



UNIL | Université de Lausanne

Unicentre

CH-1015 Lausanne

<http://serval.unil.ch>

Year : 2012

FLUID-ROCK-STRAIN FEEDBACKS IN EXTENSIONAL SHEAR ZONES

Quilichini Antoine

Quilichini Antoine, 2012, FLUID-ROCK-STRAIN FEEDBACKS IN EXTENSIONAL SHEAR ZONES

Originally published at : Thesis, University of Lausanne

Posted at the University of Lausanne Open Archive.

<http://serval.unil.ch>

Droits d'auteur

L'Université de Lausanne attire expressément l'attention des utilisateurs sur le fait que tous les documents publiés dans l'Archive SERVAL sont protégés par le droit d'auteur, conformément à la loi fédérale sur le droit d'auteur et les droits voisins (LDA). A ce titre, il est indispensable d'obtenir le consentement préalable de l'auteur et/ou de l'éditeur avant toute utilisation d'une oeuvre ou d'une partie d'une oeuvre ne relevant pas d'une utilisation à des fins personnelles au sens de la LDA (art. 19, al. 1 lettre a). A défaut, tout contrevenant s'expose aux sanctions prévues par cette loi. Nous déclinons toute responsabilité en la matière.

Copyright

The University of Lausanne expressly draws the attention of users to the fact that all documents published in the SERVAL Archive are protected by copyright in accordance with federal law on copyright and similar rights (LDA). Accordingly it is indispensable to obtain prior consent from the author and/or publisher before any use of a work or part of a work for purposes other than personal use within the meaning of LDA (art. 19, para. 1 letter a). Failure to do so will expose offenders to the sanctions laid down by this law. We accept no liability in this respect.



UNIL | Université de Lausanne

Faculté des géosciences
et de l'environnement

Institut de Minéralogie et Géochimie

FLUID-ROCK-STRAIN FEEDBACKS IN EXTENSIONAL SHEAR ZONES

Thèse de Doctorat

Présentée à la Faculté des Sciences de l'Université de Lausanne
par

Antoine Quilichini

**Géologue diplômé
Université de Montpellier II (France)**

Jury

Prof. Emmanuel Reynard, Président du Jury
Prof. Torsten Vennemann, Rapporteur
Prof. Christian Teyssier, Directeur de thèse
Prof. Lukas Baumgartner, Expert
Prof. Neil Mancktelow, Expert
Prof. Andreas Mulch, Expert

Lausanne – 2012

IMPRIMATUR

Vu le rapport présenté par le jury d'examen, composé de

Président de la séance publique :	M. le Professeur Emmanuel Reynard
Président du colloque :	M. le Professeur Emmanuel Reynard
Directeur de thèse :	M. le Professeur Christian Teyssier
Rapporteur :	M. le Professeur Torsten Vennemann
Expert interne :	M. le Professeur Lukas Baumgartner
Expert externe :	M. le Professeur Andreas Mulch
Expert externe :	M. Le Professeur Neil Mancktelow

Le Doyen de la Faculté des géosciences et de l'environnement autorise l'impression de la thèse de

Monsieur Antoine QUILICHINI

*Master Sciences et Technologies, mention Biologie, Géosciences, Agroressources, Environnement,
spécialité Terre, Eau, Environnement
Université de Montpellier II*

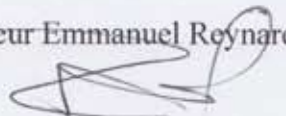
intitulée

FLUID-ROCK-STRAIN FEEDBACKS IN EXTENSIONAL SHEAR ZONES

Lausanne, le 22 mai 2012

Pour le Doyen de la Faculté des géosciences et
de l'environnement

Professeur Emmanuel Reynard



Acknowledgments:

First, I deeply thank Christian Teyssier who offered me about four years ago the opportunity to do this thesis. Although relatively quickly separated by an ocean, in the sense of the word, I will keep an unforgettable memory of the field trips in the western US and our numerous scientific discussions around a table or cheese fondues. Christian has opened for me the door to the North American continent, and has shared with me his passion for the core complexes, while leaving me a freedom of research as vast as the western US. Of course, I would like to thank Torsten Vennemann, who agreed to join and invest himself in my PhD project on the way. He has opened to me the doors of his laboratory and has always shown great availability and support when I faced scientific, methodological or administrative issues. I also thank the Swiss National Science Foundation (project 200021-117694) for funding this PhD during the four past years.

In general, I thank the jury members (Prof. Christian Teyssier, Prof. Torsten Vennemann, Prof. Andreas Mulch, Prof. Lukas Baumgartner, Prof. Neil Mancktelow and Prof. Emmanuel Reynard) for taking part in the correction and judgment of the manuscript.

This thesis is based on a multidisciplinary approach, and allowed me to interact and collaborate with many people in the fields of geosciences. Benita Putlitz and Jorge Spangenberg helped me in the Stable Isotope Laboratory, teaching me the analytical techniques and accompanying me through the years while I completed my isotopic dataset, the cornerstone of this work. Thierry Adatte and Jean-Claude Lavanchy open the doors of their laboratories, they have guided me and offered me their time so I get the chemical analyzes presented in this work. I also thank Martin Robyr for welcoming me to the University of Bern, and allowed me to perform microprobe analyses while that of Lausanne could not be used. Thanks to Matt Heizler who kindly performed the $^{40}\text{Ar}/^{39}\text{Ar}$ dating on several muscovite samples at the New Mexico Tech. I also thank William Nachlas, friend and collaborator, who accompanied me during the first two seasons of fieldwork in the western U.S., and has produced microprobe analyzes of the Kettle DSZ during his Bachelor. William has demonstrated great patience while facing my rough French accent and poor English during the first fieldwork. These two seasons of fieldwork next to him helped me to make a step forward in terms of English, and also allowed me to discover the American culture. Finally, Luc Siebenaller was able to share with me his recent PhD experience and guided me

in my doctoral work for nearly two years. Our scientific collaboration in the laboratories of the University of Lausanne and during fieldwork has not only resulted in several ongoing publications, but especially enhanced a friendship that I am sure, will not suffer the effects of time.

The next part is addressed to my family, friends and relatives, and therefore is in French.

Tout d'abord, je remercie de tout mon cœur mes parents, Isabelle et Jean-Claude, et ma sœur, Anouk, pour leur support et leur amour inconditionnel qui au fil des ans m'ont construit, portés et poussés à accomplir mes objectifs. La passion des voyages, la soif de connaissance et l'ouverture d'esprit de mes parents ont joués un rôle prépondérant dans mes choix personnels et professionnels. Aussi loin que je puisse me souvenir, mes grands-parents Jean et Lydie furent les premiers à me diriger vers la géologie, de part la recherche de minéraux et fossiles à proximité de leur maison, et en enrichissant ma collection quand l'occasion se présentait. Cette passion pour la géologie fut décuplée lorsque j'ai commencé l'université, où j'ai eu la chance de rencontrer et de me lier d'amitié avec Julie Verbeke et Jean-Christophe Wrobel-Daveau. Nous avons fait nos premiers pas dans le monde des Géosciences ensemble, et près de dix ans plus tard nous voici tous trois docteur. Votre amitié compte énormément à mes yeux, et je suis convaincu que rien ne pourrait altérer ce qui nous lie ! Je ne saurais oublier la Champ & Rado family. Plus que des amis, vous êtes une deuxième famille, et notre cheminement commun depuis la plus tendre enfance jusqu'à aujourd'hui représente pour moi de profondes racines et les fondations de l'homme que je suis devenu.

Depuis mon arrivée en Suisse, j'ai eu l'opportunité de rencontrer une foule de personnes plus chaleureuses et intéressantes les unes que les autres. Je pense en particulier à la profonde amitié que j'ai pour Sylvia Mettasch et Luc Siebenaller, et qui nous a conduit à fonder le très select club des Glory Three ! Je garderai un souvenir ému de toutes ces soirées à frôler l'autisme en marchandant diverses ressources autour de ce merveilleux jeu qu'est « Les Colons de Catans ». Sans parler de nos débats philosophiques, extrêmement enrichissant de part leur diversité, et nos différences de point de vue ; où encore de nos virées nocturnes mémorables dans Lausanne. Je pense également à Brahim Bomou et Romain Bauer ; l'escalade, la passion pour les films gores et les blagues douteuses furent les fondations de notre amitié. Nos sessions d'escalades m'ont permis à maintes reprises de relâcher la pression et ainsi d'éviter la folie lors de la fin de rédaction.

Je ne saurai faire une liste exhaustive de toutes les autres personnes chères à mon cœur à Lausanne, en France ou encore aux États-Unis qui ont compté pour moi, m'ont apporté leur soutien, leur amitié et bien plus encore au cours des quatre dernières années ; cependant je suis persuadé qu'ils/elles se reconnaîtront en lisant ces mots et accepteront mes plus sincères remerciements.

Abstract: Fluid-rock-strain feedbacks in extensional shear zones

The presence of meteoric fluids synchronous with the activity of extensional detachment zones (Famin, 2004; Mulch et al., 2007; Gébelin et al., 2011) implies that extensional systems involve fluid convection at a crustal scale, which results in high geothermal gradients within active detachment zones (Morrison and Anderson, 1998, Gottardi et al., 2011). In addition, the metamorphic reactions related to fluid infiltration in extensional shear zones can influence the rheology of the system (White and Knipe, 1978) and ultimately how strain localizes in the crust. In this thesis, two shear zones that were permeated by meteoric fluids are studied, one quartzite-dominated, and the other of granitic composition; the relations between strain, fluid, and evolving rock composition are addressed using structural, microstructural, and chemical/isotopic measurements.

The study of the Columbia River detachment that bounds the Kettle core complex (Washington, USA) demonstrates that the mylonitic fabrics in the 100 m thick quartzite-dominated detachment footwall developed within one million years. The main shearing stage occurred at $365 \pm 30^\circ\text{C}$ when oxygen isotopes of quartz and muscovite equilibrated owing to coeval deformation and dynamic recrystallization of these minerals. The detachment shear zone records a decrease in temperature, and dislocation creep during detachment shearing gave way to dissolution-precipitation and fracturing in the later stages of detachment activity. Fluid flow switched from pervasive to channelized, leading to isotopic disequilibrium between different minerals.

The Bitterroot shear zone detachment (Montana, USA) developed a 600 m thick mylonite zone, with well-developed transitions from protomylonite to ultramylonite. The localization of deformation relates directly to the intensity of feldspar hydration, a major rock-softening metamorphic reaction. Bulk-rock analyses of the mylonitic series indicate lateral mass transfer in the mylonite (no volume change), and significant volume loss in ultramylonite. The hydrogen isotope composition of phyllosilicates shows (1) the presence of an initial magmatic/metamorphic source characterized by the granodiorite in which a magmatic, and gneissic (protomylonite) foliation developed, and (2) a meteoric source that buffers the values of phyllosilicates in mylonite, ultramylonite, cataclasite, and deformed and undeformed quartz veins. The mineral oxygen isotope compositions were buffered by the host-rock compositions until chloritization of biotite started; the chlorite oxygen isotope values are negative (-10 per mil). Isotope thermometry indicates a temperature of isotopic equilibrium of the granodiorite between $600\text{-}500^\circ\text{C}$, between $500\text{-}300^\circ\text{C}$ in the mylonite, and between 300 and 200°C for brittle fabrics (cataclasite and quartz veins).

Results from this work suggest a general model for fluid-rock-strain feedbacks in detachment systems that are permeated by meteoric fluids. Phyllosilicates have preserved in their hydrogen isotope values evidence for the interaction between rock and meteoric fluids during mylonite development. Fluid flow generates mass transfer along the tectonic anisotropy, and mylonites do not undergo significant volume change, except locally in ultramylonite zones. Hydration of detachment shear zones attends mechanical grain size reduction and enhances strain softening and localization. Self-exhuming detachment shear zones evolve rapidly (a few million years) through the transition from ductile to brittle, which is partly controlled by the thermal effect of circulating surface fluids. Detachment systems are zones in the crust where strain and fluid flow are coupled; these systems evolve rapidly toward strain localization and therefore efficient exhumation.

Keywords : Extension, detachment, deformation mechanisms, metamorphic reaction, stable isotope, isotope equilibrium temperature, fluid flow, fluid-rock interaction.

Résumé : Interactions fluides-roches-déformation dans les zones de cisaillements extensives

La présence de fluide météorique synchrone à l'activité du détachement (Farmin, 2003 ; Mulch et al., 2007 ; Gébelin et al., 2011), implique que les zones de cisaillement sont des systèmes ouverts avec des cellules de convections à l'échelle crustale et un intense gradient géothermique au sein du détachement (Morrison et Anderson, 1998, Gottardi et al., 2011). De plus, les réactions métamorphiques liées à des infiltrations fluides dans les zones de cisaillement extensionnel peuvent influencer les paramètres rhéologiques du système (White and Knipe, 1978), et impliquer la localisation de la déformation dans la croûte. Dans ce manuscrit, deux zones de cisaillement infiltrées par des fluides météoriques sont étudiées, l'une étant largement quartzitique, et l'autre de nature granitique ; les relations entre déformation, fluides, et roches s'appuient sur des approches structurales, microstructurales, chimiques et isotopiques.

L'étude du détachement du Columbia river (WA, USA) met en évidence que la déformation mylonitique se développe en un million d'années. La phase de cisaillement principal s'effectue à $365 \pm 30^\circ\text{C}$ d'après les compositions isotopiques en oxygène du quartz et de la muscovite. Ces minéraux atteignent l'équilibre isotopique lors de leur recristallisation dynamique contemporaine à la déformation. La zone de cisaillement enregistre une baisse de température, remplaçant le mécanisme de glissement par dislocation par celui de dissolution-précipitation dans les derniers stades de l'activité du détachement. La dynamique de circulation fluide bascule d'une circulation pervasive à chenalisée, ce qui engendre localement la rupture des équilibres d'échange isotopiques.

La zone de cisaillement de Bitterroot (MT, USA) présente une zone mylonitique de 600m d'épaisseur, progressant des protomylonites aux ultramylonites. L'intensité de la localisation de la déformation se reflète directement sur l'hydratation des feldspaths, réaction métamorphique majeure dite de « rock softening ». Une étude sur roche totale indique des transferts de masse latéraux au sein des mylonites, et d'importantes pertes de volume dans les ultramylonites. La composition isotopique en hydrogène des phyllosilicates met en évidence la présence (1) d'une source magmatique/métamorphique originelle, caractérisée par les granodiorites ayant conservé leur foliation magmatique, jusqu'aux protomylonites, et (2) une source météorique qui tamponne les valeurs des phyllosilicates des fabriques mylonitiques jusqu'aux veines de quartz non-déformées. Les compositions isotopiques en oxygène des minéraux illustrent le tamponnement de la composition du fluide météorique par l'encaissant. Ce phénomène cesse lors du processus de chloritisation de la biotite, puisque les valeurs des chlorites sont extrêmement négatives (-10 per mil). La thermométrie isotopique indique une température d'équilibre isotopique de la granodiorite entre $600\text{-}500^\circ\text{C}$, entre $500\text{-}300^\circ\text{C}$ dans les mylonites, et entre 300 et 200°C dans les fabriques cassantes (cataclasites et veines de quartz).

Basé sur les résultats issus de ce travail, nous proposons un modèle général d'interactions fluide-roches-déformation dans les zones de détachements infiltrées par des fluides météoriques. Les zones de détachements évoluent rapidement (en quelques millions d'années) au travers de la transition fragile-ductile ; celle-ci étant partiellement contrôlée par l'effet thermique des circulations de fluide météoriques. Les systèmes de détachements sont des lieux où la déformation et les circulations fluides sont couplées ; évoluant rapidement vers une localisation de la déformation, et de ce fait, une exhumation efficace.

Mots clés : Extension, détachement, mécanismes de déformations, réactions métamorphiques, isotopes stables, thermométrie isotopique, circulation fluides, interactions fluide-roche.

TABLE OF CONTENTS

Acknowledgments	5
Abstract.....	9
Résumé	10
Chapter I : Introduction	25
1. Genesis of Metamorphic Core Complexes in the North American Cordillera:	25
2. Extensional shear zones / detachments:.....	28
3. Characterization of fluid source(s) and fluid flow in extensional SZ.....	32
3.1. Sources of fluids on Earth:	32
3.2. Stable isotope characterization of fluid sources:	33
3.2.1. Stable isotope thermometry:.....	34
3.2.2. Meteoric water:.....	34
3.2.3. Metamorphic and magmatic water:	34
3.2.4. Oxygen isotope composition of rocks:	35
3.3. Fluids in extensional shear zones:	36
3.3.1. Evidence of fluid flow in extensional shear zones:	36
3.3.2. Permeability of a shear zone:.....	38
3.3.3. Classification of fluid flow:.....	40
4. Main goals and approaches of the thesis	41
Chapter II : Methodology	45
1. Sampling strategy and microstructural study:	46
1.1. Paleostress analysis with T-Tecto 3.0:	46
1.2. Microstructural under optical microscope:.....	46
2. Preparation of samples:	46
2.1. Hydraulic press:.....	46
2.1.1. Preparation before crushing:.....	46
2.1.2. Crushing rocks:.....	47
2.2. Grinding:.....	47
3. Mineral separation:	48
4. Rock chemistry, mineral assemblages and single grain analyses:.....	49
4.1. X-ray fluorescence:.....	49
4.2. X-Ray Diffraction:.....	50
4.3. Microprobe:	50
5. Stable isotopes analyses:	50
5.1. Fluid inclusions extraction:	51
5.1.1. Extraction of CO ₂ :	51
5.1.2. Elimination of SO ₂ :	52
5.1.3. Extraction of H ₂ O:	52
5.2. Oxygen isotope analyses:	52
5.3. Hydrogen isotope analyses:.....	53
5.4. Fluid inclusions analyses:.....	53

Chapter III : Microstructural, paleostress and paleostrain evolution in an extensional shear zone: Insight from the Bitterroot shear zone (MT, USA).55

1. Introduction:	55
2. Geological setting:	57
3. Ductile and brittle fabrics of the Bitterroot shear zone:	64
3.1. Ductile fabrics:	65
3.1.1. The mylonitic series in the BSZ:	65
3.1.2. Protomylonite:	69
3.1.3. Mylonite:	70
3.1.4. Ultramylonite:.....	73
3.1.5. V1 quartz veins:.....	74
3.1.6. Cataclasites:	75
3.2. Brittle fabrics:	78
3.2.1. The brittle series in the Sweathouse section:.....	78
3.2.2. Chlorite en-echelon tension gashes, chlorite veins and epidote veins:.....	81
3.2.3. V2a and V2b quartz veins:	84
3.2.4. Breccia:	86
3.2.5. Normal faults:	87
4. Paleostrain analysis with T-Tecto 3.0:	90
4.1. Fractures with slip indicators:.....	90
4.2. Veins with no slip evidence:.....	93
5. Discussion:.....	94
5.1. Relation between ductile and brittle features:	94
5.2. Spatial and temporal evolution of the BSZ:	95
5.3. Evidence of fluid flow:	99
5.4. Rock-softening processes:	100
6. Conclusion:	101

Chapter IV : Metamorphic reactions, volume change and mass transfer in the Bitterroot shear zone: bulk-rock and single-grain analyses 103

Introduction:	103
1. Sampling strategy:	104
2. Mineral assemblages characterizing the mylonitic series and cataclasite of the BSZ....	106
3. Major and trace element variations in the mylonitic series and cataclasite of the BSZ .	107
4. Mass-balance analysis related to the different fabrics of the BSZ:	112
5. Chemistry of phyllosilicates:	118
5.1. Single grain analyses:	118
5.2. Chemiographic representation of phyllosilicates:	120
5.3. Muscovite-phengite Tschermak substitution:.....	122
5.4. Octahedral and tetrahedral substitutions:	123
6. Discussion:.....	126
6.1. Temperature of biotite chloritization inferred from biotite and chlorite compositions.	126
6.1.1. Temperature inferred from biotite compositions:.....	126
6.1.2. Temperature inferred from chlorite compositions:.....	128
6.2. Fluid-rock interaction and metamorphic reactions:.....	131
7. Conclusion:	134

Chapter V : Infiltration of meteoric fluids through an extensional shear zone from ductile to brittle deformation (Bitterroot detachment, MT, USA)	135
Introduction:	135
1. Sampling strategy:	137
2. $\delta^{18}\text{O}$ values of quartz and hydrous minerals:.....	139
3. δD values of hydrous minerals:	141
4. δD , $\delta^{13}\text{C}$, and $\delta^{18}\text{O}$ values of fluid inclusions in quartz:	142
4.1. δD values of fluid inclusions and amount of water in quartz:.....	142
4.2. $\delta^{13}\text{C}$ and $\delta^{18}\text{O}$ values of fluid inclusions in quartz:	144
5. Oxygen isotope thermometry:	145
6. Discussion:.....	149
6.1. Evolution from a closed system magmatic fluid circulation towards meteoric fluid infiltration:	149
6.2. Fluid sources from ductile towards brittle deformation:	151
6.3. Biotite and chlorite isotopic exchange behavior:	152
6.4. Temperature inferred by stable isotope compositions:.....	156
6.5. Deformation and evolution of fluid flow during exhumation	158
7. Conclusion :	162
 Chapitre VI : Infiltration of meteoric fluids in ductile crust beneath the Kettle extensional detachment (WA, USA).....	165
Abstract.....	165
Introduction	166
1. Geologic setting.....	169
2. Quartzite mylonite characteristics	172
2.1. Microstructure	172
2.1.1. UQM.....	172
2.1.2. LQM	175
2.2. Quartz crystallographic fabric	177
2.3. Fluid inclusion distribution.....	177
3. Chemistry and $^{40}\text{Ar}/^{39}\text{Ar}$ ages of mica fish:.....	177
3.1. Microprobe analysis and elemental maps.....	177
3.2. $^{40}\text{Ar}/^{39}\text{Ar}$ dating of muscovite	179
4. Stable isotope analysis.....	181
4.1. δD values of muscovite:	181
4.2. δD values of fluid inclusions in quartz ($\delta\text{D FI}_{\text{Qz}}$):.....	182
4.3. $\delta^{18}\text{O}$ values of quartz and muscovite:	183
4.4. Oxygen isotope thermometry:	184
5. Discussion.....	186
5.1. Fluid source and evolution of fluid flow	186
5.2. Chemical and isotopic evolution of quartz and muscovite during exhumation	189
5.3. Argon ages and oxygen isotope thermometry	191
5.4. Exhumation of UQM and LQM along the Kettle DSZ in space and time.	194
6. Conclusion:	194
 Chapter VII : General conclusions:.....	197
 References:	202

Appendix Chapter III.....	227
Appendix Chapter IV.....	241
Appendix Chapter V.....	329
Appendix Chapter VI.....	335

TABLE OF FIGURES

Chapter I :

Figure I-1: Geological sketch map of the North American Cordillera, from northern Mexico to southern Canada. This map shows the principal tectonics structures associated to the Cretaceous orogeny of the Cordillera and its Tertiary collapse (Hildebrand, 2009).....	26
Figure I-2 : Crustal thickness of the North American Cordillera (Coney et al., 1984). A. Paleo-crustal thickness estimated for the Early Tertiary, and B. Current crustal thickness.	28
Figure I-3 : Spatial propagation of deformation in a shear zone from ductile fabrics toward brittle fabrics (adapted from Lister and Davis, 1989).....	29
Figure I-4 : Schematic block diagram of crustal extension and localization of deformation in an evolving detachment (adapted from Lister and Davis, 1989). Orange, ductile fabrics ; Green, brittle fabrics ; Red line : detachment fault.	30
Figure I-5: Synthetic block diagram showing the different structures associated with extensional shear zones (adapted from Malavieille, 1993): 1. foliated rocks with extensional shear bands; 2. small scale normal shear zones; 3. Synkinematic granite bodies or sill, mylonitized and boudinaged; 4, stretching and mineral lineations; 5, extensional crenulation cleavage; 6, boudinage at different scales; 7, shear criteria; 8, sheath folds in zones of high shear strain; 9, folds with axes parallel to stretching lineations; 10, tight folds with subhorizontal axial planes; 11, slicken-sides on brittle detachment surfaces; 12, cataclastic breccia; 13, fractured pebbles, stretched and striated; 14, low-angle décollements in weak layer; 15, high-angle brittle faults; 16, stretched layers; 17, synsedimentary hydroplastic faults; 18, gravity folding. Colors illustrate the hanging wall (yellow) and footwall (pink), and the detachment (blue and green).	31
Figure I-6: Graphic representing the range of oxygen and hydrogen isotope compositions, which define the different fluid sources (adapted from Sheppard, 1986).	35
Figure I-7: Oxygen isotope composition according to geological contexts (Field and Fifarek, 1985).	36
Figure I-8: Pore connectivity evolution according to the development shear strain, for constant pore fluid pressure, strain rate and temperature. Boxes show strain-dependent change in grain-scale fluid distribution (Bauer et al., 2000).	39
Figure I-9 : Granular fluid pump model associated to viscous grain boundary sliding in mylonite (Fusseis et al., 2009). The motion vectors (black) illustrate the differential motion of grains. The different pressures in opening and closing pores are colour coded; b, c, Mechanisms of cavity formation on grain boundaries and triple junctions (locations respectively marked 'b' and 'c' in a): cavitation at triple junctions (b); cavitation at dislocation tangles near grain boundaries (c).....	40
Figure I-10 : Classification of different type of fluid flow during regional metamorphism with respect to permeability, deformation and heat flux (Oliver, 1996).....	41

Chapter III :

Figure III-1: Classification of fault rocks by Sibson (1977), and updated by Scholtz (1990).	56
Figure III-2: Synoptic model of a shear zone (after Scholtz, 1988).....	57
Figure III-3: Simplified geological map of the Bitterroot valley (adapted from Toth, 1983).	58
Figure III-4: Schematic W-E cross-section of the Bear Creek pluton and Sapphire pluton (A-A' transect in Figure III-3 corresponds to km 40 to 100 on this cross-section), the BSZ defines the contact between these two plutons (adapted from Foster et al., 2001, 2007).	59
Figure III-5: Two micas granodiorite of the Bear Creek pluton.....	59
Figure III-6: Schematic block diagram of the Lost Horse Canyon section.....	61
Figure III-7: Composite photograph and corresponding schematic view of the characteristic alternation of mylonite, ultramylonite, metabasite and felsic layers in the BSZ.	62
Figure III-8: Stereonet showing the mylonite and ultramylonite foliation data.	63
Figure III-9: Schematic drawing of the Sweathouse quarry, with sample numbers.....	64
Figure III-10 : A. Photomicrograph of a protolith thin section, cut vertical and parallel to the magmatic lineation; B. Phyllosilicates are highlighted (muscovite, biotite, chlorite); top right corner corresponds to east.	65
Figure III-11 : Scan of thin sections, crossed polars: A. Protolith (BT09-80) and B. Protomylonite (BT10-52), top right corner corresponds to top and east.....	67
Figure III-12: Scan of thin sections, crossed polars: C. mylonite (BT08-80) and D. mylonite to ultramylonite (BT08-48), top right corner corresponds to top and east.	68
Figure III-13: Scan of thin section, crossed polars: E. ultramylonite (BT08-34), top right corner corresponds to top and east.	69
Figure III-14: Optical micrographs of a protomylonite thin section (BT10-52), perpendicular to the foliation and parallel to the stretching lineation, sense of shear is top-to-the-east (top right corner).	70
Figure III-15: Mylonite (Myl.) and Ultramylonite (Umyl.) spatial organization in the field. For A. and B., the right top corner represents east, the plane of the photo is perpendicular to the foliation and parallel to the stretching lineation.	71
Figure III-16 : Photomicrographs of a mylonite thin section (BT08-80), perpendicular to the foliation and parallel to the stretching lineation, sense of shear is top-to-the-east (to right).....	72
Figure III-17: Photomicrographs of mylonite (A and B, BT08-45) and ultramylonite (C and D, BT08-34) thin sections, perpendicular to foliation and parallel to stretching lineation, sense of shear is top-to-the-east (top right).	73
Figure III-18: V1 quartz veins in mylonite (top picture) and in metabasite (bottom picture). Rotation and boudinage of these quartz veins is consistent with top-to-the-east shearing.	74
Figure III-19 : Photomicrographs of V1 quartz veins viewed perpendicular to the foliation and parallel to the stretching lineation, top right corner is east. A and A' have quartz ribbons in the upper part, the lower part corresponds to the contact with the granodiorite mylonite showing breakdown of feldspar porphyroclast (Or) with feldspar-quartz mixture tails (BT10-09). B and B', sheared quartz grains, and late chlorite + sericite planes (BT10-30).....	75

Figure III-20: Cataclasite bands (mm to cm scale) in mylonite, either horizontal (ultracataclasite, left), or vertical (protocataclasite, right).....	76
Figure III-21 : Photomicrographs of cataclasite, perpendicular to the foliation and parallel to the stretching lineation, top right corner corresponds to east. A and A' from a vertical Ep-rich protocataclasite (BT10-33), with large clasts of mylonite with sharp edges. B and B' show horizontal cataclasite, defined by at least 50 % of Ep-Fe-oxide matrix, and containing both rounded and angular clasts (BT10-08).	77
Figure III-22 : Photomicrographs of thin section, perpendicular to the foliation and parallel to the stretching lineation, top right corner corresponds to east. A and A' has a relative chronology of V1 quartz vein, chlorite vein, and cataclasite (BT10-28).	77
Figure III-23: Chlorite en-echelon tension gashes and conjugated epidote veins crosscut the mylonite.....	78
Figure III-24: Different generations of quartz veins. A and A', V1 quartz vein. B and B', V2a quartz veins. C and C', V2b quartz vein. Dark green symbols correspond to chlorite en-echelon tension gashes and chlorite veins, light green lines correspond to epidote veins.	79
Figure III-25: Quartz geode (center) in a V2a quartz vein.....	80
Figure III-26: Breccia overlying the granodiorite mylonite. The fault zone corresponds to the brittle detachment and displays anastomosed faults.....	81
Figure III-27: Stereonets of striated chlorite veins and chlorite tension gashes (left) and striated epidote veins (right).....	82
Figure III-28: Photomicrographs of chlorite and epidote veins perpendicular to the foliation and parallel to the stretching lineation, top right corner corresponds to east. A and A' present a normal displacement of K-feldspar along a chlorite vein; a chlorite vein crosscuts a dynamically recrystallized shear band (BT10-28). B and B' shows an epidote vein crosscutting a K-feldspar, the fluid related to the epidote veins was injected also laterally in the chlorite sigmoid (BT08-21). C and C' show an epidote vein cross-cutting a V2a quartz vein. The epidote vein is reactivated and filled with a V2b quartz vein (BT10-14).	83
Figure III-29: Stereonets of quartz veins (V2a,V2b) with lineated slickensides (left), and without lineated slickensides (right).	84
Figure III-30: Optical micrographs of quartz veins in thin section, perpendicular to the foliation and parallel to the stretching lineation, top right corner corresponds to East. A and A' correspond to a V2a quartz vein and present subhedral quartz cross-cut by an epidote vein (bottom), fluid inclusions are aligned along plans (FIPs) and are coherent with top-to-the-east sense of shear (BT10-13). B and B' show the subhedral mineral assemblage of V2b (BT10-12). C and C', correspond to a V2b quartz vein and present subhedral epidote and quartz grains, randomly distributed (BT10-31).....	85
Figure III-31: A and A', relative chronology between epidote veins (walls of V2a quartz vein), V2a, and V2b quartz veins (BT10-14).....	86
Figure III-32 : Photomicrograph of breccia thin section, perpendicular to the foliation and parallel to the stretching lineation, top right corner corresponds to east (BT10-33).....	86
Figure III-33: Stereonet of the normal fault network in the Sweathouse section.	87
Figure III-34: A. Conjugated normal faults in the Sweathouse quarry, merging into a single normal fault. B. Zoom in the normal fault zone: walls (~10cm) are characterized by silicified granodiorite (blue), the fault zone developed a bleached	

granodiorite mylonite (yellow). Note the presence of a gouge filled with clay (white) on the right border and the presence of silicified granodiorite on both sides.	88
Figure III-35: Scan of a bleached granodiorite thin section (BT10-46), top right corner corresponds to east. The irregular line delineates a zone of undeformed quartz around angular feldspar clasts.	89
Figure III-36: Paleostrain analysis of quartz veins (V2a,V2b) for the Sweathouse section. A corresponds to the paleostress field using the MSM method (red, compression; blue, extension). B provides the directions and relative magnitudes of strain axes calculated from strain tensors.	91
Figure III-37: Paleostrain field using the MSM method (upper part), direction of strain axes and relative magnitudes of strain principal axes according to fault-slip inversion (lower part) for brittle features of the Sweathouse section. A corresponds to the chlorite veins and chlorite tension gashes planes. B corresponds to epidote veins, and C corresponds to conjugated normal faults.	92
Figure III-38: Paleostress field and direction of kinematic axes for fractures with no slip evidence (red, compression; blue, extension). A presents measurement of chlorite veins and epidote veins, B show measurement of quartz veins.	93
Figure III-39: A. Graphic determination of a plane containing sigma 1 and sigma 3 related to the mylonitic foliation. B. Set of quartz veins with no slip.	95
Figure III-40: Spatial evolution of the overprinted fabrics, according to the exhumation of mylonitic rocks along the BSZ. Top, schematic cross-section of the BSZ. 1, Magmatic foliation. 2, Protomylonite. 3, Mylonite, mica fish (grey) and V1 Qz veins (white). 4, Ultramylonite and V1 Qz veins. 5, Cataclasite parallel or oblique to the mylonitic foliation. 6 Chl, Ep veins and V2a, b Qz veins (see Figure 27 for more details). 7a, brecciation. 7b, Low angle "cold fault" plane.	97
Figure III-41: Schematic appearance of the different brittle features corresponding to T=6, Figure 26. Grey sigmoid: chlorite tension gashes; green: epidote plans; V1, V2a and V2b: different generation of quartz veins.	98
Figure III-42: Schematic view of the BSZ that combines the Lost Horse and the Sweat House sections, with the different fabrics (from ductile to brittle) overprinting the two micas granodiorite (color code according to Figure III-40).	101

Chapter IV :

Figure IV-1: Location of samples on the block diagram corresponding to the Lost Horse Canyon section. Samples are listed as a function of the type of analyses, and rock type. Myl. : mylonite ; Umyl. : ultramylonite ; Cata. : cataclasite.	105
Figure IV-2: Location of samples on the schematic view of the Sweathouse section. Samples are presented in relation to rock types. Blue: mylonite ; Yellow: bleached granodiorite ; Red: cataclasite.	106
Figure IV-3: Proportion of major minerals (%) defining the mineral assemblages of fabrics affecting the granodiorite from the BSZ, determined by X-ray diffraction.	107
Figure IV-4: Variable factor map, according to the PCA performed on major elements (Top), and on trace elements (Bottom). Dim 1 and Dim 2 correspond to the correlation percentage along the x and y-axis, respectively.	109

Figure IV-5: Harker diagram showing the correlation between SiO ₂ and other major elements. White zone circles the protolith values, light grey zones the mylonite and dark grey zones the ultramylonites. Yellow dots: bleached granodiorite.....	110
Figure IV-6: Spectra of trace-element content in mylonite (orange), ultramylonite (blue) and bleached granodiorite (red). The protolith spectra of trace-element content is in grey, which can be darker when superimposed with the other spectra.....	111
Figure IV-7: Isocon diagrams for the alteration of the granodiorite with respect to the different fabrics of the BSZ. A. Three samples of the granodiorite defining the average protolith composition. B. Mylonite. C. Ultramylonites. D. Bleached granodiorite.....	111
Figure IV-8: Volume change in the different fabrics of the BSZ. Samples from the protolith do not show volume change. Samples from the mylonite highlight three tendencies: the group A is characterized by a volume-loss type, the group B by a volume-conservative type, and the group C is defined by a volume-gain type. Ultramylonite and bleached granodiorite correspond to a volume-loss type. See Appendix IV, Table IV-3,4 and 5 for details.	115
Figure IV-9: Mass changes of the major elements in the different deformation fabrics of the BSZ. A. Mylonite; B. Ultramylonite; and C. Bleached granodiorite.....	117
Figure IV-10: Single grain analysis transect in a muscovite fish (BT08-48-M18), and in a tabular biotite (BT08-63-B01), representative of the mylonite from the BSZ. The transects of the muscovite and biotite do not show significant major element variation.	119
Figure IV-11: Single grain analyses along a transect in chlorite (BT08-63-C03), and in chloritized biotite (BT08-31-C03), representative of the mylonite from the BSZ. The transect of the chlorite shows no major element variations, whereas the chloritized biotite shows major element variations that are distributed between the biotite pole and the chlorite pole.	120
Figure IV-12: Chemiographic representation of Bt, Chl, and Ms according to the major deformation fabrics characterizing the BSZ. $MR^3:2*Ca+Na+K; 3R^2:(Mg+Fe+Mn)/3; 2R^3M:(Al_{tot}-MR3)/2$. Muscovite is in grey, biotite in black, chlorite in white. A. Protolith, B. Mylonite, C. Ultramylonite, D. Cataclasite.	122
Figure IV-13: Tschermak substitution with total aluminum versus (Si+Mg+Fe) content on the basis of electron microprobe analysis of single grain transects. White micas in protolith, mylonite and ultramylonite define a muscovitic pole, only a few analyses show a trend towards a phengitic composition.....	123
Figure IV-14: Octahedral aluminium content versus Mg / (Mg+Fe) ratio of phyllosilicates from the different fabrics of the BSZ. Phyllosilicates in the protolith define narrow ranges, whereas values are more scattered in the mylonite an ultramylonite. Note that the Mg / (Mg+Fe) ratio tends to increase with strain.....	124
Figure IV-15: Ti content versus (Mg+Fe) of phyllosilicates from the different fabrics of the BSZ. Phyllosilicates in the protolith define narrow ranges, whereas values are more scattered in the mylonite an ultramylonite. Note that in biotite, the Ti content (Mg+Fe) ratio tends to decrease with respect to the strain, and define a trend toward the chlorite pole.....	125
Figure IV-16: Biotite formation temperature according to the Ti-in-biotite geothermometry of Henry et al. (2005). Number of ions are calculated on the basis of 22 oxygens. The Ti versus Mg / (Mg+Fe) plot of biotite shows that the protolith defines a narrow range, whereas mylonite is scattered about the protolith. Biotite in	

ultramylonite defines a second pole with a higher Mg / (Mg+Fe) ratio and a lower Ti content, which corresponds to lower temperature.	127
Figure IV-17: Computed temperatures of biotite and chlorite versus distance below the hanging wall. Temperatures are calculated according to Henry et al. (2005) and Vidal et al. (2005) geothermometers, respectively. Biotite shows a narrow range of temperature (650 ±50 °C), whereas chlorite ranges from 485 °C down to 270 ±20 °C.	130
Figure IV-18: Volume changes of the different fabrics with respect to the distance below the hanging wall.....	133

Chapter V :

Figure V-1: Location of mylonite samples and two Qz veins (BT10-42 and BT10-51) in the block diagram for the Lost Horse Canyon section.	138
Figure V-2: Location of sample on the schematic view of the Sweathouse section. Samples are presented as a function of the rock types. Blue: mylonite ; Red: Qz veins.	139
Figure V-3: Oxygen isotope compositions of the samples from Lost Horse and Sweathouse sections. Samples are presented in a one-dimensional diagram, according to rock type. Error bars correspond to the standard deviation between two analyses.	140
Figure V-4: Hydrogen isotope composition of the samples from the Lost Horse and the Sweathouse sections. δD values of samples are presented according to rock type. Error bars correspond to the standard deviation between two analyses.....	142
Figure V-5: Calculated amount of water (mg) per gram of quartz. Error bars correspond to standard deviations.	143
Figure V-6: Carbon isotope composition of fluid inclusions in quartz for samples from the Lost Horse and the Sweathouse sections. Values for samples are presented according to rock type. Error bars correspond to the standard deviation between two analyses.	144
Figure V-7: Oxygen isotope composition of Qz-Ms, and Qz-Bt pairs from the undeformed granodiorite. Isotherm are based on the Qz-Ms thermometer calibrated by Chacko et al. (1996), and the Qz-Bt thermometer calibrated by Bottinga and Javoy (1975).	146
Figure V-8: Oxygen isotope composition of Qz-Ms pairs, Qz-Bt pairs and Qz-Chl pairs from the mylonite. Isothermal lines are based on the Qz-Ms thermometer calibrated by Chacko et al. (1996), the Qz-Bt thermometer developed by Bottinga and Javoy (1975) and the Qz-Chl thermometer developed by Zheng (1993b).....	147
Figure V-9: Oxygen isotope composition of Qz-Ms pairs, Qz-Chl pairs and Qz-Ep pair from the Qz veins. Black square corresponds to the V1 quartz vein and the white squares to V2a, b quartz veins. Isothermal lines are based on the Qz-Ms thermometer calibrated by Chacko et al. (1996), the Qz-Chl and the Qz-Ep thermometers are after Zheng (1993b).	148
Figure V-10: Hydrogen isotope composition of the fluid inclusions in quartz with regard to the water content per gram of quartz. Black circles correspond to the mylonite, grey square to the V1 quartz veins and white squares to the V2a, b quartz veins. Error bars correspond to the standard deviations.....	150

Figure V-11: Hydrogen and oxygen isotope compositions of minerals for each rock types. The quartz values are plotted as the oxygen isotope compositions of the host grains and the hydrogen isotope composition of their included fluids. The different shapes are surrounding symbols from the same rock type.	152
Figure V-12: Oxygen isotope composition of Chl and Bt of samples from Lost Horse and Sweathouse. Black circles correspond to undeformed granodiorite and grey circles correspond to the mylonite.	154
Figure V-13: Hydrogen isotope composition of Chl and Bt pairs of samples from Lost Horse and Sweathouse. Black circles correspond to undeformed granodiorite and grey circles correspond to mylonite.	154
Figure V-14: Hydrogen isotope compositions of the Bt and Chl pairs of samples from Lost Horse and Sweathouse, according to their water content (weight percent) as measured as part of the extraction procedure of H ₂ for isotopic measurements. Black circles correspond to biotite and grey circles correspond to chlorite.....	155
Figure V-15: Schematic representation of the temperature range characterizing each rock type. Temperatures correspond to the apparent isotopic exchange equilibrium temperature for different mineral pairs.	157
Figure V-16: Hydrogen isotope compositions of Qz, Bt, Ms, Chl, Ep and fluid inclusions from the different fabrics, arranged according to the distance from the hanging wall. Temperature range given on the right corresponds to the temperatures of the fabric formation as estimated from the different isotopic thermometers of the fabric-forming minerals; they are thus not related to the depth or distance given on the left. The theoretical hydrogen isotope compositions of the fluid in equilibrium with the different hydrous minerals (δD_{wt}) are calculated based on temperatures for the Qz-Ms of the protolith and the Qz-Ep temperatures of the mylonite and the Qz veins (Appendix V, Table V-4).	159
Figure V-17: Oxygen isotope compositions of Qz, Bt, Ms, Chl, and Ep from the different rocks, arranged according to the distance from the hanging wall. Temperature range given on the right corresponds to the temperatures of the fabric formation as estimated from the different isotopic thermometers of the fabric-forming minerals; they are thus not related to the depth or distance given on the left. The oxygen isotope compositions of the fluid in equilibrium with the different fabric-forming minerals ($\delta^{18}O_{wt}$) are calculated based on temperatures of the Qz-Ms isotopic fractionation for the protolith and mylonite, and Qz-Ep isotopic fractionations for Qz veins in the mylonite (Appendix V, Table V-4).	160
Figure V-18: Schematic cross-section representing the evolution of the stable isotope composition of the BSZ. A, illustrates the hydrogen isotope composition and the fluid flow in the detachment through space and time. B, illustrates the oxygen isotope composition of the fluid flow in the detachment through space and time. Red correspond to magmatic fluid composition; purple: δD of the meteoric fluid retaining its δD_{wt} but with $\delta^{18}O_{wt}$ buffered by the host-rock; blue: meteoric fluid composition.	163
Figure V-19: Evolution of the fluid flow and the $\delta^{18}O_{wt}$ values relative to the evolution of the fabric overprinting the granodiorite of the Bear Creek Pluton. Red corresponds to magmatic fluid compositions; purple: δD meteoric fluid retaining its δD_{wt} but with $\delta^{18}O_{wt}$ buffered by the host-rock, blue: meteoric fluid composition. Length and number of arrows illustrate the volume of fluid flowing in the BSZ.....	164

Chapter VI :

- Figure VI-1: (a) Map of the Okanagan-Kettle metamorphic core complex, and localization of the Kettle detachment shear zone (DSZ) ; (b) Schematic section of the Kettle-Okanagan MCC..... 168
- Figure VI-2: The Kettle DSZ, part of the Columbia river detachment that delineates the contact between the Tertiary lower crust and the Mesozoic upper crust is highlighted at the Hall Creek Quarry (adapted from Washington State DNR, 2008). 170
- Figure VI-3: Schematic bloc diagram of the detachment units present in the Hall Creek Quarry, Inchellum, WA. C-axis fabrics orientation of quartz grains on the right side, for both UQM and LQM units..... 171
- Figure VI-4: (a) Silicified breccia, rich in oxides. (b) Upper Quartzite mylonite. (c) kink-bands in UQM. (d) Lower Quartzite mylonite. (e) Micaschist layer. (f) Sheet folds in the micaschist 173
- Figure VI-5: Thin sections have been cut perpendicular to the foliation and parallel to the lineament. The optical micrographs are West-East oriented (left to right in micrographs); top and bottom border of the thin sections are parallel to the foliation plan of the quartzite mylonite. (a), (d), and (f) optical micrographs in crossed polarized light with white lines defining the S-C-C' fabric; (b), (c) and (e) optical micrographs in natural light with localization of the fluid inclusions. 174
- Figure VI-6: Thin sections have been cut perpendicular to the foliation and parallel to the lineament. The optical micrographs are West-East oriented (left to right in micrographs); top and bottom border of the thin sections are parallel to the foliation plan of the quartzite mylonite. (a) quartz ribbons of different length in the UQM. (b) Grain size reduction of K-feldspar by hydration, producing quartz and muscovite in its tails. 176
- Figure VI-7: (a), (c), (e) Tschermak substitution substitution with total aluminum versus (Si+Mg+Fe) content, on the basis of electron microprobe analysis of single grain transects. (b), (d), (f) Al element map of micafish, transect has been measured perpendicular to the shear plane (white lines)..... 179
- Figure VI-8: $^{40}\text{Ar}/^{39}\text{Ar}$ age spectras on muscovite grains, performed by Pr. Heizler at the University of New Mexico. Results indicate constant ages through the section, the mean-value is 50.5 ± 0.3 My. The small error bars are justified by the wide plateaus. 180
- Figure VI-9: (a) Hydrogen isotope composition of muscovite as a function of the distance below the detachment. (b) Hydrogen isotope composition of quartz fluid inclusions as a function of the distance below the detachment. In both graphs, the error bars correspond to the standard deviation of the duplicates. Simplified cross-section on left side : UQM – Upper Quartzite Mylonite ; S - micaschiste layer ; LQM – Lower Quartzite Mylonite. 182
- Figure VI-10: Oxygen isotope composition of quartz (dark grey) and muscovite (light grey) as a function of the distance below the detachment. $\delta^{18}\text{O}_{\text{Qz}}$ and $\delta^{18}\text{O}_{\text{Ms}}$ are relatively constant in the lower quartzite mylonite and highly variable in the upper quartzite mylonite. Simplified cross-section on left side : UQM – Upper Quartzite Mylonite ; S - micaschiste layer ; LQM – Lower Quartzite Mylonite..... 183
- Figure VI-11: Calculated Qz-Ms oxygen isotope equilibrium temperature versus the distance below the detachment. The temperatures reflect relatively constant

oxygen isotope fractionations between Qtz and Ms for the LQM, $355 \pm 20^\circ\text{C}$; but large changes in fractionation for the UQM, $390 \pm 200^\circ\text{C}$. For two samples (white stars in black circles) temperatures cannot be calculated as the $\delta^{18}\text{O}_{\text{Qtz}}$ is lower than the $\delta^{18}\text{O}_{\text{Ms}}$. Simplified cross-section on left side: UQM – Upper Quartzite Mylonite; S - micaschiste layer; LQM – Lower Quartzite Mylonite..... 185

Figure VI-12: Summarize for both UQM and LQM of results for each type of analyses according to a time, temperature axis..... 187

Figure VI-13: (a) Schematic cross-section of the Kettle DSZ, showing the pathways of both UQM and LQM in space and time : t=1 corresponds to amphibolite facies, t=2 corresponds to early greenschist facies, t=3 corresponds to late greenschist facies. (b) Zoom at t=3 onto the Hall Creek section. (c) Evolution of the microstructure and isotopic composition of the UQM and LQM during exhumation..... 193

Chapter VII :

Figure VII-1: Schematic model of fluid flow through an extensional shear zone. 1. Surface fluids flow through the detachment fault and connect with cataclasites. 2. Cataclasites connect to the ultramylonite at the brittle-ductile transition, and surface-derived fluids keep flowing through ultramylonites. 3. At a depth where deformation is distributed, the surface-derived fluids flowing through the ultramylonite are released in the mylonite and flow pervasively in the broad ductile shear zone..... 200

Chapter I : Introduction

This thesis explores the deepest regions of fossil hydrothermal systems that formed during early Cenozoic extension of the North American Cordillera and that have been exhumed to the surface by tectonics and erosion. A combined field, geochemical, and stable isotope study of these regions helps understand how fluid circulations influence the thermal budget and the deformation of the crust.

Hydrothermal alteration in extensional shear zones has been recognized beneath the detachment zones that bound metamorphic core complexes (MCC) in the North American Cordillera (Kerrick et al., 1984; Nesbitt and Muehlenbach, 1989, 1991; Fricke et al., 1992; Morrison and Anderson, 1998; Mulch et al., 2004, 2007; Gébelin et al., 2011; Gottardi et al., 2011). In this thesis, the term detachment shear zone is used to describe the highly sheared rocks that are located immediately beneath what is generally considered the brittle detachment fault that defines metamorphic core complexes. In such extensional settings the role of fluids in the exhumation process has been studied extensively using various approaches. Previous work has highlighted general trends, which are summarized in this section, regarding the metamorphic reactions, the geothermal gradients, and the flow of fluids and volatiles and/or volume changes in the units that make up the detachment shear zone. The purpose of this chapter is to address the current state of understanding of fluid-rock-strain interactions in order to present the context in which this thesis was conceived and carried out.

1. Genesis of Metamorphic Core Complexes in the North American Cordillera:

The Cordillera located in the western regions of the North American continent is oriented broadly north-south and extends over 6000 km from Canada to Mexico. The non-collisional orogeny of the North American Cordillera is controlled by two major geodynamic events. From late Jurassic to early Tertiary a compressional phase is evidenced by the Sevier thrust belt (Figure I-1), accommodated by thin-skinned thrust systems that define the hinterland of the Cordillera (Armstrong, 1968; Fleck, 1970; Allmendinger et al., 1984, 1992; Heller et al., 1986; Miller and Gans, 1989; Wannamaker et al., 1997; Taylor et al., 2000; Decelles, 2004; Lawton, 2009).

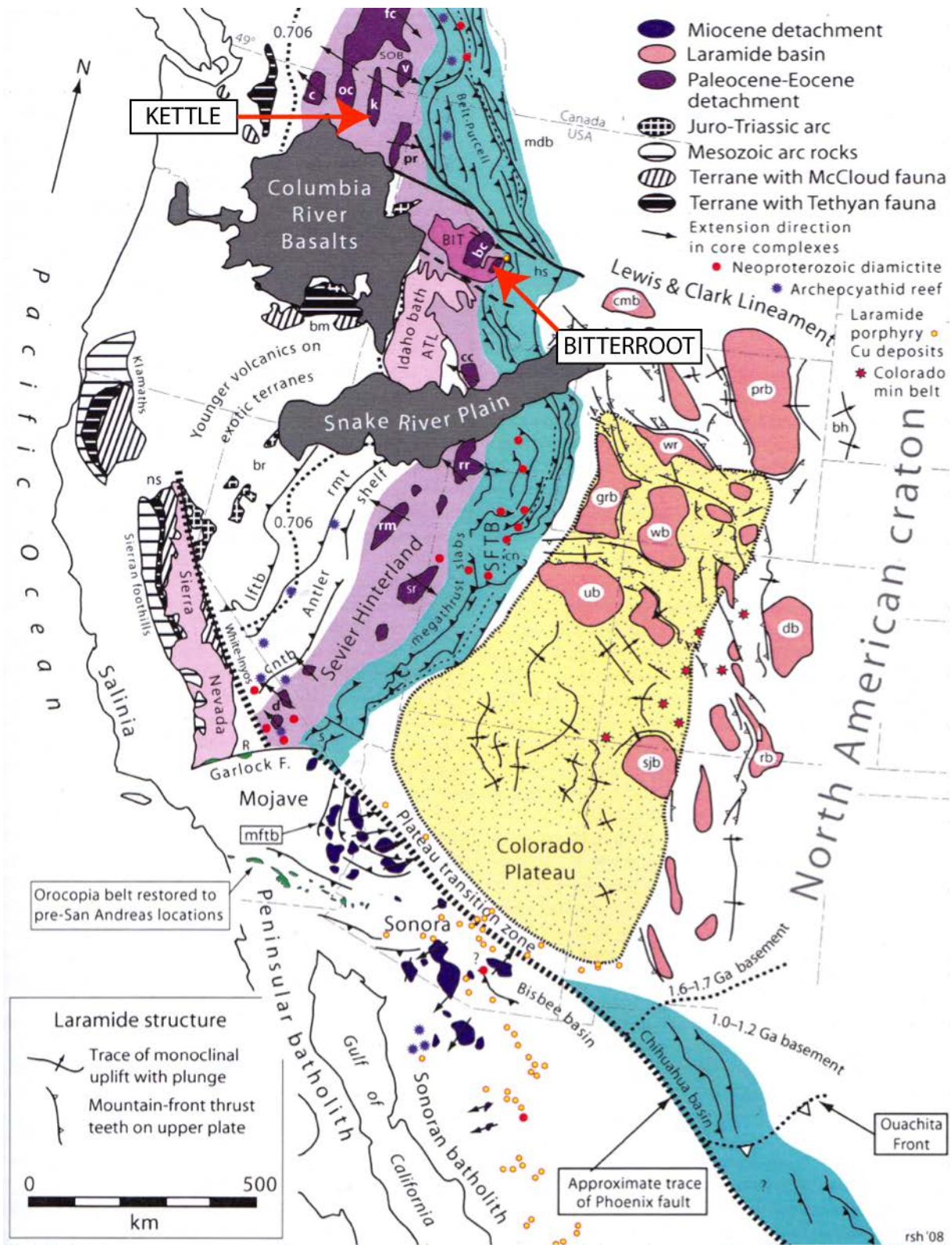


Figure I-1: Geological sketch map of the North American Cordillera, from northern Mexico to southern Canada. This map shows the principal tectonics structures associated to the Cretaceous orogeny of the Cordillera and its Tertiary collapse (Hildebrand, 2009).

From late Cretaceous to Eocene (75-55 Ma), a second pulse is evidenced by the Laramide thrust belt, with thick-skinned thrust faults developed to the east of the front of the Sevier thrust belt (Brown, 1983 ; Erslev, 1993 ; Johnson et al., 1984 ; Karlstrom et al., 2002 ; Decelles, 2004). At about 75 Ma, deformation started to affect the Sevier foreland, but Sevier deformation continues well into the Laramide (Bird, 1998). Several sediment-filled basins related to the Laramide uplift lay east to the Laramide front of deformation (Dickinson et al., 1988; Mix et al., 2011) and can be observed in the Colorado plateau (Figure I-1). At that time, the paleo-thickness of the North American Cordillera crust estimated by Coney et al. (1984) ranges between 40 and 60 km (Figure I-2).

In the early Cenozoic, a major geodynamic change engenders crustal thinning beneath the North American Cordillera. Several geologic processes leading to the Cenozoic extension of the Cordillera have been proposed: (1) the Mesozoic over-thickened crust, characterized by a low-relief, high-elevation hinterland plateau (the “Nevadaplano”) and a topographically rugged frontal thrust belt experiences gravitational collapse (Coney et al., 1984; Hodges et al., 1992; McQuarrie and Chase, 1999; Decelles, 2004;); (2) a hypothetical west-dipping subduction zone is reversed in an east-dipping subduction zone at about 55 Ma and generates extension and arc magmatism and to a greater extent, collapse of the thickened crust (Hildebrand, 2009); (3) removal of the subducting Farallon flat-slab and its sinking northeastward into the mantle resulted in upwelling of hot asthenosphere and softening of the lithosphere, which collapsed (Saltus and Thompson, 1995; Humphreys, 1995; Sigloch et al., 2008; Liu et al., 2010); (4) a wave of uplift, extension, and volcanism propagated from southern British Columbia to Nevada/Arizona and generated a wave of uplift, followed by a wave of extension and formation of core complexes, which was accompanied by a wave of volcanism; this scenario may be related to the propagation of a slab-window during the Cenozoic (Mix et al., 2011)

Independent of the geologic process responsible of the Cenozoic extension affecting the North American Cordillera, lateral and vertical flow of partially molten crust related to crustal extension are intimately linked to the development of MCC (Lister and Davis, 1989; Malavieille, 1993; Brun et al., 1994; Rey et al., 2001; Teyssier, 2005). The North American Cordillera displays over 25 MCC that are aligned along the N-S axis of the Cordillera (Crittenden et al., 1980; Coney, 1980, 1984; Armstrong, 1982, 1991a). The MCC developed during Paleocene-Eocene in southern Canada (Brown, 1983; Armstrong et al., 1991b; Norlander et al., 2001; Teyssier, 2005; Glombick, 2006; Johnson, 2006), from Eocene to

Oligo-Miocene in northern and central US (Foster et al., 1997, 2001, 2007; Wells et al., 2000; Mulch et al., 2007) and during Miocene in northern Mexico (Anderson et al., 1980; Nourse et al., 1994) (Figure I-1). The most recent expression of crustal thinning in the US is the Basin and Range province (Figure I-1), and it is Miocene to present in age (Zobak et al., 1981; Thatcher et al., 1999; Wernicke and Snow, 1998; Bird, 2002; Hammond and Thatcher, 2004); the present crustal thickness ranges between 20 and 30 km (Figure I-2B). Consequently, the MCC from the Cordillera are post-Sevier-Laramide orogeny, predate the late Cenozoic Basin-and-Range extension, and indicate a north to south migration of MCC formation.

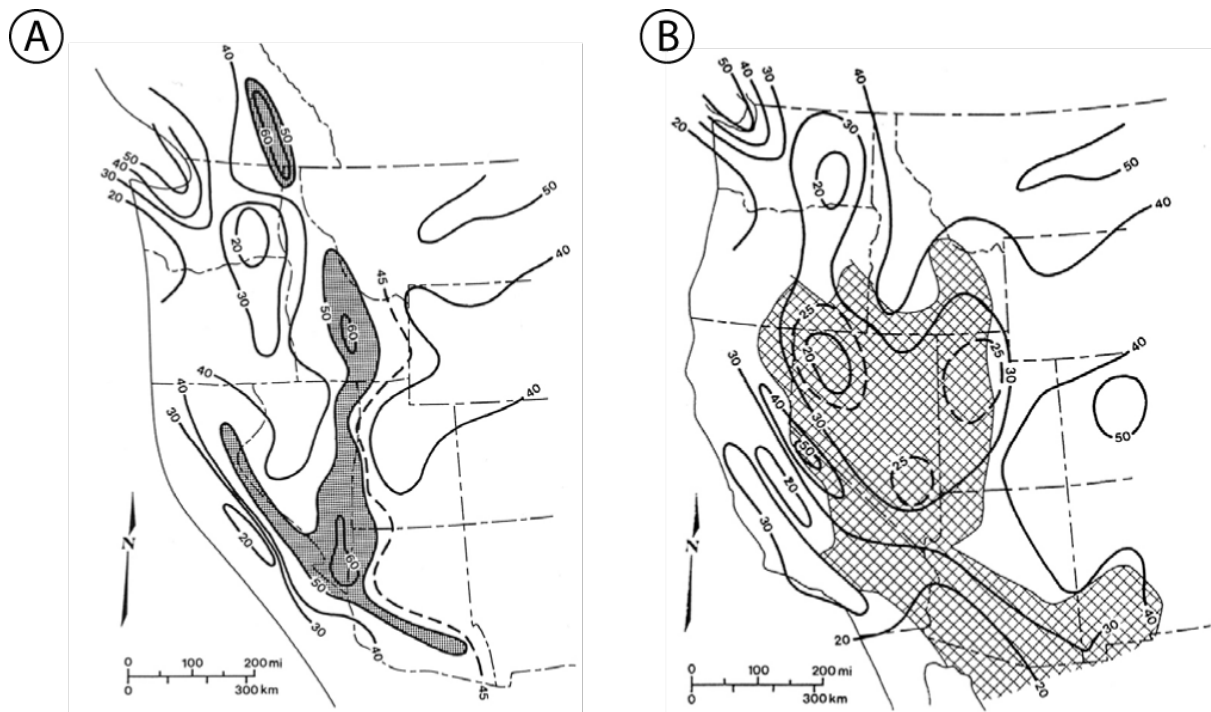


Figure I-2 : Crustal thickness of the North American Cordillera (Coney et al., 1984). A. Paleo-crustal thickness estimated for the Early Tertiary, and B. Current crustal thickness.

The work presented in this thesis is based on two detachment shear zones that are linked to Eocene extension. The Columbia River detachment shear zone represents the eastern border of the Okanogan-Kettle dome (OC and K in Figure I-1), and the Bitterroot detachment shear zone delineates the contact between the Bear Creek pluton and the Sapphire block (BC in Figure I-1).

2. Extensional shear zones / detachments :

Since the 1970s, the scientific community has proposed three models of crustal thinning. McKenzie (1972) proposed a crustal thinning model accommodated by pure shear, rifting-type, inducing brittle deformation in the upper crust accompanied by asthenospheric

rebound. A second model was proposed by Wernicke (1981), based on the low angle normal faults of the Basin-and-Range Province. Wernicke (1981) proposed that strain localizes in a shear zone that transects the lithosphere, and that thinning is accommodated dominantly by this simple shear zone. These two models are based on initiation of crustal thinning in the upper crust, with a propagation of deformation at the lithosphere scale. These models imply a rise of the Moho in the vicinity of a MCC, which contradicts the seismic data indicating a flat Moho in the Basin-and-Range. Finally, Davis et al. (1983) proposed a model of crustal thinning by combination of pure and simple shear (general shear). The originality of this work comes from the idea that the deformation is initiated in the ductile domain and propagates to the brittle domain (Figure I-3).

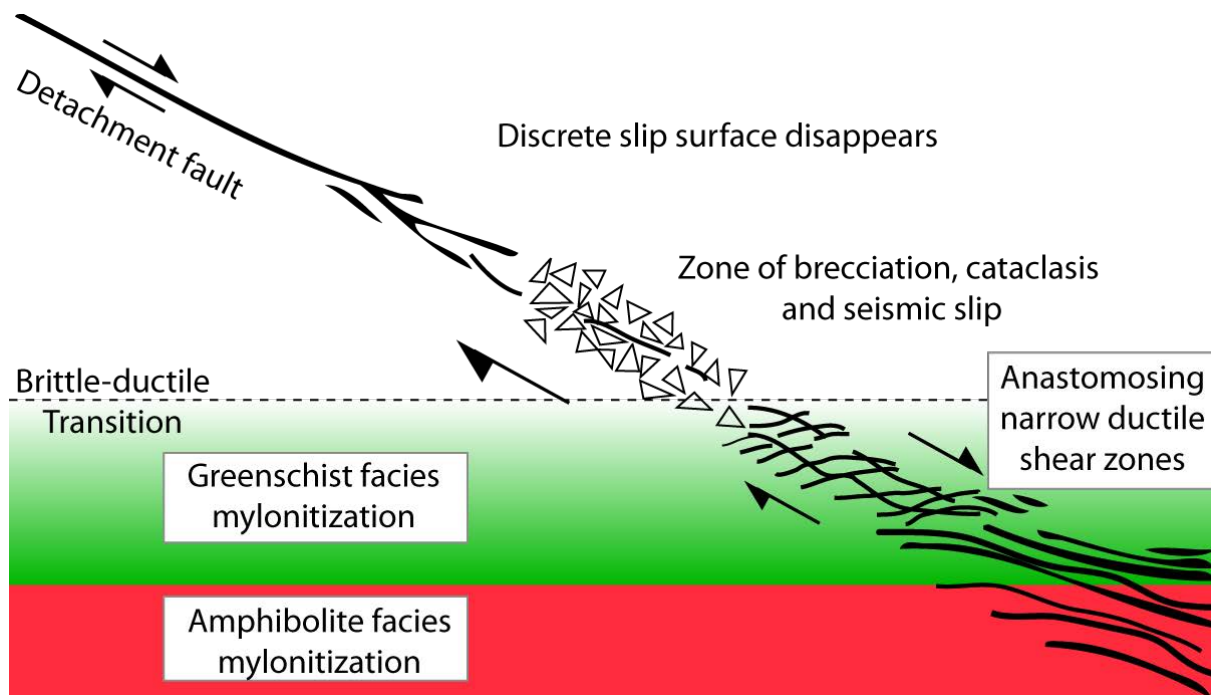


Figure I-3 : Spatial propagation of deformation in a shear zone from ductile fabrics toward brittle fabrics (adapted from Lister and Davis, 1989).

A fourth model proposes that overthickened crust leads to a partial melting of the middle crust, resulting in a detachment zone associated to the emplacement of a leucogranite batholith (Vanderhaeghe et al., 1999). The lower crust underlying the detachment zones experiences ductile thinning by both lateral flow and upwelling flow (Vanderhaeghe et al., 1999; Teyssier, 2005; Liu et al., 2010). Rise of the lower crust towards the surface in case of a free-boundary collapse forms migmatite domes and develops a rolling-hinge detachment during boudinage instability (Teyssier et al., 2005). Note that in the Simplon fault zone (Switzerland), the comparison between a thermochronological dataset and numerical

modeling established that the thermochronological pattern is better reproduced by a low-angle detachment that maintained a 30° dip, rather than by a rolling hinge model (Campani et al., 2010a).

Following their recognition in the North American Cordillera (Davis and Coney, 1979; Coney, 1980), MCC's have been observed and documented in different extensional settings around the world, for example the Aegean Sea (Lister et al., 1984; Jolivet et al., 1998; Forster and Lister, 2009; Huet et al., 2011), China (Davis et al., 2002; Liu et al., 2005; Lin et al., 2008) or Papua New Guinea (Baldwin et al., 1993; Abers, 2002; Spencer, 2009). The MCC's of the North American Cordillera are extensional structures generated by crustal thinning (Davis and Coney, 1979, Coney, 1980; Dewey, 1988; Armstrong et al., 1991; Vanderhaeghe et al., 1999, 2003; Liu, 2001; Foster et al., 1997, 2001, 2002, 2007; Teyssier, 2005; Mix et al., 2011; Vogl et al., 2012), and are characterized by two principal units: a brittlely deformed hanging wall lying over a metamorphic core that is ductilely deformed, and which can include migmatitic domes (Thor-Odin, Valhalla, Pioneers, Ruby Ranges MCC), gneiss domes (Okanogan-Kettle dome) or granitic batholiths (Bitterroot lobe), in which magnetic fabrics also define a domal shape (Sidman et al., 2005).

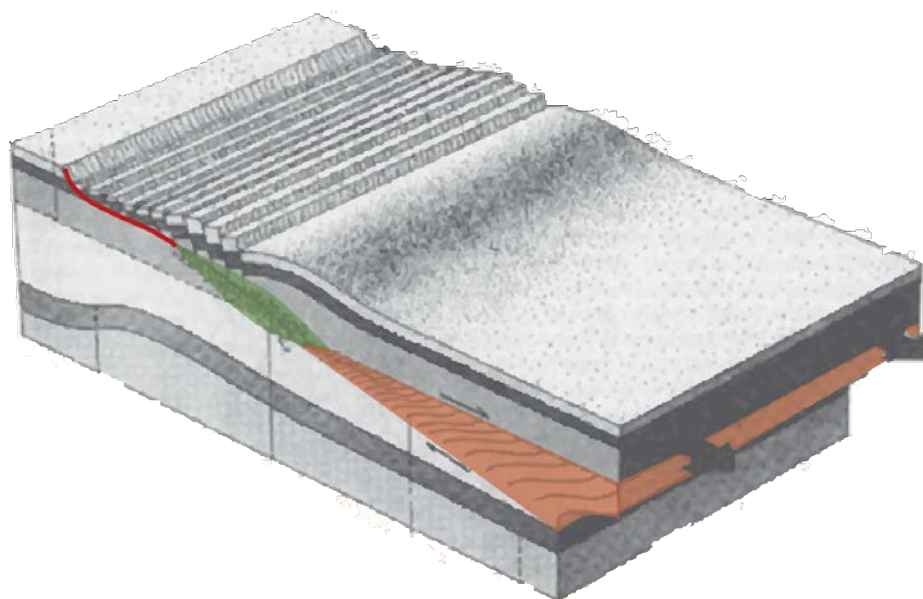


Figure I-4 : Schematic block diagram of crustal extension and localization of deformation in an evolving detachment (adapted from Lister and Davis, 1989). Orange, ductile fabrics ; Green, brittle fabrics ; Red line : detachment fault.

Detachment systems accommodate most of the deformation generated by the exhumation of MCC. They juxtapose the contact of the high-grade metamorphic, partially molten, or magmatic middle crust with the relatively unmetamorphosed upper crust (Coney, 1980; Dewey, 1988; Armstrong et al., 1991; Vanderhaeghe et al., 1999). Such a layer can be tens to hundreds of meters thick and is characterized by the superposition of brittle structures over ductile fabrics (Davis, 1983; Malavieille, 1993) (Figure I-4). Detachments are self-exhuming systems and are, therefore, excellent natural examples to observe and study the continuous transition from ductile to brittle deformation (Campani et al., 2010b), since ductile and brittle fabrics are juxtaposed within the same unit and record a continuous period of exhumation (Figure I-5).

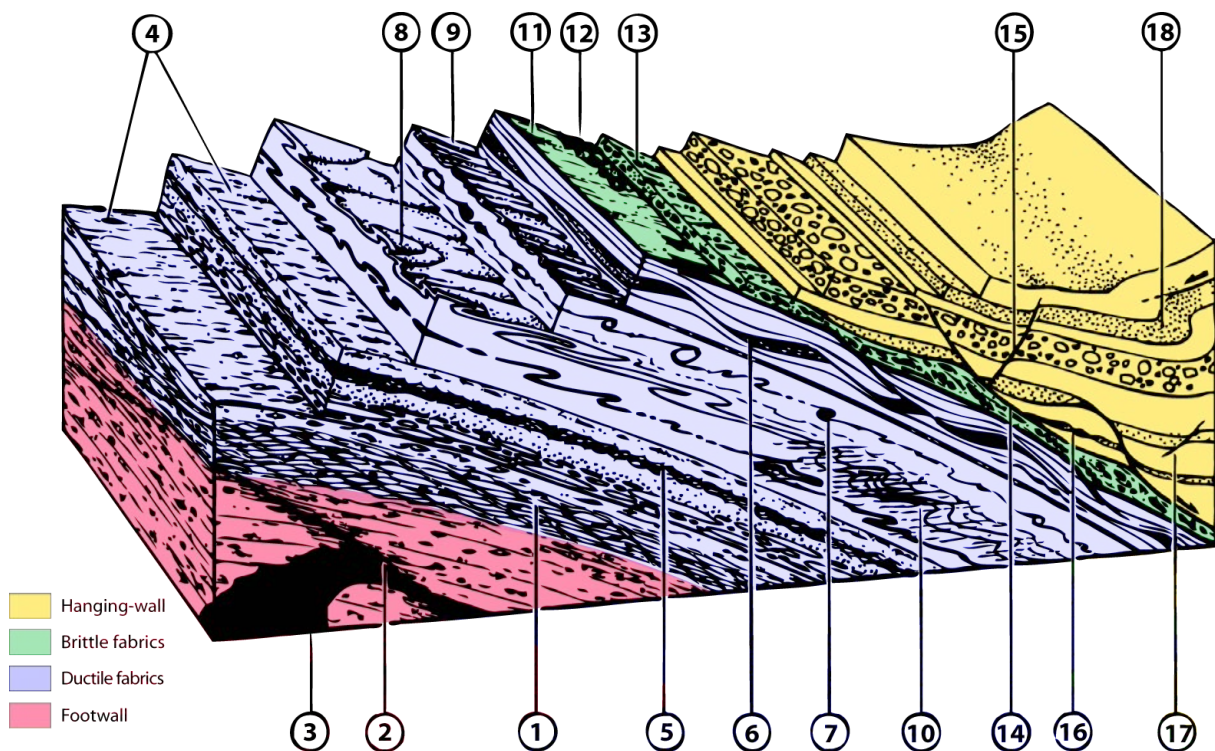


Figure I-5: Synthetic block diagram showing the different structures associated with extensional shear zones (adapted from Malavieille, 1993): 1. foliated rocks with extensional shear bands; 2. small scale normal shear zones; 3. Synkinematic granite bodies or sill, mylonitized and boudinaged; 4. stretching and mineral lineations; 5. extensional crenulation cleavage; 6. boudinage at different scales; 7. shear criteria; 8. sheath folds in zones of high shear strain; 9. folds with axes parallel to stretching lineations; 10. tight folds with subhorizontal axial planes; 11. slicken-sides on brittle detachment surfaces; 12. cataclastic breccia; 13. fractured pebbles, stretched and striated; 14. low-angle decollements in weak layer; 15. high-angle brittle faults; 16. stretched layers; 17. synsedimentary hydroplastic faults; 18. gravity folding. Colors illustrate the hanging wall (yellow) and footwall (pink), and the detachment (blue and green).

Mylonite and ultramylonite fabrics correspond to ductilely deformed rocks, showing general evidence of intense non-coaxial shearing, such as S-C fabrics, shear bands, sigma and delta porphyroclasts, and mica fish (Passchier, 1987, Passchier and Trouw 2005; Mancktelow et al., 2002; Tripathy et al., 2009). Brittle fabrics correspond to breccia, cataclasite, pseudotachylite, and veining (Sibson, 1986; Scholz, 1988, 1992; Lister and Davis, 1989; Malavieille, 1993). The most brittle expression of a detachment is a low-angle normal fault called the “detachment fault” (Davis, 1988; Malavieille, 1993). Crustal extension generates high-angle normal faults in the hanging wall, which can connect with the detachment at different depths.

3. Characterization of fluid source(s) and fluid flow in extensional SZ

In this thesis, the term fluid is used to describe a mix of an aqueous phase and volatile elements, in order to avoid any confusion with silicate liquids. The term reservoir corresponds to a volume of rock containing a volume of fluid, in our case the metamorphic core complex acts as a reservoir. As for the fluid sources in the reservoir, they can be variable in space and time.

3.1. Sources of fluids on Earth:

Apart from seawater, which covers approximately 70% of the Earth’s surface, the most common source of continental fluid corresponds to meteoric fluids, which includes all fluids precipitated at the Earth’s surface. These fluids can travel by surface runoff and ground water flow and penetrate the crust via open structures such as fractures or faults. Diagenetic fluids correspond to the fluid that is extracted from the rocks during compaction. While originally meteoric or seawater, these fluids evolve during diagenesis and interact with organic and inorganic matter (Clayton; 1966; Sheppard, 1986; Dubessy and Ramboz, 1986). This has the effect of altering the amount of volatile elements and the isotopic composition and possibly the pH of the fluid (Lawrence and Gieskes, 1981; Sheppard, 1986; Davisson et al., 1994, 1996). These two sources of fluids (meteoric and diagenetic, or formation water) characterize the majority of fluids flowing near the top of, and through the brittle crust. Metamorphic fluids that are released during metamorphism play an important role in promoting and controlling metamorphic reactions. During the prograde path, metamorphic reactions can release fluids, which are generally released during the destabilization and (re)crystallization of originally hydrated minerals at moderate temperatures, such as phyllosilicates (Dixon and Williams, 1983; O’Hara, 1988; O’Hara and Blackburn, 1989; Hippert, 1998; Kwon et al.,

2009). Magmatic fluids can be released into the host rock during the adiabatic ascent of magma toward the surface and during its crystallization (Sheppard et al., 1971; Kamili et al., 1996; Ambrosio, 2010). These fluids are enriched in incompatible elements and related to the formation of ore deposits over thousands of years; for example, epithermal gold deposits are located in the vicinity of active or fossil magmatic zones and metamorphic shear zones (Criss et al., 1983; Criss et al., 1990; Berger et al., 1990; Xiong and Zhai, 1992; Steinmüller, 2001; Levresse et al., 2004; Zhai et al., 2009; Bongiolo et al. 2011). Finally, the presence of fluid in the mantle is still poorly understood, however, dehydration of the subducting slab with its sediment cover appears to be the most common way to bring fluids into the mantle, thus defining a mantle fluid source if the fluids have re-equilibrated with the mantle phases (Hirschmann, 2006; Hirschmann et al., 2009). Alternatively, these fluids may be primary in origin (juvenile fluids).

3.2. Stable isotope characterization of fluid sources:

Elements such as hydrogen (H), carbon (C) or oxygen (O) consist of an assemblage of different isotopes that incorporate two or more distinct stable isotopes. R refers to the atomic ratio N^*/N of a heavy (N^*) to a light (N) isotope, where R can represent $^2\text{H}/^1\text{H}$, $^{13}\text{C}/^{12}\text{C}$ and $^{18}\text{O}/^{16}\text{O}$. The measured ratio in the isotopic composition of a sample (x) is normalized to a standard (std) and provides a dimensionless δ -values, defined by the following equation:

$$\delta_x = 1000 * (R_x - R_{\text{std}}) / R_{\text{std}}$$

The factor of 1000 converts the δ -values to per mil (‰), and this formula defines the isotopic values of hydrogen (δD), carbon ($\delta^{13}\text{C}$) and oxygen ($\delta^{18}\text{O}$), according to the following equations:

$$\delta\text{D} = 1000 * [((^2\text{H}/^1\text{H})_x / (^2\text{H}/^1\text{H})_{\text{VSMOW}}) - 1]$$

$$\delta^{13}\text{C} = 1000 * [((^{13}\text{C}/^{12}\text{C})_x / (^{13}\text{C}/^{12}\text{C})_{\text{PDB}}) - 1]$$

$$\delta^{18}\text{O} = 1000 * [((^{18}\text{O}/^{16}\text{O})_x / (^{18}\text{O}/^{16}\text{O})_{\text{VSMOW}}) - 1]$$

The most common standard for carbon isotopes is referred to as “PDB” and represent a Cretaceous belemnite from the Peedee Formation of South Carolina (Craig, 1957). Craig (1961) determined the hydrogen and oxygen isotopic compositions of seawater as near 0‰, and this defines the value of seawater as a standard (VSMOW, Vienna Standard Mean Ocean Water as the ratio is defined by the International Atomic Energy Agency (IAEA) in Vienna).

3.2.1. *Stable isotope thermometry:*

If thermo-barometric conditions are favorable to stable isotope diffusion, equilibrium of isotopic fractionation between fluid and host-rock can be reached. The isotopic fractionation is a function of temperature. Therefore, if isotopic equilibrium is reached between a mineral and a fluid, or between two minerals, it is possible to estimate the isotope equilibrium temperature (Urey, 1951; Bottinga and Javoy, 1975; Clayton, 1972; Zheng, 1993, Chacko et al. 1996; Vennemann and O'Neil, 1996). The $\delta^{18}\text{O}$ values of the mineral assemblage, complemented by δD values of hydrous minerals if present, hence may help to constrain not only the source of the fluid present during diffusion and/or (re)crystallization of minerals, but also the temperature of isotope equilibrium.

3.2.2. *Meteoric water:*

Craig (1961) demonstrated that the isotopic enrichment/depletion, relative to seawater, displays a linear correlation between the δD and $\delta^{18}\text{O}$ values over the entire range for meteoric water which has not undergone excessive secondary evaporation. The linear correlation between the isotopic composition of hydrogen and oxygen from meteoric fluids is called the Global Meteoric Water Line (GMWL):

$$\delta\text{D} = 8 * \delta^{18}\text{O} + 10\text{‰}$$

In addition, the isotopic fractionation between the vapor and liquid phase on evaporation implies that the isotopic compositions of oxygen and hydrogen are depleted in heavy isotopes in the atmosphere, providing them low to extremely negative isotope values. Note that the δD and $\delta^{18}\text{O}$ values of meteoric water are decreasing with increasing latitudes (Epstein et al., 1970; Taylor, 1979). The isotopic fractionation is also a function of altitude of precipitation; hence the isotopic composition of meteoric fluids can be considered a marker of temporal evolution of topography (e.g., Chamberlain et al., 1999; Garzzone et al., 2000; Poage and Chamberlain, 2002; Mulch et al., 2004, 2007; Currie et al., 2005 ; Rowley and Currie, 2006; Mix et al., 2011).

3.2.3. *Metamorphic and magmatic water:*

Regarding metamorphic and magmatic fluids, stable isotope analyses of fluid inclusions in minerals as well as those of the minerals have shown that these two sources of fluids have distinct stable isotope compositions. The hydrogen and oxygen isotope composition of metamorphic and magmatic fluids are based on mineral-water fractionation at a given

temperature since exchange during post-metamorphic/magmatic processes can modify both the δD and $\delta^{18}O$ values of the fluid inclusions (Sheppard, 1986). Metamorphic fluids are characterized by $\delta^{18}O$ values ranging from 5 to 25 ‰ and δD values between -20 and -70 ‰ (Taylor, 1974; Rye et al., 1976; Sheppard et al., 1977, 1985; Field and Fifarek; 1985).

In contrast, magmatic fluids define a uniform composition, with $\delta^{18}O$ values ranging from 5 to 10 ‰, and δD values between -40 and -80 ‰ (Sheppard et al., 1969; Chappell et al., 1974; Taylor, 1986; Nabelek et al., 1983; Sheppard, 1986; Field and Fifarek; 1985). In these cases, the fluid $\delta^{18}O$ and δD values no longer plot on the GMWL (Figure I-6).

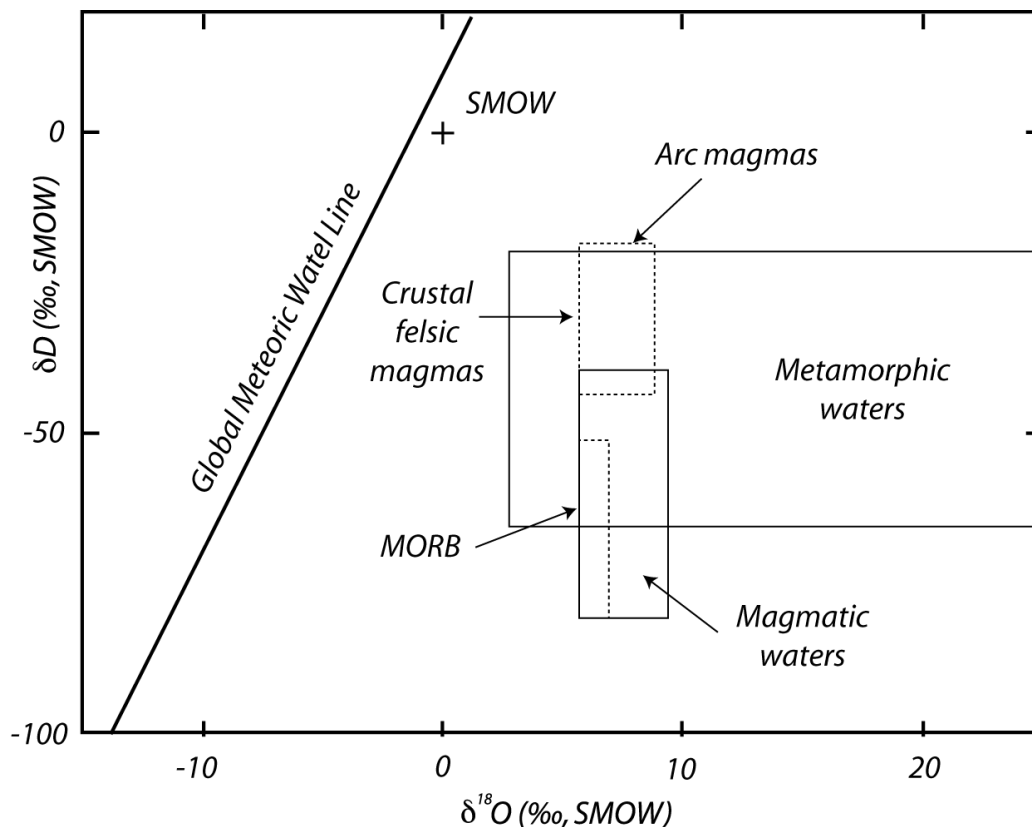


Figure I-6: Graphic representing the range of oxygen and hydrogen isotope compositions, which define the different fluid sources (adapted from Sheppard, 1986).

3.2.4. Oxygen isotope composition of rocks:

To highlight the interactions between different sources of fluids and rock types, Field and Fifarek (1985) compiled a database of stable isotope compositions of the main geological settings (Figure I-7). They demonstrate that the oxygen isotope composition varies from one geological setting to another. For example, igneous rocks have $\delta^{18}O$ values of between 5 and 15 ‰, where the value in oxygen gradually increases from basalt / gabbro to rhyolite / granite. Sedimentary rocks are characterized by high oxygen isotope values, ranging from 10 to 40 ‰.

As for hydrothermal deposits, they are characterized by compositions ranging from -10 to 20 ‰. The characterization of isotopic compositions of fluids and minerals, and the observation of isotopic compositions characteristic of various types of geological settings have naturally been used to address the questions of fluid-rock interaction, the volume of fluid (according to the source) available in the reservoir, the type of fluid flow that permits isotopic exchange, and also the relationship between fluid flow, fluid-rock exchange, and strain.

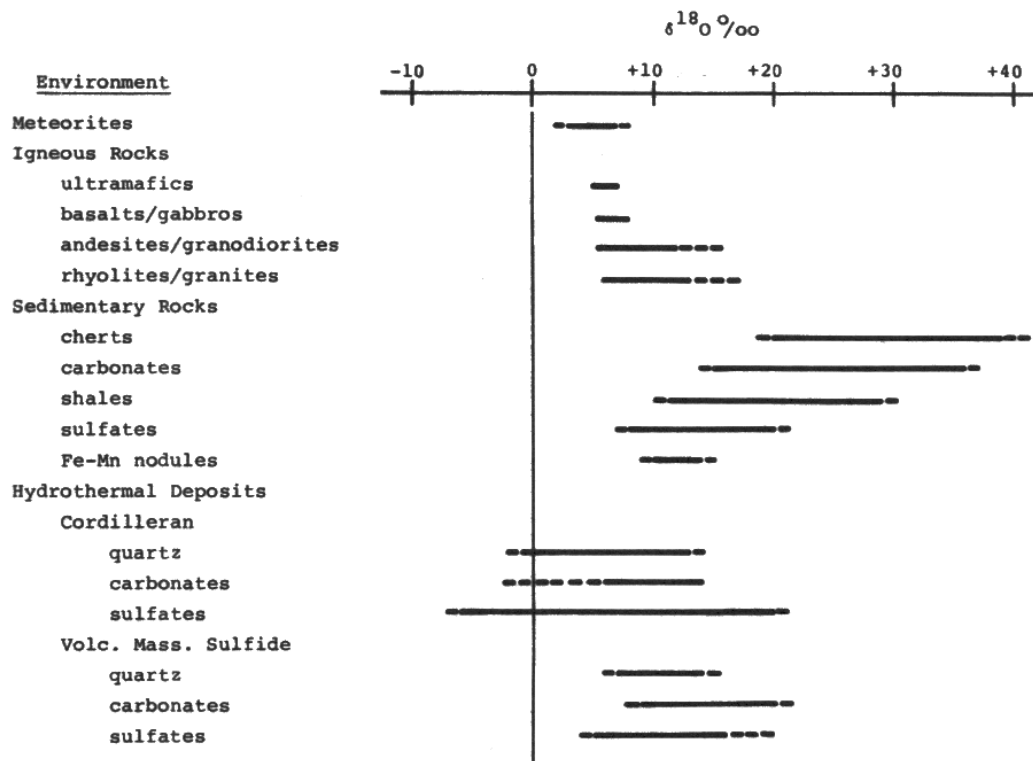


Figure I-7: Oxygen isotope composition according to geological contexts (Field and Fifarek, 1985).

3.3. Fluids in extensional shear zones:

3.3.1. Evidence of fluid flow in extensional shear zones:

Studies of detachments in the North American Cordilleran core complexes suggest that meteoric fluids permeate detachment zones, as recorded by the hydrogen isotope composition of fabric-forming minerals such as white mica, biotite, and amphibole (Morrison and Anderson, 1998; Criss and Fleck, 1990; Losh, 1997; Mulch et al., 2004; 2007; Gottardi et al., 2011; Gébelin et al., 2011). Hydrothermal alteration of breccia in a detachment has been demonstrated in the Sweathouse section, along the Bitterroot detachment (Kerrick and Hyndman, 1986). In contrast to the isotopic composition of the mineral assemblages of the breccia, the $\delta^{18}\text{O}$ values for both quartz and feldspar in the mylonite have preserved their

protolith isotopic composition. The shear zone acts as a high-permeability conduit for discharge of large volumes of magmatic and/or metamorphic fluids at moderate temperature during ductile deformation (Kerrick et al., 1984), even if it corresponds to a low fluid-rock ratio (Kerrick and Hyndman, 1986). Meteoric fluids may infiltrate the system only during the latest stages of activity on the detachment, i.e. at a shallow structural level and temperature below 300°C, and promote elevated fluid-rock ratios.

However, Nesbitt and Muehlenbachs (1989, 1991) highlighted the infiltration of meteoric fluid in the ductile domain in an extensional shear zone, and the presence of meteoric fluids can be detected down to paleo-depths on the order of 10-15 km. These authors proposed that crustal-scale convection of fluids can bring meteoric fluids down to such depths. This is corroborated by the work of Fricke et al. (1992), which shows that the meteoric fluids have reached the ductile domain, beyond the brittle-ductile transition. The brittle-ductile transition thus cannot be considered as an impermeable barrier for meteoric fluids. Evidence of meteoric fluid flowing through detachment and extensional shear zones is now common (Morrison and Anderson, 1998; Mulch et al., 2006, 2007; Gébelin, 2011; Gottardi et al., 2011), but the processes responsible for the burial or infiltration of meteoric fluids to 10-15 km depths remain unconstrained. Sibson (1975) proposed a mechanism of seismic pumping for hydrothermal fluid transport, using the fault surface as passageways for flow. A dilatancy / fluid diffusion model may explain the intermittent fluid flow triggered by seismic activity along faults, moving fluids from one crustal environment to another. The hydraulic head that is generated by the topography of an orogen may be involved in moving "cold" fluids downward, toward the shear zone and then "hot" fluids upward in the direction of decreasing hydraulic head along ductile shear zones and faults (Upton et al., 2000; Nemcok et al., 2009; Craw et al., 2010).

In parallel, Morrison and Anderson (1998) demonstrated through stable isotope analyses that most of the cooling of the mylonite from the Whipple core complex (CA, USA) is the result of advective heat extraction by meteoric fluids, rather than by conductive cooling. The steep thermal gradient observed in the Raft River detachment (Gottardi et al., 2011) also suggests that meteoric fluid "cooled" the detachment, extracting the advective heat by convective fluid flow. In this scenario, the "cold" meteoric fluid flows toward the "hot" detachment, developing a convection cell that acts as a cooling system during detachment activity. Fluids become more buoyant when approaching the detachment, which drives meteoric fluids upward and away from the detachment. Consequently, a combination of

seismic pumping, topographically-driven fluid flow, and heat advection mechanisms may be necessary to trigger convection cells, which become self-driven once they are established. As such, buoyancy-driven fluid flow is controlled by porosity-permeability of the upper crust and is driven by high heat flow at the base of the system, beneath the detachment, where heat is advected by crustal thinning and/or magma intrusions. This hydrothermal convective flow is focused in the detachment for the duration of activity of the detachment and at relatively high temperature (300-500°C), resulting potentially in significant fluid-rock interaction and isotopic exchange.

3.3.2. Permeability of a shear zone:

Quantifying fluid fluxes in detachment zones is a challenge because permeability of ductilely deforming rocks is a dynamic quantity that is poorly understood. Bauer et al. (2000) proposed that mechanisms such as dissolution-precipitation and development of ductile fabrics, from the protolith to mylonite, lead to a progressive interconnectivity of a dynamic porosity. At very low strain, pore connectivity is low (Figure I-8, I), but only a small shear strain is required to increase the formation of dilatant shear surfaces (Figure I-8, II); this stage may correspond to protomylonite. At intermediate to high strain, pore connectivity increases gradually with strain, which generates a competition between processes that create interconnected pores, like hydrofracturing or dissolution, and processes which destroy pore connectivity, such as grain boundary migration (Figure I-8, III). Finally, at moderate temperature or high strain rates, transient fluctuations in pore fluid pressure may enhance fracture propagation and lead to an interconnected fluid flow network along narrow high-strain shear bands (Figure I-8, IV).

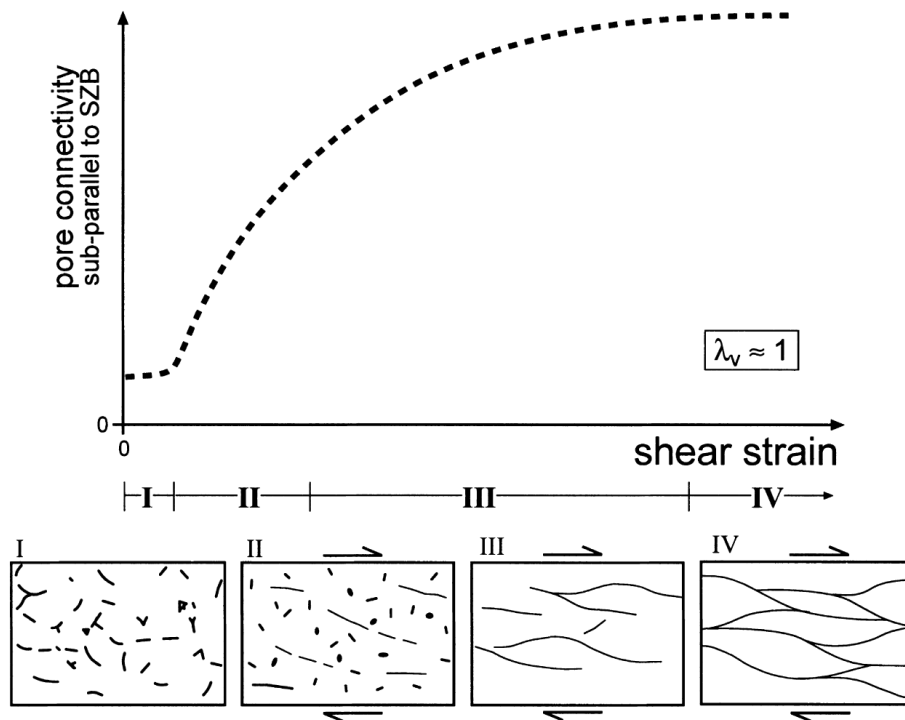


Figure I-8: Pore connectivity evolution according to the development shear strain, for constant pore fluid pressure, strain rate and temperature. Boxes show strain-dependent change in grain-scale fluid distribution (Bauer et al., 2000).

In parallel, Mancktelow et al. (1998) proposed that a fine mylonitic porosity may develop by accumulation of intragranular fluid inclusions to the grain boundary and by cavitation of grain boundaries during grain boundary sliding. Grain-boundary sliding and the associated opening and closing of grain-boundary pores gives rise to grain-scale fluid pressure differences between neighboring pores (Figure I-9), initiating a granular fluid pump (Fusseis et al., 2009). Pore fluid pressures decrease due to the local porosity increase and the solute concentration in the fluids are oversaturated leading to precipitation of phases in order to re-establish local chemical equilibrium (Herwegh et al., 2011). Then, the granular fluid pump model solves the inherent problem of high lithostatic pressures by considering pore fluid pressure as a quantity that varies on the grain scale (Fusseis et al., 2009).

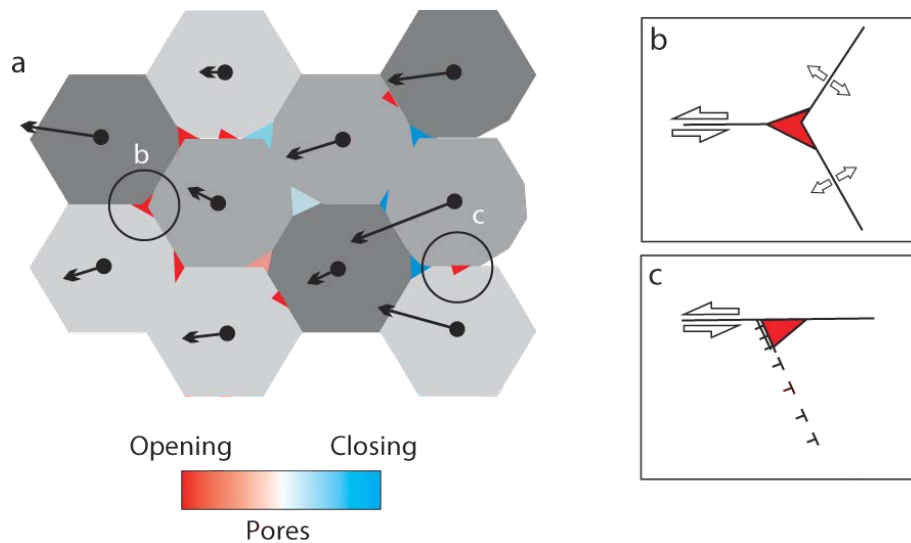


Figure I-9 : Granular fluid pump model associated to viscous grain boundary sliding in mylonite (Fusseis et al., 2009). The motion vectors (black) illustrate the differential motion of grains. The different pressures in opening and closing pores are colour coded; b, c, Mechanisms of cavity formation on grain boundaries and triple junctions (locations respectively marked 'b' and 'c' in a): cavitation at triple junctions (b); cavitation at dislocation tangles near grain boundaries (c).

A dynamic equilibrium between lithostatic pressure, pore fluid pressure, and pressure from chemical reactions is achieved if, in addition to dissolution and precipitation, an aqueous fluid is advectively transferred into these cavities from nearby collapsing pores (Fusseis et al., 2009). Grain boundary sliding-induced cavitation may at least partly help to explain enhanced grain-scale fluid flow in ductile shear zones (Rybacki et al., 2008, Fusseis et al., 2009).

3.3.3. Classification of fluid flow:

Oliver (1996) proposed a classification of fluid flow based on scale, degree of equilibration between fluid and rock, and several other parameters (Figure I-10). A closed system is defined as a rock-fluid system in which the rock does not show evidence of interaction with an external fluid. If such a system contains fractures, closed system implies that the fluid is generated in-situ, the mass-balance is constant, and the fluid remains in isotopic equilibrium with the rock. In an open system the rock-fluid system is controlled by an external fluid source, implying that a large volume of fluid can infiltrate the system and buffer the host rock. In this case, Oliver (1996) distinguished two types of fluid flow: (a) channelized fluid flow focused through particular locations while other locations remain relatively unaffected; (b) pervasive fluid flow, which requires that, at a certain scale, the entire volume of rock interacts and exchanges with an external fluid. Note that these

definitions of fluid flow, such as open and closed system notions are scale dependent, and could shift for example from channelized fluid flow on one scale to pervasive fluid flow on another scale.

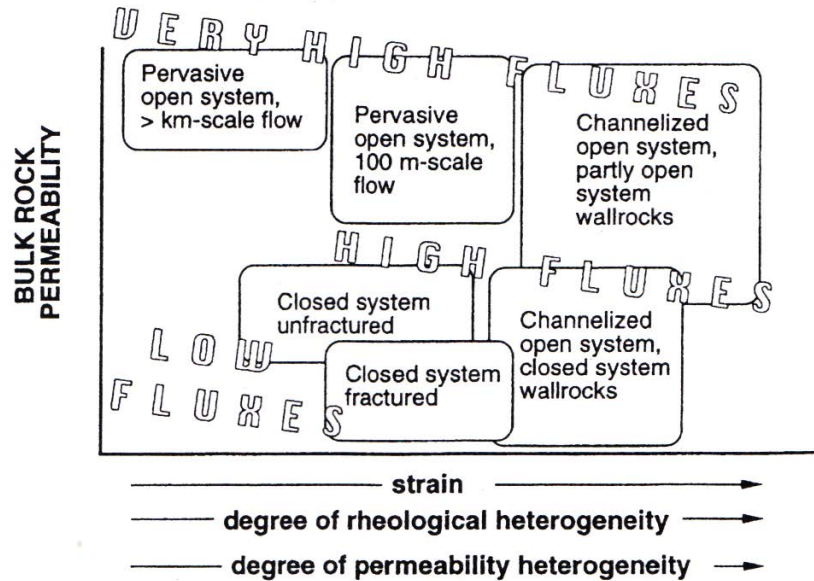


Figure I-10 : Classification of different type of fluid flow during regional metamorphism with respect to permeability, deformation and heat flux (Oliver, 1996).

4. Main goals and approaches of the thesis

The influence of fluid-rock interaction on deformation processes and rock composition in shear zones remains unclear; yet it is of major interest for understanding crustal deformation, geothermal activity (Zehner et al., 2006; Faulds et al., 2005; Person, 2008), and economic geology (Kerrick et al. 1984; Person et al., 2007; Kolb, 2008).

This thesis is based on a detailed study of two detachment systems that are exposed in the North American Cordillera: the Bitterroot detachment system, Bitterroot lobe (MT, USA), which affects a relatively isotropic granodiorite footwall, and the Kettle detachment system, Kettle Dome (WA, USA), which is localized in quartzite-dominated lithologies.

Methods and protocols employed during the thesis work are listed in Chapter II. Chapter III presents the field and structural geological context in which the Bitterroot detachment system was analyzed. This work integrates and complements published work on the lithologies and structures in this detachment system. The different fabrics, from ductile to brittle, that affect the granodiorite of the Bitterroot lobe are described and interpreted, and a microstructural analysis provides a framework for the strain history. Based on the relative

chronology between fabrics and structures, a sampling strategy for bulk chemical composition, mineralogy, and isotopic analysis was developed in order to answer the following questions:

What is the relationship between fluid(s) and strain localization?

Fluid flow is likely one of the major parameters controlling the dynamics of extensional shear zones. In order to understand the chemical changes related to strain localization occurring in the granodiorite, X-ray diffraction, microprobe analyses of phyllosilicates, and bulk-rock analyses were conducted on the main fabrics of the Bitterroot detachment system. Samples of protolith, mylonite, ultramylonite, and cataclasite were collected in order to monitor through bulk-rock analysis the chemical changes that occurred during fluid-rock interaction. Based on the mobility of elements, the bulk-rock analyses provide a way to quantify volume change and mass transfer (Gresens, 1967, Grant, 2005, Podelvin et al., 1993,) as well as fluid-rock ratios (O'Hara, 1988; Glazner and Bartley, 1991) affecting the different fabrics. The results, presented in Chapter IV, display a clear relationship between mineralogical assemblages and chemical composition, fluid-rock interaction, and strain localization.

How do fluids and fluid flow evolve in space and time in an extensional detachment system?

Mineralization associated with fluid flow through shear zones permits to identify the fluid pathways and to a greater extent, quantify the plumbing system during the activity of the shear zone.

Chapter V aims to demonstrate that mineralized veins and faults allow us to construct a map of the plumbing system within a detachment system that was active at or near the evolving brittle-ductile transition. Correlating the stable isotope results, performed on grains and fluid inclusions identified as part of the structural study, furnish a complete dataset for mapping a brittle-ductile plumbing system in 4 dimensions (2D+time+temperature), at the detachment scale. The 4D model extracted from the Sweathouse and Lost Horse sections of the Bitterroot detachment system improves our understanding of a fluid-assisted detachment migration through time.

What is the impact of fluid flow on exhumation along extensional SZ?

Recrystallization processes, metamorphic hydration reactions can be defined as rock softening fluid-enhanced processes (Hippert, 1998; Mancktelow, 2003; Nakamura et al., 2005). Trends of elemental exchange and patterns of isotopic variation can be compared and evaluated to resolve the style and mechanisms of fluid transport during exhumation of the core complex. In Chapter VI, interpretations based on stable isotope compositions, white mica chemical compositions and $^{40}\text{Ar}/^{39}\text{Ar}$ ages of the Kettle detachment address the permeability of rocks deforming in the ductile regime and the thermal and mechanical consequences of fluid flow in extensional detachment systems. In particular, results from this chapter suggest that evolution of fluid-rock interaction with respect to recrystallization processes in the mylonite must be related to the spatial and temporal evolution of strain localization.

Chapter II : Methodology

A multi-disciplinary approach has been conducted in order to characterize and quantify the fluid-rock-strain feedbacks in extensional shear zones. Protocols and methods used in the thesis are listed in this section. This work was performed based on the observation of geological processes ranging from mesoscopic to the atomic scale. The thesis is organized according to the observation of such phenomena, from the large to the small scale as follows:

- **Recognition and sampling units / fabrics in the field:**

This part of the work consists in compiling several vertical profiles within shear zones, ranging from the protolith (if you have access) to the hanging wall. Outcrops only rarely allow a complete profile across the shear zone to be taken; several profiles have thus juxtaposed to obtain a complete section across the shear zone.

- **Microstructural characterization:**

During the first stage, a microstructural study at the macroscopic scale has been conducted in the shear zones in order to highlight the evolution of the shear zone in space and time. As a second stage a microstructural study at the microscopic scale was performed in order to complete the macroscopic observations, also allowing the mineralogical assemblages to be characterized and the deformation mechanisms, invisible to the eye, to be revealed.

- **Geochemical analysis:**

Bulk-rock analyses highlight the chemical variations as a function of the strain rate of deformation and / or deformation domains (ductile/brittle). This study is complemented by single-grain analysis on phyllosilicates in order to characterize the chemical changes also at the micrometer scale.

- **Stable isotope analysis:**

Analysis of the isotopic compositions of oxygen, hydrogen, and carbon were performed on silicates and phyllosilicates, as well as on fluid inclusions in quartz in order to highlight the isotopic exchange between minerals and fluids. This study allows for a characterization of the source of the fluids present during the recrystallization of minerals, and also to constrain the isotopic equilibrium temperatures between minerals and fluids.

1. Sampling strategy and microstructural study:

Three field campaigns have led to the recognition of different units and / or fabrics characterizing extensional shear zones. Macroscopic observations in the field have controlled the sampling strategy. While sampling, microstructural measurements (foliation, stretching lineation, slip plane, fault planes,...) have been performed systematically on ductile and/or brittle fabrics in order to characterize the paleostress evolution associated with the activity of the detachment.

1.1. Paleostress analysis with T-Tecto 3.0:

The results presented in the chapter III were obtained using T-Tecto 3.0 software (Zalohar, 2008). Processing the brittle microtectonic measurements allows accessing the direction kinematic axes and paleostress fields according to the Multiple-Slip-Method (MSM). The MSM is an extension of methods from Kostrov (1974), Molnar (1983), as well as a method proposed by Marrett and Allmendinger (1990, 1991) and Cladouhos and Allmendinger (1993). The best-fit paleostress and paleostrain tensors are determined by fault-slip data inversion.

1.2. Microstructural study using an optical microscope:

Thin sections were produced at the University of Lausanne. The microstructural analyses at the grain scale were carried out using a polarized light microscope. Microscopic observations allow us to highlight the evolution of textures and fabrics (either ductile or brittle) that affect the different units of the detachments.

2. Preparation of samples:

The following protocols are largely based on the protocols present on the Modus Operandi section of the Centre d'Analyse Minérale website (<http://www.unil.ch/cam>), differences rely on slight differences according to the experience's user and the precision required for different type of analysis.

2.1. Hydraulic press:

2.1.1. Preparation before crushing:

Samples are cut using a diamond saw for rocks (the one to make the chips of thin sections) to produce pieces smaller than 5x5x5 cm. Indeed, the pyramid-shaped pieces are

easier to crush. The limit of 5 cm comes from the ring of protection. For all samples, any parts of alteration or pieces marked by permanent marker were removed.

2.1.2. Crushing rocks:

The pieces of rock are laid out onto the support base, surrounded by a protective ring to: a) avoid putting fingers into the press during pressing, and, b) prevent the rock pieces to go in all directions. The ring is well positioned in order to avoid it being pressed by the piston.

The control lever is turned in the horizontal position "down" and the piston starts to crush the rock. A hand has to be kept on the lever during the entire process, which permits to stop pressing immediately if problems arise. The lever is turned to "neutral" position (middle position) as soon as the sound of the crushing stops. Then, the lever is turned in position "up" until the protective ring can be removed. The crushed items are pushed in the tray with the small metal spatula, the pieces larger than 5 mm are put on the base and pressed again.

Between each sample, the table and all of the press pieces are brushed using a soft brush. The base support is removed and the piston and the base support are vigorously brushed with a wire brush, followed by a wet paper towel to remove completely the dust and metal deposit. The rock dust can be removed with compressed air with an emphasis on the support of the piston and the base support.

2.2. Grinding:

The work surface is cleaned with a wet tissue and dried with a paper towel; the ventilation has to be switched on. A paper sheet protects the work surface; one more is also placed above in order to recover the rock powder (to be changed between each sample). All the vessels (including the grinder) are cleaned with water and dried, and are ready to complete the filling, or remove the rock powder from the tungsten grinder.

Using the scale, approximately 60 g of material to be ground is weighed on paper. This amount of rock has to be distributed in the central area of the grinder, between the central cylinder and the ring, taking care not to leave any rock powder on top of the central cylinder or on the ring.

The grinder is placed on its base in the middle of the mill and the lever is lowered. During this operation, it is preferable to place a paper (A4 sheet folded three times, in 8 layers) between the base of the lever and the grinder in order to prevent the escape of dust from the grinder. The milling time is programmed using the timer. The typical time is about 5

seconds for stable isotopes analysis (fraction has to remain larger than 100 microns) and 30 to 60 seconds according to the stiffness of the rock being ground for bulk-rock analysis (fraction has to be smaller than 40 microns). This operation has to be repeated until the desired particle size is reached in a sufficient amount.

Between each sample, the table and all the pieces of the tungsten grinder are cleaned with water and brushed using a soft brush and finally dried with compressed air.

3. Mineral separation:

The mineral separation has been performed using a Frantz magnetic separator. All the pieces of the Frantz are cleaned with ethanol, in order to remove any type of grease that could retain the grains on the glide surfaces. Consequently, once the pieces are cleaned, they are not handled with naked hands to avoid contamination of cleaned surfaces. The work surface is cleaned with a wet tissue and dried with a paper towel. Paper is also used to protect the work surface; one piece of paper is placed over the work surface but underneath the magnetic separator in order to recover the rock powder (to be changed between each sample).

Before starting the magnetic separation, the sieved grains of a selected sample are washed in a beaker with water. For particle size smaller than 250 microns, a drop of liquid soap is added to the water, in order to lower the surface tension of the water and assure that phyllosilicates can sink. This action has to be repeated two to three times, until the water remains clean. The sample in the beaker is rinsed with pure ethanol in an ultrasonic tank for 30-60 seconds. Once the ethanol is decanted, the wet sample is disposed on a paper and dried under an infrared light. When the sample is dry, it has to be sieved. It is up to the user to select the particle size that has to be separated; this as a function of the grain size of the given sample.

For the samples analyzed in this thesis, the first set-up for the Frantz magnetic separator are: 10° inclination on the short axis and 5° inclination on the long axis; the amperage is fixed at 1A. Such a setup allows pure quartz and feldspar grains to be separated from the other minerals containing iron (“magnetic fraction”). Once the totality of the sample went through the magnetic separator, the set-up of the Frantz is changed for a second passage of the former “magnetic” fraction: inclination remains unchanged for both axis but the amperage is lowered to 0.5A. The “non-magnetic” separate obtained with the second setup now contains the phyllosilicate fraction while minerals richer in iron such as magnetite, hematite, garnet, etc. still remain in the “magnetic” fraction. This approach is repeated at higher amperage to

separate other targeted minerals. The Frantz magnetic separation can be combined with a sub-horizontal shaking table in order to increase the purity of the separates, notably the mica separation. The shaking table has to be previously cleaned with ethanol, for the same reason as was given for the Frantz. Phyllosilicate as sheet-like minerals will tend to be displaced horizontally along the micro-corrugations, while the non-platy minerals such as quartz and feldspar grains roll down and fall into a collecting rail. Consequently, one rail is collecting the “non-platy” minerals such as quartz and feldspar, and another rail collects the platy sheet-silicates. Beakers are placed at the extremity of both rails in order to collect the separates.

The Frantz magnetic separation and the shaking table separation have to be repeated until the desired degree of purity (>95%) is attained. If such a purity of separate cannot be reached, which is often the case, a final separation is done by hand-picking using a binocular microscope.

Such separates of >95% purity were used for the stable isotope analysis. All the stable isotope analyses were performed in the Stable Isotope Laboratory at the University of Lausanne, Switzerland.

4. Rock chemical composition, mineral assemblages and single grain analyses:

Bulk-rock analyses were performed by X-ray fluorescence (XRF) over 22 samples (at least 2-3 samples per rock type to be representative), and provide the concentration of 13 major elements and 23 traces elements. Bulk-rock analyses were used to examine the compositional changes and mass/volume changes related to fluid flow during the detachment activity. In parallel, the X-ray diffraction (XRD) on the same samples permits to semi-quantitatively determine the mineral proportions in the rocks. XRD has been used to identify changes in mineral proportions relative to the strain history. Single grain analyses were performed with an electron microprobe, to identify compositional variations on a sample to grain scale.

4.1. X-ray fluorescence:

Major and trace element concentrations were determined by X-ray fluorescence spectrometry, using a X-ray spectrometer Philips PW2400 at the University of Lausanne. Measurements of trace elements are done on pressed powder tablets of 4 cm in diameter, or melted tablets for determination of major elements. Their production requires a quantity of

powder of 10-15 g, with a grain size lower than 80 μm . XR fluorescence analysis was done using a Rhodium (Rh) anode as X-ray tube, which is a good compromise for light elements (major) and heavy elements (traces). Detection limits are at approximately 0.01% for majors and 1 to 5 ppm for trace elements.

4.2. X-Ray Diffraction:

Mineralogical analyses were performed at the University of Lausanne using a X-TRA Thermo-Arl Diffractometer following the Kübler's procedure (Kübler, 1987; Adatte et al., 1996) with an accuracy better than 5%. Measurements were done on fine-grained powder tablets (<80 μm) for each sample.

4.3. Microprobe:

Qualitative and quantitative microchemical observations of mica were gathered using a Jeol-8200 Electron Microprobe in the Geoscience Department, at the University of Bern (CH). Compositional measurements of the mica grains were made using the electron microprobe; specific mica (biotite, muscovite, and chlorite) and epidote grains were selected for analysis based on geometry. Operating conditions of mica analyses were 15 kV and 15 nA, to avoid beam damage during the 90 second total analysis time. In addition, microprobe analyses of single grains have been conducted on transects perpendicular to the mica cleavages, using approximately 10 μm steps. Standardization was performed with the following standards: SiO_2 : H081_anor81; MgO : H015_fors15; K_2O : H088_orth88; F: H035_phlog35; FeO : H101_alma101; TiO_2 : B45_ilme45; Al_2O_3 : H081_anor81; CaO : H081_anor81; Na_2O : H003_albi3; MnO : H044_teph44. The accuracy of major element determinations is better than $\pm 1\%$ of the total values.

5. Stable isotopes analyses:

Stable isotopes compositions are used to interpret the characteristics of fluid-rock interactions. Coupling oxygen and hydrogen isotope compositions is a powerful tool, because aqueous fluids are rich in these elements that they can profoundly modify the host-rock isotopic composition. The hydrogen isotope composition of hydrated minerals permits the source of the fluid which had interacted with the mineral during its growth to be estimated. While the oxygen isotope composition permits to compute the isotope equilibrium

temperature for a difference in composition between two minerals, or between a mineral and a fluid as well as the determination of the isotopic composition of the fluid and hence its origin.

5.1. Fluid inclusions extraction:

Samples selected for fluid inclusion extraction were previously handpicked in order to isolate at least one gram of pure quartz in order to avoid possible contamination during extraction. The weight of analyzed samples ranged between 1 and 2 grams. And the sample has to be dried overnight at 70°C before being placed in the extraction line.

The pure silica glass tube containing the sample is fixed on the extraction line and the sample evacuated to a vacuum of better than 10^{-3} mbars while heated to about 110°C. A liquid nitrogen trap ($\sim -195^\circ\text{C}$) is placed on the extraction line to trap the H_2O , CO_2 and possibly other gases such as SO_2 extracted from the sample. The sample is step-heated from 300, 400, 450°C up to 800°C in order to distinguish the amount of extracted fluid at each step by its pressure rise. H_2O is then extracted from the fluid inclusions by heating the quartz samples in vacuum to temperatures in excess of 650 to 800°C and, after distillation under vacuum from CO_2+CH_4 (latter oxidized at 760°C using CuO), it is trapped within a 6 mm (outside diameter) Pyrex® tube containing approximately 150 mg of zinc shavings. The exposure of the residual gases not trapped with liquid nitrogen in the first U-trap to heated CuO converts the H_2 as well as CH_4 to H_2O and CO_2 . The water fraction of H_2 and CH_4 is separated together with water directly obtained from the fluid inclusions while the CO_2 from CH_4 is transferred with the rest of the CO_2 . The CO_2 and CH_4 converted to CO_2 using CuO are trapped in a different small Pyrex® vial. Another vial containing 2-5 grams of fine silver phosphate powder is used to trap SO_2 from the CO_2 and CH_4 gas fraction, as this would inhibit proper analyses at the mass spectrometer.

5.1.1. Extraction of CO_2 :

Liquid nitrogen and ethanol are mixed in order to reach a temperature for the cold trap of about -75°C . The liquid nitrogen trap (-195°C) is then replaced by the trap at -75°C on the first U-trap of the vacuum extraction line. Consequently, the CO_2 previously trapped will sublime while H_2O and any SO_2 will remain trapped. If the amount of CO_2 extracted is sufficient (measured using a vacuum manometer) for analysis, the CO_2 is transferred into the CO_2 vial using vacuum distillation and a liquid nitrogen trap. To ensure a complete transfer of CO_2 in the receiving vial, 3 minutes are required for the transfer. The trap is then removed

and the vial isolated by melting the glass with a torch. The CO₂ vial is then ready for analysis on the mass spectrometer.

5.1.2. Elimination of SO₂:

If SO₂ is present with H₂O during the oxidation of Zn before moving the vial to the mass spectrometer, it interferes with the hydrogen isotopic analysis. SO₂ has to be removed from the extraction line by a reaction with silver phosphate powder at room temperature. Since it is not possible to predict if the sample contains SO₂ or not, all samples were treated in the following way:

The H₂O and possibly SO₂ that remained trapped in the U-trap at -75°C are vacuum distilled to the vial containing the silver phosphate and using liquid nitrogen. 3 minutes are allocated for transferring the gas phases. The vial is then closed and the liquid nitrogen trap removed. Then about 5 minutes are allowed for the gases to react with the silver phosphate powder at room temperature. The silver phosphate powder then traps the SO₂ and only H₂O remains in the vial. This will be transferred to the zinc-containing vial.

5.1.3. Extraction of H₂O:

H₂O present in the vial containing the silver phosphate powder has to be transferred back to the zinc-containing vial with the help of liquid nitrogen and vacuum distillation. This step requires at least 5 minutes for transferring H₂O because the water tends to condense on the walls of the vials and between the grains of silver phosphate powder, even at very low pressure or vacuum. Using a hair-drier as heat source to warm the vial's walls and extraction line during the 5 minutes transfer can speed up the evaporation and enhances the transfer.

Once the transfer of H₂O is done, the vial is sealed with the help of a gas torch, and finally the cold trap is removed. The H₂O vial obtained is then placed in an oven at 500 °C for 15 minutes in order to oxidize the zinc and convert water to hydrogen gas for analyses on the mass spectrometer.

5.2. Oxygen isotope analyses:

The δ¹⁸O values of minerals were measured using a CO₂-laser fluorination line coupled to a Finnigan MAT 253 mass spectrometer. At least two standard quartz samples (NBS 28: 9.64‰) were used for each run; most of the pairs were measured during the same run with 1-2 mg of material. Samples were loaded in pits within a platinum sample holder, which was

dried in an oven (110°C) for an hour after loading, and then placed in the chamber. The chamber was evacuated to a vacuum of about 10^{-6} mbar for a minimum of one hour, and then pre-fluorinated overnight (50 mbars of F₂). Samples were heated with a CO₂-laser in about 50 mbars of F₂ by rastering the beam over the entire sample. Oxygen liberated was purified through an extraction line, by passing the gas over heated KCl salt (T = 150 °C) to react out the F₂ as chlorine gas (Cl₂). Oxygen was then absorbed onto a molecular sieve 5Å held at liquid nitrogen temperatures (-196°C). O₂ was expanded into the inlet of the Finnigan MAT 253 mass spectrometer. Stable oxygen isotope ratios are reported in the delta (δ) notation as the permil (‰) deviation relative to the Vienna Standard Mean Ocean Water (VSMOW).

The analytical reproducibility obtained by standard measurements was better than 0.2 ‰ but for some analytical results better than 0.1 ‰. Deviations from the expected standard value were observed, and results obtained on samples were therefore corrected for this bias.

5.3. Hydrogen isotope analyses:

The δD values of hydrated minerals were measured with a TC-EA (high temperature reduction, thermo-chemical elemental analyzer) linked to a Finnigan MAT Delta Plus XL mass spectrometer. Each sample was weighed into a silver cup at between 1.5 to 3 mg, according to the weight percent of water in each hydrated mineral. Analyses were replicated and normalized with an in-house kaolinite (Kaolinite # 17: -125‰) and a biotite (G1: -66‰) standard. Replicate hydrogen isotope analyses of the standard used for the set of samples had an average precision better than 1 ‰.

5.4. Fluid inclusions analyses:

Hydrogen isotope compositions of the H₂O vials were analyzed using a Finnigan MAT 253 mass spectrometer as H₂. The analytical reproducibility obtained by standards measurements (MOW: 5.7 ‰; LIPE: -53.9 ‰; INH: -113.1 ‰) was better than 2‰ with some results better than 1 ‰. Results obtained on samples were corrected for the bias of the deviations from the expected standard value.

Carbon and oxygen isotope compositions of the CO₂ + CH₄ (latter converted to CO₂) vials were measured with a GasBench II linked to a Finnigan MAT Delta Plus XL mass spectrometer. The glass vials containing the gases were broken in an atmosphere of ultrapure He and the gas passed via a gas chromatograph to separate the CO₂ into the mass spectrometer. Analytical uncertainty (2σ) is better than 0.1 ‰ for δ¹³C.

Chapter III : Microstructural, paleostress and paleostrain evolution in an extensional shear zone: Insight from the Bitterroot shear zone (MT, USA).

Introduction:

The Bitterroot shear zone (BSZ), defined by a 500-1500 m thick zone of mylonitic rocks, is an ideal shear zone for studying a strain gradient associated with exhumation, since the protolith is considered as relatively isotropic. Several propositions of nomenclature of shear zone-related rocks have been proposed (Zeck, 1974; Sibson, 1977; White, 1982; Scholtz; 1990; Malavieille, 1983), and this topic remains controversial since a nomenclature has to take into account a wide range of parameters such as textures, deformation mechanisms, presence of fabrics or not, strain rate, recovery rate, and cohesion. The definition of mylonite, as proposed by Mawer (1986 a,b), accounts for the composite foliation and various kinematic indicators that are common features of mylonitic rocks. Mylonite occurs in shear zones and develops primarily by ductile deformation processes on a grain scale, although the intensity of mylonitization indicates considerable strain heterogeneity on that scale. Progressive mylonitization leads to local shear bands, corresponding to intensely foliated ultramylonite almost devoid of porphyroclasts (Sibson, 1979). Based on the classification proposed by Sibson (1977), Scholtz (1990) introduced a textural classification of fault rocks ranging from fault breccia to blastomylonite. This updated classification implies (Figure III-1) that both random- and foliated-fabric fault rocks can occur in the upper crustal, brittle regime; Sibson (1977) used distinguished fault rocks of the brittle frictional regime (random fabric) from those of the plastic regime (planar and linear fabric). Description of the different textures observed through the BSZ are based on the Scholtz textural classification, even if in this case, the fabrics do correspond to an evolution from plastic (ductile domain) to frictional regime (brittle domain), as defined by Sibson (1977). The recognition of the different fabrics in the field defined the sampling strategy in order to study, at both the macroscopic and microscopic scales, the deformation mechanisms that are related to the different fabrics.

		Random fabric		Foliated		
Incohesive	Fault breccia (visible fragments > 30% of rock mass)		?			
	Fault gouge (visible fragments < 30% of rock mass)		Foliated gouge			
Cohesive	Nature of matrix	Glass-devitrified glass	Pseudotachylyte		?	
			Crush breccia (fragments > 0.5 cm) Fine crush breccia (0.1 < fragments < 0.5 cm) Crush microbreccia (fragments < 0.1 cm)		0-10	
	Tectonic reduction in grain size dominates grain growth by recrystallization and neomineralization	Cataclasite series	Mylonite series	Protocataclasite	Protomylonite	10-50
				Cataclasite	Mylonite	50-90
				Ultracataclasite	Ultramylonite	90-100
Grain growth pronounced	?		Blastomylonite			
			Percent of matrix			

Figure III-1: Classification of fault rocks by Sibson (1977), and updated by Scholtz (1990).

Variations in parameters such as strain rate, temperature or effective pressure influence the deformation mechanisms in extensional shear zones. Deformation mechanisms include cracking and frictional sliding, pressure solution, dislocation creep, diffusion creep, creep cavitation, and grain boundary sliding. Each of these deformation mechanisms is characterized by a distinct set of microstructures and a specific range of pressure-temperature-fluid conditions. There are relatively few grain scale deformation mechanisms that combine to allow the large-scale deformation of a heterogeneous rock mass (Schmid, 1982; Knipe, 1989). However, different deformation mechanisms from brittle deformation to dislocation creep (ductile) may take place synchronously. Cataclasis of strong minerals, such as feldspar, can occur simultaneously with crystal-plastic deformation and dynamic recrystallization of weaker minerals, such as quartz or phyllosilicates (Simpson, 1985, Nyman et al., 1992). (Figure III-2). Thus, the competition between strain rate and rate of recovery or recrystallization is a major parameter of the texture of rocks related to shear zones.

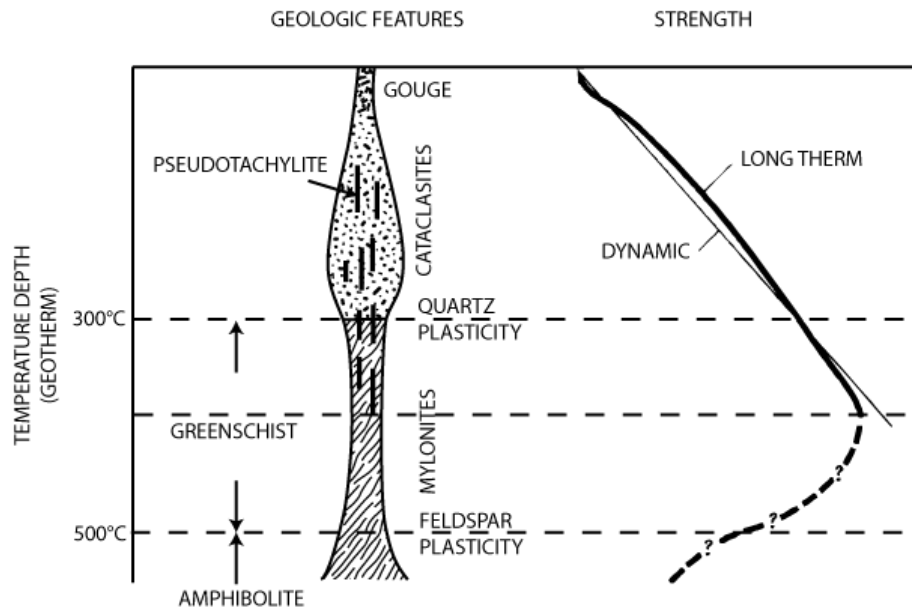


Figure III-2: Synoptic model of a shear zone (after Scholtz, 1988).

1. Geological setting:

During the Eocene, collapse of the North American Cordillera produced crustal thinning on the orogen scale and generated exhumation of metamorphic core complexes (MCC) as well as magma-dominated domains, such as the Idaho-Bitterroot batholith. Denudation of the batholith occurred dominantly by extension on the Bitterroot shear zone (BSZ) (Foster et al., 1997, 2001, 2007). In the study area, the shear zone and its footwall consist of the Bear Creek pluton (Toth, 1983), which occupies a part of the Bitterroot lobe at the eastern end of the Idaho-Bitterroot batholith (Figure III-3). The hanging wall of the BSZ consists of the approximately 15 km thick Sapphire block, which is made up of Belt Supergroup (Hyndman, 1983). Near the BSZ, the Belt metasediments are metamorphosed to amphibolite facies and intruded by numerous dikes and other granite bodies that emanated from the underlying Idaho-Bitterroot batholith. Further east, the Sapphire block contains only slightly metamorphosed Belt sequences. The BSZ is a 500-1500 m thick mylonite zone that accommodated eastward displacement of the Sapphire block from the roof of the Idaho-Bitterroot batholith (Figure III-4); in the study area mylonitization is restricted to variously sheared Bear Creek pluton. The Bear Creek protolith is a late Cretaceous to Eocene granodiorite intrusion (Toth, 1983). The pluton intruded at depths of 17-25 km (6-8 kbar) between 75 and 48 Ma (Chase et al., 1978; Hyndman, 1983; Foster and Fanning, 1997) and defines the Bitterroot lobe.

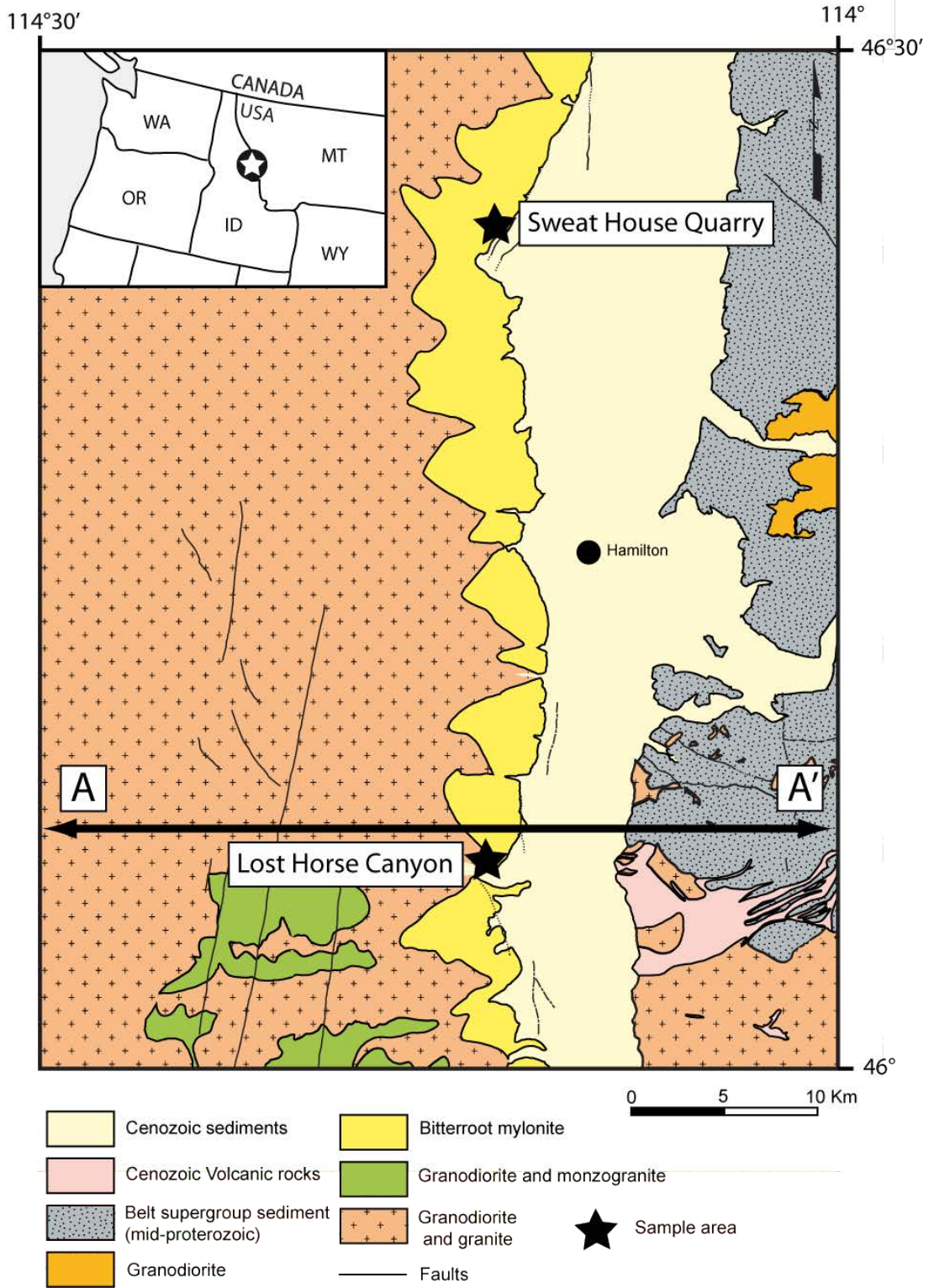


Figure III-3: Simplified geological map of the Bitterroot valley (adapted from Toth, 1983).

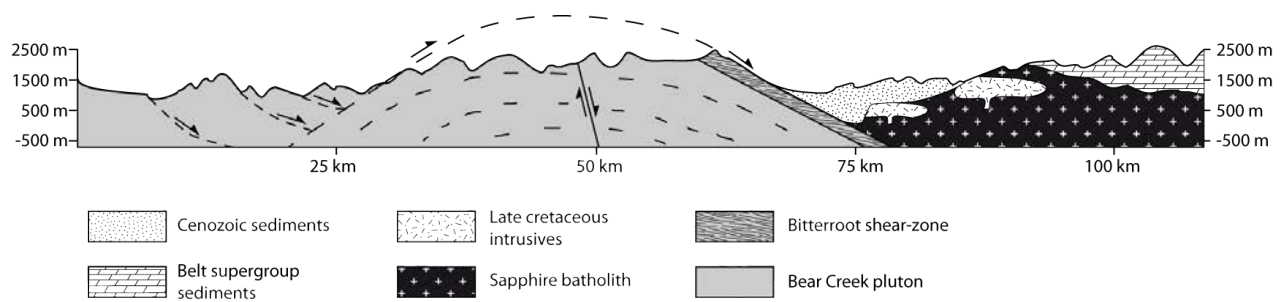


Figure III-4: Schematic W-E cross-section of the Bear Creek pluton and Sapphire pluton (A-A' transect in Figure III-3 corresponds to km 40 to 100 on this cross-section), the BSZ defines the contact between these two plutons (adapted from Foster et al., 2001, 2007).

The Bear Creek pluton is defined by a two-mica granodiorite and contains a magmatic foliation that is commonly defined by alignment of biotite grains (Figure III-5). The average magmatic foliation defines a N-S elongated dome (Sidman et al., 2005) (Figure III-4), as evidenced by decreasing metamorphic grade in those directions and by the curvature of cooling age distributions (Foster and Raza, 2002). The Bear Creek pluton was intruded by Eocene epizonal plutons, such as the Paradise pluton in the southern margin of the Bitterroot lobe, and by syntectonic mafic dikes that are randomly oriented in the batholith (Toth, 1983; Garmezy, 1983; Foster and Raza, 2002; Foster et al., 2007). A few normal faults affect the Bear Creek pluton and contain quartz veins with lobate edges.



Figure III-5: Two micas granodiorite of the Bear Creek pluton.

A 500-1500 m thick mylonite zone defines the BSZ and extends ~100 km north-south along the Bitterroot valley, with a fairly constant dip of 20-30° to the east. Sampling was conducted at two localities across the BSZ. The Lost Horse canyon traverse (Figure III-3) provides ~1000 m of structural section with a fairly continuous deformation gradient upward from the undeformed footwall granodiorite to protomylonite, mylonite, and ultramylonite, although mylonite and ultramylonite alternate locally.

In the Lost Horse Canyon section, the protomylonite zone represents a progressive transition, over ~200 m, between the undeformed granodiorite and the mylonite-ultramylonite sequence (Figure III-6). Protomylonitic deformation occurred at high temperature (~600°C) probably prior to pegmatite complete crystallization (LaTour and Barnett, 1987; Hyndman and Myers, 1988). Deformation took place initially under amphibolite-facies conditions during the late stage of magmatic crystallization of the footwall plutons (Kerrick and Hyndman, 1986, LaTour and Barnett, 1987, Foster et al., 2007). Strain localization under greenschist-facies conditions leads to the development of ultramylonite bands characterized by a decrease in modal proportion and grain size of plagioclase and K-feldspar porphyroclasts. Ultramylonite bands are present near the base of the mylonitic shear zone, but ultramylonite-mylonite alternations are more common at the top of the section (Figure III-6). The mylonite and ultramylonite fabrics affecting the granodiorite indicate increased strain localization from the deepest structural units toward the detachment. Metabasite dikes and pegmatite veins are partially to totally transposed into the mylonitic foliation (Figure III-7) and affected by intense planar and linear fabrics with top-to-the-east shear indicators (sigmoid porphyroclasts, S-C fabrics, shear bands). Cataclasite zones are parallel or oblique to the mylonitic foliation and occur from the base to the top of the Lost Horse Canyon section. However, cataclasite zones are more pronounced and abundant at the top of the section.

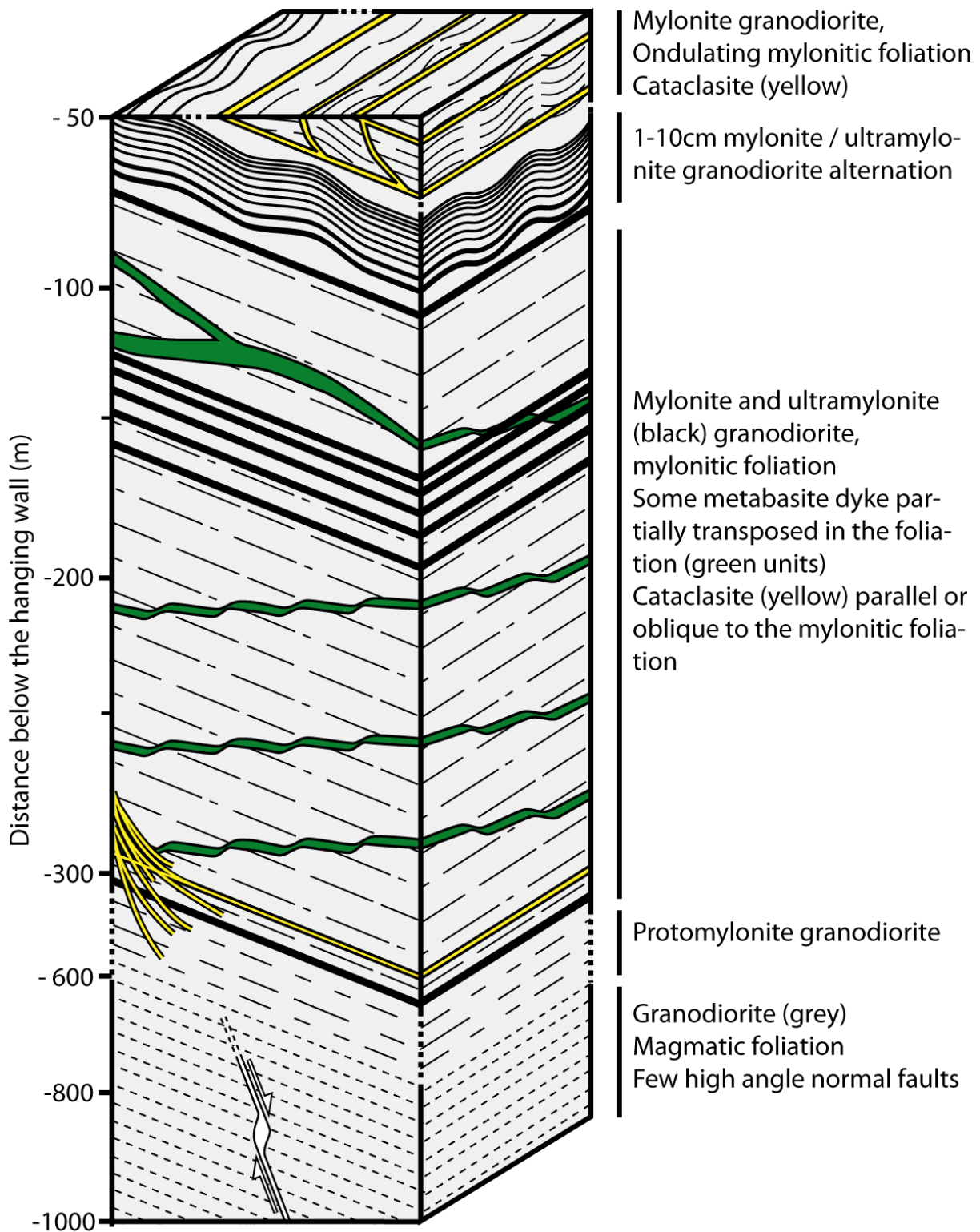


Figure III-6: Schematic block diagram of the Lost Horse Canyon section.

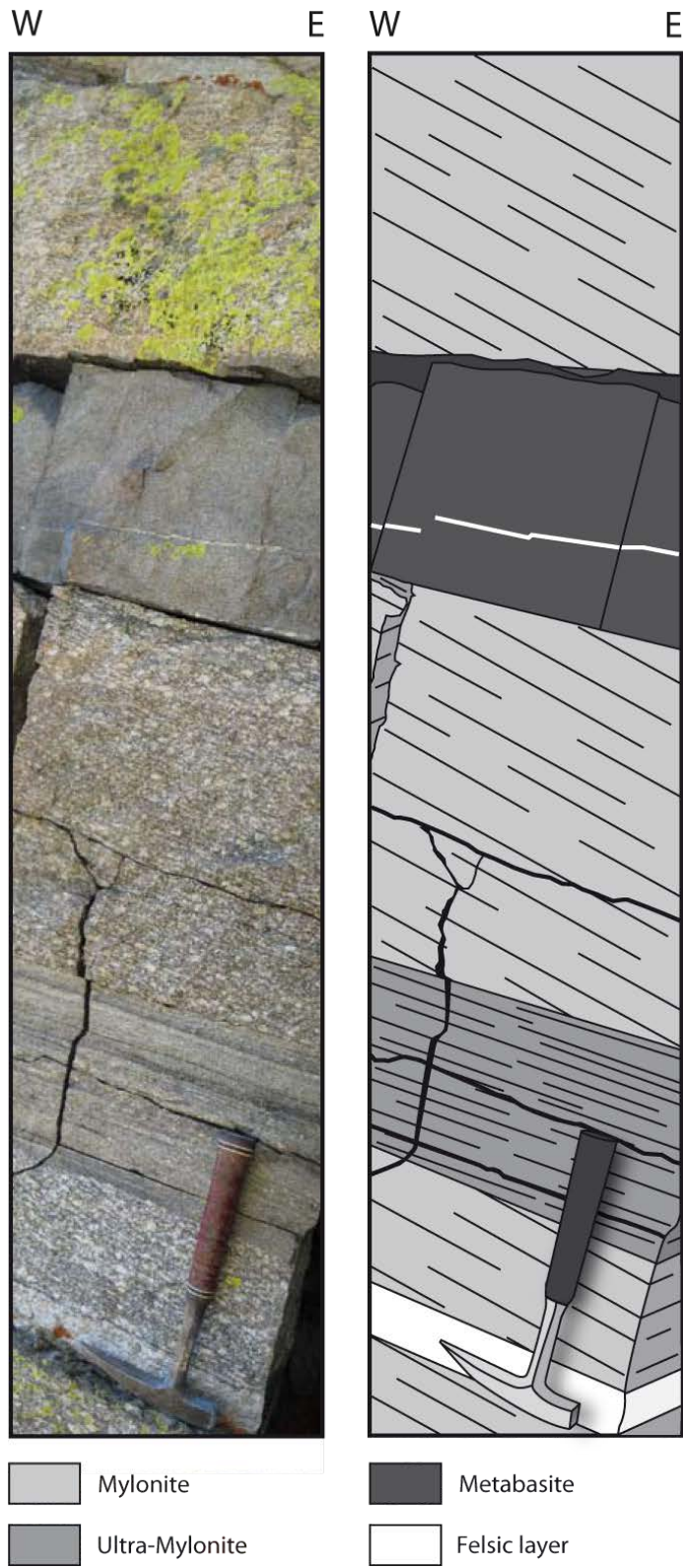


Figure III-7: Composite photograph and corresponding schematic view of the characteristic alternation of mylonite, ultramylonite, metabasite and felsic layers in the BSZ.

In both sections, mylonite and ultramylonite foliation measurements are constant throughout the BSZ. The average strike and dip of the mylonitic foliation is 018/22E, with a stretching lineation trending N119 (Figure III-8). The $\sim 11^\circ$ difference between the plunge direction of the mylonitic foliation (N108) and the stretching lineation indicates a slight dextral component of the BSZ.

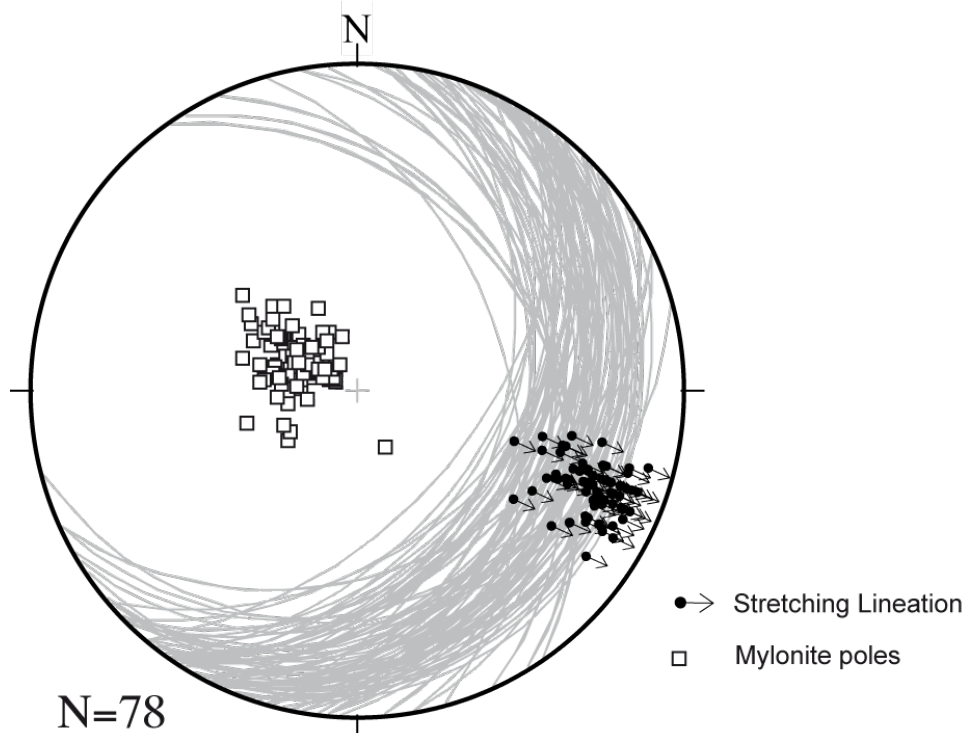


Figure III-8: Stereonet showing the mylonite and ultramylonite foliation data.

The upper part of the BSZ was sampled at the Sweathouse quarry (Figure III-3), which displays ~ 100 m of section. The Sweathouse quarry is of specific interest since it is the only place along the BSZ where chloritized breccia has been preserved and lies structurally above the mylonitic shear zone (Figure III-9). The brittle structures affecting the granodiorite mylonite are chlorite tension gashes and veins, several generations of quartz veins, and high-angle conjugate normal faults (Figure III-9). The volumetric proportion of chlorite in the breccia is less than 5 % (Kerrich and Hyndman, 1986), but the breccia contains epidote in greater quantity. Fragments of mylonite in the breccia indicate that mylonites were brecciated at low greenschist-facies conditions, at temperatures of 100 to 300 $^\circ\text{C}$ in the brittle regime (Kerrich and Hyndman, 1986). Given the high degree of silicification of this unit, which is very resistant to erosion as a result, and the presence of abundant chlorite and epidote, it is highly probable that the breccia experienced intense fluid-rock interaction.

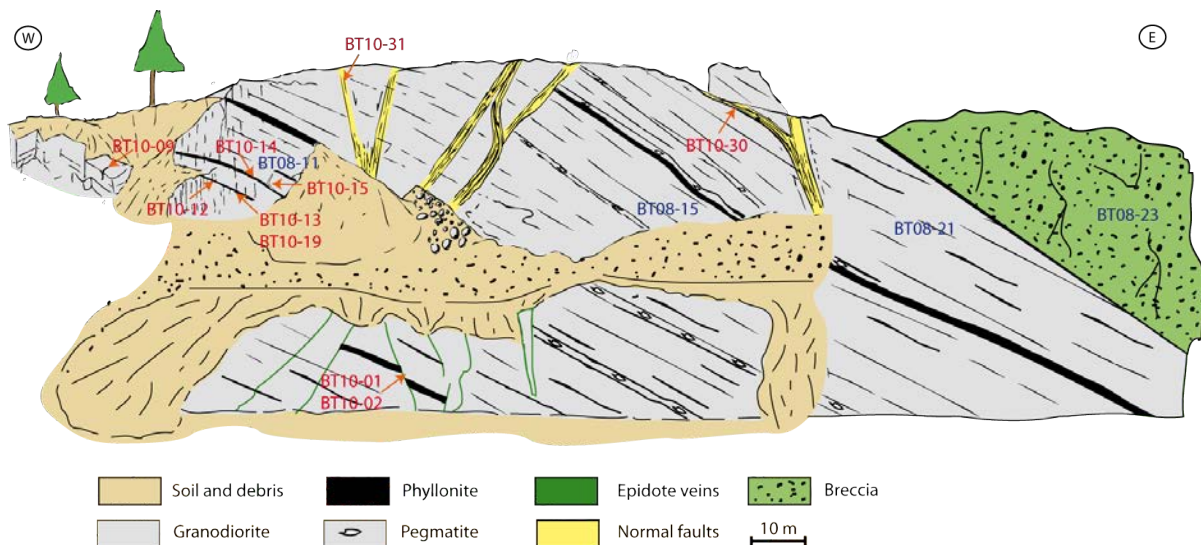


Figure III-9: Schematic drawing of the Sweathouse quarry, with sample numbers.

Combining the Lost Horse Canyon and the Sweathouse quarry sections offers a complete overview of the ductile to brittle fabrics that affected the Bear Creek pluton during exhumation. In the next section, a description of structures and microstructures in the different mylonitic states of the Bear Creek pluton provides a framework in which the analysis of fluid-rock interaction was conducted in this study.

2. Ductile and brittle fabrics of the Bitterroot shear zone:

Fabrics observed across the BSZ are described in this section on outcrop scale and also using a microscope. The mineral composition was determined petrographically and with the use of X-ray diffraction (see chapter IV.2 for more detail).

The Bear Creek pluton is a two-mica granodiorite in the Bitterroot lobe and contains plagioclase (~48%) and K-feldspar megacrysts (~27%), up to a few centimeters in size, quartz (~21%) with variable grain sizes (0.01 up to 0.1 mm), phyllosilicate (muscovite, biotite, chlorite, <0.1 mm long) (~3%), and accessory minerals (1%). The granodiorite shows magmatic textures with K-feldspar megacrysts surrounded by reaction aureoles defined by plagioclase, quartz, and phyllosilicates (Figure III-10), and myrmekitic aggregates (Simpson, 1985). Phyllosilicates are either included or located at the vicinity of K-feldspar minerals. Plagioclase, quartz, and phyllosilicates define a matrix surrounding K-feldspar megacrysts (Figure III-11A). Chloritization of biotite is highlighted by chlorite in interlayers of biotite or by complete chloritization of biotite, and is probably associated to retrogression during exhumation. Since the aim is to differentiate the fabrics characterizing the BSZ, the two-mica granodiorite of the Bear Creek pluton is referred to in this study as the “protolith”.

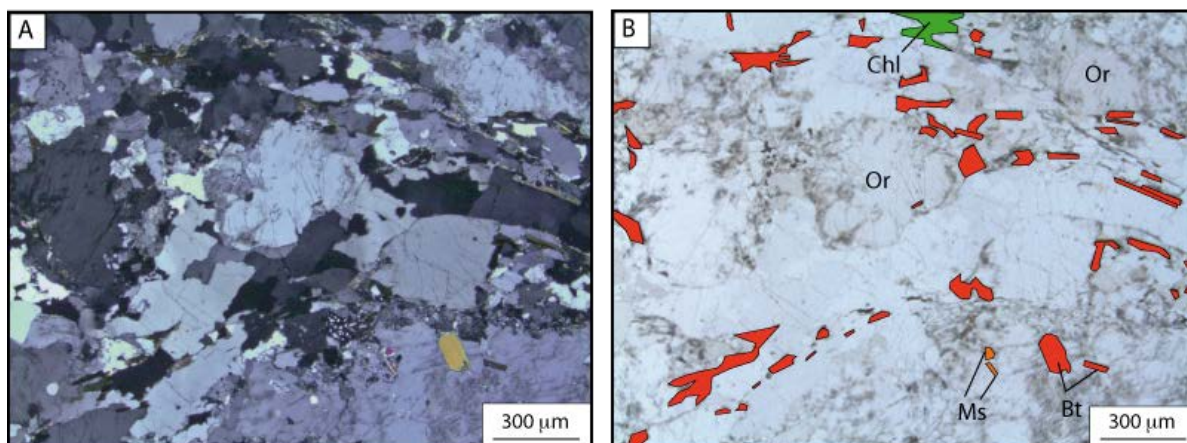


Figure III-10 : A. Photomicrograph of a protolith thin section, cut vertical and parallel to the magmatic lineation; B. Phyllosilicates are highlighted (muscovite, biotite, chlorite); top right corner corresponds to east.

2.1. Ductile fabrics:

2.1.1. The mylonitic series in the BSZ

Protomylonitic fabrics are present in the structurally lower part of the BSZ in the Lost Horse canyon section, where the granodiorite shows a weak to moderately developed foliation and lineation. Along this section continuity of fabric from magmatic to solid-state has been documented on the basis of the anisotropy of magnetic susceptibility fabrics (Sidman et al., 2005). The protomylonite is characterized by weak foliation and stretching lineation, with slight sigmoid-shaped feldspar porphyroclasts consistent with east-directed sense of shear (Figure III-11B). Given the continuity of fabrics from magmatic to solid state, the base of the BSZ is gradual; for our purpose here we define the base of the BSZ by the first appearance of the protomylonitic fabrics, located approximately 600 m structurally below the uppermost exposed portion of the mylonite zone (Figure III-6).

Mylonitic fabrics in the BSZ become more prominent upward across the shear zone and give way to ultramylonite zones toward the top of the section (Figure III-6). The transition between protomylonite and mylonite is marked by the occurrence of meter-thick mylonite zones; some thin bands (5-10 cm) of ultramylonite also exist. The top 400 m of the section is dominated by granodiorite mylonite (>90%), with ultramylonite bands (<10%) becoming thinner and more closely spaced toward the top. Mylonite and ultramylonite from the top 100 m of the Lost Horse section have the same characteristics as those in the Sweathouse section in terms of fabric development and orientation.

The mylonite samples of the BSZ show a relatively constant microstructure throughout the Lost Horse Canyon section, characterized by a matrix (> 50%) composed of phyllosilicates + quartz + plagioclase, dynamically recrystallized quartz and phyllosilicates (mica fish define S-C fabric), and grain-size reduction of K-feldspar porphyroclasts relative to the protolith (Figure III-12C). The microstructure of mylonite-ultramylonite at the top of the Lost Horse Canyon section, where mylonite and ultramylonite layers alternate with 1-10 cm spacing, shows a fine-grained matrix (> 80 %), a higher degree of grain-size reduction, and S-C fabrics that are more pronounced. Ultramylonite bands are melanocratic, rarely more than 20 cm thick, and show a well-developed foliation and stretching lineation on the sample scale. Ultramylonite bands have more than 90 % fine grained matrix, the feldspar porphyroclasts are a few millimeters in size, which indicates significant grain-size reduction, and have a sigmoidal shape consistent with top-to-the-east sense of shear (Figure III-13E).

Thin cataclasite zones are present in both the Lost Horse and Sweathouse sections, but the Sweathouse section offers unique exposure, in the Bitterroot Valley, of a thick and continuously exposed cataclasite zone. Well-developed cataclasite is an important observation in a detachment system, as it may represent the brittle-ductile boundary (White, 2001). In addition, quartz veins that are sheared to various degrees abound in the BSZ (both Lost Horse and Sweathouse sections) and are a good indication that fluids were present during deformation.

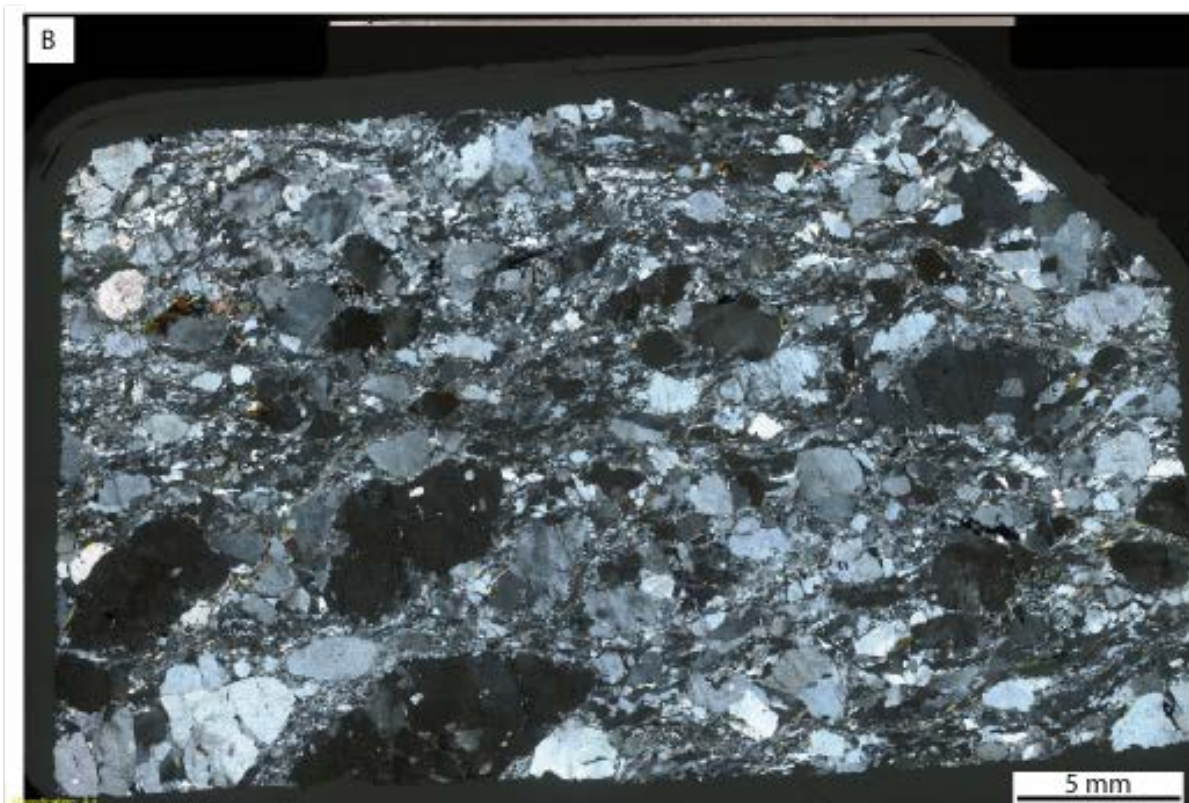
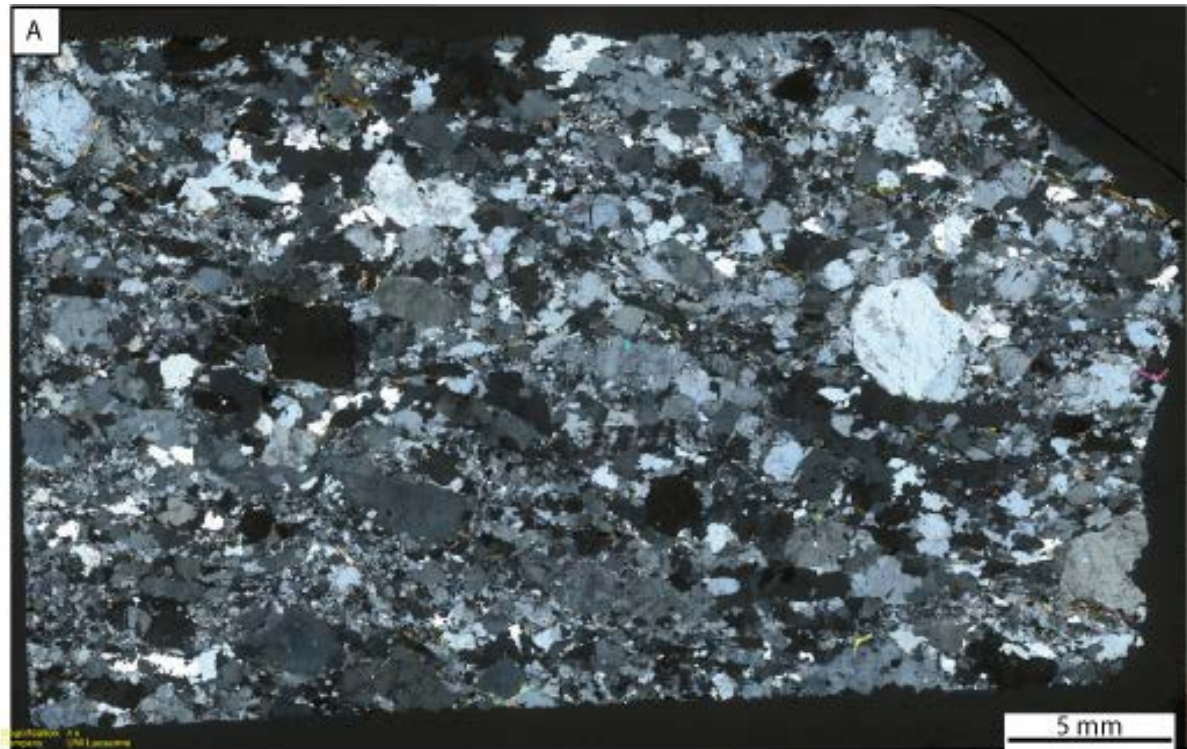


Figure III-11 : Scan of thin sections, crossed polars: A. Protolith (BT09-80) and B. Protomylonite (BT10-52), top right corner corresponds to top and east.

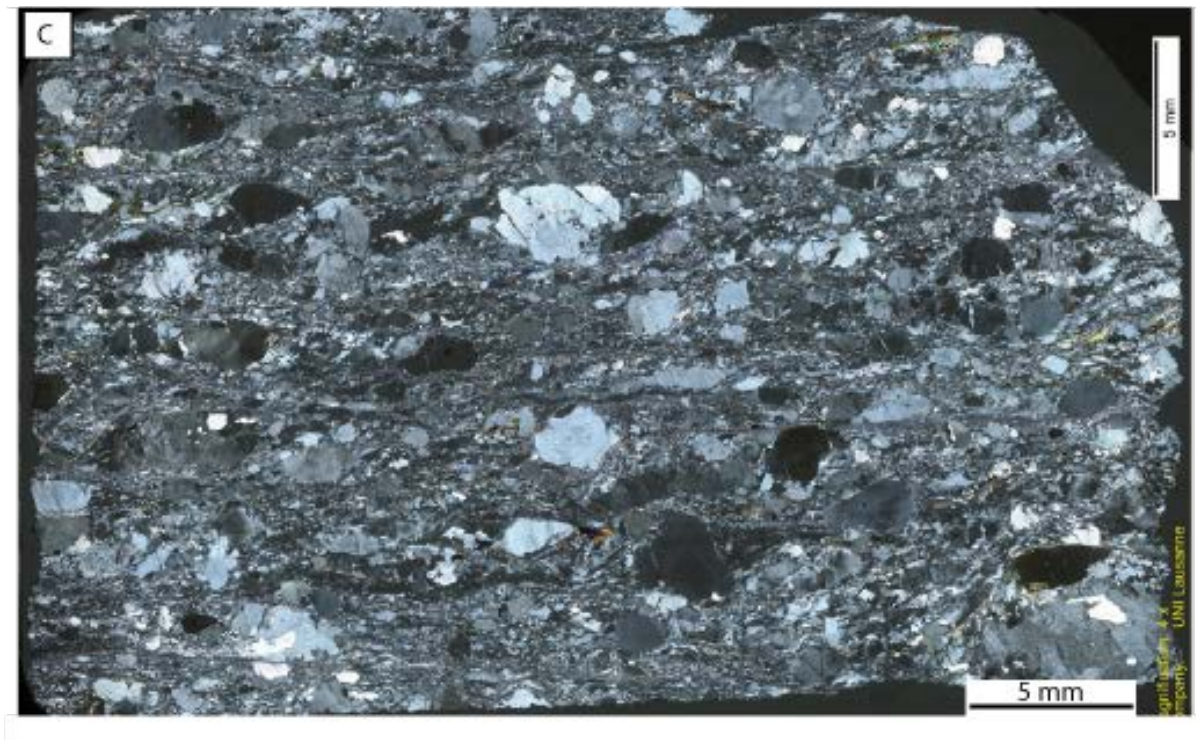


Figure III-12: Scan of thin sections, crossed polars: C. mylonite (BT08-80) and D. mylonite to ultramylonite (BT08-48), top right corner corresponds to top and east.



Figure III-13: Scan of thin section, crossed polars: E. ultramylonite (BT08-34), top right corner corresponds to top and east.

2.1.2. Protomylonite:

In terms of microstructure, the protomylonite differs from the protolith because of the development of local microshear zones and some sigmoidal feldspar porphyroclasts. Minerals of the protomylonite are principally in the same proportion to those defined for the protolith, except about 10 % of secondary minerals represented in, but not restricted to, microshear zones (Figure III-14A). Primary minerals are plagioclase, orthoclase, quartz, biotite, muscovite and Fe-Ti oxides, as well as minerals related to the deformation are plagioclase (including plagioclase in myrmekite, Figure III-14B), orthoclase, quartz, biotite and muscovite. Like the protolith, the protomylonite shows chloritized biotite, which likely relates to partial retrogression during exhumation. The fluid inclusion planes (FIPs) in feldspar porphyroclasts are sub-vertical, east-dipping, and constant from one grain to another. Bands of elongated quartz grains (0.2-0.5 mm) define discrete microshear zones (<1 cm long, <0.5 mm large), and biotite and muscovite fish are located at the vicinity of these microshear zones (Figure III-14A). Protomylonite fabrics overprint the magmatic fabric of the Bear Creek pluton granodiorite and is overprinted by mylonite and ultramylonite fabrics.

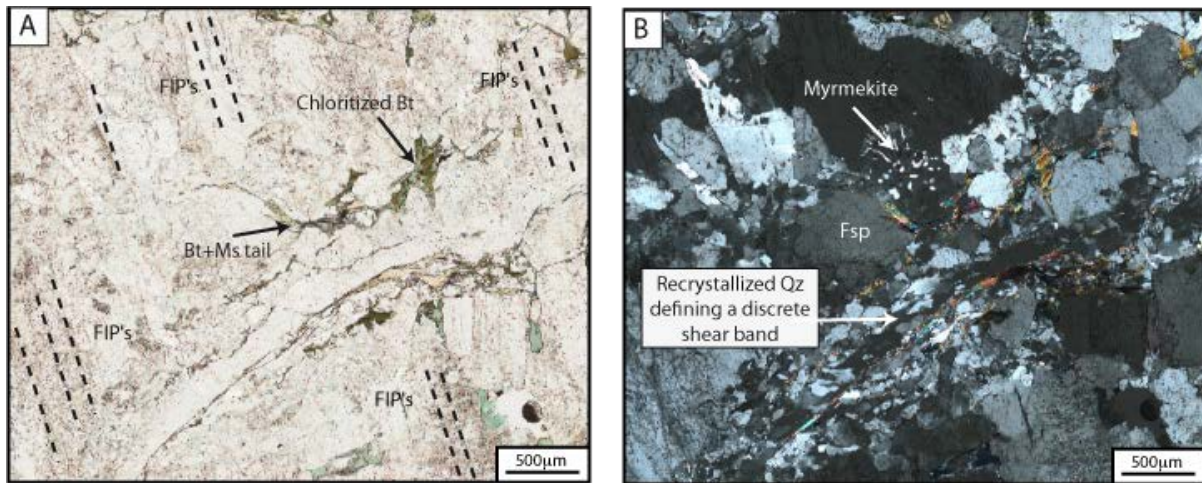


Figure III-14: Optical micrographs of a protomylonite thin section (BT10-52), perpendicular to the foliation and parallel to the stretching lineation, sense of shear is top-to-the-east (top right corner).

2.1.3. Mylonite:

Mylonite is defined by a pronounced foliation and strong stretching lineation, with C-S fabrics consistent with a top-to-the-east sense of shear. Compared to the protomylonitic granodiorite, the mylonite shows a fine-grained matrix that surrounds feldspar porphyroclasts, which average 1-3 cm in size (Figure III-15. B).

The granodiorite mylonite is quite uniform in composition and is composed of ~40 % plagioclase and 20 % K-feldspar porphyroclasts (0.3-5 mm), 30 % quartz with variable grain size (0.01 up to 0.20 mm), and about 10 % phyllosilicate (muscovite, biotite, chlorite; 0.1-0.3 mm), which is consistent with the XRD analyses presented in chapter IV. The granodiorite mylonite microstructure is characterized by C-S fabric, delineated by elongated quartz grains (0.1-0.2 mm) and muscovite fish (0.1-0.3 mm), and by C' bands defined by very fine (10 µm) quartz grains.

Quartz in the C-S fabric and C' bands shows variable grain size reduction at the thin section scale, compared to the undeformed granodiorite (Figure III-16). The nearly pure quartz ribbons that define the C shear bands have a uniform grain size (50 µm); quartz grains within ribbons are recrystallized, show triple-junction grain boundaries, and are either equant (Figure III-16A) or sigmoidal in shape (Figure III-16B).

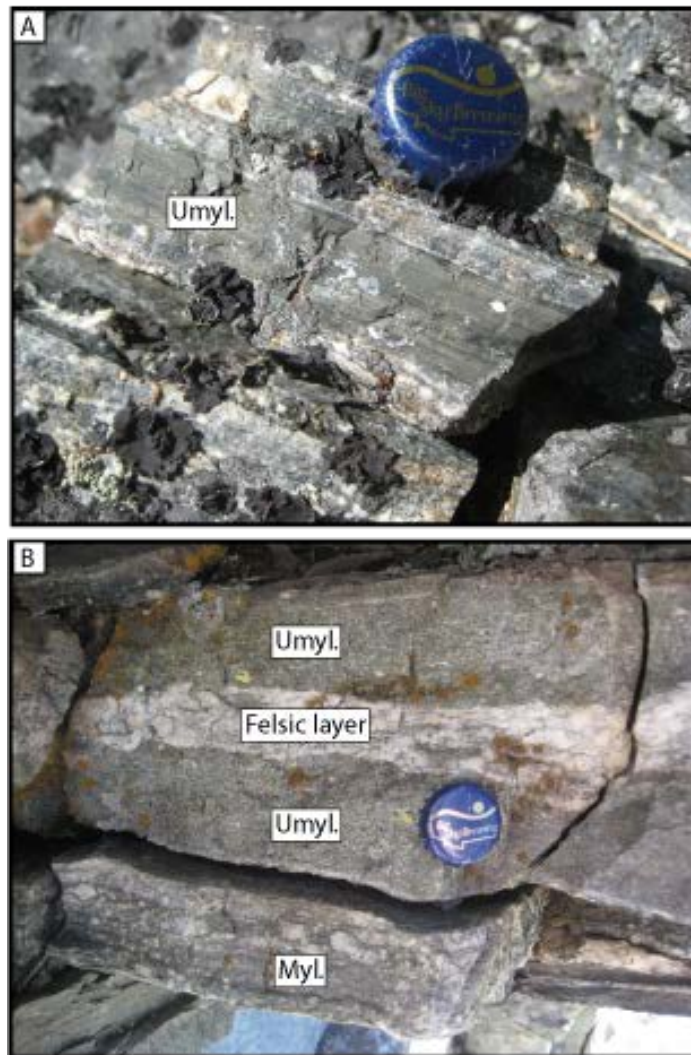


Figure III-15: Mylonite (Myl.) and Ultramylonite (Umyl.) spatial organization in the field. For A. and B., the right top corner represents east, the plane of the photo is perpendicular to the foliation and parallel to the stretching lineation.

The feldspar porphyroclasts show consistent orientations of FIPs within single grains, but these orientations are different from one grain to the other; this may indicate that feldspar grains rotated during deformation. The feldspar porphyroclasts are affected by brittle deformation, showing tilted blocks (dominoes) (Figure III-17A and B) and elongated asymmetric tails in their pressure shadows, consistent with the top-to-the-east shearing. The tails are characterized by $\sim 10 \mu\text{m}$ feldspar grains dispersed in a fine grain matrix of mica and quartz (Figure III-16A and B). The phyllosilicates + quartz tails in the pressure shadows of K-feldspar porphyroclasts suggest a combination of mechanical and chemical breakdown of feldspars in both the Sweathouse and Lost Horse granodiorite mylonites (Figure III-16).

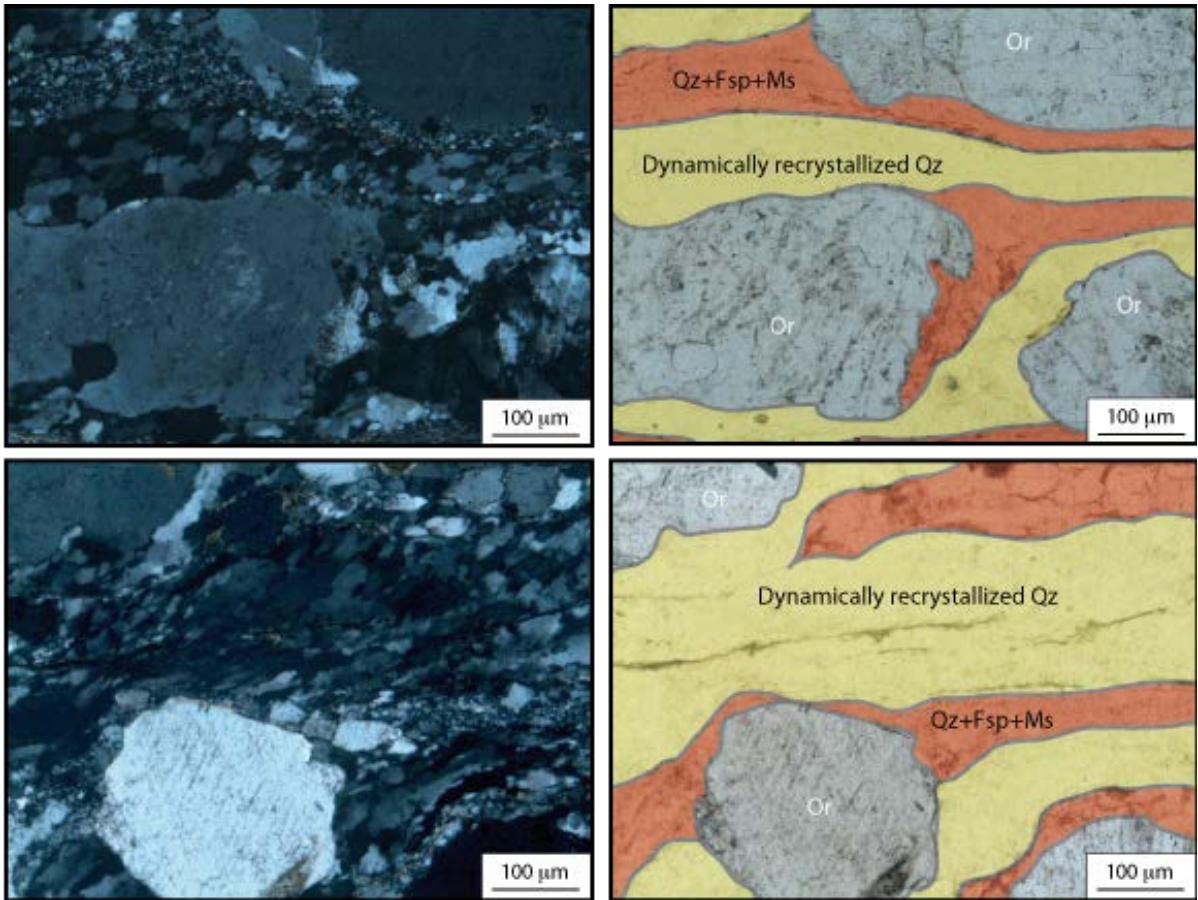


Figure III-16 : Photomicrographs of a mylonite thin section (BT08-80), perpendicular to the foliation and parallel to the stretching lineation, sense of shear is top-to-the-east (to right).

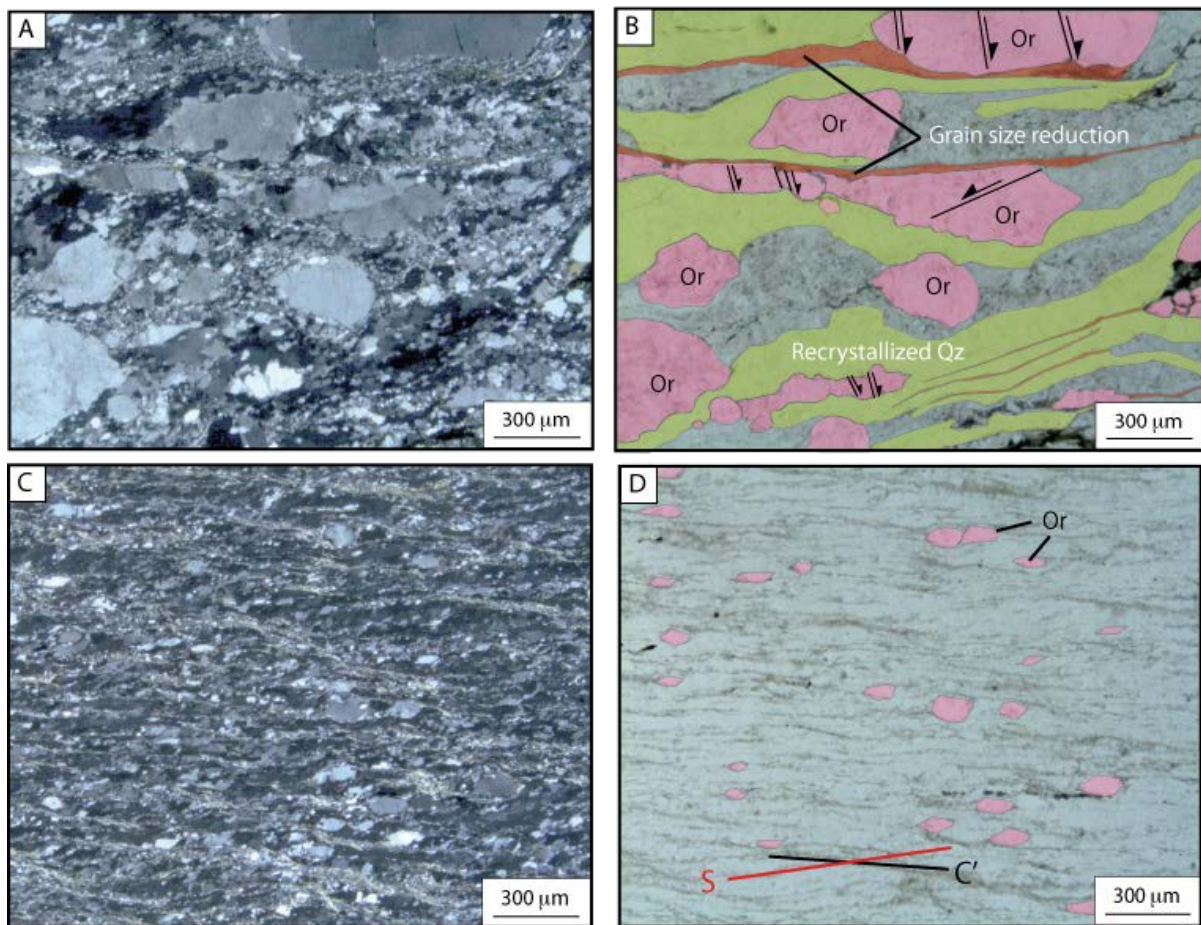


Figure III-17: Photomicrographs of mylonite (A and B, BT08-45) and ultramylonite (C and D, BT08-34) thin sections, perpendicular to foliation and parallel to stretching lineation, sense of shear is top-to-the-east (top right).

2.1.4. Ultramylonite:

In a plane perpendicular to foliation and parallel to the stretching lineation, ultramylonite bands are generally parallel to the average foliation of the BSZ, with the exception of some ultramylonite zones that cross-cut the mylonite foliation at a slightly shallower dip angle (closer to horizontal).

The granodiorite ultramylonite is composed of ~30% plagioclase, 40% quartz with variable grain size (0.01 up to 0.2 mm), 15 % K-feldspar porphyroclasts (0.3-5 mm), 15 % phyllosilicate (muscovite, biotite, chlorite; 0.1-0-3 mm), consistent with XRD analyses (cf. Chapter IV.2). The amount of phyllosilicates increases within the ultramylonite compared to the mylonite. Ultramylonite is characterized by a very fine-grained matrix (<10 μm) that mantles rounded feldspar clasts (0.1 mm). The fine grain size of the matrix makes it difficult to recognize mineral species optically, except the feldspar clasts that show clear shear-sense

indicators (Figure III-17A and C). Quartz grains range from a few microns to 0.1-0.2 mm, and K-feldspar grains are 0.1-0.3 mm "fish like" clasts. The C' surfaces are mostly defined by the alignment of phyllosilicate and are strongly expressed in the ultramylonite. Quartz and feldspar porphyroclasts experienced intense grain size reduction in the granodiorite ultramylonite compared to the mylonite.

2.1.5. V1 quartz veins:

The first set of quartz veins (V1) is characterized by partial to complete transposition into the foliation of the mylonitic fabric and shows a strong stretching lineation, wavy and lobate vein boundaries, and no visible mineralization except quartz. V1 are a few centimeters thick, and their partial transposition is indicated by recumbent folds (Figure III-18, top) or sigmoidal shapes (Figure III-18, bottom), consistent with top-to-the-east sense of shear.



Figure III-18: V1 quartz veins in mylonite (top picture) and in metabasite (bottom picture). Rotation and boudinage of these quartz veins is consistent with top-to-the-east shearing.

The V1 quartz veins are composed of > 95 % quartz and < 5 % phyllosilicates (muscovite and/or chlorite). Within the veins, elongate quartz grains (0.1-0.4 mm) and mica fish (0.1-0.2 mm) define the S-C fabric. Transposition of V1 veins produces quartz ribbons

characterized by intense deformation and recrystallization. (Figure III-19A). In some veins, dynamic recrystallization is expressed along shear bands, and in others, is affecting the entire quartz vein (Figure III-19A and B, respectively). Dynamic recrystallization is accommodated by bulging of grain boundaries and subgrain rotation (regimes 1-2 of Hirth and Tullis, 1992). The V1 quartz veins do not contain FIPs, and instead the fluid inclusions (FI) are focused at or near the grain boundaries of recrystallized quartz.

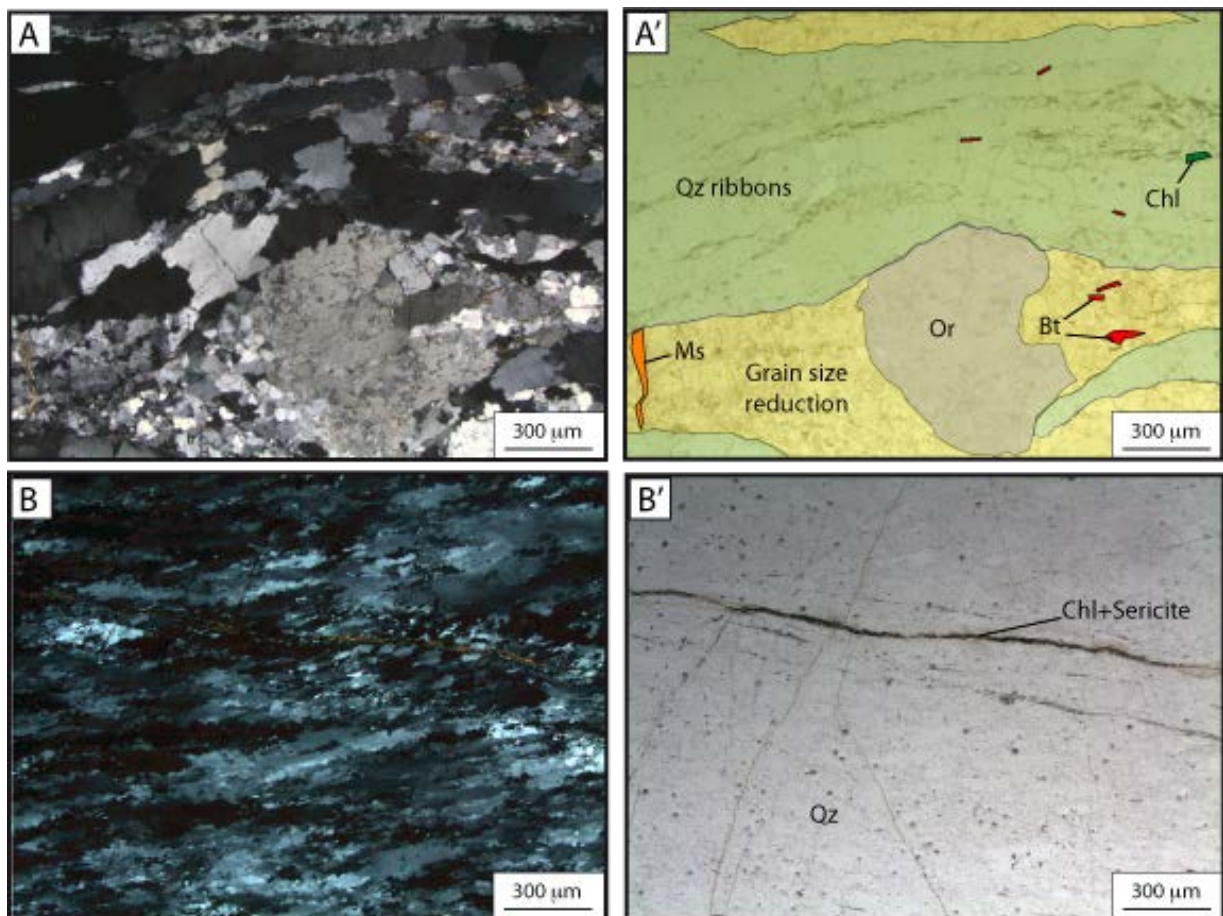


Figure III-19 : Photomicrographs of V1 quartz veins viewed perpendicular to the foliation and parallel to the stretching lineation, top right corner is east. A and A' have quartz ribbons in the upper part, the lower part corresponds to the contact with the granodiorite mylonite showing breakdown of feldspar porphyroclast (Or) with feldspar-quartz mixture tails (BT10-09). B and B', sheared quartz grains, and late chlorite + sericite planes (BT10-30).

2.1.6. Cataclasite:

In the Lost Horse and the Sweathouse sections, protocataclasite (30 % matrix, Figure III-20) to ultracataclasite (90 % matrix, Figure III-20) can be a few millimeters to tens of centimeters thick and tend to be better expressed towards the top of the sections. Cataclasite zones crosscut all ductile fabrics within the BSZ. The cataclasite matrix is chlorite-rich, and

angular feldspar clasts show heterogeneous sizes. In both the Lost Horse Canyon and Sweathouse quarry sections, cataclasite has been observed either discordant or parallel to the mylonitic foliation, and in general, the high-angle cataclasite zones connect those parallel to mylonitic foliation.



Figure III-20: Cataclasite bands (mm to cm scale) in mylonite, either horizontal (ultracataclasite, left), or vertical (protocataclasite, right).

Cataclasites display angular clasts and some rounded clasts of granodiorite mylonite, which range from 0.1 to 5.0 mm. The matrix has heterogeneous grain size (<0.1 mm), and is mostly composed of epidote and Fe-oxides. The matrix is generally observed mantling the mylonite clasts, but can also be observed as epidote clusters. These clusters show sharp boundaries with the surrounding feldspar, and are probably related to space opening (void) generated during cataclastic flow (Figure III-21A and A'). In terms of relative chronology, cataclasite zones crosscut the V1 quartz veins and are crosscut by chlorite veins (Figure III-22A and A').

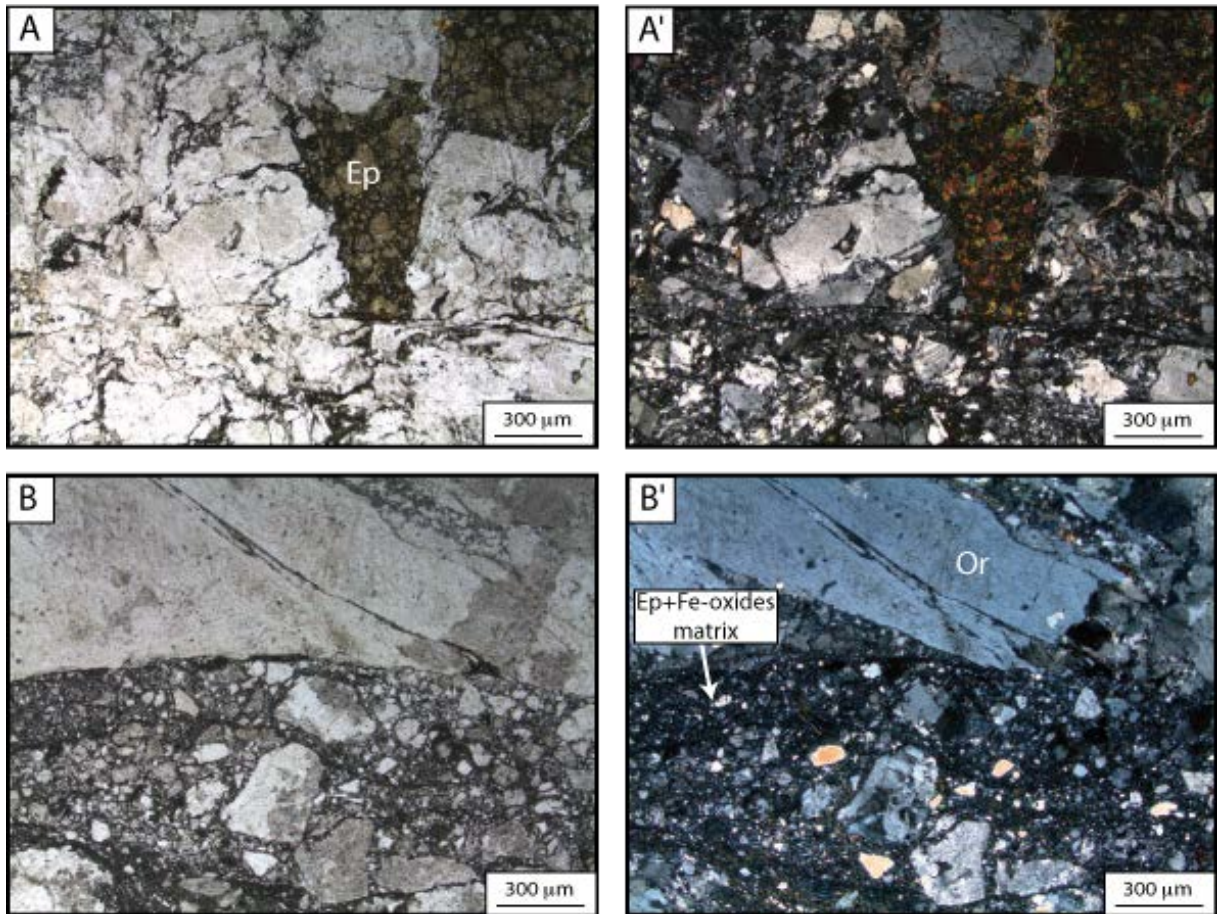


Figure III-21 : Photomicrographs of cataclasite, perpendicular to the foliation and parallel to the stretching lineation, top right corner corresponds to east. A and A' from a vertical Ep-rich protcataclasite (BT10-33), with large clasts of mylonite with sharp edges. B and B' show horizontal cataclasite, defined by at least 50 % of Ep-Fe-oxide matrix, and containing both rounded and angular clasts (BT10-08).

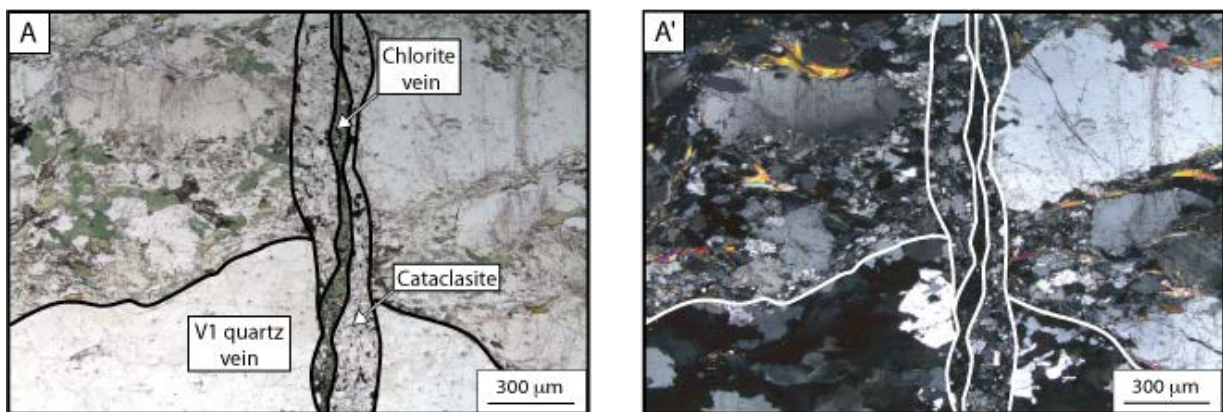


Figure III-22 : Photomicrographs of thin section, perpendicular to the foliation and parallel to the stretching lineation, top right corner corresponds to east. A and A' has a relative chronology of V1 quartz vein, chlorite vein, and cataclasite (BT10-28).

2.2. Brittle fabrics:

2.2.1. The brittle series in the Sweathouse section:

Numerous brittle features affect the mylonitic series in the Sweathouse section and may be related to the stage when the extensional shear zone underwent brittle deformation. Chlorite en-echelon tension gashes, chlorite veins, epidote veins, a second set of quartz veins, chloritized breccia, and normal faults are listed in this section and will be studied in more exhaustive details in the following sections (Appendix III, Table III-1).

Mylonite in the Sweathouse section displays chlorite tension gashes organized along conjugate planes. Some of the chlorite tension gashes are crosscut by chlorite or epidote veins (Figure III-23). Epidote veins are commonly meter-long and a few mm thick. Steeply dipping epidote veins tend to connect with foliation-parallel epidote veins. Epidote veins commonly used the "en echelon" chlorite tension gashes as weakness planes to localize and grow (Figure III-23); epidote veins are also observed as discrete planes cutting through the mylonite granodiorite at high angles.

In contrast to V1 quartz veins, which are older than the chlorite and epidote veins (Figure III-24A and A'), a second set of veins crosscuts at least the chlorite veins and in some cases the epidote veins.



Figure III-23: Chlorite en-echelon tension gashes and conjugated epidote veins crosscut the mylonite.

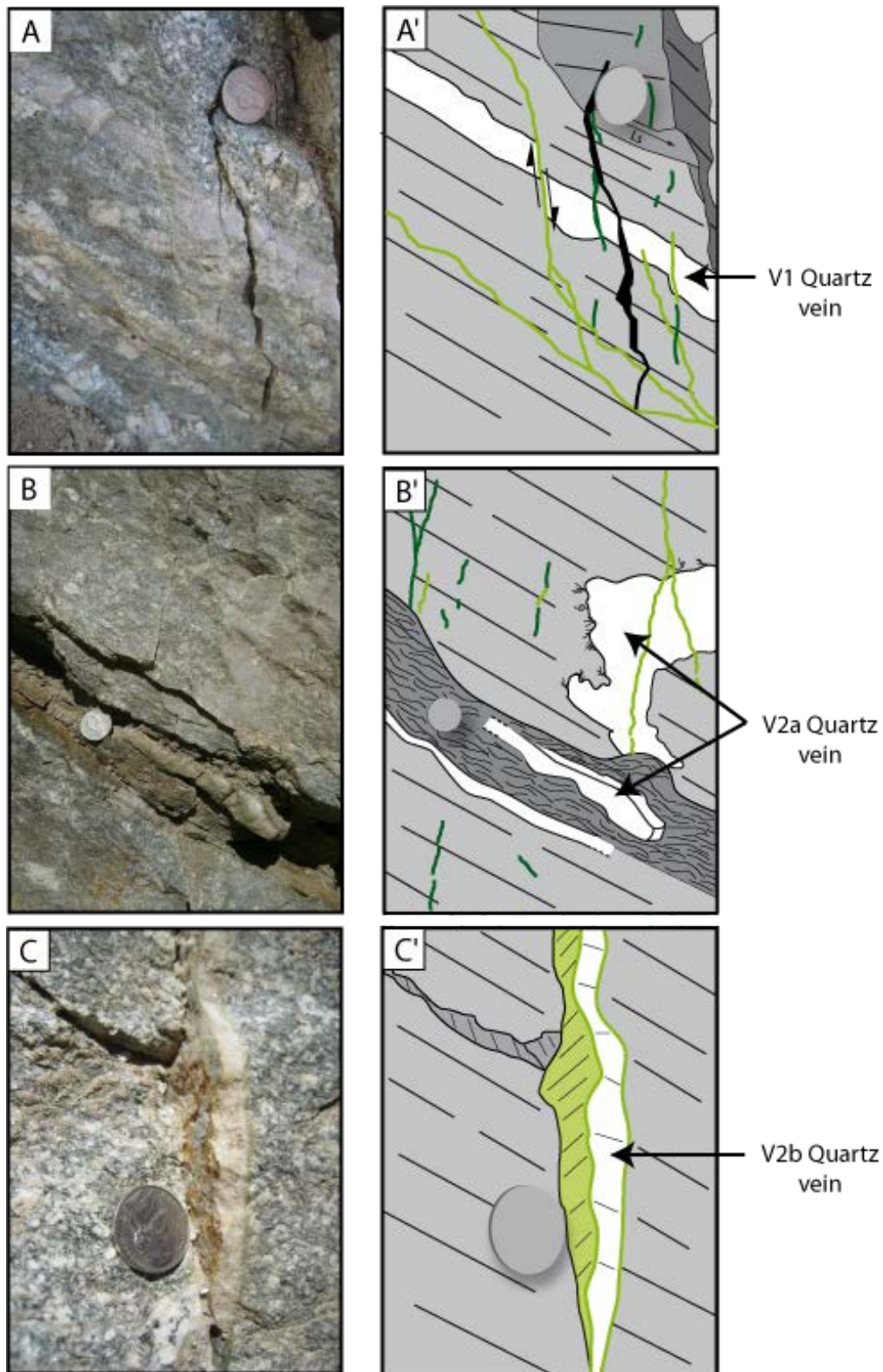


Figure III-24: Different generations of quartz veins. A and A', V1 quartz vein. B and B', V2a quartz veins. C and C', V2b quartz vein. Dark green symbols correspond to chlorite en-echelon tension gashes and chlorite veins, light green lines correspond to epidote veins.



Figure III-25: Quartz geode (center) in a V2a quartz vein.

The second set of quartz veins encountered in the field can be divided into two groups. The first group, V2a, is either parallel or slightly oblique to the mylonitic foliation (Figure III-24, B and B'). In contrast to V1, V2a veins are characterized by mm to cm sized undeformed quartz and contain mylonite and phyllonite clasts. Locally, they are also distinguished by the presence of faceted quartz crystals (geodes) and Fe-oxide mineralization (Figure III-25). The second group of the second set of quartz veins, V2b, corresponds to veins oriented at a high angle to the mylonitic foliation, with sharp vein boundaries; they may also contain oxide mineralization (Figure III-24, C and C'). V2b quartz veins crosscut V1 quartz veins, and slickensides on the V2b boundaries indicate a normal fault movement. V2b and V2a quartz veins have been observed mutually crosscutting each other, implying more or less synchronous development. V1 and V2a quartz veins are crosscut by epidote-bearing veins while the V2b quartz veins are epidote-rich, and are in general bordered by epidote veins (Figure III-24C and C').

A network of high-angle normal faults can be observed in the mylonites near the top of the Sweathouse section, where a chloritized breccia overlies the mylonite across a low-angle normal fault (Figure III-26). The fault zone corresponds to an intensively cataclased mylonite, associated to anastomosing normal faults. The mylonite underneath the fault zone presents an undulating / anastomosed foliation and a dense network of chlorite and epidote veins.

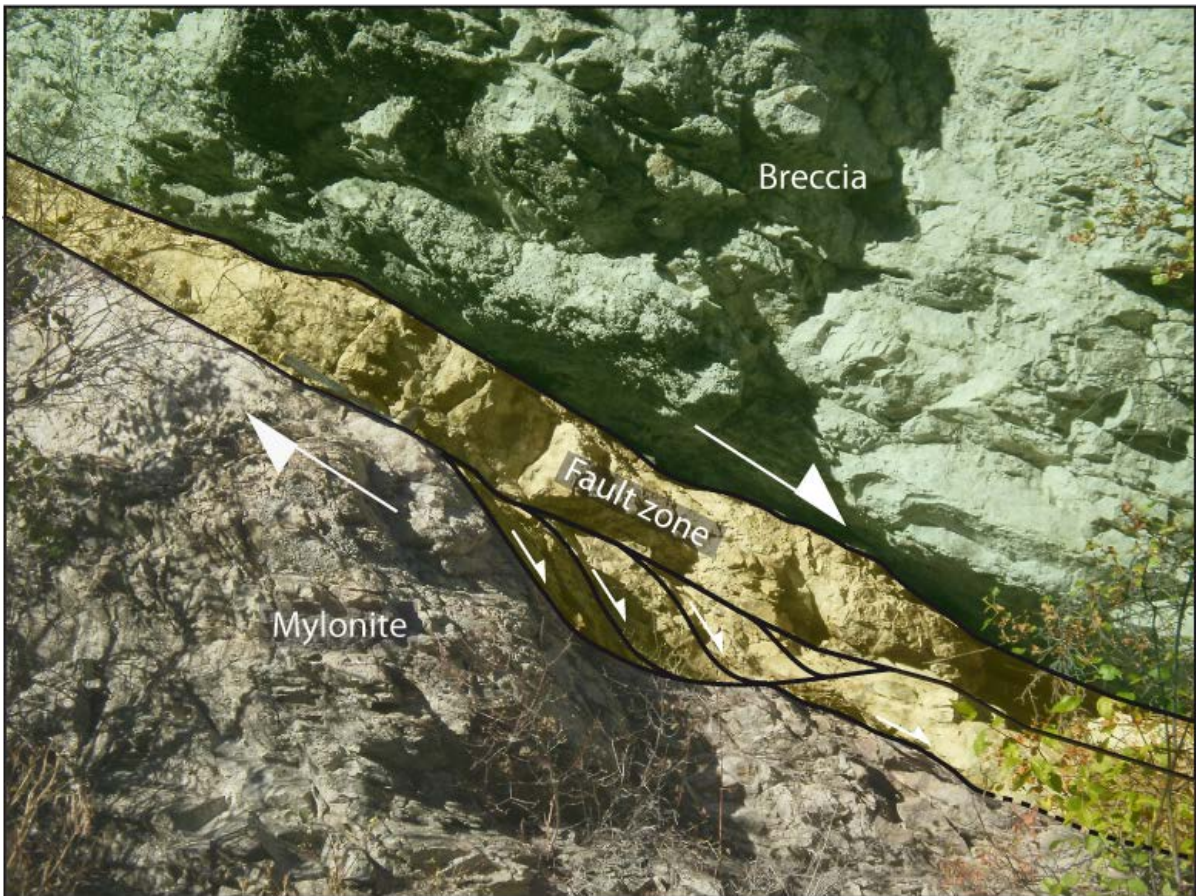


Figure III-26: Breccia overlying the granodiorite mylonite. The fault zone corresponds to the brittle detachment and displays anastomosed faults.

2.2.2. Chlorite en-echelon tension gashes, chlorite veins and epidote veins:

Chlorite en-echelon tension gashes and chlorite veins are NE-SW oriented; where present, slickenlines reveal normal displacement along them (Figure III-27, left), which is also observed at a microscale (Figure III-28 A and A'). Others veins are simply tension fractures. None of the chlorite tension gashes and chlorite veins observed under the microscope display shear deformation. Chlorite tension gashes are organized along planes, and chlorite veins are mostly pure, with minute amounts of oxides; chlorite grains in the veins are equant (Figure III-28 A and A'). The veins can be several meters long and only a few millimeters thick.

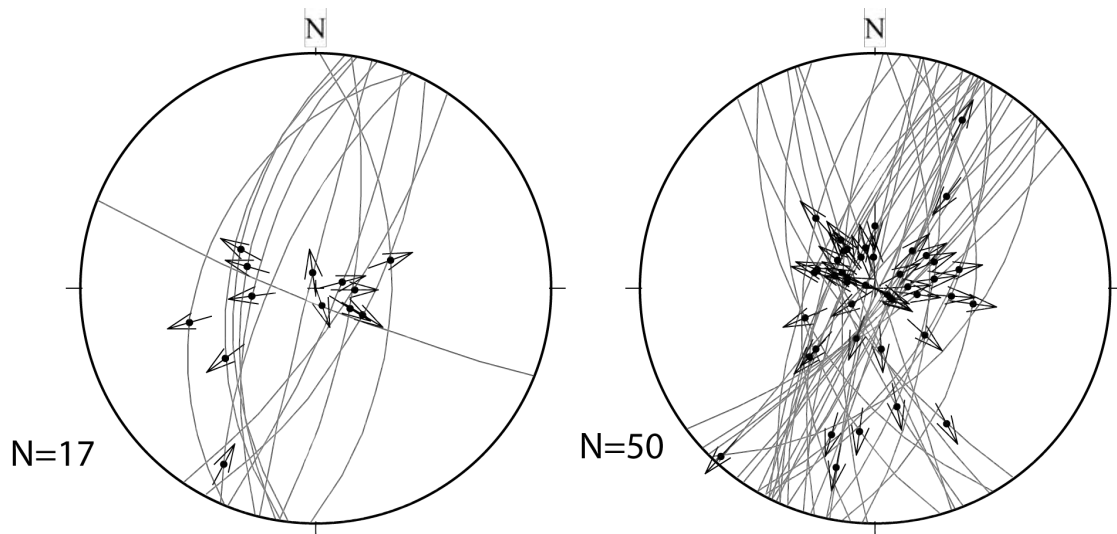


Figure III-27: Stereonets of striated chlorite veins and chlorite tension gashes (left) and striated epidote veins (right).

Like chlorite veins, epidote veins are mostly NE-SW oriented and are steeply dipping to the east or to the west (Figure III-27, right). Epidote veins can be pure or associated with very fine-grained quartz. Subhedral epidote and quartz grain size range from ten to a hundred micron. The veins locally contain angular clasts of granodiorite mylonite or cataclasite (Figure III-28 B and B'). Epidote veins are crosscutting the S-C bands and microshear zones at high angle, while subhedral epidote and quartz are observed in sub-horizontal planes and chlorite-rich sigmoid at the vicinity of epidote veins (Figure III-28 B and B'). The presence of subhedral epidote and quartz crystals in sub-horizontal planes of the mylonite may indicate a local lateral injection of the fluid related to the epidote veins.

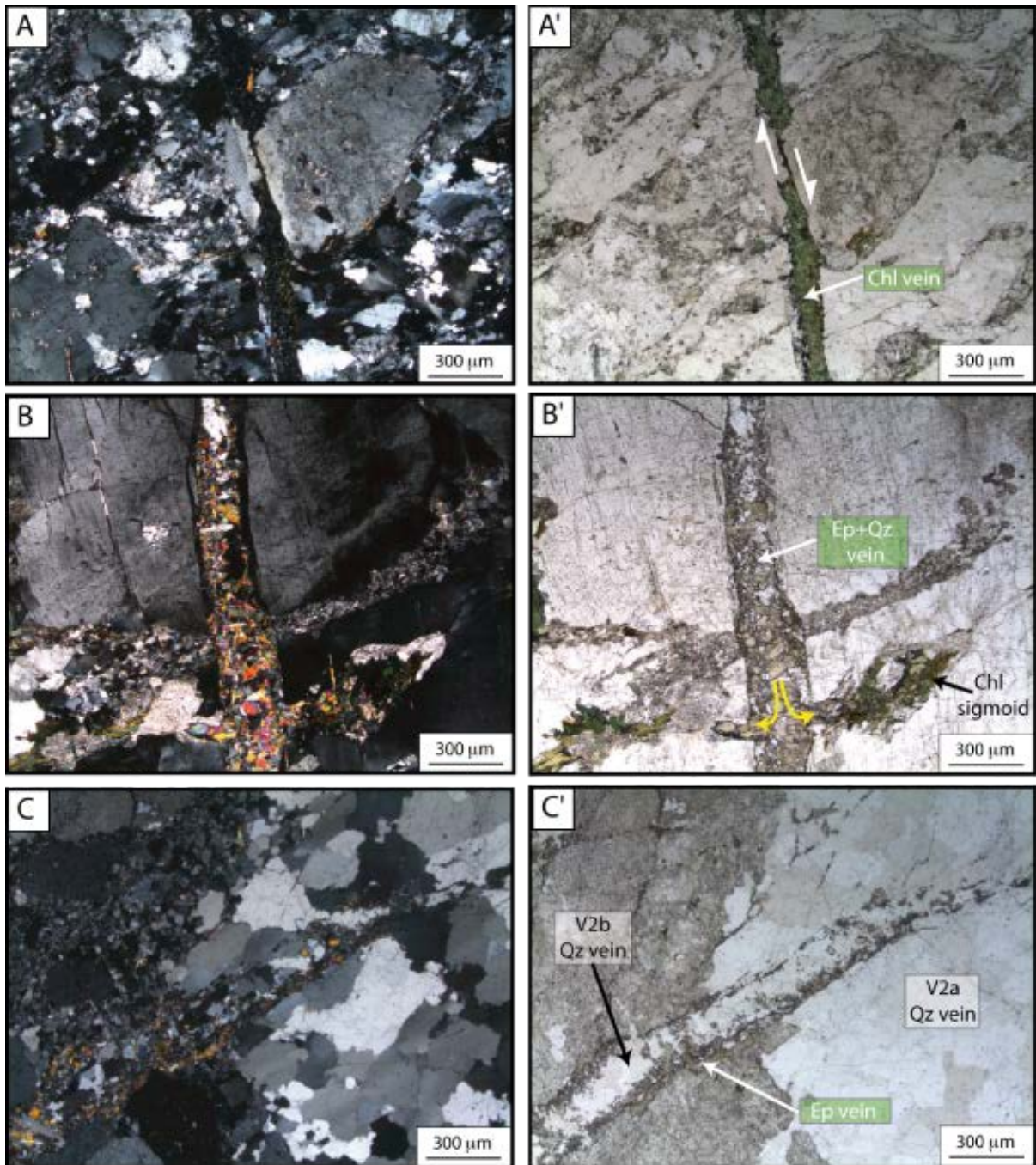


Figure III-28: Photomicrographs of chlorite and epidote veins perpendicular to the foliation and parallel to the stretching lineation, top right corner corresponds to east. A and A' present a normal displacement of K-feldspar along a chlorite vein; a chlorite vein crosscuts a dynamically recrystallized shear band (BT10-28). B and B' shows an epidote vein crosscutting a K-feldspar, the fluid related to the epidote veins was injected also laterally in the chlorite sigmoid (BT08-21). C and C' show an epidote vein cross-cutting a V2a quartz vein. The epidote vein is reactivated and filled with a V2b quartz vein (BT10-14).

2.2.3. V2a and V2b quartz veins:

The second set of quartz veins (V2a, V2b) is NE-SW oriented, relatively steeply dipping to the east or to the west. When observed, lineated slickensides on V2 quartz veins indicate normal fault movement (Figure III-29, left) and show the same distribution of orientations as the veins that are devoid of slickenside (Figure III-29, right).

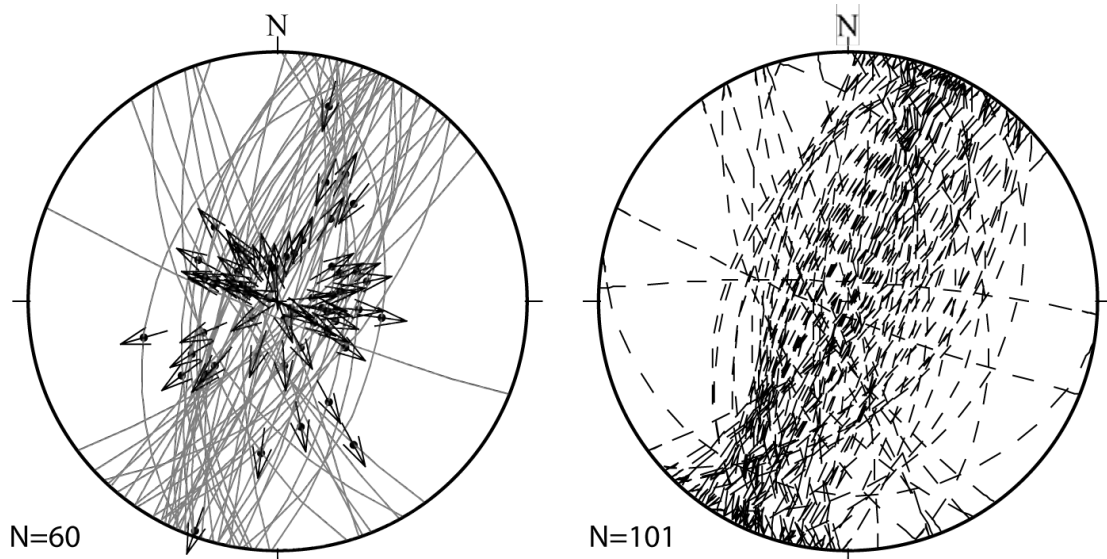


Figure III-29: Stereonets of quartz veins (V2a,V2b) with lineated slickensides (left), and without lineated slickensides (right).

V2a quartz veins are composed of ~98% quartz and ~2% phyllosilicates (Ms-Chl) and Fe-oxides (Figure III-30A and A'). V2a quartz veins reveal automorphic quartz (0.1 up to 0.6 mm), can contain clasts of granodiorite mylonite and show discordant sharp vein boundaries (Figure III-31A and A'); V2a veins are either cross-cutting or parallel to the mylonitic foliation, and are crosscut by epidote veins (Figure III-30A and A').

V2b quartz veins (Figure III-30B and B') are composed by ~90% quartz, ~5% phyllosilicates (Ms-Chl), and ~5% epidote and minute amounts of Fe-oxides. V2b veins are defined by automorphic quartz (0.1 up to 0.6 mm), muscovite (< 0.3 mm), chlorite (< 0.3 mm), epidote (0.1 up to 0.6 mm). The V2b quartz veins form a network, where the quartz veins can be either cross-cutting or parallel to the mylonitic foliation; V2b veins are commonly cross-cutting V2a quartz veins (Figure III-31A and A'). Some of the epidote veins border V2b quartz veins, which may indicate that epidote veins were reopened and filled with V2b quartz veins. The second set of quartz veins (V2a and V2b) display a high density of a single generation of FIPs; the FIPs in these veins are consistently dipping east (Figure III-30A', B' and C').

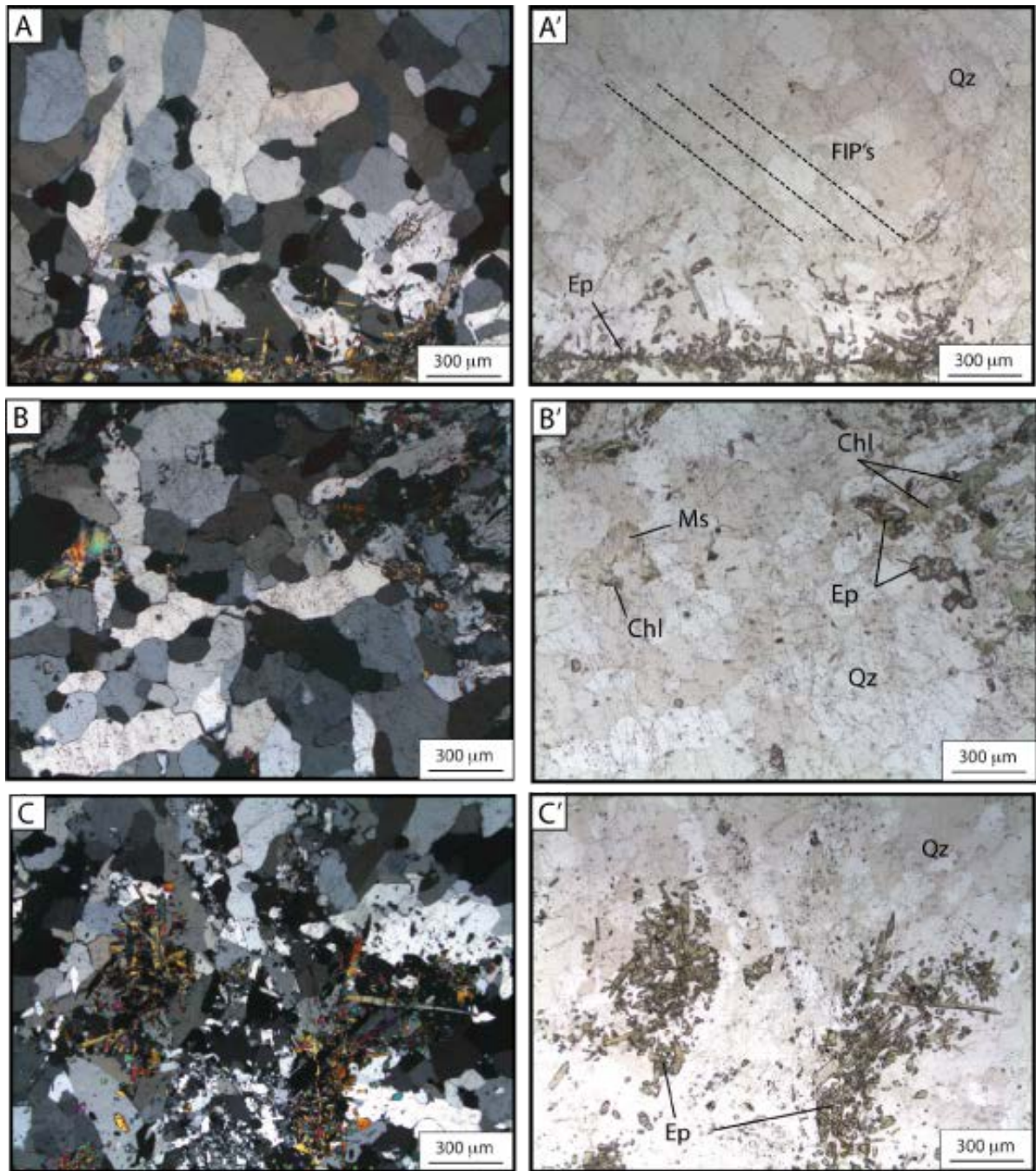


Figure III-30: Optical micrographs of quartz veins in thin section, perpendicular to the foliation and parallel to the stretching lineation, top right corner corresponds to East. A and A' correspond to a V2a quartz vein and present subhedral quartz cross-cut by an epidote vein (bottom), fluid inclusions are aligned along plans (FIPs) and are coherent with top-to-the-east sense of shear (BT10-13). B and B' show the subhedral mineral assemblage of V2b (BT10-12). C and C', correspond to a V2b quartz vein and present subhedral epidote and quartz grains, randomly distributed (BT10-31).

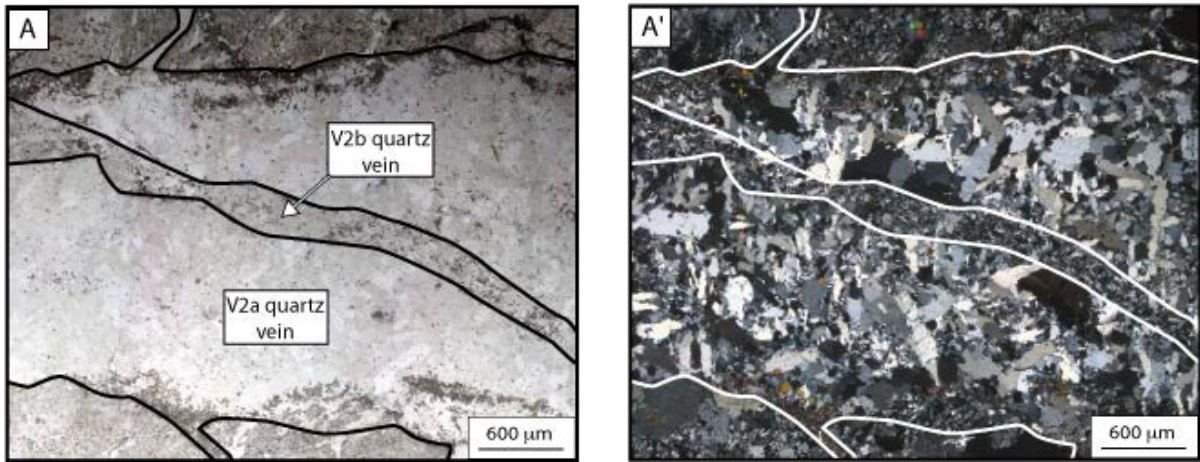


Figure III-31: A and A', relative chronology between epidote veins (walls of V2a quartz vein), V2a, and V2b quartz veins (BT10-14).

2.2.4. Breccia:

In the chloritized breccia, quartz, plagioclase, and feldspar clasts are angular, mantled by a fine grain quartz-feldspar matrix. The brecciated matrix is composed either of a fine-grained quartz-feldspar mixture, or is rich in chlorite and epidote. A spatial organization between the two different matrices could not be teased out. Grain sizes are mostly heterogeneous and quartz grain size is lower than a few microns. No distinctive microstructures can be observed in the breccia, and brittle deformation and fluid-rock interaction appear to have erased any previous fabrics. The breccia from the Sweathouse section is characterized by intensively chloritized and brecciated granodiorite mylonite (Figure III-32).

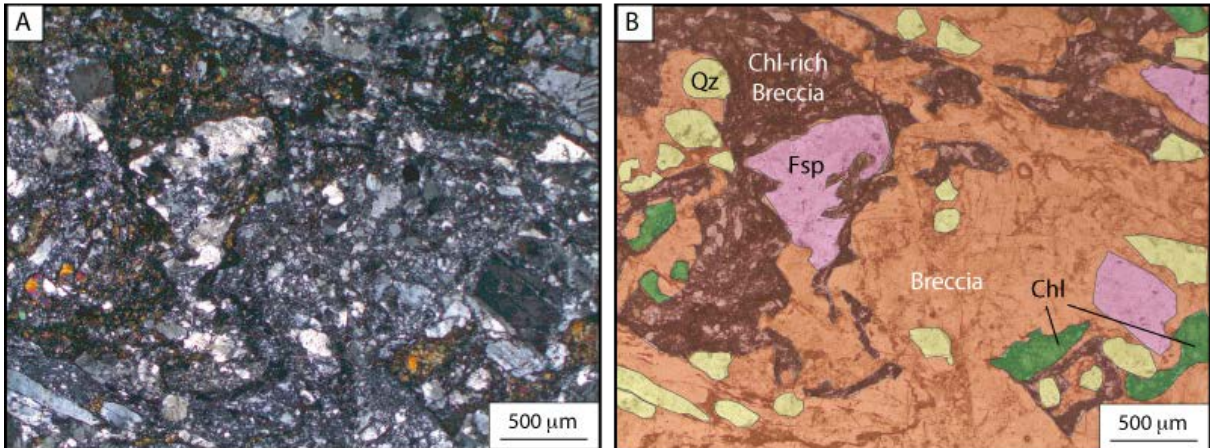


Figure III-32 : Photomicrograph of breccia thin section, perpendicular to the foliation and parallel to the stretching lineation, top right corner corresponds to east (BT10-33).

2.2.5. Normal faults:

Sub-vertical normal faults are generally NE-SW oriented, dipping to the east and to the west. According to the lineated slickensides on the fault planes, faults show both sinistral and normal movement, defining a conjugate fault network with oblique normal slip (Figure III-33). In some cases, relatively low-angle normal faults ($\sim 45^\circ$) appear to connect with high-angle normal faults (Figure III-34, A).

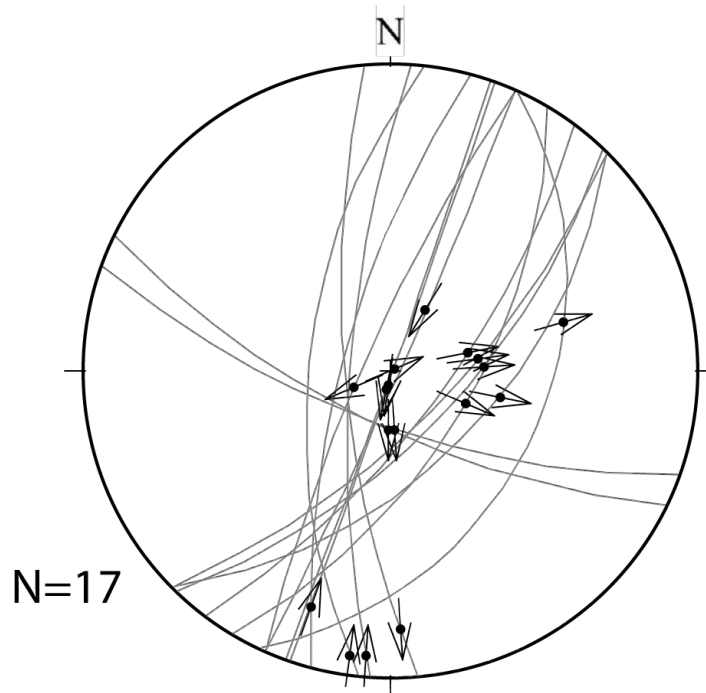


Figure III-33: Stereonet of the normal fault network in the Sweathouse section.

The normal faults show silicified walls ($\sim 10\text{cm}$), with a significant increase of quartz matrix, mineralization of millimeter size pyrite, and a decrease of feldspar porphyroclasts, which are replaced by quartz and Fe-oxide geodes. The core of fault zones is composed of a bleached granodiorite (significant decrease of silica), corresponding to compacted angular feldspar clasts that are randomly oriented. The bleached granodiorite is also defined by significant increase in chlorite, the appearance of epidote in the matrix, and localized bands of automorphic quartz mantling feldspar clasts (Figure III-35). The bleached granodiorite is a loose rock unit that is commonly bounded by clay-rich gouge (Figure III-34, B).

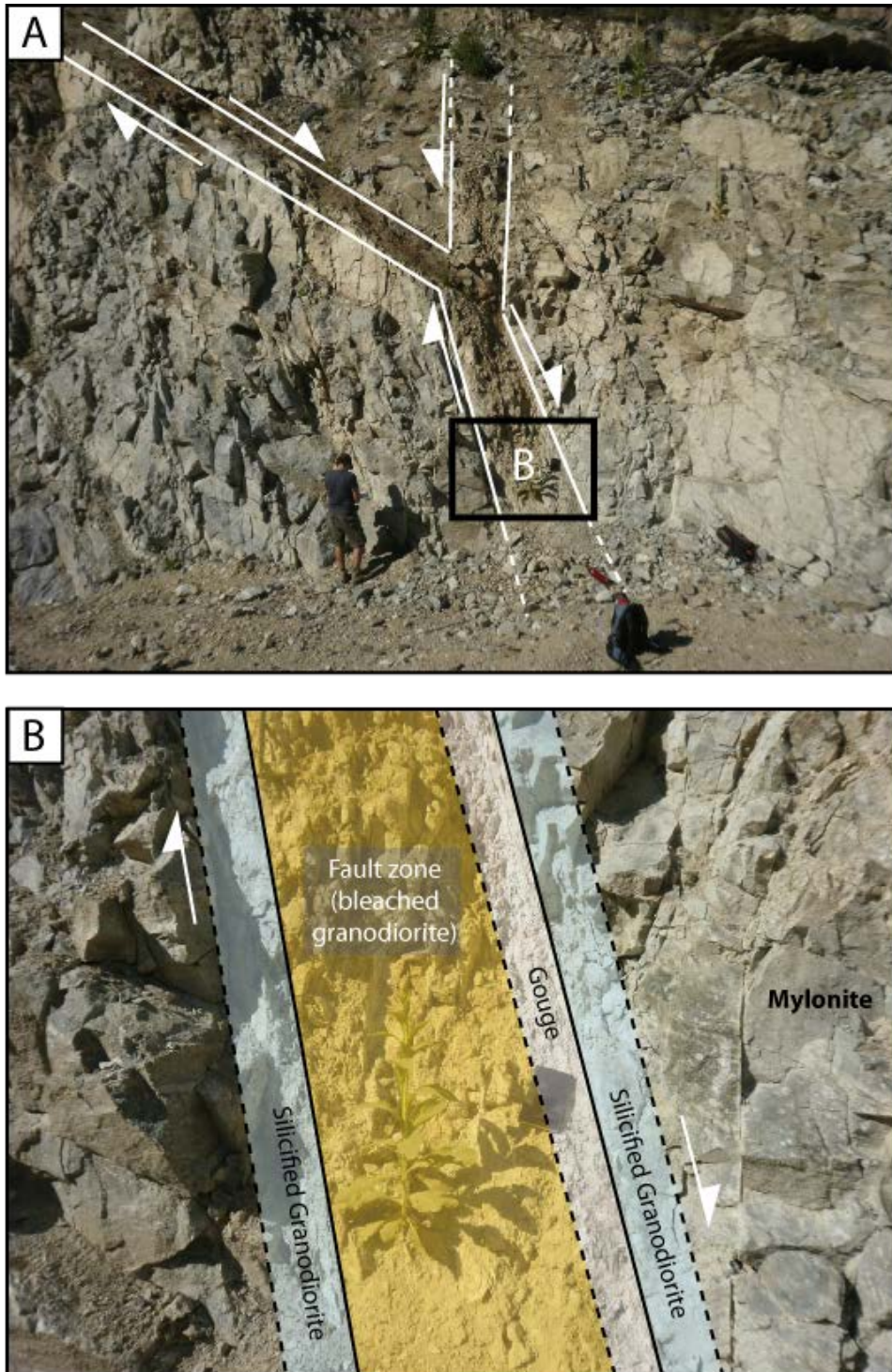


Figure III-34: A. Conjugated normal faults in the Sweathouse quarry, merging into a single normal fault. B. Zoom in the normal fault zone: walls (~10cm) are characterized by silicified granodiorite (blue), the fault zone developed a bleached granodiorite mylonite (yellow). Note the presence of a gouge filled with clay (white) on the right border and the presence of silicified granodiorite on both sides.

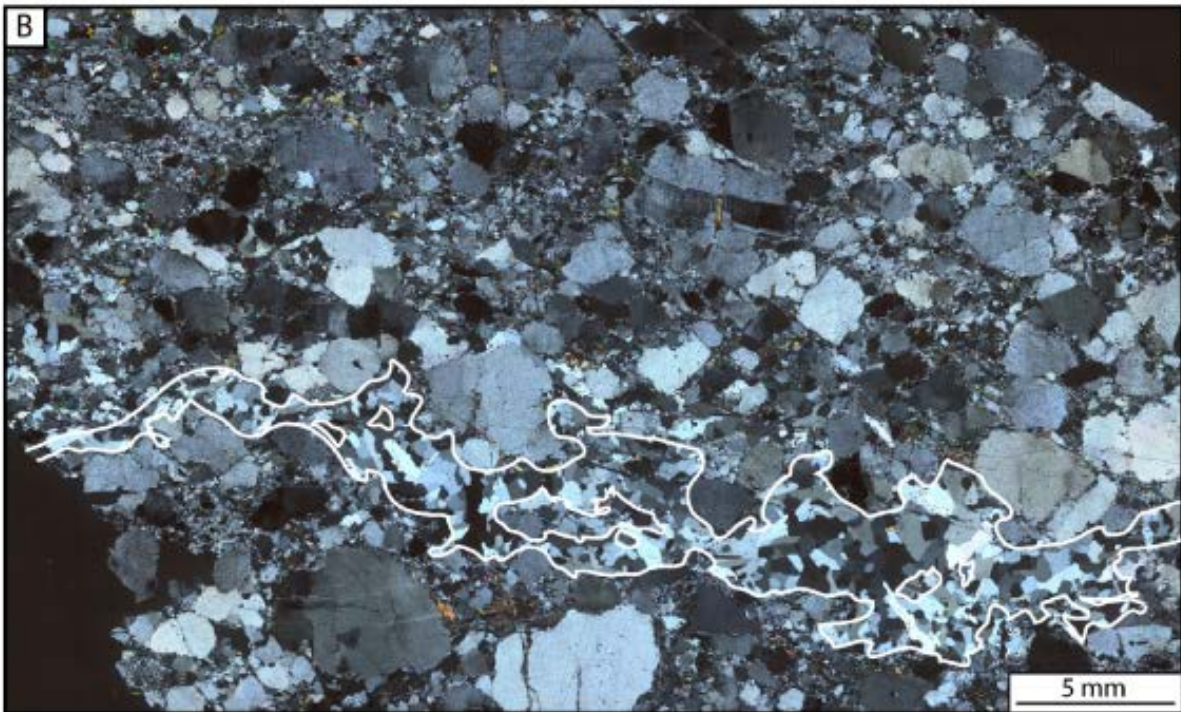


Figure III-35: Scan of a bleached granodiorite thin section (BT10-46), top right corner corresponds to east. The irregular line delineates a zone of undeformed quartz around angular feldspar clasts.

3. Paleostrain analysis with T-Tecto 3.0:

The following results were obtained using T-Tecto 3.0 software (Žalohar et al., 2008). Processing the brittle microtectonic measurements allows access to the directions of kinematic axes and paleostress fields according to the Multiple-Slip-Method (MSM). The MSM is an extension of methods from Kostrov (1974), Molnar (1983), as well as a methods proposed by Angelier (1984), Marrett and Allmendinger (1990,1991), and Cladouhos and Allmendinger (1993). Ductile structures cannot be analyzed by fault-slip inversion due to the high probability that such structures may have been rotated during their formation and exhumation. The best-fit paleostrain tensors of the brittle features are determined by fault-slip data inversion. Results for each rock type are presented in stereonet according to the lower hemisphere stereographic projection.

The brittle features are presented in two groups. The first group of data corresponds to brittle features where lineated slickenslides show a slip direction, allowing T-Tecto to run a fault-slip data inversion. The second group of data corresponds to tension fractures filled with chlorite, epidote or quartz, with no evidence of slip.

3.1. Fractures with slip indicators:

The fault-slip data inversion calculates the direction of principal strain axis and the relative values of principal strain, where X corresponds to the short axis, Y to the intermediate axis and Z to the long axis of a theoretical strain ellipsoid. Based on the X, Y and Z values, the Flinn parameter (k) permits to determine the shape of the strain ellipsoid, defined by the following equation:

$$\mathbf{k} = (\mathbf{X}/\mathbf{Y} - 1) / (\mathbf{Y}/\mathbf{Z} - 1)$$

The strain ellipsoid is characterized by two domains: the flattening field is defined by $0 < k < 1$, and the constriction field is defined by $1 < k < \infty$. Notice that the datasets for the different groups, especially for the chlorite veins and faults, are small and statistically not robust; however, results provide a qualitative measure of paleostrain in the BSZ.

The directions of strain axes for quartz veins with lineated slickenslides show maximum compression vertical and maximum extension horizontal (Figure III-36A). The fault-slip data inversion in T-Tecto 3.0 provides the direction of principal strain axis: ϵ_1 : 002 / 86; ϵ_2 : 206 / 14; ϵ_3 : 117 / 04 (Figure III-36B). The relative values of principal strain indicate a 66% of shortening along Z, and 33% increase along X and Y, indicating radial extension.

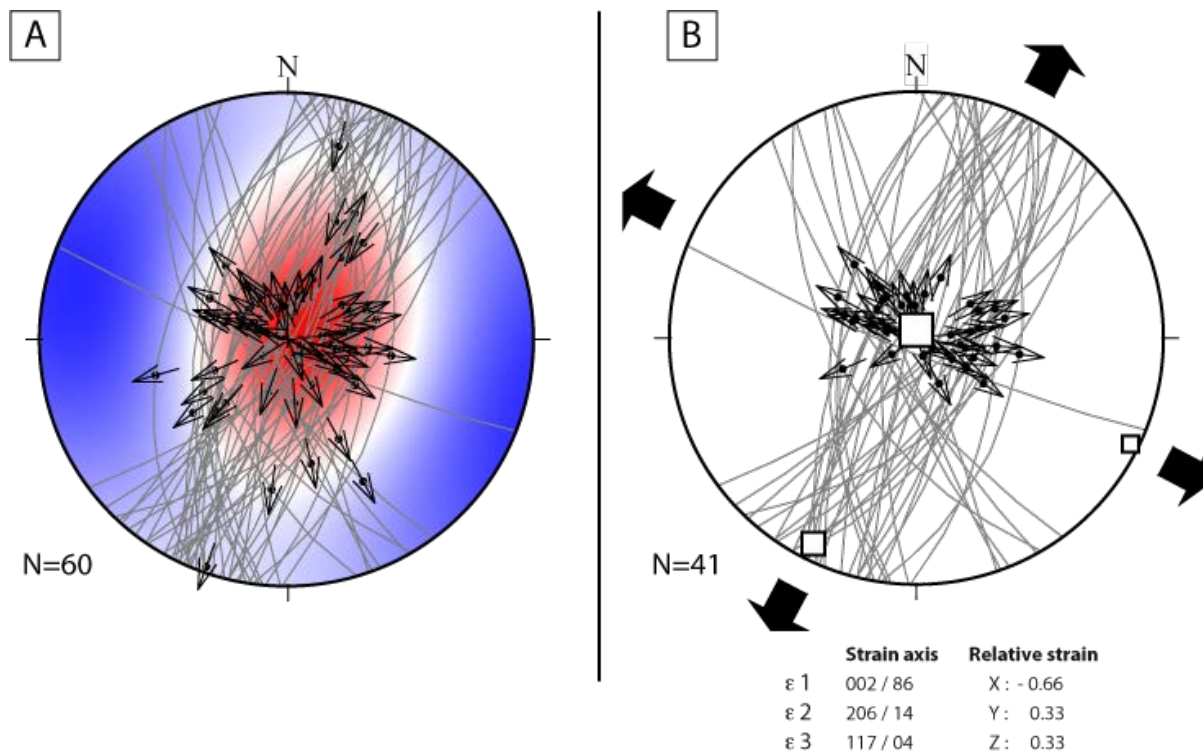


Figure III-36: Paleostress analysis of quartz veins (V2a,V2b) for the Sweathouse section. A corresponds to the paleostress field using the MSM method (red, compression; blue, extension). B provides the directions and relative magnitudes of strain axes calculated from strain tensors.

The presence of lineated slickenslides on chlorite veins implies that the chlorite veins acted as microfaults. The direction of strain axes, according to the paleostress method, show the maximum compression vertical and maximum extension horizontal (Figure III-37A). The fault-slip data inversion in T-Tecto 3.0 provides the following directions of principal strain axes: $\epsilon 1$: 002 / 86; $\epsilon 2$: 225 / 03; $\epsilon 3$: 134 / 03 (Figure III-37A). The relative values of principal strain indicate a 62% of shortening along Z, and 31% increase along X and Y. Like the quartz veins, the principal strain axis and the relative strain values show that the maximum compression is vertical and extension is radial.

Most epidote veins also show a slip direction, the direction of kinematic axes show also the maximum compression vertical and maximum extension horizontal (Figure III-37B). The fault-slip data inversion in T-Tecto 3.0 provides the directions of principal strain axes: $\epsilon 1$: 002 / 86; $\epsilon 2$: 201 / 04; $\epsilon 3$: 110 / 01 (Figure III-37B). The relative values of principal strain indicate a 58% of shortening along Z, and 25% increase along Y and 34% increase along X. These relative strain values indicate radial extension, with a preferred WNW-ESE direction of extension.

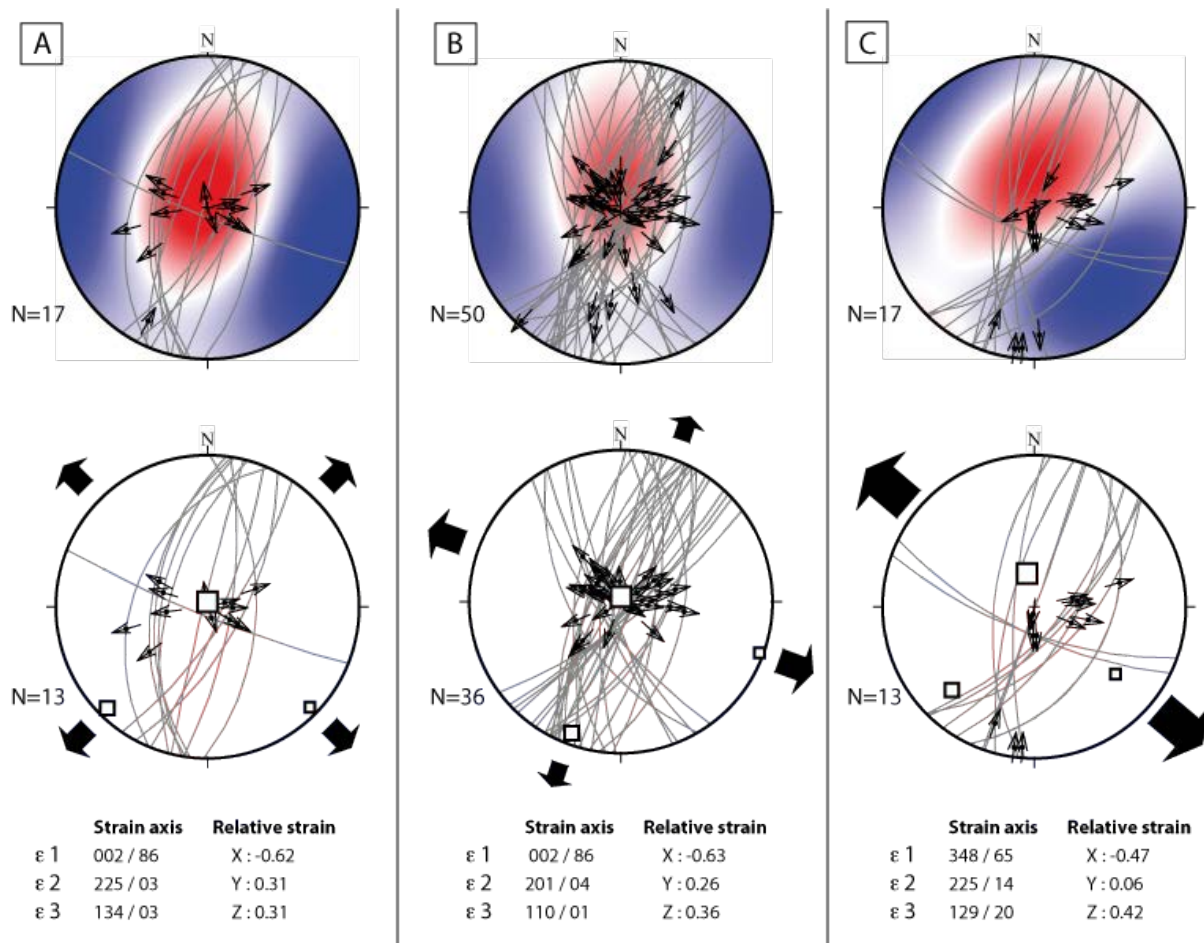


Figure III-37: Paleostain field using the MSM method (upper part), direction of strain axes and relative magnitudes of strain principal axes according to fault-slip inversion (lower part) for brittle features of the Sweathouse section. A corresponds to the chlorite veins and chlorite tension gashes planes. B corresponds to epidote veins, and C corresponds to conjugated normal faults.

The conjugate normal faults have been run in the T-Tecto fault-slip data inversion and provide direction of strain axes with a maximum compression subvertical (slightly tilted to the N) and maximum extension subhorizontal (Figure III-37C). The directions of principal strain axes are: ϵ_1 : 348 / 65; ϵ_2 : 225 / 14; ϵ_3 : 129 / 20 (Figure III-37C). The relative values of principal strain indicate a 47% of shortening along Z, and 6% increase along Y and 42% increase along X. The relative values of principal strain axes indicate that the maximum extension is oriented SE-NW in a regime that tends toward plane strain.

The Flinn parameter tends to 0 for the quartz veins and chlorite veins, $k=0.04$ for the epidote veins and $k=0.34$ for the normal faults. All the brittle features have a Flinn parameter lower than 1, and fall in the flattening field. According to this qualitative approach, T-Tecto fault-slip data inversion indicates that brittle features from the Sweathouse section were generated by a tectonic regime dominated by radial extension. In contrast, the paleostain

field, combined with the distribution of the strike of veins, which is dominantly NE-SW, appears to indicate a tectonic regime dominated by plane-strain extension.

3.2. Veins with no slip evidence:

Chlorite, epidote, and quartz veins with no slip evidence are likely related to tension fractures. Measurements of this group of veins can be introduced as tension fractures into T-Tecto 3.0 in order to obtain the paleostress field and the direction of strain axes. Results are presented according to two groups, one with the chlorite and epidote veins (Figure III-38A), and the other with quartz veins (Figure III-38B). Independently of the nature of the veins, the two groups show similar results with sub-horizontal maximum extension oriented WNW-ESE (~N120). The strike consistency of the two sets of veins and the maximum extension indicate that these veins are related to a tectonic regime dominated by plane-strain extension.

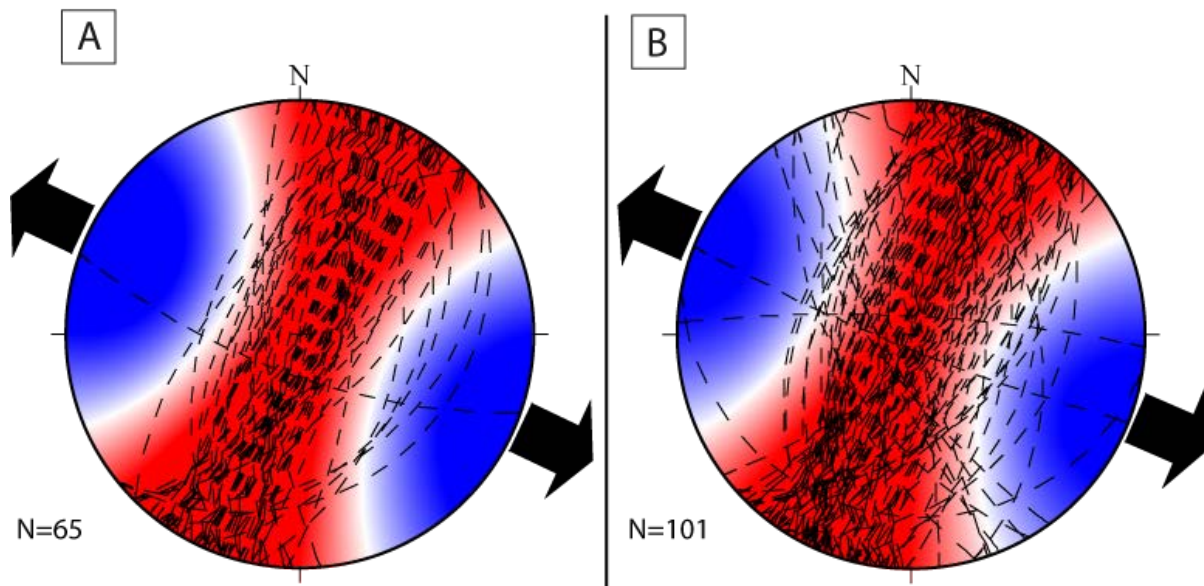


Figure III-38: Paleostress field and direction of kinematic axes for fractures with no slip evidence (red, compression; blue, extension). A presents measurement of chlorite veins and epidote veins, B show measurement of quartz veins.

4. Discussion:

The Bear Creek pluton displays a magmatic foliation defining a N-S elongated dome. On its eastern border, mylonitic fabrics define the BSZ and overprint the magmatic foliation. The spatial evolution from protomylonite to ultramylonite fabrics indicates a strain gradient at the shear zone scale. The upward increase in the frequency of alternation between mylonite and ultramylonite in the upper part of the shear zone, up to every 10 cm at the very top of the section, likely reflects strain localization during shear zone activity. The macroscopic and microscopic study of the BSZ, coupled with the paleostrain study of veins and fractures, provide a good basis for discussing the spatial and temporal evolution of the BSZ. This structural evolution defined the rationale for a targeted sampling strategy that was conducted to better understand the chemical and stable isotopic evolution of rocks and minerals during localized deformation in the presence of fluids.

4.1. Relation between ductile and brittle features:

Despite the consistency of the mylonitic and ultramylonitic foliations, the possibility remains that these structures have rotated during exhumation. It is reasonable to think that such ductile structures may have rotate around a subhorizontal axis corresponding to the protolith dome axis. The stretching lineation and the pole to mylonitic foliation, which can be approximated as the directions of finite extension and finite contraction, respectively, define a subvertical plane striking ~N120 (Figure III-39)

The T-Tecto fault-slip data inversion indicates that brittle features from the Sweathouse section were generated by a tectonic regime dominated by extension. The relative strain values provided by fault-slip data inversion are sensitive to several inputs such as cohesion and friction angle along faults, which implies that the relative strain values must be interpreted with caution. Given the consistency of the strike and dip orientations of the veins and the direction of strain axes, a tectonic regime dominated by plane-strain extension responsible for all the brittle features appears to be realistic. Evidence for radial extension, which is supported by small datasets, may indicate that gravitational spreading may have affected the brittle evolution of the shear zone, perhaps during the waning stages of the horizontal pull exerted by regional extensional boundary conditions.

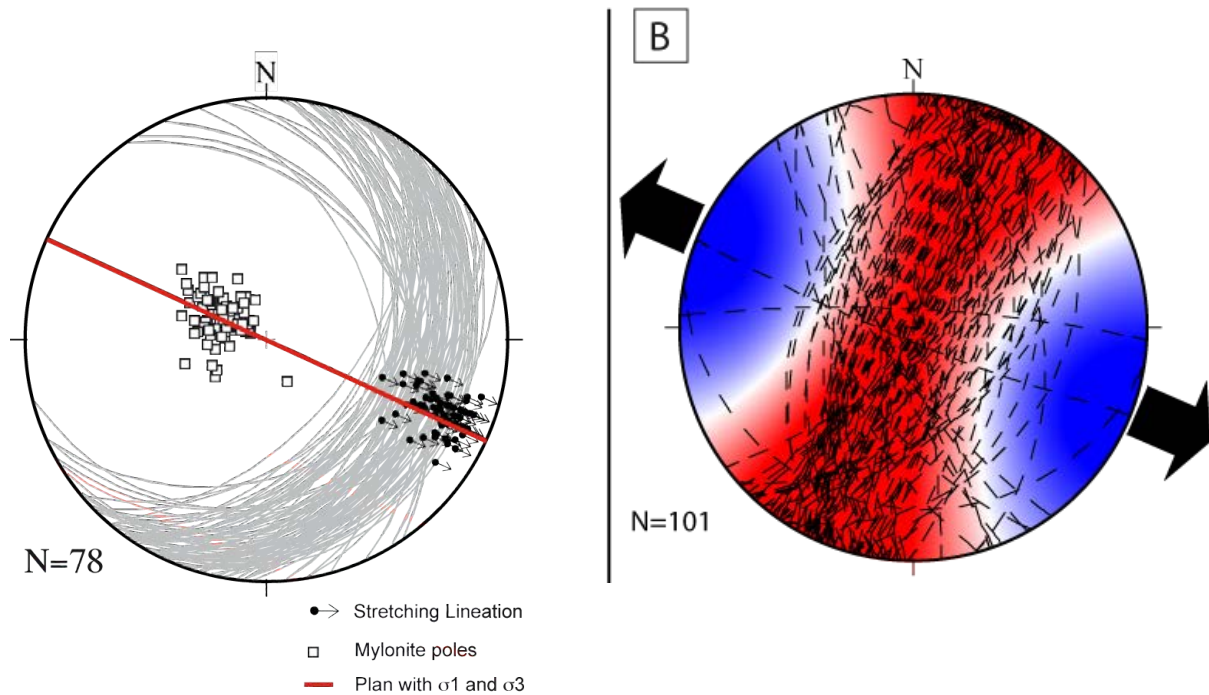


Figure III-39: A. Graphic determination of a plane containing sigma 1 and sigma 3 related to the mylonitic foliation. B. Set of quartz veins with no slip.

Both ductile and brittle units from the Sweathouse and Lost Horse sections indicate an ESE-WNW direction of extension (\sim N120) (Figure III-39 A and B). Thus, ductile and brittle structures were likely generated during the same protracted kinematic event. No major tectonic events have affected the Idaho batholith since Eocene. Hence, the BSZ represents a continuum in the detachment history from ductile to brittle deformation, where rocks migrated through the brittle-ductile transition during exhumation. Moreover, the different type of veins related to the brittle deformation and normal faults, which put the chloritized breccia directly over the mylonitic fabrics of the Sweathouse quarry, show the same strain regime. If the brittle features retained their initial orientation, it may indicate that the shear zone did not experience significant rotation or tilting since its exhumation.

4.2. Spatial and temporal evolution of the BSZ:

The BSZ affects the relatively isotropic Bear Creek pluton and displays a strain gradient from the protolith toward the hanging wall, over a 600 m thick section, as observed in the Lost Horse Canyon and the Sweathouse quarry. Figure III-40 shows schematically the proposed evolution of structures in space and time (stages 1 to 7). Other than the magmatic fabric (stage 1) that characterizes the Bear Creek pluton (Sidman et al., 2005), the deepest structural evidence of shearing related to shear zone activity is the 200 m structural section of

protomylonite (stage 2). The protomylonite zone grades upward into a mylonite zone (stage 3) that shows an increasing frequency of ultramylonite zones toward the top of the BSZ, which consists of decimeter- and centimeter-scale alternation of mylonite and ultramylonite (stage 4). The intensely deformed V1 quartz veins that are transposed into the mylonitic foliation were probably generated by fluid overpressure during mylonite development. These ductile fabrics were overprinted by brittle features, as observed especially well in the Sweathouse quarry. These features include chlorite en-echelon tension gashes and chlorite veins, V2a quartz veins and epidote veins, and V2b quartz veins (Figure III-41) that progressively affected the mylonite (stages 5, 6). By that time, a network of conjugate high-angle normal faults developed in the upper part of the shear zone (stage 7a, b). At low to moderate temperature (300-100°C; Hyndman et al., 1988), the granodiorite mylonite underwent brecciation (stage 7a). A low-angle normal fault corresponding to the detachment fault is the last expression of activity in the BSZ (stage 7b) and brings the breccia on top of the granodiorite mylonite in the Sweathouse quarry.

Cataclasite indicates a semi-brittle deformation regime (White, 2001), since cataclastic flow occurs simultaneously by frictional grain size reduction and crystal plastic deformation. In the BSZ cataclasite, the cataclasite contains mylonite clasts, indicating that cataclastic flow overprinted mylonite and likely ultramylonite deformation. In the Sweathouse quarry cataclasite, frictional grain size reduction is highlighted by the brittle behavior of mylonite clasts, while crystal plastic deformation affected the epidote and quartz rich matrix. Thus, it is proposed that the brittle-ductile transition in the BSZ is characterized by the transition from mylonite to cataclasite (stage 5).

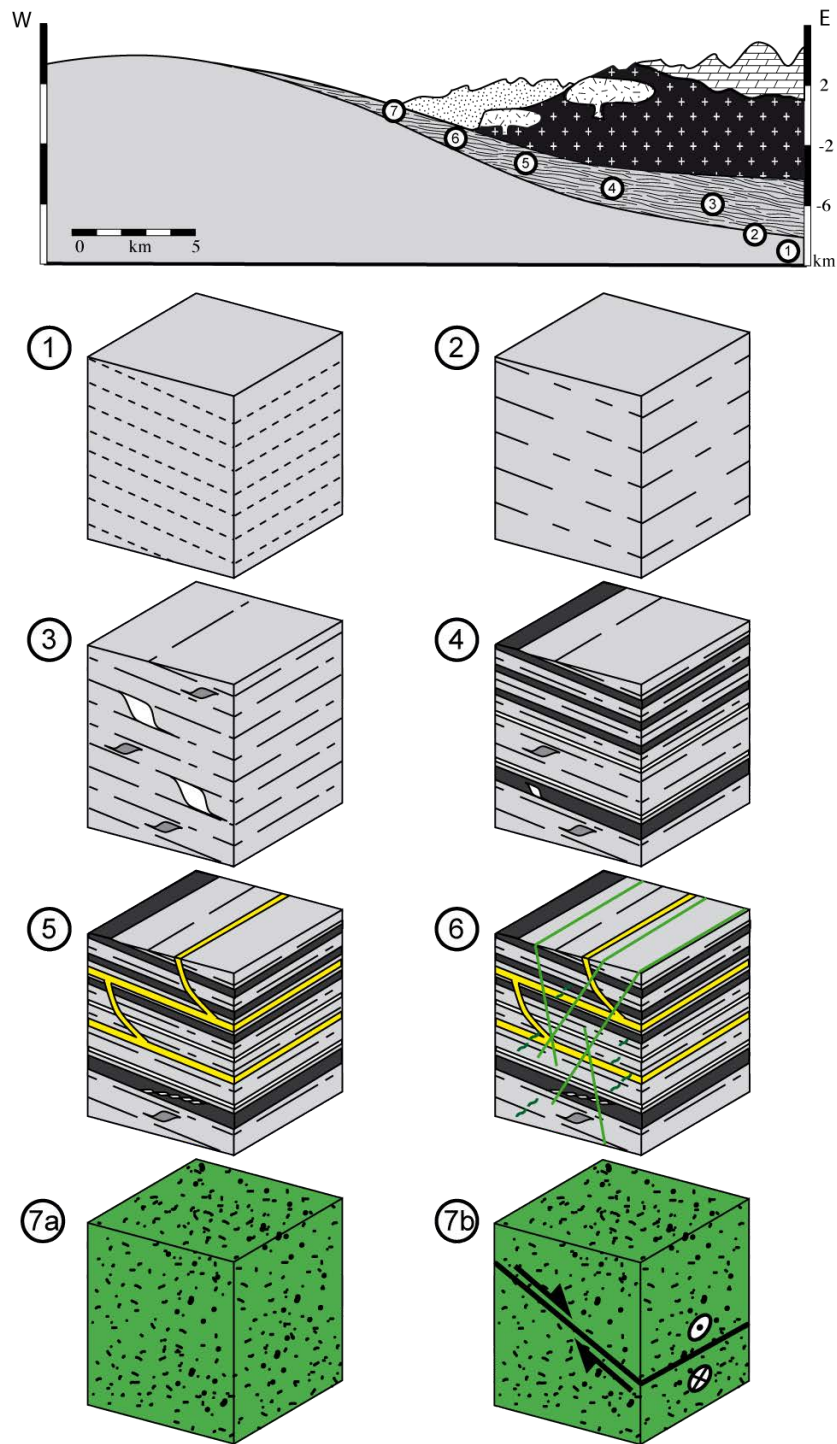


Figure III-40: Spatial evolution of the overprinted fabrics, according to the exhumation of mylonitic rocks along the BSZ. Top, schematic cross-section of the BSZ. 1, Magmatic foliation. 2, Protomylonite. 3, Mylonite, mica fish (grey) and V1 Qz veins (white). 4, Ultramylonite and V1 Qz veins. 5, Cataclasite parallel or oblique to the mylonitic foliation. 6 Chl, Ep veins and V2a, b Qz veins (see Figure 27 for more details). 7a, brecciation. 7b, Low angle “cold fault” plane.

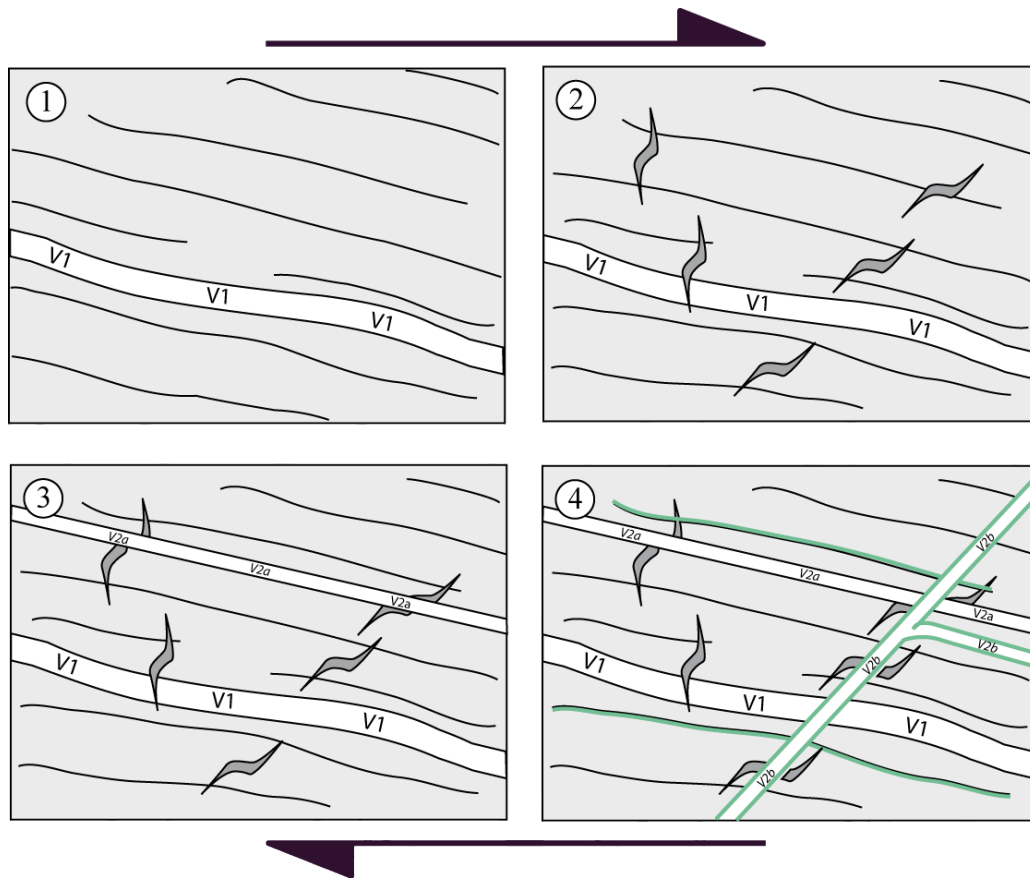


Figure III-41: Schematic appearance of the different brittle features corresponding to T=6, Figure 26. Grey sigmoid: chlorite tension gashes; green: epidote plans; V1, V2a and V2b: different generation of quartz veins.

The paleostrain analysis demonstrates that the BSZ displays a continuum of deformation from ductile to brittle regimes. However, the temporal evolution of the ductile fabrics leading to a strain gradient at the shear zone scale remains unclear. Two hypotheses for the shear zone evolution can be put forward to explain the spatial strain gradient from protomylonite to mylonite-ultramylonite alternation in the upper part of the BSZ: (1) strain is localized in the upper part of the shear zone and the mylonitization front migrates downward while the shear zone widens; (2) broad strain including magmatic fabrics at depth induces the development of a thick shear zone, and strain progressively localized upward in the section during exhumation to form mylonite and ultramylonite bands that are most abundant at the top of the section.

The consistency of fabrics in the Lost Horse Canyon shear zone between the magmatic fabric in the Bear Creek pluton (Foster and Raza, 2002; Sidman et al., 2005) and the protomylonite –to-ultramylonite sequence suggests that strain was distributed through an initially broad shear zone in the pluton. Strain localization in the upper part of the shear zone

as evidenced by the narrow mylonite-ultramylonite alternation (1-10 cm scale) may indicate that the shear zone progressively reduced its actively deforming thickness by localizing strain upward. However, the constant grain-scale microstructure and grain size reduction of feldspar porphyroclasts over 400 m of mylonitic section in the Lost Horse Canyon suggests that mylonitic processes most characteristic of the upper part of the section reached deeply into the BSZ to produce mylonite bands in the protomylonite section during exhumation and cooling. Consequently, the spatial organization of the ductile fabrics related to the shear zone activity does not permit to categorically exclude one or the other of the proposed hypothesis for the dynamics of this shear zone. The chemical and stable isotope analyses presented in the next chapters will help discuss this problem further.

4.3. Evidence of fluid flow:

Sheared V1 quartz veins, cross-cutting both mylonite and ultramylonite, are evidence for local fluid flow contemporaneous with ductile deformation. At the microscale, mylonite shows a significant increase of phyllosilicate with respect to the protolith (+5-10%). Phyllosilicates are hydrated minerals, where water content can reach 3-4 wt. % in muscovite and biotite, and 8-12 wt. % in chlorite (Bailey, 1989). Such an increase of phyllosilicate in the mylonite and ultramylonite likely implies an input of fluid(s) in the deforming host-rock, and thus evidences fluid flow at the microscale.

At the Sweathouse quarry, the relationship between the silicified walls of the fault zone and the silica-poor inner fault zone remains unclear, but fluid flow through the fault zone was likely responsible for such a phenomenon. A possible explanation is fluid-assisted dissolution of silica from the inner core of the fault zone and expulsion of silica-rich fluids toward the walls of the fluid conduit. Such a configuration would indicate induced weakening mechanism of the fault. If the silicified fault walls are associated with intense hydrothermal fluid flow along the fault plane, possible strengthening, though silicification, of the fault network could have maintained localized hydrothermal activity.

The gouge and the precipitation of pyrite and replacement of feldspar by quartz-Fe oxides geodes in the silicified walls support the idea that a certain amount of fluid circulated through the fault zone. We saw previously that the cataclasite contains a Chl-Ep-rich matrix, and the more intense the cataclasis, the higher the chlorite content. The fault gouge may have previously been a chlorite-rich ultracataclasite, in which the chlorite altered to clay, with the

help of fluid at low temperature. Additionally, the numerous quartz, chlorite, and epidote veins reveal significant fluid flow when the shear zone underwent brittle deformation.

4.4. Rock-softening processes:

The protomylonite develops discrete microshear zones sub-parallel to the mylonitic foliation of the BSZ. These microshear zone are characterized by elongated quartz grains and dynamically recrystallized fine grains of quartz formed by grain boundary bulging recrystallization. Mylonites show well-developed S-C fabrics, and quartz ribbons parallel to the mylonitic foliation. Quartz ribbons in mylonite show synkinematic muscovite fish and quartz is dominated by subgrain rotation (Figure III-16 B and B') and/or grain boundary migration (Hirth and Tullis, 1992) (Figure III-16 A and A'). As it can be observed from Figure III-11 to 13, the amount of quartz ribbons increases with respect to the strain, from the protomylonite toward the ultramylonite fabrics. The microstructures of the quartz evolve from bulging (protomylonite) to grain boundary migration (mylonite and ultramylonite), and would reflect a change of recrystallization mechanism with increased strain (Mancktelow, 2003). The crystal-plastic deformation of quartz grains accommodates a considerable amount of slip along the shear bands parallel to the foliation (Fusseis et al., 2009). The recrystallization mechanism of quartz, and the significant increase of quartz ribbons with respect to the strain may be associated with a rock softening process.

The second process of rock softening affecting the ductile fabrics is the mechanical and chemical breakdown of feldspar during deformation and hydration processes, respectively. Synkinematic hydration of feldspar results in generating quartz and phyllosilicate in pressure shadows of feldspar porphyroclasts (O'Hara, 1988; Kwon et al., 2009). Quartz and phyllosilicates in the pressure shadows are mantling feldspar clasts, which denotes a reaction-assisted mechanism transforming feldspar clasts into aggregates of quartz and muscovite in the feldspar pressure shadows (Hippert, 1998; Handy et al., 1999). Mechanical and chemical breakdown of feldspar implies a decrease in the proportion of feldspar in the granodiorite mylonite, and an increase in quartz and phyllosilicate. According to Hippert (1998), the disruption of feldspar porphyroclast leads to a dramatic increase in strain accommodation and represent the ultimate cause of strain localization. Such process is in good agreement with microscale observation in the ultramylonite, where both feldspar and quartz grains show intense grain size reduction.

5. Conclusion:

The combined Lost Horse Canyon and Sweathouse sections show the most complete deformation history related to Eocene exhumation experienced by the Bear Creek pluton. The continuum of deformation from ductile to brittle deformation of the BSZ footwall (Figure III-42) follows this spatial (ductile, brittle) and temporal evolution (brittle):

Emplacement of the Bear Creek pluton -> protomylonite - wide mylonite shear zone - V1 quartz veins, ductilely deformed - strain localization evidenced by ultramylonite bands, mostly expressed in the upper part of the shear zone -> cataclasites -> chlorite tension gashes and chlorite veins -> V2a quartz veins -> epidote veins and V2b quartz veins -> Breccia and high angle normal faults (hydrothermal activity) -> Detachment fault.

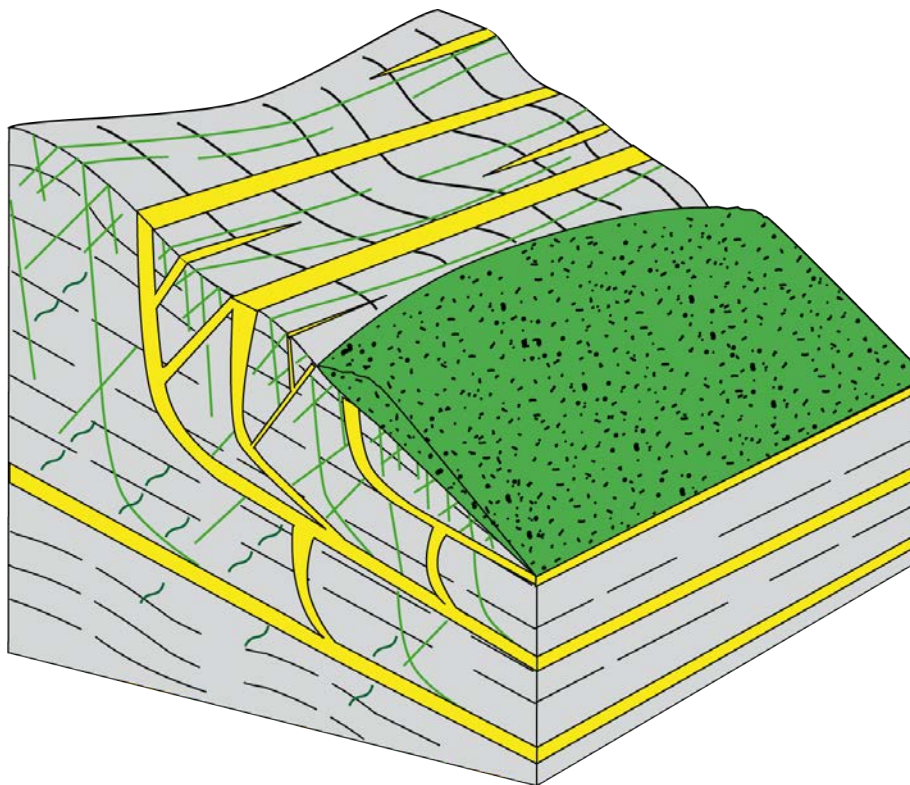


Figure III-42: Schematic view of the BSZ that combines the Lost Horse and the Sweat House sections, with the different fabrics (from ductile to brittle) overprinting the two micas granodiorite (color code according to Figure III-40).

The relative chronology developed through the structural, microstructural, and paleostrain studies provides an important tool for tracking the spatial and temporal fluid flow related to the detachment history. The sampling strategy for the geochemistry and stable isotope analyses presented in the following chapters was based on this relative chronology. Fluid flow and fluid-rock interaction related to the ductile regime will be examined through

the mineral assemblages generated by the rock-softening processes in the mylonite and the first generation of veins (V1). Fluid flow and fluid-rock interaction related to the brittle regime will be examined through the second population of quartz veins (V2a and b), which present differences with V1 quartz veins in terms of (1) deformation (V1 sheared and V2a and b remain undeformed) (2) mineralogy (no epidote in V1, V2a), and (3) spatial organization of the fluid inclusions (FI at grain boundaries in V1, and FIPs in V2a and V2b).

Chapter IV : Metamorphic reactions, volume change and mass transfer in the Bitterroot shear zone: bulk-rock and single-grain analyses

Introduction:

Along with pressure and temperature, the volume of fluid contained in a certain volume of rock (fluid-rock ratio) is an important factor in metamorphism because fluids can inhibit or accelerate mineral reactions (Greenwood, 1961). These reactions can consume or release metamorphic fluids, which has a direct impact on effective pressure (difference between lithostatic and hydrostatic pressure). The effective pressure plays a role on mechanisms of deformation and strength of rocks (Secor, 1965; Phillips, 1972; Sibson, 1985), which can also be influenced by grain size, composition and texture of the rocks. Consequently, rheological parameters can be influenced by reactions related to fluid infiltration (White and Knipe, 1978).

In a sheared rock recrystallizing during retrograde metamorphism, the presence of aqueous fluids results in the formation of hydrous minerals (micas), which have lower frictional strength than the original mineral (feldspar). Such a metamorphic reaction is referred to as a “rock softening reaction” (White and Knipe, 1978; Simpson, 1985; Hippert, 1998; Collettini et al., 2009; Holdsworth et al., 2010; Collettini, 2011) and contributes to softening of the shearing rock along with grain size reduction and the development of crystallographic preferred orientation. Deformation and metamorphic reactions occur simultaneously in extensional shear zones. It is very likely that the localization of deformation influences fluid flow. Although it is difficult to determine whether strain localization is influenced by fluid circulation. The presence of fluids appears to enhance the localization of deformation, but is unlikely initiating localization.

Fluids enable feldspar hydration and dissolution of quartz, which allows strain accommodation by volume loss in shear zones (O’Hara and Blackburn, 1989). Based on variations in element concentration between a protolith and an altered rock, Gresen (1967) proposed an equation allowing the calculation of the composition-volume variations during metasomatic alteration. This equation, rewritten by Grant (1986), provides a simple way to quantify gains and losses in mass transfer. Since then, several studies have been conducted on volume change affecting shear zones; they show a wide range of results: O’Hara (1988) found

a volume loss of about 60% in a thrust fault; Tartèse et al.'s (2011) results indicate a 25% volume gain in a transpressional shear zone. In an extensional setting, the development of a connected porosity may lead to vigorous fluid flow that may allow not only removal but also addition of material to the shear zone (Hippert, 1998).

In this chapter, the mineral assemblages and chemical variations are investigated with respect to the fabrics affecting the granodiorite of the Bear Creek pluton. Since the phyllosilicates were most likely recrystallizing during retrograde metamorphism and contain the major elements of the rock, single grain analyses have been conducted on micas and chlorite in order to trace chemical variations as a function of strain and conditions of deformation at the grain scale. Finally, based on Grant's (1986) equation and on the least-square method approach to mass transport developed by Baumgartner et al. (1995), volume change through the Bitterroot shear zone is discussed in terms of mass-transfer at the shear zone scale.

1. Sampling strategy:

The Bitterroot shear zone (BSZ) deformed the Bear Creek pluton during the Eocene; the shear zone footwall is considered relatively isotropic and uniform in composition (granodiorite). Therefore, the BSZ offers an ideal place for quantifying fluid/rock interaction related to strain and deformation mechanisms, from grain scale to shear zone scale.

Two vertical sections of the BSZ provide a continuum of deformation, from ductile to brittle regimes. The Lost Horse Canyon section is about 1 km wide and displays an evolution from magmatic fabric in the structurally deepest outcrops to alternating bands of mylonite and ultramylonite zones in the upper part of the section. The Sweathouse section corresponds to the highest part of the shear zone, where the detachment fault is preserved and puts in contact the mylonite below with chloritized breccia above.

The different rock types that characterize the BSZ were sampled over three field seasons (BT08, BT09, BT10). X-Ray Fluorescence (XRF) and X-Ray Diffraction (XRD) analyses were performed on 22 samples (cf. Chapter II for methodology). Of those, 18 samples from the Lost Horse section (Figure IV-1) were analyzed: 3 samples from the protolith, 9 from mylonite, 4 from ultramylonite and 2 from cataclasite). The dataset is complemented with samples from the Sweathouse section (Figure IV-2): two mylonite samples in order to compare the results with the Lost Horse section (BT10-03 and -17), and 2 bleached granodiorite samples (BT10-04 and -16).

Major element compositions of phyllosilicate were obtained by microprobe analyses on 10 samples over the two sections. The Lost Horse Canyon section displays 8 of these samples (Figure IV-1), where the deepest protolith sample (BT09-80T) was selected in order to define the magmatic composition of the phyllosilicates. Mylonite samples are distributed across the Lost Horse section, except BT08-15 located in the Sweathouse quarry (Figure IV-2). The cataclastic detachment fault of the Sweathouse section was also analyzed (BT10-33).

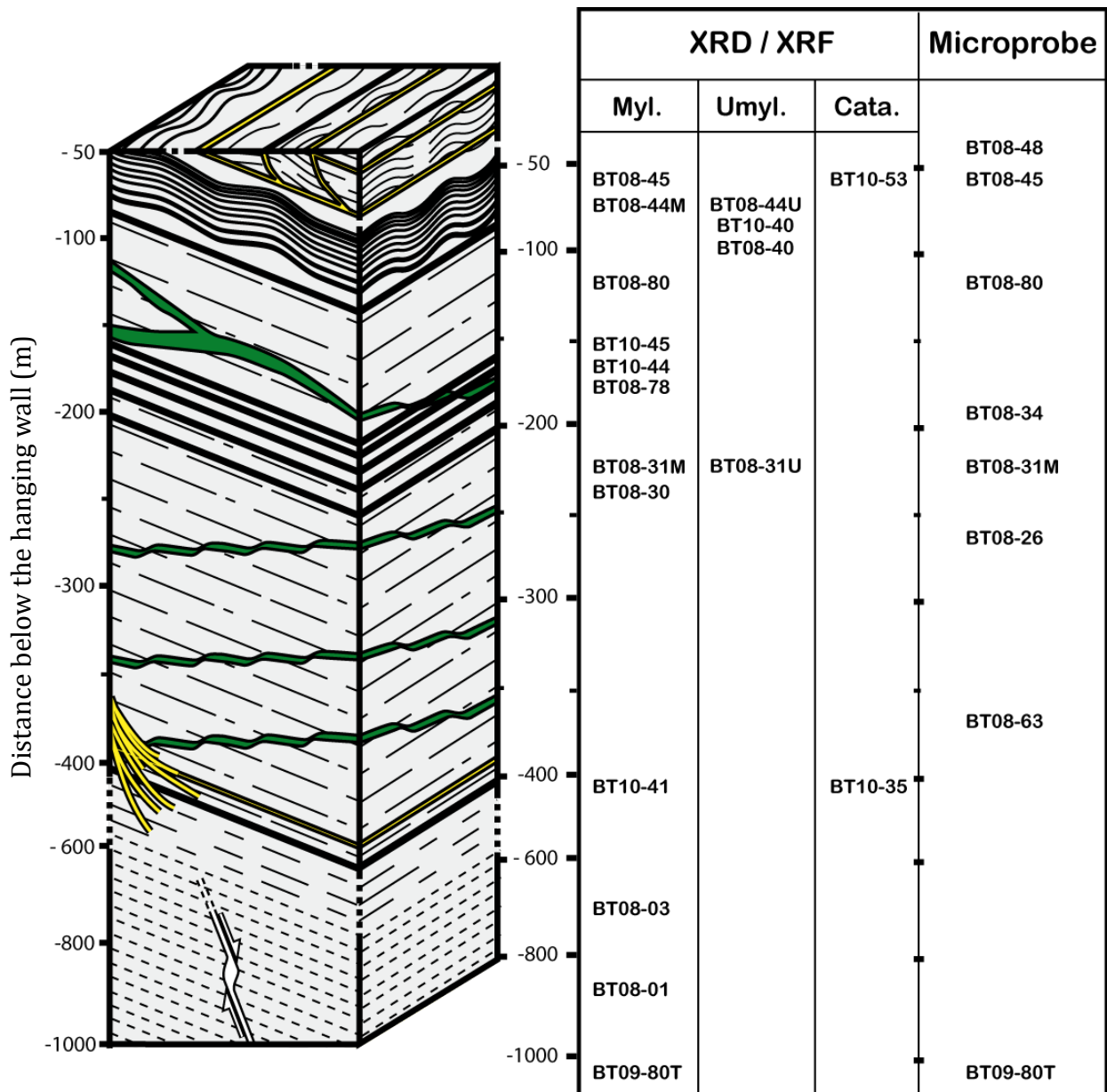


Figure IV-1: Location of samples on the block diagram corresponding to the Lost Horse Canyon section. Samples are listed as a function of the type of analyses, and rock type. Myl. : mylonite ; Umyl. : ultramylonite ; Cata. : cataclasite.

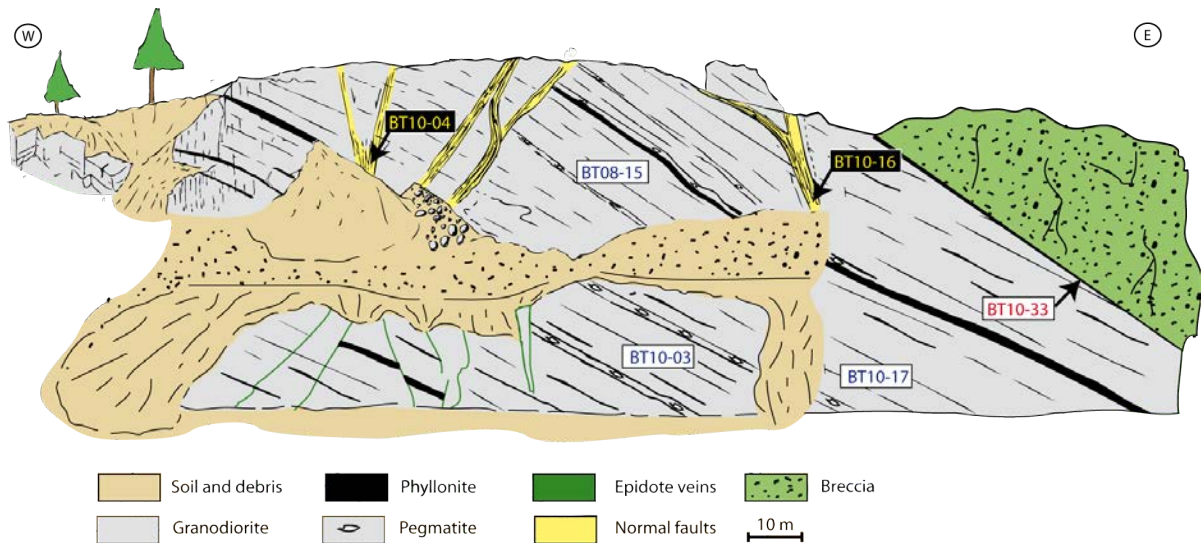


Figure IV-2: Location of samples on the schematic view of the Sweathouse section. Samples are presented in relation to rock types. Blue: mylonite ; Yellow: bleached granodiorite ; Red: cataclasite.

X-ray fluorescence analyses were conducted in order to characterize the evolution of bulk-rock chemistry with respect to strain. Major and trace elements were measured on protolith, mylonite, ultramylonite, bleached granodiorite, and cataclasite. In addition, single grain analyses were performed using an electron microprobe on muscovite, biotite, and chlorite in order to access the chemical variation of major elements from the core to the rims of phyllosilicates. The aim of this study is to examine the effect of deformation on muscovite, biotite, and chlorite recrystallization and growth, and therefore to better understand the variations in chemical and isotopic compositions.

2. Mineral assemblages characterizing the mylonitic series and cataclasite of the BSZ

The proportion of major minerals was determined semi-quantitatively by X-ray Diffraction (XRD) analyses (Appendix IV, Table IV-1). These analyses were performed on each sample where bulk-rock chemical analyses were run (Figure IV-3). Mineral abbreviations in this chapter are after Whitney and Evans (2010).

Mylonite and cataclasite have a similar major mineral composition: 42% plagioclase, 26% K-feldspar, 25% quartz, 5% phyllosilicates and 2% other minerals. The XRD analyses highlight a decrease of feldspar content (-10%) and a relative increase of quartz content (+5%) compared to the protolith. Ultramylonite and bleached granodiorite show major mineral composition changes. Ultramylonite has a decrease of feldspar content (-30% for both

feldspars) and an increase of quartz content (+20%) compared to the granodiorite. The bleached granodiorite shows the largest mineral content variations, with a decrease of quartz (-15%) and K-feldspar content (-15%), while the plagioclase content shows a relative increase of +30%.

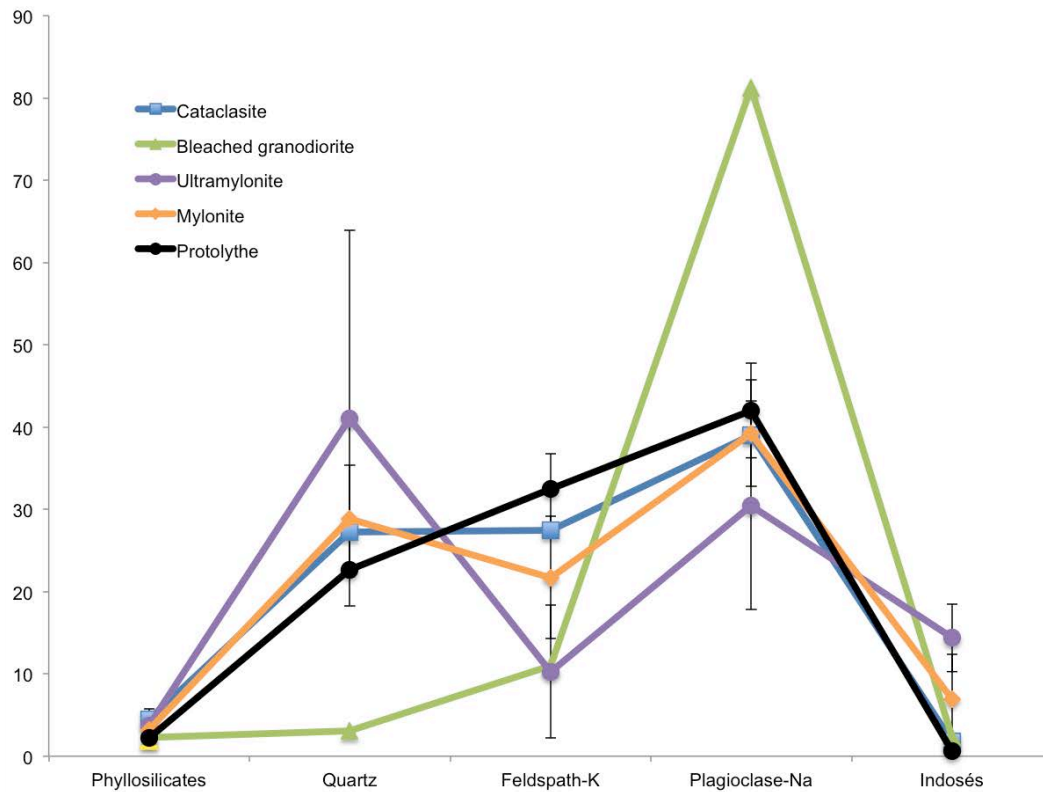


Figure IV-3: Proportion of major minerals (%) defining the mineral assemblages of fabrics affecting the granodiorite from the BSZ, determined by X-ray diffraction.

3. Major and trace element variations in the mylonitic series and cataclasite of the BSZ

Major and trace element concentrations were determined for the same samples that were used for XRD analyses. The amount of rock necessary for reliable bulk-rock analyses for the granodiorite should be about 2 kg for granodiorite with centimeter-sized feldspar, but in our case, the samples used for the major and trace element analyses were 0.5 kg before crushing. The following results are, therefore, only semi-qualitative (Appendix IV, Table IV-2) for the protolith samples, and qualitative for mylonite and ultramylonite samples since the grain size is sub-centimetric.

A principal component analysis (PCA) was performed on the 22 samples together with output for 13 variables for the major elements and 23 variables for the trace elements (Figure

IV-4). The PCA was computed using “R” software and FactoMineR package, and provides a statistical approach for determining correlation and anti-correlation between the different variables (major and trace elements). The computed PCA highlights a principal dimension describing 67% of the variables and opposing SiO_2 and K_2O to Fe_2O_3 , TiO_2 , K_2O , MgO , MnO , CaO , P_2O_5 , NiO , Cr_2O_3 , and LOI (H_2O) (Figure IV-4, top). For the trace elements, the PCA shows a poorer correlation, with a principal factor explaining 33 % of the variables, which is not sufficient to determine if an element opposes the others (Figure IV-4, bottom).

PCA indicates that SiO_2 and K_2O are anti-correlated with the other major elements. The Harker’s diagrams in Figure IV-5 show the correlation existing between SiO_2 and other major elements. For each diagram the three samples from the protolith define a narrow zone. In contrast, the mylonite and ultramylonite show that SiO_2 and K_2O content are anti-correlated with the Al_2O_3 , Fe_2O_3 , TiO_2 , CaO , P_2O_5 , and LOI contents. In terms of SiO_2 , Al_2O_3 and K_2O contents, the mylonite and ultramylonite show element concentrations that are either higher or lower than those characterizing the protolith. The bleached granodiorite is characterized by a 5-15 wt% decrease of SiO_2 compared to the protolith content. Except for the Na_2O content, which is twice as high as in the other BSZ deformed rocks, bleached granodiorite presents the same element concentrations as do the mylonite and ultramylonite.

In terms of trace element variations, the protolith shows consistent element concentrations through the three analyzed samples (Figure IV-6). Compared to the protolith concentrations, the mylonite has higher concentrations in Zr, Sr, Co, Ce, Ba, La, and S. In contrast, in the ultramylonite the concentration of Sr and Ba are lower, while Zr, Rb, Zn, Ni, Co, Cr and Sc are higher with respect to protolith concentrations. Bleached granodiorite has a similar trace-element spectrum to that of the protolith, except for a decrease in Sr and Ba content (Figure IV-6).

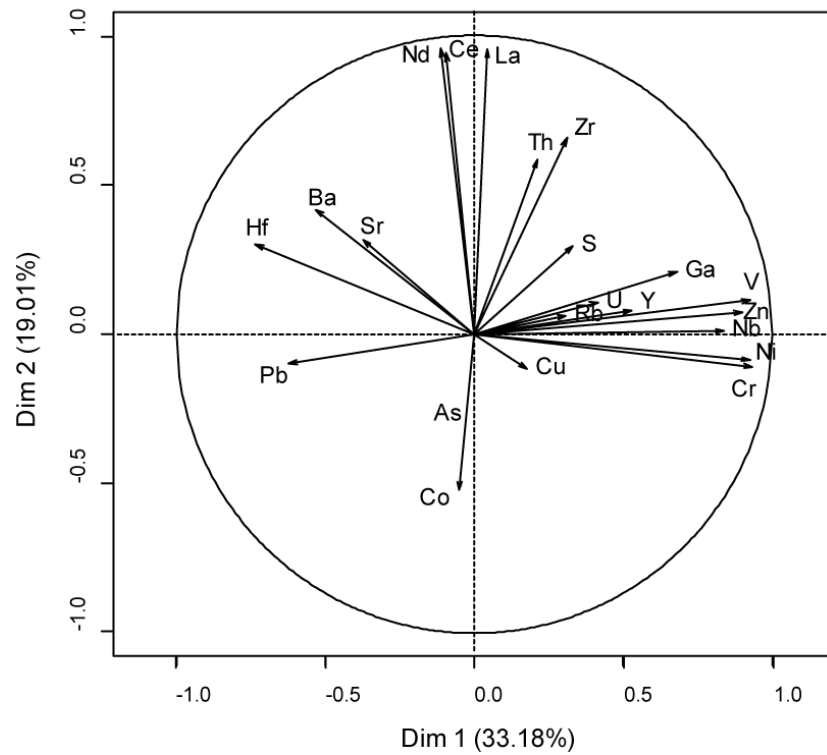
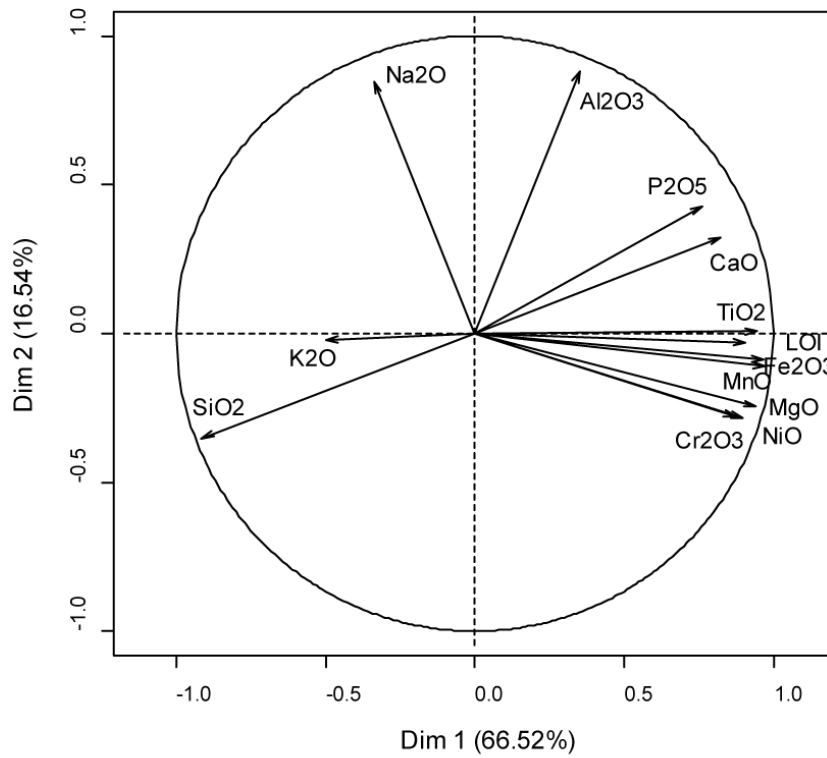


Figure IV-4: Variable factor map, according to the PCA performed on major elements (Top), and on trace elements (Bottom). Dim 1 and Dim 2 correspond to the correlation percentage along the x and y-axis, respectively.

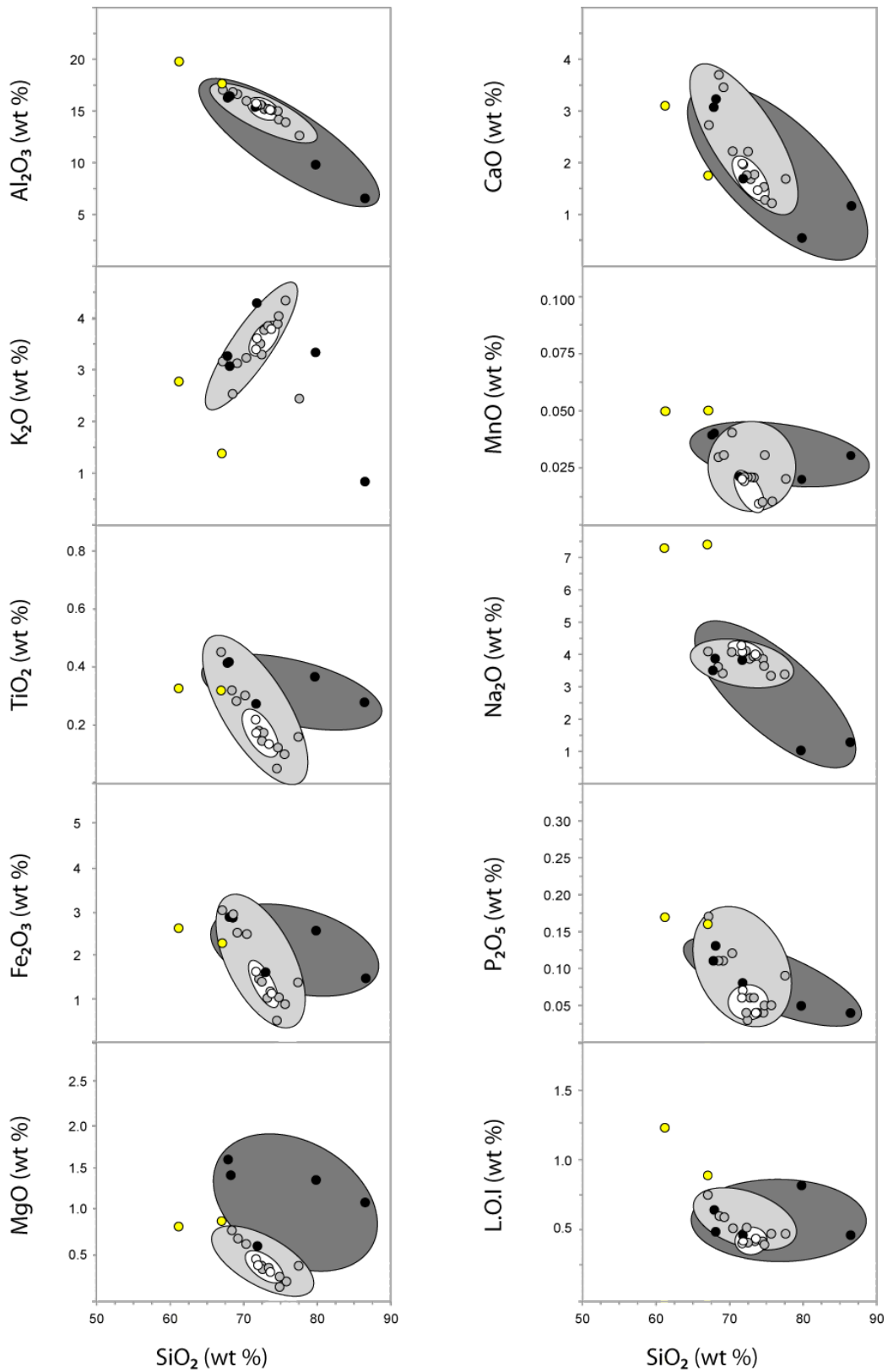


Figure IV-5: Harker diagram showing the correlation between SiO_2 and other major elements. White zone circles the protolith values, light grey zones the mylonite and dark grey zones the ultramylonites. Yellow dots: bleached granodiorite.

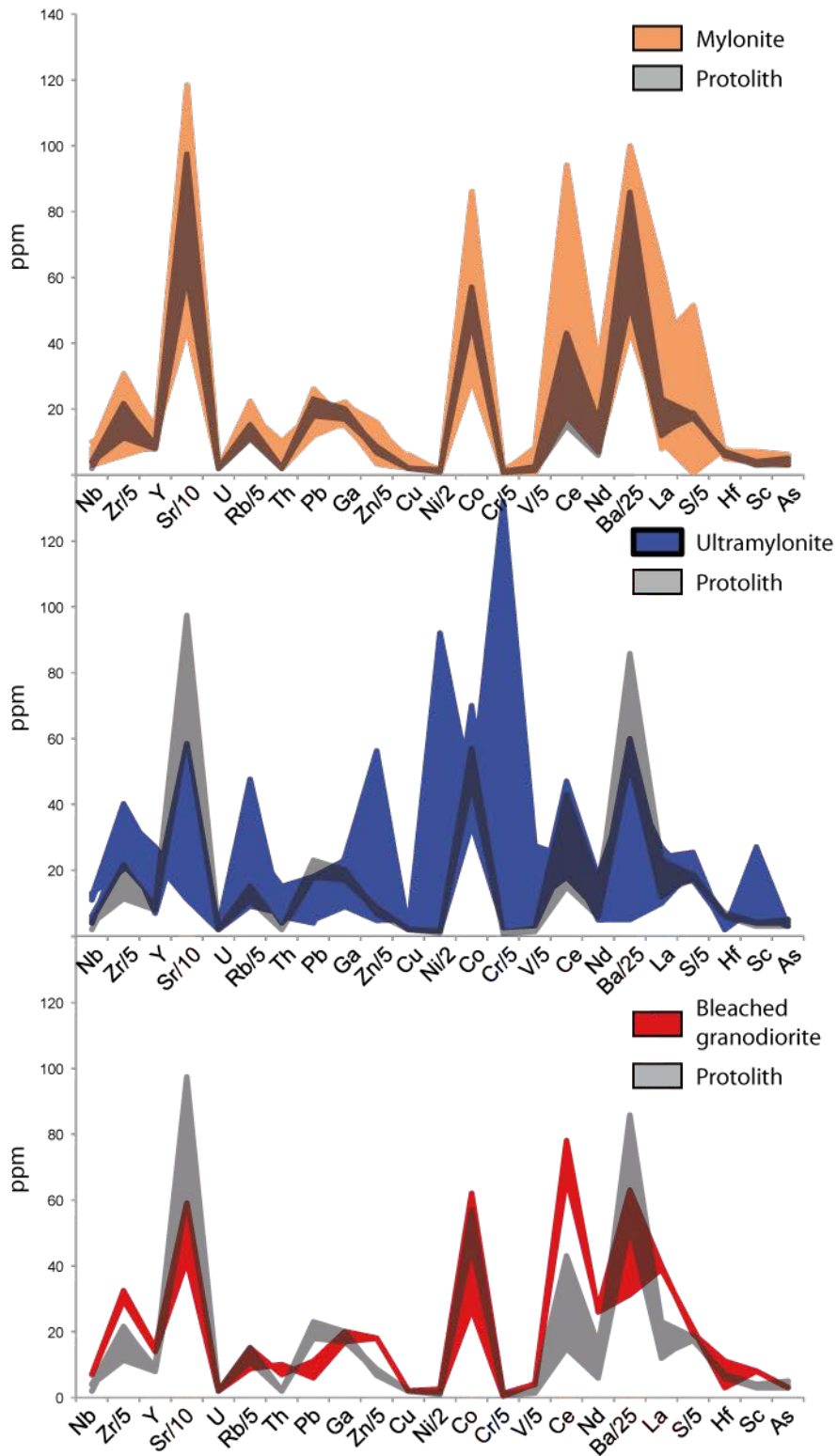


Figure IV-6: Spectra of trace-element content in mylonite (orange), ultramylonite (blue) and bleached granodiorite (red). The protolith spectra of trace-element content is in grey, which can be darker when superimposed with the other spectra.

4. Mass-balance analysis related to the different fabrics of the BSZ:

The fluid/rock interaction can be estimated by comparing major and trace-element concentrations of “altered” rocks (C_a) with respect to a parent rock (C_p). Determination of concentration changes during mylonitization can be calculated by following the equation (1) (Grant, 1986; Potdevin and Marquer, 1987; Olsen and Grant, 1991; Sturm, 2003, Grant, 2005):

$$\Delta C_i/C_i^A = [(M^B/M^A)(C_i^B/C_i^A)] - 1 \quad (1)$$

$\Delta C_i/C_i^A$ corresponds to the ratio of changes to original amount, C_i^A and C_i^B describe the concentrations of a certain element (i) in the parent rock (A) and in the altered rock (B). The volume changes (V^B/V^A) can be estimated by taking the reciprocal of the isocon line (M^A/M^B) where M represents mass (?) and following the equation (2) (Olsen and Grant, 1991; Sturm, 2003):

$$V^B/V^A = [(M^B/M^A)(\rho^B/\rho^A)] \quad (2)$$

In the BSZ, the parent rock, or protolith, is a granodiorite. According to the XRD results, deformation related to the detachment activity modified the proportion of the different minerals, but not the mineral assemblages. Since the density of quartz, feldspar, and phyllosilicates ranges from 2.5 to 2.7 g/cm³, it is thought that the deformation affecting the granodiorite may not be reflected by the density of the deformed granodiorite. Indeed, Glazner and Bartley (1991) have measured densities of 2.61±001 and 2.69±004 g/cm³ for a granodiorite and a mylonite, respectively. Such densities provide a density factor $\rho^B/\rho^A = 1.030$, and according to equation (2), it implies a classification in three types: (1) a volume-conservative type when $M^B/M^A \approx 1$, (2) a volume-gain type when $M^B/M^A \gg 1$, and (3) a volume-loss type when $M^B/M^A \ll 1$.

The isocon method (Grant, 1986) provides a quantitative evaluation of chemical gain and loss in mass transfer, based on species (major and/or trace elements), major and/or trace are assumed to remain immobile in the process, which define a straight line through the origin called an isocon (Figure IV-7). The immobile species can be determined either graphically (Grant, 1986; Hippert, 1998; Kwon et al., 2009) or statistically (Baumgartner et al., 1995; Mori et al., 2003). The least-square approach of Baumgartner et al. (1995) provides a statistically rigorous approach for quantifying the immobile species with their overlapping cone method (Appendix IV, Table IV-3,4 and 5). Such an approach provides an unbiased

choice of isocon, but neither takes into account the geochemical characteristics of the species involved nor the process being studied (Grant, 2005).

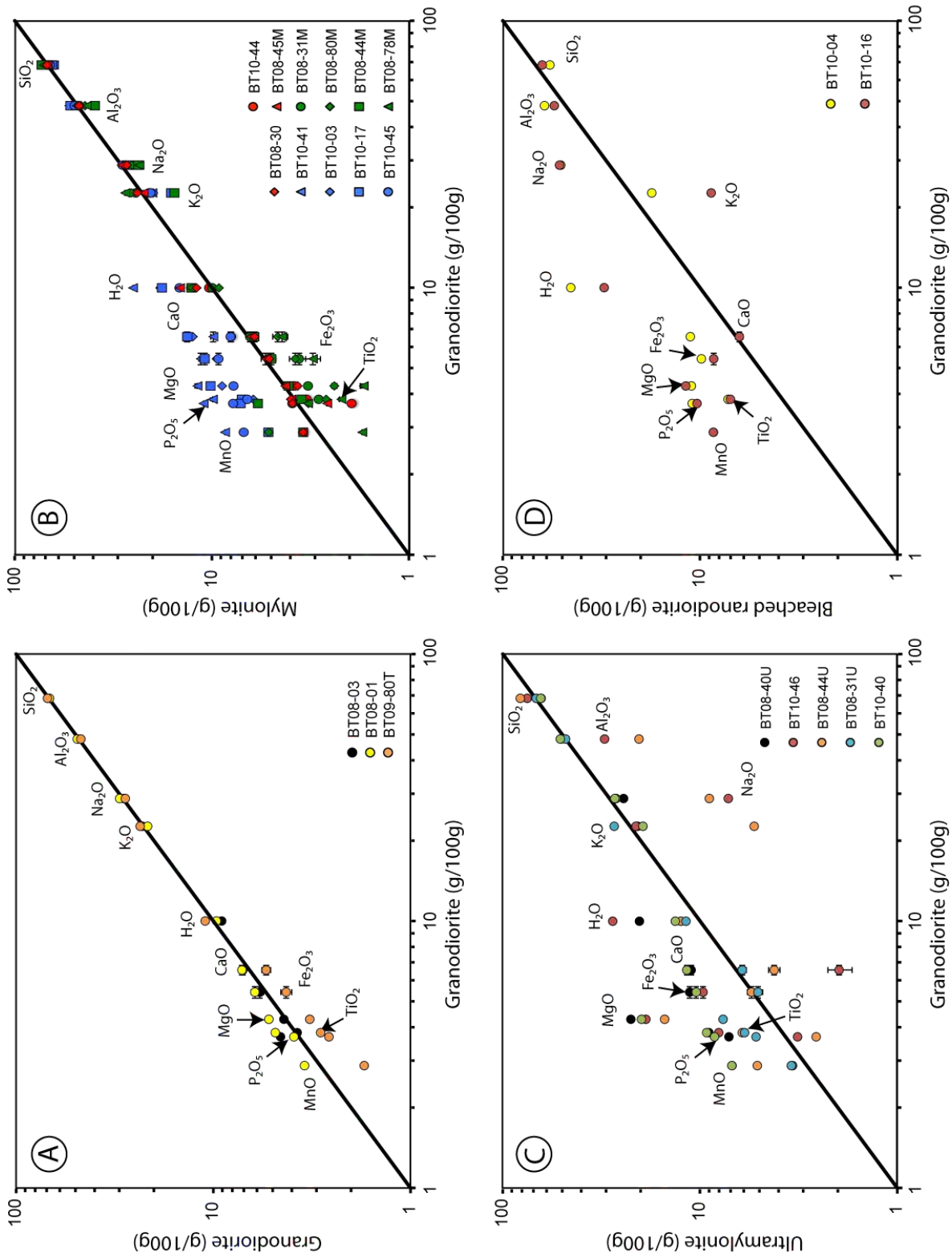


Figure IV-7: Isocon diagrams for the alteration of the granodiorite with respect to the different fabrics of the BSZ. A. Three samples of the granodiorite defining the average protolith composition. B. Mylonite. C. Ultramylonites. D. Bleached granodiorite.

In shear zones, mass transport calculations are largely based on the five following immobile species: TiO_2 , Al_2O_3 , MgO , Fe_2O_3 and Zr (Grant, 1986; O'Hara, 1988; Mohanty and Ramsay, 1984; Goddard and Evans, 1995; Hippert, 1998; Manatschal et al., 2000; Kwon et al., 2009; Tartèse et al., 2011). Consequently, this study aims to combine the two approaches in order to constrain both statistics and geochemical characteristics of the system. In a first step, the major and trace-element concentration changes of each sample relative to the average protolith composition (3 samples) have been evaluated with the software "Isocone_2_IBM" (Baumgartner et al., 1995), where species have log-normal concentrations and the error for both protolith and samples corresponds to the logarithm of the average standard deviation (1σ) of the protolith. The software provides a list of several dozens of possible isocons, thus the choice of the best isocon for each sample is based on (1) an isocon defined by the presence of most of the five immobile species listed above, and (2) the largest number of additional immobile species defining the isocon.

Major element concentrations are plotted against the corresponding average concentrations of the protolith in Figure IV-8, the species are scaled in order to increase the graphical dispersion of species along the isocon. The scaling factor applied to each species corresponds to $1/(1\sigma)$, where 1σ is the standard deviation of each average protolith species. The three granodiorite samples collected at 150 m from one another show major element compositions aligned along the isocon, even if BT09-80T have lower values in terms of MnO, MgO, Fe_2O_3 and CaO (Figure IV-8A). Mylonite samples show a scattered distribution of the species concentrations, and three groups of samples are graphically determined: a group defined by a majority of element concentrations above the isocon (blue group, Figure IV-8B), a group with element concentrations aligned along the isocon (red group, Figure IV-8B), and a group with a majority of element concentrations below the isocon (green group, Figure IV-8C). Ultramylonite and bleached granodiorite have the most scattered major element concentrations relative to the average protolith concentrations. The dispersion of the major element concentrations with respect to the different strain facies (mylonite, cataclasite) provides a first indication of the fluid-rock ratio experienced by these rocks.

Since it is assumed that deformation processes are not accompanied by large density changes, the mass changes calculated using "Isocone_2_IBM" (Baumgartner et al., 1995) correspond to the volume changes. The results for the protolith samples indicate a conservative-volume type, while the mylonite samples defines three groups (Figure IV-8). Group A (blue group in Figure IV-8B) shows volume changes of -22 ± 5 % down to -47 ± 4 %,

which is indicative of a volume loss. Group B (red group in Figure IV-8B) ranges between 0 ± 2 % and 4 ± 2 % and corresponds to a conservative-volume type, and group C (green group in Figure IV-8B) shows volume changes ranging from 7 ± 3 % up to 25 ± 5 %, which is indicative of a volume gain. The ultramylonite shows volume changes ranging from -17 ± 4 % down to -46 ± 7 %, indicative of volume loss. Finally, the two samples from the bleached granodiorite show volume losses of -44 ± 3 %.

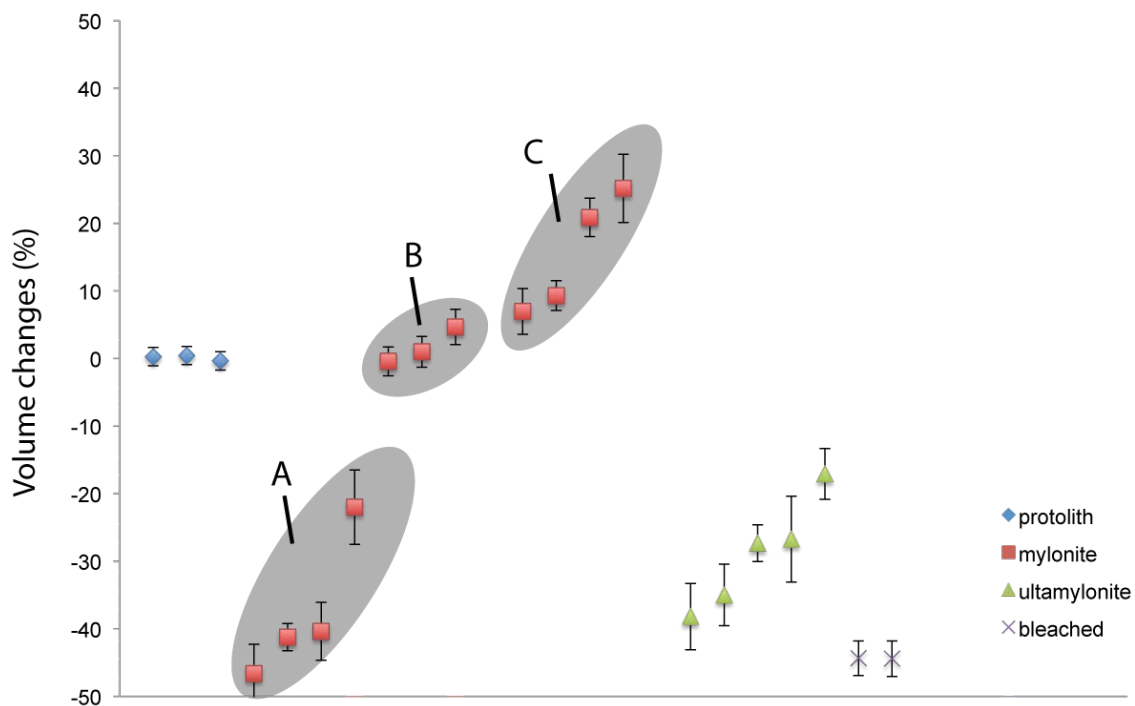


Figure IV-8: Volume change in the different fabrics of the BSZ. Samples from the protolith do not show volume change. Samples from the mylonite highlight three tendencies: the group A is characterized by a volume-loss type, the group B by a volume-conservative type, and the group C is defined by a volume-gain type. Ultramylonite and bleached granodiorite correspond to a volume-loss type. See Appendix IV, Table IV-3,4 and 5 for details.

Mass changes of elements are provided by the “Isocone_2_IBM” software (Baumgartner et al., 1995). Mylonites from group A (purple lines in Figure IV-9) are characterized by volume loss and show:

- a mass decrease of SiO_2 , Al_2O_3 , K_2O , NaO ,
- a relative mass increase of insoluble elements such as TiO_2 , Fe_2O_3 , MgO , and MnO .

Mylonites from group B are isovolumetric and show no significant mass changes of major elements (orange lines in Figure IV-9), while mylonites from group C (blue lines in Figure IV-9), characterized by volume gain show:

- a mass increase of SiO₂, MnO, and K₂O,
- a relative mass decrease of TiO₂, Fe₂O₃, and MgO due to dilution of these elements.

In contrast, calculated mass changes in ultramylonite samples show a regular pattern (Figure IV-9B):

- a mass increase of TiO₂ and MgO,
- a mass decrease of SiO₂, Al₂O₃, CaO, K₂O, and NaO.

Samples of the bleached granodiorite also show a regular pattern of mass changes (Figure IV-9C):

- a mass increase of MgO, MnO, H₂O,
- a mass decrease of SiO₂, Al₂O₃, CaO, and K₂O.

Ultramylonite and bleached granodiorite are characterized by significant volume loss (> -15 %), thus the apparent mass increase of species in these rocks is a direct result of changes in concentration.

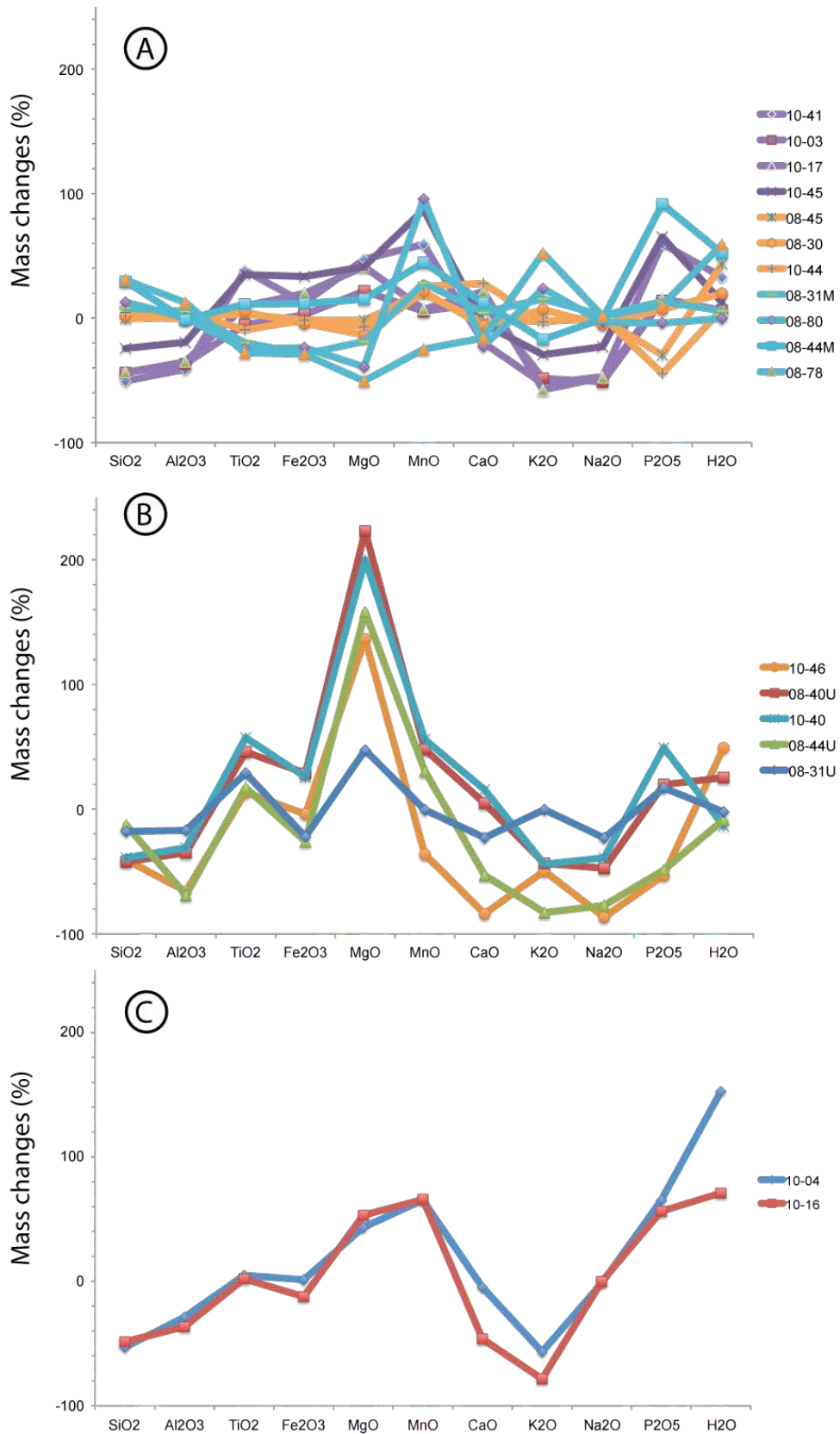


Figure IV-9: Mass changes of the major elements in the different deformation fabrics of the BSZ. A. Mylonite; B. Ultramylonite; and C. Bleached granodiorite.

5. Chemistry of phyllosilicates:

5.1. Single grain analyses:

Microprobe analyses have been performed on several muscovite, biotite, and chlorite grains along a transect perpendicular to the shear plane (Appendix IV, Table IV-6, 7, and 8). Besides the tabular muscovite in the protolith, the analyzed muscovite grains in mylonite are mica fish that are scattered in a matrix of quartz (cf. Chapter III.2.1) or are bordering feldspar porphyroclasts. The muscovite composition is relatively constant (sample BT08-48-M18) and does not have major element variations on mineral transects across and along the grains (Figure IV-10). Analyzed muscovite grains have a composition in SiO₂ of 46 wt%, in Al₂O₃ of 33 wt%, in K₂O of 11 wt%, in FeO of 3 wt% and in MgO of 1 wt%.

Biotite is rarely observed with fish shape, but is rather tabular and commonly included in feldspar porphyroclasts. Biotite is unaltered or partially chloritized (Figure IV-10, Figure IV-11). Where biotite is unaltered, it has no change in chemical composition. For example, analysis BT08-63-B01 has a SiO₂ content of about 35 wt%, 20 wt% of FeO, 18 wt% of Al₂O₃ and about 10 wt% of both MgO and K₂O (Figure IV-10). A pure chlorite (BT08-63-C03), representative of the chlorite composition observed in the section, has a composition of 26 wt% of SiO₂, 27 wt% of FeO, 21 wt% of Al₂O₃, 13 wt% of MgO and null for K₂O (Figure IV-11). Transects in pure chlorite show no zoning and have a constant composition throughout the section.

Where biotite is chloritized, the zoning observed under the optical microscope is also reflected in the chemical compositions. Sheets of chlorite are interspersed with biotite sheets (Figure IV-11). The transect in a chloritized biotite (BT08-31-C03) illustrates the process of chloritization of biotite: the major element compositions are highly variable (several wt%), particularly for SiO₂, FeO and K₂O contents. These values are not representative of major element diffusion between biotite and chlorite. The mixed composition of major elements corresponds to a matrix effect correction in the analysis that can generate 5-10% error per element; owing to this effect, values become intermediate between pure pole values for biotite and chlorite.

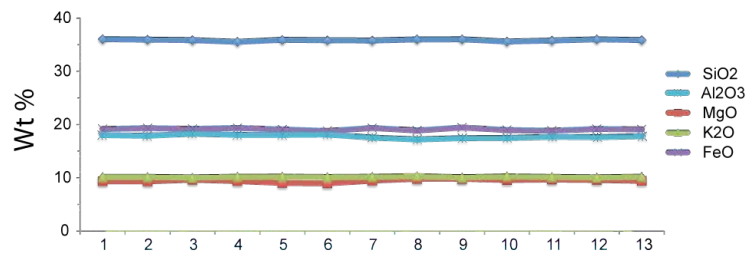
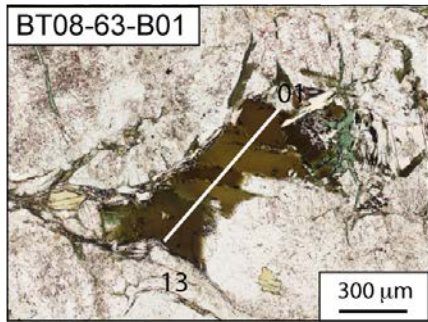
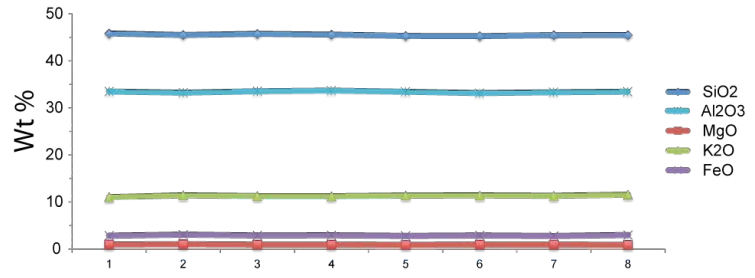
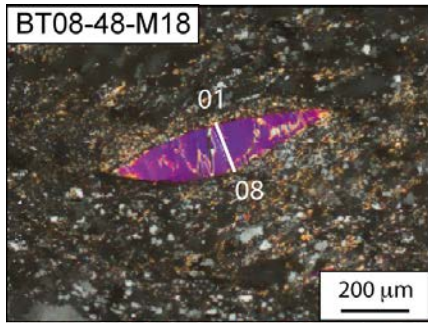


Figure IV-10: Single grain analysis transect in a muscovite fish (BT08-48-M18), and in a tabular biotite (BT08-63-B01), representative of the mylonite from the BSZ. The transects of the muscovite and biotite do not show significant major element variation.

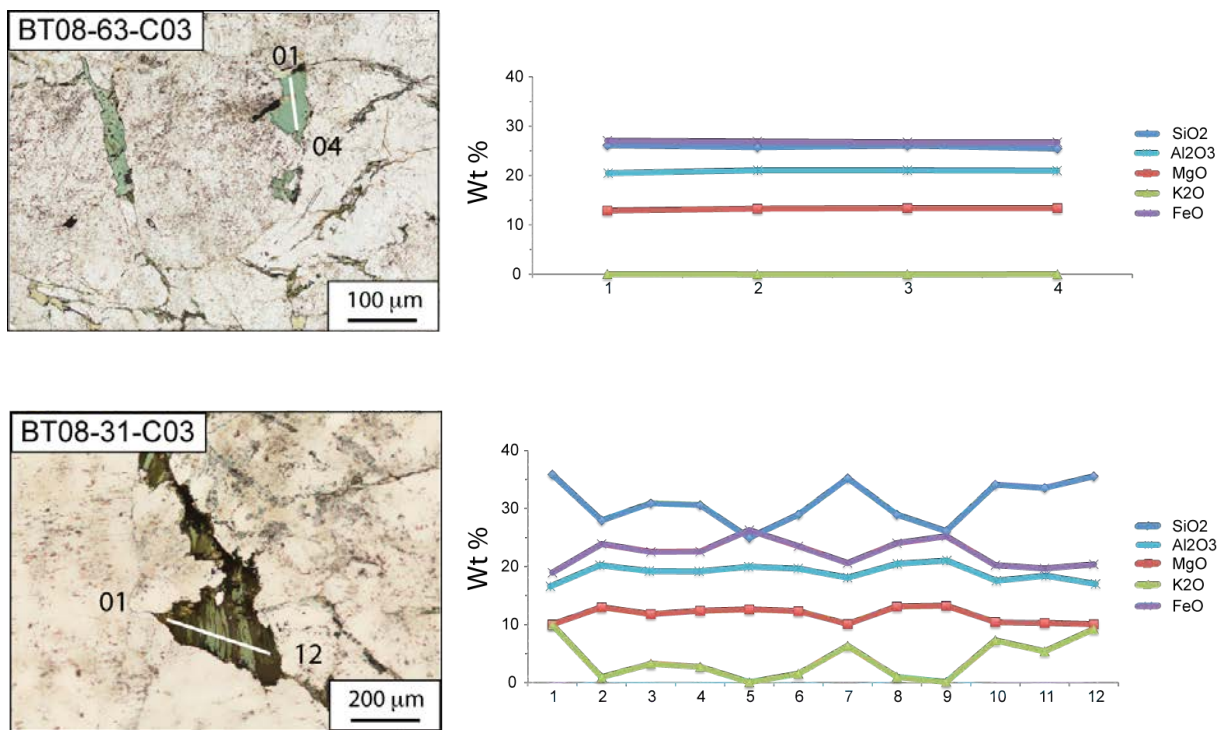


Figure IV-11: Single grain analyses along a transect in chlorite (BT08-63-C03), and in chloritized biotite (BT08-31-C03), representative of the mylonite from the BSZ. The transect of the chlorite shows no major element variations, whereas the chloritized biotite shows major element variations that are distributed between the biotite pole and the chlorite pole.

The fact that the total wt% of some analyses (Appendix IV, Table IV-6, 7, and 8) is lower than what is expected for phyllosilicates can be explained as follows: (1) the polishing of the thin section may be problematic since the phyllosilicates are softer than the rest of the mineral assemblage and may, therefore, have surface irregularities during the analysis; (2) the low total wt% may also come from a partial void where the beam contacts the sample, since the phenomenon of chloritization generates volume loss (Kogure et al., 2000) and could preserve voids in the interlayers.

5.2. Chemiographic representation of phyllosilicates:

The chemical analysis of phyllosilicates, at a grain scale, was conducted to determine whether the deformation of the granodiorite induces composition changes of biotite, muscovite and chlorite. The number of ions is calculated on the basis of 11 oxygens for biotite and muscovite, and on the basis of 14 oxygens for chlorite. A chemiographic representation of the microprobe dataset is done in $MR^3-3R^2-2R^3M$ coordinates, where $MR^3 = 2*Ca+Na+K$; $3R^2 = (Mg+Fe+Mn)/3$ and $2R^3M = (Al_{tot}-MR3)/2$. Figure IV-12 displays the

different fields of composition of natural phyllosilicates (Velde, 1972, 1977a, 1977b, 1995). Plotting the microprobe results on the chemiographic representation provides a first estimate on the validity and quality of the phyllosilicates analyses in this study.

In the protolith (Figure IV-12 A), muscovite is characterized by a MR^3 between 45 and 55 %, a $2R^3M$ between 35 and 50 % and a $3R^2$ lower than 15 %. Biotite has a MR^3 between 40 and 50 %, a $2R^3M$ between 15 and 35 % and a $3R^2$ between 25 and 40 %. Chlorite is defined by MR^3 below 10 %, a $2R^3M$ between 45 and 50 % and a $3R^2$ between 45 and 55 %. muscovite, biotite and chlorite of the protolith thus define three distinct poles, corresponding to their respective field of composition on the ternary diagram.

In the mylonites (Figure IV-12 B), muscovite has MR^3 , $3R^2$ and $2R^3M$ values that differ by a few percent from that defined for the protolith. Biotite has a MR^3 between 0 and 60 %, a $2R^3M$ between 10 and 50 % and a $3R^2$ 20 to 50 %. Chlorite is defined by MR^3 between 0 and 60 %, a $2R^3M$ between 10 and 50 % and a $3R^2$ between 30 and 55 %. muscovite, biotite, and chlorite of the mylonite thus define similar poles to those observed in the protolith; nevertheless some values of biotite and chlorite are spread from one pole to the other.

In the ultramylonite (Figure IV-12 C), muscovite is characterized by a MR^3 between 45 and 55%, a $2R^3M$ between 15 and 25% and a $3R^2$ lower than 15 %. Biotite and chlorite have a MR^3 between 35 and 50 %, a $2R^3M$ between 15 and 25 % and a $3R^2$ between 25 and 40 %. The poles are still similar to those defined in the protolith, and a few values are spread between biotite and chlorite poles.

Finally, chlorite analyzed in a cataclasite (Figure IV-12 D) is defined by MR^3 less than 5 % (except for one data at 10 %), a $2R^3M$ between 40 and 50 % and a $3R^2$ 50 to 60 %. Chlorite in the cataclasite thus defines a pole similar by a few percent to that for the chlorite pole defined in the protolith.

Thus, a selection in the data was performed in order to remove analyses indicating a mixed composition between chlorite and biotite. The selection is largely based on the K_2O and H_2O contents. However, analyses showing characteristic major element compositions of biotite and chlorite, but with totals of a few percent lower than expected (3-5 wt% for biotite, and 8-12 wt% for chlorite) were retained for reasons presented in the previous section.

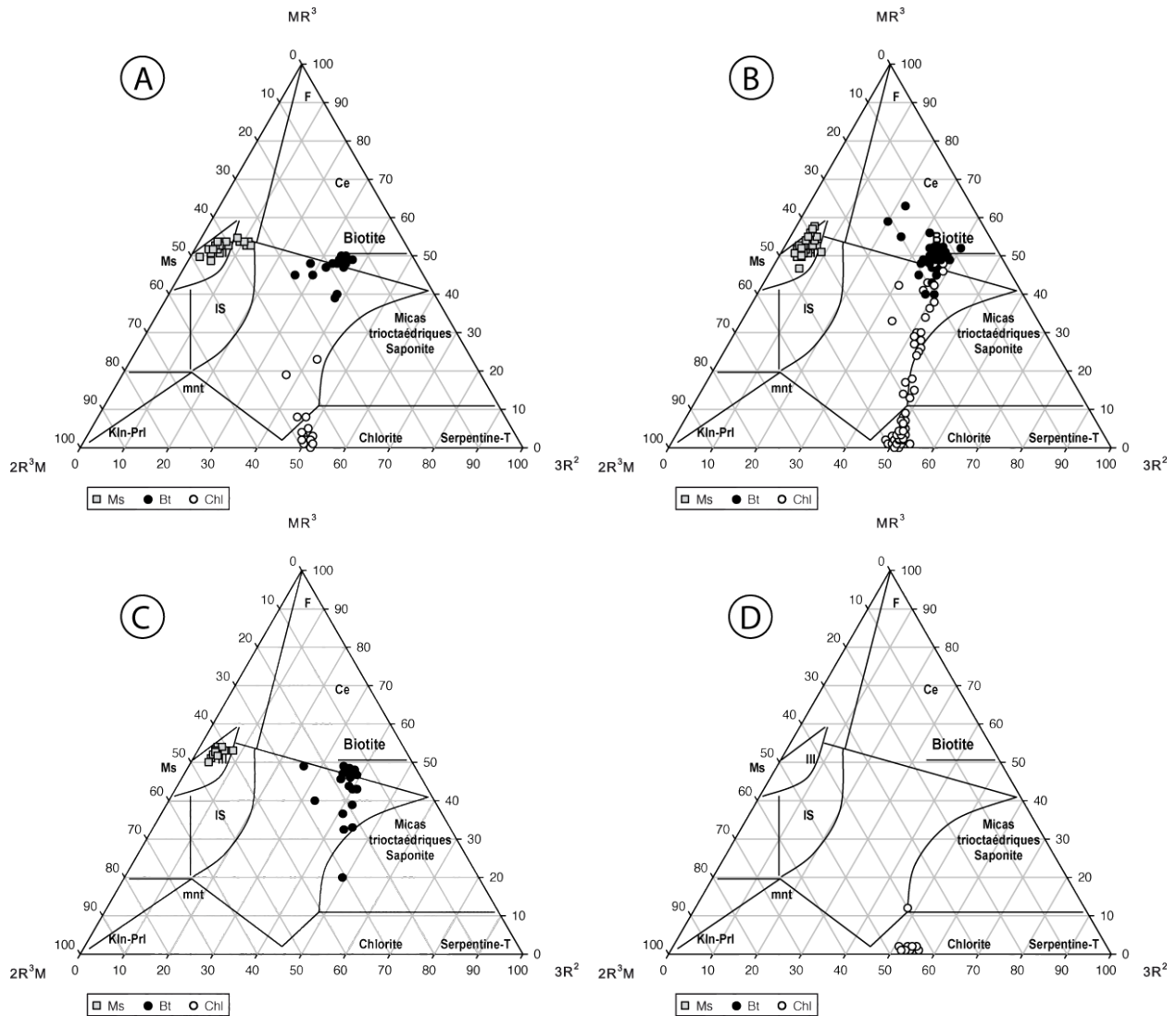


Figure IV-12: Chemiographic representation of Bt, Chl, and Ms according to the major deformation fabrics characterizing the BSZ. $MR^3: 2 * Ca + Na + K$; $3R^2: (Mg + Fe + Mn) / 3$; $2R^3M: (Al_{tot} - MR^3) / 2$. Muscovite is in grey, biotite in black, chlorite in white. A. Protolith, B. Mylonite, C. Ultramylonite, D. Cataclasite.

5.3. Muscovite-phengite Tschermak substitution:

Muscovite major elements have been reported in total aluminum (apfu) versus $\Sigma(Si + Mg + Fe^{2+})$ (apfu) diagrams in order to highlight the possible Tschermak substitution in white mica corresponding to phengitic-muscovitic compositions (Figure IV-13). The number of ions is calculated on the basis of 11 oxygens.

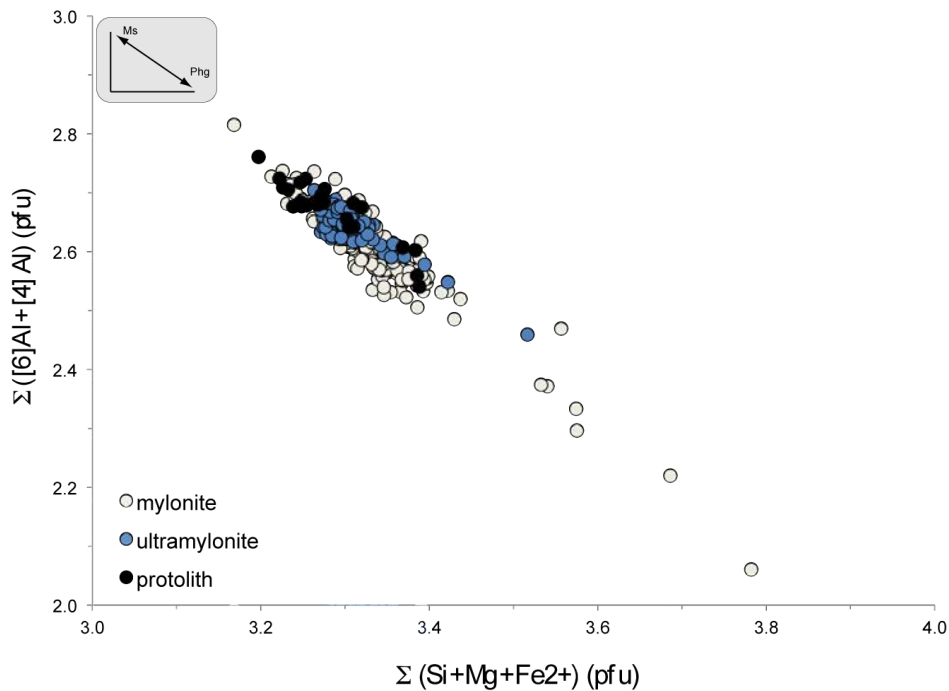


Figure IV-13: Tschermak substitution with total aluminum versus (Si+Mg+Fe) content on the basis of electron microprobe analysis of single grain transects. White micas in protolith, mylonite and ultramylonite define a muscovitic pole, only a few analyses show a trend towards a phengitic composition.

Over 95 % of white micas are defined by $\Sigma(\text{Si} + \text{Mg} + \text{Fe}^{2+})$ between 3.2 and 3.4 (apfu) and between 2.5 and 2.8 of total aluminum (apfu). According to Tschermak substitution, these white micas have an almost pure muscovitic composition. Whether the muscovite is from the protolith, the mylonites, or the ultramylonites, major element compositions of muscovite define a single domain. Only a few values of muscovite from the mylonite tend toward the phengitic pole.

5.4. Octahedral and tetrahedral substitutions:

The number of ions is calculated on the basis of 11 oxygens for biotite and muscovite, and on the basis of 14 oxygens for chlorite. Biotite, muscovite, and chlorite are plotted on a $\text{Mg} / (\text{Mg} + \text{Fe})$ versus octahedral aluminium (pfu) diagram, and are separated according to the different fabrics of the BSZ (Figure IV-14). In terms of octahedral aluminium, muscovite has the highest content, ranging from 1.5 up to 1.8 pfu. The octahedral aluminium content ranges from 0.9 to 1.25 pfu in chlorite and is lower than 0.5 in biotite. The $\text{Mg} / (\text{Mg} + \text{Fe})$ ratios of biotite, muscovite, and chlorite from the protolith define narrow ranges, while values are more scattered in the mylonites. Indeed, the $\text{Mg} / (\text{Mg} + \text{Fe})$ ratio of muscovite in the mylonite tends to increase up to 0.2 with respect to the protolith. Biotite from the mylonite shows an $\text{Mg} /$

(Mg+Fe) ratio ranging from 0.3 up to 0.55, and presents a ratio either lower or higher than the protolith biotite ratio. Muscovite and biotite from the ultramylonite show the highest Mg / (Mg+Fe) ratio. Biotite from the ultramylonite shows the most significant increase of the Mg / (Mg+Fe) ratio and defines a distinctive pole with ratio 0.35 higher than in the protolith. Chlorite from the cataclasite shows a Mg / (Mg+Fe) ratio over 0.5, defining the highest ratios for the chlorite group.

According to these observations, the Mg/(Mg+Fe) versus octahedral aluminum (pfu) diagram highlights a correlation between the Mg/(Mg+Fe) ratio and the various deformation fabrics of the BSZ.

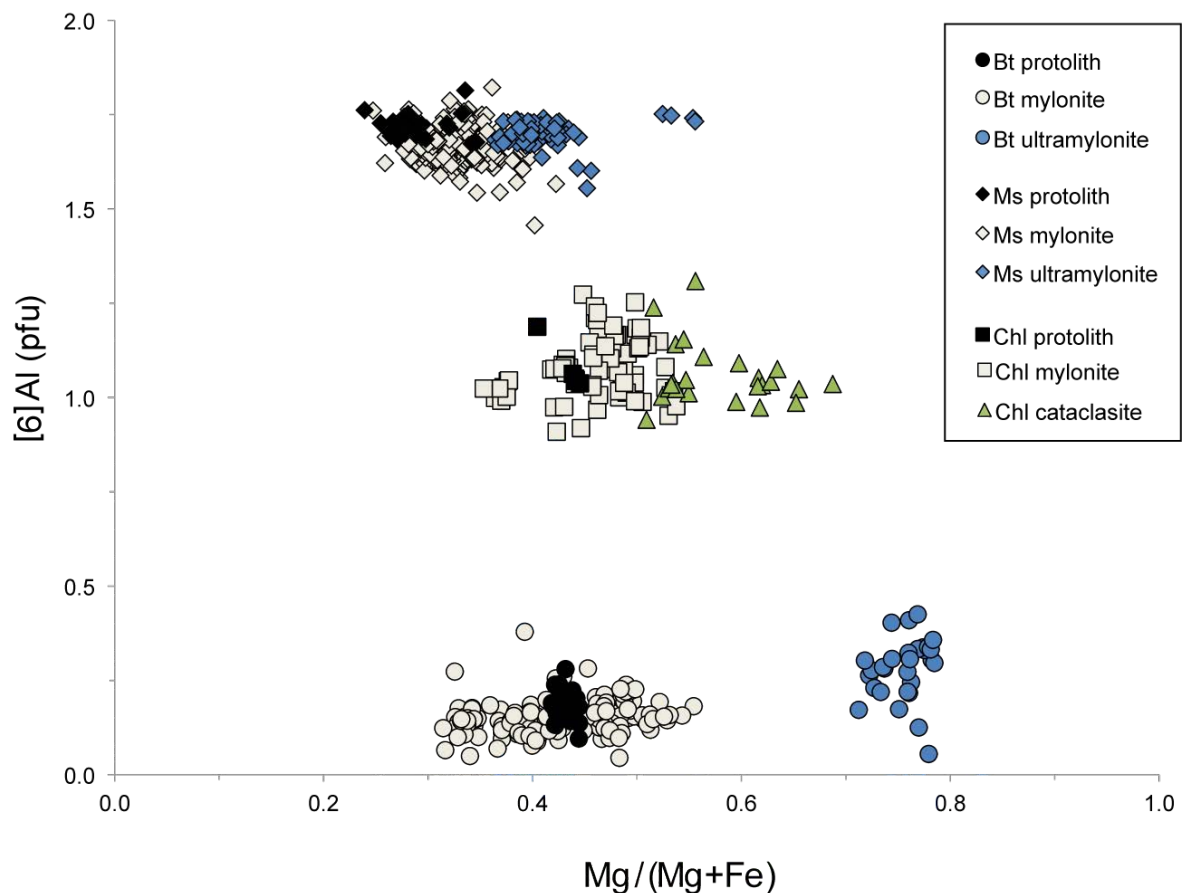


Figure IV-14: Octahedral aluminium content versus Mg / (Mg+Fe) ratio of phyllosilicates from the different fabrics of the BSZ. Phyllosilicates in the protolith define narrow ranges, whereas values are more scattered in the mylonite and ultramylonite. Note that the Mg / (Mg+Fe) ratio tends to increase with strain.

Phyllosilicates are also plotted on the Σ (Mg + Fe²⁺) versus Ti (pfu) diagram (Figure IV-15). Muscovite of the protolith, mylonite, and ultramylonite define a single domain with Σ (Mg + Fe²⁺) lower than 0.5, and Ti content lower than 0.1 pfu. Chlorite of the protolith, mylonite, and ultramylonite also defines a single domain characterized by a very low Ti content (<0.05 pfu) and a Σ (Mg + Fe²⁺) ranging from 3.5 up to 4.5. Biotite from the protolith has Ti content ranging from 0.15 and 0.20 pfu and a Σ (Mg + Fe²⁺) between 2 and 2.2, while biotite from mylonite has a similar Σ (Mg + Fe²⁺) to the protolith but shows a larger range of Ti content (0.10-0.25 pfu). Biotite from ultramylonite shows the lowest Ti content of the biotite group, with values lower than 0.10 pfu, while Σ (Mg + Fe²⁺) increases slightly towards the chlorite group.

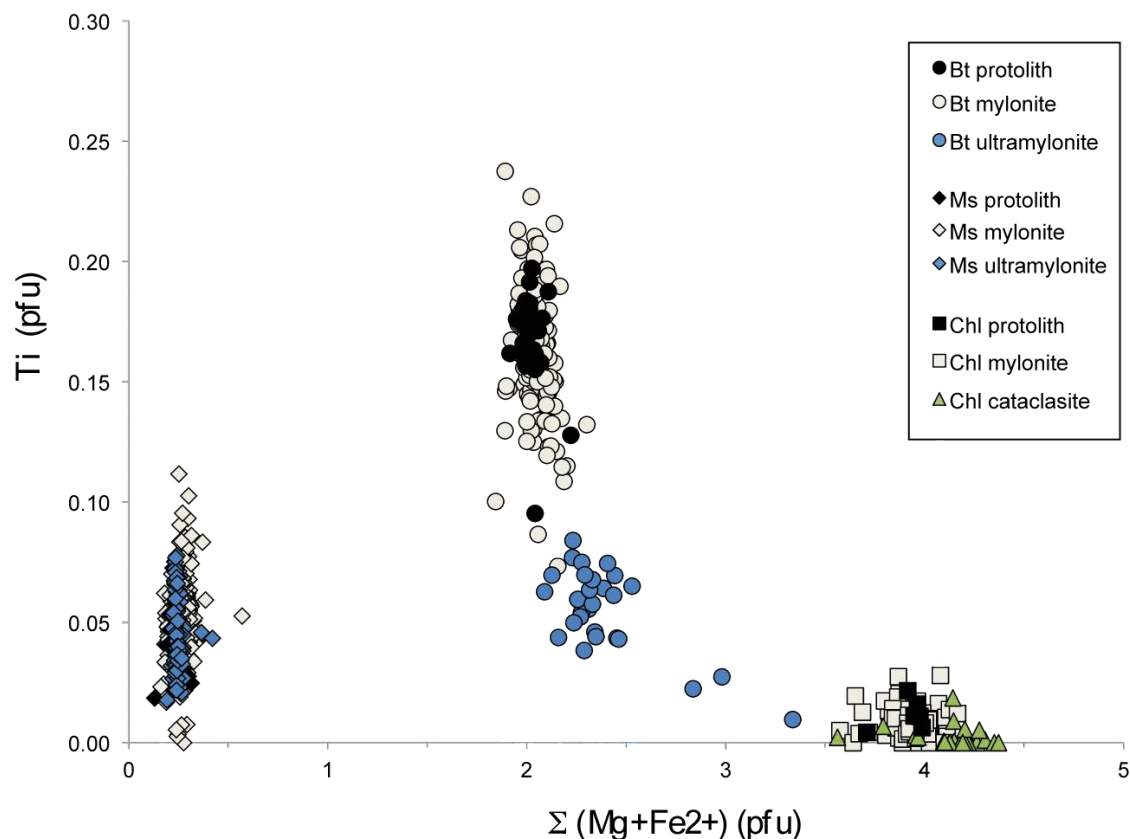


Figure IV-15: Ti content versus (Mg+Fe) of phyllosilicates from the different fabrics of the BSZ. Phyllosilicates in the protolith define narrow ranges, whereas values are more scattered in the mylonite and ultramylonite. Note that in biotite, the Ti content (Mg+Fe) ratio tends to decrease with respect to the strain, and define a trend toward the chlorite pole.

6. Discussion:

The protolith samples have mineral assemblage and major and trace element compositions that are relatively homogeneous for the three samples collected at 150 m intervals. Mylonites have variations in terms of mineral assemblage and geochemistry. These chemical variations correspond to higher, equal or lower major element concentrations than those of the average composition of the protolith. Ultramylonite samples has the most pronounced variations in major and trace elements for the ductile fabrics of BSZ. The bleached granodiorite, corresponding to the core of high-angle normal faults, has the greatest variation in mineralogy and geochemistry in the BSZ. XRD analyses show an evolution in the mineral assemblage proportion with respect to the fabrics of the BSZ. The bulk-rock and single grain analyses support this observation since the bulk rock and phyllosilicate chemical compositions evolve with strain localization.

The temperature of chloritization of biotite is discussed first, since major element compositions of biotite and chlorite allow calculation of their crystallization temperature. In a second step, the Isocon method (Grant, 2005; Baumgartner et al., 1991, 1995) will highlight the volume changes relative to the different fabrics of the BSZ, and also the change in mass of each major element. This last point, combined with XRD results will be the basis to discuss the metamorphic reactions that can generate such volume changes.

6.1. Temperature of biotite chloritization inferred from biotite and chlorite compositions.

6.1.1. Temperature inferred from biotite compositions:

To evaluate the temperature of crystallization of biotite and chlorite, two geothermometers based on their compositions were used. The first is an empirically calibrated geothermometer based on the Ti content, temperature and the X-Mg ($Mg / (Mg+Fe)$) ratio of biotite (Henry et al., 2005). This geothermometer is calibrated for a pressure range of 4-6 kbar, and temperatures between 480°C and 800°C. As required for the Ti-in-biotite geothermometer, the Ti content of biotite is based on 22 oxygens in this section.

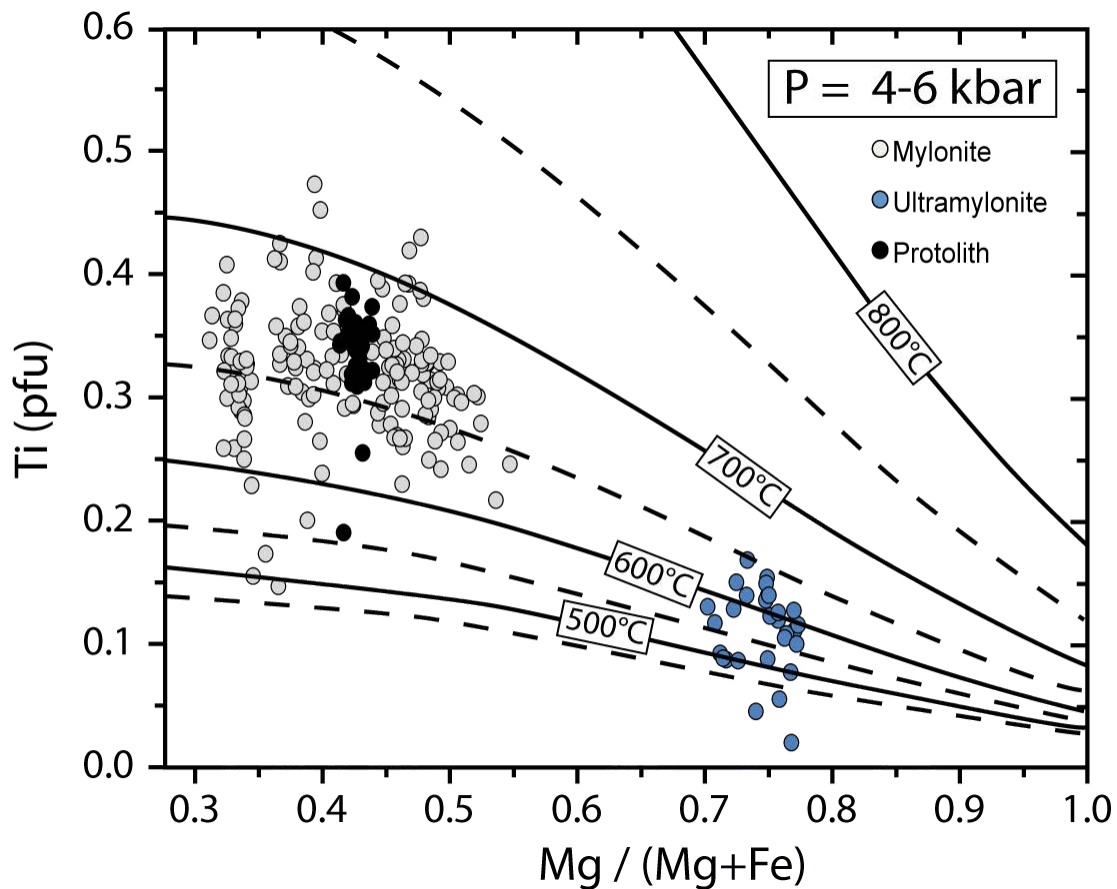


Figure IV-16: Biotite formation temperature according to the Ti-in-biotite geothermometry of Henry et al. (2005). Number of ions are calculated on the basis of 22 oxygens. The Ti versus $Mg / (Mg+Fe)$ plot of biotite shows that the protolith defines a narrow range, whereas mylonite is scattered about the protolith. Biotite in ultramylonite defines a second pole with a higher $Mg / (Mg+Fe)$ ratio and a lower Ti content, which corresponds to lower temperature.

The presence of ilmenite or rutile in the rock ensures that the biotite is saturated in Ti (Guidotti, 1977). However, ilmenite or rutile is only present in rare metabasite layers, which comprise < 5 % of the mylonites (Toy et al., 2010), so it is also difficult to constrain the activity of titanium in the quartzofeldspathic rocks during mylonitization. The Ti-in-biotite thermometer provides temperature estimates <50 °C different from those obtained from other thermometers in rocks lacking graphite, and with low-Al biotite (Henry et al., 2005). Consequently, the estimated chemical equilibrium temperature with the Ti-in-biotite geothermometry corresponds to a minimum temperature in this study.

Henry et al. (2005) proposed that for biotite with a $Mg / (Mg+Fe) > 0.65$, the Ti-substitution is governed by the Ti-Tschermak substitution occurring in octahedral and tetrahedral layer misfit. When $Mg / (Mg+Fe) < 0.65$, the Ti deprotonation is the dominant mechanism for Ti-substitution, which is mostly influenced by high temperature and a

reduction of the $f(\text{O}_2)$. This is consistent with the chemical composition of biotite in ultramylonite, where the octahedral aluminium content increases (Figure IV-14) while the Ti content decreases (Figure IV-15) with respect to $\text{Mg} / (\text{Mg}+\text{Fe})$. Conversely, biotite in the mylonite has a constant octahedral aluminum content, but varies in divalent cation (Mg, Mn, Fe) content with respect to biotite from the protolith (Figure IV-14).

The biotite values are plotted in a $\text{Mg} / (\text{Mg}+\text{Fe})$ versus Ti content diagram (Figure IV-16), with non-linear isotherms defined by Henry et al. (2005). Biotite in the protolith has an average chemical equilibration temperature of 670 ± 20 °C (over 39 analyses). Biotite in the mylonite has an average chemical equilibration temperature of 660 ± 30 °C (over 161 analyses). In ultramylonite BT08-34, the average chemical equilibration temperature is 580 ± 60 °C (over 27 analyses). According to the calculated temperature of chemical equilibrium, biotite from the mylonite has an average chemical equilibration temperature in the same range as the protolith's, although mylonite values are more scattered. This implies that biotite from the mylonite preserved the chemical composition of the peak temperature biotite present in the protolith. In contrast, biotite from the ultramylonite indicates a temperature decrease of ~ 100 °C with respect to the protolith. Ultramylonites are commonly thought to develop at greenschist facies (Lister and Davis, 1989); in the BSZ, Ti content in biotite in the ultramylonite could be partially equilibrated, and the temperature provided with the Ti-in-biotite geothermometry could be overestimated.

6.1.2. Temperature inferred from chlorite compositions:

Three main substitutions occur in chlorite: the Fe-Mg-1 substitution, the Tschermak substitution ($\text{Al}^{\text{IV}}\text{Al}^{\text{VI}}\text{Si}-1(\text{Mg},\text{Fe})-1$), and the di/trioctahedral substitution ($(\text{Mg},\text{Fe}^{2+})_3\Box-1\text{Al}-2$). Different thermometers have been developed based on the chemical compositions of chlorite (Cathelineau and Nieva 1985 ; Cathelineau 1988 ; Hillier and Velde 1992 ; Vidal et al., 2001, 2005, 2006; Inoue et al. 2009). For example, Cathelineau and Nieva (1985) and Cathelineau (1988) proposed an empirical calibration based on the correlation between the tetrahedral aluminum occupancy (Al^{IV}) and/or the octahedral vacancy as a function of temperature deduced from fluid inclusions in fossil geothermal systems. All these thermometers suggest that the Al^{IV} content of chlorite depends on the temperature at which it forms (Cathelineau and Nieva, 1985; Hillier and Velde 1992; Zang and Fyfe 1995). Substitution of Al^{3+} for Fe^{3+} also occurs in chlorite, and the analysis of the iron speciation in the chlorite reveals that divalent iron and trivalent iron are most likely located in two different crystallographic environments in the structure (Munoz et al., 2006). Most medium and high

temperature chlorites contain <10 % Fe³⁺, which is consistent with the low $f(\text{O}_2)$ conditions imposed by the presence of graphite, whereas high Fe³⁺ contents are predicted for low temperature chlorite (Vidal et al., 2006).

Chlorite temperatures have been calculated using chlorite compositions and following the method of Vidal et al. (2005, 2006). These authors propose a geothermometer based on four thermodynamic components (Mg-amesite, clinochlore, daphnite, and Mg-sudoite) in a solid solution model that accounts for the Fe-Mg, Tschermak, and di/trioctahedral substitutions. This geothermometer is calibrated for a wide range of pressure and temperature conditions (100–850°C, 0.5–20 kbar). Since Fe³⁺ can influence the number of vacancies in the chlorite structure, and probably affects the activity of the chlorite end-members, a simultaneous estimate of Fe³⁺ in chlorite and equilibrium temperature for the Chl-Qtz-H₂O assemblage can be done at the given pressure of 4 kbar. Such an estimate has been proposed with a temperature difference of 20 °C and $a_{\text{H}_2\text{O}} = 1$, using a temperature scatter of 20 °C and a criterion based on the convergence of equilibria (Vidal et al. 2005).

Based on these criteria, a single chlorite value has been retained for the protolith (BT09-80-C08-5) and provides a temperature of 485°C. The temperatures determined from the mylonite samples range from 270 ±20 °C (over 4 values) to 390 ±90 °C (over 8 values). Chlorite from the protolith and the mylonite define a first population where the Fe³⁺ content and the X Mg ratio are anti-correlated with temperature (Appendix IV, Table IV-9). In contrast, chlorite from the cataclasite shows an increase in the Fe³⁺ content and the X Mg ratio with respect to protolith and mylonite, indicative of a second population of chlorite, providing a temperature of 280±25°C (over 12 values).

Computed chlorite and biotite temperatures are plotted as a function of distance below the hanging wall in Figure IV-17. With the exception of biotite from the ultramylonite, biotite shows a narrow range of chemical equilibrium temperatures throughout the section, which is in good agreement with the statement that compositions of phyllosilicates do not re-equilibrate significantly by lattice diffusion with variation in P–T conditions (Vidal et al., 2006).

In contrast, chlorite from the protolith defines the highest biotite chloritization temperature, and the chlorite temperatures in mylonitic footwall tend to decrease toward the hanging wall (arrow, Fig. III.15). Thus, the chlorite composition may indicate a trend of decreasing chloritization temperatures of the BSZ toward the hanging wall. According to

Vidal et al. (2006), the redox conditions may become more oxidizing during exhumation, which might result from a progressive meteoric fluid infiltration as the BSZ rocks returned towards the surface. Based on this idea, the appearance of a second population of chlorite in cataclasite, with an estimated average Fe^{3+} content about 20 % higher than in the mylonite (see appendix), would imply a drastic change in the fluid-rock ratio during detachment activity, at $T < 300\text{ }^{\circ}C$.

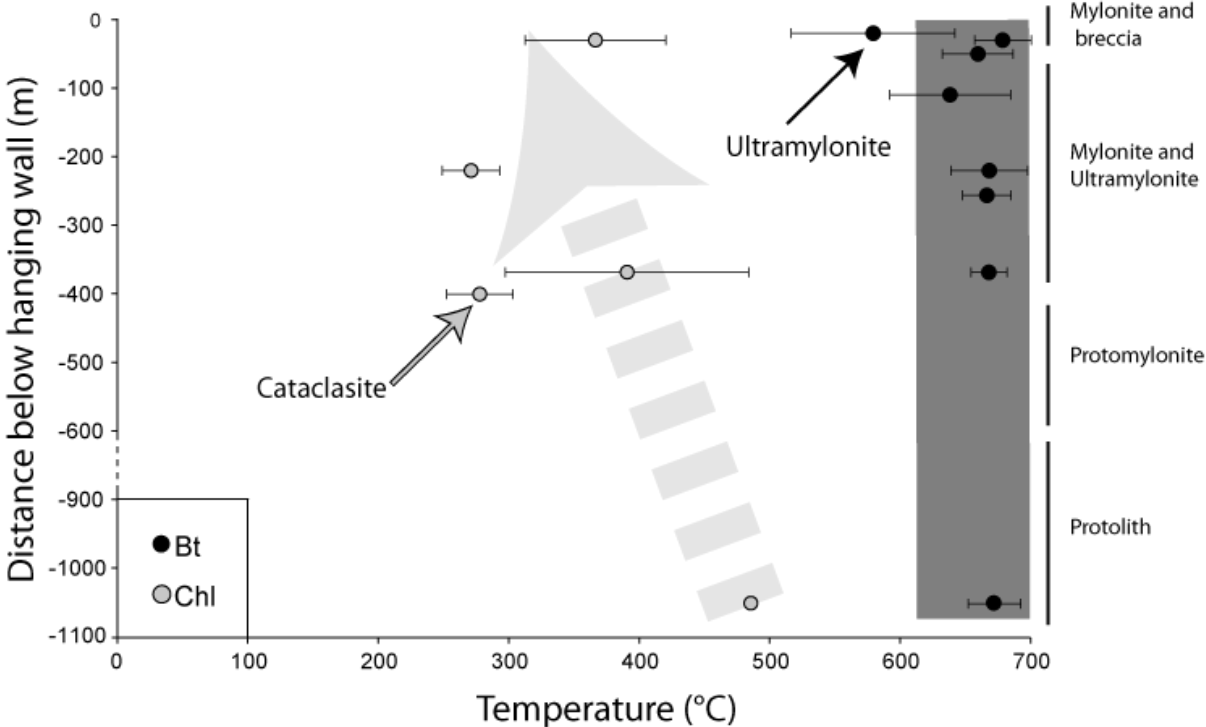
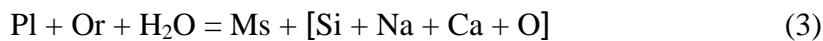
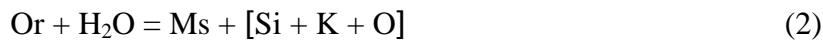
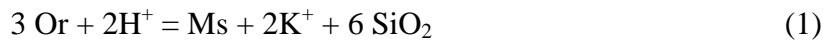


Figure IV-17: Computed temperatures of biotite and chlorite versus distance below the hanging wall. Temperatures are calculated according to Henry et al. (2005) and Vidal et al. (2005) geothermometers, respectively. Biotite shows a narrow range of temperature ($650 \pm 50\text{ }^{\circ}C$), whereas chlorite ranges from $485\text{ }^{\circ}C$ down to $270 \pm 20\text{ }^{\circ}C$.

6.2. Fluid-rock interaction and metamorphic reactions:

Previous work on compressional tectonic settings (thrusting) has proposed that mylonitization is accompanied by volume loss (O'Hara, 1988; Dipple et al., 1990; Goddard and Evans, 1995; Tartèse et al., 2011; Raimondo et al., in press). A different scenario is expected for extensional settings because of porosity development and consequent fluid flow, allowing removal and addition of matter to the shear zone (Glazner and Bartley, 1991; Hippert, 1998, Kwon et al., 2009; Tschegg and Grasemann, 2009). This section investigates the possible relations among volume gains and losses in the different deformation facies (protolith, mylonitic series, cataclastic rocks) of the BSZ, metamorphic reactions, and other geological processes.

The XRD analyses suggest that feldspar (Or+Pl) content decreases when quartz and phyllosilicate content increase. Such a process is referred to in the literature as fluid-assisted feldspar breakdown reaction and leads to rock softening by producing quartz and phyllosilicates according to the following reactions:



A combination of reaction (1) (O'Hara, 1988), with reactions (2) and (3) (Kwon et al., 2009) may explain the mobility of major elements in the mylonite (SiO_2 , Al_2O_3 , K_2O , Na_2O and MnO) and in the ultramylonite (SiO_2 , Al_2O_3 , CaO , K_2O and Na_2O). Note that hydration of feldspar may lead to volume loss via a decrease in the molar volume of the reaction products (Hippert, 1998). The volume loss in mylonite (group A) and ultramylonite is largely accommodated by fluid-assisted breakdown of feldspar, and elements in excess such as Si, K, Na and Ca are mobilized by fluid flow. In this case, silica leaching requires that the fluid be undersaturated with respect to silica. Mylonite from groups B and C show petrological evidence of fluid-assisted breakdown of feldspar (see chapter 2); however, the computed volume changes indicate either conservative volume or volume gain with a mass increase of SiO_2 , MnO and K_2O at the sample scale. In this case, the silica increase requires that the fluid be saturated with respect to silica.

Extensional shear zones are characterized by large fluid-rock ratio (Glazner and Bartley, 1991), and hydrogen isotope compositions indicate that fluids interacting with the mylonite

are surface-derived fluids (e.g., Nesbitt and Muehlenbachs, 1989, 1991; Fricke et al., 1992; Morrison and Anderson, 1998; Mulch et al., 2007; Gébelin et al., 2011). The bleached granodiorite, sampled in high-angle fault cores, shows significant volume loss ($-44 \pm 3\%$) and decrease of the quartz content (-20%) with respect to the protolith. The high-angle normal faults are supposed to constitute a preferential pathway for surface fluids along the shear zone (Sibson, 1975; McCaig, 1988; Famin, 2004). According to the volume changes and the evolution of the mineralogical assemblage, these downwelling fluids can dissolve silica in the fault core. In this case, surface-derived fluids reach the ductile shear zone being partially saturated in silica. Estimates of the fluid-rock ratio in the conduits carrying surface fluids, or in the shear zone, depends directly on the rate of silica saturation of the surface-derived fluids. Since the rate of silica saturation during infiltration into the shear zone has to be estimated, the fluid-rock ratio in mylonite and ultramylonite can only be approximated. Assuming that the initial fluid was undersaturated in silica, Glazner and Bartley (1991) obtained a fluid-rock ratio in mylonite of 500 and 160 at 300 °C and 400 °C, respectively. O'Hara assumed a 50 % and 90 % saturated fluid at 400 °C and 4 kbar and obtained a fluid-rock ratio in mylonite of between 10^2 and 10^3 (O'Hara, 1988). These two studies converge toward the concept of high fluid-rock ratios in shear zones and agree that the fluid-rock ratio calculated is dependent on the silica saturation of the fluid.

Volume change in mylonites reflects the interaction with silica-undersaturated fluids in the case of volume loss and silica-saturated fluids in the case of volume gain. Considering that surface fluids are silica undersaturated, the volume changes in mylonite indicate an evolution in the silica saturation of the surface-derived fluid during fluid flow along the shear zone. Then, volume changes in mylonite may suggest a mechanism of either lateral or vertical mass transfer and volume compensation by major element transport in a surface-derived fluid throughout the shear zone.

7. Conclusion:

The single grain analyses conducted on phyllosilicates have highlighted that biotite in the protolith and mylonites have preserved the magmatic peak temperature experienced by the protolith ($670\pm 30^\circ\text{C}$), while biotite in the ultramylonite could be partially re-equilibrated, providing consequently an over-estimated temperature. Temperatures of biotite chloritization associated with greenschist-facies retrograde reactions in the BSZ indicate a trend of decreasing temperatures from 485°C down to $270 \pm 20^\circ\text{C}$ towards the hanging wall. The appearance of a second generation of newly-formed chlorite in the cataclasite implies a drastic change in the fluid-rock ratio at $T < 300^\circ\text{C}$.

Muscovite grains display fish shape in both mylonite and ultramylonite, and the X(Mg) in muscovites increases from the protolith to mylonite and is the highest in ultramylonite. The X(Mg) and the mica fish shape are indicative of recrystallization during shear zone activity. Meanwhile, muscovite shows no evidence of Tschermak substitution in the protolith, mylonite, and ultramylonite. The Tschermak substitution is largely described in the literature as pressure-dependent (Auzanneau, 2010; Bucher-Nurminen, 1987; Massonne and Schreyer, 1987; Konopasek, 1998; Zanazzi and Pavese, 2002). Thus, recrystallization of muscovite in mylonite and ultramylonite may occur under isobarometric conditions.

Muscovite grains are characterized by a Fe content higher than the Mg content, and could reflect that bulk composition may be the controlling factor for the X(Mg) variations (Guidotti, 1970; Guidotti, 1977; Mohr and Newton, 1983). The protolith of the BSZ is near-isotropic and most of the bulk composition of rocks in the shear zone are related to different degrees of fluid-rock ratio interaction. Consequently, the X(Mg) increases from the protolith towards ultramylonite appears to highlight an increasing fluid-rock ratio as a function of strain intensity.

The bulk-rock analyses, associated with variations of the mineralogical assemblage with respect to the different fabrics indicate that the surface-derived fluid dissolved quartz during the downward fluid migration towards the shear zone. The volume changes occurring in the mylonite and ultramylonite are related to: (1) the fluid-assisted breakdown of feldspar to muscovite (with/without quartz) and (2) depends to the saturation of silica (but also K, Ca, Na) in the fluid. The heterogeneous volume loss (mylonite, ultramylonite) and volume gain (mylonite) throughout the section suggest a mechanism of lateral mass transfer parallel to foliation, with a final balance that is most likely isovolumetric at the shear zone scale.

Chapter V : Infiltration of meteoric fluids through an extensional shear zone from ductile to brittle deformation (Bitterroot detachment, MT, USA)

Introduction:

Detachments accompanying the exhumation of metamorphic core complexes (MCC) juxtapose metamorphosed, and in some cases partially melted crust (footwall), with an upper crust affected by brittle deformation (hanging wall). Detachments commonly record the transition from ductile to brittle deformation. In theory, this transition is described as a permeability barrier between the fluid-rich brittle crust and the fluid-depleted intermediate crust (e.g., Yardley and Valley, 1994); the permeability contrast at this crustal interface has the potential to generate fluid circulation.

Most ductile deformation mechanisms tend to decrease the permeability of rocks, unless they are accompanied by dilatant pore opening or fracturing (Zhang et al., 1994). The effective pressure is most likely the parameter that most influences permeability in ductilely deforming rocks, since a low effective pressure can promote dilatancy and fractures even in rocks experiencing ductile deformation. However, Bauer (2000) proposes a model where (1) the pore connectivity of sheared rocks increases with respect to the shear strain, and (2) the dynamic pore connectivity is a competition between development of fabrics and dynamic recrystallization. Grain-boundary sliding, associated to opening and closing of grain-boundary pores give rise to grain-scale fluid pressure differences between neighbouring pores, initiating a granular fluid pump that provides steady, non-episodic fluid transfer on the timescales defined by diffusion creep (Fusseis et al., 2009).

Syntectonic fluid flow in the detachment is undeniable, and post-deformational modification of pore space seems unlikely (Fusseis et al., 2009). Cavitation creep, viscous grain-boundary sliding and dissolution in quartzo-feldspathic rocks may increase the synkinematic grain-boundary porosity (Rybacki et al., 2008; Fusseis et al., 2009). The increased porosity enhances fluid flow in shear zones, where fluid-rock ratio can reach values as high as 160-500 at 400 and 300 °C, respectively (Glazner and Bartley, 1991).

Hydrothermal systems associated with Cenozoic epizonal plutonism in the Idaho batholith are demonstrated by fluid-rock interaction that lowered the oxygen isotope values of

feldspar by up to 20 ‰ and the hydrogen isotope values of biotite by up to 100 ‰ with respect to a typical magmatic isotope composition of these minerals (Criss et al., 1983). Most of the epithermal and mesothermal Au-Ag ore deposits are also associated with low oxygen isotope composition in the southern part of the Idaho batholith (Criss et al., 1983; Xiong and Zhai, 1992).

In the Bitterroot shear zone, the mylonites and chlorite breccia were generated by deformation that accommodated displacement of the hanging wall in response to removal of the Bitterroot dome carapace towards the east (Hyndman, 1983). Kerrich and Hyndman (1986) showed that the oxygen isotope composition of feldspar underwent a negative shift as much as -10 ‰ relative to magmatic values in both mylonite and breccia in the Sweathouse quarry. The negative shift in oxygen isotope composition occurred because feldspar exchanged with a large volume of meteoric fluid as the rock cooled down to a temperature of about 150 °C. In contrast, quartz is resistant to oxygen isotope exchange at temperatures lower than 300 °C (Taylor, 1974; Bottinga and Javoy, 1973; Criss and Taylor, 1983); as a result, Kerrich and Hyndman (1986) did not observe significant shifts of the quartz and muscovite oxygen isotope compositions in the mylonite, and thus estimated that mylonitic deformation occurred at about 550 ±50 °C, and that meteoric fluids infiltrated the breccia at about 350 °C.

In more recent studies of other detachment shear zone systems, the stable isotope composition of hydrous minerals collected in the ductile part of the systems have systematically revealed that surface-derived fluids infiltrated not just the brittle-ductile part of the detachment, but also the ductile fabrics (Nesbitt and Muehlenbach, 1989, 1991; Fricke et al., 1992; Morrison and Anderson, 1998; Mulch et al., 2007; Gébelin et al., 2011; Gottardi et al., 2011). Following these studies, the present work has focused on the acquisition of hydrogen and oxygen isotope composition profiles through the Bitterroot shear zone in order to verify the results of Kerrich (1984, 1986), and to explore the range of temperatures and in which deformation fabrics developed in the presence of meteoric fluids. Feldspar oxygen isotope composition have been neglected in this study since Kerrich and Hyndman (1986) demonstrated that feldspar equilibrates with meteoric fluid as the shear zone rocks cooled to a temperature as low as 150 °C, which is characteristic of the brittle domain. Instead, the hydrogen and oxygen stable isotope compositions were analyzed for quartz (Qz), biotite (Bt), muscovite (Ms), and chlorite (Chl) in the mylonite, and quartz, muscovite, chlorite, and epidote (Ep) in the quartz veins. Mineral abbreviations are after Whitney and Evans (2010).

Complementary fluid inclusion analyses provide further results directly on the fluid that interacted with the rocks during detachment activity.

1. Sampling strategy:

The Bitterroot shear zone (BSZ) deformed the near-isotropic Bear Creek pluton. Therefore, the BSZ offers an ideal place for quantifying fluid/rock interaction and fluid flow related to strain and deformation mechanisms through a stable isotope study. The Lost Horse and the Sweathouse sections provide a complete section through the BSZ, from the protolith toward the detachment fault, which juxtaposes the mylonite with the chloritized breccia.

This chapter presents the stable isotope compositions of quartz, biotite, muscovite, chlorite, epidote and fluid inclusions in quartz. Stable isotope analyses were made on 3 protolith samples, 1 protomylonite, 14 mylonites – 12 in Lost Horse Canyon, and 2 in Sweathouse sections (Figure V-1), 12 quartz veins (V1, V2a, V2b) – 10 from Sweathouse and 2 in Lost Horse Canyon sections (Figure V-2), and one breccia. Ultramylonite is not represented in this chapter because ultramylonite contains a homogeneous grain size that is too small for proper mineral separation.

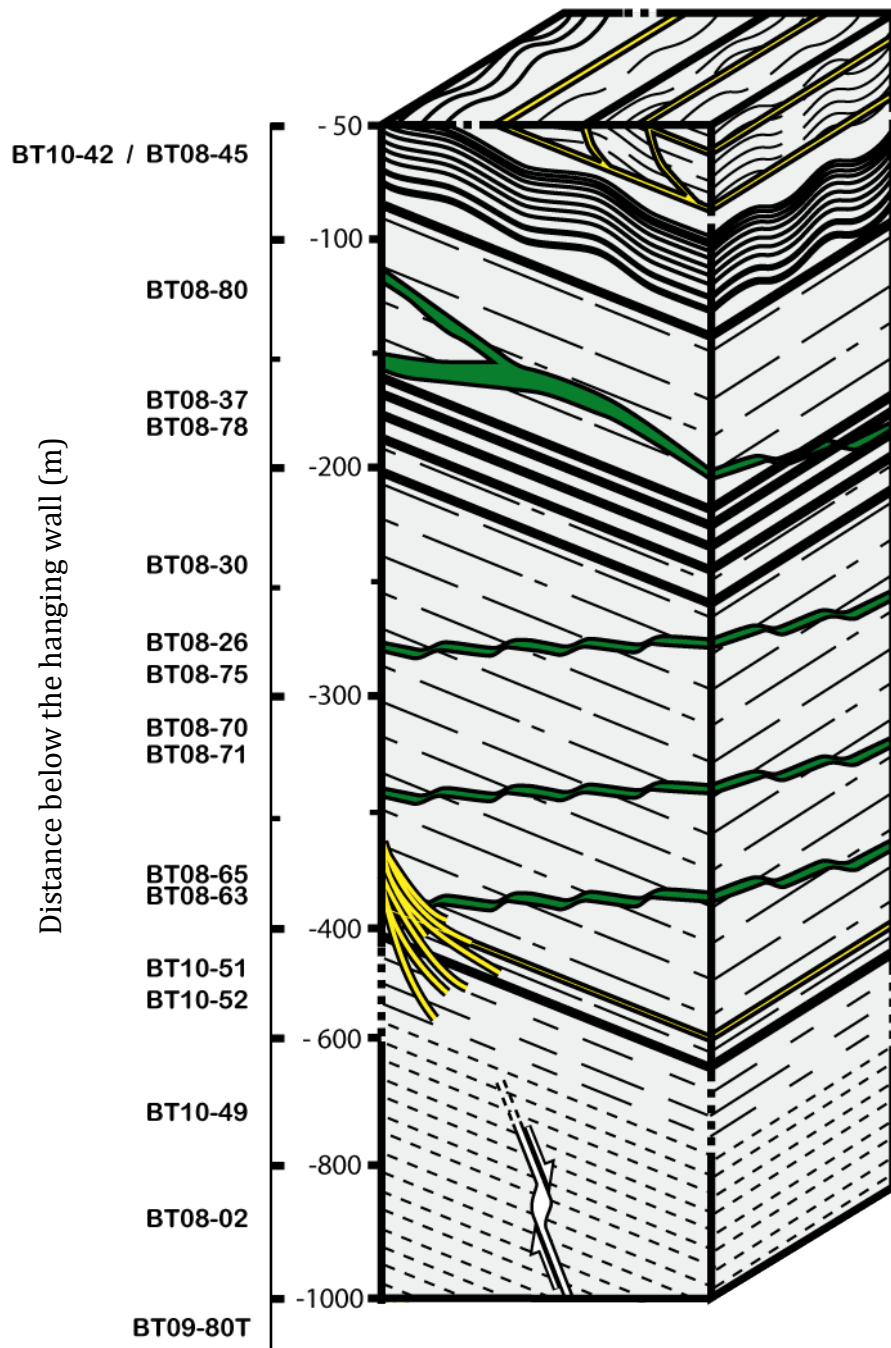


Figure V-1: Location of mylonite samples and two Qz veins (BT10-42 and BT10-51) in the block diagram for the Lost Horse Canyon section.

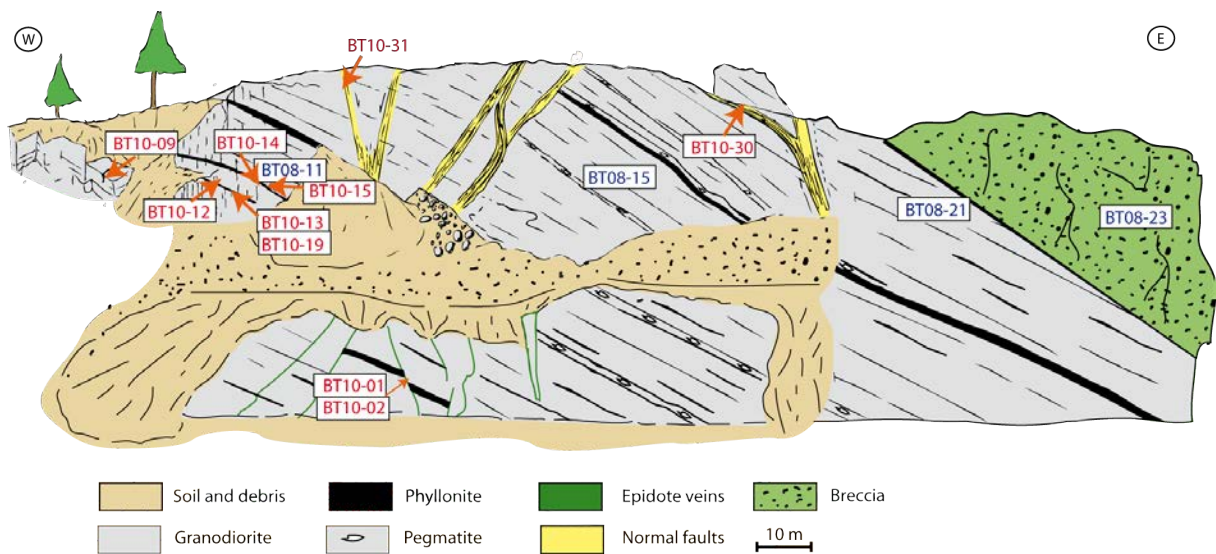


Figure V-2: Location of sample on the schematic view of the Sweathouse section. Samples are presented as a function of the rock types. Blue: mylonite ; Red: Qz veins.

2. $\delta^{18}\text{O}$ values of quartz and hydrous minerals:

Measurements of $^{18}\text{O}/^{16}\text{O}$ ratios for quartz (expressed as $\delta^{18}\text{O}_{\text{Qz}}$ values), biotite ($\delta^{18}\text{O}_{\text{Bt}}$), muscovite ($\delta^{18}\text{O}_{\text{Ms}}$), chlorite ($\delta^{18}\text{O}_{\text{Chl}}$), and epidote ($\delta^{18}\text{O}_{\text{Ep}}$) were conducted from samples of undeformed granodiorite (protolith), mylonite, breccia and V1, V2a, and V2b quartz veins (Appendix V, Table V-1).

The $\delta^{18}\text{O}_{\text{Qz}}$ values of undeformed granodiorite have a range from 9.6 ± 0.4 up to 10.1 ± 0.3 ‰, and the mylonitized granodiorite has a range of $\delta^{18}\text{O}_{\text{Qz}}$ from 8.5 ± 0.1 up to 10.9 ± 0.1 ‰. The breccia, which is thought to be a mylonite or ultramylonite that underwent cataclastic flow and brittle deformation, has a $\delta^{18}\text{O}_{\text{Qz}}$ value of 2.4 ± 0.5 ‰. Thus, the $\delta^{18}\text{O}_{\text{Qz}}$ value of the breccia is about 7‰ lower than the average $\delta^{18}\text{O}_{\text{Qz}}$ value of mylonite. The quartz veins have two distinctive populations of $\delta^{18}\text{O}_{\text{Qz}}$ values: the V1 quartz veins have a range from 8.7 ± 0.7 up to 10.7 ± 0.1 ‰, and the V2a,b quartz veins have values from -5.5 ± 2.4 ‰ down to -6.9 ± 0.2 ‰. The V1 quartz veins have $\delta^{18}\text{O}_{\text{Qz}}$ values in the same range as the granodiorite, whereas the second population of veins (V2a, b) has an extremely low $\delta^{18}\text{O}_{\text{Qz}}$ value. The difference between V1 and V2a, b quartz veins implies that the two populations of quartz veins were derived from different fluids and/or formed at different temperatures.

Regarding hydrous minerals, biotite was found only in the undeformed granodiorite and mylonite. The $\delta^{18}\text{O}_{\text{Bt}}$ values of the undeformed granodiorite fall in a narrow range from 5.4 ± 0.1 ‰ down to 4.5 ± 0.1 ‰, while the $\delta^{18}\text{O}_{\text{Bt}}$ values from the mylonite have a wide range

from 4.2 ± 0.2 ‰ down to -5.4 ± 1.5 ‰. The $\delta^{18}\text{O}_{\text{Ms}}$ values of the undeformed granodiorite and the protomylonite have a narrow range from 7.7 ± 0.1 ‰ down to 7.2 ± 0.1 ‰ and the $\delta^{18}\text{O}_{\text{Ms}}$ values of the mylonite have a range from 8.5 ± 0.1 ‰ down to 5.1 ± 0.1 ‰. Muscovite was found in sufficient amounts in only one sample of V1 quartz veins and it has a $\delta^{18}\text{O}_{\text{Ms}}$ value of 7.8 ± 0.1 ‰, a value in the same range as muscovite in the undeformed granodiorite, protomylonite, and mylonite. In contrast, the $\delta^{18}\text{O}_{\text{Ms}}$ values of the V2a, b quartz veins have a range from 8.5 ± 0.5 ‰ down to -1.9 ± 0.1 ‰.

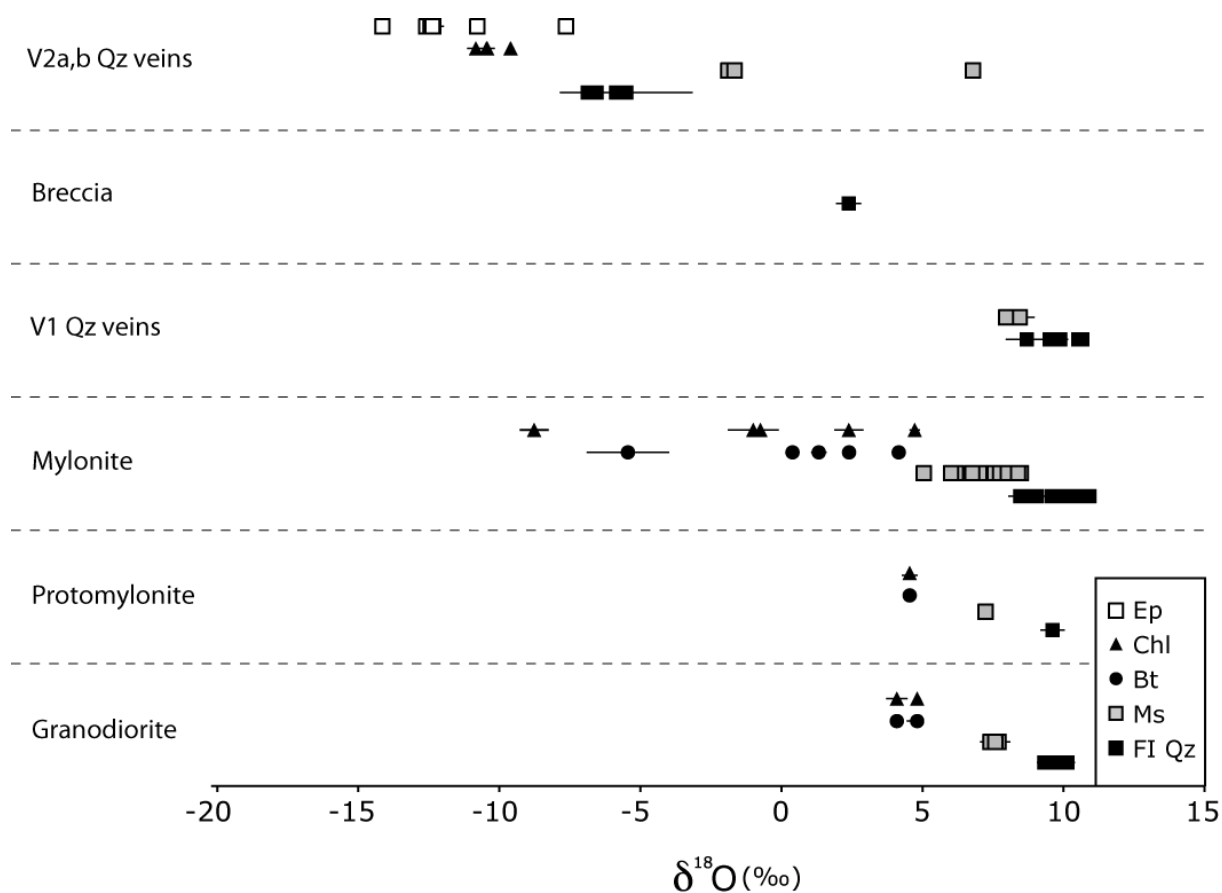


Figure V-3: Oxygen isotope compositions of the samples from Lost Horse and Sweathouse sections. Samples are presented in a one-dimensional diagram, according to rock type. Error bars correspond to the standard deviation between two analyses.

Chlorite has been observed in every unit, from the protolith to the breccia. The $\delta^{18}\text{O}_{\text{Chl}}$ values of the undeformed granodiorite are in a narrow range from 4.8 ± 0.1 ‰ to 4.1 ± 0.4 ‰, and the $\delta^{18}\text{O}_{\text{Chl}}$ values of the mylonite have a wide range from 4.7 ± 0.2 ‰ down to -8.8 ± 0.5 ‰. No chlorite has been observed in the V1 quartz veins but the $\delta^{18}\text{O}_{\text{Chl}}$ values from the V2 (a and b) quartz veins are even lower than those from the mylonite with values between -9.6 ± 0.1 and -10.8 ± 0.1 ‰. Finally, no epidote was found in the mylonite and in V1 quartz veins,

but epidote extracted from the V2a, b quartz veins have the most negative $\delta^{18}\text{O}$ values in the Sweathouse quarry, with a $\delta^{18}\text{O}_{\text{Ep}}$ in a range from -7.6 ± 0.1 ‰ down to -14.2 ± 0.2 ‰.

The oxygen isotope compositions of quartz, biotite, muscovite, chlorite, and epidote are compared in Figure IV-1. This diagram draws the attention to an essential point: the oxygen isotope compositions present two poles for all the analyzed minerals, except for epidote. There is one pole characterized by negative $\delta^{18}\text{O}$ values, which is mostly represented by the V2a, b quartz veins, and another pole by positive $\delta^{18}\text{O}$ values, defined by the undeformed granodiorite minerals. Minerals such as biotite and chlorite from the mylonite are distributed from one pole to another. Finally, a spread of isotopic values between the two poles is observed in both mylonites and V2 quartz veins.

3. δD values of hydrous minerals:

The hydrogen isotopic compositions of biotite ($\delta\text{D}_{\text{Bt}}$), muscovite ($\delta\text{D}_{\text{Ms}}$), chlorite ($\delta\text{D}_{\text{Chl}}$) and epidote ($\delta\text{D}_{\text{Ep}}$) have been analyzed in the granodiorite, the mylonite, the breccia and the quartz veins (Appendix V, Table V-2), when present in those rocks (epidote in V2a, b quartz veins only, for example). The undeformed granodiorite and the protomylonite have a hydrogen isotopic composition for biotite, chlorite, and muscovite of -82 ‰ down to -93 ‰, -71 ‰ down to -79 ‰, and -61 ‰ down to -69 ‰, respectively (Figure V-4). The $\delta\text{D}_{\text{Bt}}$, $\delta\text{D}_{\text{Chl}}$ and $\delta\text{D}_{\text{Ms}}$ values of the undeformed granodiorite are in good agreement with those for phyllosilicates interacting with magmatic fluids (Suzuoki and Epstein, 1976; Field and Fifarek, 1985; Kuroda et al., 1986; Wilamowski, 2002). The mylonite also has constant hydrogen isotope composition throughout the section. The $\delta\text{D}_{\text{Bt}}$ and $\delta\text{D}_{\text{Ms}}$ values of the mylonite are in a range of -136 down to -155 ‰, and -127 down to -150 ‰, respectively, and chlorite has δD values between -126 and -152 ‰. Such negative values of the biotite, chlorite, and muscovite in the mylonite and breccia imply that these phyllosilicates recrystallized in presence of low-D fluids, probably meteoric fluids (Morrison and Anderson, 1998; Mulch et al., 2007; Gébelin et al., 2011; Gottardi et al., 2011).

The hydrous minerals in both V1 and V2 quartz veins also have low absolute δD values. Despite the absence of biotite and the presence of epidote, quartz veins have similar hydrogen isotope values of chlorite and muscovite compared to the mylonite. The $\delta\text{D}_{\text{Ms}}$ and $\delta\text{D}_{\text{Chl}}$ have a range of -139 down to -143 ‰, and -144 down to -153 ‰, respectively. Epidote has a $\delta\text{D}_{\text{Ep}}$ ranging from -127 down to -139 ‰.

The hydrogen isotope compositions of biotite, muscovite, chlorite, and epidote have been plotted in a one-dimensional diagram (Figure V-4) for comparison. This graph is consistent with the oxygen isotope results: the hydrogen isotope compositions present two poles for all analyzed minerals, except for epidote which falls in the most negative pole. There is one pole characterized by the phyllosilicates from the undeformed granodiorite with a $\delta D > -100$ ‰ and another pole characterized by the phyllosilicates from the mylonite and the quartz veins with a $\delta D < -120$ ‰.

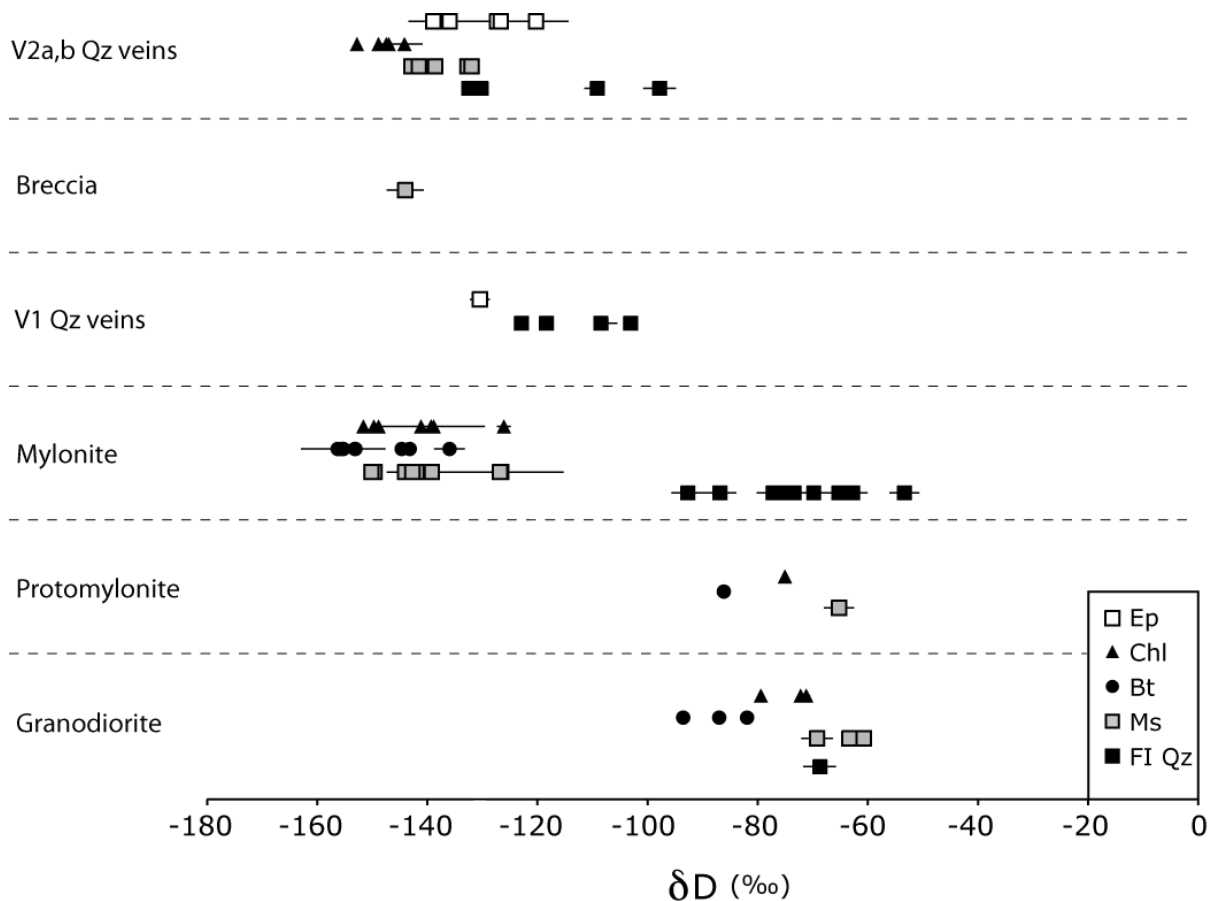


Figure V-4: Hydrogen isotope composition of the samples from the Lost Horse and the Sweathouse sections. δD values of samples are presented according to rock type. Error bars correspond to the standard deviation between two analyses.

4. δD , $\delta^{13}C$, and $\delta^{18}O$ values of fluid inclusions in quartz:

4.1. δD values of fluid inclusions and amount of water in quartz:

The hydrogen isotope compositions of fluid inclusions in quartz (δD_{FI-Qz}) from the undeformed granodiorite average to a value of -69 ± 3 ‰ (Figure V-4). The δD_{FI-Qz} from the

mylonite have a range of values from $-53 \pm 3\text{‰}$ down to $-92 \pm 3\text{‰}$ and the quartz veins (V1, V2a, V2b) have $\delta D_{\text{FI Qz}}$ values of $-98 \pm 3\text{‰}$ down to $-133 \pm 1\text{‰}$. Note that, independent of the large $\delta^{18}\text{O}_{\text{Qz}}$ difference observed between the V1, V2a and V2b veins, the $\delta D_{\text{FI Qz}}$ of all quartz vein populations is relatively constant.

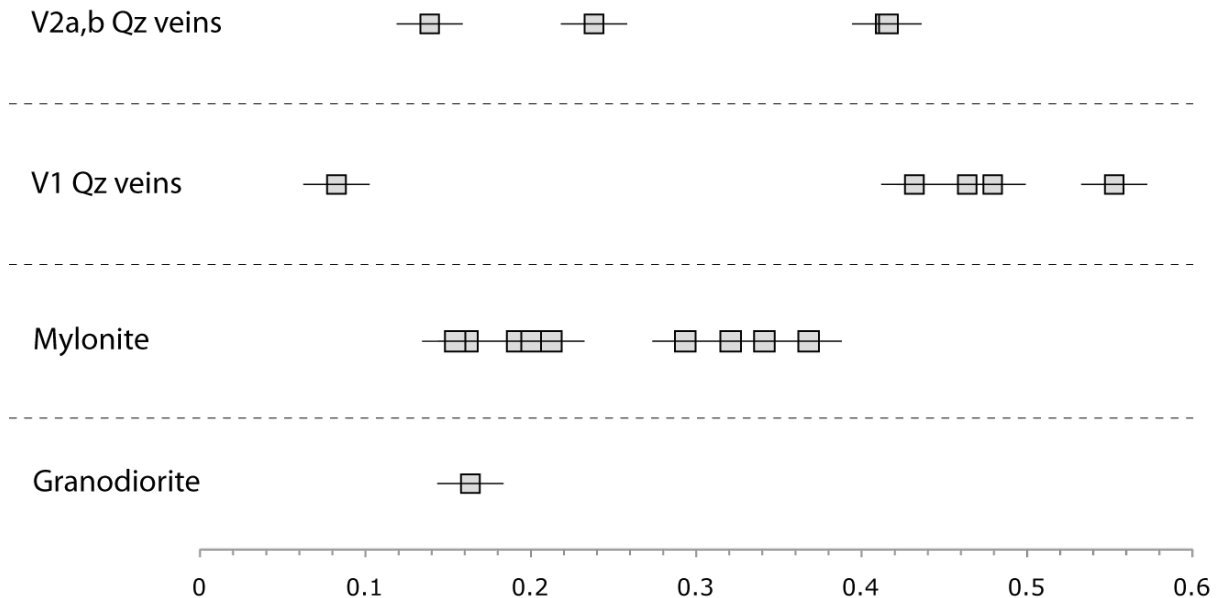


Figure V-5: Calculated amount of water (mg) per gram of quartz. Error bars correspond to standard deviations.

The amount of water contained in each vial was calculated with the help of the vials prepared from standard waters used for the calibration of the isotopic compositions and the mass-spectrometer voltage for the hydrogen gas signal. The amount of water (mg) of each standard is known as it was weighed before combining the water with the zinc in the vacuum tube (a weighted capillary tube, frozen under vacuum and liquid nitrogen into the vial with zinc), and the mass-spectrometer provides a voltage (mV) of H_2 gas pressure according to the amount of water released by the vials. Varying the amount of water in the standard vials permits to calculate a linear correlation between the water content of each vial and the voltage provided by the mass-spectrometer.

The undeformed granodiorite contains 0.16 ± 0.02 mg of water per gram of quartz ($\text{mg}_{\text{wt}}/\text{g}_{\text{Qz}}$), and the mylonite has a water content from 0.15 ± 0.02 up to 0.37 ± 0.02 $\text{mg}_{\text{wt}}/\text{g}_{\text{Qz}}$ (Figure V-5). The V1 quartz veins water content varies from 0.08 ± 0.02 up to 0.55 ± 0.02 $\text{mg}_{\text{wt}}/\text{g}_{\text{qz}}$ and the V2a, b quartz veins range from 0.14 ± 0.02 up to 0.44 ± 0.02 $\text{mg}_{\text{wt}}/\text{g}_{\text{Qz}}$. The undeformed granodiorite has one of the lowest water contents per gram of quartz while the

granodiorite mylonite and V2a, b quartz veins are characterized by a large range of water content per gram of quartz. Finally, the V1 quartz veins have the highest water content of the analyzed samples, except one value that is even lower than the one from the undeformed granodiorite.

4.2. $\delta^{13}C$ and $\delta^{18}O$ values of fluid inclusions in quartz:

Concerning carbon isotope compositions ($\delta^{13}C$ values), the undeformed granodiorite and the mylonite have $\delta^{13}C$ values that range from -20.6 ± 0.2 ‰ down to -24.7 ± 0.3 ‰ (Appendix V, Table V-3). The V1 quartz veins have higher $\delta^{13}C$ values comprised between -11.7 ± 0.1 ‰ and -12.2 ± 0.2 ‰. Unfortunately, the amount of CO_2 and/or CH_4 extracted from the quartz fluid inclusions of the V2 (a and b) quartz veins were insufficient for analysis, which suggests that the quartz fluid inclusions from the V2 quartz veins were mostly aqueous fluid inclusions.

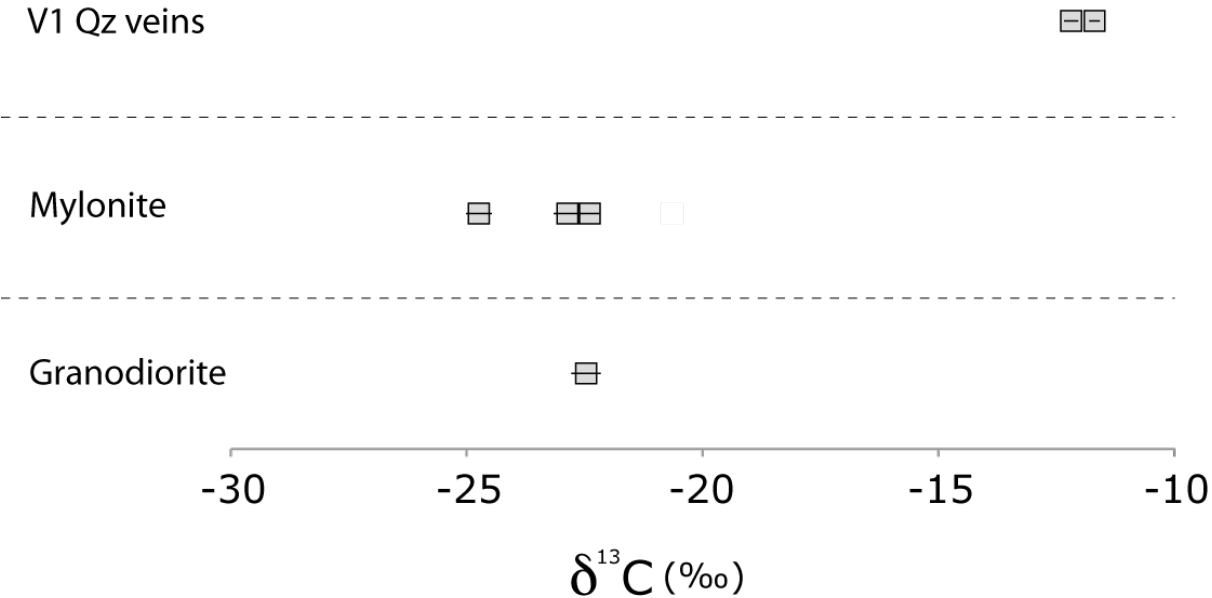


Figure V-6: Carbon isotope composition of fluid inclusions in quartz for samples from the Lost Horse and the Sweathouse sections. Values for samples are presented according to rock type. Error bars correspond to the standard deviation between two analyses.

5. Oxygen isotope thermometry:

Isotope exchange equilibrium temperatures can be calculated based on the difference in $\delta^{18}\text{O}$ values ($\Delta^{18}\text{O}_{\text{X-Y}}$ or $1000\ln\alpha_{\text{X-Y}}$) of mineral pairs, as long as it can be assumed that the mineral pair reached oxygen isotope equilibrium. Several oxygen isotope thermometers are available for the mineral assemblages that characterize the various rock types of the BSZ. The following calculations are based on isotopic thermometers calibrated by Chacko et al. (1996) for the Qz-Ms pairs ($\Delta^{18}\text{O}_{\text{Qz-Ms}}$), by Bottinga and Javoy (1975) for the Qz-Bt pairs ($\Delta^{18}\text{O}_{\text{Qz-Bt}}$), and by Zheng (1993b) for the Qz-Chl ($\Delta^{18}\text{O}_{\text{Qz-Chl}}$) and Qz-Ep pairs ($\Delta^{18}\text{O}_{\text{Qz-Ep}}$). The isotopic thermometers have been chosen in order to fit their temperature range of calibration given the expected moderate temperatures of deformation related to detachment activity. The isotopic thermometers are based on the following equations:

$$(1) \Delta^{18}\text{O}_{\text{Qz-Ms}} = 1.350x^2 + 0.042x^4 - 0.0086x^6; \text{ with } x = 10^3\text{T}^{-1}$$

$$(2) \Delta^{18}\text{O}_{\text{Qz-Bt}} = 0.400x^2 - 3.10; \text{ with } x = 10^3\text{T}^{-1}$$

$$(3) \Delta^{18}\text{O}_{\text{Qz-Chl}} = 3.990x^2 - 8.11x + 2.35; \text{ with } x = 10^3\text{T}^{-1}$$

$$(4) \Delta^{18}\text{O}_{\text{Qz-Ep}} = 0.420x^2 + 3.05x - 1.27; \text{ with } x = 10^3\text{T}^{-1}$$

The mineral assemblages from the undeformed granodiorite and protomylonite give temperatures that range between 470 ± 60 °C and 580 ± 20 °C according to $T_{\text{Qz-Ms}}$, with an average temperature of 520 ± 50 °C (one standard deviation). The Qz-Bt isotopic thermometer gives a temperature of between 520 ± 20 °C and 560 ± 10 °C and an average temperature of 540 ± 20 °C (Figure V-7). From the quartz-chlorite mineral pair, $T_{\text{Qz-Chl}}$ has a range from 310 ± 20 °C to 360 ± 40 °C, which gives an average temperature of 340 ± 30 °C.

The mylonite has Qz-Ms isotope exchange equilibrium temperatures in the range from 320 ± 20 °C up to 725 ± 50 °C, with an average temperature of 450 ± 110 °C (Figure V-8). The Qz-Bt pairs give temperatures that range from 220 ± 30 °C up to 440 ± 10 °C with an average temperature of 340 ± 80 °C. The Qz-Chl pairs give temperatures from 0 ± 10 °C up to 280 ± 10 °C, with an average temperature of 140 ± 110 °C. Removing the two samples above 600 °C corresponding to the top section, and probably in isotopic disequilibrium, the average for Qz-Ms pairs have an isotope exchange equilibrium temperature for the mylonite of 420 ± 60 °C.

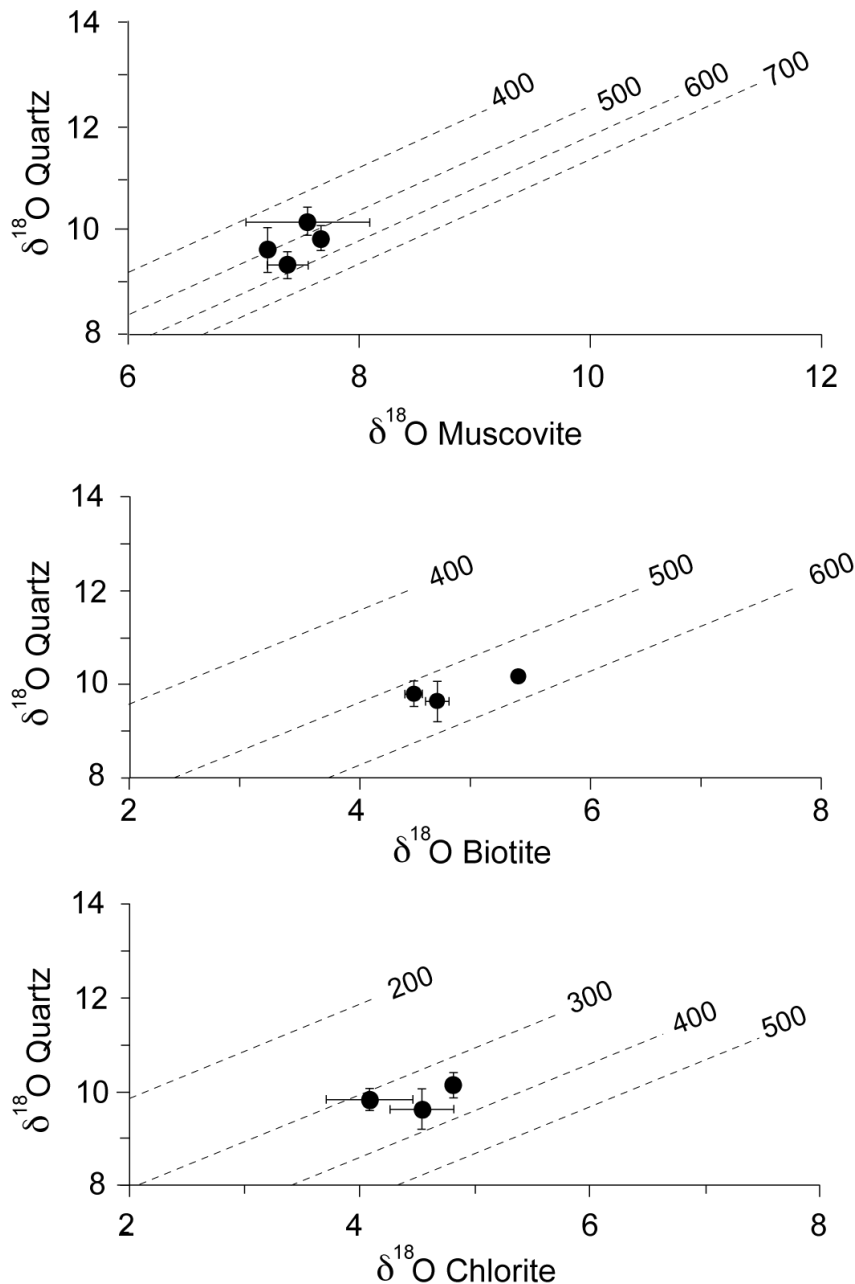


Figure V-7: Oxygen isotope composition of Qz-Ms, and Qz-Bt pairs from the undeformed granodiorite. Isotherm are based on the Qz-Ms thermometer calibrated by Chacko et al. (1996), and the Qz-Bt thermometer calibrated by Bottinga and Javoy (1975).

The single V1 quartz vein with muscovite provides a temperature of 450 ± 50 °C, which is in the temperature domain defined by Qz-Ms thermometry of the mylonite. The Qz-Ms thermometry of the V2a, b quartz vein indicates isotopic disequilibrium between quartz and muscovite because the $\delta^{18}\text{O}$ values of muscovite are always higher than those of the quartz.

The isotope exchange equilibrium temperature provided by the Qz-Chl thermometer (Zheng, 1993b) for the V2a, b have a range from 370 ± 150 °C to 660 ± 20 °C, with an average temperature of 500 ± 150 °C. While the Qz-Ep isotope thermometer has a temperature

range from 180 ± 10 °C to 290 ± 20 °C, with an average temperature of 220 ± 50 °C, once the sample with unrealistic temperature is removed ($T_{Qz-Ep} > 1100$ °C). The Qz-Ep thermometer appears to give temperatures in a domain (200-300 °C) that is to be expected for undeformed veins at the brittle-ductile transition.

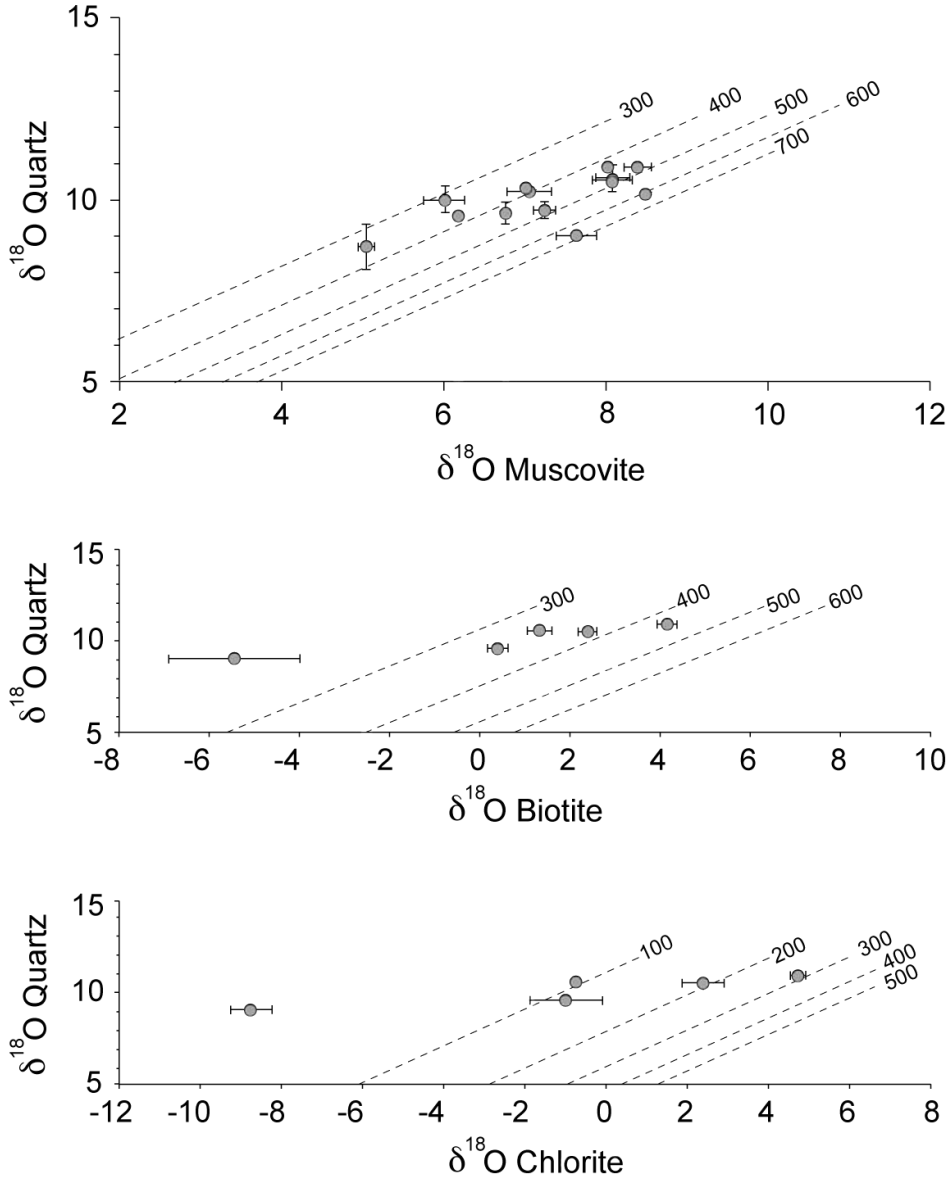


Figure V-8: Oxygen isotope composition of Qz-Ms pairs, Qz-Bt pairs and Qz-Chl pairs from the mylonite. Isothermal lines are based on the Qz-Ms thermometer calibrated by Chacko et al. (1996), the Qz-Bt thermometer developed by Bottinga and Javoy (1975) and the Qz-Chl thermometer developed by Zheng (1993b).

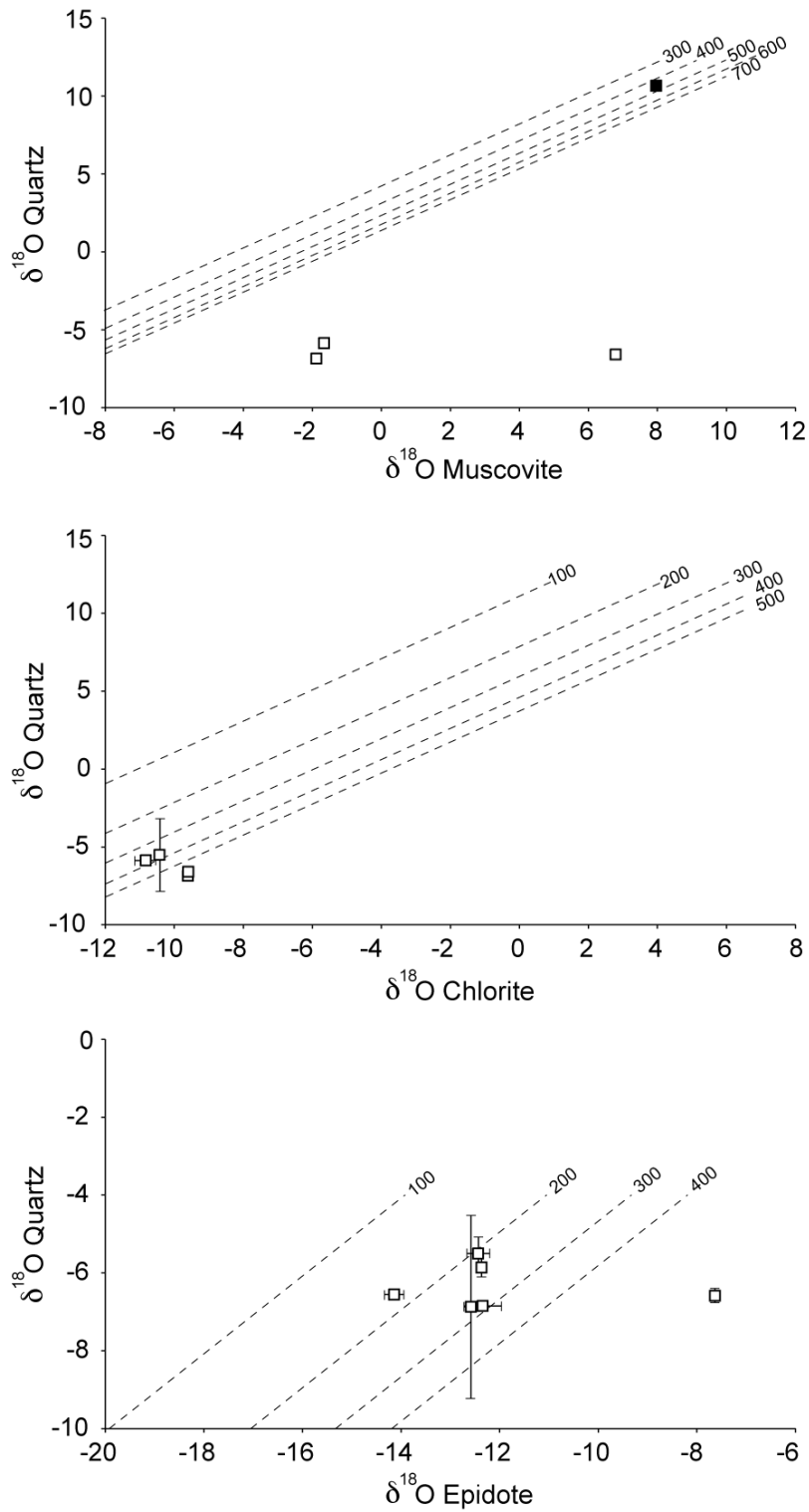


Figure V-9: Oxygen isotope composition of Qz-Ms pairs, Qz-Chl pairs and Qz-Ep pair from the Qz veins. Black square corresponds to the V1 quartz vein and the white squares to V2a, b quartz veins. Isothermal lines are based on the Qz-Ms thermometer calibrated by Chacko et al. (1996), the Qz-Chl and the Qz-Ep thermometers are after Zheng (1993b).

6. Discussion:

The protolith samples in the deepest units of the section have δD values > -90 ‰ (Bt-Chl-Ms), whereas the mylonite has constant, low δD values (< -120 ‰) throughout the entire section, independent of the distance from the hanging wall. Since the hydrogen isotope composition of hydrous minerals may allow for an identification of the fluid source, the δD values of the Lost Horse and Sweathouse sections suggest that the undeformed granodiorite interacted with a different fluid compared to the mylonite and the different quartz veins.

As such, the isotopic study of the BSZ supports a minimum of two fluid sources in rocks related to the shear zone and to the MCC, presenting a spatial organization and defining different degrees of fluid-mineral equilibration. The fluid-rock-strain interaction will be discussed here in order to highlight the mechanism of meteoric fluid percolation in a ductilely deformed shear zone and its implication for exhumation dynamics.

6.1. Evolution from a closed system magmatic fluid circulation towards meteoric fluid infiltration:

As a reminder, and based on the literature, a typical hydrogen isotope composition of sheet silicates interacting with magmatic fluids during their growth is around -40 to -80 ‰ (e.g., Sheppard, 1986). Sheet silicates that grow in the presence of meteoric water may have hydrogen isotope compositions in a range from -120 ‰ to -160 ‰ (e.g., Fricke et al., 1992; Mulch et al., 2004).

The hydrogen isotope compositions for biotite and muscovite of the undeformed granodiorite, the protolith of the mylonite, have a range that is typical for sheet silicates that have interacted with a magmatic fluid. The δD_{Ms} and δD_{Bt} values of the protolith support muscovite, chlorite, and biotite crystallization in the presence of a magmatic fluid. All the sheet silicates from the mylonites and the quartz veins have low absolute δD values (-150 ‰ $< \delta D < -130$ ‰). These sheared units and quartz veins within them thus have hydrogen isotope values of sheet silicates that suggest an interaction with low-deuterium meteoric fluids.

In addition, a typical magmatic fluid is thought to have a hydrogen isotope composition of -40 to -80 ‰ and meteoric fluids between 0 and -150 ‰, depending on their evaporative source, but also the topography in the area of precipitation, and the fluid-rock interaction and temperature thereof (Field and Fifarek, 1985). Consequently, the $\delta D_{FI Qz}$ of the undeformed

granodiorite should be representative of the initial magmatic fluids that equilibrated with the phyllosilicates, and the $\delta D_{FI\ Qz}$ of the quartz veins (V1, V2a, V2b) would represent the meteoric fluids that infiltrated the detachment. The hydrogen compositions of fluid inclusions in quartz from the mylonite are distributed between the magmatic fluid pole and the meteoric fluid pole (Figure V-4). In order to test this scenario, the water content per gram of quartz has been plotted against the δD_{FI} value (Figure V-10). Both mylonite and quartz veins (V1 and V2a,b) groups have a negative correlation between the water content per gram of quartz and the δD_{FI} value. Even if the water content per gram of quartz cannot be directly linked to the volume of fluid flowing in the detachment, Figure V-10 shows that the higher the water content per gram of quartz, the lower the δD_{FI} value. Based on this observation, and that phyllosilicates of the mylonite also have low δD values throughout the section, it can be concluded that the volume of fluid infiltrating the detachment was sufficient to buffer and lower the δD values of the phyllosilicates, but not necessarily enough to maintain their own initially low values. Such an assumption could explain the distribution of the δD_{FI} values from the magmatic fluid toward the meteoric fluid pole.

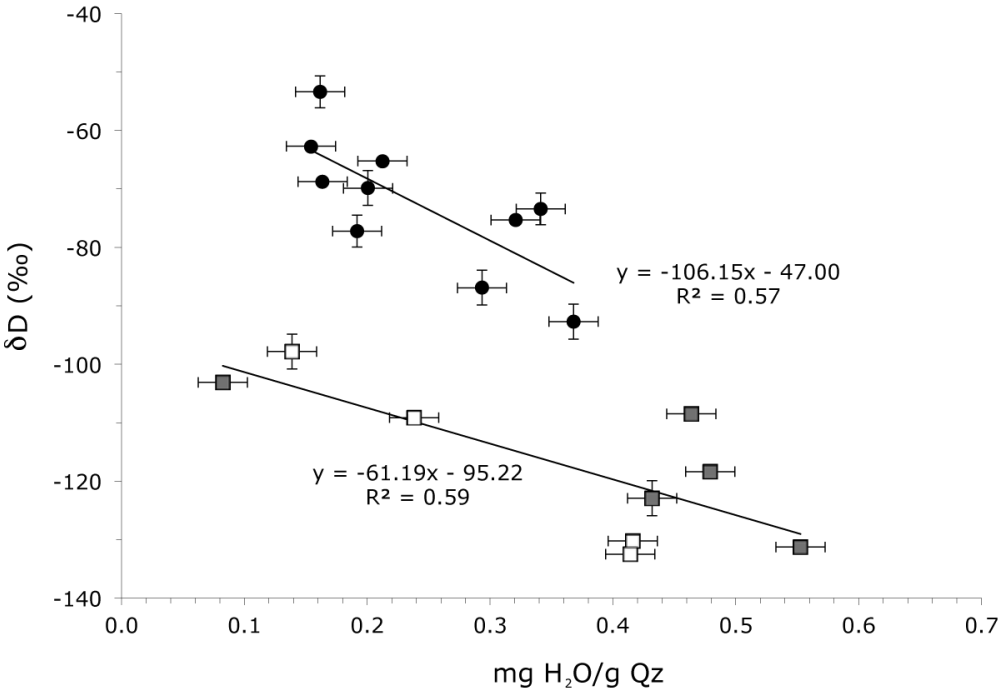


Figure V-10: Hydrogen isotope composition of the fluid inclusions in quartz with regard to the water content per gram of quartz. Black circles correspond to the mylonite, grey square to the V1 quartz veins and white squares to the V2a, b quartz veins. Error bars correspond to the standard deviations.

Field and Fifarek (1985) compiled a database of $\delta^{13}\text{C}$ values according to geological environments. The typical $\delta^{13}\text{C}$ values of igneous rocks have a range from -5 down to -10 ‰. In a volcanic/geothermal system, the $\delta^{13}\text{C}$ values of CO_2 are in a range of $+2$ ‰ down to -10 ‰, and the $\delta^{13}\text{C}$ values of CH_4 is from -16 down to -32 ‰. Finally, the hydrothermal field (CaCO_3) shows $\delta^{13}\text{C}$ values that range from $+2$ down to -10 ‰. According to the Field and Fifarek compilation (1985), the $\delta^{13}\text{C}$ values of the quartz fluid inclusions of the granodiorite are in the range for volcanic/geothermal CH_4 . The $\delta^{13}\text{C}$ values from the quartz fluid inclusions of quartz veins V1 could be either within the igneous rock range or that for hydrothermal solutions. Based on the very low hydrogen isotope composition of the fluid inclusions of the quartz veins, it seems reasonable to suggest a hydrothermal origin for the $\delta^{13}\text{C}$ values of CO_2 in the quartz veins.

6.2. Fluid sources from ductile towards brittle deformation:

The BSZ interacted with at least two fluid sources, and the interaction with these two sources appears to be strongly conditioned by the strain rate experienced by the different rock units. One of the fluid sources is the protolith and the protomylonite. Minerals and fluid inclusions have retained compositions typical of magmatic values in terms of stable isotope compositions ($\delta^{18}\text{O} > 5$ ‰; $\delta\text{D} > -90$ ‰, Figure V-11). The second source is identified in the V2a, b quartz veins, where isotopic values are compatible with meteoric water compositions, whether for minerals or fluid inclusions ($\delta^{18}\text{O} < 0$ ‰, $\delta\text{D} < -120$ ‰, Figure V-11).

Units such as the mylonite, the V1 quartz veins, and breccia have mineral and fluid compositions between these two poles (Figure V-11). The mylonite has relatively constant hydrogen isotope values for the hydrous minerals, with values corresponding to meteoric fluids. Concerning the fluid inclusions in the mylonite, their isotopic compositions range between the magmatic and meteoric source poles. This may indicate a potential mixing of the two sources in the mylonite (Figure V-11). The $\delta^{18}\text{O}_{\text{Qz}}$ and the $\delta^{18}\text{O}_{\text{Ms}}$ of mylonite are similar to those of the protolith, whereas the $\delta^{18}\text{O}_{\text{Bt}}$ and the $\delta^{18}\text{O}_{\text{Chl}}$ have large variations. Just as for the mylonite, V1 quartz veins have oxygen isotope compositions similar to those of the granodiorite protolith in terms of $\delta^{18}\text{O}_{\text{Qz}}$; however, the fluid inclusions in quartz of these veins have δD values corresponding to meteoric water compositions. Finally, the breccia has a $\delta^{18}\text{O}_{\text{Qz}}$ midway between the magmatic source and the meteoric source poles. Though the breccia was initially a mylonite, the $\delta^{18}\text{O}_{\text{Qz}}$ values of the breccia indicate a fluid-rock interaction much more pronounced than in the mylonite.

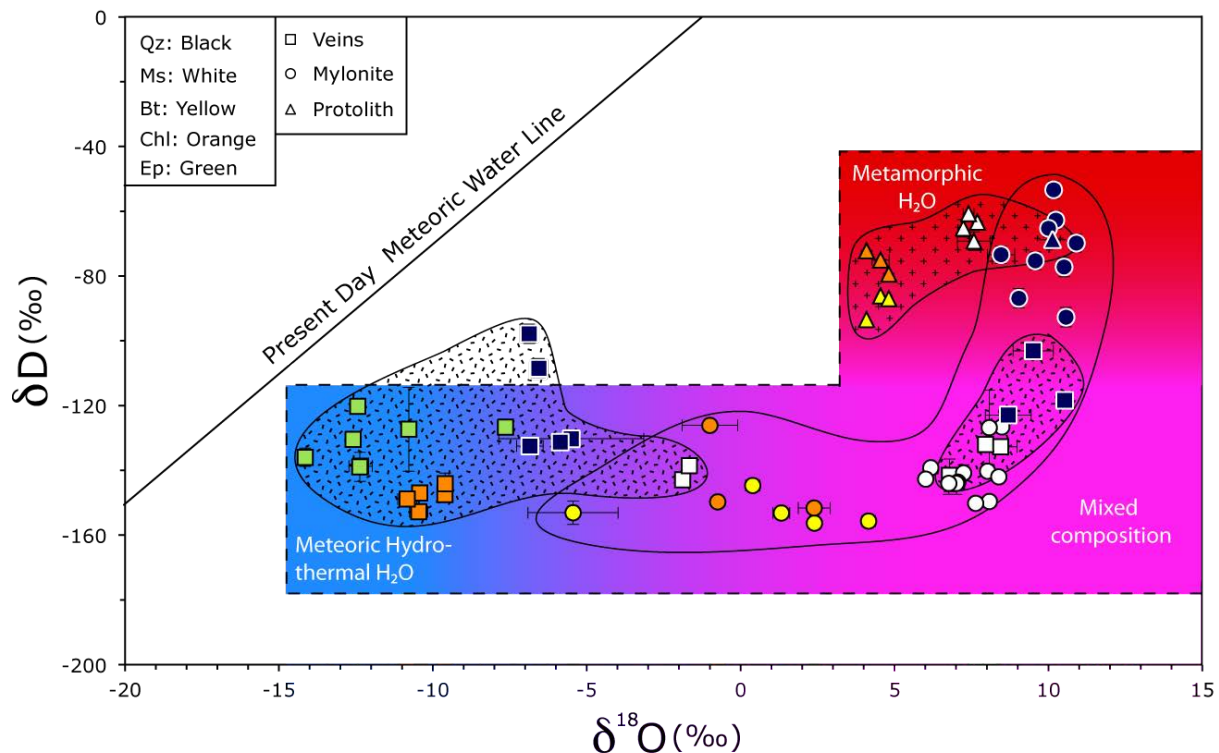


Figure V-11: Hydrogen and oxygen isotope compositions of minerals for each rock types. The quartz values are plotted as the oxygen isotope compositions of the host grains and the hydrogen isotope composition of their included fluids. The different shapes are surrounding symbols from the same rock type.

In the BSZ, the hydrogen isotope compositions of hydrous minerals present in the mylonite and V1 quartz veins are characterized by a meteoric hydrogen composition while the oxygen isotope composition is very heterogeneous. The isotopic composition variations of chlorite, biotite, and fluid inclusions in mylonite and quartz veins V1 may, therefore, represent a front of infiltration of meteoric fluids in the shear zone. Such an interpretation could have important implications in terms of stable isotope thermometry, and will be discussed in the following section.

6.3. Biotite and chlorite isotopic exchange behavior:

The oxygen isotope compositions of biotite and chlorite from the mylonite cover a range from being in equilibrium at high temperatures with magmatic to meteoric fluid compositions (Figure V-11). However, it appears that biotite and chlorite pairs in each sample of the mylonite have similar oxygen isotope compositions. This is important for stable isotope thermometry based on biotite and chlorite and for interpretations on these minerals apparent equilibrium.

The $\delta^{18}\text{O}_{\text{Bt}}$ and $\delta^{18}\text{O}_{\text{Chl}}$ values of the undeformed granodiorite and the mylonite have been plotted together in Figure V-12. This graph shows a positive linear correlation between $\delta^{18}\text{O}_{\text{Bt}}$ and $\delta^{18}\text{O}_{\text{Chl}}$, with a correlation coefficient of 0.98. The biotite and chlorite pairs from the undeformed granodiorite cluster towards higher values, whereas the biotite and chlorite pairs of the mylonite are distributed along a line extrapolating towards lower values. Figure V-12 illustrates: (1) the chloritization of biotite occurring in the mylonite due to hydrothermal alteration (Eggleton and Banfield, 1985; Fiebig and Hoefs, 2002, Wilamowski, 2002), which has already been highlighted in the microprobe section (chapter IV.2.4), and (2) the likely increasing fluid/rock ratio or at least increasing fluid-mineral exchange with low $\delta^{18}\text{O}$ fluids towards the range of lower values within the mylonite. Indeed, it has been demonstrated in the previous section that the undeformed granodiorite only interacted with a magmatic fluid (cluster towards the higher values, Figure V-12). Eggleton and Banfield (1985) demonstrated that only oxygen bound to the octahedral sites are capable of exchanging with the surrounding fluids at relatively low temperatures (below approximately 400°C) since oxygen has strong bonds in the tetrahedral sites. However, Fiebig and Hoefs (2002) have shown that chloritization in approximate isotopic equilibrium with the fluid involves both octahedral and tetrahedral sites within the sheets of biotite for oxygen isotope exchange. Diffusion of oxygen between biotite and fluids can occur at temperature as low as 300°C (Fortier and Gilletti, 1991), and Fiebig and Hoefs (2002) describe chloritization of biotite as a dissolution-precipitation process rather than a simple diffusional exchange, since they observed a direct correlation between the degree of chloritization and the oxygen isotope variation. Chloritization of biotite in the mylonite may thus occur as a recrystallization process at temperatures below about 300°C.

According to the oxygen isotope compositions, chlorite is formed in the presence of a fluid depleted in the heavy oxygen isotope, that is meteoric fluids. Furthermore, the extent of chloritization being related to the final $\delta^{18}\text{O}$ values suggest that chlorite is formed at fluid/rock ratios sufficiently high so that the fluid is no longer buffered by the surrounding rock.

In contrast to oxygen isotope compositions of biotite and chlorite, the $\delta\text{D}_{\text{Bt}}$ and the $\delta\text{D}_{\text{Chl}}$ values of the mylonite do not show a trend that parallels that of the oxygen isotope variations. The $\delta\text{D}_{\text{Bt}}$ and the $\delta\text{D}_{\text{Chl}}$ values define two distinct clusters, with the undeformed granodiorite in the upper right corner and the mylonite in the lower left corner (Figure V-13).

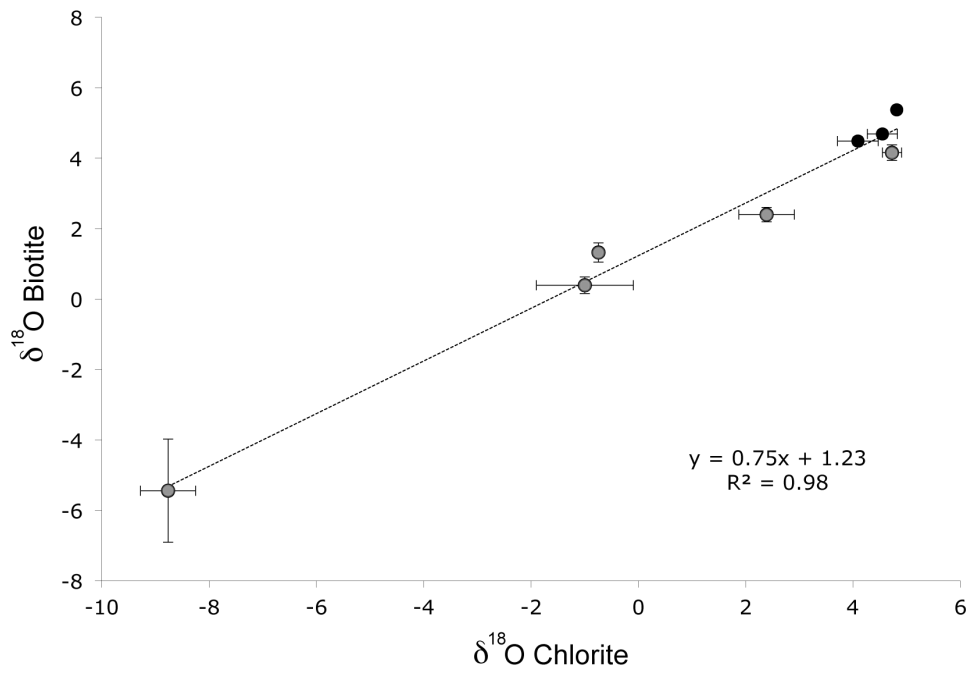


Figure V-12: Oxygen isotope composition of Chl and Bt of samples from Lost Horse and Sweathouse. Black circles correspond to undeformed granodiorite and grey circles correspond to the mylonite.

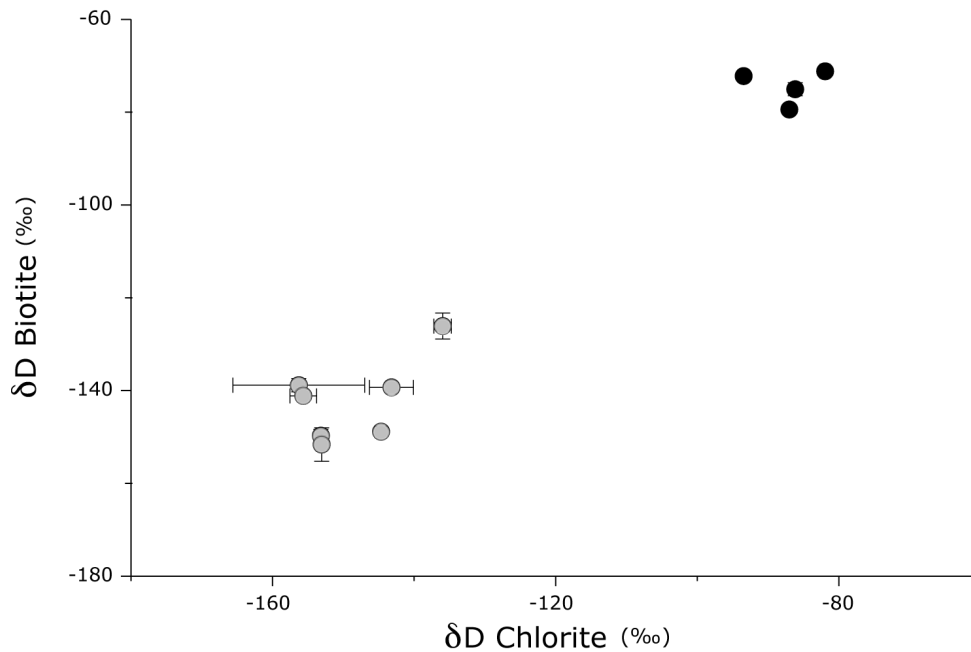


Figure V-13: Hydrogen isotope composition of Chl and Bt pairs of samples from Lost Horse and Sweathouse. Black circles correspond to undeformed granodiorite and grey circles correspond to mylonite.

This clustering of values implies that both biotite and chlorite in the granodiorite are still in equilibrium with a magmatic fluid, while those in the mylonite were crystallizing in a fluid where the H-budget was dominated by the exotic fluid that is likely to be of meteoric origin.

The water contents (wt%) determined for the minerals as part of the hydrogen extraction procedure are plotted relative to the δD_{Bt} and the δD_{Chl} values of the appropriate mineral in Figure V-14 and given in Appendix V, Table V-3. As a reminder, the average water content of a biotite is around 2-4 wt%, and 9-12 wt% for chlorite. The water contents of biotite and chlorite of the undeformed granodiorite are in good agreement with the stoichiometrically required theoretical water contents of the pure minerals. However, the water contents of biotite and chlorite from the mylonite are distributed along the y-axis, but they are not mixing. As such, the data in the mylonite may be interpreted as chloritization of the biotite that may or may not have been accompanied by a change in the isotopic composition of the newly formed mineral. As hydrogen diffusion is easier compared to that of oxygen, and given that the aqueous fluid phase contains a higher proportion of H compared to a typical granodiorite, even at relatively low fluid/rock ratios, both residual biotite and newly formed chlorite will have re-equilibrated with the new fluid.

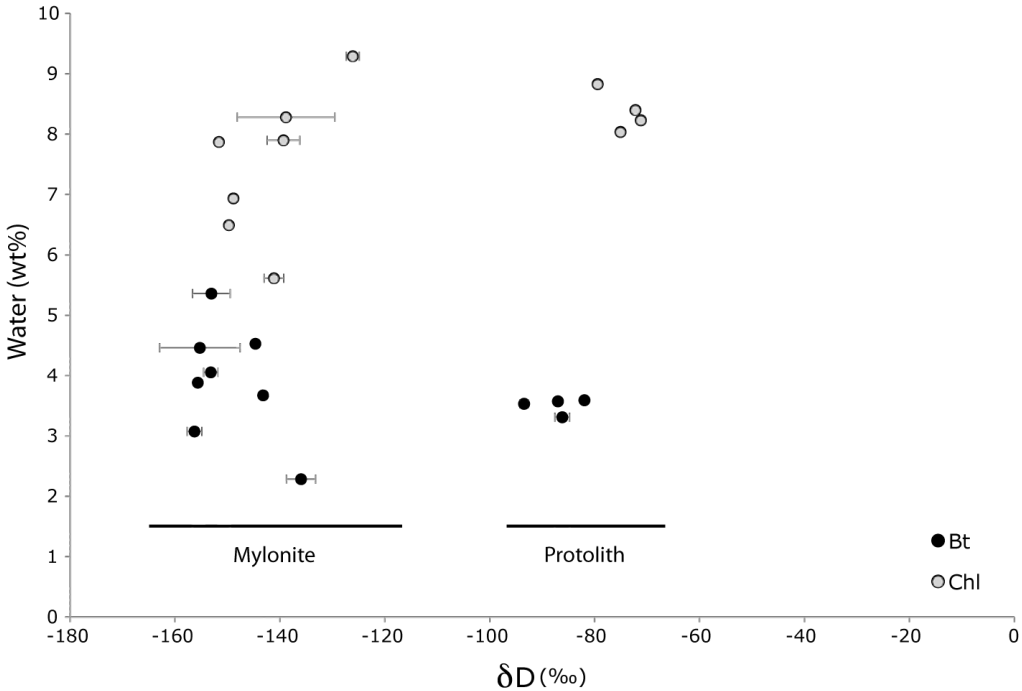


Figure V-14: Hydrogen isotope compositions of the Bt and Chl pairs of samples from Lost Horse and Sweathouse, according to their water content (weight percent) as measured as part of the extraction procedure of H₂ for isotopic measurements. Black circles correspond to biotite and grey circles correspond to chlorite.

6.4. Temperature inferred by stable isotope compositions:

In the undeformed granodiorite, the isotopic exchange equilibrium temperature obtained with the Qz-Bt and Qz-Ms pairs are in good agreement in that most of the mineral pairs give an apparent equilibrium temperature of between 500 to 600 °C, which could very well represent closure temperatures in a slowly cooled intrusive, granodioritic rock. In contrast, the Qz-Chl isotopic thermometer provide temperature about 200 °C lower compared to those of the Qz-Ms and Qz-Bt pairs. As discussed in the previous section, this relation indicates that the chlorite from the undeformed granodiorite is not in isotopic equilibrium with the other minerals. The chlorite isotopic disequilibrium with other minerals implies that the process of chloritization occurs at a temperature lower than the isotopic closure temperature of biotite, muscovite, and quartz, even in the undeformed granodiorite. A temperature range of about 200-300 °C seems to be reasonable for such a process. Since the oxygen and hydrogen isotope compositions of chlorite are typical for magmatic rocks in the undeformed granodiorite, it follows that they are in equilibrium with the magmatic fluid but at lower temperatures compared to the other mineral phases.

In the mylonite, the Qz-Ms isotopic thermometer applied to the mylonite gives apparent equilibration temperatures of between 350 °C up to 550 °C, which are typical for rocks experiencing greenschist facies deformation. In contrast, the Qz-Bt and the Qz-Chl isotopic fractionations in most cases give isotope exchange equilibrium temperatures lower than the closure temperature of chlorite and biotite and lower than the other mineral pairs (Graham et al., 1987; Fortier and Gilletti, 1991). The large $\delta^{18}\text{O}_{\text{Bt}}$ and $\delta^{18}\text{O}_{\text{Chl}}$ variations compared to the small range of $\delta^{18}\text{O}_{\text{Qz}}$ values also indicate that the Qz-Bt and the Qz-Chl temperature variations are largely related to the chloritization of hydrous micas. However, the hydrogen isotope compositions of biotite from the mylonite suggests that meteoric fluid percolated the mylonitic shear zone at high to moderate temperature ($T > 400$ °C), since the biotite re-equilibrated during recrystallization with the new fluid. As such, the shear zone can be considered as an open system, from the early stage of mylonitization (400-500 °C, Figure V-15) until the chloritization process under low greenschist facies conditions (250-350 °C, Figure V-15).

Such an scenario is supported by the presence of the muscovite bearing V1 quartz vein in the mylonite, where the isotope exchange equilibrium temperature of Qz-Ms pair is 450 ± 50 °C. Since the hydrogen isotope composition of the muscovite from the V1 quartz vein is -132 ± 1.2 ‰, meteoric fluids likely percolated the BSZ at temperatures of 400-500 °C.

The V2b quartz veins have apparent isotope exchange equilibrium temperatures of 500 ± 150 °C for the Qz-Chl pairs, and 220 ± 50 °C for the Qz-Ep pairs. Epidote and chlorite are the minerals present in the BSZ that have the lowest closure temperatures in terms of oxygen and hydrogen diffusion (Graham et al., 1980, 1981, 1987, 1991). The chlorite veins correspond to the first structures affecting the mylonite under brittle regime, and chlorite is mostly found at the edges of the V2b quartz veins (cf. Chapter III.3.2). As such the chlorite may represent a different generation of growth compared to the quartz. Consequently, the temperatures calculated from the Qz-Chl mineral pairs are not necessarily isotopic equilibrium temperatures. Since automorphic epidote was only found in the V2b quartz veins, epidote was likely the last hydrous mineral that interacted with the fluids. If the quartz in the vein also formed at this temperature and/or was open to oxygen isotope exchange with the epidote, the Qz-Ep isotopic thermometer may indicate temperatures of formation for the V2b quartz vein of 200-300 °C (Figure V-15). The breccia formed by intense brittle deformation contains automorphic chlorite and epidote. In this case it can be assumed that the mylonite was brecciated at temperatures close to or lower than those corresponding to the V2b quartz veins (Figure V-15).

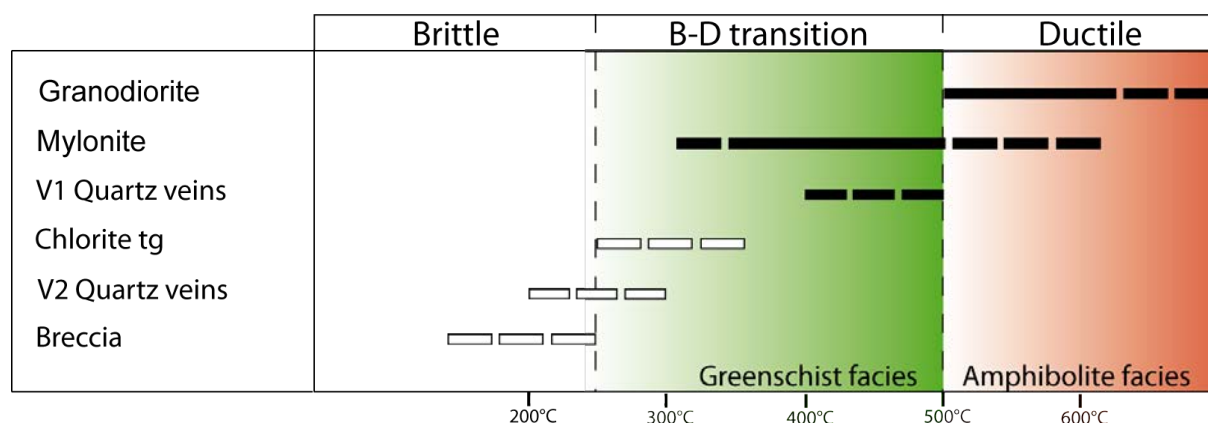


Figure V-15: Schematic representation of the temperature range characterizing each rock type. Temperatures correspond to the apparent isotopic exchange equilibrium temperature for different mineral pairs.

6.5. Deformation and evolution of fluid flow during exhumation

In summary of the previous observations, the undeformed granodiorite interacted with a magmatic fluid in a closed system during the ascent of the pluton, and its constituent minerals crystallized at temperatures down to 500-600 °C. During mylonitization of this granodiorite as part of the detachment activity, the granodiorite was open to interaction with a meteoric fluid at temperatures below 500 °C. These results allow for the calculation of the isotopic fractionation between fluid and minerals (Figure V-16) and hence the isotopic compositions of the fluids given the average hydrogen and oxygen isotope compositions of the constituent minerals in these rocks. The calculated stable isotope composition of the fluid is given as δD_{wt} and $\delta^{18}O_{wt}$ values. For magmatic fluids, the theoretical δD values are between -45 and -60 ‰ (Figure V-16), and theoretical $\delta^{18}O_{wt}$ values are between 6.5 up to 9.5 ‰ (Figure V-17). In contrast, meteoric fluid δD values may have a range from -80 ‰ down to -130 ‰ (Figure V-16), in good agreement with the δD_{FI} values measured for inclusions in the quartz veins. $\delta^{18}O_{wt}$ values of fluids are calculated to have a range from -8 down to -16 ‰ (Figure V-17). The $\delta^{18}O_{wt}$ values corresponding to meteoric fluids with the above range of δD values is between -12 and -20 ‰, when plotted on the Global Meteoric Water Line (GMWL; Craig, 1961).

The oxygen and hydrogen isotopic compositions of silicates from the protolith and the protomylonites are consistent with the theoretical values of a magmatic fluid. In contrast, the hydrogen isotope compositions of the sheet silicates from the mylonite indicate that the minerals grew in the presence of meteoric fluids. However, based on the equilibrium fractionation between mineral and water at a given temperature, the $\delta^{18}O_{wt}$ values in equilibrium with silicates from the mylonite are 20 ‰ higher than the $\delta^{18}O_{wt}$ expected for pure meteoric waters. Indeed, the $\delta^{18}O_{wt}$ values in equilibrium with the mylonite are in a similar range to those of magmatic fluids.

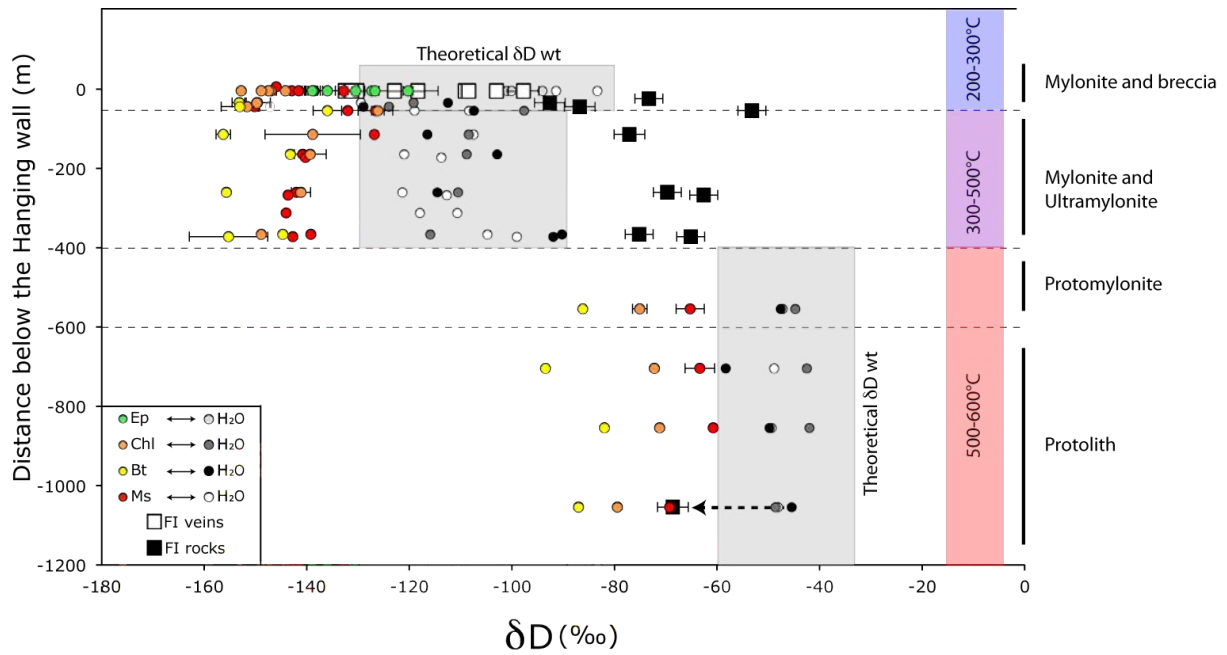


Figure V-16: Hydrogen isotope compositions of Qz, Bt, Ms, Chl, Ep and fluid inclusions from the different fabrics, arranged according to the distance from the hanging wall. Temperature range given on the right corresponds to the temperatures of the fabric formation as estimated from the different isotopic thermometers of the fabric-forming minerals; they are thus not related to the depth or distance given on the left. The theoretical hydrogen isotope compositions of the fluid in equilibrium with the different hydrous minerals (δD_{wt}) are calculated based on temperatures for the Qz-Ms of the protolith and the Qz-Ep temperatures of the mylonite and the Qz veins (Appendix V, Table V-4).

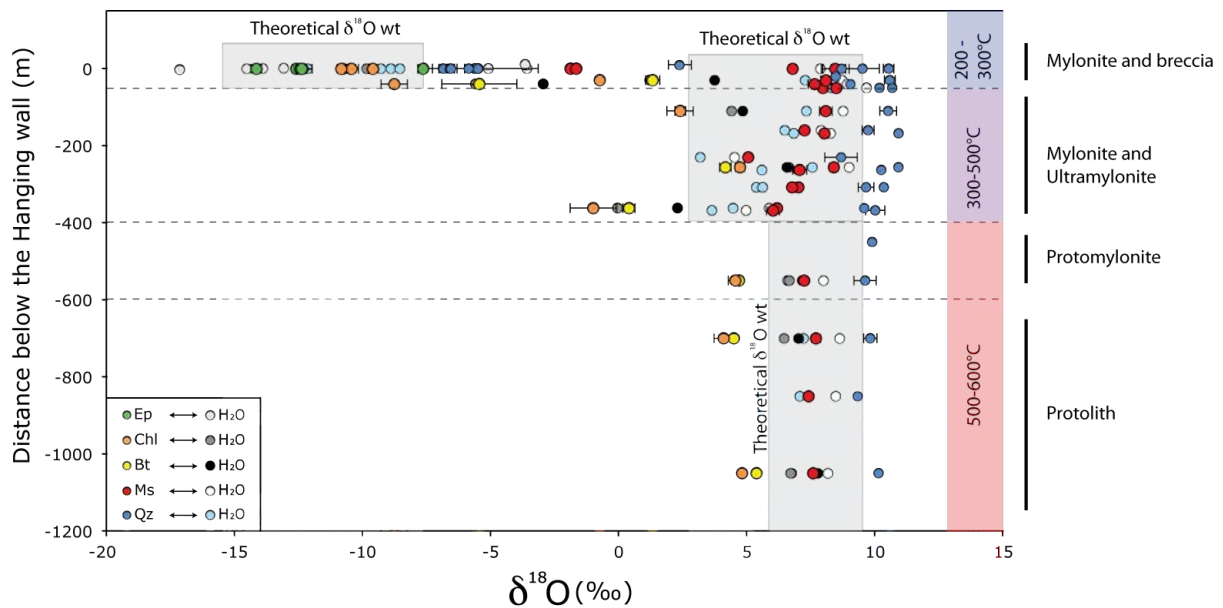


Figure V-17: Oxygen isotope compositions of Qz, Bt, Ms, Chl, and Ep from the different rocks, arranged according to the distance from the hanging wall. Temperature range given on the right corresponds to the temperatures of the fabric formation as estimated from the different isotopic thermometers of the fabric-forming minerals; they are thus not related to the depth or distance given on the left. The oxygen isotope compositions of the fluid in equilibrium with the different fabric-forming minerals ($\delta^{18}\text{O}_{\text{wt}}$) are calculated based on temperatures of the Qz-Ms isotopic fractionation for the protolith and mylonite, and Qz-Ep isotopic fractionations for Qz veins in the mylonite (Appendix V, Table V-4).

The infiltrating fluids during mylonitization were thus buffered by the rocks in terms of their oxygen isotope but not hydrogen isotope compositions, as the amount of hydrogen in the rocks prior to exchange is relatively small compared to that for oxygen. The isotopic composition of fluid inclusions in quartz from the protolith suggest to be partially equilibrated meteoric fluids, since their values are mid-way between magmatic and meteoric fluids. The hydrogen isotope compositions of buffered origin are also observed in the δD_{FI} values from quartz of the mylonite, located midway between the values characterizing the meteoric and magmatic fluids. In this case, the hydrogen isotope compositions of the sheet silicates indicate an isotopic equilibrium with meteoric fluids, or fluids that are partially buffered by the host-rocks during the process of mylonitization, until quartz and muscovite reach their isotopic closure temperatures.

As a reminder, the continental crust contains about 44 wt. % oxygen, and even higher if expressed in vol % or mol %. Oxygen is the most abundant element in rocks, whereas hydrogen is a minor or trace element (e.g., Criss, 1999). However, hydrogen has a lower atomic mass and size compared to oxygen and hence the diffusion of hydrogen is five times faster compared to that for oxygen and the closure temperatures for diffusion are also lower for hydrogen exchange. In this case, the volume of fluid required for changing the oxygen isotope bulk-rock composition of a unit is several orders of magnitude larger than that required for changing the hydrogen isotope bulk-rock composition.

In this case, it can be assumed that the volume of meteoric fluid that has percolated in the mylonitic BSZ was sufficient for shifting the hydrogen isotope composition of all hydrous minerals. However, since quartz and muscovite from the mylonite retain their magmatic oxygen isotope compositions, the volume of fluid was insufficient to shift the oxygen isotope composition of the shear zone. The meteoric fluid has thus influenced the mylonite in terms of its hydrogen isotope composition, but oxygen isotope composition of the fluid is still buffered by the rock.

However, the process of chloritization shows that chlorite is approaching, or reaches an isotopic equilibrium with a fluid characterized by a low- ^{18}O oxygen isotope composition. Indeed, Kerrich and Hyndman (1986) have shown in the Sweathouse section that the oxygen isotope compositions of feldspars and chlorites from mylonite and breccia show a pronounced interaction with meteoric fluids at temperatures from 350 °C and probably down to temperatures below 200 °C.

This implies that at temperature below 300 °C, the volume of fluid percolating in the granodiorite and the breccia is sufficient to buffer the oxygen isotope composition of minerals still capable of isotopic exchange or of newly formed minerals at this temperature, such as chlorite and some feldspars. V2a and b quartz veins have oxygen and hydrogen isotope compositions which confirm that the hydrothermal process that affected the BSZ at 200-300 °C was characterized by fluids of meteoric isotopic composition.

7. Conclusion :

Magmatic fluid was present during cooling of the granodiorite magma until the early stages of the detachment activity. In terms of fluid, the early stage of the Bear Creek Pluton exhumation along the BSZ (protomylonite) can still be defined as a “closed system” (Figure V-18 and t = 1, 2 of Figure V-19). When the granodiorite develops a mylonitic fabric, at T = 400 to 500 °C, the system opens and connects the detachment to an external meteoric fluid source (Figure V-18 and t = 3 of Figure V-19). Biotite isotope composition demonstrates that small amounts of meteoric fluid infiltrates the mylonite at temperatures $\geq 400^{\circ}\text{C}$. However, the mylonite silicates suggest interaction with a fluid of mixed magmatic and meteoric isotope composition, which highlights an infiltration of meteoric fluid through the entire section during the mylonitization process. This meteoric fluid infiltration is more expressed in terms of oxygen isotope compositions at the top of the section and diminishes towards the protolith (Figure V-18 and t = 4, 5 Figure V-19). The late stage of the detachment activity, when T $\leq 300^{\circ}\text{C}$, is dominated by fluid flow that retains its meteoric composition for both oxygen and hydrogen isotope compositions (Figure V-18 and t = 6, 7 Figure V-19). Consequently, the evolution of the oxygen isotope compositions in the detachment implies a spatial and temporal evolution of the fluid/rock ratio in the detachment. A pervasive infiltration of meteoric fluids occurs throughout the entire shear zone while deformation is accommodated by mylonitization of the granodiorite and (t = 3, 4, 5 Figure V-19). During exhumation, strain localizes in the upper part of the shear zone, developing intense ultramylonite / mylonite alternation and cataclasite, infiltration of meteoric fluid is channelized and increases the fluid-rock ratio (t = 5, 6, 7 Figure V-19).

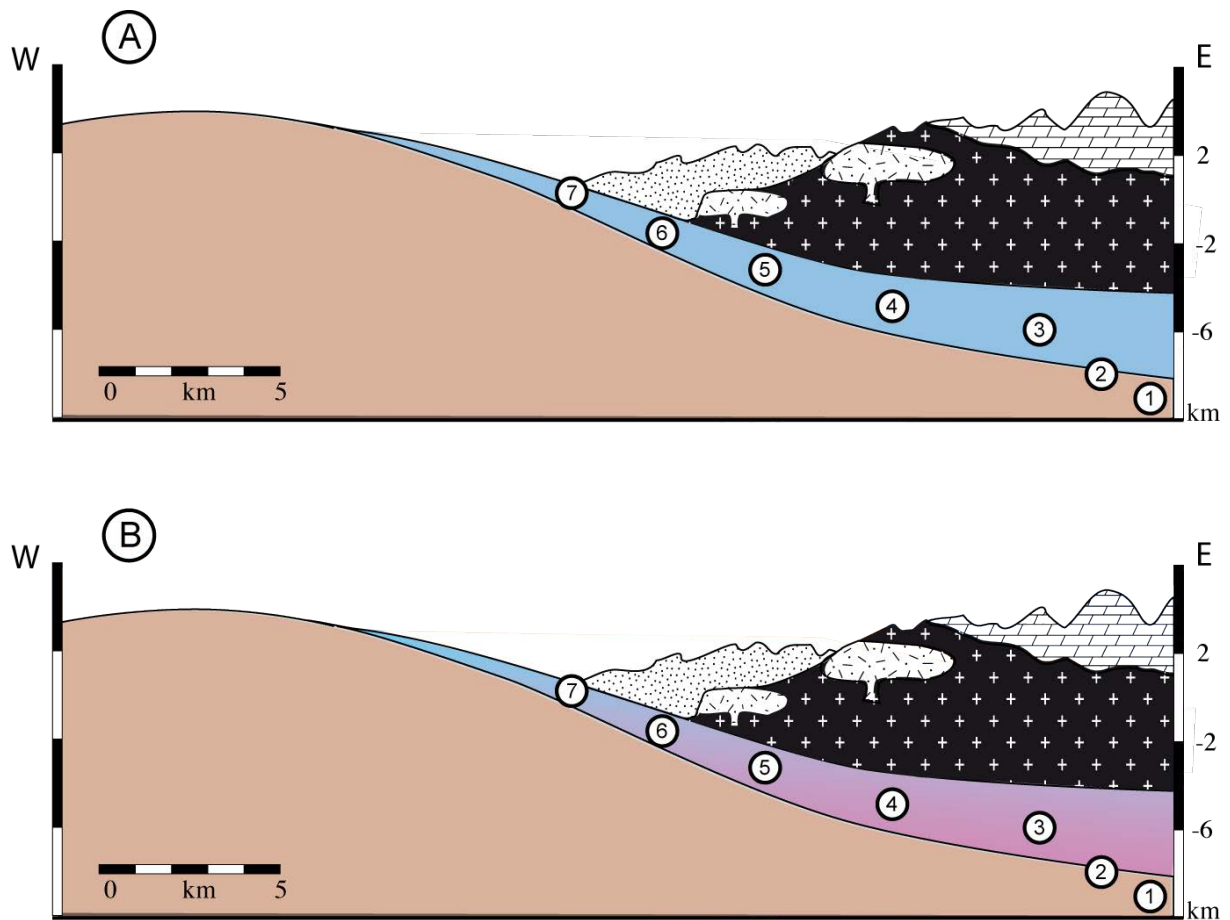


Figure V-18: Schematic cross-section representing the evolution of the stable isotope composition of the BSZ. A, illustrates the hydrogen isotope composition and the fluid flow in the detachment through space and time. B, illustrates the oxygen isotope composition of the fluid flow in the detachment through space and time. Red correspond to magmatic fluid composition; purple: δD of the meteoric fluid retaining its δD_{wt} but with $\delta^{18}O_{wt}$ buffered by the host-rock; blue: meteoric fluid composition.

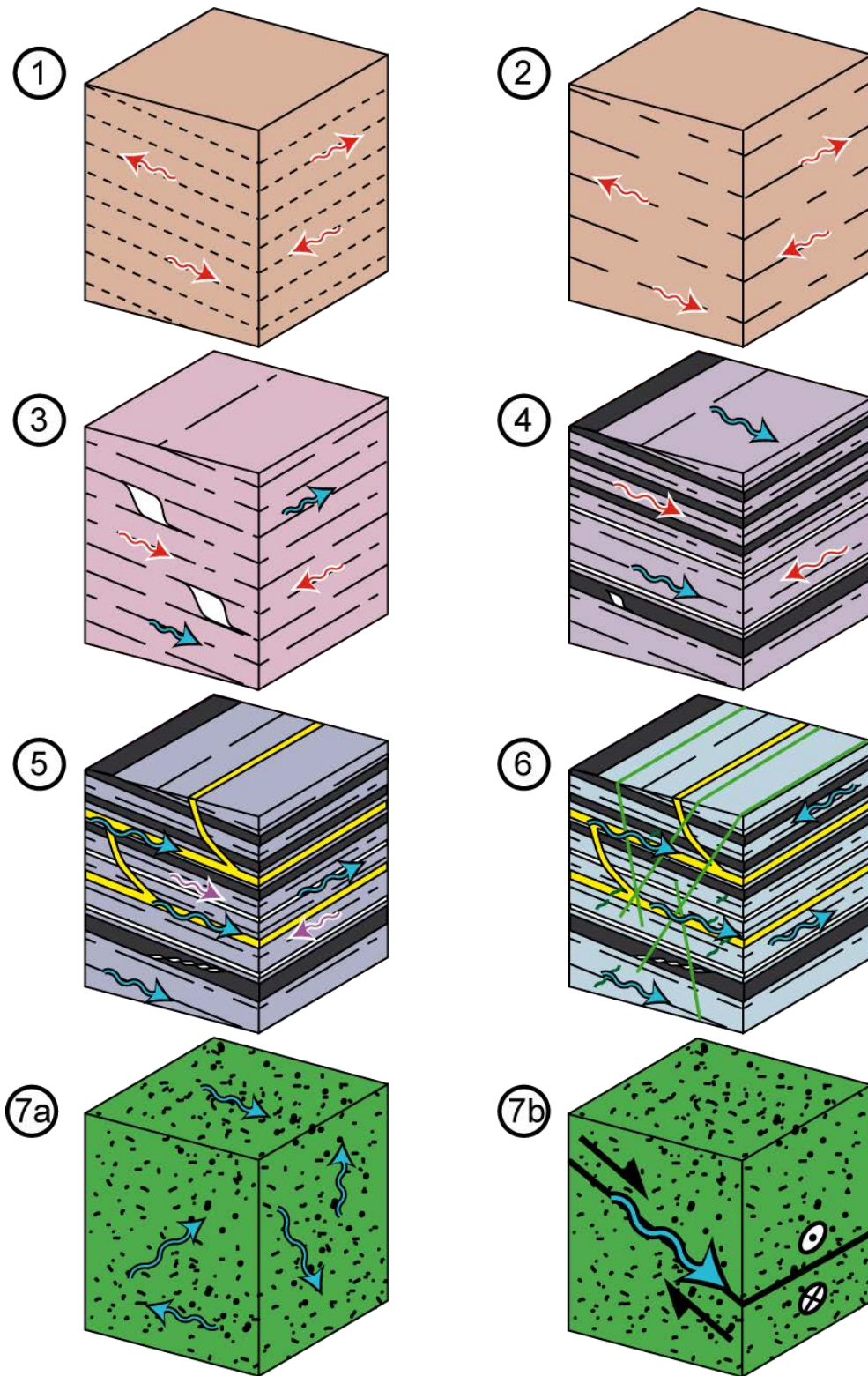


Figure V-19: Evolution of the fluid flow and the $\delta^{18}\text{O}_{\text{wt}}$ values relative to the evolution of the fabric overprinting the granodiorite of the Bear Creek Pluton. Red corresponds to magmatic fluid compositions; purple: δD meteoric fluid retaining its $\delta\text{D}_{\text{wt}}$ but with $\delta^{18}\text{O}_{\text{wt}}$ buffered by the host-rock, blue: meteoric fluid composition. Length and number of arrows illustrate the volume of fluid flowing in the BSZ.

Chapter VI : Infiltration of meteoric fluids in ductile crust beneath the Kettle extensional detachment (WA, USA)

A. Quilichini¹, L. Siebenaller², W. Nachlas³, C. Teyssier³, T. Vennemann¹, M. T. Heizler⁴, A. Mulch^{5,6,7}

¹Institut de Minéralogie et Géo chimie, Université de Lausanne, 1015 Lausanne, Switzerland

²Institut de Recherche pour le Développement, Université Paul Sabatier - Toulouse 3, 31062, Toulouse, France

³Department of Earth Sciences, University of Minnesota, Minneapolis, Minnesota 55455, USA

⁴New Mexico Geochronology Research Laboratory, New Mexico Tech, Socorro, New Mexico 87801-4796, USA

⁵Biodiversity and Climate Research Centre (BiK-F), Senckenberganlage 25, 60325 Frankfurt/Main, Germany

⁶Institut für Geowissenschaften, Goethe Universität Frankfurt, Altenhöferallee 1, 60438 Frankfurt/Main, Germany

⁷Senckenberg, Senckenberganlage 25, 60325 Frankfurt/Main, Germany

(Submitted to the Geological Society of America Bulletin)

Abstract

Meteoric fluid flow along crustal-scale extensional detachment systems has been documented in many extensional terrains, yet the interaction among fluids, deformation/recrystallization processes, and rock chemical composition remains enigmatic. Here is documented the microstructural evolution of a quartzite mylonite (quartz + muscovite ± feldspar) in the Kettle detachment shear zone (Washington, USA), which defines the footwall of the Columbia River detachment and bounds the Kettle dome metamorphic core complex. Across the shear zone quartz microstructures evolved from grain boundary migration recrystallization to subgrain rotation mechanisms, with attending changes in muscovite chemical compositions, quartz-muscovite oxygen isotope composition, and degree of fluid-rock interaction. Over 150 m of section, hydrogen isotope ratios (δD) from synkinematic muscovite are constant ($\delta D = -130 \text{ ‰}$) and consistent with a meteoric fluid source. Quartz-muscovite oxygen isotope thermometry indicates equilibrium fractionation temperatures of $\sim 365 \pm 30^\circ\text{C}$ in the lower part of the section, where quartz recrystallization was dominated by grain boundary migration recrystallization. In the upper part of the section, muscovite shows

increasing intra-grain compositional zoning, and quartz microstructure is dominated by subgrain rotation recrystallization, bulging recrystallization, and solution-precipitation. Meteoric fluids permeated the evolving mylonite section, while ductile deformation propagated upward toward the brittle detachment during exhumation and cooling; the preserved microstructural and isotopic exchange signature occurred over a short time as indicated by consistent argon ages comprised between 51 and 50 Ma over the whole section. Pervasive fluid flow became increasingly channelized over the time scale of detachment shear zone activity, leading to microstructural heterogeneity and large shifts in quartz oxygen isotope values on a meter scale. Localization culminated by activation of the brittle detachment surface, which rapidly exhumed the mylonitic footwall.

Introduction

In detachment systems that bound metamorphic core complexes (MCC) fluids may convect from the surface to the detachment along faults and fractures that serve as zones of recharge and discharge within the brittle crust (Fricke et al., 1992; Morrison and Anderson, 1998; Person et al., 2007). This fluid flow is driven by high heat input beneath the detachment (Rey et al., 2009a and b; Gottardi et al., 2011), where heat is advected by crustal thinning and intrusion of crustal-derived melts. This hydrothermal convective flow is narrowly focused at the footwall-hanging wall interface for the duration of activity of detachment tectonics at moderate temperatures (500-300°C), resulting in significant fluid-rock interaction and isotopic exchange (O'Hara et al., 1997; Holk and Taylor, 1997, 2007; Mulch et al., 2006, 2007; Person et al., 2007; Gébelin et al., 2011; Campani et al., in press).

Studies of the hydrogen isotope ratios of fabric-forming minerals such as muscovite, biotite, and amphibole in detachments of North American Cordilleran core complexes suggest that meteoric fluids can permeate the shear zone that typically exists in the upper part of the detachment footwall (e.g. Morrison and Anderson, 1998; Criss and Fleck, 1990; Losh, 1997; Mulch et al., 2004; 2007; Gottardi et al., 2011; Gébelin et al., 2011). Processes such as convective fluid flow and seismic pumping (Sibson et al., 1975), changes in fluid salinity, and the presence of a relatively large hydraulic head are likely responsible for the transport of surface fluids down to depths of ~10 km to the detachment footwall, where fluid and rock interact at elevated temperature (Person et al., 2007).

Fluid-rock interaction during detachment activity feeds back into crustal deformation. Bulk-rock analyses of mylonite zones indicate that these zones experience a 20-60% volume

loss over the duration of detachment tectonics (O'Hara, 1988; O'Hara and Blackburn, 1989; Yang et al., 1998). The presence of water during dynamic recrystallization and mylonite formation promotes the breakdown of feldspar and the growth of mechanically weak hydrous phases (mica, chlorite) that tend to further localize deformation (Janeck and Evans, 1988).

Here is examined the impact of the feedback between the dynamic recrystallization of quartz and the oxygen isotope fractionation that takes place between quartz and muscovite in a setting in which synkinematic muscovite grew in the presence of a meteoric fluid. Mylonitic quartzite is of particular interest as it is largely bi-mineralic, which simplifies the analysis of isotopic exchange between fluids and minerals. The approach used here focuses on a quartzite unit located in the footwall of the Columbia River detachment that bounds the Kettle dome (Washington, USA). We examine the relationships among quartz-muscovite microstructures, the chemical composition and $^{40}\text{Ar}/^{39}\text{Ar}$ ages of muscovite, and the oxygen ($\delta^{18}\text{O}$) and hydrogen (δD) isotopic compositions of the fabric forming minerals in the mylonite. Results support a strong link between fluid flow, dynamic recrystallization, and equilibrium fractionation of oxygen isotopes.

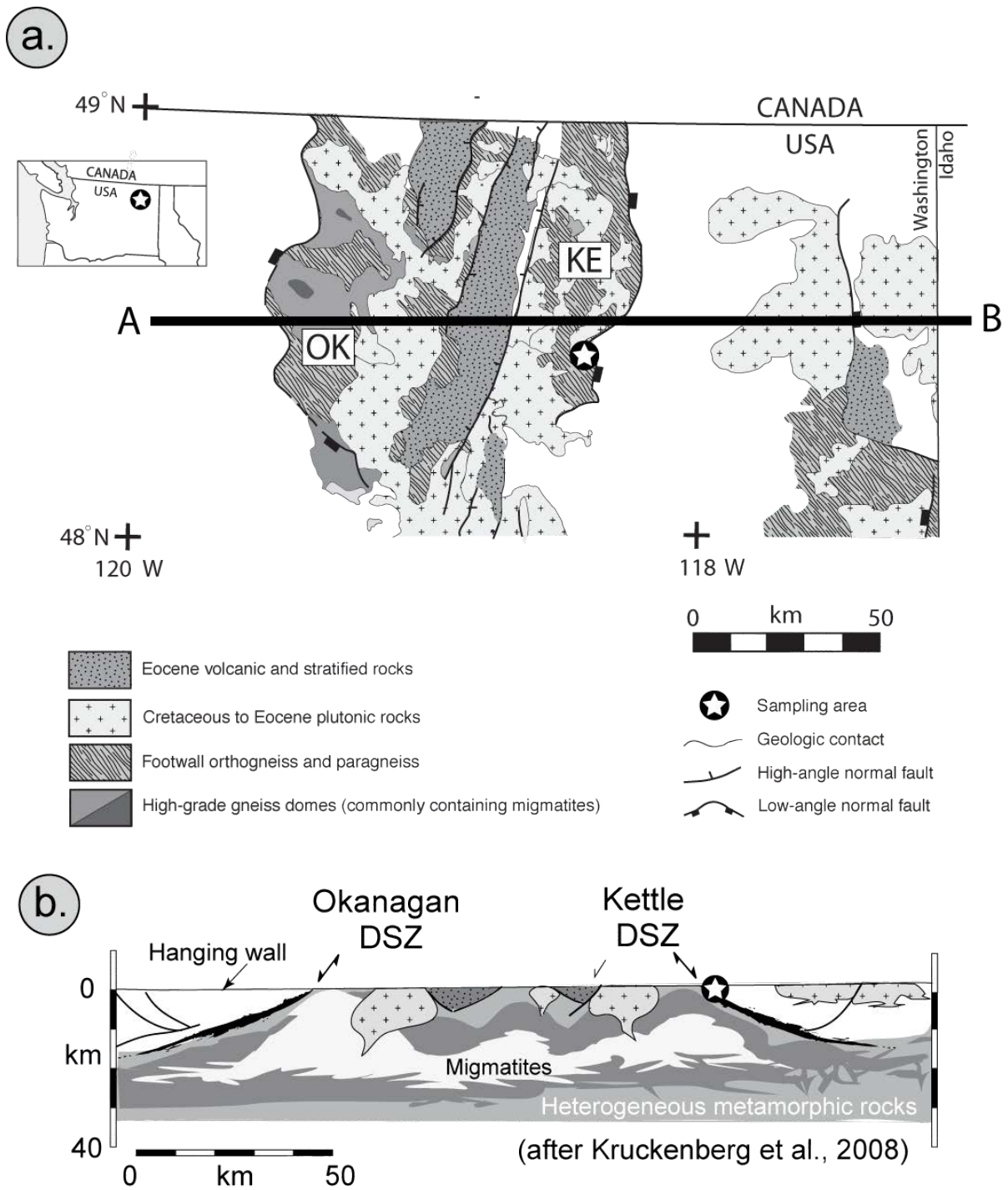


Figure VI-1: (a) Map of the Okanagan-Kettle metamorphic core complex, and localization of the Kettle detachment shear zone (DSZ) ; (b) Schematic section of the Kettle-Okanagan MCC.

1. Geologic setting

To the north of the Snake River plain, the North American Cordillera is characterized by the formation of metamorphic core complexes (MCC) that are bounded by detachment shear zones (Coney, 1980; Armstrong, 1982; Coney, 1980; Foster and Raza, 2002). The Columbia River detachment defines the eastern border of the Kettle dome MCC (Figure VI-1a& b), which was exhumed during Eocene time (Cheney, 1977, 1980; Mulch et al. 2007). The immediate footwall of the Columbia River detachment consists of a section of mylonitic rocks (Rhodes and Cheney, 1981), which at this latitude are dominated by quartzite (Figure VI-2). In the following, we use the term Kettle detachment shear zone (DSZ) to describe sheared rocks that make up the footwall of the Kettle detachment fault.

Foliation in the Kettle DSZ dips shallowly to the east, and lineation is oriented E-W (~N100) and plunges ~20° to the E. Outcrop and thin section observations indicate consistent top-to-the-east sense of shear, consistent with Columbia River detachment kinematics and exhumation of the Kettle dome (Mulch et al., 2006, 2007; Cubley and Pattison, 2009). Samples across the Kettle DSZ were collected from the Hall Creek quarry (Inchelium, WA), which provides ~150 m of continuous section of mylonitic quartzite. High-resolution sampling (5-10 m) complements the initial study of Mulch et al. (2007).

In the Hall Creek quarry we sampled a particularly good exposure of the hanging wall as well as footwall units of the Columbia River detachment (Figure VI-3). Ordovician marine metasediments (Miles, 1985) define the hanging wall and structurally overlie a 20 m thick breccia and cataclasite layer (brittle part of the detachment). The 20 m thick unit was affected by intense brittle deformation, and the high density of randomly oriented quartz veins suggests that fluid-filled fractures were present during deformation (Figure VI-4a). The breccia and cataclasite layers correspond to the uppermost part of the detachment system, where the host rock is silicified and contains abundant secondary oxides. As a result, identifying the protolith of this unit is problematic.

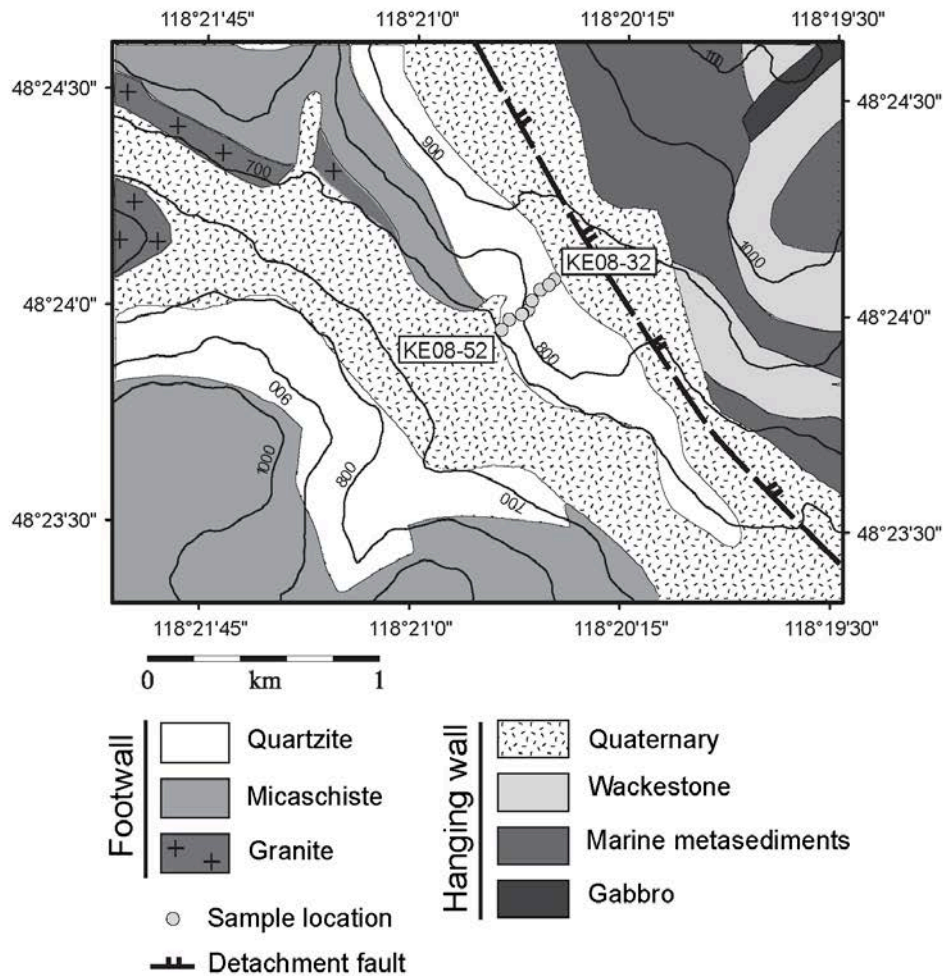


Figure VI-2: The Kettle DSZ, part of the Columbia river detachment that delineates the contact between the Tertiary lower crust and the Mesozoic upper crust is highlighted at the Hall Creek Quarry (adapted from Washington State DNR, 2008).

Underneath the breccia/cataclasite unit, a 20-30 m of section of mylonite displays alternating layers of quartzite and micaschist 1-10 cm thick (Figure VI-4b). Foliation in this unit, here called the upper quartzite mylonite (UQM), is wavy, and lineation is weakly developed. The UQM is characterized by the presence of numerous brittle structures such as kink-bands and high-angle normal faults, with displacements up to a few centimeters (Figure VI-4c). The UQM is a zone of mylonitic deformation overprinted by pervasive brittle deformation.

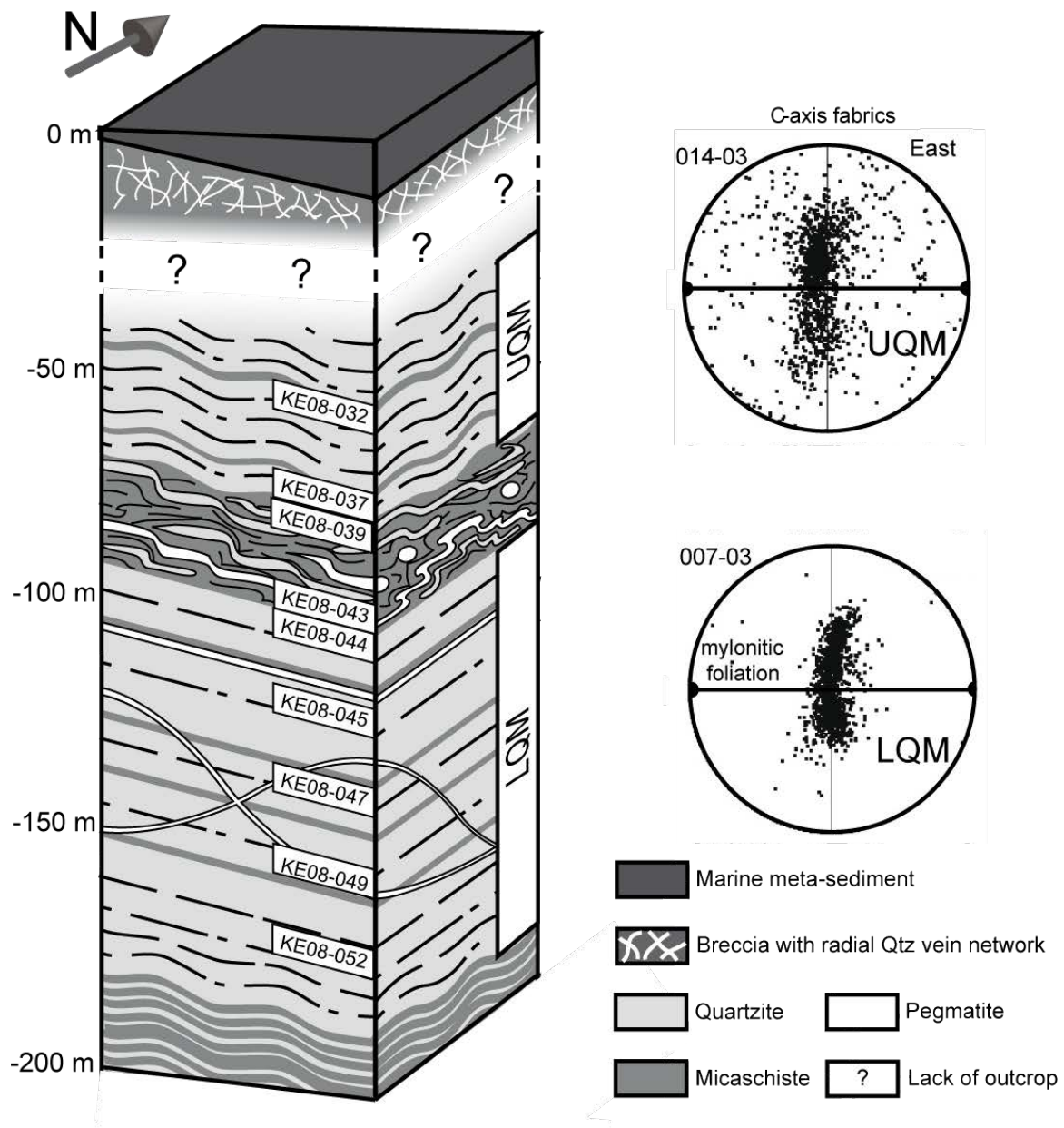


Figure VI-3: Schematic bloc diagram of the detachment units present in the Hall Creek Quarry, Inchellum, WA. C-axis fabrics orientation of quartz grains on the right side, for both UQM and LQM units.

The deepest part of the exposed Kettle DSZ is another 50 m thick layer of muscovite-bearing quartzite (lower quartzite mylonite, LQM). This quartzite mylonite displays planar foliation and a strong stretching lineation (Figure VI-4d). This unit is characterized by 10-20 cm thick quartzite layers that are separated by thin mica-rich layers, a few mm to cm thick, or sheared transposed pegmatite veins that can reach 10 cm in thickness. A 5 m thick layer near the base of the LQM hosts 1-10 cm thick quartzite-micaschist alternations similar to UQM, although brittle structures are absent.

The transition from UQM to LQM is marked by a 20 m thick schist layer (Figure VI-4e) where no evidence of brittle faulting could be detected. This schist layer contains quartzite mylonite lenses and sheared pegmatite veins that are affected by recumbent folds with extremely attenuated limbs (Figure VI-4f). Except for the pegmatite veins, this metasedimentary sequence of UQM, LQM, and intercalated schist layers can be interpreted as transposed sedimentary layering with original alternations of sandstone and mudstone (Mills, 1985). The Kettle DSZ, and to a greater extent the Columbia River detachment, was metamorphosed to amphibolite facies and retrogressed under greenschist-facies conditions (Vanderhaeghe et al., 2003; Mulch, 2004, 2006, 2007). Based on the variable intensity of deformation, pegmatite bodies are interpreted to have intruded pre- to syn-mylonitization.

2. Quartzite mylonite characteristics

2.1. Microstructure

The microstructural study is based on representative samples from both UQM and LQM. Observations were made in thin sections that are cut perpendicular to foliation and parallel to the stretching lineation.

2.1.1. UQM

The mineral mode in UQM is 88% quartz, 2% K-feldspar, 8% muscovite, and 2% oxides. Quartz grains display a heterogeneous grain size distribution with small subgrains (0.01-0.05mm) mantling larger quartz grains (0.1 to 0.3 mm) (Figure VI-5a), and subgrains record a well-developed crystallographic preferred orientation (Figure VI-3). The UQM displays thin quartz ribbons, several hundred microns in length (Figure VI-6a). Muscovite grains have variable aspect ratios and dominantly form lenticular mica fish (Grothenthuis, 2003) with wavy boundaries. Isolated K-feldspar grains are porphyroclastic, typically >0.5 mm in size, and show tails in the pressure shadows characterized by recrystallized quartz and muscovite (Figure VI-6b). The UQM displays an S-C fabric (Lister and Snoke, 1984) that is defined by elongate quartz grains, mica fish, and sigmoidal foliation. This S-C fabric is systematically cut by C' shear bands with approximately ~ 200-400 μm spacing.

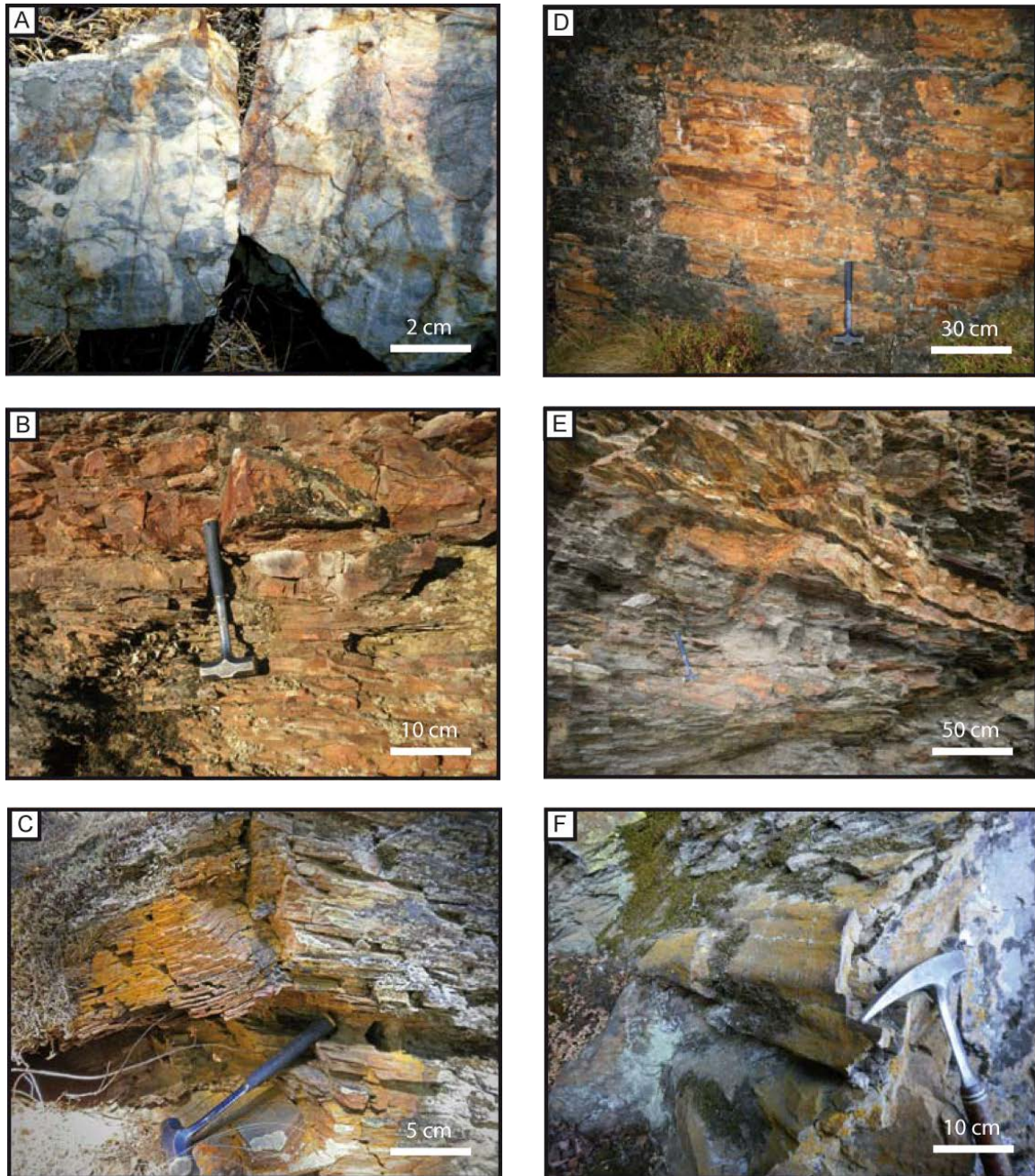


Figure VI-4: (a) Silicified breccia, rich in oxides. (b) Upper Quartzite mylonite. (c) kink-bands in UQM. (d) Lower Quartzite mylonite. (e) Micaschist layer. (f) Sheet folds in the micaschist .

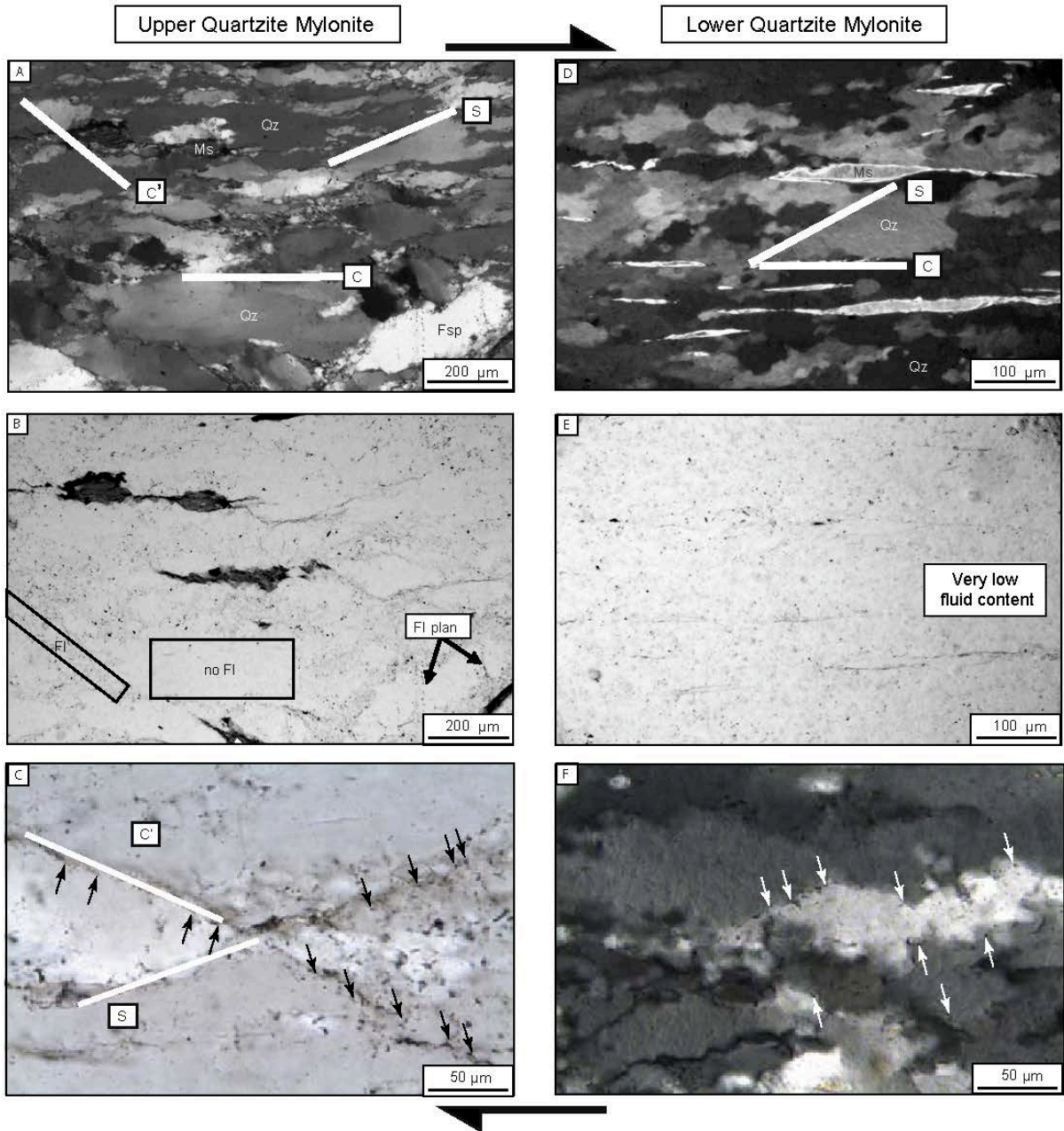


Figure VI-5: Thin sections have been cut perpendicular to the foliation and parallel to the lineament. The optical micrographs are West-East oriented (left to right in micrographs); top and bottom border of the thin sections are parallel to the foliation plan of the quartzite mylonite. (a), (d), and (f) optical micrographs in crossed polarized light with white lines defining the S-C-C' fabric; (b), (c) and (e) optical micrographs in natural light with localization of the fluid inclusions.

The presence of small quartz grains (10-50 μm) along irregular quartz grain boundaries indicates bulging of grain boundaries (Hirth and Tullis, 1992; Stipp et al., 2002). Recrystallized grains along grain boundaries have a size similar to that of subgrains (Figure VI-5a), indicating that recrystallization was achieved dominantly by subgrain rotation (Passchier and Trouw, 2005). Serrated grain boundaries and the presence of recrystallized subgrains indicate that the UQM experienced dynamic recrystallization in the bulging and subgrain rotation dislocation creep regimes 1 to 2 of Hirth and Tullis (1992) and Stipp et al. (2002).

2.1.2. LQM

The LQM is composed of 95% quartz and 5% muscovite. The quartz grain size is rather uniform at approximately 100 μm (Figure 5d); quartz grains have lobate boundaries and are mostly devoid of intracrystalline deformation features (undulatory extinction) or subgrains. Muscovite forms lozenge-shape lenticular mica fish (Ten Grotenhuis et al., 2003). LQM quartzite is largely devoid of feldspar, and oxide minerals occur in trace abundance compared to UQM.

The S-C fabric, defined by elongate quartz and mica fish, is well developed in LQM. However, C' shear bands are absent (Figure VI-5d). Quartz c-axes have a strong preferred orientation, with an asymmetry consistent with top-to-the-east shearing. The uniform quartz recrystallized grain size and the strong crystallographic fabric suggest that LQM deformed in the dislocation creep regime 3 of Hirth and Tullis (1992) that is dominated by grain boundary migration.

Microstructural observations reveal a significant difference in quartz microstructure between UQM and LQM that corresponds to quartz recovery mechanisms (dislocation creep regime 1-2 versus regime 3; Hirth and Tullis, 1992). Grain boundary migration (Drury and Urai, 1990) prevails in LQM, whereas bulging and subgrain rotation recrystallization dominate in UQM. This evolution in recrystallization mechanisms occurs spatially across the 20 m thick schist layer between the two quartzite units.

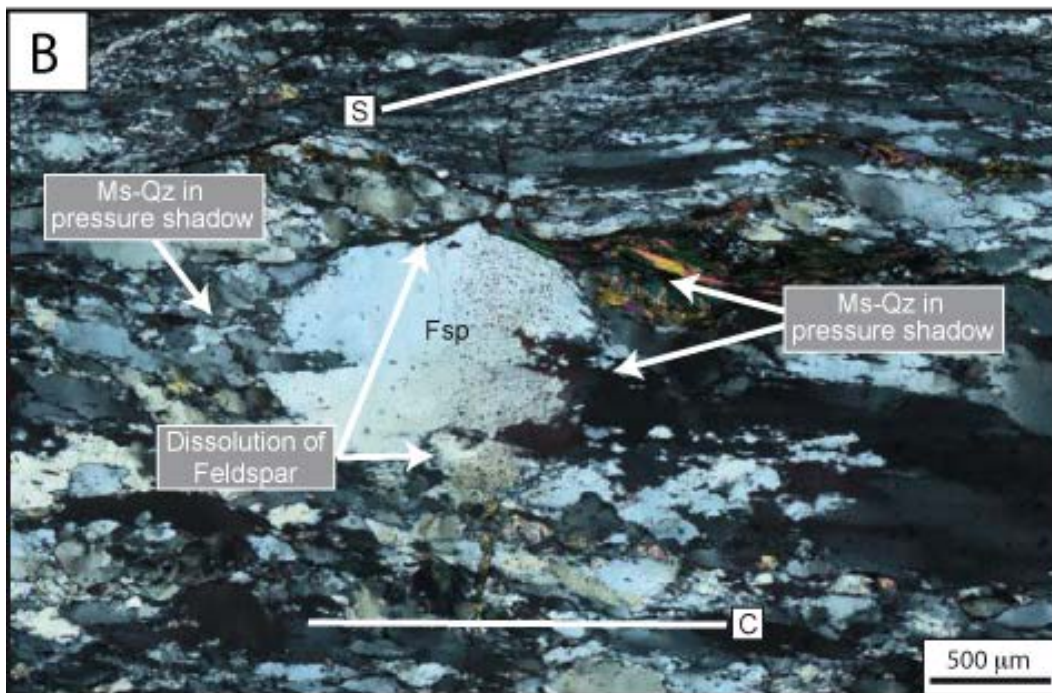
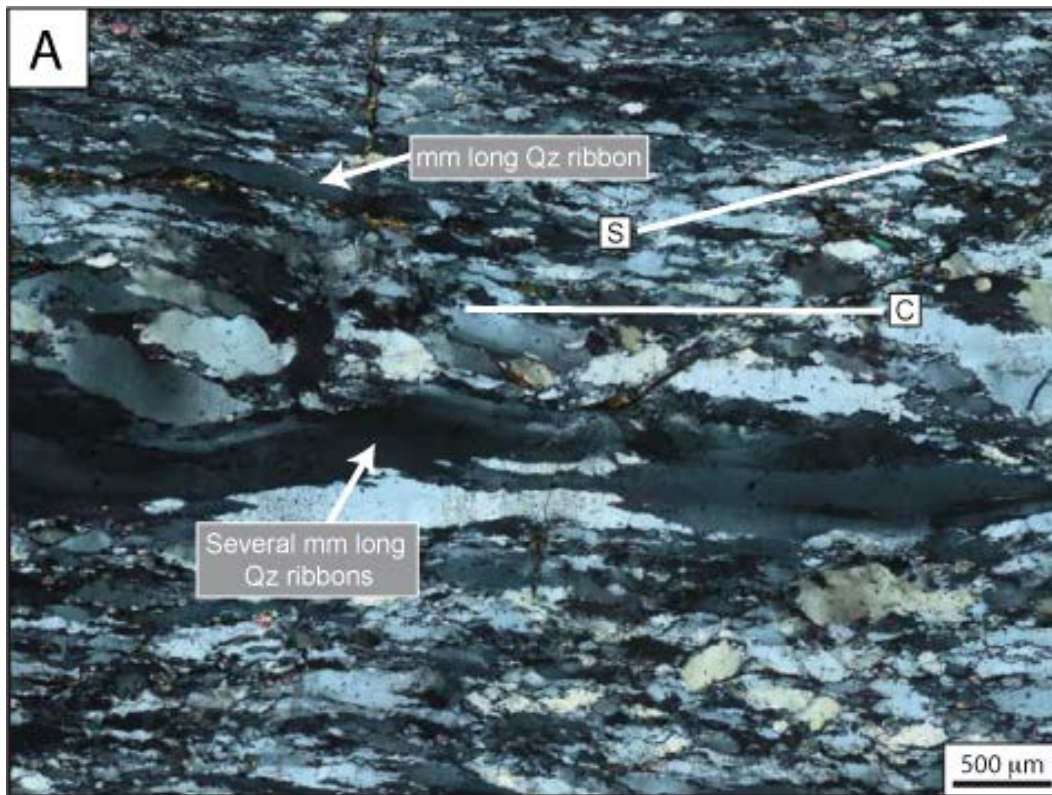


Figure VI-6: Thin sections have been cut perpendicular to the foliation and parallel to the lineament. The optical micrographs are West-East oriented (left to right in micrographs); top and bottom border of the thin sections are parallel to the foliation plan of the quartzite mylonite. (a) quartz ribbons of different length in the UQM. (b) Grain size reduction of K-feldspar by hydration, producing quartz and muscovite in its tails.

2.2. Quartz crystallographic fabric

Quartz c-axis fabrics from two samples (UQM and LQM units) were analyzed by electron backscatter diffraction (EBSD). C-axes are distributed on a partial single girdle oriented normal to lineation, with a slight inclination and a concentration of axes near the center of the stereonet (Figure VI-3). This c-axis fabric indicates that deformation in both units was accommodated by prism and rhomb glide systems along the $\langle a \rangle$ direction, in agreement with top-to-the-east shearing (Passchier and Trow, 2005). The UQM c-axis fabric is slightly more scattered than LQM, but both likely developed under similar T and kinematic conditions.

2.3. Fluid inclusion distribution

Another notable distinction between UQM and LQM is the density and distribution of fluid inclusions (FI) with respect to microstructures. In the UQM, FI are common in the vicinity of C' shear bands and are concentrated along quartz subgrain boundaries (Figure VI-5b & c). FI are also found within fluid inclusion planes (FIP) (Lespinasse and Pecher, 1986) crosscutting K-feldspar grains (Figure VI-5b). In the LQM, FI are rare and are only preserved in the vicinity of grain boundaries (Figure VI-5e & f).

3. Chemical composition and $^{40}\text{Ar}/^{39}\text{Ar}$ ages of mica fish:

3.1. Microprobe analysis and elemental maps

Qualitative and quantitative microchemical observations of muscovite were gathered using a CamScan Series II Scanning Electron Microscope (SEM) and a Cameca SX-50 Electron Microprobe (EMP) in the Geosciences Department, Virginia Polytechnic Institute and State University. Specific muscovite grains were selected for analysis based on geometry (Appendix VI Table V-1); 10 grains were analyzed from 3 samples spaced approximately 50 m within the section (KE08-032, KE08-045 and KE08-052 at -57, -117, and -168 m, respectively, Figure VI-3). The SEM was used to generate secondary electron (SE) and back-scattered electron (BSE) images that allowed selection of particular regions of interest for quantitative EMP analysis. Operating conditions for BSE analysis were: accelerating voltage of 20.0 kV with a working distance of 35 mm. Compositional measurements (EDS and WDS) of muscovite grains were made using the EMP including quantitative compositional determination and variance (EPMA) (15 kV accelerating voltage and 20 nA beam current)

and elemental mapping of muscovite grains (WDS; 15 kV and 75 nA with a dwell time of 1024 microseconds per pixel).

Additional EMP analyses of single grains were conducted perpendicular to the muscovite cleavage at 10 μm intervals. Major element compositions from single grain transects are reported as total aluminium (atoms per fugacity units, apfu) versus $\Sigma(\text{Si}+\text{Mg}+\text{Fe})$ (apfu) diagrams to highlight possible Tschermak (phengite-muscovite) substitution in muscovite.

Zoning of muscovite composition between core and rim are measurable for most major elements and zoning is particularly clear for Al, Mg, and Si (element maps, Figure VI-7a & b). The cores of these muscovite grains have a $\Sigma(\text{Si}+\text{Mg}+\text{Fe})$ composition of 3.5 ± 0.1 apfu and a total aluminium composition of 2.5 ± 0.1 apfu, corresponding to a 1:1 proportion of muscovite to phengite. The rims show a $\Sigma(\text{Si}+\text{Mg}+\text{Fe})$ composition of 3.25 ± 0.1 apfu and a total aluminium composition of 2.7 ± 0.1 apfu, and tend towards a higher muscovite proportion. Most (>80%) UQM muscovite grains display a higher Mg-Si content in the core, while Al content decreases toward the core (Figure VI-7a). The unzoned muscovite from the UQM (<20%) falls in the same composition range ($\Sigma(\text{Si}+\text{Mg}+\text{Fe})$ 3.25 ± 0.1 apfu; $\Sigma(\text{Al})$ 2.7 ± 0.1 apfu) as the rims of zoned muscovite.

In contrast, muscovite analyzed from LQM shows no significant core to rim zoning (Figure VI-7d & f). According to the Mg, Al, and Si content (Figure VI-7c & e), the muscovite composition of the lower quartzite has a $\Sigma(\text{Si}+\text{Mg}+\text{Fe})$ composition of 3.5 ± 0.1 apfu and a total aluminium composition of 2.5 ± 0.1 apfu, corresponding to a 1:1 proportion of muscovite to phengite. Muscovite compositions from the top of LQM (KE08-45) are slightly more scattered, indicating a possible trend toward UQM compositional patterns.

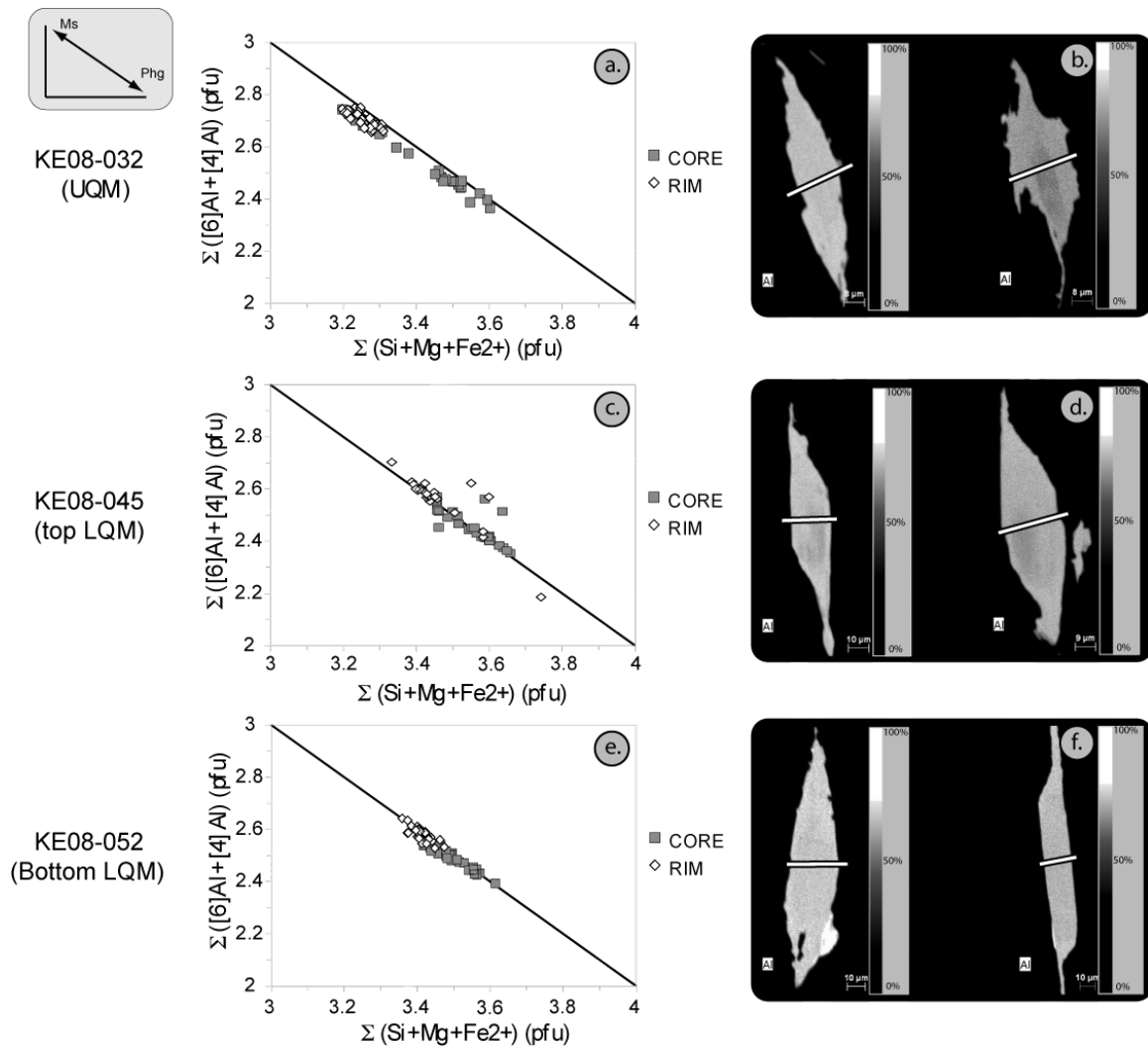


Figure VI-7: (a), (c), (e) Tschermak substitution substitution with total aluminum versus (Si+Mg+Fe) content, on the basis of electron microprobe analysis of single grain transects. (b), (d), (f) Al element map of micafish, transect has been measured perpendicular to the shear plane (white lines).

3.2. $^{40}Ar/^{39}Ar$ dating of muscovite

Muscovite of the Hall Creek section was analyzed at New Mexico Tech (NM, USA) by furnace step heating $^{40}Ar/^{39}Ar$ geochronology (Appendix VI, Table V-2). Muscovite grains from 0.12 to 0.60 mm were separated using a Frantz magnetic separator. Hand-picking under a binocular microscope eliminated grains that were affected by weathering, alteration, or mineral inclusions. Muscovite separates ranging in weight between 6 and 23 mg were analyzed by furnace step heating $^{40}Ar/^{39}Ar$ geochronology. Calculated plateau ages include at least 65% of total ^{39}Ar released in at least six successive steps.

The apparent $^{40}Ar/^{39}Ar$ ages of muscovite samples are all within a very narrow age range between 50 to 51 Ma, with no trend as a function of position in the section (Figure

VI-8). All six argon release spectra share common features, including slightly elevated age steps over the first 10-15% of ^{39}Ar release, followed by a broad flat segment from which ages have been calculated. No significant difference in the shape of release spectra or the calculated ages can be detected between samples from the UQM (KE08-32 and KE08-39) and LQM (KE08-44, KE08-45, KE08-47, and KE08-49) units (Figure VI-3).

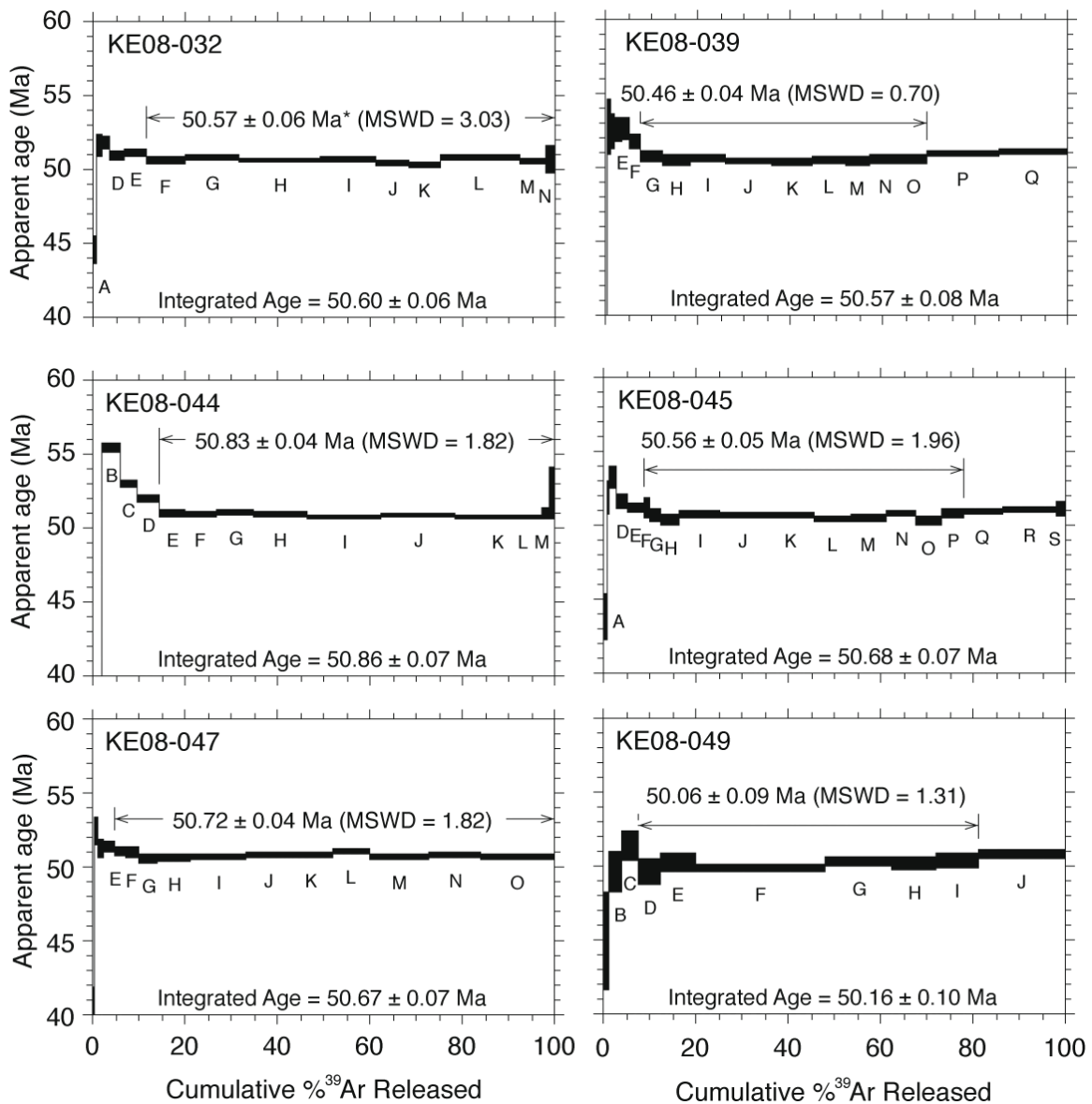


Figure VI-8: $^{40}\text{Ar}/^{39}\text{Ar}$ age spectras on muscovite grains, performed by Pr. Heizler at the University of New Mexico. Results indicate constant ages through the section, the mean-value is 50.5 ± 0.3 My. The small error bars are justified by the wide plateaus.

4. Stable isotope analysis

Quartz and muscovite grains were separated using a Frantz magnetic separator, followed by hand picking under a binocular microscope to obtain fractions with >95% purity. All stable isotope analyses were performed in the Stable Isotope Laboratory at the University of Lausanne. The $\delta^{18}\text{O}$ values of quartz and muscovite were measured using a CO_2 -laser fluorination line coupled to a Finnigan MAT 253 mass spectrometer. Each sample was replicated and normalized with in-house kaolinite and biotite standards. Two quartz standards (NBS 28) were used for each run. Most of the mineral pairs were measured as part of the same sequence using 1 to 2 mg of quartz or muscovite. The δD values of muscovite were measured in continuous flow mode with a TC-EA (high temperature reduction) linked to a Finnigan MAT Delta Plus XL mass spectrometer.

Samples selected for fluid inclusion extraction were hand-picked in order to isolate at least one gram of pure quartz and to avoid possible contamination by inclusions or other contaminants. The weight of analyzed samples ranges between 1 and 2 g. The pure silica glass tube containing the sample is fixed on the extraction line, then the sample is step-heated to 300, 400, 450, and up to 500°C in order to distinguish the amount of extracted fluid at each step by its pressure rise. H_2O is extracted from the fluid inclusions by heating the quartz samples in vacuum to temperatures in excess of 500°C and is trapped within a smaller Pyrex® vial containing approximately 150 mg of zinc shavings. A cold trap filled with liquid nitrogen allows trapping of H_2O in the tube containing zinc. This trap is removed at the end of the last heating step after cutting and hermetically closing the tube using a gas burner. The H_2O vial obtained is then placed in an oven at 500°C for 15 minutes in order to oxidize the zinc and release hydrogen. Hydrogen isotope compositions of the H_2 vials are analyzed using a Finnigan MAT 253 mass spectrometer.

4.1. δD values of muscovite:

δD values measured for muscovite (Figure VI-9a) remain relatively constant throughout the vertical extent of the section (-129‰ to -134‰), independent of the unit analyzed (quartzite, micaschist, pegmatite). The values are typical for muscovite that has equilibrated with a homogeneous fluid of low D/H ratio. The narrow range of muscovite δD values and their low absolute values may indicate that muscovite recrystallized in the presence of meteoric fluids (e.g. Morrison and Anderson, 1998; Mulch et al., 2004; Mulch et al. 2007; Gottardi et al., 2011; Gébelin et al., 2011).

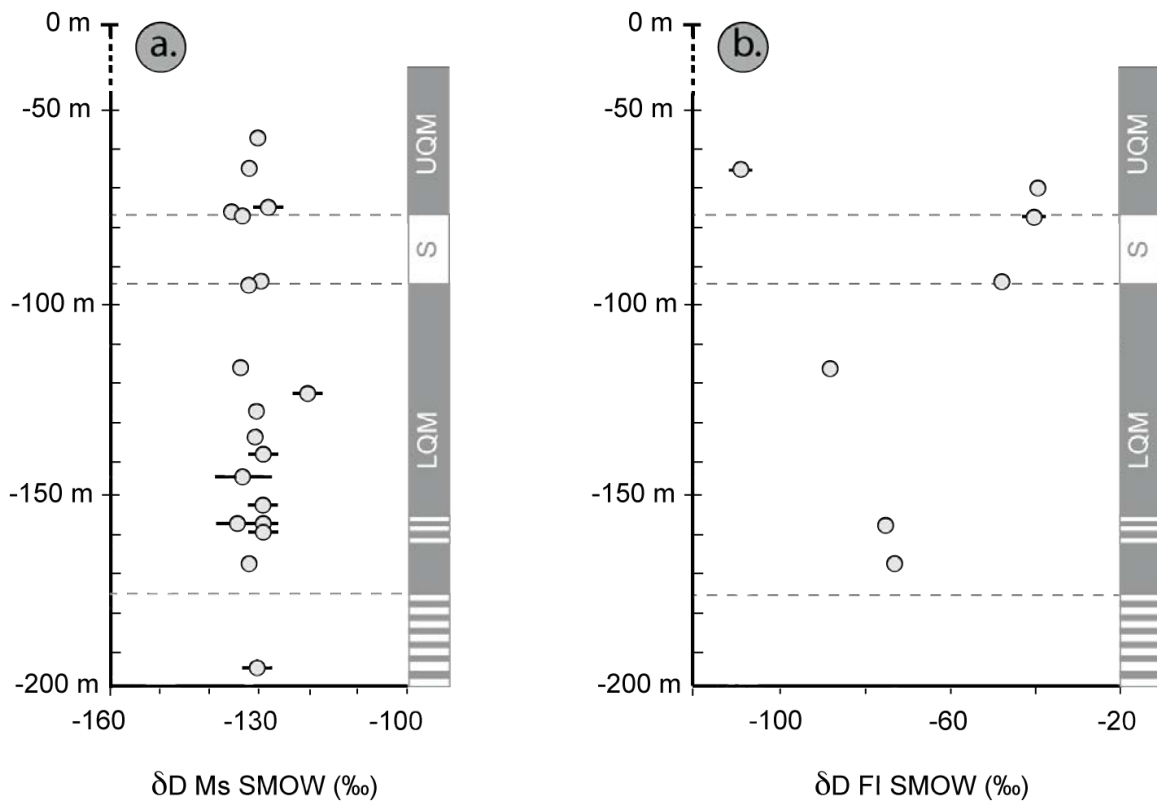


Figure VI-9: (a) Hydrogen isotope composition of muscovite as a function of the distance below the detachment. (b) Hydrogen isotope composition of quartz fluid inclusions as a function of the distance below the detachment. In both graphs, the error bars correspond to the standard deviation of the duplicates. Simplified cross-section on left side : UQM – Upper Quartzite Mylonite ; S - micaschist layer ; LQM – Lower Quartzite Mylonite.

4.2. δD values of fluid inclusions in quartz ($\delta D FI_{Qz}$):

Extraction of fluid inclusion from 7 pure quartz samples produced sufficient H_2 for mass spectrometric analysis. These seven samples are distributed through the section: two samples come from UQM (-65 and -70 m), two from lenses of quartzite in the micaschist layer (-77 and -94 m), and three from LQM (-117, -158 and -168 m) (Figure VI-9b).

In UQM, sample KE08-33 shows a $\delta D FI_{Qz}$ of $-109 \pm 1\text{‰}$ and sample KE08-35 a $\delta D FI_{Qz}$ of $-39 \pm 3\text{‰}$. In the lenses of quartzite which borders the upper and lower parts of the micaschist layer, the sample KE08-39 has a value of $-40 \pm 3\text{‰}$ and sample KE08-43 has a value of $-48 \pm 3\text{‰}$. In LQM, the samples show $\delta D FI_{Qz}$ of $-88 \pm 1\text{‰}$, $-75 \pm 3\text{‰}$, and $-73 \pm 3\text{‰}$ for KE08-45, KE08-47 and KE08-52, respectively (Appendix VI, Table V-3).

Few samples had a sufficient amount of fluid to be measured along the section; therefore results are not robust, but some contrast is seen between LQM and the rest of the

section. In LQM the three samples provide a $\delta D FI_{Qz}$ mean value of $-79 \pm 8\%$. In contrast, $\delta D FI_{Qz}$ in UQM varies by 70‰ between KE08-33 and KE08-35, and in the micaschist layer between UQM and LQM, the values are relatively constant at around $-44 \pm 4\%$. The hydrogen isotope composition of fluid inclusions shows significant shifts (several tens ‰) from one unit to the other. LQM is characterized by low $\delta D FI_{Qz}$ ($\approx -80\%$), while the micaschist layer shows deuterium-rich values ($\delta D FI_{Qz} \approx -45\%$). UQM shows one deuterium-rich sample ($\delta D FI_{Qz} \approx -40\%$) and one sample with very low $\delta D FI_{Qz}$ ($\approx -110\%$).

4.3. $\delta^{18}O$ values of quartz and muscovite:

Measurements of $^{18}O/^{16}O$ ratios for quartz ($\delta^{18}O_{Qz}$) and muscovite ($\delta^{18}O_{Ms}$) are presented in Figure VI-10. The $\delta^{18}O_{Qz}$ values show a wide range from 12.9 ‰ down to 4.0 ‰, while $\delta^{18}O_{Ms}$ values vary slightly between 9.7‰ and 5.6‰ (Appendix VI, Table V-3). Two groups of values with characteristic spatial distributions are distinguished and correspond to UQM and LQM units.

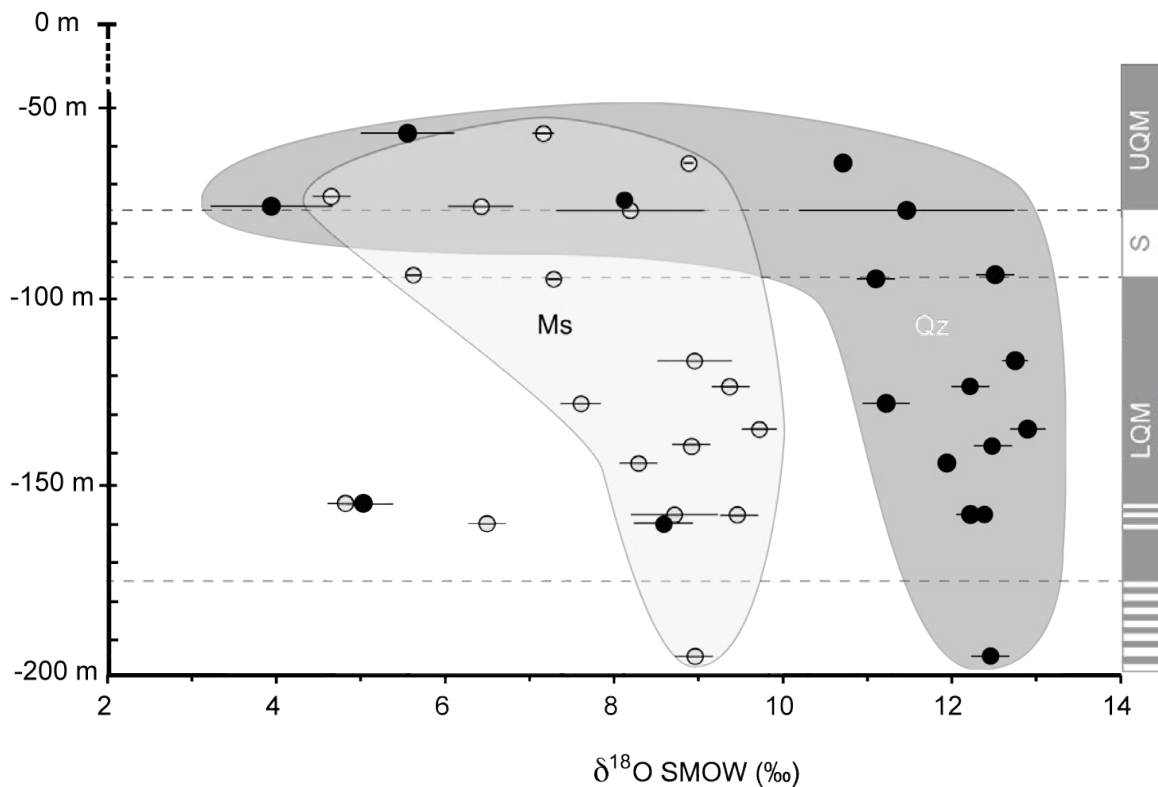


Figure VI-10: Oxygen isotope composition of quartz (dark grey) and muscovite (light grey) as a function of the distance below the detachment. $\delta^{18}O_{Qz}$ and $\delta^{18}O_{Ms}$ are relatively constant in the lower quartzite mylonite and highly variable in the upper quartzite mylonite. Simplified cross-section on left side : UQM – Upper Quartzite Mylonite ; S - micaschist layer ; LQM – Lower Quartzite Mylonite.

In UQM, $\delta^{18}\text{O}_{\text{Qz}}$ values range from $4.0\pm 0.7\text{‰}$ (KE08-37) to $10.7\pm 0.1\text{‰}$ with a mean value of $7.1\pm 3.0\text{‰}$ ($n=5$; KE08-32 to KE08-37, 012-03). $\delta^{18}\text{O}_{\text{Ms}}$ values range from $4.7\pm 0.05\text{‰}$ (012-03) to $8.9\pm 0.1\text{‰}$ (KE08-37) with a mean value of $6.8\pm 1.8\text{‰}$ ($n=4$). Two quartzite lenses from the micaschist layer have $\delta^{18}\text{O}_{\text{Qz}}$ values of $11.5\pm 1.5\text{‰}$ and $12.5\pm 0.0\text{‰}$, and $\delta^{18}\text{O}_{\text{Ms}}$ values of $8.2\pm 0.9\text{‰}$ and $5.6\pm 0.1\text{‰}$, respectively (KE08-39 and KE08-43).

In LQM, $\delta^{18}\text{O}_{\text{Qz}}$ values range from $11.1\pm 0.2\text{‰}$ (KE08-44) to $12.9\pm 0.2\text{‰}$ (KE08-47), with a mean value of $12.2\pm 0.6\text{‰}$ ($n=12$; KE08-44 to KE08-52, 000-03 to 011-03). $\delta^{18}\text{O}_{\text{Ms}}$ range from $7.3\pm 0.1\text{‰}$ (KE08-44) up to $9.7\pm 0.2\text{‰}$ (KE08-47), with a mean value of $\delta^{18}\text{O}_{\text{Ms}}$ throughout LQM of $8.7\pm 0.8\text{‰}$ ($n=12$). Two samples (009-03 and 004-03) show $\delta^{18}\text{O}_{\text{Qz}}$ and $\delta^{18}\text{O}_{\text{Ms}}$ values several ‰ lower than the average $\delta^{18}\text{O}_{\text{Qz}}$ and $\delta^{18}\text{O}_{\text{Ms}}$ values in LQM. Samples 009-03 and 004-03 (-154 and -160 m, respectively) are located in the 5-10 m thick part near the base of the LQM where the lithology is defined by a 1-10 cm alternation of micaschist and quartzite.

The UQM is characterized by a wide variation of quartz and muscovite oxygen isotope compositions. In contrast, $\delta^{18}\text{O}_{\text{Qz}}$ and $\delta^{18}\text{O}_{\text{Ms}}$ mean values of LQM are $12.2 \pm 0.6\text{‰}$ and $8.7 \pm 0.8\text{‰}$, respectively. The $\delta^{18}\text{O}_{\text{Qz}}$ mean value in UQM is 5‰ lower than the $\delta^{18}\text{O}_{\text{Qz}}$ mean value in LQM, and the $\delta^{18}\text{O}_{\text{Ms}}$ mean value in UQM is 2‰ lower than $\delta^{18}\text{O}_{\text{Ms}}$ mean value in LQM. Consequently, UQM and LQM preserve distinct spatial variations in $\delta^{18}\text{O}_{\text{Qz}}$ and $\delta^{18}\text{O}_{\text{Ms}}$.

4.4. Oxygen isotope thermometry:

If quartz and muscovite attained isotopic equilibrium during detachment activity, the difference in $\delta^{18}\text{O}$ values ($\Delta^{18}\text{O}_{\text{Qz-Ms}}$) permits the calculation of an isotope exchange equilibrium temperature. Several calibrations exist for temperature-dependent oxygen isotope exchange in the quartz-muscovite system (Bottinga and Javoy, 1975; Eslinger et al., 1979; Mattews et Schliestedt, 1984; Chacko et al., 1996). The calibration of Chacko et al. (1996) covers a temperature range from 123°C up to 1227°C and is based on the following equation:

$$\Delta^{18}\text{O}_{\text{Qz-Ms}} = 1.350x + 0.042x^2 - 0.0086x^3; \text{ with } x = 10^6\text{T}^{-2}$$

Equilibrium fractionation temperatures (Figure VI-11) range from 333°C to 393°C for LQM, with a mean value of $365^{\circ}\text{C} \pm 30^{\circ}\text{C}$. Calculated temperatures in UQM attain a mean of $390 \pm 200^{\circ}\text{C}$; the large variation being a direct consequence of the wide range in oxygen isotope compositions of quartz and muscovite in this unit. Samples KE08-032 and KE08-037

from UQM even show $\delta^{18}\text{O}_{\text{Qz}}$ values lower than those of $\delta^{18}\text{O}_{\text{Ms}}$, implying a negative $\Delta^{18}\text{O}_{\text{Qz-Ms}}$. Consequently, UQM temperature calculations are not considered reliable owing to the lack of oxygen isotope equilibrium of the mineral pair.

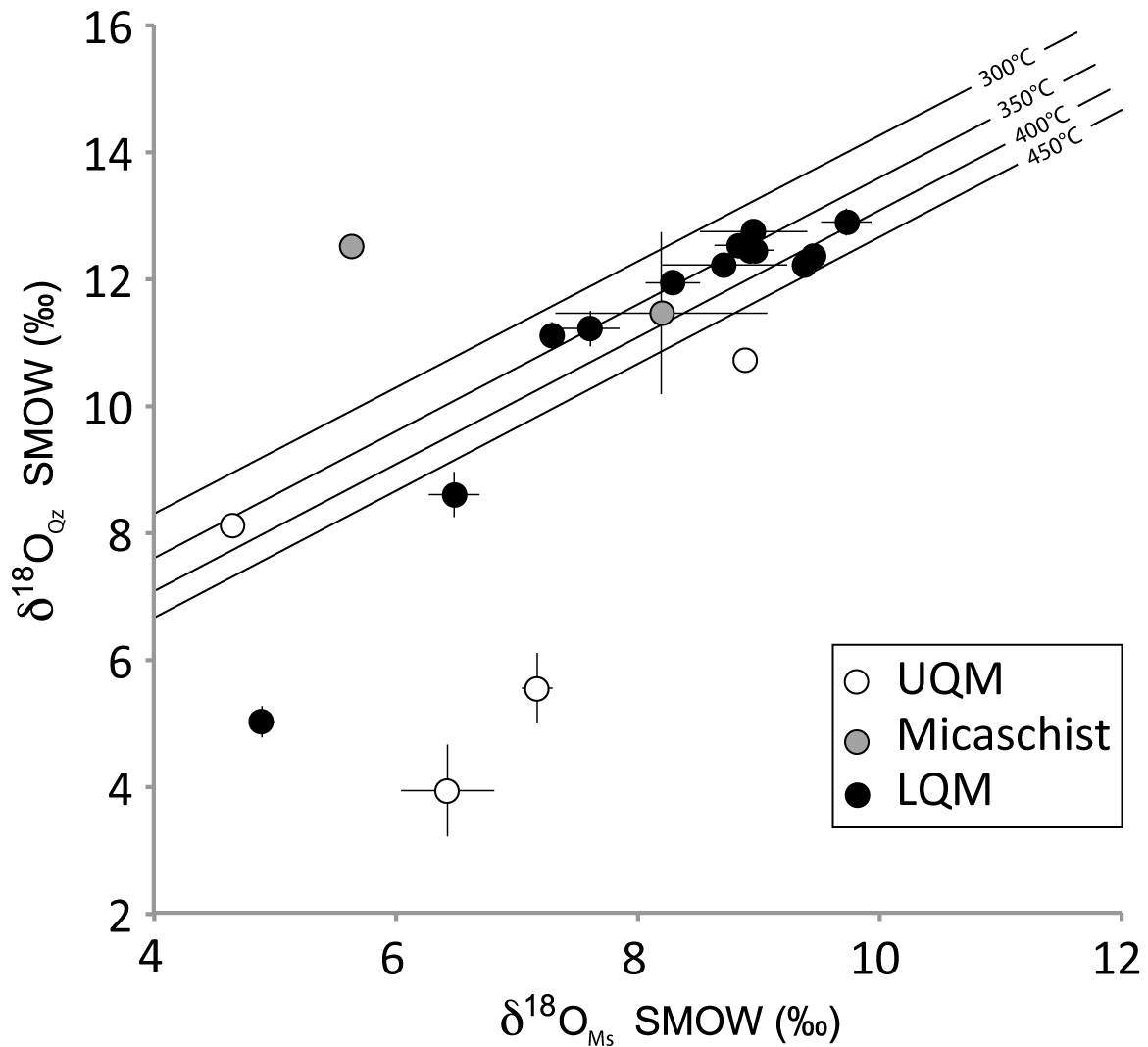


Figure VI-11: Calculated Qz-Ms oxygen isotope equilibrium temperature versus the distance below the detachment. The temperatures reflect relatively constant oxygen isotope fractionations between Qtz and Ms for the LQM, $355 \pm 20^\circ\text{C}$; but large changes in fractionation for the UQM, $390 \pm 200^\circ\text{C}$. For two samples (white stars in black circles) temperatures cannot be calculated as the $\delta^{18}\text{O}_{\text{Qz}}$ is lower than the $\delta^{18}\text{O}_{\text{Ms}}$. Simplified cross-section on left side: UQM – Upper Quartzite Mylonite; S - micaschist layer; LQM – Lower Quartzite Mylonite.

5. Discussion

One important characteristic of the Kettle DSZ is that meteoric fluids permeated the uppermost levels of ductile crust beneath the brittle detachment and participated in the growth of synkinematic mica fish in quartzite mylonite. The different ways in which UQM and LQM units recorded deformation, metamorphism, and fluid-rock interaction in the presence of meteoric water provide insight into the dynamics of this detachment system. Microstructural evidence shows that LQM experienced dislocation creep dominated by quartz grain boundary migration recrystallization; in this unit, muscovite is compositionally homogeneous and both, $\delta^{18}\text{O}_{\text{ms}}$ and $\delta^{18}\text{O}_{\text{Qz}}$ are relatively constant, suggesting oxygen isotope exchange at $T = 365 \pm 30^\circ\text{C}$. In contrast, UQM is characterized by more complex microstructures involving solution-precipitation, subgrain-rotation recrystallization, and the formation of discrete C' shear bands. In UQM synkinematic mica fish are compositionally zoned, which indicates a change in the chemical environment and/or conditions during mineral growth. Oxygen isotope compositions of quartz and muscovite in UQM did not attain isotopic equilibrium, and in some cases quartz $\delta^{18}\text{O}_{\text{Qz}}$ values are shifted to values lower than those of muscovite. Here we suggest that UQM and LQM preserve different stages of the evolution of the Kettle DSZ and therefore record a history of deformation and fluid-rock interaction during cooling and exhumation of the detachment system.

5.1. Fluid source and evolution of fluid flow

The nature of the fluid assisting the recrystallization process can be characterized on the basis of the hydrogen isotopic composition of muscovite and FI analyses in UQM and LQM: $\delta\text{D}_{\text{Ms}}$ values are remarkably low and constant ($\delta\text{D}_{\text{Ms}} = -130 \pm 5 \text{‰}$) over the entire detachment shear zone and indicate that muscovite from both UQM and LQM exchanged isotopically with meteoric water (Sheppard, 1986; Criss, 1991). All muscovite grains in the studied section have been deformed into mica fish, which implies that the muscovite grains likely grew synkinematically during ductile shearing. It is unlikely that grain-scale (hydrogen) isotope exchange occurred subsequent to crystallization and deformation in the shear zone, given the undisturbed $^{40}\text{Ar}/^{39}\text{Ar}$ systematics of analyzed muscovite. Thus, the Kettle DSZ footwall quartzite deformed ductilely in the presence of evolved meteoric fluids under greenschist-facies conditions. Synkinematic muscovite from the entire section was buffered isotopically by the hydrogen composition of meteoric fluids, and therefore significant amount of surface fluids infiltrated the detachment during ductile shearing ($t=2$, Figure VI-12).

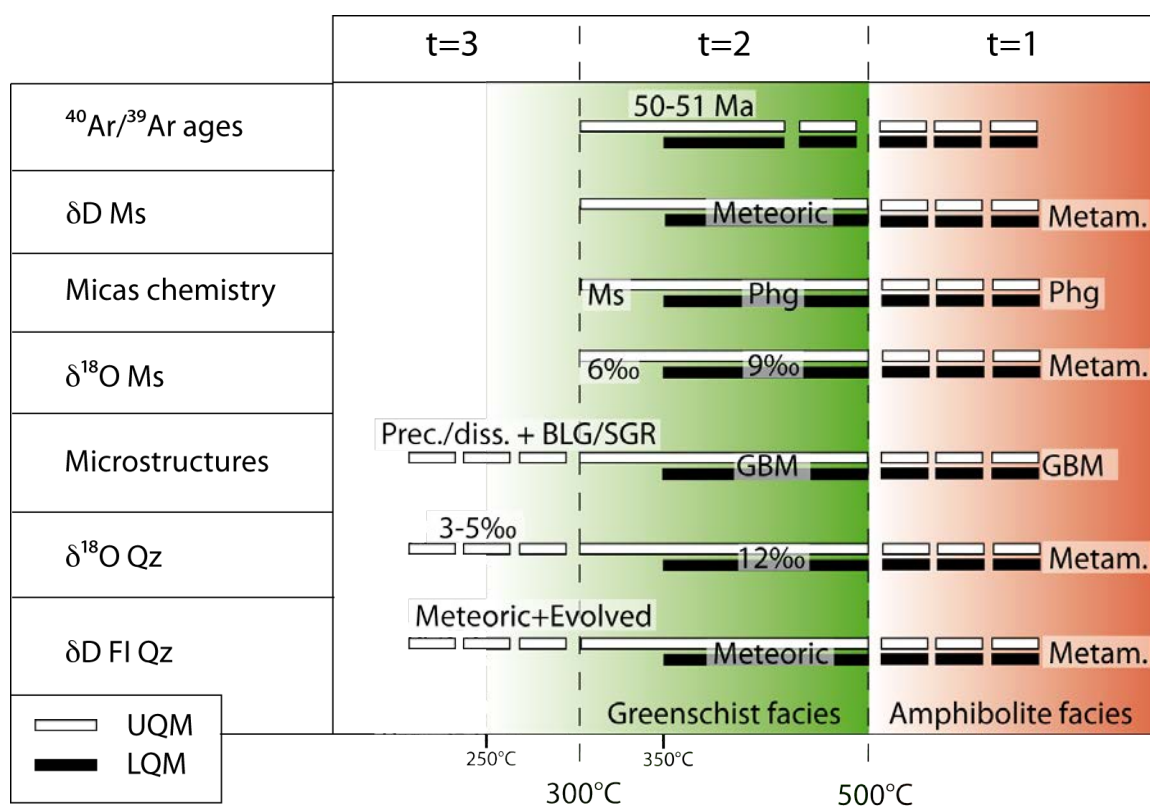


Figure VI-12: Summarize for both UQM and LQM of results for each type of analyses according to a time, temperature axis.

In the absence of in-situ isotopic analyses, it is not possible to further evaluate whether the chemical zoning of muscovite is accompanied by a variation in $\delta\text{D}_{\text{Ms}}$ on the grain scale. However, given the uniform $\delta\text{D}_{\text{Ms}}$ values over the entire section, which includes both zoned and unzoned muscovite, meteoric fluids likely penetrated the Kettle DSZ during the duration of muscovite growth, independent of the chemical environment in which muscovite grew.

The limited dataset of δD values from quartz fluid inclusions precludes solid interpretations but nevertheless highlights wide variations of δD in UQM, while LQM δD values are nearly constant. In UQM, variability in δD values span 70‰, with one value clearly indicative of meteoric (-110‰), and the other as metamorphic / hydrothermal (-40‰) fluids, implying that this unit either interacted with fluids derived from two separate sources (meteoric and metamorphic), or represents a meteoric fluid (-110‰), and a time-integrated, rock-buffered meteoric fluid (-40‰). The uniform $\delta\text{D}_{\text{Ms}}$ values in UQM does suggest that a single fluid source (meteoric) participated in the growth of muscovite at time interval t=2 (Figure VI-12). Based on these observations, the simplest scenario is that incoming fluids were of meteoric origin throughout the history of the detachment and exchanged isotopically with rock to various degrees during protracted hydrothermal circulation.

In LQM, the $\delta D FI_{Qz}$ values are nearly constant ($\sim -80\text{‰}$), which implies that this unit records a single source of fluid in fluid inclusions. The difference between δD_{Ms} (-130‰) and $\delta D FI_{Qz}$ (-80‰) is approximately 50‰ . The theoretical hydrogen isotopic fractionation equation of Suzuoki and Epstein (1976) for a fluid in equilibrium with muscovite is $\sim 30\text{‰}$ at 350°C and $\sim 50\text{‰}$ at 300°C . Therefore, the $\delta D FI_{Qz}$ values measured in LQM are representative of the fluid that assisted muscovite recrystallization at relatively low deformation temperatures. Fluid inclusions in LQM are not located in fracture planes but are concentrated at the vicinity of quartz grain boundaries that migrated during dynamic recrystallization, suggesting that the fluid was likely circulating along migrating grain boundaries. The consistency of hydrogen isotopic compositions from both muscovite and fluid inclusions in quartz indicates that quartz, muscovite, and fluid reached isotopic equilibrium during deformation of LQM. As a result, the quartz-muscovite oxygen isotope thermometer is reliable and accurately reflects the temperature of recrystallization ($T = 365 \pm 30^\circ\text{C}$).

In UQM, some fluid inclusions represent “fresh meteoric fluid” and others are from a fluid that continued to interact with quartzite by circulation within UQM at elevated temperature ($t=3$, Figure VI-12) or with fluids that are of metamorphic origin. Given that the aqueous fluid phase contains a higher proportion of H compared to a typical quartzite mylonite, even at relatively low fluid/rock ratios, the δD composition of the fluid may not change dramatically during dynamic recrystallization. Assuming that the $\delta D FI_{Qz}$ corresponds to the δD value characterizing meteoric fluid composition prior to fluid-rock interaction, then the $\delta^{18}\text{O}$ values of the meteoric fluid were -6‰ for a $\delta D FI_{Qz} = -40\text{‰}$, and -15‰ for a $\delta D FI_{Qz} = -110\text{‰}$ if the meteoric waters plotted along the Global MWL (Craig, 1961). The theoretical isotopic fractionation between quartz and H_2O (Clayton, 1972; Zhang et al., 1989; Zheng, 1993) at 200°C and 300°C yields values of 12‰ and 7‰ , respectively. Based on the calculated $\delta^{18}\text{O}$ meteoric composition prior to dynamic recrystallization, each of these fluid compositions can potentially shift the oxygen isotope composition of quartz by 10‰ and shift the muscovite oxygen isotope composition by 2‰ until muscovite reached its isotopic closure temperature.

The homogenization of $\delta^{18}\text{O}$ values is enhanced by isotopic exchange during dynamic recrystallization by grain boundary migration in quartzite mylonite (Kirschner and Teyssier, 1997). Nakamura et al. (2005) also showed that grain boundary migration is the primary control for oxygen isotope diffusion under hydrothermal conditions. In addition, the presence

of fluids at grain boundaries has been suggested to improve grain boundary mobility (e.g., Mancktelow, 2004). Consequently, pervasive fluid flow associated with grain boundary migration may enhance and accelerate the exchange of oxygen isotopes in quartz and muscovite, leading to isotopic equilibrium within LQM. In contrast, large shifts in $\delta^{18}\text{O}_{\text{Qz}}$ within UQM and heterogeneous microstructures reflecting dynamic recrystallization by bulging, subgrain-rotation recrystallization, and solution-precipitation suggest that fluid flow was channelized in the UQM, where meteoric fluid buffered the fluid-rock isotopic system within meter-thick preferential pathways.

5.2. Chemical and isotopic evolution of quartz and muscovite during exhumation

The heterogeneity in Mg-Si-Al content in muscovite increases upward, toward the detachment, and the Tschermak substitution decreases closer to the brittle-ductile transition. This differential Tschermak substitution is largely described in the literature as pressure-dependent (Auzanneau, 2010; Bucher-Nurminen, 1987; Massonne and Schreyer, 1987; Konopasek, 1998; Zanazzi and Pavese, 2002). The decreasing pressure associated to the exhumation of the metamorphic core complex is in good agreement with the Tschermak substitution (phengitic core, muscovitic rims) occurring in micas. Another reason could be that the muscovitic composition of rims from zoned muscovite as well as unzoned muscovite are related to the sericitization reaction of K-feldspar in the presence of a fluid phase. The sericitization reaction of K-feldspar is governed by a dissolution-precipitation mechanism and may be facilitated by infiltrating fluids. Thus, the evolution from phengitic composition toward muscovitic composition could be due to a near isothermal pressure decrease or to feldspar hydration.

The Kettle DSZ section shows two populations of synkinematic muscovite. Zoned muscovite in UQM has core compositions similar to unzoned muscovite from LQM, and rims are Al-rich and depleted in Mg-Si relative to cores. These rims have the same major element composition as that of unzoned muscovite in UQM. We propose that the Mg-Si rich muscovite population (LQM + cores of zoned UQM muscovite) represents an early stage of syn-kinematic muscovite crystallization. At some point the deformation and recrystallization front left LQM, and UQM continued to deform under a changed chemical and thermomechanical environment. This evolution is consistent with a progressive localization of deformation upward, toward the brittle detachment fault.

The relative consistency of $\delta^{18}\text{O}$ values in LQM suggests that the quartz-muscovite pairs approached oxygen isotope equilibrium while LQM experienced GBM dislocation creep (t=2, Figure VI-12). The pattern of $\delta^{18}\text{O}$ values through the whole section supports the interpretation that UQM may have started at fairly consistent $\delta^{18}\text{O}$ values seen in LQM. Oxygen isotope fractionation is temperature dependent, with the fluid-mineral fractionation increasing with decreasing temperature. Muscovite from both UQM and LQM with phengitic to muscovitic compositions recrystallized at temperatures higher than 350°C, according to LQM stable isotope thermometry. In UQM the unzoned muscovite grains and the muscovitic rims zoned grains represent a later stage of muscovite growth. The $\delta^{18}\text{O}$ values of quartz and muscovite in UQM are similar to two samples near the base of LQM (004-03 and 009-03) and are several permil lower than in LQM, suggesting continued isotopic exchange with low-dD fluid in UQM while the late-stage muscovite were (re-)crystallizing. This exchange likely occurred during cooling at $T < 365 \pm 30^\circ\text{C}$ (t=2, Figure VI-12).

$\delta^{18}\text{O}_{\text{Qz}}$ in UQM was shifted to values as low as 3.9‰ toward a more or less complete exchange with a fluid that was depleted in ^{18}O (Figure VI-10). The resultant oxygen isotope quartz-muscovite disequilibrium started when dynamic recrystallization in UQM changed from grain boundary migration to bulging and subgrain-rotation recrystallization. The wide variations of both quartz and muscovite $\delta^{18}\text{O}$ values in UQM (e.g. 009-03 and 004-03) are indicative of isotopic disequilibrium. Indeed, KE08-032 and KE08-037 also have low $\delta^{18}\text{O}$ values of 5.6‰ and 3.9‰, respectively. These two samples also have higher values of $\delta^{18}\text{O}$ for muscovite compared to quartz (Appendix VI, Table V-3), which is inconsistent with equilibrium fractionation.

The variations in $\delta^{18}\text{O}_{\text{Qz}}$ values of the UQM may be explained by the presence of quartz grains that were unaffected or only partially affected by dynamic recrystallization and that retained their original $\delta^{18}\text{O}_{\text{Qz}}$ compositions (Giletti, 1985; Zheng et al., 1998; Nakamura et al., 2005). None of the samples analyzed display a typical low-temperature oxygen isotope composition of authigenic quartz (15-25‰) (Williams et al., 1997; Girard et al., 2001).

In contrast, the low $\delta^{18}\text{O}_{\text{Qz}}$ values of KE08-032 and KE08-037 indicate a much higher fluid-rock interaction with meteoric water that is depleted in the heavy oxygen isotope (-10 to -20‰). If muscovite had already cooled below its closure temperature to oxygen isotopic exchange (<300°C), lattice diffusion of oxygen is ineffective in quartz grains (Kerrick et al., 1976; Farvera and Yunda, 1991). Then, quartz grains may have continued to exchange oxygen with a heavy oxygen depleted fluid during a dissolution-precipitation process that

accompanies retrogression at temperatures below 300°C, while muscovite has already reached its closure temperature for oxygen isotope exchange ($t=3$, Figure VI-12). This microstructural overprint coeval with localized meteoric fluid flow likely shifted the UQM and the base of the LQM towards isotopic disequilibrium.

5.3. Argon ages and oxygen isotope thermometry

The consistency of $^{40}\text{Ar}/^{39}\text{Ar}$ ages (51-50 Ma, Figure VI-8) indicates that the closure of muscovite to argon diffusion occurred nearly contemporaneous over the entire section. In detachment systems deformation contributes to exhumation and cooling owing to the rapid juxtaposition of hot footwall with cool hanging wall (e.g., Gottardi et al., 2011). Therefore, $^{40}\text{Ar}/^{39}\text{Ar}$ cooling ages potentially close to deformation/recrystallization ages (Mulch et al., 2006, 2007). The LQM unit shows a single unzoned population of muscovite with relatively constant $\delta^{18}\text{O}$ values of quartz and muscovite, which suggests isotopic equilibrium for this mineral pair at $T \sim 365 \pm 30^\circ\text{C}$. This temperature is significantly below the closure-temperature range for commonly accepted argon diffusion in muscovite ($\geq 400^\circ\text{C}$, Harrison et al., 2009). This is particularly true for the coarse grain sizes analyzed in this study (250-600 μm) and for the rapid cooling detachment system of the Kettle DSZ. Therefore, we interpret the argon ages in LQM as deformation and recrystallization ages.

The Mg-Si rich muscovite population in LQM and the Mg-Si rich cores of mica fish in UQM represent an early stage of synkinematic muscovite crystallization, suggesting that muscovites in UQM share a part of their chemical and thermal stability with muscovites from LQM. In UQM however, the chemically distinct muscovite that makes up population 2 and also occupies the rims around mica fish clearly represents a later stage of muscovite growth. Yet, no difference is detected in the argon spectra from LQM and UQM muscovite populations. Future work should concentrate on single-grain analyses in order to identify a potential age difference between the two populations of muscovite. However, based on the results presented here, we can only conclude that the cessation of muscovite deformation/crystallization was quasi-simultaneous over the studied section, even though the microstructural, oxygen isotopic, and chemical patterns do indicate a likely migration of deformation upward with the localization of latest deformation (ductile-to-brittle) in the UQM unit. The ages of 51-50 Ma recorded in the Kettle DSZ mylonite units likely mark the rapid cessation of deformation-recrystallization in this detachment system.

These results can be compared to $^{40}\text{Ar}/^{39}\text{Ar}$ dating of recrystallized muscovite at the latitude of the Thor-Odin dome ~250 km further north in British Columbia (Vanderhaeghe et al., 2003; Mulch et al., 2004). Argon release spectra and single-grain laser analyses indicate that the ~200 m thick mylonite zone in the footwall of the Columbia River detachment was active from 49 to 48 Ma. Mulch et al. (2007) also obtained an $^{40}\text{Ar}/^{39}\text{Ar}$ age of 49.1 ± 0.3 Ma on muscovite from a quartzite mylonite sampled on Kamloops Island, which is located 40 km to the N-NE of our sampled Kettle DSZ section. Together with the present results (51-50 Ma), this age distribution implies that the Columbia River detachment propagated from the Okanagan-Kettle dome (WA, USA) towards the Thor-Odin dome (BC, CA) to the north over 2-3 Ma, between 51-50 Ma and 49-48 Ma.

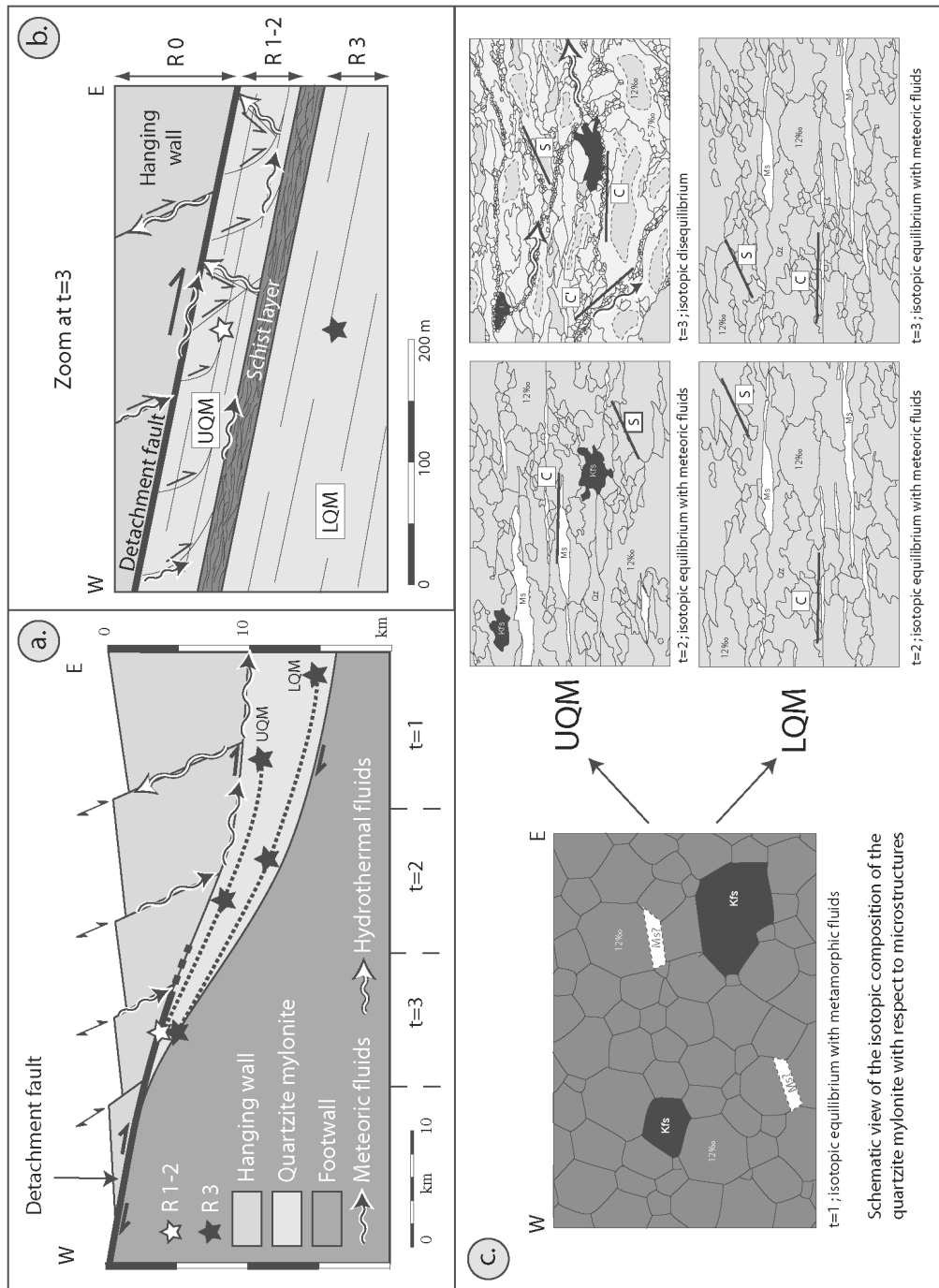


Figure VI-13: (a) Schematic cross-section of the Kettle DSZ, showing the pathways of both UQM and LQM in space and time : t=1 corresponds to amphibolite facies, t=2 corresponds to early greenschist facies, t=3 corresponds to late greenschist facies. (b) Zoom at t=3 onto the Hall Creek section. (c) Evolution of the microstructure and isotopic composition of the UQM and LQM during exhumation.

5.4. Exhumation of UQM and LQM along the Kettle DSZ in space and time.

The textural, microchemical, and isotopic relations in the Kettle DSZ yield insight into the mode of exhumation of UQM and LQM. In our model, the microstructural and chemical/isotopic signatures in LQM and UQM were acquired at different times during the evolution of the Kettle DSZ, until the units were juxtaposed in the late stage of detachment activity (Figure VI-13a & b). This interpretation allows UQM and LQM to experience different dislocation creep regimes (Figure VI-13c): At $t=1$, both UQM and LQM experience grain boundary migration recrystallization under amphibolite-facies conditions. During dynamic recrystallization, all minerals present in UQM and LQM are assumed to be in isotopic equilibrium with a hypothetically coexisting metamorphic fluid. At $t=2$, both UQM and LQM begin to deform under greenschist-facies conditions. Quartz grains recrystallize under higher flow stress conditions (higher strain rate?) and muscovite fish are developed (LQM preserved microstructure). During this stage ($t=2$) the Kettle DSZ was infiltrated by meteoric fluid, as indicated by low- δD muscovite values in both LQM and UQM. Flow of this meteoric fluid was pervasive (grain scale) and sufficiently vigorous to attain oxygen isotope equilibrium of recrystallizing quartz and muscovite at $T = 365^{\circ}\text{C} \pm 30^{\circ}\text{C}$.

By $t=3$, UQM and LQM were structurally juxtaposed. Meteoric fluid inflow was channelized along S-C-C' fabrics and induced local (dm to m) isotopic shifts in recrystallized quartz throughout UQM and even near the base of LQM (Figure VI-13c). The 1-10 cm quartzite-micaschist alternations defining UQM and the 5-10 m thick section near the base of LQM correspond to units with oxygen isotope disequilibrium. Then, at $t=3$, layers such as mica schist may have localized strain and fluid flow. This local disequilibrium precludes the application of the quartz-muscovite oxygen isotope thermometry.

6. Conclusion:

This study demonstrates the temporal and spatial relationships between dynamic recrystallization and fluid-rock interaction in mylonitic footwall quartzite of the Eocene Kettle detachment shear zone. The quartzite mylonite can be divided into an upper (UQM) and lower (LQM) unit that initially deformed by similar dynamic recrystallization processes involving grain boundary migration recrystallization under greenschist-facies conditions. Meteoric fluids permeated the quartzite mylonite and imparted a uniformly low δD in muscovite; fluid flow occurred on the grain (boundary) scale throughout the mylonitic quartzite section at temperatures of $365^{\circ}\text{C} \pm 30^{\circ}\text{C}$. During the late(r) stages of exhumation

UQM underwent a distinct evolution, providing insight into the nature and rate of processes in detachments. LQM “fossilized” the early microstructure and fluid-rock interaction, while strain migrated into UQM, which experienced infiltration of late fluids localized along discrete pathways. The quartz microstructure in UQM evolved towards a recrystallization regime involving bulging and subgrain rotation, and fluid flow concentrated in meter-scale layers where quartz was extremely depleted in ^{18}O and D. The quartzite-micaschist alternation corresponds to units showing isotopic disequilibrium and may be paramount in controlling the localization of fluid flow while the detachment evolved towards brittle deformation. The muscovite $^{40}\text{Ar}/^{39}\text{Ar}$ ages are the ages of deformation and recrystallization and are uniform throughout the quartzite section (51-50 Ma). This result indicates that mylonite development, hydration of the detachment shear zone, migration of deformation within the mylonitic quartzite, and cooling and exhumation of the mylonitic rocks occurred rapidly (~1 myr). We conclude that the deformation and hydration processes in detachment shear zones are likely coupled, leading to mechanical instabilities and strain localization that collectively promote rapid exhumation of footwall rocks.

Chapter VII : General conclusions:

This thesis brings evidence that the fluid-rock-strain feedbacks in extensional shear-zones follow complex patterns and are influenced by several parameters such as the spatial and temporal evolution, temperature, source and volume of fluid, isotropic/anisotropic initial configuration, bimineralic/polymineralic system, and strain intensity experienced by rocks. However, comparing the Kettle shear zone and the Bitterroot shear zone brings out some similarities.

The exhumation of metamorphic core complexes along shear zones occurs in a short period of time. Most detachments from the North American Cordillera support a rapid cooling history that reflects a rapid exhumation history during which high-grade metamorphic rocks or magma bodies are advected toward the surface and then cool rapidly. The Bear Creek pluton intruded at 55-54 Ma (Foster et al., 1997), and experienced rapid exhumation after 50 Ma (Foster et al., 2001, 2007). Based on zircon fission-track ages, the Bitterroot complex was at a temperature of < 200-250°C by 40-38Ma. The cooling history of the Kettle shear zone remains to be deciphered, but according to the muscovite $^{40}\text{Ar}/^{39}\text{Ar}$ data presented in Chapter VI, the Kettle shear zone experienced mylonitic deformation during a short period of time, from 51 to 50 Ma.

The single grain chemical analyses conducted on phyllosilicates from the Bitterroot shear zone have highlighted that the biotite in both protolith and mylonites have preserved the magmatic peak temperature experienced by the protolith ($670\pm 30^\circ\text{C}$), which is in good agreement with peak metamorphism condition ($650-750^\circ\text{C}$, 6-8 kbar) defined for the Bitterroot complex in the literature (House et al., 1997; Foster et al., 2001). Magmatic/metamorphic fluids are the fluid sources that interacted with the rocks, as long as the system remains closed (protolith and protomylonite, Figure VII-1).

The bulk-rock elemental analysis in the BSZ demonstrated that in a ductile shear zone affecting a relatively isotropic rock and associated pervasive fluid flow, the heterogeneous volume variation of mylonite suggests that the pluton was not as isotropic as we assumed. However, the constant volume loss of ultramylonite throughout the BSZ implies interaction with an unsaturated fluid and consequently downward fluid flow and mass transfer parallel to the foliation. The final balance is most likely isovolumetric at the shear zone scale. The volume changes occurring in the mylonite and ultramylonite are related to (1) local

heterogeneities in the pluton (mylonite), (2) fluid-assisted breakdown of feldspar in muscovite (\pm quartz), and (3) the saturation of silica (\pm K, Ca, Na) in the fluid.

According to Qz-Ms oxygen isotope thermometry, the Bitterroot shear zone initiated at a temperature close to 500°C, and rocks within the shear zone were ductilely deformed down to 300°C. Biotite in the ultramylonite could be partially reequilibrated, providing an over-estimated Ti-in-Bt temperature (580 \pm 60°C). As soon as the ductile shear zone develops a mylonitic texture, the S-C fabric and dynamically recrystallized quartz ribbons increase significantly the pore connectivity and act as fluid pathways, allowing surface-derived fluids to infiltrate the ductilely deforming rocks. Hydration of feldspar and strain partitioning distributed in quartz ribbons lead to dynamic recrystallization and grain size reduction, which enhances the sheared rock ability for ductile flow. Fluid-assisted reaction softening implies strain localization and a positive feedback loop, leading to the development of the mylonitic shear zone and ultimately ultramylonite bands. Chloritization of biotite occurs synchronously to the mylonitic deformation in the Bitterroot shear zone, and in the presence of surface-derived fluids as indicated by the low oxygen and hydrogen isotope values of chlorite in mylonites. The production of hydrous minerals, such as chlorite, in the ductilely deformed rock implies the storage of surface-derived fluids in the rock, fluids can be remobilized as long as hydrous minerals keep recrystallizing. The temperatures of biotite chloritization associated with greenschist-facies retrograde reactions in the Bitterroot shear zone indicate a trend of decreasing temperatures from 485°C down to 270 \pm 20°C toward the hanging wall. Such temperatures are in good agreement with the temperature calculated from Qz-Ms oxygen isotope thermometry and imply that surface-derived fluids infiltrates the ductilely deformed shear zone at low to moderate temperatures (\sim 200-500°C).

Microstructures, major element chemistry, and oxygen isotope compositions of muscovite are constant through the 400 m of mylonite in the BSZ. In the Kettle shear zone, the core of the muscovite from the upper quartzite mylonite, and the unzoned muscovite from the lower quartzite mylonite have the same major element compositions. This observation indicates that the shear zone is chemically uniform, in terms of micas, and the recurring low-dD of mica means that both the Bitterroot and the Kettle shear zones were pervasively infiltrated by surface-derived fluids. These results would indicate that at a certain point of the detachment activity, the two shear zones were broader. Yet, the overprinting fabrics in both Bitterroot and Kettle shear zones make it impossible to determine if the shear zones started broader or more localized. Strain localization in the upper part of the shear zone is evidenced

by the 1-10 cm mylonite and ultramylonite alternation in the Lost Horse Canyon, and by the microstructural evolution and increased isotopic disequilibrium in the Kettle shear zone (Figure VII-1). However, the Lost Horse Canyon also displays some mylonite and ultramylonite in the protomylonite part of the shear zone, and the Kettle shear zone shows isotopic disequilibrium in a narrow quartzite-mica schist layer at the base of the lower quartzite mylonite. Consequently, strain localization does not appear unidirectional. Most likely, strain localization is partitioned at the shear zone scale. Meanwhile, in both detachments systems, the strain localization is better expressed in the upper part of the shear zone.

At $T < 300^{\circ}\text{C}$ (Figure VII-1), exhumation was mostly accommodated by brittle frictional deformation along the detachment fault until the rocks reached the near-surface. Several brittle features affected the mylonite once they underwent brittle deformation. The Sweathouse section shows evidence of significant fracturing associated with a tectonic regime that was dominated by plane-strain extension. Such brittle features contain hydrous minerals with characteristic surface fluid isotopic values.

Contrary to previous models proposed in the literature, the results from this thesis lead to a new model where surface fluids infiltrate the shear zone along the detachment fault. Meteoric fluids flow along the fracture and high-angle normal fault and are assumed to feed the extensional shear zone. Fluids flow downward along the detachment fault, toward the ductile part of the broad shear zone, where mylonitic deformation takes place.

Indeed, the bulk-rock analyses associated with the mineralogical assemblage variations with respect to the different fabrics indicate that surface fluids dissolved quartz from the core of high-angle normal faults and cataclasite zones during downward fluid migration. High-angle faults and cataclasite zones acts as the plumbing system for fluid flow and provide a connected system which allows surface fluids to flow downward along the brittle part of the shear zone toward the brittle-ductile transition (Figure VII-1.1).

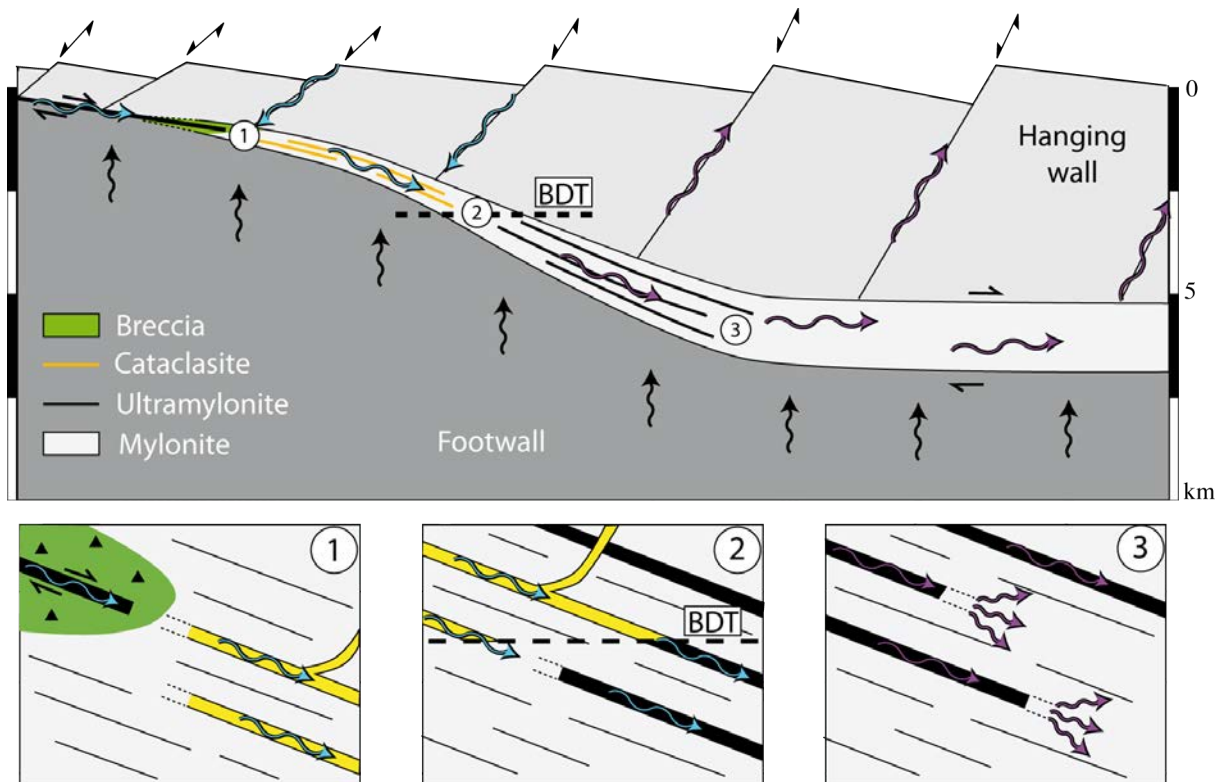


Figure VII-1: Schematic model of fluid flow through an extensional shear zone. 1. Surface fluids flow through the detachment fault and connect with cataclasites. 2. Cataclasites connect to the ultramylonite at the brittle-ductile transition, and surface-derived fluids keep flowing through ultramylonites. 3. At a depth where deformation is distributed, the surface-derived fluids flowing through the ultramylonite are released in the mylonite and flow pervasively in the broad ductile shear zone.

At the brittle-ductile transition, surface fluids keep flowing downward in a channelized way through the ultramylonite (Figure VII-1.2), as evidenced by the volume loss measured from ultramylonite zones. Such fluids are no longer considered as surface fluids and are now surface-derived fluids, since their chemical and isotopic compositions evolve while interacting with the ductilely deformed rocks. As proposed by Simpson (1977), seismic and chemical pumping can drag surface-derived fluids downward, against the thermal and fluid buoyancy gradients associated with the shear zone.

At a depth where deformation is distributed through the broad extensional shear zone (mylonitic deformation), the fluids flowing downward through ultramylonite are released in the mylonitic shear zone and flow pervasively (Figure VII-1.3). As long as the rock experiences ductile deformation, fluid flow is pervasive at the shear zone scale, and channelized along grain boundaries at the grain scale. The volume of fluid penetrating the

mylonite during deformation is sufficiently large to buffer the hydrogen isotope composition of phyllosilicate in the entire shear zone, while the rock buffers the oxygen isotope composition of the meteoric fluid. When the shear zone is anisotropic (Kettle shear zone), fluid flow can be perturbed by impermeable layers (for example schist layers), which implies that fluid flows laterally and/or along shear bands at the brittle-ductile transition.

The surface-derived fluids that are not consumed by mica growth in mylonite can potentially migrate upward through the mylonitic shear zone, toward the surface along high-angle normal faults connected to the extensional shear zone. Besides removing heat from the detachment shear zone, such upward fluid migration may lead to ore mineralization near the hanging wall and/or the supra-detachment basin related to the extensional system (Figure VII-1).

To conclude, self-exhuming extensional shear zones evolve rapidly through the transition from ductile to brittle, while surface-derived fluids flow downward, toward the mylonitic shear zone at a faster rate than rocks are exhumed. The positive feedback loops between development of a mylonitic fabric and infiltration of surface-derived fluid in the ductilely deformed rocks of the shear zone have been demonstrated in this thesis; these feedback loops tend to enhance the exhumation process. Extensional shear zones are zones in the crust where strain and fluid flow are coupled; these systems evolve rapidly toward strain localization and therefore efficient exhumation.

References:

- Abers, G.A., Ferris, A., Craig, M., Davies, H., Lerner-Lam, A.L., Mutter, J.C. and Taylor, B., 2002. Mantle compensation of active metamorphic core complexes at Woodlark rift in Papua New Guinea. *Nature*, 418, 862-865.
- Allmendinger, R.W., Miller, D.M., and Jordan, T.E., 1984. Known and inferred Mesozoic deformation in the hinterland of the Sevier belt, northwest Utah. in Kerns, G. J., and Kerns, R.L., eds., *Geology of northwest Utah, southern Idaho and northeast Nevada*: Utah Geological Association, 21 p.
- Allmendinger, R.W., 1992. Chapter 13: Thrust and fold tectonics of the western United States exclusive of the accreted terranes. in Burchfiel, B. C., Lipman, P., and Zoback, M. L., eds., *The Cordilleran orogen; Conterminous U. S.*: Boulder, Colorado, Geological Society of America, 583 p.
- Ambrosio, M., Doveri, M., Fagioli, M. T., Marini, L., Principe, C. and Raco, B, 2010. Water-rock interaction in the magmatic-hydrothermal system of Nisyros Island (Greece). *Journal of Volcanology and Geothermal Research*, 192, 1-2, 57-68.
- Anderson, T.H., Silver, L.T. and Salas, G. A., 1980. Distribution and U-Pb isotope ages of some lineated plutons, northwestern Mexico. in *Cordilleran Metamorphic Core Complexes*, edited by M.D. Crittenden, Sr., Coney, P.J. and Davis, G.H., Geological Society of America Memoirs, 153, 269-283.
- Angelier, J., 1984. Tectonic analysis of fault-slip data. *Journal of Geophysical Research*, 89, 5835-5848.
- Armstrong, R.L., 1968. Sevier Orogenic Belt in Nevada and Utah. *Geological Society of America Bulletin*, 79, 4, 429-458.
- Armstrong, R.L. 1982. Cordilleran metamorphic core complexes - From Arizona to southern Canada. *Annual Review of Earth and Planetary Science*, 10, 129-154.
- Armstrong, R. L. and Ward, P., 1991a. Evolving geographic patterns of Cenozoic magmatism in North American Cordillera: The temporal and spatial association of magmatism and metamorphic core complexes. *Journal of Geophysical Research*, 96, 13201-13224.
- Armstrong, R.L., Parrish, R. R., Van Der Heyden, P., Scott, K., Runkle, D. and Brown, R.L., 1991b. Early Proterozoic basement exposures in the southern Canadian Cordillera: core

- gneiss of Frenchman Cap, Unit of Grand Forks Gneiss and the Vasseaux Formation. *Canadian Journal of Earth Sciences*, 28, 1169-1201.
- Auzanneau, E. and M. Schmidt, 2010. Titanium in phengite: a geobarometer for high temperature eclogites. *Contributions to Mineralogy and Petrology*, 159, 1, 1-24.
- Bailey, S.W, 1989. *Hydrous Phyllosilicates (exclusive of micas)*. Mineralogical Society of America, 19, 1318p.
- Baldwin, S.L., Lister, G.S., Hill, E.J., Foster, D.A. and McDougall, I., 1993. Thermochronologic constraints on the tectonic evolution of active metamorphic core complexes, D'entrecasteaux Islands, Papua New Guinea. *Tectonics*, 12, 3, 611-628.
- Bauer, P., Palm, S. and Handy, M.R., 2000. Strain localization and fluid pathways in mylonite: inferences from in situ deformation of a water-bearing quartz analogue (norcamphor). *Tectonophysics*, 320, 141-165.
- Baumgartner, L.P. and Ferry, J. M. 1991. A model for coupled fluid-flow and mixed-volatile mineral reactions with applications to regional metamorphism. *Contributions to Mineralogy and Petrology*, 106, 3, 273-285.
- Baumgartner, L.P. and Olsen, S.N, 1995. A least-squares approach to mass transport calculations using the isocon method. *Economic Geology and the Bulletin of the Society of Economic Geologists*, 90, 1261-1270.
- Berger, B. R. and Bonham Jr, H. F., 1990. Epithermal gold-silver deposits in the western United States: time-space products of evolving plutonic, volcanic and tectonic environments. *Journal of Geochemical Exploration*, 36, 1-3, 103-142.
- Bird, P., 1998. Kinematic history of the Laramide orogeny in latitudes 35-49N, western United States. *Tectonics*, 17, 780-801.
- Bird, P. 2002. Stress direction history of the western United States and Mexico since 85 Ma. *Tectonics*, 21, 3, 12.
- Bongiolo, E.M., Renac, C., Mexias, A.S., Gomes, M.E.B., Ronchi, L.H. and Patrier-Mas, P, 2011. Evidence of Ediacaran glaciation in southernmost Brazil through magmatic to meteoric fluid circulation in the porphyry, epithermal Au-Cu deposits of Lavras do Sul. *Precambrian Research*, 189, 3-4, 404-419.
- Bottinga, Y. and Javoy, M., 1973. Comments on oxygen isotope geothermometry. *Earth and*

- Planetary Science Letters, 20, 250-265.
- Bottinga, Y. and Javoy, M., 1975. Oxygen isotope partitioning among the minerals in igneous and metamorphic rocks. *Reviews in Geophysics and Space Physics*, 13, 401-418.
- Brown, R.L. and Read, P.B., 1983. Shuswap terrane of British Columbia: A Mesozoic "core complex". *Geology*, 11, 164-168.
- Brun, J.P., Sokoutis, D. and Van Den Driessche, J., 1994. Analogue modeling of detachment fault systems and core complexes. *Geology*, 22, 4, 319-322.
- Bucher-Nurminen, K., 1987. A recalibration of the chlorite-biotite-muscovite geobarometer. *Contributions to Mineralogy and Petrology*, 96, 4, 519-522.
- Campani M., Herman, F. and Mancktelow, N., 2010a. Two- and three-dimensional thermal modeling of a low-angle detachment: the exhumation history of the Simplon Fault Zone, central Alps. *Journal of Geophysical Research*, 115, B10420.
- Campani M., Mancktelow, N., Seward, D., Rolland, Y., Müller, W. and Guerra, I., 2010b. Geochronological evidence for continuous exhumation through the ductile-brittle transition along a crustal-scale low-angle normal fault: Simplon Fault Zone, central Alps. *Tectonics*, 29, TC3002.
- Campani, M., Mulch, A., Kempf, O., Schlunegger, F. and Mancktelow, N., in press. Miocene paleotopography of the Central Alps. *Earth and Planetary Science Letters*.
- Cathelineau, M. and Nieva, D., 1985. A chlorite solid solution geothermometer. The Los Azufres (Mexico) geothermal system. *Contributions to Mineralogy and Petrology*, 91, 235-244.
- Cathelineau, M., 1988. Cation site occupancy in chlorites and illites as a function of temperature. *Clay Minerals* 23, 471-485.
- Chacko, T., Hu, X.S., Mayeda, T.K., Clayton, R.N. and Goldsmith, J.R., 1996. Oxygen isotope fractionations in muscovite, phlogopite, and rutile. *Geochimica et Cosmochimica Acta*, 60, 25957-2608.
- Chamberlain, C.P., Poage, M.A., Craw, D. and Reynolds, R.C., 1999. Topographic development of the Southern Alps recorded by the isotopic composition of authigenic clay minerals, South Island, New Zealand, *Chemical Geology*, 155, 279-294.
- Chappell, B.W. and White, A.J.R., 1974. Two contrasting granite types. *Pacific Geology*, 8,

173-174.

- Chase, R.B., Bickford, M.E. and Tripp, S.E., 1978. Rb-Sr and U-Pb isotopic studies of the northeastern Idaho batholith and border zone. *Geological Society of America Bulletin*, 89, 1325-1334.
- Cheney, E. S., 1977. The Kettle Dome; the southern extension of the Shuswap terrane into Washington. *Abstracts with Programs - Geological Society of America*, 9, 7, 926.
- Cheney, E. S., 1980. Kettle dome and related structures of northeastern Washington. In: *Cordilleran metamorphic core complexes* (eds Crittenden, M. D., Coney, P. J. and Davis, G. H). *Geological Society of America Memoir* 153, 463-483.
- Cladouhos, T.T. and Allmendinger, R.W., 1993. Finite strain and rotation from fault slip data., *Journal of Structural Geology*, 15, 771-784.
- Clayton, R.N., Friedman, I., Graf, D.L., Mayeda, T.K., Meents, W.F. and Shimp, N.F., 1966. The Origin of Saline Formation Waters 1. Isotopic Composition. *Journal of Geophysical Research* 71, 16, 3869-3882.
- Clayton, R.N., O'Neil, J.R. and Mayeda, T.K., 1972. Oxygen isotope exchange between quartz and water. *Journal of Geophysical Research*, 77, 3057-3067.
- Collettini, C., Niemeijer, A., Viti, C., Marone, C., 2009. Fault zone fabric and fault weakness. *Nature* 462, 907-910.
- Collettini, C., 2011. The mechanical paradox of low-angle normal faults: Current understanding and open questions. *Tectonophysics* 510, 253-268.
- Coney, P.J. 1980. Cordilleran metamorphic core complexes; an overview. In: *Cordilleran metamorphic core complexes* (edited by Crittenden M.D, C. P. J. and Davis, G. H.) 153. *Geological Society of America*, 7-34.
- Coney, P.J. and Harms, T.A. 1984. Cordilleran metamorphic core complexes: Cenozoic extensional relics of Mesozoic compression. *Geology*, 12, 550-554.
- Craig, H., 1957. Isotopic standards for carbon and oxygen and correction factors for mass-spectrometric analysis of carbon dioxide. *Geochimica et Cosmochimica Acta*, 12, 1-2, 133-149.
- Craig, H. 1961. Isotopic variations in meteoric waters. *Science* 133.
- Criss R.E. and Taylor, H.P., 1983. An $^{18}\text{O}/^{16}\text{O}$ and D/H study of Tertiary hydrothermal

- systems in the southern half of the Idaho batholith. *Geological Society of America Bulletin*, 94, 5, 640-663.
- Criss, R.E., Gregory, R.T., and Taylor Jr, H.P., 1987. Kinetic theory of oxygen isotopic exchange between minerals and water. *Geochimica et Cosmochimica Acta*, 51, 5, 1099-1108.
- Criss, R.E and Fleck, R.J., 1990. Oxygen isotope map of the giant metamorphic-hydrothermal system around the northern part of the Idaho batholith, USA. *Applied Geochemistry*, 5, 641-655.
- Criss, R. E., 1991. *The Principles of Stable Isotope Distribution*. 254 pp., Oxford Univ. Press, New York.
- Criss, R. E., 1999. *The Principles of Stable Isotope Distribution*. 264 pp., Oxford Univ. Press, New York.
- Crittenden, M.D., Coney, P.J. and Davis, G.H., 1980. Cordilleran metamorphic core complexes. *Geological Society of America Memoirs*, 153, 496.
- Cubley, J.F. and Pattison, D.R.M., 2009. Pressure contrast across the Kettle River normal fault, British Columbia. *Geological Survey of Canada Current Research*, 9, 25p.
- Currie, B.S., Rowley, D.B. and Tabor, N.J., 2005. Middle Miocene paleoaltimetry of southern Tibet: Implications for the role of mantle thickening and delamination in the Himalayan orogen, *Geology*, 33, 181–184.
- Davis, G. and Coney, P.J. 1979. Geologic development of the Cordilleran metamorphic core complexes. *Geology* 7, 120-124.
- Davis, G., Lister, G. and Reynolds S., 1983. Interpretation of Cordilleran core complexes as evolving crustal shear zones in an extending orogen. *Geological Society of America Abstract Programs.*, 12, 311.
- Davis, G.A, 1988. Rapid upward transport of mid-crustal mylonitic gneisses in the footwall of a Miocene detachment fault, Whipple Mountains, southeastern California. *Geologische Rundschau*, 77, 1, 191-209.
- Davis, G.A., Darby, B.J., Yadong, Z. and Spell, T.L., 2002. Geometric and temporal evolution of an extensional detachment fault, Hohhot metamorphic core complex, Inner Mongolia, China. *Geology*, 30, 11, 1003-1006.

- Davisson, M.L, Presser, T.S and Criss, R.E, 1994. Geochemistry of tectonically expelled fluids from the northern Coast Ranges, Rumsey Hills, California. *Geochimica et Cosmochimica Acta*, 58, 1687-1699.
- Davisson, M.L and Criss, R.E, 1996. Na-Ca-Cl relations in basinal fluids. *Geochimica et Cosmochimica Acta*, 60, 2743-2752.
- DeCelles, P.G., 2004. Late Jurassic to Eocene evolution of the Cordilleran thrust belt and foreland basin system, western U.S.A. *American Journal of Science*, 304, 2, 105-168.
- Dewey, J. F. 1988. Extensional collapse of orogens. *Tectonics*, 7, 6, 1123-1139.
- Dipple, G.M., Wintsch, R.P., and Andrews, M.S., 1990. Identification of the scales of differential element mobility in a ductile shear zone. *Journal of Metamorphic Geology*, 8, 645-661.
- Dickinson, W. R., Klute, M.A., Hayes, M.J., Janecke, S.U., Lundin, E.R., McKittrick, M.A., and Olivares, D., 1988. Paleogeographic and paleotectonic setting of Laramide sedimentary basins in the central Rocky Mountain region. *Geological Society of America Bulletin*, 100, 1023-1039.
- Dixon, J. and Williams, G. 1983. Reaction softening in mylonites from the Arnaboll thrust southerland. *Scottish Journal of Geology*, 19, 157-168.
- Drury, M. R. and Urai, J. L., 1990. Deformation-related recrystallization processes. *Tectonophysics*, 172 , 3-4, 235-253.
- Dubessy, J. and Ramboz, C., 1986. The history of organic nitrogen from early diagenesis to amphibolite facies: mineralogical, chemical and isotopic consequences. 5th Int. Symp. Water-Rock Interaction, Reykjavik, 171-174.
- Eggleton, R.A and Banfield, J.F, 1985. The alteration of granitic biotite to chlorite. *American Mineralogist*, 70, 902-910.
- Epstein, S., Sharp, R.P. and Gow, A.J., 1970. Antarctic Ice Sheet: Stable Isotope Analyses of Byrd Station Cores and Interhemispheric Climatic Implications. *Science*, 168, 1570-1572.
- Erslev, E. A., 1993. Thrusts, back-thrusts and detachment of Rocky Mountain foreland arches. *in* Schmidt, C. J., Chase, R. B., and Erslev, E. A., editors, Laramide basement deformation in the Rocky Mountain foreland of the western United States: Geological Society of America Special Paper 280, 339-358.

- Eslinger, E.V., Savin, S.M. and Yeh, H., 1979. Oxygen isotope geothermometry of diagenetically altered shales. *SEPM Special Publication*, 26, 113-124.
- Famin, V., 2004. Incursion de fluides dans une zone de cisaillement ductile (Tinos, Cyclades, Grèce): Mécanismes d'infiltration et implications tectoniques. Unpublished thesis, Université Paris VI.
- Farvera, J.R. and Yunda, R.A., 1991. Oxygen diffusion in quartz: Dependence on temperature and water fugacity. *Chemical Geology*, 90, 1-2, 55-70.
- Faulds, J.E., Henry, C.D., Coolbaugh, M.F., Garside, L.J., and Castor, S.B., 2005. Late Cenozoic strain field and tectonic setting of the northwestern Great Basin, western USA: Implications for geothermal activity and mineralization, *in* Rhoden, H.N., Steininger, R.C., and Vikre, P.G., eds., *Geological Society of Nevada Symposium 2005: Window to the World*, Reno, Nevada, 1091-1104.
- Fiebig, J. and Hoefs, J., 2002. Hydrothermal alteration of biotite and plagioclase as inferred from intragranular oxygen isotope- and cation-distribution patterns. *European Journal of Mineralogy*, 14, 49-60.
- Field, C.W. and Fifarek, R.H., 1985. Light stable-isotope systematics in the epithermal environment. In: Berger, B.R. and Bethke, P.M. (eds.). *Geology and Geochemistry of Epithermal Systems*. *Reviews in Economic Geology*, 2, 99-128.
- Fleck, R.J., 1970. Tectonic Style, Magnitude, and Age of Deformation in the Sevier Orogenic Belt in Southern Nevada and Eastern California. *Geological Society of America Bulletin*, 81, 6, 1705-1720.
- Forster, M. and Lister, G., 2009. Core-complex-related extension of the Aegean lithosphere initiated at the Eocene-Oligocene transition. *Journal of Geophysical Research*, 114, B2, B02401.
- Fortier, S.M., and Giletti, B.J., 1991. Volume self-diffusion of oxygen in biotite, muscovite, and phlogopite micas. *Geochimica et Cosmochimica Acta*, 55, 1319-1330.
- Foster, D.A. and Fanning, C.M., 1997. Geochronology of the northern Idaho batholith and the Bitterroot metamorphic core complex: magmatism preceding and contemporaneous with extension. *Geological Society of America Bulletin*, 109, 379-394.
- Foster, D. A., Schafer, C., Fanning, C. M. and Hyndman, D. W. 2001. Relationships between crustal partial melting, plutonism, orogeny, and exhumation: Idaho-Bitterroot batholith.

- Tectonophysics, 342, 3-4, 313-350.
- Foster, D.A. and Raza, A., 2002. Low-temperature thermochronological record of exhumation of the Bitterroot metamorphic core complex, northern Cordilleran Orogen. *Tectonophysics* 349, 23– 36.
- Foster, D.A., P.T. Doughty, T.J. Kalakay, C.M Fanning, S. Coyner, W.C. Grice, and J.J. Vogl, 2007, Kinematics and timing of exhumation of Eocene metamorphic core complexes along the Lewis and Clark fault zone, northern Rocky Mountains, USA, in Till, A., Roeske, S., Sample, J., and Foster, D.A., eds., *Exhumation along major continental strike-slip systems: Geological Society of America Special Paper 434*, 205-229.
- Fournier, R.O, Potter, R.W., 1982. An equation correlating the solubility of quartz in water from 25 to 900°C at pressures up to 10,000 bars. *Geochemica Cosmochimica Acta*, 46, 1969-1973.
- Fricke, H.C., Wickham, S.M. and O’Neil, J.R., 1992. Oxygen and hydrogen isotope evidence for meteoric water infiltration during mylonitization and uplift in the Ruby Mountains-East Humboldt Range core complex, Nevada. *Contributions to Mineralogy and Petrology*, 111, 203-221.
- Fusseis, F., Regenauer-Lieb, K., Liu, J., Hough, R. M. and De Carlo, F., 2009. Creep cavitation can establish a dynamic granular fluid pump in ductile shear zones. *Nature*, 459, 974-977.
- Garmezzy, L., 1983. Geology and geochronology of the southeast border of the Bitterroot dome: implications for the structural evolution of the mylonite carapace. PhD dissertation, Pennsylvania State University, University Park, Pennsylvania.
- Garzzone, C.N., Quade, J, DeCelles, P.G. and English, N.B., 2000. Predicting paleoelevation of Tibet and the Himalaya from d_{18O} vs. altitude gradients in meteoric water across the Nepal Himalaya, *Earth Planet. Sci. Lett.*, 183, 215–229.
- Gébelin, A., Mulch, A., Teyssier, C., Vennemann, T.W., Heizler, M. and Seaton, N.C.A., 2011. Oligo-Miocene extensional tectonics and fluid flow across the Northern Snake Range detachment system, Nevada. *Tectonics*, 30, TC5010.
- Giletti, B.J., 1985. The nature of oxygen transport within minerals in the presence of hydrothermal water and the role of diffusion. *Chemical Geology*, 53, 197-206.
- Girard J.P., Munz I., Johansen H., Hill S. and Canham A., 2001. Condition and timing of

- quartz cementation in Brent reservoirs, Hild Field, North Sea: constraints from fluid inclusions and SIMS oxygen isotope microanalysis. *Chemical Geology*, 176, 1-4, 73-92.
- Glazner, A.F., and Bartley, J.M., 1991. Volume loss, fluid flow and state of strain in extensional mylonites from the central Mojave Desert, California: *Journal of Structural Geology*, 13, 587-594.
- Glombick, P., 2006. A reappraisal of the tectonic significance of early Tertiary low-angle shear zones exposed in the Vernon map area (82 L), Shuswap metamorphic complex, southeastern Canadian Cordillera. *Canadian Journal of Earth Sciences*, 43, 245-268.
- Goddard, J.V., and Evans, J.P., 1995. Chemical changes and fluid–rock interaction in faults of crystalline thrust sheets, northwestern Wyoming. *USA Journal of Structural Geology*, 17, 533–547.
- Gottardi, R., Teyssier, C., Mulch, A., Venneman, T.W. and Wells, M.L., 2011. Preservation of extreme transient geotherm in the Raft River detachment shear zone, *Geology*, 39, 759-762.
- Graham, C.M., Sheppard, S.M. F. and Heaton, T.H.E., 1980. Experimental hydrogen studies. 1. Systematics of hydrogen isotope fractionation in the epidote-H₂O, zoisite-H₂O and AlO(OH)-H₂O. *Geochimica et Cosmochimica Acta*, 44, 2, 353-364.
- Graham, C.M., 1981. Experimental hydrogen isotope studies: III. Diffusion of hydrogen in hydrous minerals, and stable isotope exchange in metamorphic rocks. *Contributions to Mineralogy and Petrology*, 76, 216-228.
- Graham, C.M., Viglino, J. A. and Harmon, R. S. 1987. Experimental-study of hydrogen-isotope exchange between aluminous chlorite and water and of hydrogen diffusion in chlorite. *American Mineralogist*, 72, 5-6, 566-579.
- Graham C.M. and Elphick S.C., 1991. Some experimental constraints on the role of hydrogen in oxygen and hydrogen diffusion and Al-% interdiffusion in silicates. In *Diffusion, Atomic Ordering and Mass Transport, Advances in Physical Geochemistry*, 8, 248-285.
- Grant, J.A., 1986. The isocon diagram – a simple solution to Gresens' equation for metasomatic alteration: *Economic Geology*, 81, 1976–1982.
- Grant, J.A., 2005. Isocon analysis: a brief review of the method and applications. *Physics and Chemistry of the Earth*, 30, 997-1004.

- Gratier, J.P., Guiguet, R., Renard, F., Jenatton, L., and Bernard, D., 2009. A pressure solution creep law for quartz from indentation experiments. *Journal of Geophysical Research*, 114, B03403.
- Greenwood, H.J., 1961. The system NaAlSi₂O₆-H₂O-argon: Total pressure and water pressure in metamorphism. *Journal of Geophysical Research*, 66, 3923-3946.
- Gresens, R.L., 1967. Composition-volume relationships of metasomatism. *Chemical Geology*, 2, 47-65.
- Guidotti, C.V., 1970. The Mineralogy and Petrology of the Transition from the Lower to Upper Sillimanite Zone in the Oquossoc Area, Maine. *Journal of Petrology*, 11, 2, 277-336.
- Guidotti, C.V., 1977. Micas in metamorphic rocks. *Reviews in Mineralogy*, 13, 357-468.
- Hammond, W.C. and Thatcher, W., 2004. Contemporary tectonic deformation of the Basin and Range province, western United States: 10 years of observation with the Global Positioning System. *Journal of Geophysical Research-Solid Earth*, 109, B8, 21.
- Heller, P.L., Bowdler, S.S., Chambers, H.P., Coogan, J.C., Hagen, E.S., Shuster, M.W., Winslow, N.S. and Lawton, T.F., 1986. Time of initial thrusting in the Sevier orogenic belt, Idaho-Wyoming and Utah. *Geology*, 14, 5, 388-391.
- Henry, D.J., Guidotti, C.V., and Thomson, J.A., 2005. The Ti-saturation surface for low-to medium pressure metapelitic biotites: implications for geothermometry and Ti substitution mechanisms. *American Mineralogist*, 90, 375-382.
- Herwegh, M., Linckens, J., Ebert, A., Berger, A. and Brodhag, S.H., 2011. The role of second phases for controlling microstructural evolution in polymineralic rocks: A review. *Journal of Structural Geology*, 33, 12, 1728-1750.
- Hildebrand, R.S., 2009. Did Westward Subduction Cause Cretaceous-Tertiary Orogeny in the North American Cordillera? *Geological Society of America Special Papers*, 457, 1-71.
- Hillier, S. and Velde, B. 1992. Octahedral occupancy and the chemical composition of diagenetic (low-temperature) chlorites. *Clay Minerals*, 26, 146-168.
- Hippertt, J.F., 1998. Breakdown of feldspar, volume gain and lateral mass transfer during mylonitization of granitoid in a low metamorphic grade shear zone. *Journal of Structural Geology Structures and Properties of High Strain Zones in Rocks*, 20, 2-3, 175-193.

- Hirschmann, M.M., 2006. Water, melting, and the deep Earth H₂O cycle. *Annual Review of Earth and Planetary Sciences* 34, 629-653.
- Hirschmann, M.M. and Dasgupta, R., 2009. The H/C ratios of Earth's near-surface and deep reservoirs, and consequences for deep Earth volatile cycles. *Chemical Geology*, 262, 1-2, 4-16.
- Hirth, G., and Tullis, J. 1992. Dislocation creep regimes in quartz aggregates. *Journal of Structural Geology*, 14, 145-159.
- Hodges, K.V., and Walker, J.D., 1992. Extension in the Cretaceous Sevier orogen, North American Cordillera. *Geological Society of America Bulletin*, 104, 560-569.
- Holk, G.J., and Taylor, H.P.Jr., 1997. 18O/16O homogenization of the middle crust during anatexis: The Thor-Odin metamorphic core complex, British Columbia. *Geology*, 25, 1, 31-34.
- Holk, G.J., and H.P.Jr. Taylor, 2007. 18O/16O Evidence for contrasting hydrothermal regimes involving magmatic and meteoric-hydrothermal waters at the Valhalla metamorphic core complex, British Columbia, *Economic Geology*, 102, 1063-1078.
- Huet, B., Le Pourhiet, L., Labrousse, L., Burov, E.B. and Jolivet, L., 2011. Formation of metamorphic core complex in inherited wedges: A thermomechanical modelling study. *Earth and Planetary Science Letters*, 309(3-4), 249-257.
- Humphreys, E.D., 1995. Post-Laramide removal of the Farallon slab, western United States. *Geology*, 23, 987-990.
- Hyndman, D.W., 1983. The Idaho batholith and associated plutons, Idaho and Western Montana. In: Roddick, J.A. (Ed.), *Circum-Pacific Plutonic Terranes*. Geological Society of America Memoir, 159, 213-240.
- Hyndman, D.W. and Myers, S.A., 1988. The transition from amphibolite-facies mylonite to chloritic breccia and role of the mylonite in formation of Eocene epizonal plutons, Bitterroot dome, Montana. *Geologische Rundschau*, 77, 211-226.
- Inoue, A., Meunier, A., Patrier-Mas, P., Rigault, C., Beaufort, D., and Vieillard, P., 2009. Application of chemical geothermometry to low-temperature trioctahedral chlorites. *Clays and Clay Minerals* 57, 371-382.
- Janeck, S.U and Evans, J.P, 1988. Feldspar-influenced rock rheologies. *Geology*, 16, 12,

1064-1067.

- Jolivet, L., Goffe, B., Bousquet, R., Oberhansli, R. and Michard, A. 1998. Detachments in high-pressure mountain belts, Tethyan examples. *Earth and Planetary Science Letters*, 160, 1-2, 31-47.
- Johnson, R.A., Karlstrom, K.E., Smithson, S.B., and Houston, R.S., 1984. Gravity profiles across the Cheyenne Belt, a Precambrian crustal suture in southeastern Wyoming. *Journal of Geodynamics*, 1, 445–471.
- Johnson, B.J. 2006. Extensional shear zones, granitic melts, and linkage of overstepping normal faults bounding the Shuswap metamorphic core complex, British Columbia. *Geological Society of America Bulletin*, 118, 366-382.
- Karlstrom, K., Bowring, S.A., Chamberlain, K.R., Dueker, K.G., Eshete, T., Erslev, E.A., Farmer, G.L., Hiezler, M., Humphreys, E.D., Johnson, R.A., Keller, G.R., Kelley, S.A., Levander, A., Magnani, M.B., Matzel, J.P., McCoy, A. M., Miller, K.C., Morozova, E.A., Pazzaglia, F.J., Prodehl, C., Rumpel, H.M., Shaw, C.A., Sheehan, A.F., Shoshitaishvili, E., Smithson, S.B., Snelson, C.M., Stevens, L.M., Tyson, A.R., and Williams, M.L., 2002. Structure and evolution of the lithosphere beneath the Rocky Mountains: Initial results from the CD-ROM experiment. *GSA Today*, 12, 4–9.
- Kerrich, R., 1976. Some effects of tectonic recrystallization on fluid inclusions in vein quartz. *Contributions to Mineralogy and Petrology*, 59, 192–202.
- Kerrich, R., La Tour, T.E. and Willmore, L. 1984. Fluid participation in deep fault zones: evidence from geological, geochemical $^{18}\text{O}/^{16}\text{O}$ relations. *Journal of Geophysical Research* H 88, 4331-4343.
- Kerrich, R. and Hyndman, D.W., 1986. Thermal and fluid regimes in the Bitterroot lobe – Sapphire block detachment zone, Montana: evidence from $^{18}\text{O}/^{16}\text{O}$ and geologic relations. *Geological Society of America Bulletin*, 97, 147–155.
- Kirschner, D.L. and Teyssier, C., 1997. Effect of deformation on oxygen isotope exchange in the Heavitree Quartzite, Ruby Gap duplex, central Australia. *Journal of Structural Geology* 17, 10, 1407-1423.
- Knipe, R. J. 1989. Deformation mechanisms - Recognition from natural tectonites *Journal of Structural Geology*, 11, 127-146.
- Kolb, J., 2008. The role of fluids in partitioning brittle deformation and ductile creep in

- auriferous shear zones between 500 and 700 C. *Tectonophysics*, 446, 1-15.
- Konopasek, J., 1998. Formation and destabilization of the high pressure assemblage garnet-phengite-paragonite (Krusne hory Mountains, Bohemian Massif): The significance of the Tschermak substitution in the metamorphism of pelitic rocks. *Lithos*, 42, 3-4, 269-284.
- Kostrov, V.V., 1974. Seismic moment and energy of earthquakes, and seismic flow of rocks. *Izvestiya Academy of Sciences of the USSR (Physics of Solid Earth)*, 1, 23-40.
- Kuroda, Y., Yamada, T., Kobayashi, H., Ohtomo, Y., Yagi, M. and Matsuo, S., 1986. Hydrogen isotope study of the granitic rocks of the Ryoke belt, Central Japan. *Chemical Geology: Isotope Geoscience section*, 58, 4, 283-302.
- Kwon, S., Park, Y., Park, C. and Kim, H.S. 2009. Mass-balance analysis of bulk-rock chemical changes during mylonitization of a megacryst-bearing granitoid, Cheongsan shear zone, Korea. *Journal of Asian Earth Sciences*, 35, 6, 489-501.
- LaTour, T.E. and Barnett, R.L., 1987. Mineralogical changes accompanying mylonitization in the Bitterroot dome of the Idaho batholith: implications for the timing of deformation. *Geological Society of America Bulletin*, 98, 356-363.
- Lawrence, J.R. and Gieskes, J.M., 1981. Constraints on Water Transport and Alteration in the Oceanic Crust From the Isotopic Composition of Pore Water. *Journal of Geophysical Research*. 86, B9, 7924-7934.
- Lawton, T.F., 2009. Compositional Trends within a Clastic Wedge Adjacent to a Fold-Thrust Belt: Indianola Group, Central Utah, U.S.A. In: *Foreland Basins*. Blackwell Publishing Ltd., 411-423.
- Lespinasse, M. and Pecher, A., 1986. Microfracturing and regional stress field: a study of the preferred orientations of fluid-inclusion planes in a granite from the Massif Central, France. *Journal of Structural Geology*, 8, 169-180.
- Levresse, G., Cheilletz, A., Gasquet, D., Reisberg, L., Deloule, E., Marty, B. and Kyser, K., 2004. Osmium, sulphur, and helium isotopic results from the giant Neoproterozoic epithermal Imiter silver deposit, Morocco: evidence for a mantle source. *Chemical Geology*, 207, 1-2, 59-79.
- Lin, W., Faure, M., Monié, P., Schärer U. and Panis D., 2008. Mesozoic Extensional Tectonics in Eastern Asia: The South Liaodong Peninsula Metamorphic Core Complex (NE China). *Journal of Geology*, 116, 2, 134-154.

- Lister, G.S. and Snoke, A.W., 1984. S-C Mylonites. *Journal of Structural Geology*, 6, 617-638.
- Lister, G.S., Banga, G. and Feenstra, A. 1984. Metamorphic core complexes of Cordilleran type in the Cyclades, Aegean Sea, Greece. *Geology*, 12, 4, 221-225.
- Lister, G.S. and Davis, G. A. 1989. The origin of metamorphic core complexes and detachment faults formed during Tertiary continental extension in the northern Colorado River region, U.S.A. *Journal of Structural Geology*, 11, 1/2, 65-94.
- Liu, M., 2001. Cenozoic extension and magmatism in the North American Cordillera: the role of gravitational collapse. *Tectonophysics*, 342, 407-433.
- Liu, J., Davis, G.A., Lin, Z. and Wu, F., 2005. The Liaonan metamorphic core complex, Southeastern Liaoning Province, North China: A likely contributor to Cretaceous rotation of Eastern Liaoning, Korea and contiguous areas. *Tectonophysics*, 407, 1-2, 65-80.
- Liu, L., Gurnis, M., Seton, M., Saleeby, J., Muller, R.D., and Jackson, J.M., 2010. The role of oceanic plateau subduction in the Laramide orogeny. *Nature Geoscience*, 3, 353-357.
- Losh, S., 1997. Stable isotope and modeling studies of fluid-rock interaction associated with the Snake Range and Mormon Peak detachment faults, Nevada. *Geological Society of America Bulletin*, 109, 300-323.
- Malavieille, J., 1993. Late orogenic extension in mountain belts: insights from the Basin and Range and the Late Paleozoic Variscan Belt. *Tectonics*, 12, 5, 1115-1130.
- Manatschal, G., Marquer, D. and Früh-Green, G.L., 2000. Channelized fluid flow and mass transfer along a rift-related detachment fault (Eastern Alps, Southeast Switzerland). *Geological Society of America Bulletin*, 112, 1, 21-33.
- Mancktelow, N.S., Grujic, D. and Johnson, E.L., 1998. An SEM study of porosity and grain boundary microstructure in quartz mylonites, Simplon Fault Zone, Central Alps. *Contributions to Mineralogy and Petrology*, 131, 1, 71-85.
- Mancktelow, N.S., Arbaret, L. and Pennacchioni, G., 2002. Experimental observations on the effect of interface slip on rotation and stabilisation of rigid particles in simple shear and a comparison with natural mylonites. *Journal of Structural Geology*, 24, 3, 567-585.
- Mancktelow, N.S. and Pennacchioni, G., 2004. The influence of grain boundary fluids on the microstructure of quartz-feldspar mylonites. *Journal of Structural Geology*, 26, 47-69.

- Manning, C.E., 1994. The solubility of quartz in H₂O in the lower crust and upper mantle. *Geochimica et Cosmochimica Acta*, 58, 4831-4839.
- Marrett, R. and Allmendinger, R.W., 1990. Kinematic analysis of fault-slip data. *Journal of Structural Geology*, 12, 973-986.
- Marrett, R. and Allmendinger, R.W., 1991. Estimates of strain due to brittle faulting: sampling of fault populations. *Journal of Structural Geology*, 13, 735-738.
- Massonne, H.J. and Schreyer W., 1987. Phengite geobarometry based on the limiting assemblage with K-feldspar, phlogopite, and quartz. *Contributions to Mineralogy and Petrology*, 96, 2, 212-224.
- Mawer, C.K., 1986a. What is a mylonite? *Geoscience Canada*, 13, 33-34.
- Mawer, C.K., 1986b. State of strain in a quartzite mylonite, central Australia. *Journal of Structural Geology*, 5, 401-409.
- McCaig, A.M., 1988. Deep fluid circulations in fault zones. *Geology*, 16, 867-870.
- McKenzie, D. 1972. Active tectonics of the Mediterranean region. *Geophys. J. Roy. Astron. Soc.* 30, 109-185.
- McQuarrie, N., and Chase, C.G., 1999. Raising the Colorado Plateau. *Geology*, 28, 91-94.
- Miller, E. L. and Gans, P. B., 1989. Cretaceous crustal structure and metamorphism in the hinterland of the Sevier thrust belt, western U.S. Cordillera. *Geology*, 17, 1, 59-62.
- Mills, J.W., 1985. Geologic maps of the Marcus and Kettle Falls quadrangles, Stevens and Ferry counties, Washington. Washington Division of Geology and Earth Resources.
- Mix, H.T., Mulch, A., Kent-Corson, M.L. and Chamberlain, C.P., 2011. Cenozoic migration of topography in the North American Cordillera. *Geology* 39, 1, 87-90.
- Mohanty, S. and Ramsay, J.G., 1994. Strain partitioning in ductile shear zone: an example from a lower Pennine nappe of Switzerland. *Journal of Structural Geology*, 16, 663-676.
- Mohr, D.W. and Newton, R.C., 1983. Kyanite-staurolite metamorphism in sulfidic schists of the Anakeesta Formation, Great Smoky Mountains, North Carolina. *American Journal of Science*, 283, 2, 97-134.
- Molnar, P., 1983. Average regional strain due to slip on numerous faults of different orientations. *Journal of Geophysical Research*, 88, 6430-6432.

- Mori, Y., Nishiyama, T., and Yanagi, T., 2003. Mass transfer paths in alteration zones around carbonate veins in the Nishisonogi Metamorphic Rocks, southwest Japan. *American Mineralogist*, 88, 611–623.
- Morrison, J. and Anderson, L.J., 1998. Footwall Refrigeration Along a Detachment Fault: Implications for the Thermal Evolution of Core Complexes. *Science*, 279, 63-66.
- Mulch, A., Teyssier, C., Cosca, M.A., Vanderhaeghe O. and Vennemann, T.W., 2004. Reconstructing paleoelevation in eroded orogens. *Geology*, 32, 6, 525-528.
- Mulch, A., Teyssier, C., Cosca, M.A. and Vennemann, T.W., 2006. Thermomechanical analysis of strain localization in a ductile detachment zone. *Journal of Geophysical Research*, 111, B12405.
- Mulch, A., Teyssier, C., Cosca, M.A. and Chamberlain, C.P., 2007. Stable isotopes paleoaltimetry of Eocene core complexes in the North American Cordillera. *Tectonics*, 26, 1-13.
- Munoz, M., de Andrade, V., Vidal, O., Lewin, E., Pascarelli, S. and Susisi, J., 2006. Redox and speciation micromapping using dispersive X-ray absorption spectroscopy : Application to iron in chlorite mineral of a metamorphic rock thin section. *G-cube*, 7, 11, 1-10.
- Nabelek, P.I., O'Neil, J.R. and Papike, J.J., 1983. Vapor phase exsolution as a controlling factor in hydrogen isotope variation in granitic rocks: the Notch Peak granitic stock, Utah. *Earth and Planetary Science Letters*, 66, 137-150.
- Nakamura, M., Yurimoto, H. and Watson, B.E., 2005. Grain growth control of isotope exchange between rocks and fluids. *Geology*, 33, 10, 829-832.
- Nemcok, M., Schamel, S. and Gayer, R., 2009. Thrustbelts: Structural Architecture, Thermal Regimes and Petroleum Systems. Cambridge University Press, 556 pages.
- Nesbitt, B.E., and Muehlenbachs, K., 1989. Origins and movement of fluids during deformation and metamorphism in the Canadian Cordillera: *Science*, 245, 733-736.
- Nesbitt, B.E., and Muehlenbachs, K., 1991. Stable isotopic constraints on the nature of the syntectonic fluid regime of the Canadian Cordillera: *Journal of Geophysical Research*, 18, 963-966.
- Norlander, B.H., Whitney, D.L., Teyssier, C. and Vanderheaghe, O., 2001. Partial melting and decompression of the Thor-Odin dome, Shuswap metamorphic core complex,

- Canadian Cordillera. *Lithos*, 61, 103-125.
- Nourse, J., Anderson, T. and Silver, L., 1994. Tertiary metamorphic core complexes in Sonora, northwestern Mexico. *Tectonics*, 13, 5, 1161-1182.
- Nyman, M.W., Law, R.D., and Smelik, E.A., 1992. Cataclastic deformation mechanism for the development of core-mantle structures in amphibole. *Geology*, 20, 455-458.
- O'Hara, K.D., 1988. Fluid flow and volume loss during mylonitization: an origin for phyllonite in an overthrust setting. *Tectonophysics*, 156, 21-34.
- O'Hara, K.D., and Blackburn, W.H., 1989. Volume loss model for trace element enrichments in mylonites. *Geology*, 17, 524-527.
- O'Hara, K.D., Sharp, Z.D., Moecher, D.P. and Jenkin, G.R., 1997. The effect of deformation on oxygen isotope exchange in quartz and feldspar and the significance of isotopic temperatures in mylonites. *Journal of Geology*, 105, 193-204.
- Oliver, N.H.S., 1996. Review and classification of structural controls on fluid flows during regional metamorphism. *Journal of Metamorphic Geology*, 14, 477-492.
- Olsen, S.N. and Grant, J.A., 1991. Isocon analysis of migmatization in the Front Range, Colorado, USA. *Journal of Metamorphic Geology*, 9, 2, 151-164.
- Passchier, C.W., 1987. Stable positions of rigid objects in non-coaxial flow, a study in vorticity analysis. *Journal of Structural Geology*, 9, 5-6, 679-690.
- Passchier, C.W. and Trouw R.A.J., 2005. *Microtectonics*. Springer Berlin Heidelberg New York, 322 p.
- Peacock, S.M., 1993. The importance of blueschist -> eclogite dehydration reactions in subducting slabs. *Geological Society of America Bulletin*, 105, 684-694.
- Person, M., Mulch, A., Teyssier, C. and Gao, Y., 2007. Isotope transport and exchange within metamorphic core complexes. *Am. J. Sci.*, 307, 555-589.
- Person, M. 2008. *Hydrologic Models of Modern and Fossil Geothermal Systems within the Great Basin: Implications for Carlin-Type Gold Mineralization*. Geosphere.
- Phillips, W.J., 1972. Hydraulic fracturing and mineralization. *Geological Society of London Journal*, 128, 337-359.
- Poage, M.A., and Chamberlain, C.P., 2002. Stable isotopic evidence for a Pre-Middle Miocene rain shadow in the western Basin and Range: Implications for the

- paleotopography of the Sierra Nevada. *Tectonics*, 21, 4, 1034.
- Potdevin, J.L., and Marquer, D., 1987. Méthodes de quantification des transferts de matière par les fluides dans les roches métamorphiques déformées. *Geodinamica acta* 1, 193-206.
- Raimondo, T., Clark, C., Hand, M. and Faure, K (in press). Assessing the geochemical and tectonic impacts of fluid–rock interaction in mid-crustal shear zones: a case study from the intracontinental Alice Springs Orogen, central Australia. *Journal of Metamorphic Geology*, 29, 8, 821-850.
- Renard, F., Gratier, J.P., and Jamtveit, B., 2000. Kinetics of crack-sealing, intergranular pressure solution, and compaction around active faults. *Journal of Structural Geology* 22, 1395-1407.
- Rey, P., Vanderhaeghe, O. and Teyssier, C., 2001. Gravitational collapse of the continental crust: definitions, regimes, mechanisms and modes. *Tectonophysics*, 342, 435-449.
- Rey, P., Teyssier, C. and Whitney, D.L., 2009a. Extension rates, crustal melting, and core complex dynamics. *Geology*, 37, 391-394.
- Rey, P., Teyssier, C. and Whitney, D.L., 2009b. The role of partial melting and extensional strain rates in the development of metamorphic core complexes. *Tectonophysics*, 477, 135-144.
- Rowley, D.B., and Currie, B.S., 2006. Palaeo-altimetry of the late Eocene to Miocene Lunpola basin, central Tibet. *Nature*, 439, 677 – 681.
- Rybacki, E., Wirth, R. and Dresen, G., 2008. High-strain creep of feldspar rocks: Implications for cavitation and ductile failure in the lower crust. *Geophysical Research Letters*, 35, 4, 1-5.
- Rye, R.O., Schuiling, R.D., Rye, D.M. and Jansen, J.B.H., 1976. Carbon, hydrogen, and oxygen isotope studies of the regional metamorphic complex at Naxos, Greece. *Geochimica et Cosmochimica Acta*, 40, 1031-1049.
- Rhodes, B.P. and Cheney, E.S., 1981. Low-angle faulting and the origin of Kettle Dome, a metamorphic core complex in northeastern Washington. *Geology*, 9, 8, 366-369.
- Saltus, R.W., and Thompson, G.A., 1995. Why is it downhill from Tonopah to Las Vegas?: A case for mantle plume support of the high northern Basin and Range. *Tectonics*, 14, 1235-1244.

- Schmid, S.M. 1982. Microfabric studies as indicators of deformation mechanisms and flow laws operative in mountain building. In: Mountain building processes. Academic Press, London, 95-110.
- Scholz, C.H., 1988. The brittle-plastic transition and the depth of seismic faulting. *Geologische Rundschau*, 77, 319-328.
- Scholz, C. H. 1992. The mechanics of earthquakes and faulting. Cambridge University Press, Cambridge.
- Secor, D.T, 1965. Role of fluid pressure in jointing. *American Journal of Science*, 263, 633-646.
- Sheppard, S.M.F., Nielsen, R.L. and Taylor, H.P., 1969. Oxygen and hydrogen isotope ratios in clay minerals from porphyry copper deposits. *Economic Geology*, 64, 755-777.
- Sheppard, S.M.F., Nielsen, R.L. and Taylor, H.P., 1971. Hydrogen and oxygen isotope ratios in minerals from porphyry copper deposits. *Economic Geology*, 66, 4, 515-542.
- Sheppard, S.M.F., Brown, P.E. and Chambers, A.D., 1977. The Lilloise intrusion, east Greenland: Hydrogen isotope evidence for the efflux of magmatic water into the contact metamorphic aureole. *Contributions to Mineralogy and Petrology*, 63, 2, 129-147.
- Sheppard, S.M.F. and Harris, C., 1985. Hydrogen and oxygen isotope geochemistry of Ascension Island lavas and granites: variation with crystal fractionation and interaction with sea water. *Contributions to Mineralogy and Petrology*, 91, 1, 74-81.
- Sheppard, S.M.F., 1986. Characterization and isotopic variations in natural waters, *Reviews in Mineralogy*, 16, 165-184.
- Sibson, R.H, Moore, J.McM and Rankin, A.H, 1975. Seismic pumping - a hydrothermal fluid transport mechanism. *Journal of the Geological Society of London*, 131, 653-659.
- Sibson, R. H. 1977. Fault rocks and fault mechanisms. *Journal of the Geological Society of London* 133, 191-213.
- Sibson, R.H. 1979. Transient discontinuities in ductile shear zone. *Journal of Structural geology*, 2, 165-171.
- Sibson, R.H., 1985. A note on fault reactivation. *Journal of Structural Geology* 7, 751-754.
- Sibson, R.H., 1986. Earthquakes and rock deformation in crustal fault zones. *Annual Review of Earth and Planetary Sciences*, 14, 149-175.

- Sidman, D., Ferré, E.C., Teyssier, C. and Jackson, M., 2005. Magnetic fabric and microstructure of a mylonite: Example from the Bitterroot Shear Zone, Western Montana. In: Bruhn, D. & Burlini, L. (eds) *High-Strain Zones: Structure and Physical Properties*. Geological Society, London, Special Publications, 245, 143-163.
- Sigloch, K., McQuarrie, N., and Nolet, G., 2008. Two-stage subduction history under North America inferred from multiple-frequency tomography. *Nature Geoscience*, 1, 458-462.
- Simpson, C., 1985. Deformation of granitic rocks across the brittle-ductile transition. *Journal of Structural geology*, 7, 503-511.
- Spencer, J.E., 2009. Structural analysis of three extensional detachment faults with data from the 2000 Space-Shuttle Radar Topography Mission. *GSA Today*, 20, 8, 4-10.
- Steinmüller, K., 2001. Modern hot springs in the southern volcanic Cordillera of Peru and their relationship to Neogene epithermal precious-metal deposits. *Journal of South American Earth Sciences*, 14, 4, 377-385.
- Stipp, M., Stunitz, H., Heilbronner, R., and Schmid, S. M., Dynamic recrystallization of quartz: correlation between natural and experimental conditions. From: De Meer, S., Drury, M. R., De Bresser, J. H. P., and Pennock, G. M. (eds) 2002. *Deformation Mechanisms, Rheology and Tectonics: Current Status and Future Perspectives*. Geological Society of London, Special Publications, 200, 171-190.
- Sturm, R., 2003. SHEARCALC – a computer program for the calculation of volume change and mass transfer in a ductile shear zone. *Computers and Geosciences*, 29, 587–610.
- Suzuoki, T. and Epstein, S., 1976. Hydrogen isotope fractionation between OH-bearing minerals and water. *Geochim. Cosmochim. Acta*, 40, 1229-1240.
- Tartèse, R., Boulvais, P., Poujol, M., Chevalier, T., Paquette, J.-L., Ireland, T. R. and Deloule, E., 2011. Mylonites of the South Armorican Shear Zone: Insights for crustal-scale fluid flow and water-rock interaction processes. *Journal of Geodynamics*- In press.
- Taylor, H.P Jr., 1974. The application of oxygen and hydrogen isotope studies to problems of hydrothermal alteration and ore deposition. *Economic Geology*, 69, 843-883.
- Taylor, H.P Jr., 1979. Oxygen and hydrogen isotope relationships in hydrothermal mineral deposits. In Barnes, H.L. (ed.) *Geochemistry of hydrothermal ore deposit*, 2d edition, 236-277.

- Taylor, B.E, 1986. Magmatic volatiles: isotopic variations of C, H and S. *Reviews in Mineralogy*, 16, 185-219.
- Taylor, W.J., Bartley, J. M., Martin, M.W., Geissman, J.W., Walker, J.D., Armstrong, P.A. and Fryxell, J.E., 2000. Relations between hinterland and foreland shortening: Sevier orogeny, central North American Cordillera. *Tectonics*, 19, 6, 1124–1143.
- Ten Grotenhuis, S.M., Trouw, R.A.J. and Passchier, C.W., 2003. Evolution of micafish in mylonitic rocks. *Tectonophysics*, 372, 1-21.
- Teysier, C., 2005. Flow of partially molten crust and origin of detachments during collapse of the Cordilleran Orogen. *Geological Society of London*, 245, 39-64.
- Thatcher, W., Foulger, G.R., Julian, B.R., Svarc, J., Quilty, E. and Bawden, G.W., 1999. Present-Day Deformation Across the Basin and Range Province, Western United States. *Science*, 283, 5408, 1714-1718.
- Toth, M.I., 1983. Reconnaissance geological map of the Selway-Bitterroot Wilderness, Idaho county, Idaho and Missoula and Ravalli Counties, Montana. United States Geological Survey Miscellaneous Field Studies Map MF-1495-B, scale 1:125,000.
- Toy, V.G., Craw, D., Cooper, A.F. and Norris, R.J, 2010. Thermal regime in the central Alpine Fault zone, New Zealand: Constraints from microstructures, biotite chemistry and fluid inclusion data. *Tectonophysics* 485, 178-192.
- Tripathy, N.R., Srivastava, H.B. and Mamtani, M.A., 2009. Evaluation of a regional strain gradient in mylonitic quartzites from the footwall of the Main Central Thrust Zone (Garhwal Himalaya, India): Inferences from finite strain and AMS analyses. *Journal of Asian Earth Sciences*, 34, 1, 26-37.
- Tschegg, C., and Grasemann, B., 2009. Deformation and alteration of a granodiorite during low-angle normal faulting (Serifos, Greece). *Lithosphere*, 1, 139-154.
- Upton, P., Grant Caldwell, T., Page Chamberlain, C., Craw, D., James, Z., Jiracek, G.J., Koons, P.O. and Wannamaker, P.E., 2000. Fluids in a backthrust regime (Southern Alps, New Zealand). *Journal of Geochemical Exploration*, 69-70, 517-521.
- Urey, H.C, Lowenstam, H.A, Epstein, S., and McKinney, C.R, 1951. Measurements of paleotemperatures and temperatures of the upper Cretaceous of England, Danmark, and the southeastern United States *Geological Society of America Bulletin*, 62, 399-416.

- Vanderhaeghe, O., Burg, J.P. and Teyssier, C., 1999. Exhumation of migmatitic terrains in the hinterland of two collapsed orogens. In: Exhumation processes (edited by Ring, U., Brandon, M., Willet, S. & Lister, G.) 154. Geological Society of London Special Paper, 181-204.
- Vanderhaeghe, O., Teyssier, C., McDougall, I. and Dunlap W. J., 2003. Cooling and exhumation of the Shuswap Metamorphic Core Complex constrained by $^{40}\text{Ar}/^{39}\text{Ar}$ thermochronology, Geological Society of America Bulletin, 115, 200 – 216.
- Velde, B., and A. M. Brusewitz, 1972. The transformation of natural clay minerals at elevated temperatures and pressures. Geol. Foren. in Stockholm Forhand, 94, 449-458.
- Velde, B., and D. Rumble IIIrd, 1977a. Alumina content of chlorite in muscovite-bearing assemblages. In Carnegie institution of Washington, Year book, 76, 621-623.
- Velde, B., 1977b. Clays and clay minerals in natural and synthetic systems. Elsevier, Amsterdam, 218 p.
- Velde, B., 1995. Origin and mineralogy of clays. Springer Verlag, Berlin, 334 p.
- Vennemann T.W. and O'Neil J.R., 1996. Hydrogen isotope exchange between hydrous minerals and molecular hydrogen: I. A new approach for the determination of hydrogen isotope fractionation at moderate temperatures. Geochimica et Cosmochimica Acta, 60, 2437-2451.
- Vidal, O., Parra, T. and Trotet, F. 2001. A thermodynamic model for Fe-Mg aluminous chlorite using data from phase equilibrium experiments and natural pelitic assemblages in the 100 degrees to 600 degrees C, 1 to 25 kb range. American Journal of Science, 301, 6, 557-592.
- Vidal, O., Parra, T. and Vieillard, P., 2005. Thermodynamic properties of the Tschermak solid solution in Fe-chlorite: Application to natural examples and possible role of oxidation. American Mineralogist, 90, 2-3, 347-358.
- Vidal, O., De Andrade, V. Lewin, E. Munoz, M. Parra, T. and Pascarelli, S., 2006. P-T-deformation-Fe³⁺/Fe²⁺ map at the thin section scale using Chl-Mica local equilibria and comparison with XANES mapping: Application to a garnet-bearing metapelite from Sambagawa (Japan), Journal of Metamorphic Geology, 24, 669–683.
- Vogl, J.J., Foster, D.A., Fanning, C.M., Kent, K.A., Rodgers, D.W. and Diedesch, T., 2012. Timing of extension in the Pioneer metamorphic core complex with implications for the

- spatial-temporal pattern of Cenozoic extension and exhumation in the northern U.S. Cordillera. *Tectonics* 31, 1, TC1008.
- Wannamaker, P.E., Johnston, J., Booker, M., and Stodt, J.A., 1997. Anatomy of the Southern Cordilleran Hingeline, Utah and Nevada, from deep resistivity profiling. *Geophysics*, 62, 1069-1086.
- Washington Division of Geology and Earth Resources, 2008. Digital Geology of the Washington State at 1:100.000 Scale version 2.0.
- Wells, M., Snee, L. and Blythe, A., 2000. Dating of major normal fault systems using thermochronology: An example from the Raft River detachment, Basin and Range, western United States. *Journal of Geophysical Research*, 105, B7, 16303-16327.
- Wernicke, B., 1981. Low-angle normal faults in the Basin and Range Province: nappe tectonics in an extending orogen. *Nature* 291, 645-648.
- Wernicke, B. and Snow, J. K., 1998. Cenozoic tectonism in the central basin and range: Motion of the Sierran Great Valley block. *International Geology Review*, 40, 5, 403-410.
- White, S. H. and Knipe, R. J., 1978. Transformation- and reaction-enhanced ductility in rocks. *Journal of the Geological Society of London*, 135, 513-516.
- White, S.H, 1982. Fault rocks of the Moine Thrust Zone: a guide to their nomenclature. *Texture and Microstructures*. 4, 211-221.
- White, S.R, 2001. Textural and microstructural evidence for semi-brittle flow in natural fault rocks with varied mica contents. *International Journal of Earth Sciences*, 90 , 14-27.
- Whitney, D.L., and Evans, B.W., 2010. Abbreviations for names of rock-forming minerals. *American Mineralogist*, 95, 185-187.
- Wilamowski, A., 2002. Chloritization and polytypism of biotite in the Lomnica granite, Karkonosze Massif, Sudetes, Poland: stable isotope evidence. *Chemical Geology* 182, 2-4, 529-547.
- Williams, L., Herving R.L. and Bjørlykke K., 1997. New evidence for the origin of quartz cements in hydrocarbon reservoirs revealed by oxygen isotopes microanalyses. *Geochimica et Cosmochimica Acta*, 61, 2529-2538.
- Xiong, Y. and Zhai, Y., 1992. Oxygen isotope studies of epithermal systems: A review. *Chinese Journal of Geochemistry*, 11, 4, 329-343.

- Yang, X. Y., O'Hara, K.D., and Moecher, D.P., 1998. Distinction between tectonic mixing and mass transfer processes in a ductile shear zone. *Journal of Structural Geology*, 20, 8, 1089-1103.
- Žalohar, J. and Vrabec, M., 2008. Combined (paleo)stress and kinematic analysis of fault-slip data: the Multiple-slip method. *Journal of Structural Geology*.
- Zanazzi, P.F and Pavese A., 2002. Behavior of micas at high pressure and high temperature. *Reviews in Mineralogy and Geochemistry*, 46, 99-116.
- Zang, W. and Fyfe, W.S. 1995. Chloritization of the hydrothermally altered bedrock at the Igarapé Bahia gold deposit, Carajás, Brazil. *Mineralium Deposita*, 30, 1, 30-38.
- Zeck, H.P, 1974. Cataclasites, hemicataclasites, holocataclasites, blastoditto- and myloblastites-cataclastic rocks. *American Journal of Science*, 274, 1064-1073.
- Zehner, R.E, Coolbaugh, M.F, and Shevenell, L., 2006. Regional Groundwater Geochemical Trends in the Great Basin: Implications for Geothermal Exploration. *GRC Transactions*, 30, 112-124.
- Zhai, W., Sun, X., Sun, W., Su, L., He, X. and Wu, Y., 2009. Geology, geochemistry, and genesis of Axi: A Paleozoic low-sulfidation type epithermal gold deposit in Xinjiang, China. *Ore Geology Reviews*, 36, 4, 265-281.
- Zhang L.G., Liu J.X., Zhou H.B. and Chen Z.S., 1989. Oxygen isotope fractionation in the quartz-water-salt system. *Economic Geology*, 89, 1643-1650.
- Zhang, S., Paterson, M.S. and Cox, S.F. 1994. Porosity and permeability evolution during hot isostatic pressing of calcite aggregates. *Journal of Geophysical Research*, 99, 15741-15760.
- Zheng, Y.F., Fu, B., Li, Y., Xiao, Y. and Li, S., 1998. Oxygen and hydrogen isotope geochemistry of ultrahigh-pressure eclogites from the Dabie Mountains and the Sulu terrane. *Earth and Planetary Science Letters*, 155, 113–129.
- Zheng, Y.F., 1993b. Calculation of oxygen isotope fractionation in hydroxyl-bearing silicates. *Earth and Planetary Science Letters*, 120, 247-263.

APPENDIX
CHAPTER III

Table III.1: List of the microstructural measurements from the BSZ. Ls: Stretching lineament; P dir. : pitch direction.

LOCALITY	ROCK	TYPE	MEASURE	Ls	PITCH	P DIR.	MOVE
Lost Horse Overview	myl	S1	45 S 16	107			
Lost Horse Overview	myl	S1	13 E 21	107			
Lost Horse Overview	myl	S1	65 S 23	112			
Lost Horse Overview	myl	S1	22 E 8	105			
Valley- BT10-52	proto myl	S1	108 S 78	108			
Road Topsection	myl	S1	12 E 25	112			
Road Topsection	myl	S1	18 E 30	114			
SweatHouse	myl	S1	28 E 34	113			
SweatHouse	myl	S1	36 E 32	113			
SweatHouse	myl	S1	33 E 36	105			
SweatHouse	pegmatite	S1	45 E 32	113			
SweatHouse	myl	S1	32 E 23				
SweatHouse	phyllonite	S1	32 E 43				
Lost Horse Overview	myl	S1	45 S 16	107			
Lost Horse Overview	myl	S1	22 E 8	105			
Lost Horse Overview	myl	S1	12 E 25	112			
BT08-006	protolith	S1	40 E 25				
BT08-007	protolith	S1	50 E 17				
BT08-008	protolith	S1	48 E 21				
BT08-009	protolith	S1	35 E 45				
BT08-012	protolith	S1	34 E 32				
BT08-013	protolith	S1	49 E 39				
BT08-014	protolith	S1	35 E 33	114			
BT08-015	protolith	S1	24 E 24				
BT08-016	protolith	S1	58 E 21				
BT08-017	protolith	S1	40 E 38				
BT08-024	myl	S1	35 E 16	119			
BT08-026	myl	S1	48 E 16	107			
BT08-027	myl	S1	44 E 29	109			
BT08-029	myl	S1	30 E 15				
BT08-030	myl	S1	30 E 11				
BT08-031	Umyl+myl	S1	56 E 11	110			
BT08-032	myl	S1	3 E 20	114			
BT08-033	Umyl+myl	S1	21 E 13	110			
BT08-035	myl	S1	25 E 40	108			
BT08-037	myl	S1	38 E 14	126			
BT08-038	myl	S1	35 E 23	107			
BT08-039	myl	S1	16 E 18	114			
BT08-040	UMyl	S1	19 E 20	119			
BT08-041	myl	S1	19 E 21	119			
BT08-042	UMyl	S1	27 E 20	116			
BT08-043	myl	S1	25 E 20	110			
BT08-044	Umyl+myl	S1	25 E 23	112			
BT08-045	myl	S1	26 E 28	110			
BT08-046	myl	S1	30 E 10	120			

Table III.1: List of the microstructural measurements from the BSZ. Ls: Stretching lineament; P dir. : pitch direction.

LOCALITY	ROCK	COMMENTS	STRIKE	Ls	PITCH	P DIR.	MOVE
BT08-047	myl	S1	20 E 11	110			
BT08-048	myl	S1	24 E 24	114			
BT08-049	Umyl+myl	S1	29 E 16	112			
BT08-050	Umyl	S1	35 E 26	112			
BT08-051	myl	S1	35 E 27	112			
BT08-052	myl	S1	25 E 15	114			
BT08-053	myl	S1	27 E 9	114			
BT08-063	myl	S1	24 E 18	115			
BT08-064	myl	S1	10 E 20	110			
BT08-065	myl	S1	30 E 12	114			
BT08-066	myl	S1	34 E 19	114			
BT08-067	myl	S1	29 E 15	110			
BT08-068	myl	S1	49 E 12	114			
BT08-069	myl	S1	26 E 19	114			
BT08-070	myl	S1	48 E 21	110			
BT08-071	Umyl+myl	S1	34 E 14	112			
BT08-073	Umyl+myl	S1	44 E 22	115			
BT08-074	myl	S1	30 E 14	106			
BT08-075	myl	S1	36 E 18	115			
BT08-076	myl	S1	46 E 20	115			
BT08-077	myl	S1	28 E 10	116			
BT08-078	myl	S1	38 E 22	113			
BT08-079	myl	S1	40 E 12	118			
BT08-080	myl	S1	75 E 20	120			
BT09-080	myl	S1	60 E 24	110			
BT09-081	Umyl	S1	170 E 18				
BT09-087	Proto myl	S1	35 E 38	120			
BT09-089	myl	S1	5 E 27	122			
BT09-090	myl	S1	32 E 38	120			
BT09-091	ahl-rich brecci	S1	65 S 32	125			
BT09-095	myl	S1	16 E 30	110			
BT09-100	myl	S1	11 E 30	110			
BT09-102	myl	S1	10 E 28	108			
BT09-104	myl	S1	7 E 33	102			
BT09-105	myl	S1	5 E 34	105			
BT09-106	myl	S1	15 E 35	107			
BT09-108	myl	S1	148 E 28	110			
BT09-109	myl	S1	170 E 25	120			
BT09-110	myl	S1	175 E 28				
BT09-111	myl	S1	5 E 22	110			
BT09-112	myl	S1	25 E 24	110			
BT09-114	myl	S1	155 E 29	102			
SweatHouse	pegmatite	S1	38 E 37	115			
SweatHouse	pegmatite	S1	16 E 41	104			
SweatHouse	Umyl	S1	34 E 34	114			

Table III.1: List of the microstructural measurements from the BSZ. Ls: Stretching lineament; P dir. : pitch direction.

LOCALITY	ROCK	COMMENTS	STRIKE	Ls	PITCH	P DIR.	MOVE
SweatHouse	myl	S1	45 S 41	125			
Lost Horse quarry	myl	S1	28 E 26	109			
SweatHouse	myl	Qz vein+geode	40 E 46	125			
SweatHouse	myl	Qz vein+geode	20 E 80		0		D
SweatHouse	myl	Qz vein+geode	28 E 79				
SweatHouse	myl	Qz vein+geode	28 W 65				
SweatHouse	myl	Qz vein+geode	3 W 62				
SweatHouse	myl	Qz vein+geode	27 W 69				
SweatHouse	myl	Qz vein+geode	24 W 40	143			
SweatHouse	myl	Qz vein+geode	24 E 46	124			N
SweatHouse	myl	Qz vein+geode	20 W 46				
SweatHouse	myl	Qz vein+geode	20 W 66		13	N	S
SweatHouse	myl	Qz vein+geode	32 W 76				
SweatHouse	myl	Qz vein+geode	43 E 54	132			N
SweatHouse	myl	Qz vein+geode	12 E 70				
SweatHouse	myl	Qz vein+geode	33 E 25	23			D
SweatHouse	myl	Qz vein+Epd+Chl	6 W 56		62	N	ND
SweatHouse	myl	Qz vein+Epd+Chl	25 W 76				
SweatHouse	myl	Qz vein+Epd+Chl	21 W 63				
SweatHouse	myl	Qz vein+Epd+Chl	24 W 69		80	N	N
SweatHouse	myl	Qz vein+Epd+Chl	15 W 65		52	S	ND
SweatHouse	myl	Qz vein+Epd+Chl	28 W 77		52	S	N
SweatHouse	myl	Qz vein+Epd+Chl	53 S 75		76	N	N
SweatHouse	myl	Qz vein+Epd+Carb	26 W 76		63	N	I
SweatHouse	myl	Qz vein+Epd+Carb	27 E 88		12	N	S
SweatHouse	myl	Qz vein+Epd	4 W 78				
SweatHouse	myl	Qz vein+Epd	37 E 88				
SweatHouse	myl	Qz vein+Epd	26 W 77				
SweatHouse	myl	Qz vein+Epd	38 E 89				
SweatHouse	myl	Qz vein+Epd	20 W 59		57	S	
SweatHouse	myl	Qz vein+Epd	27 W 71				
SweatHouse	myl	Qz vein+Epd	26 E 81		90		N
SweatHouse	myl	Qz vein+Epd	13 W 54				
SweatHouse	myl	Qz vein+Epd	14 E 67		89	N	
SweatHouse	myl	Qz vein+Epd	25 W 65				
SweatHouse	myl	Qz vein+Epd	22 W 68		84	N	N
SweatHouse	pegmatite	Qz vein+Epd	16 E 83		90		N
SweatHouse	myl	Qz vein+Epd	24 W 60		85	S	N
SweatHouse	myl	Qz vein+Epd	30 E 58		64	N	N
SweatHouse	myl	Qz vein+Epd	28 E 56		77	N	N
SweatHouse	myl	Qz vein+Epd	26 W 76		87	S	N
SweatHouse	myl	Qz vein+Epd	48 S 44	127			N
SweatHouse	myl	Qz vein+Epd	43 E 82		62	N	N
SweatHouse	myl	Qz vein+Epd	42 N 85		37	N	S
SweatHouse	myl	Qz vein+Epd	47 S 79		61	NE	SN

Table III.1: List of the microstructural measurements from the BSZ. Ls: Stretching lineament; P dir. : pitch direction.

LOCALITY	ROCK	COMMENTS	STRIKE	Ls	PITCH	P DIR.	MOVE
SweatHouse	myl	Qz vein+Epd	45 S 79		78	NE	N
SweatHouse	myl	Qz vein+Epd	44 E 47	124			
SweatHouse	myl	Qz vein+Epd	44 E 47		2	S	D
SweatHouse	myl	Qz vein+Chl	35 W 83		61	N	
Lost Horse quarry	myl	Qz vein+Chl	6 E 87				
Lost Horse quarry	myl	Qz vein+Chl	23 N 38		58	S	N
Lost Horse quarry	myl	Qz vein+Chl	28 E 64		89	S	N
Lost Horse quarry	myl	Qz vein+Chl	7 W 52		77	N	N
Lost Horse quarry	myl	Qz vein+Chl	14 W 87		83	N	N
Lost Horse quarry	myl	Qz vein+Chl	10 W 56		86	N	N
Lost Horse quarry	myl	Qz vein+Chl	9 W 49		55	S	N
Lost Horse quarry	myl	Qz vein+Chl	112 S 83		84	E	N
Lost Horse quarry	myl	Qz vein+Chl	1 E 54		77	N	N
Lost Horse quarry	myl	Qz vein+Chl	9 E 72		83	S	N
Valley- BT10-52	proto myl	Qz vein+Chl	28 E 89		90		N
Road Topsection	myl	Qz vein Epd+Chl	30 W 85		90		N
Road Topsection	myl	Qz vein Epd+Chl	164 W 53		34	S	S
Road Topsection	myl	Qz vein Epd+Chl	151 W 76		90		N
Road Topsection	myl	Qz vein Epd+Chl	150 W 54		86	N	N
Road Topsection	myl	Qz vein Epd+Chl	17 W 45				
Road Topsection	myl	Qz vein Epd+Chl	27 W 69		80	N	N
Road Topsection	myl	Qz vein Epd+Chl	158 W 74		77	N	N
Road Topsection	myl	Qz vein Epd+Chl	158 W 74		37	S	SN
Road Topsection	myl	Qz vein Epd+Chl	144 W 72		67	N	N
Road Topsection	myl	Qz vein Epd+Chl	144 W 72		25	S	SN
Road Topsection	myl	Qz vein Epd+Chl	173 E 35	112			
Road Topsection	myl	Qz vein Epd+Chl	25 E 88		64	S	N
Road Topsection	myl	Qz vein Epd+Chl	11 W 86		75	N	N
Road Topsection	myl	Qz vein Epd+Chl	161 E 88		70	N	N
Road Topsection	myl	Qz vein Epd+Chl	12 E 63		80	N	N
Road Topsection	myl	Qz vein Epd+Chl	8 E 44		90		N
Road Topsection	myl	Qz vein Epd+Chl	2 W 74		83	N	N
Road Topsection	myl	Qz vein Epd+Chl	18 W 75		89	N	N
Road Topsection	myl	Qz vein Epd+Chl	28 W 77		80	N	N
Road Topsection	myl	Qz vein Epd+Chl	160 W 82		62	S	ND
Road Topsection	myl	Qz vein Epd+Chl	160 W 82		63	N	NS
Lost Horse Overview	myl	Qz vein	93 N 81				
Lost Horse Overview	myl	Qz vein	164 E 33				
Lost Horse Overview	myl	Qz vein	100 S 14				
Valley- BT10-49	protolith	Qz vein	40 E 68		81	S	N
Valley- BT10-49	protolith	Qz vein	34 E 63		83	N	N
Valley- BT10-49	protolith	Qz vein	44 E 54		84	N	N
Valley- BT10-49	protolith	Qz vein	35 E 71		74	N	N
Valley- BT10-49	protolith	Qz vein	23 W 85		70	N	N
Valley- BT10-49	protolith	Qz vein	5 E 59		50	S	N

Table III.1: List of the microstructural measurements from the BSZ. Ls: Stretching lineament; P dir. : pitch direction.

LOCALITY	ROCK	COMMENTS	STRIKE	Ls	PITCH	P DIR.	MOVE
Valley- BT10-49	protolith	Qz vein	15 E 67				
Valley- BT10-49	protolith	Qz vein	22 W 89		67	N	N
SweatHouse	myl	Qz vein	35 E 84				
SweatHouse	myl	Qz vein	15 E 34				
SweatHouse	myl	Qz vein	34 E 76				
SweatHouse	myl	Qz vein	35 E 84				
SweatHouse	myl	Qz vein	38 W 85		47	N	N
SweatHouse	myl	Qz vein	24 E 83		30	N	S
SweatHouse	myl	Qz vein	28 E 89				
SweatHouse	myl	Qz vein	16 E 87				
SweatHouse	myl	Qz vein	23 W 89				N
SweatHouse	myl	Qz vein	36 W 83				
SweatHouse	myl	Qz vein	14 E 75		85	N	N
SweatHouse	myl	Qz vein	38 W 85		47	N	?
Lost Horse quarry	myl	Qz vein	9 E 72		37	N	DN
Lost Horse quarry	myl	Qz vein	30 W 66				
SweatHouse	myl	Qz tension gashe	34 E 76				D
SweatHouse	myl	Chl tension gashe	30 W 73				
SweatHouse	myl	Chl tension gashe	8 W 70				
SweatHouse	myl	Chl tension gashe	38 W 89				
SweatHouse	myl	Chl tension gashe	2 W 66				
SweatHouse	myl	Chl tension gashe	10 W 80				
SweatHouse	myl	Chl tension gashe	36 E 77				
SweatHouse	myl	Chl tension gashe	33 E 80				
SweatHouse	myl	Chl tension gashe	27 E 70				
SweatHouse	myl	Tardive fault	116 S 70		81	E	N
SweatHouse	myl	Tardive fault	110 S 70		81	E	N
SweatHouse	myl	Faults below breccia	37 E 70		68	N	N
SweatHouse	myl	Faults below breccia	44 E 65		66	N	N
SweatHouse	myl	Faults below breccia	50 E 30	90			
SweatHouse	myl	fault+cataclasite	175 W 73		10	S	S
SweatHouse	myl	fault+cataclasite	6 W 60		4	S	D
SweatHouse	myl	fault+cataclasite	15 W 72		12	S	D
SweatHouse	myl	fault+cataclasite	4 W 75		4	S	D
SweatHouse	myl	fault+cataclasite	24 E 87		64	N	I
SweatHouse	myl	fault+cataclasite	24 W 80		79	S	N
SweatHouse	myl	fault+calcite	35 W 78		79	S	
SweatHouse	myl	fault+calcite	35 W 78		88	S	N
Valley- BT10-52	proto myl	fault	19 E 89		83	S	N
Valley- BT10-52	proto myl	fault	18 E 89		90		N
Valley- BT10-52	proto myl	fault	20 E 89		89	N	N
Valley- BT10-52	proto myl	fault	20 E 89		85	S	N
Lost Horse Overview	myl	fault	45 E 54		70	N	N
SweatHouse	myl	fault	10 E 43	105			N
SweatHouse	myl	fault	23 E 89				N

Table III.1: List of the microstructural measurements from the BSZ. Ls: Stretching lineament; P dir. : pitch direction.

LOCALITY	ROCK	COMMENTS	STRIKE	Ls	PITCH	P DIR.	MOVE
SweatHouse	myl	fault	12 E 70				N
SweatHouse	myl	fault	45 S 69		65	NE	N
SweatHouse	myl	fault	31 E 60		86	N	N
SweatHouse	phylionite	fault	25 E 36		55	N	S
Lost Horse quarry	myl	Epd+Carb	3 E 64		70	S	N
SweatHouse	myl	Epd vein	12 W 89		14	S	S
SweatHouse	myl	Epd vein	20 W 89				
SweatHouse	myl	Epd vein	14 E 75		75		
SweatHouse	myl	Epd vein	50 E 22	116			
SweatHouse	myl	Epd vein	40 E 85		60	N	
SweatHouse	myl	Epd vein	35 E 80				
SweatHouse	myl	Epd vein	24 E 89				
SweatHouse	myl	Epd vein	35 W 77		25	N	
SweatHouse	myl	Epd vein	20 W 59		57	S	
SweatHouse	Umyl	Epd vein	35 E 34	115			
SweatHouse	Umyl	Epd vein	35 E 34	55			
SweatHouse	myl	Epd vein	26 E 80		90		N
SweatHouse	myl	Epd vein	22 E 78		24	S	ND
SweatHouse	myl	Epd vein	22 E 78		24	S	D
SweatHouse	myl	Epd vein	36 E 84		77	N	N
SweatHouse	myl	Epd vein	34 E 85		65	N	N
SweatHouse	myl	Chl+Epd	45 W 52				N
SweatHouse	myl	Chl+Epd	32 W 74				
SweatHouse	myl	Chl+Epd	15 W 61		79		N
SweatHouse	myl	Chl+Epd	28 W 62				
SweatHouse	myl	Chl+Epd	15 E 76				
SweatHouse	myl	Chl+Epd	18 E 76				
SweatHouse	myl	Chl+Epd	15 E 85				
SweatHouse	myl	Chl+Epd	20 E 70				
SweatHouse	myl	Chl+Epd	20 E 78				
SweatHouse	myl	Chl+Epd	14 E 77				
SweatHouse	myl	Chl+Epd	34 E 74		80	N	N
SweatHouse	myl	Chl+Epd	24 W 69		10	S	D
Lost Horse Overview	myl	Chl vein	22 E 79		82	N	N
SweatHouse	myl	Cataclasite	20 W 46				
SweatHouse	myl	Cataclasite	20 W 66		30	N	S
SweatHouse	myl	Cataclasite	27 E 79		6	N	S
SweatHouse	myl	Cataclasite	24 W 55				N
Lost Horse quarry	myl	Cataclasite	10 W 85		83	S	N
Lost Horse Overview	myl	C' band myl.	164 E 40				
SweatHouse	myl	C' band myl.	40 E 50	108			
Lost Horse Overview	myl	C band myl.	145 E 30				
Lost Horse Overview	myl	S band myl.	64 N 22				

Table III.2: List of samples from the BSZ.

Samples	Description	Localities	UTM (11N)	WGS84	Elevation
			(m)	(m)	(m)
BT08-001	Granodiorite	Lost Horse Canyon	0700563	5112636	
BT08-002	Granodiorite	Lost Horse Canyon	0700203	5112842	
BT08-003	Granodiorite	Lost Horse Canyon	0707449	5111126	
BT08-004	Granodiorite	Lost Horse Canyon	0708239	5110924	
BT08-005	Peg+Granodiorite ultramylonite	Lost Horse Canyon	0711646	5109137	
BT08-006	Granodiorite mylonite	Sweat House Quarry	0713117	5144162	
BT08-007	Granodiorite mylonite	Sweat House Quarry	0713126	5144142	
BT08-008	Granodiorite mylonite	Sweat House Quarry	0713132	5144140	
BT08-009	Granodiorite mylonite	Sweat House Quarry	0713164	5144151	
BT08-010	Mafic dyke	Sweat House Quarry	0713159	5144118	
BT08-011	Granodiorite mylonite	Sweat House Quarry	0713015	5143894	
BT08-012	Granodiorite mylonite	Sweat House Quarry	0713184	5144146	
BT08-013	Granodiorite mylonite	Sweat House Quarry	0713177	5144116	
BT08-014	Granodiorite mylonite	Sweat House Quarry	0713176	5144113	
BT08-015	Granodiorite mylonite	Sweat House Quarry	0713198	5144128	
BT08-016	Granodiorite mylonite	Sweat House Quarry	0713191	5144112	
BT08-017	Granodiorite mylonite	Sweat House Quarry	0713238	5144107	
BT08-018	Granodiorite mylonite	Sweat House Quarry	0713251	5144109	
BT08-019	Pegmatite	Sweat House Quarry	0713260	5144108	
BT08-020	Granodiorite mylonite	Sweat House Quarry	0713270	5144110	
BT08-021	Granodiorite mylonite	Sweat House Quarry	0713290	5144109	
BT08-022	Brecchia	Sweat House Quarry	0713412	5144155	
BT08-023	Brecchia	Sweat House Quarry	0713490	5144157	
BT08-024	Granodiorite mylonite	Lost Horse Canyon (top)	0710782	5109957	1675
BT08-025	Granodiorite ultramylonite	Lost Horse Canyon (top)	0710768	5109980	1685
BT08-026	Granodiorite mylonite	Lost Horse Canyon (top)	0710768	5109980	1685
BT08-027	Granodiorite mylonite	Lost Horse Canyon (top)	0710791	5109986	1695
BT08-028	Metabasite	Lost Horse Canyon (top)	0710791	5109986	1695
BT08-029	Granodiorite mylonite	Lost Horse Canyon (top)	0710781	5109986	1706
BT08-030	Granodiorite mylonite	Lost Horse Canyon (top)	0710805	5109968	1713
BT08-031	Granodiorite ultramylonite/mylonite	Lost Horse Canyon (top)	0710824	5109980	1722
BT08-032	Granodiorite mylonite	Lost Horse Canyon (top)	0710818	5109978	1725
BT08-033	Granodiorite ultramylonite/mylonite	Lost Horse Canyon (top)	0710848	5109980	1735
BT08-034	Granodiorite mylonite	Lost Horse Canyon (top)	0710848	5109980	1735
BT08-035	Granodiorite mylonite	Lost Horse Canyon (top)	0710846	5109982	1745
BT08-036	Pegmatite	Lost Horse Canyon (top)	0710870	5109985	1758
BT08-037	Granodiorite mylonite	Lost Horse Canyon (top)	0710870	5109985	1758
BT08-038	Granodiorite mylonite	Lost Horse Canyon (top)	0710876	5110031	1770
BT08-039	Granodiorite mylonite	Lost Horse Canyon (top)	0710872	5110046	1780
BT08-040	Granodiorite ultramylonite	Lost Horse Canyon (top)	0710917	5110054	1810
BT08-041	Granodiorite mylonite	Lost Horse Canyon (top)	0710917	5110054	1810
BT08-042	Granodiorite ultramylonite	Lost Horse Canyon (top)	0710914	5110112	1824

Table III.2: List of samples from the BSZ.

Samples	Description	Localities	UTM (11N)	WGS84	Elevation
			(m)	(m)	(m)
BT08-043	Granodiorite mylonite	Lost Horse Canyon (top)	0710924	5110088	1832
BT08-044	Granodiorite ultramylonite/mylonite	Lost Horse Canyon (top)	0710930	5110087	1839
BT08-045	Granodiorite mylonite	Lost Horse Canyon (top)	0710919	5110125	1849
BT08-046	Granodiorite mylonite	Lost Horse Canyon (top)	0710925	5110111	1843
BT08-047	Granodiorite mylonite	Lost Horse Canyon (top)	0710936	5110097	1843
BT08-048	Granodiorite mylonite	Lost Horse Canyon (top)	0710934	5110081	1843
BT08-049	Granodiorite ultramylonite/mylonite	Lost Horse Canyon (top)	0710932	5110068	1841
BT08-050	Granodiorite ultramylonite	Lost Horse Canyon (top)	0710925	5110059	1842
BT08-051	Granodiorite mylonite	Lost Horse Canyon (top)	0710925	5110059	1842
BT08-052	Granodiorite mylonite	Lost Horse Canyon (top)	0710925	5110048	1839
BT08-053	Granodiorite mylonite	Lost Horse Canyon (top)	0710921	5110035	1835
BT08-054	Granodiorite mylonite	Blodgett Canyon			
BT08-055	Granodiorite mylonite	Blodgett Canyon			
BT08-056	Granodiorite mylonite	Blodgett Canyon			
BT08-057	Granodiorite mylonite	Blodgett Canyon			
BT08-058	Granodiorite mylonite	Blodgett Canyon			
BT08-059	Granodiorite mylonite	Blodgett Canyon			
BT08-060	Granodiorite mylonite	Blodgett Canyon			
BT08-061	Granodiorite mylonite	Blodgett Canyon			
BT08-062	Granodiorite mylonite	Blodgett Canyon			
BT08-063	Granodiorite mylonite	Lost Horse Quarry (bottom)	0711628	5109112	1324
BT08-064	Granodiorite mylonite	Lost Horse Quarry (bottom)	0711642	5109119	1334
BT08-065	Granodiorite mylonite	Lost Horse Quarry (bottom)	0711652	5109115	1349
BT08-066	Granodiorite mylonite	Lost Horse Quarry (bottom)	0711664	5109129	1361
BT08-067	Granodiorite mylonite	Lost Horse Quarry (bottom)	0711637	5109155	1371
BT08-068	Granodiorite mylonite	Lost Horse Quarry (bottom)	0711629	5109160	1382
BT08-069	Granodiorite mylonite	Lost Horse Quarry (bottom)	0711589	5109149	1394
BT08-070	Granodiorite mylonite	Lost Horse Quarry (bottom)	0711592	5109202	1406
BT08-071	Granodiorite ultramylonite	Lost Horse Quarry (bottom)	0711596	5109211	1414
BT08-072	Pegmatite	Lost Horse Quarry (bottom)	0711588	5109216	1423
BT08-073	Granodiorite ultramylonite	Lost Horse Quarry (bottom)	0711588	5109216	1423
BT08-074	Granodiorite mylonite	Lost Horse Quarry (bottom)	0711592	5109241	1435
BT08-075	Granodiorite mylonite	Lost Horse Quarry (bottom)	071578	5109269	1459
BT08-076	Granodiorite mylonite	Lost Horse Quarry (bottom)	0711594	5109293	1482
BT08-077	Granodiorite mylonite	Lost Horse Quarry (bottom)	0711595	5109367	1500
BT08-078	Granodiorite mylonite	Lost Horse Quarry (bottom)	0711604	5109388	1519
BT08-079	Granodiorite mylonite	Lost Horse Quarry (bottom)	0711596	5109426	1549
BT08-080	Granodiorite mylonite	Lost Horse Quarry (bottom)	0711575	5109472	1574
BT09-080	Granodiorite mylonite	Twins lake -Lost Horse canyon	0693025	5114292	2032
BT09-081	Granodiorite ultramylonite	Twins lake -Lost Horse canyon	0712552	5113078	1651

Table III.2: List of samples from the BSZ.

Samples	Description	Localities	UTM (11N) (m)	WGS84 (m)	Elevation (m)
BT09-082	Granodiorite mylonite	Twins lake -Lost Horse canyon	0712552	5113078	1651
BT09-083	Chlorite-Qz rock	Sweat House Quarry	0713531	5144095	1196
BT09-084	Chl-rich breccia	Sweat House Quarry	0713496	5144152	1233
BT09-085	Pegmatite	Sweat House Quarry	0713439	5144202	1255
BT09-086	Granodiorite mylonite	Sweat House Quarry	0713426	5144214	1259
BT09-087	Granodiorite mylonite	Sweat House Quarry	0711230	5144710	1509
BT09-088	Micaschiste	Sweat House Quarry	0711230	5144710	1509
BT09-089	Granodiorite mylonite	Sweat House Quarry	0712691	5144426	1312
BT09-090	Granodiorite mylonite	Sweat House Quarry	0713004	5144151	1241
BT09-091	Chl-rich breccia	Sweat House Quarry	0713350	5144037	1209
BT09-092	Chl-rich breccia	Sweat House Quarry	0713324	5144031	1223
BT09-093	Chl-rich breccia	Sweat House Quarry	0713340	5144059	1236
BT09-094	Chl-rich breccia	Sweat House Quarry	0713383	5144068	1245
BT09-095	Granodiorite mylonite	Blodgett Canyon	0712984	5128064	1568
BT09-096	Chl-rich breccia	Blodgett Canyon	0712710	5127736	1310
BT09-097	Granodiorite	Blodgett Canyon	0709500	5128190	1491
BT09-098	Granodiorite	Blodgett Canyon	0709500	5128190	1491
BT09-099	Chl-rich breccia	Blodgett Canyon	0712802	5127810	1340
BT09-100	Granodiorite mylonite	Blodgett Canyon	0712968	5128043	1554
BT09-101	U-Granodiorite myloniteo	Blodgett Canyon	0712968	5128043	1554
BT09-102	Granodiorite mylonite	Blodgett Canyon	0712981	5128024	1539
BT09-103	Qz vein	Blodgett Canyon	0713019	5128017	1521
BT09-104	Granodiorite mylonite	Blodgett Canyon	0713019	5128017	1521
BT09-105	Granodiorite mylonite	Blodgett Canyon	0713038	5128000	1504
BT09-106	Granodiorite mylonite	Blodgett Canyon	0713041	5127973	1487
BT09-107	-				
BT09-108	Granodiorite mylonite	Blodgett Canyon	0713039	5127950	1467
BT09-109	Granodiorite mylonite	Blodgett Canyon	0713056	5127940	1443
BT09-110	Granodiorite mylonite	Blodgett Canyon	0713073	5127916	1426
BT09-111	Granodiorite mylonite	Blodgett Canyon	0713030	5127894	1403
BT09-112	Granodiorite mylonite	Blodgett Canyon	0712933	5127897	1401
BT09-113	Metabasite	Blodgett Canyon	0712933	5127897	1401
BT09-114	Granodiorite mylonite	Blodgett Canyon	0712875	5127885	1374
BT09-115	Diorite	Blodgett Canyon	0712777	5127848	1351
BT09-116	Granodiorite	Sapphyre block	0278414	5119540	1544
BT09-117	Granodiorite	Sapphyre block	0269020	5131284	1266

Table III.2: List of samples from the BSZ.

Samples	Description	Localities	UTM (11N)	WGS84	Elevation
			(m)	(m)	(m)
BT10-001	Qz+Epd vein	Sweat House	0713050	5144151	1171
BT10-002	Qz+Epd vein	Sweat House	0713050	5144151	1171
BT10-003	Granodiorite mylonite	Sweat House	0713050	5144151	1171
BT10-004	Bleached Granodiorite	Sweat House	0713050	5144151	1171
BT10-005	Silicified Granodiorite	Sweat House	0713050	5144151	1171
BT10-006	Metabasite	Sweat House	0713050	5144151	1171
BT10-007	Calcite in Epd+ChalcoPy+Si fracture	Sweat House	0713050	5144151	1171
BT10-008	Epdt vein + Chl tension gashes	Sweat House	0713050	5144151	1171
BT10-009	Pure Qz vein cross-cutting S1	Sweat House	0713117	5144162	
BT10-010	Phyllonite	Sweat House	0713164	5144151	1171
BT10-011	Phyllonite	Sweat House	0713164	5144151	1171
BT10-012	Parrallelized Qz vein with geode	Sweat House	0713164	5144151	1171
BT10-013	Mineralized Qz vein with geode	Sweat House	0713164	5144151	1171
BT10-014	Pure Qz vein cross-cutting S1	Sweat House	0713164	5144151	1171
BT10-015	Qz+Epd+Chl vein in bleached grano.	Sweat House	0713164	5144151	1171
BT10-016	BLEached Granodiorite	Sweat House	0713164	5144151	1171
BT10-017	Granodiorite mylonite	Sweat House	0713184	5144146	
BT10-018	Metabasite	Sweat House	0713176	5144113	
BT10-019	Mineralized Qz vein with geode	Sweat House	0713164	5144151	1171
BT10-020	Bleached Granodiorite	Sweat House	0713164	5144151	1171
BT10-021	Metabasite	Sweat House	0713164	5144151	1171
BT10-022	Qz+Epd vein	Sweat House	0713164	5144151	1171
BT10-023	Partially silicified grano. mylonite	Sweat House	0713164	5144151	1171
BT10-024	Silicified Granodiorite mylonite	Sweat House	0713164	5144151	1171
BT10-025	Cataclasite	Sweat House	0713164	5144151	1171
BT10-026	Phyllonite	Sweat House	0713164	5144151	1171
BT10-027	Mineralisation	Sweat House	0713164	5144151	1171
BT10-028	Chl vein	Sweat House	0713164	5144151	1171
BT10-029	Granodiorite ultramylonite	Sweat House			
BT10-030	Parrallelized Qz vein	Sweat House			
BT10-031	Mineralized Qz vein, vertical in a fault	Sweat House	0713490	5144157	
BT10-032	Cataclased Granodiorite mylonite	Sweat House	0713490	5144157	
BT10-033	Transition layer with carbonates	Sweat House	0713490	5144157	
BT10-034	Cataclasite (vertical pipe)	Lost Horse Quarry	0711623	5109118	
BT10-035	Cataclasite (horizontal pipe)	Lost Horse Quarry	0711623	5109118	
BT10-036	Cataclasite (top section)	Lost Horse Quarry	0711575	5109472	
BT10-037	Bleached/silicified Grano. mylonite	Lost Horse Quarry	0711575	5109472	
BT10-038	Pseudo-cataclasite	Lost Horse Quarry	0711575	5109472	
BT10-039	Cataclasite	Lost Horse Quarry	0711575	5109472	
BT10-040	Granodiorite ultramylonite	Lost Horse Quarry	0711575	5109472	
BT10-041	Granodiorite mylonite (block)	Lost Horse Quarry	0711623	5109118	

Table III.2: List of samples from the BSZ.

Samples	Description	Localities	UTM (11N)	WGS84	Elevation
			(m)	(m)	(m)
BT10-042	Qz vein cross-cutting S1	Road LostHorse Overview	0712098	5111651	1678
BT10-043	Qz vein cross-cutting S1	Lost Horse Overview	0710867	5110081	
BT10-044	Granodiorite mylonite	Lost Horse Overview	0710867	5110081	
BT10-045	Granodiorite mylonite	Lost Horse Overview	0710867	5110081	
BT10-046	Granodiorite ultramylonite	Lost Horse Overview	0710867	5110081	
BT10-047	Diorite	Lost Horse Overview	0710867	5110081	
BT10-048	Granodiorite	Protolythe	0700177	5112791	1597
BT10-049	Granodiorite	Protolythe	0704713	5111266	
BT10-050	Granodiorite	Protolythe	0704713	5111266	1477
BT10-051	Mineralized Qz vein	Protolythe	0704713	5111266	
BT10-052	Granodiorite proto-mylonite	Protolythe	0707347	5111149	1400
BT10-053	Cataclasite	Road LostHorse Overview	0712562	5113084	1642
BT10-054	Qz vein transposed	Road LostHorse Overview	0712562	5113084	
BT10-055	Qz vein cross-cutting S1	Road LostHorse Overview	0712562	5113084	
BT10-056	Qz vein cross-cutting S1	Road LostHorse Overview	0712562	5113084	

APPENDIX
CHAPTER IV

Table IV.1: X-Ray Diffraction analysis, and semi-qualitative proportion of minerals.

Samples	Rock	Distance	Intensity (cps)							Quartz peak Deviation
			Micas	Kaolinite	Phyllosilicate	Quartz	K-Feldspar	Plagioclase	Calcite	
			8.80	12.41	19.90	26.65	27.50	27.9-28.0	29.43	
BT09-80	Protolith	-1060	897.50	123.33	19.00	10449.17	5869.17	4757.50	26.58	0.07
BT08-01	Protolith	-860	369.17	113.33	20.00	5522.50	1891.67	5516.67	26.66	0.01
BT08-03	Protolith	-710	504.17	100.83	22.00	5645.00	2292.50	4630.00	26.56	0.09
BT10-41	Mylonite	-420	695.83	467.50	20.00	4215.00	991.67	3146.67	26.50	0.15
BT08-30M	Mylonite	-240	349.17	107.50	22.36	5690.00	1402.50	2977.50	26.50	0.15
BT08-31M	Mylonite	-230	317.50	81.67	19.00	6822.50	1432.50	2891.67	26.62	0.03
BT08-78	Mylonite	-180	115.83	132.50	28.00	8015.00	2488.33	2350.00	26.50	0.15
BT10-44	Mylonite	-180	309.17	169.17	15.00	6668.33	1095.83	3441.67	26.54	0.11
BT10-45	Mylonite	-160	1165.00	106.67	27.00	5716.67	1520.83	3304.17	26.56	0.09
BT08-80	Mylonite	-120	265.00	89.17	24.00	7545.83	1495.83	2878.33	26.68	0.03
BT08-44M	Mylonite	-70	362.50	105.83	22.00	10025.00	909.17	3856.67	26.60	0.05
BT08-45	Mylonite	-60	652.50		27.00	6253.33	1286.67	4333.33	26.58	0.07
BT10-03	Mylonite	-50	961.67	361.67	20.00	6615.00	1166.67	3989.17	26.66	0.01
BT10-17	Mylonite	-40	1713.33	319.17	23.26	4996.67	637.50	1995.00	26.66	0.01
BT08-31U	Ultramylonite	-230	769.17	58.33	22.00	6450.83	941.67	2284.17	26.66	0.01
BT08-40U	Ultramylonite	-100	1357.50	73.33	37.75	5788.33	519.17	2885.00	26.58	0.07
BT08-44U	Ultramylonite	-80	615.83		16.00	15008.33		760.83	26.64	0.01
BT10-40	Ultramylonite	-70	1254.17	61.67	18.00	5116.67	415.00	2454.17	26.50	0.15
BT10-04	Bleached	-50	266.67	812.50	17.00	261.67	2184.17	15899.17	26.80	0.15
BT10-16	Bleached	-40	261.67	440.83	26.00	1364.17	378.33	8969.17	26.68	0.03
BT10-35	Cataclasite	-410	262.50	435.83	32.00	7187.50	3372.50	5081.67	26.64	0.01
BT10-53	Cataclasite	-60	73.33	1555.83	38.00	3764.17		2453.33	26.66	0.01

Table IV.1: X-Ray Diffraction analysis, and semi-qualitative proportion of minerals.

	Rock	Distance	Phyllosilicates	Quartz	K-Feldspar	Plagioclase	Calcite	Undosed
			(%)	(%)	(%)	(%)	(%)	(%)
BT09-80	Protolith	-1060	1.6	25.1	43.2	29.4	0.0	0.7
BT08-01	Protolith	-860	2.4	20.8	24.1	52.3	0.0	0.3
BT08-03	Protolith	-710	2.7	21.9	30.2	44.2	0.0	0.9
	Average		2.2 ± 0.6	22.6 ± 2.2	32.5 ± 9.7	42.0 ± 11.6	0.0	0.6 ± 0.3
BT08-41	Mylonite	-420	3.1	22.3	17.0	40.1	0.0	17.5
BT08-30M	Mylonite	-240	3.3	28.9	24.3	38.2	0.0	5.2
BT08-31M	Mylonite	-230	2.8	32.6	22.5	36.9	0.0	5.3
BT08-78	Mylonite	-180	4.3	35.2	34.1	24.4	0.0	2.0
BT10-44	Mylonite	-180	2.2	29.0	15.2	40.0	0.0	13.6
BT10-45	Mylonite	-160	4.0	26.7	24.0	40.4	0.0	4.9
BT08-80	Mylonite	-120	3.5	34.9	23.4	34.9	0.0	3.2
BT08-44M	Mylonite	-70	3.0	38.2	13.1	39.2	0.0	6.4
BT08-45	Mylonite	-60	3.8	24.4	17.3	48.9	0.0	5.6
BT10-03	Mylonite	-50	2.8	29.5	17.6	46.7	0.0	3.3
BT10-17	Mylonite	-40	3.6	30.5	15.2	35.2	0.0	15.5
	Average		3.2 ± 0.6	28.9 ± 6.4	21.7 ± 7.4	39.3 ± 6.5	0.0	6.9 ± 5.5
BT08-31U	Ultramylonite	-230	3.3	31.7	19.6	29.9	0.0	15.5
BT08-40U	Ultramylonite	-100	6.7	28.9	9.2	36.2	0.0	19.1
BT08-44U	Ultramylonite	-80	2.3	75.3	0.0	13.2	0.0	9.2
BT10-40	Ultramylonite	-70	2.7	28.5	12.5	42.7	0.0	13.6
	Average		3.8 ± 2.0	41.1 ± 22.8	10.3 ± 8.1	30.5 ± 12.7	0.0	14.4 ± 4.1
BT10-04	Bleached	-50	1.2	0.6	16.8	78.2	0.5	2.8
BT10-16	Bleached	-40	3.3	5.5	5.2	84.2	0.0	1.8
	Average		2.3 ± 1.5	3.0 ± 3.5	11.0 ± 8.2	81.2 ± 4.2	0.2 ± 0.3	2.3 ± 0.7
BT10-35	Cataclasite	-410	4.5	27.3	27.5	39.0	0.0	1.8
BT10-53	Cataclasite	-60	6.9	21.1	0.0	30.9	0.0	41.0
	Average		5.7 ± 1.7	24.2 ± 4.3	13.7 ± 19.4	35.0 ± 5.7	0.0	21.4 ± 27.8

Table IV.2: Major and trace element concentrations determined by X-Ray Fluorescence

Samples	Rock	Distance	Locality	SiO2 wt-%	TiO2 wt-%	Al2O3 wt-%	Fe2O3 wt-%	MnO wt-%	MgO wt-%	CaO wt-%	Na2O wt-%	K2O wt-%	P2O5 wt-%	LOI wt-%	Cr2O3 wt-%	NiO wt-%	Somme wt-%
BT09-80T	Protolith	-1060	LH	73.59	0.13	15.11	1.13	0.01	0.23	1.50	4.00	3.70	0.04	0.31	-	-	99.76
BT08-01	Protolith	-860	LH	71.69	0.22	15.74	1.63	0.02	0.37	1.98	4.28	3.39	0.06	0.27	-	-	99.68
BT08-03	Protolith	-710	LH	71.82	0.17	15.53	1.54	0.02	0.31	1.96	4.08	3.61	0.07	0.26	-	-	99.37
BT10-41	myl	-420	LH	67.15	0.45	17.04	3.02	0.05	0.84	2.73	4.09	3.16	0.17	0.70	-	-	99.41
BT08-30	myl	-240	LH	72.81	0.18	15.17	1.36	0.02	0.26	1.68	3.87	3.77	0.06	0.33	-	-	99.51
BT08-31M	myl	-230	LH	73.33	0.13	15.21	0.96	0.02	0.23	1.77	3.94	3.85	0.06	0.28	-	-	99.78
BT08-78	myl	-180	LH	75.70	0.10	13.91	0.82	0.01	0.12	1.22	3.34	4.34	0.05	0.36	-	-	99.96
BT10-44	myl	-180	LH	72.47	0.15	15.51	1.35	0.02	0.27	2.22	4.00	3.29	0.03	0.29	-	-	99.60
BT10-45	myl	-160	LH	70.38	0.30	15.98	2.45	0.04	0.55	2.22	4.07	3.23	0.12	0.41	-	-	99.76
BT08-80	myl	-120	LH	74.77	0.12	14.18	1.00	0.03	0.17	1.28	3.65	4.04	0.05	0.26	-	-	99.54
BT08-44M	myl	-70	LH	77.58	0.16	12.63	1.33	0.02	0.29	1.69	3.39	2.44	0.09	0.35	-	-	99.96
BT08-45	myl	-60	LH	72.29	0.18	15.61	1.42	0.02	0.30	1.76	4.11	3.50	0.04	0.41	-	-	99.65
BT10-03	myl	-50	SW	69.14	0.28	16.63	2.51	0.03	0.63	3.46	3.42	3.13	0.11	0.51	-	-	99.85
BT10-17	myl	-40	SW	68.51	0.32	16.83	2.88	0.03	0.72	3.70	3.62	2.53	0.11	0.50	-	-	99.77
BT08-31U	Umyl	-230	LH	71.80	0.27	15.48	1.35	0.02	0.54	1.69	3.83	4.29	0.08	0.33	0.01	-	99.70
BT08-40	Umyl	-100	LH	67.81	0.41	16.28	2.99	0.04	1.60	3.07	3.51	3.26	0.11	0.57	0.01	-	99.67
BT10-40	Umyl	-80	LH	68.12	0.42	16.43	2.78	0.04	1.41	3.23	3.87	3.07	0.13	0.38	-	-	99.88
BT08-44U	Umyl	-70	LH	86.48	0.28	6.56	1.45	0.03	1.08	1.17	1.29	0.84	0.04	0.35	-	-	99.56
BT10-04	Bleached	-50	SW	61.22	0.33	19.78	2.61	0.05	0.79	3.10	7.29	2.77	0.17	1.28	-	-	99.39
BT10-16	Bleached	-40	SW	67.05	0.32	17.64	2.26	0.05	0.84	1.75	7.40	1.38	0.16	0.87	-	-	99.73
BT10-35	Cataclasisite	-410	LH	72.02	0.25	15.21	1.23	0.02	0.27	1.11	4.16	3.92	0.05	1.10	-	-	99.32
BT10-53	Cataclasisite	-60	LH	60.67	0.75	17.12	4.71	0.07	3.74	4.76	3.64	1.15	0.21	2.93	0.02	0.01	99.75

Table IV.2: Major and trace element concentrations determined by X-Ray Fluorescence

Samples	Rock	Distance	Locality	Nb	Zr	Y	Sr	U	Rb	Th	Pb	Ga	Zn	Cu	Ni	Co	Cr	V	Ce	Nd	Ba	La	S	Hf	Sc	As
BT09-80T	Protolith	-1060	LH	4	57	8	610	-	75	2	23	20	37	2	2	57	4	7	15	6	1319	12	94	6	3	3
BT08-01	Protolith	-860	LH	4	108	8	923	-	55	2	18	18	43	2	2	50	5	12	43	16	1763	21	89	6	4	3
BT08-03	Protolith	-710	LH	2	105	9	974	-	63	2	18	17	40	2	3	47	5	11	25	11	2145	23	92	6	4	4
BT10-41	myl	-420	LH	6	147	14	1183	-	84	7	15	21	79	2	3	32	4	41	94	33	2496	63	98	8	4	4
BT08-30	myl	-240	LH	7	83	16	738	-	91	2	17	21	40	2	2	29	4	10	22	8	1589	19	93	6	5	3
BT08-31M	myl	-230	LH	6	44	10	741	-	98	2	18	18	39	2	2	47	6	10	19	8	1389	11	85	7	4	6
BT08-78	myl	-180	LH	4	38	8	630	-	86	2	15	15	23	6	2	39	5	7	18	7	1909	10	3	8	3	6
BT10-44	myl	-180	LH	6	69	12	852	-	75	2	20	17	36	2	2	86	5	17	26	10	1239	17	88	7	3	4
BT10-45	myl	-160	LH	10	76	12	856	-	102	2	16	21	69	5	3	56	8	21	37	10	1637	20	101	5	4	3
BT08-80	myl	-120	LH	8	76	12	448	-	111	4	21	17	30	2	2	41	2	10	26	11	1227	23	86	7	4	3
BT08-44M	myl	-70	LH	7	65	10	702	-	57	2	12	16	35	5	2	67	7	17	24	8	1102	15	171	7	6	4
BT08-45	myl	-60	LH	5	97	10	861	-	83	2	17	18	40	4	2	56	3	10	37	12	1536	21	86	6	5	3
BT10-03	myl	-50	SW	7	134	12	665	-	97	6	22	20	61	2	3	43	6	29	50	23	1421	31	157	7	7	6
BT10-17	myl	-40	SW	8	153	13	646	-	91	10	19	22	64	2	2	41	8	32	58	22	1198	41	257	6	7	5
BT08-31U	Umyl	-230	LH	4	146	7	390	-	140	15	18	23	45	2	3	34	18	24	47	18	1170	27	84	6	4	4
BT08-40	Umyl	-100	LH	6	116	13	584	-	91	4	14	21	62	3	8	40	56	54	18	8	1498	20	97	5	7	3
BT10-40	Umyl	-80	LH	5	109	11	572	-	95	5	13	21	62	3	9	41	38	42	30	15	1244	21	101	6	7	5
BT08-44U	Umyl	-70	LH	11	180	27	133	-	46	7	5	9	24	5	3	70	13	16	24	5	126	10	102	2	9	5
BT10-04	Bleached	-50	SW	7	162	15	590	-	75	7	11	20	90	2	3	27	2	21	67	27	1573	40	97	11	8	3
BT10-16	Bleached	-40	SW	7	148	14	416	-	44	10	6	17	90	2	5	62	6	20	78	26	782	39	104	3	8	3
BT10-35	Cataclasite	-410	LH	6	113	10	898	-	79	3	15	17	34	2	4	42	5	15	53	19	2065	41	88	6	2	5
BT10-53	Cataclasite	-60	LH	6	129	15	616	-	34	3	11	22	72	60	63	39	198	83	24	10	866	26	115	2	20	3

Table IV.3: Mass changes of elements of mylonites, the calculation is based on the least square approach to mass transport calculation Baumgartner et al. (2005).

BT10-41							
Component		parent	±	altered	±	% Change	# Times Sig
SiO2	*	72.43	1.06	67.25	1.06	-50.5	10.9
Al2O3	*	15.47	0.32	17.07	0.32	-41.1	2.4
TiO2		0.17	0.05	0.45	0.05	38.1	0.2
Fe2O3		1.44	0.27	3.02	0.27	12.3	0.8
MgO	*	0.31	0.07	0.84	0.07	47.3	0.3
MnO		0.02	0.01	0.05	0.01	59.3	0.0
CaO		1.81	0.28	2.73	0.28	-19.8	0.8
K2O	*	3.57	0.16	3.16	0.16	-52.7	0.6
Na2O	*	4.12	0.14	4.10	0.14	-47.0	0.7
P2O5	*	0.06	0.02	0.17	0.02	59.7	0.1
H2O	*	0.28	0.03	0.70	0.03	33.1	0.1
Nb		3.33	1.15	6.01	1.15	-4.0	6.0
Zr		90.08	28.64	147.22	28.64	-12.9	81.9
Y		8.34	0.58	14.02	0.58	-10.4	14.6
Sr		836.38	197.26	1184.73	197.26	-24.4	516.4
Rb	*	64.38	10.08	84.12	10.08	-30.3	24.9
Th		2.00	0.01	7.01	0.01	86.7	5.5
Pb	*	19.69	2.89	15.02	2.89	-59.3	6.3
Ga	*	18.35	1.53	21.03	1.53	-38.9	4.3
Zn		40.03	3.00	79.12	3.00	5.5	10.2
Cu		2.00	0.01	2.00	0.01	-46.6	3.0
Ni		2.33	0.58	3.00	0.58	-31.4	3.7
Co	*	51.37	5.13	32.05	5.13	-66.7	12.6
Cr		4.67	0.58	4.01	0.58	-54.3	6.7
V	*	10.01	2.65	41.06	2.65	118.9	13.2
Ce		27.69	14.20	94.14	14.20	81.2	56.7
Nd		11.01	5.00	33.05	5.00	60.4	19.3
Ba		1743.80	413.74	2499.65	413.74	-23.6	1034.9
La	*	18.69	5.86	63.09	5.86	80.0	25.5
S	*	91.75	2.52	98.14	2.52	-42.9	14.5
Hf		6.01	0.01	8.01	0.01	-28.8	9.6
Sc		3.67	0.58	4.01	0.58	-41.8	5.5
As		3.33	0.58	4.01	0.58	-36.0	5.2
Total	% masse		-46.6	±	4.4		

Table IV.3: Mass changes of elements of mylonites, the calculation is based on the least square approach to mass transport calculation Baumgartner et al. (2005).

BT10-03							
Component		parent	±	altered	±	% Change	# Times Sig
SiO2	*	72.43	1.06	69.05	1.06	-43.9	4.6
Al2O3	*	15.47	0.32	16.61	0.32	-36.7	1.1
TiO2		0.17	0.05	0.28	0.05	-5.3	0.1
Fe2O3		1.44	0.27	2.51	0.27	2.8	0.7
MgO		0.31	0.07	0.63	0.07	21.7	0.2
MnO		0.02	0.01	0.03	0.01	5.5	0.0
CaO		1.81	0.28	3.46	0.28	12.0	0.8
K2O	*	3.57	0.16	3.13	0.16	-48.5	0.4
Na2O	*	4.12	0.14	3.42	0.14	-51.2	0.4
P2O5		0.06	0.02	0.11	0.02	14.1	0.0
H2O		0.28	0.03	0.51	0.03	6.5	0.1
Nb		3.33	1.15	6.99	1.15	23.4	6.2
Zr		90.08	28.64	133.82	28.64	-12.5	73.7
Y		8.34	0.58	11.98	0.58	-15.4	12.9
Sr	*	836.38	197.26	664.13	197.26	-53.2	404.0
Rb		64.38	10.08	96.87	10.08	-11.2	23.2
Th		2.00	0.01	5.99	0.01	76.3	4.8
Pb	*	19.69	2.89	21.97	2.89	-34.4	5.7
Ga	*	18.35	1.53	19.97	1.53	-35.9	3.2
Zn		40.03	3.00	60.92	3.00	-10.4	7.3
Cu		2.00	0.01	2.00	0.01	-41.2	2.7
Ni		2.33	0.58	3.00	0.58	-24.5	3.5
Co	*	51.37	5.13	42.94	5.13	-50.8	10.1
Cr		4.67	0.58	5.99	0.58	-24.5	6.9
V	*	10.01	2.65	28.96	2.65	70.3	9.8
Ce		27.69	14.20	49.93	14.20	6.2	36.2
Nd		11.01	5.00	22.97	5.00	23.1	14.7
Ba	*	1743.80	413.74	1419.14	413.74	-52.0	808.4
La		18.69	5.86	30.96	5.86	-2.5	15.7
S		91.75	2.52	156.79	2.52	0.7	8.0
Hf		6.01	0.01	6.99	0.01	-31.4	8.6
Sc		3.67	0.58	6.99	0.58	12.2	6.5
As		3.33	0.58	5.99	0.58	5.7	5.7
Total	% masse		-41.2	±	2.0		

Table IV.3: Mass changes of elements of mylonites, the calculation is based on the least square approach to mass transport calculation Baumgartner et al. (2005).

BT10-17							
Component		parent	±	altered	±	% Change	# Times Sig
SiO2	*	72.43	1.06	68.50	1.06	-43.6	8.7
Al2O3	*	15.47	0.32	16.83	0.32	-35.1	1.9
TiO2		0.17	0.05	0.32	0.05	9.8	0.1
Fe2O3		1.44	0.27	2.88	0.27	19.8	0.8
MgO	*	0.31	0.07	0.72	0.07	41.4	0.2
MnO		0.02	0.01	0.03	0.01	7.0	0.0
CaO	*	1.81	0.28	3.70	0.28	21.5	0.8
K2O	*	3.57	0.16	2.53	0.16	-57.6	0.5
Na2O	*	4.12	0.14	3.62	0.14	-47.7	0.6
P2O5		0.06	0.02	0.11	0.02	15.7	0.0
H2O		0.28	0.03	0.50	0.03	6.0	0.1
Nb		3.33	1.15	8.00	1.15	43.0	6.8
Zr		90.08	28.64	152.97	28.64	1.5	78.4
Y		8.34	0.58	13.00	0.58	-7.0	13.3
Sr	*	836.38	197.26	645.87	197.26	-53.9	406.2
Rb		64.38	10.08	90.98	10.08	-15.6	23.3
Th	*	2.00	0.01	10.00	0.01	198.2	7.3
Pb	*	19.69	2.89	19.00	2.89	-42.4	5.8
Ga	*	18.35	1.53	22.00	1.53	-28.5	3.8
Zn		40.03	3.00	63.99	3.00	-4.6	8.4
Cu		2.00	0.01	2.00	0.01	-40.4	2.7
Ni		2.33	0.58	2.00	0.58	-48.9	3.1
Co	*	51.37	5.13	40.99	5.13	-52.3	11.2
Cr		4.67	0.58	8.00	0.58	2.2	7.8
V	*	10.01	2.65	31.99	2.65	90.8	10.5
Ce		27.69	14.20	57.99	14.20	24.9	39.3
Nd		11.01	5.00	22.00	5.00	19.3	14.3
Ba	*	1743.80	413.74	1197.76	413.74	-59.0	796.7
La		18.69	5.86	40.99	5.86	31.1	18.3
S	*	91.75	2.52	256.95	2.52	67.3	13.5
Hf		6.01	0.01	6.00	0.01	-40.4	8.1
Sc		3.67	0.58	7.00	0.58	13.9	6.5
As		3.33	0.58	5.00	0.58	-10.6	5.2
Total	% masse		-40.4	±	4.3		

Table IV.3: Mass changes of elements of mylonites, the calculation is based on the least square approach to mass transport calculation Baumgartner et al. (2005).

BT10-45							
Component		parent	±	altered	±	% Change	# Times Sig
SiO2	*	72.43	1.06	70.33	1.06	-24.3	6.5
Al2O3	*	15.47	0.32	15.96	0.32	-19.4	1.4
TiO2		0.17	0.05	0.30	0.05	34.9	0.1
Fe2O3	*	1.44	0.27	2.45	0.27	33.4	0.6
MgO		0.31	0.07	0.55	0.07	41.3	0.2
MnO	*	0.02	0.01	0.04	0.01	87.1	0.0
CaO		1.81	0.28	2.22	0.28	-4.5	0.5
K2O	*	3.57	0.16	3.23	0.16	-29.4	0.4
Na2O	*	4.12	0.14	4.07	0.14	-22.9	0.4
P2O5	*	0.06	0.02	0.12	0.02	65.2	0.0
H2O		0.28	0.03	0.41	0.03	12.7	0.1
Nb		3.33	1.15	9.99	1.15	133.9	7.5
Zr		90.08	28.64	75.95	28.64	-34.1	50.5
Y		8.34	0.58	11.99	0.58	12.2	11.2
Sr		836.38	197.26	855.43	197.26	-20.2	357.8
Rb		64.38	10.08	101.93	10.08	23.9	21.3
Th		2.00	0.01	2.00	0.01	-22.0	2.3
Pb	*	19.69	2.89	15.99	2.89	-36.6	4.5
Ga		18.35	1.53	20.99	1.53	-10.6	3.1
Zn	*	40.03	3.00	68.95	3.00	34.6	7.4
Cu		2.00	0.01	5.00	0.01	95.0	3.9
Ni		2.33	0.58	3.00	0.58	0.3	2.9
Co	*	51.37	5.13	55.96	5.13	-14.9	9.6
Cr		4.67	0.58	7.99	0.58	33.7	6.9
V	*	10.01	2.65	20.99	2.65	63.7	7.2
Ce		27.69	14.20	36.98	14.20	4.3	27.1
Nd		11.01	5.00	9.99	5.00	-29.0	8.6
Ba		1743.80	413.74	1635.91	413.74	-26.7	692.6
La		18.69	5.86	19.99	5.86	-16.4	11.1
S	*	91.75	2.52	100.93	2.52	-14.1	9.1
Hf		6.01	0.01	5.00	0.01	-35.0	6.4
Sc		3.67	0.58	4.00	0.58	-14.9	4.3
As		3.33	0.58	3.00	0.58	-29.8	3.6
Total	% masse		-22.0		±	5.5	

Table IV.3: Mass changes of elements of mylonites, the calculation is based on the least square approach to mass transport calculation Baumgartner et al. (2005).

BT08-45							
Component		parent	±	altered	±	% Change	# Times Sig
SiO2	*	72.43	1.06	72.34	1.06	-0.6	2.1
Al2O3		15.47	0.32	15.62	0.32	0.5	0.6
TiO2		0.17	0.05	0.18	0.05	3.3	0.1
Fe2O3		1.44	0.27	1.42	0.27	-1.6	0.4
MgO		0.31	0.07	0.30	0.07	-1.6	0.1
MnO		0.02	0.01	0.02	0.01	19.5	0.0
CaO		1.81	0.28	1.76	0.28	-3.3	0.4
K2O		3.57	0.16	3.50	0.16	-2.2	0.2
Na2O		4.12	0.14	4.12	0.14	-0.6	0.2
P2O5		0.06	0.02	0.04	0.02	-29.7	0.0
H2O	*	0.28	0.03	0.41	0.03	43.3	0.0
Nb		3.33	1.15	5.00	1.15	49.4	4.2
Zr		90.08	28.64	97.06	28.64	7.5	48.0
Y		8.34	0.58	10.01	0.58	19.5	9.0
Sr		836.38	197.26	861.51	197.26	2.6	307.8
Rb		64.38	10.08	83.05	10.08	28.6	16.5
Th		2.00	0.01	2.00	0.01	-0.4	2.0
Pb		19.69	2.89	17.01	2.89	-14.1	3.7
Ga		18.35	1.53	18.01	1.53	-2.2	2.2
Zn		40.03	3.00	40.02	3.00	-0.4	4.4
Cu		2.00	0.01	4.00	0.01	99.2	3.1
Ni		2.33	0.58	2.00	0.58	-14.6	2.1
Co		51.37	5.13	56.03	5.13	8.7	7.6
Cr		4.67	0.58	3.00	0.58	-36.0	3.9
V		10.01	2.65	10.01	2.65	-0.4	4.1
Ce		27.69	14.20	37.02	14.20	33.1	24.4
Nd		11.01	5.00	12.01	5.00	8.7	8.1
Ba		1743.80	413.74	1536.90	413.74	-12.3	569.1
La		18.69	5.86	21.01	5.86	12.0	9.9
S	*	91.75	2.52	86.05	2.52	-6.6	4.0
Hf		6.01	0.01	6.00	0.01	-0.4	5.9
Sc		3.67	0.58	5.00	0.58	35.9	4.3
As		3.33	0.58	3.00	0.58	-10.4	3.1
Total	% masse		-0.4	±	2.1		

Table IV.3: Mass changes of elements of mylonites, the calculation is based on the least square approach to mass transport calculation Baumgartner et al. (2005).

BT08-30							
Component		parent	±	altered	±	% Change	# Times Sig
SiO2	*	72.43	1.06	72.96	1.06	1.5	2.1
Al2O3		15.47	0.32	15.20	0.32	-0.8	0.6
TiO2		0.17	0.05	0.18	0.05	4.8	0.1
Fe2O3		1.44	0.27	1.36	0.27	-4.4	0.4
MgO		0.31	0.07	0.26	0.07	-13.4	0.1
MnO		0.02	0.01	0.02	0.01	21.1	0.0
CaO		1.81	0.28	1.68	0.28	-6.4	0.4
K2O	*	3.57	0.16	3.77	0.16	6.7	0.2
Na2O	*	4.12	0.14	3.87	0.14	-5.3	0.2
P2O5		0.06	0.02	0.06	0.02	7.0	0.0
H2O	*	0.28	0.03	0.33	0.03	19.8	0.0
Nb		3.33	1.15	7.01	1.15	112.0	5.4
Zr		90.08	28.64	83.17	28.64	-6.8	44.1
Y		8.34	0.58	16.03	0.58	93.8	12.5
Sr		836.38	197.26	739.56	197.26	-10.8	283.9
Rb	*	64.38	10.08	91.19	10.08	43.0	17.4
Th		2.00	0.01	2.00	0.01	1.0	2.0
Pb		19.69	2.89	17.04	2.89	-12.8	3.7
Ga	*	18.35	1.53	21.04	1.53	15.7	2.3
Zn		40.03	3.00	40.08	3.00	1.0	4.4
Cu		2.00	0.01	2.00	0.01	1.0	2.0
Ni		2.33	0.58	2.00	0.58	-13.4	2.1
Co	*	51.37	5.13	29.06	5.13	-42.9	5.9
Cr		4.67	0.58	4.01	0.58	-13.4	4.2
V		10.01	2.65	10.02	2.65	1.0	4.1
Ce		27.69	14.20	22.05	14.20	-19.8	18.5
Nd		11.01	5.00	8.02	5.00	-26.5	6.7
Ba		1743.80	413.74	1592.35	413.74	-7.9	573.6
La		18.69	5.86	19.04	5.86	2.9	9.3
S		91.75	2.52	93.20	2.52	2.4	4.1
Hf		6.01	0.01	6.01	0.01	1.0	5.9
Sc		3.67	0.58	5.01	0.58	37.8	4.3
As		3.33	0.58	3.01	0.58	-9.2	3.1
Total		% masse	1.0	±	2.3		

Table IV.3: Mass changes of elements of mylonites, the calculation is based on the least square approach to mass transport calculation Baumgartner et al. (2005).

BT10-44							
Component		parent	±	altered	±	% Change	# Times Sig
SiO2	*	72.43	1.06	72.57	1.06	4.7	2.2
Al2O3	*	15.47	0.32	15.53	0.32	5.2	0.6
TiO2		0.17	0.05	0.15	0.05	-9.5	0.1
Fe2O3		1.44	0.27	1.35	0.27	-1.6	0.4
MgO		0.31	0.07	0.27	0.07	-6.9	0.1
MnO		0.02	0.01	0.02	0.01	25.6	0.0
CaO	*	1.81	0.28	2.22	0.28	27.9	0.5
K2O		3.57	0.16	3.30	0.16	-3.2	0.2
Na2O		4.12	0.14	4.00	0.14	1.6	0.2
P2O5	*	0.06	0.02	0.03	0.02	-44.6	0.0
H2O		0.28	0.03	0.29	0.03	7.1	0.0
Nb		3.33	1.15	6.01	1.15	88.3	4.7
Zr		90.08	28.64	69.10	28.64	-19.7	39.9
Y		8.34	0.58	12.02	0.58	50.6	10.0
Sr		836.38	197.26	853.20	197.26	6.6	298.9
Rb		64.38	10.08	75.11	10.08	22.1	15.3
Th		2.00	0.01	2.00	0.01	4.7	1.9
Pb		19.69	2.89	20.03	2.89	6.4	3.9
Ga		18.35	1.53	17.02	1.53	-3.0	2.1
Zn		40.03	3.00	36.05	3.00	-5.8	4.1
Cu		2.00	0.01	2.00	0.01	4.7	1.9
Ni		2.33	0.58	2.00	0.58	-10.3	2.1
Co	*	51.37	5.13	86.12	5.13	75.3	9.9
Cr		4.67	0.58	5.01	0.58	12.2	4.6
V	*	10.01	2.65	17.02	2.65	77.8	5.7
Ce		27.69	14.20	26.04	14.20	-1.6	19.6
Nd		11.01	5.00	10.01	5.00	-4.8	7.2
Ba		1743.80	413.74	1240.74	413.74	-25.6	508.0
La		18.69	5.86	17.02	5.86	-4.8	8.7
S		91.75	2.52	88.12	2.52	0.4	4.0
Hf		6.01	0.01	7.01	0.01	22.1	6.3
Sc		3.67	0.58	3.00	0.58	-14.3	3.2
As		3.33	0.58	4.01	0.58	25.6	3.5
Total	% masse		4.7	±	2.6		

Table IV.3: Mass changes of elements of mylonites, the calculation is based on the least square approach to mass transport calculation Baumgartner et al. (2005).

BT08-31M							
Component		parent	±	altered	±	% Change	# Times Sig
SiO2	*	72.43	1.06	73.30	1.06	8.2	2.5
Al2O3	*	15.47	0.32	15.20	0.32	5.3	0.6
TiO2		0.17	0.05	0.13	0.05	-19.8	0.1
Fe2O3	*	1.44	0.27	0.96	0.27	-28.7	0.3
MgO		0.31	0.07	0.23	0.07	-18.9	0.1
MnO		0.02	0.01	0.02	0.01	28.3	0.0
CaO		1.81	0.28	1.77	0.28	4.5	0.4
K2O	*	3.57	0.16	3.85	0.16	15.4	0.2
Na2O	*	4.12	0.14	3.94	0.14	2.2	0.2
P2O5		0.06	0.02	0.06	0.02	13.3	0.0
H2O		0.28	0.03	0.28	0.03	5.8	0.0
Nb		3.33	1.15	6.00	1.15	92.4	4.7
Zr	*	90.08	28.64	43.98	28.64	-47.7	34.4
Y		8.34	0.58	10.00	0.58	28.3	8.8
Sr		836.38	197.26	740.72	197.26	-5.1	276.3
Rb	*	64.38	10.08	97.96	10.08	63.0	18.1
Th		2.00	0.01	2.00	0.01	7.0	1.9
Pb		19.69	2.89	17.99	2.89	-2.2	3.7
Ga		18.35	1.53	17.99	1.53	5.0	2.1
Zn		40.03	3.00	38.99	3.00	4.3	4.3
Cu		2.00	0.01	2.00	0.01	7.0	1.9
Ni		2.33	0.58	2.00	0.58	-8.3	2.1
Co		51.37	5.13	46.98	5.13	-2.0	6.8
Cr		4.67	0.58	6.00	0.58	37.5	5.1
V		10.01	2.65	10.00	2.65	7.0	4.0
Ce		27.69	14.20	18.99	14.20	-26.5	16.9
Nd		11.01	5.00	8.00	5.00	-22.1	6.5
Ba		1743.80	413.74	1388.48	413.74	-14.6	525.0
La		18.69	5.86	11.00	5.86	-37.0	7.3
S		91.75	2.52	84.97	2.52	-0.9	4.3
Hf		6.01	0.01	7.00	0.01	24.8	6.2
Sc		3.67	0.58	4.00	0.58	16.8	3.7
As		3.33	0.58	6.00	0.58	92.4	4.7
Total	% masse		7.0	±	3.4		

Table IV.3: Mass changes of elements of mylonites, the calculation is based on the least square approach to mass transport calculation Baumgartner et al. (2005).

BT08-80							
Component		parent	±	altered	±	% Change	# Times Sig
SiO2	*	72.43	1.06	74.95	1.06	12.9	1.9
Al2O3		15.47	0.32	14.21	0.32	0.4	0.5
TiO2		0.17	0.05	0.12	0.05	-24.7	0.1
Fe2O3		1.44	0.27	1.00	0.27	-23.7	0.3
MgO	*	0.31	0.07	0.17	0.07	-39.1	0.1
MnO	*	0.02	0.01	0.03	0.01	95.7	0.0
CaO	*	1.81	0.28	1.29	0.28	-22.8	0.3
K2O	*	3.57	0.16	4.05	0.16	23.8	0.2
Na2O		4.12	0.14	3.65	0.14	-3.3	0.2
P2O5		0.06	0.02	0.05	0.02	-3.9	0.0
H2O		0.28	0.03	0.26	0.03	-0.3	0.0
Nb		3.33	1.15	8.02	1.15	162.2	5.9
Zr		90.08	28.64	76.19	28.64	-7.6	40.5
Y		8.34	0.58	12.03	0.58	57.3	9.9
Sr	*	836.38	197.26	449.10	197.26	-41.4	226.9
Rb	*	64.38	10.08	111.27	10.08	88.6	19.7
Th		2.00	0.01	4.01	0.01	118.6	3.0
Pb		19.69	2.89	21.05	2.89	16.6	3.9
Ga		18.35	1.53	17.04	1.53	1.3	2.0
Zn	*	40.03	3.00	30.07	3.00	-18.0	3.7
Cu		2.00	0.01	2.00	0.01	9.3	1.9
Ni		2.33	0.58	2.00	0.58	-6.3	2.0
Co		51.37	5.13	41.10	5.13	-12.6	6.2
Cr		4.67	0.58	2.00	0.58	-53.2	3.3
V		10.01	2.65	10.02	2.65	9.3	3.9
Ce		27.69	14.20	26.06	14.20	2.7	19.1
Nd		11.01	5.00	11.03	5.00	9.3	7.4
Ba		1743.80	413.74	1230.00	413.74	-23.0	492.0
La		18.69	5.86	23.06	5.86	34.8	10.1
S		91.75	2.52	86.21	2.52	2.5	3.7
Hf		6.01	0.01	7.02	0.01	27.5	6.2
Sc		3.67	0.58	4.01	0.58	19.3	3.6
As		3.33	0.58	3.01	0.58	-1.7	3.0
Total	% masse		9.3	±	2.2		

Table IV.3: Mass changes of elements of mylonites, the calculation is based on the least square approach to mass transport calculation Baumgartner et al. (2005).

BT08-44M							
Component		parent	±	altered	±	% Change	# Times Sig
SiO2	*	72.43	1.06	77.43	1.06	29.5	1.9
Al2O3		15.47	0.32	12.60	0.32	-1.3	0.5
TiO2		0.17	0.05	0.16	0.05	11.3	0.1
Fe2O3		1.44	0.27	1.32	0.27	11.8	0.4
MgO		0.31	0.07	0.29	0.07	15.2	0.1
MnO		0.02	0.01	0.02	0.01	44.7	0.0
CaO		1.81	0.28	1.68	0.28	12.3	0.4
K2O	*	3.57	0.16	2.44	0.16	-17.1	0.2
Na2O		4.12	0.14	3.38	0.14	-0.6	0.2
P2O5	*	0.06	0.02	0.09	0.02	91.6	0.0
H2O	*	0.28	0.03	0.35	0.03	52.2	0.0
Nb		3.33	1.15	6.99	1.15	153.7	5.2
Zr		90.08	28.64	64.87	28.64	-12.6	35.8
Y		8.34	0.58	9.98	0.58	45.0	8.4
Sr		836.38	197.26	700.64	197.26	1.5	252.2
Rb		64.38	10.08	56.89	10.08	7.2	12.3
Th		2.00	0.01	2.00	0.01	20.9	1.8
Pb	*	19.69	2.89	11.98	2.89	-26.3	2.9
Ga		18.35	1.53	15.97	1.53	5.5	1.9
Zn		40.03	3.00	34.93	3.00	5.8	3.7
Cu	*	2.00	0.01	4.99	0.01	202.2	3.7
Ni		2.33	0.58	2.00	0.58	3.6	1.9
Co	*	51.37	5.13	66.87	5.13	57.9	7.9
Cr		4.67	0.58	6.99	0.58	81.3	5.5
V	*	10.01	2.65	16.97	2.65	105.3	5.5
Ce		27.69	14.20	23.95	14.20	4.8	17.5
Nd		11.01	5.00	7.98	5.00	-12.0	6.0
Ba		1743.80	413.74	1099.86	413.74	-23.6	444.0
La		18.69	5.86	14.97	5.86	-2.9	7.6
S	*	91.75	2.52	170.67	2.52	125.6	5.5
Hf		6.01	0.01	6.99	0.01	41.0	5.9
Sc		3.67	0.58	5.99	0.58	97.9	4.7
As		3.33	0.58	3.99	0.58	45.0	3.4
Total	% masse		20.9	±	2.8		

Table IV.3: Mass changes of elements of mylonites, the calculation is based on the least square approach to mass transport calculation Baumgartner et al. (2005).

BT08-78							
Component		parent	±	altered	±	% Change	# Times Sig
SiO2	*	72.43	1.06	75.51	1.06	30.8	2.6
Al2O3	*	15.47	0.32	13.88	0.32	12.6	0.6
TiO2		0.17	0.05	0.10	0.05	-27.8	0.0
Fe2O3	*	1.44	0.27	0.81	0.27	-29.0	0.3
MgO	*	0.31	0.07	0.12	0.07	-50.5	0.1
MnO		0.02	0.01	0.01	0.01	-24.9	0.0
CaO		1.81	0.28	1.22	0.28	-16.0	0.3
K2O	*	3.57	0.16	4.33	0.16	52.2	0.3
Na2O		4.12	0.14	3.33	0.14	1.5	0.2
P2O5		0.06	0.02	0.05	0.02	10.5	0.0
H2O	*	0.28	0.03	0.36	0.03	59.0	0.0
Nb		3.33	1.15	3.99	1.15	50.2	3.3
Zr	*	90.08	28.64	37.91	28.64	-47.1	29.5
Y		8.34	0.58	7.98	0.58	20.1	7.2
Sr		836.38	197.26	628.46	197.26	-5.7	236.0
Rb	*	64.38	10.08	85.79	10.08	67.3	15.8
Th		2.00	0.01	2.00	0.01	25.2	1.8
Pb		19.69	2.89	14.96	2.89	-4.6	3.1
Ga		18.35	1.53	14.96	1.53	2.5	1.8
Zn	*	40.03	3.00	22.94	3.00	-28.0	3.2
Cu	*	2.00	0.01	5.99	0.01	275.4	4.3
Ni		2.33	0.58	2.00	0.58	7.3	1.9
Co		51.37	5.13	38.90	5.13	-4.8	5.8
Cr		4.67	0.58	4.99	0.58	34.1	4.3
V		10.01	2.65	6.98	2.65	-12.4	3.1
Ce		27.69	14.20	17.96	14.20	-18.6	15.1
Nd		11.01	5.00	6.98	5.00	-20.3	5.6
Ba		1743.80	413.74	1904.33	413.74	37.3	579.4
La		18.69	5.86	9.98	5.86	-32.9	6.4
S	*	91.75	2.52	2.99	2.52	-95.9	3.5
Hf		6.01	0.01	7.98	0.01	66.9	6.5
Sc		3.67	0.58	2.99	0.58	2.5	2.9
As		3.33	0.58	5.99	0.58	125.2	4.6
Total	% masse		25.2	±	5.0		

Table IV.4: Mass changes of elements of ultramylonites, the calculation is based on the least square approach to mass transport calculation Baumgartner et al. (2005).

08-31U							
Component		parent	±	altered	±	% Change	# Times Sig
SiO2	*	72.43	1.06	71.86	1.06	-17.84	4.18
Al2O3	*	15.47	0.32	15.50	0.32	-16.89	0.97
TiO2		0.17	0.05	0.27	0.05	29.02	0.09
Fe2O3	*	1.44	0.27	1.35	0.27	-22.08	0.44
MgO	*	0.31	0.07	0.54	0.07	47.45	0.16
MnO		0.02	0.01	0.02	0.01	-0.54	0.01
CaO	*	1.81	0.28	1.69	0.28	-22.80	0.46
K2O		3.57	0.16	4.29	0.16	-0.31	0.33
Na2O	*	4.12	0.14	3.83	0.14	-22.97	0.31
P2O5		0.06	0.02	0.08	0.02	17.12	0.03
H2O		0.28	0.03	0.33	0.03	-2.13	0.05
Nb		3.33	1.15	4.00	1.15	-0.54	3.94
Zr		90.08	28.64	146.13	28.64	34.48	65.90
Y		8.34	0.58	7.01	0.58	-30.39	8.50
Sr	*	836.38	197.26	390.34	197.26	-61.31	279.78
Rb	*	64.38	10.08	140.12	10.08	80.57	25.29
Th	*	2.00	0.01	15.01	0.01	521.79	10.53
Pb	*	19.69	2.89	18.02	2.89	-24.20	4.31
Ga		18.35	1.53	23.02	1.53	4.15	2.82
Zn		40.03	3.00	45.04	3.00	-6.75	5.45
Cu		2.00	0.01	2.00	0.01	-17.08	2.17
Ni		2.33	0.58	3.00	0.58	6.57	2.85
Co	*	51.37	5.13	34.03	5.13	-45.09	7.51
Cr	*	4.67	0.58	18.02	0.58	219.63	13.07
V	*	10.01	2.65	24.02	2.65	98.90	7.81
Ce		27.69	14.20	47.04	14.20	40.81	30.43
Nd		11.01	5.00	18.02	5.00	35.72	11.08
Ba	*	1743.80	413.74	1171.02	413.74	-44.33	594.19
La		18.69	5.86	27.02	5.86	19.85	12.42
S	*	91.75	2.52	84.07	2.52	-24.03	6.23
Hf		6.01	0.01	6.01	0.01	-17.08	6.52
Sc		3.67	0.58	4.00	0.58	-9.50	4.14
As		3.33	0.58	4.00	0.58	-0.54	3.94
Total		% masse	-17.1	±	3.8		

Table IV.4: Mass changes of elements of ultramylonites, the calculation is based on the least square approach to mass transport calculation Baumgartner et al. (2005).

08-40U							
Component		parent	±	altered	±	% Change	# Times Sig
SiO2	*	72.43	1.06	67.86	1.06	-42.18	9.14
Al2O3	*	15.47	0.32	16.29	0.32	-34.82	2.01
TiO2		0.17	0.05	0.41	0.05	45.91	0.13
Fe2O3		1.44	0.27	3.00	0.27	28.85	0.76
MgO	*	0.31	0.07	1.60	0.07	222.92	0.41
MnO		0.02	0.01	0.04	0.01	47.94	0.02
CaO		1.81	0.28	3.08	0.28	4.74	0.72
K2O	*	3.57	0.16	3.27	0.16	-43.36	0.53
Na2O	*	4.12	0.14	3.51	0.14	-47.39	0.57
P2O5		0.06	0.02	0.11	0.02	19.70	0.04
H2O	*	0.28	0.03	0.57	0.03	25.34	0.08
Nb		3.33	1.15	6.00	1.15	11.20	5.61
Zr		90.08	28.64	116.08	28.64	-20.37	68.16
Y		8.34	0.58	13.01	0.58	-3.60	13.02
Sr	*	836.38	197.26	584.40	197.26	-56.84	390.20
Rb		64.38	10.08	91.06	10.08	-12.48	23.04
Th		2.00	0.01	4.00	0.01	23.62	3.57
Pb	*	19.69	2.89	14.01	2.89	-56.04	5.46
Ga	*	18.35	1.53	21.01	1.53	-29.19	3.77
Zn		40.03	3.00	62.04	3.00	-4.26	8.41
Cu		2.00	0.01	3.00	0.01	-7.30	3.07
Ni		2.33	0.58	8.01	0.58	111.88	6.14
Co	*	51.37	5.13	40.03	5.13	-51.79	11.10
Cr	*	4.67	0.58	56.04	0.58	641.48	39.15
V	*	10.01	2.65	54.04	2.65	233.50	16.39
Ce	*	27.69	14.20	18.01	14.20	-59.81	25.67
Nd	*	11.01	5.00	8.01	5.00	-55.01	9.75
Ba	*	1743.80	413.74	1499.02	413.74	-46.78	808.24
La		18.69	5.86	20.01	5.86	-33.76	12.97
S	*	91.75	2.52	97.07	2.52	-34.52	12.33
Hf		6.01	0.01	5.00	0.01	-48.47	7.60
Sc		3.67	0.58	7.00	0.58	18.06	6.37
As		3.33	0.58	3.00	0.58	-44.40	4.30
Total		% masse	-38.2	±	4.9		

Table IV.4: Mass changes of elements of ultramylonites, the calculation is based on the least square approach to mass transport calculation Baumgartner et al. (2005).

08-44U							
Component		parent	±	altered	±	% Change	# Times Sig
SiO2	*	72.43	1.06	86.79	1.06	105.39	8.41
Al2O3	*	15.47	0.32	6.58	0.32	22.51	1.81
TiO2		0.17	0.05	0.28	0.05	0.25	0.10
Fe2O3		1.44	0.27	1.46	0.27	2.10	0.51
MgO	*	0.31	0.07	1.08	0.07	0.45	0.28
MnO		0.02	0.01	0.03	0.01	0.03	0.02
CaO	*	1.81	0.28	1.17	0.28	2.64	0.49
K2O	*	3.57	0.16	0.84	0.16	5.20	0.46
Na2O	*	4.12	0.14	1.29	0.14	6.00	0.51
P2O5	*	0.06	0.02	0.04	0.02	0.09	0.03
H2O		0.28	0.03	0.35	0.03	0.41	0.06
Nb		3.33	1.15	11.04	1.15	4.85	8.25
Zr		90.08	28.64	180.64	28.64	131.07	79.39
Y		8.34	0.58	27.10	0.58	12.13	20.31
Sr	*	836.38	197.26	133.48	197.26	1217.01	308.35
Rb	*	64.38	10.08	46.16	10.08	93.69	17.13
Th		2.00	0.01	7.03	0.01	2.91	5.21
Pb	*	19.69	2.89	5.02	2.89	28.65	4.44
Ga	*	18.35	1.53	9.03	1.53	26.69	3.03
Zn	*	40.03	3.00	24.09	3.00	58.25	6.41
Cu		2.00	0.01	5.02	0.01	2.91	3.96
Ni		2.33	0.58	3.01	0.58	3.39	3.04
Co		51.37	5.13	70.25	5.13	74.75	11.39
Cr		4.67	0.58	13.05	0.58	6.80	10.05
V		10.01	2.65	16.06	2.65	14.56	6.21
Ce		27.69	14.20	24.09	14.20	40.30	23.80
Nd	*	11.01	5.00	5.02	5.00	16.02	7.93
Ba	*	1743.80	413.74	126.45	413.74	2537.40	613.62
La	*	18.69	5.86	10.04	5.86	27.19	9.87
S	*	91.75	2.52	102.37	2.52	133.50	11.30
Hf	*	6.01	0.01	2.01	0.01	8.74	5.88
Sc		3.67	0.58	9.03	0.58	5.34	7.15
As		3.33	0.58	5.02	0.58	4.85	4.70
Total		% masse	-26.7	±	6.3		

Table IV.4: Mass changes of elements of ultramylonites, the calculation is based on the least square approach to mass transport calculation Baumgartner et al. (2005).

10-29							
Component		parent	±	altered	±	% Change	# Times Sig
SiO2	*	72.43	1.06	53.56	1.06	-46.36	3.98
Al2O3	*	15.47	0.32	14.75	0.32	-30.74	0.95
TiO2	*	0.17	0.05	0.75	0.05	212.94	0.21
Fe2O3	*	1.44	0.27	9.15	0.27	362.87	1.83
MgO	*	0.31	0.07	9.21	0.07	2085.01	2.22
MnO	*	0.02	0.01	0.20	0.01	755.96	0.08
CaO	*	1.81	0.28	4.73	0.28	89.00	0.87
K2O	*	3.57	0.16	3.58	0.16	-27.15	0.32
Na2O	*	4.12	0.14	1.54	0.14	-72.93	0.29
P2O5	*	0.06	0.02	0.18	0.02	127.22	0.06
H2O	*	0.28	0.03	2.06	0.03	430.22	0.21
Nb	*	3.33	1.15	13.03	1.15	183.44	9.56
Zr		90.08	28.64	102.20	28.64	-17.50	58.17
Y		8.34	0.58	22.04	0.58	91.63	17.19
Sr	*	836.38	197.26	348.69	197.26	-69.70	309.90
Rb	*	64.38	10.08	238.47	10.08	169.44	39.92
Th		2.00	0.01	6.01	0.01	118.00	4.58
Pb	*	19.69	2.89	4.01	2.89	-85.23	3.97
Ga		18.35	1.53	24.05	1.53	-4.84	3.03
Zn	*	40.03	3.00	281.56	3.00	411.04	21.87
Cu		2.00	0.01	2.00	0.01	-27.31	2.36
Ni	*	2.33	0.58	184.37	0.58	5633.96	127.60
Co	*	51.37	5.13	44.09	5.13	-37.70	8.63
Cr	*	4.67	0.58	661.31	0.58	10190.92	457.93
V	*	10.01	2.65	137.27	2.65	896.45	39.98
Ce		27.69	14.20	24.05	14.20	-36.98	23.77
Nd		11.01	5.00	12.02	5.00	-20.67	9.57
Ba	*	1743.80	413.74	735.46	413.74	-69.35	618.02
La		18.69	5.86	24.05	5.86	-6.58	12.42
S		91.75	2.52	127.25	2.52	0.80	6.77
Hf	*	6.01	0.01	2.00	0.01	-75.76	5.89
Sc	*	3.67	0.58	27.05	0.58	435.12	19.02
As		3.33	0.58	3.01	0.58	-34.62	3.80
Total		% masse	-27.3	±	2.7		

Table IV.4: Mass changes of elements of ultramylonites, the calculation is based on the least square approach to mass transport calculation Baumgartner et al. (2005).

10-40							
Component		parent	±	altered	±	% Change	# Times Sig
SiO2	*	72.43	1.06	68.03	1.06	-38.90	7.74
Al2O3	*	15.47	0.32	16.41	0.32	-30.81	1.71
TiO2	*	0.17	0.05	0.42	0.05	57.42	0.13
Fe2O3		1.44	0.27	2.77	0.27	25.91	0.71
MgO	*	0.31	0.07	1.41	0.07	199.95	0.36
MnO		0.02	0.01	0.04	0.01	55.97	0.02
CaO		1.81	0.28	3.23	0.28	15.62	0.71
K2O	*	3.57	0.16	3.07	0.16	-44.02	0.46
Na2O	*	4.12	0.14	3.87	0.14	-38.90	0.50
P2O5		0.06	0.02	0.13	0.02	49.30	0.05
H2O		0.28	0.03	0.38	0.03	-13.29	0.06
Nb		3.33	1.15	4.99	1.15	-2.49	4.98
Zr		90.08	28.64	108.86	28.64	-21.29	64.33
Y		8.34	0.58	10.99	0.58	-14.29	11.74
Sr	*	836.38	197.26	571.29	197.26	-55.53	369.81
Rb		64.38	10.08	94.88	10.08	-3.83	22.49
Th		2.00	0.01	4.99	0.01	62.57	4.07
Pb	*	19.69	2.89	12.98	2.89	-57.04	5.06
Ga	*	18.35	1.53	20.97	1.53	-25.52	3.48
Zn		40.03	3.00	61.92	3.00	0.70	7.83
Cu		2.00	0.01	3.00	0.01	-2.49	2.99
Ni		2.33	0.58	8.99	0.58	150.64	6.72
Co	*	51.37	5.13	40.95	5.13	-47.99	10.29
Cr	*	4.67	0.58	37.95	0.58	429.72	26.82
V	*	10.01	2.65	41.95	2.65	172.93	13.01
Ce		27.69	14.20	29.96	14.20	-29.52	27.60
Nd		11.01	5.00	14.98	5.00	-11.27	11.25
Ba	*	1743.80	413.74	1242.45	413.74	-53.54	743.31
La		18.69	5.86	20.97	5.86	-26.88	12.68
S	*	91.75	2.52	100.87	2.52	-28.38	10.65
Hf		6.01	0.01	5.99	0.01	-34.98	7.65
Sc		3.67	0.58	6.99	0.58	24.18	6.24
As		3.33	0.58	4.99	0.58	-2.49	4.98
Total		% masse	-35.0	±	4.5		

Table IV.4: Mass changes of elements of ultramylonites, the calculation is based on the least square approach to mass transport calculation Baumgartner et al. (2005).

10-46							
Component		parent	±	altered	±	% Change	# Times Sig
SiO2	*	72.43	1.06	79.95	1.06	-40.57	17.52
Al2O3	*	15.47	0.32	9.84	0.32	-65.72	3.76
TiO2		0.17	0.05	0.37	0.05	13.50	0.14
Fe2O3		1.44	0.27	2.57	0.27	-3.84	0.80
MgO	*	0.31	0.07	1.34	0.07	136.59	0.36
MnO		0.02	0.01	0.02	0.01	-36.17	0.02
CaO	*	1.81	0.28	0.55	0.28	-83.78	0.70
K2O	*	3.57	0.16	3.34	0.16	-49.53	0.92
Na2O	*	4.12	0.14	1.03	0.14	-86.48	1.02
P2O5	*	0.06	0.02	0.05	0.02	-53.01	0.04
H2O	*	0.28	0.03	0.78	0.03	49.28	0.12
Nb		3.33	1.15	12.03	1.15	94.09	9.39
Zr		90.08	28.64	201.46	28.64	20.50	96.82
Y		8.34	0.58	23.05	0.58	48.94	19.32
Sr	*	836.38	197.26	113.26	197.26	-92.71	444.70
Rb		64.38	10.08	113.26	10.08	-5.16	29.98
Th		2.00	0.01	6.01	0.01	61.81	4.91
Pb	*	19.69	2.89	8.02	2.89	-78.07	7.06
Ga	*	18.35	1.53	16.04	1.53	-52.90	5.39
Zn	*	40.03	3.00	31.07	3.00	-58.22	11.38
Cu		2.00	0.01	7.02	0.01	88.80	5.51
Ni		2.33	0.58	6.01	0.58	38.67	5.16
Co	*	51.37	5.13	36.08	5.13	-62.16	15.90
Cr		4.67	0.58	25.06	0.58	189.07	18.37
V	*	10.01	2.65	34.08	2.65	83.23	11.48
Ce		27.69	14.20	31.07	14.20	-39.61	32.28
Nd		11.01	5.00	11.03	5.00	-46.05	11.76
Ba	*	1743.80	413.74	819.87	413.74	-74.65	914.11
La	*	18.69	5.86	15.03	5.86	-56.65	14.02
S	*	91.75	2.52	85.19	2.52	-50.00	22.61
Hf	*	6.01	0.01	4.01	0.01	-64.03	8.31
Sc		3.67	0.58	7.02	0.58	3.04	6.82
As		3.33	0.58	5.01	0.58	-19.09	5.57
Total		% masse	-46.0	±	7.5		

Table IV.5: Mass changes of elements of bleached granodiorite, the calculation is based on the least square approach to mass transport calculation Baumgartner et al. (2005).

10-04							
Component		parent	±	altered	±	% Change	# Times Sig
SiO2	*	72.43	1.06	61.41	1.06	-52.97	6.17
Al2O3	*	15.47	0.32	19.85	0.32	-28.82	1.43
TiO2		0.17	0.05	0.33	0.05	4.81	0.12
Fe2O3		1.44	0.27	2.62	0.27	1.25	0.73
MgO		0.31	0.07	0.79	0.07	43.35	0.23
MnO		0.02	0.01	0.05	0.01	65.34	0.02
CaO		1.81	0.28	3.11	0.28	-4.85	0.74
K2O	*	3.57	0.16	2.78	0.16	-56.71	0.42
Na2O		4.12	0.14	7.31	0.14	-1.51	0.49
P2O5	*	0.06	0.02	0.17	0.02	65.34	0.06
H2O	*	0.28	0.03	1.28	0.03	152.57	0.14
Nb		3.33	1.15	7.02	1.15	16.79	6.39
Zr		90.08	28.64	162.53	28.64	0.32	83.10
Y		8.34	0.58	15.05	0.58	0.09	14.71
Sr	*	836.38	197.26	591.91	197.26	-60.70	417.89
Rb	*	64.38	10.08	75.24	10.08	-35.08	22.18
Th		2.00	0.01	7.02	0.01	94.71	5.46
Pb	*	19.69	2.89	11.04	2.89	-68.93	5.44
Ga	*	18.35	1.53	20.06	1.53	-39.27	3.52
Zn	*	40.03	3.00	90.29	3.00	25.14	9.33
Cu		2.00	0.01	2.01	0.01	-44.36	2.86
Ni		2.33	0.58	3.01	0.58	-28.49	3.58
Co	*	51.37	5.13	27.09	5.13	-70.73	10.37
Cr	*	4.67	0.58	2.01	0.58	-76.16	5.99
V		10.01	2.65	21.07	2.65	16.79	8.06
Ce		27.69	14.20	67.22	14.20	34.71	44.05
Nd		11.01	5.00	27.09	5.00	36.58	16.58
Ba	*	1743.80	413.74	1578.10	413.74	-49.72	866.68
La		18.69	5.86	40.13	5.86	19.23	18.45
S	*	91.75	2.52	97.31	2.52	-41.06	9.09
Hf		6.01	0.01	11.04	0.01	1.95	10.68
Sc		3.67	0.58	8.03	0.58	21.45	7.19
As		3.33	0.58	3.01	0.58	-49.95	4.65
Total	% masse	-44.360	±	2.555			

Table IV.5: Mass changes of elements of bleached granodiorite, the calculation is based on the least square approach to mass transport calculation Baumgartner et al. (2005).

10-16							
Component		parent	±	altered	±	% Change	# Times Sig
SiO2	*	72.43	1.06	67.11	1.06	-48.60	6.36
Al2O3	*	15.47	0.32	17.66	0.32	-36.48	1.46
TiO2		0.17	0.05	0.32	0.05	2.08	0.12
Fe2O3		1.44	0.27	2.26	0.27	-12.31	0.68
MgO	*	0.31	0.07	0.84	0.07	53.08	0.24
MnO		0.02	0.01	0.05	0.01	65.93	0.02
CaO	*	1.81	0.28	1.75	0.28	-46.31	0.62
K2O	*	3.57	0.16	1.38	0.16	-78.48	0.41
Na2O		4.12	0.14	7.41	0.14	-0.25	0.50
P2O5	*	0.06	0.02	0.16	0.02	56.29	0.06
H2O	*	0.28	0.03	0.87	0.03	70.97	0.10
Nb		3.33	1.15	7.01	1.15	16.66	6.40
Zr		90.08	28.64	148.12	28.64	-8.60	79.61
Y		8.34	0.58	14.01	0.58	-6.69	14.24
Sr	*	836.38	197.26	416.34	197.26	-72.34	404.70
Rb	*	64.38	10.08	44.04	10.08	-61.99	20.09
Th	*	2.00	0.01	10.01	0.01	177.93	7.37
Pb	*	19.69	2.89	6.00	2.89	-83.06	5.30
Ga	*	18.35	1.53	17.01	1.53	-48.49	3.43
Zn	*	40.03	3.00	90.07	3.00	25.01	9.36
Cu		2.00	0.01	2.00	0.01	-44.42	2.86
Ni		2.33	0.58	5.00	0.58	19.11	4.53
Co	*	51.37	5.13	62.05	5.13	-32.87	11.80
Cr		4.67	0.58	6.00	0.58	-28.56	7.16
V		10.01	2.65	20.02	2.65	11.16	7.85
Ce		27.69	14.20	78.06	14.20	56.65	48.84
Nd		11.01	5.00	26.02	5.00	31.50	16.20
Ba	*	1743.80	413.74	782.64	413.74	-75.06	801.53
La		18.69	5.86	39.03	5.86	16.13	18.20
S	*	91.75	2.52	104.09	2.52	-36.91	9.34
Hf	*	6.01	0.01	3.00	0.01	-72.21	7.78
Sc		3.67	0.58	8.01	0.58	21.32	7.19
As		3.33	0.58	3.00	0.58	-50.00	4.66
Total	% masse	-44.418	±	2.632			

Table IV.6: Major element analyses of muscovites. The single grain analyses were performed with an electron microprobe.

	BT09-80-M02-1	BT09-80-M02-3	BT09-80-M02-4	BT09-80-M02-5	BT09-80-M02-6	BT09-80-M02-7	BT09-80-M02-8	BT09-80-M01-3	BT09-80-M01-4
SiO ₂	45.89	45.28	44.83	45.09	44.52	45.20	45.74	45.53	45.21
Al ₂ O ₃	33.41	34.10	33.85	33.76	34.12	34.15	33.63	32.75	33.51
TiO ₂	0.61	1.15	1.44	0.62	1.11	1.11	0.89	0.49	0.68
FeO	3.22	3.34	3.34	3.28	3.45	3.35	3.63	4.07	3.69
MgO	0.68	0.69	0.63	0.67	0.63	0.65	0.76	1.07	0.76
MnO	0.00	0.00	0.00	0.00	0.02	0.03	0.02	0.01	0.02
K ₂ O	10.99	11.06	11.05	11.07	11.08	11.10	11.12	10.76	11.31
CaO	0.02	0.00	0.00	0.00	0.01	0.01	0.00	0.03	0.00
Na ₂ O	0.43	0.56	0.52	0.51	0.53	0.60	0.43	0.34	0.36
F	0.10	0.18	0.00	0.07	0.15	0.20	0.10	0.16	0.08
Total	95.35	96.37	95.67	95.08	95.61	96.39	96.33	95.21	95.62
<i>Numbers of ions on the basis of 11 oxygens</i>									
Si	3.080	3.018	3.007	3.041	2.995	3.014	3.048	3.070	3.040
Al IV	0.920	0.982	0.993	0.959	1.005	0.986	0.952	0.930	0.960
Σ T	4.000	4.000	4.000	4.000	4.000	4.000	4.000	4.000	4.000
Al VI	1.723	1.698	1.684	1.725	1.701	1.699	1.689	1.673	1.696
Ti	0.031	0.057	0.073	0.031	0.056	0.056	0.044	0.025	0.034
Fe	0.163	0.168	0.169	0.167	0.175	0.168	0.182	0.207	0.187
Mg	0.068	0.069	0.063	0.068	0.063	0.065	0.076	0.107	0.076
Mn	0.000	0.000	0.000	0.000	0.001	0.002	0.001	0.001	0.001
Σ R	1.984	1.992	1.988	1.990	1.995	1.990	1.993	2.012	1.994
Ca	0.001	0.000	0.000	0.000	0.001	0.001	0.000	0.002	0.000
Na	0.056	0.073	0.068	0.067	0.069	0.077	0.056	0.044	0.047
K	0.941	0.941	0.946	0.952	0.951	0.944	0.945	0.925	0.970
Σ A	0.999	1.013	1.014	1.020	1.021	1.022	1.001	0.971	1.017
F	0.005	0.005	0.005	0.005	0.005	0.005	0.005	0.005	0.005

Table IV.6: Major element analyses of muscovites. The single grain analyses were performed with an electron microprobe.

	BT09-80-M01-5	BT09-80-M01-7	BT09-80-M03-2	BT09-80-M03-3	BT09-80-M03-6	BT09-80-M04-2	BT09-80-M04-3	BT09-80-M04-4	BT08-63-M09-3
SiO ₂	45.64	45.35	45.16	45.39	45.20	44.99	45.59	44.90	45.31
Al ₂ O ₃	34.14	34.60	33.89	34.16	34.06	34.54	34.66	35.04	32.68
TiO ₂	0.61	0.43	0.78	0.92	0.71	0.94	1.07	0.81	0.77
FeO	3.63	3.22	3.44	3.48	3.33	3.04	3.00	2.97	3.86
MgO	0.86	0.64	0.65	0.64	0.68	0.59	0.55	0.47	0.84
MnO	0.05	0.02	0.03	0.00	0.03	0.02	0.02	0.00	0.01
K ₂ O	10.35	11.17	10.99	10.99	10.57	11.04	11.19	11.08	11.19
CaO	0.07	0.01	0.05	0.00	0.03	0.00	0.00	0.02	0.00
Na ₂ O	0.33	0.44	0.58	0.51	0.48	0.54	0.46	0.44	0.40
F	0.21	0.15	0.18	0.06	0.30	0.16	0.02	0.15	0.20
Total	95.88	96.02	95.75	96.15	95.40	95.86	96.56	95.88	95.25
<i>Numbers of ions on the basis of 11 oxygens</i>									
Si	3.043	3.028	3.030	3.026	3.036	3.010	3.022	3.001	3.063
Al IV	0.957	0.972	0.970	0.974	0.964	0.990	0.978	0.999	0.937
Σ T	4.000	4.000	4.000	4.000	4.000	4.000	4.000	4.000	4.000
Al VI	1.726	1.752	1.710	1.711	1.733	1.735	1.731	1.762	1.667
Ti	0.031	0.022	0.039	0.046	0.036	0.047	0.053	0.041	0.039
Fe	0.182	0.162	0.174	0.175	0.168	0.153	0.150	0.149	0.196
Mg	0.085	0.063	0.065	0.064	0.068	0.059	0.054	0.047	0.084
Mn	0.003	0.001	0.002	0.000	0.002	0.001	0.001	0.000	0.001
Σ R	2.026	2.000	1.990	1.995	2.007	1.995	1.990	1.999	1.987
Ca	0.005	0.001	0.004	0.000	0.002	0.000	0.000	0.001	0.000
Na	0.043	0.057	0.076	0.066	0.063	0.070	0.060	0.057	0.052
K	0.880	0.952	0.941	0.935	0.906	0.942	0.946	0.945	0.965
Σ A	0.928	1.010	1.020	1.001	0.971	1.013	1.006	1.003	1.017
F	0.005	0.005	0.005	0.005	0.005	0.005	0.005	0.005	0.005

Table IV.6: Major element analyses of muscovites. The single grain analyses were performed with an electron microprobe.

	BT08-63-M09-4	BT08-63-M10-2	BT08-63-M10-3	BT08-63-M10-4	BT08-63-M10-5	BT08-63-M10-6	BT08-63-M12-2	BT08-63-M12-3	BT08-63-M12-4
SiO ₂	45.57	45.06	45.45	45.79	44.95	45.45	45.44	45.03	45.31
Al ₂ O ₃	32.75	31.57	33.08	32.89	32.90	32.81	32.87	33.51	33.08
TiO ₂	0.76	1.16	0.61	1.07	1.12	1.12	0.70	0.43	0.63
FeO	3.66	4.66	3.68	3.42	3.69	3.48	3.54	3.51	3.48
MgO	0.88	1.47	0.85	0.82	0.76	0.86	0.79	0.81	0.82
MnO	0.03	0.05	0.04	0.00	0.02	0.00	0.02	0.02	0.01
K ₂ O	11.31	10.93	11.23	11.46	11.41	11.37	11.26	11.32	11.21
CaO	0.00	0.02	0.01	0.00	0.00	0.00	0.00	0.01	0.04
Na ₂ O	0.34	0.26	0.29	0.35	0.41	0.36	0.40	0.37	0.37
F	0.17	0.03	0.05	0.14	0.18	0.15	0.15	0.05	0.25
Total	95.47	95.21	95.29	95.93	95.44	95.60	95.17	95.06	95.21
<i>Numbers of ions on the basis of 11 oxygens</i>									
Si	3.071	3.051	3.062	3.069	3.037	3.059	3.069	3.043	3.061
Al IV	0.929	0.949	0.938	0.931	0.963	0.941	0.931	0.957	0.939
ΣT	4.000	4.000	4.000	4.000	4.000	4.000	4.000	4.000	4.000
Al VI	1.672	1.570	1.690	1.668	1.658	1.662	1.686	1.713	1.696
Ti	0.039	0.059	0.031	0.054	0.057	0.057	0.036	0.022	0.032
Fe	0.186	0.238	0.187	0.173	0.188	0.176	0.180	0.179	0.177
Mg	0.088	0.149	0.085	0.082	0.077	0.087	0.079	0.082	0.083
Mn	0.002	0.003	0.002	0.000	0.001	0.000	0.001	0.001	0.001
ΣR	1.986	2.019	1.995	1.976	1.980	1.981	1.983	1.996	1.988
Ca	0.000	0.001	0.001	0.000	0.000	0.000	0.000	0.001	0.003
Na	0.044	0.034	0.038	0.045	0.054	0.047	0.052	0.049	0.049
K	0.972	0.944	0.965	0.980	0.984	0.976	0.970	0.976	0.966
ΣA	1.017	0.979	1.005	1.025	1.038	1.023	1.022	1.025	1.018
F	0.005	0.005	0.005	0.005	0.005	0.005	0.005	0.005	0.005

Table IV.6: Major element analyses of muscovites. The single grain analyses were performed with an electron microprobe.

	BT08-63-M12-5	BT08-63-M11-2	BT08-63-M11-3	BT08-63-M11-4	BT08-63-M11-5	BT08-63-M11-6	BT08-63-M01-2	BT08-63-M01-3	BT08-63-M02-1
SiO ₂	45.31	45.38	45.56	45.49	45.76	45.40	45.05	45.00	45.27
Al ₂ O ₃	33.06	33.41	32.42	32.14	32.02	31.94	31.72	32.77	32.26
TiO ₂	0.68	0.55	0.84	0.95	1.14	1.22	1.69	1.15	1.23
FeO	3.87	3.66	3.89	3.95	3.88	3.97	4.14	3.65	4.17
MgO	0.88	0.77	0.99	1.01	1.02	0.95	1.03	0.86	0.86
MnO	0.00	0.00	0.04	0.05	0.06	0.04	0.03	0.02	0.00
K ₂ O	11.22	11.24	11.62	11.27	10.53	11.19	11.09	11.15	11.24
CaO	0.00	0.01	0.00	0.00	0.00	0.01	0.05	0.04	0.00
Na ₂ O	0.39	0.39	0.25	0.33	0.36	0.47	0.33	0.39	0.45
F	0.08	0.09	0.25	0.26	0.23	0.24	0.22	0.05	0.00
Total	95.49	95.49	95.86	95.46	95.00	95.43	95.34	95.08	95.49

Numbers of ions on the basis of 11 oxygens

Si	3.051	3.052	3.069	3.074	3.090	3.070	3.050	3.043	3.054
Al IV	0.949	0.948	0.931	0.926	0.910	0.930	0.950	0.957	0.946
ΣT	4.000	4.000	4.000	4.000	4.000	4.000	4.000	4.000	4.000
Al VI	1.675	1.702	1.643	1.634	1.638	1.616	1.583	1.655	1.619
Ti	0.034	0.028	0.042	0.048	0.058	0.062	0.086	0.058	0.063
Fe	0.196	0.185	0.197	0.201	0.197	0.202	0.211	0.186	0.212
Mg	0.089	0.077	0.100	0.102	0.103	0.096	0.104	0.087	0.086
Mn	0.000	0.000	0.002	0.003	0.003	0.002	0.002	0.001	0.000
ΣR	1.995	1.992	1.985	1.987	2.000	1.978	1.985	1.988	1.980
Ca	0.000	0.000	0.000	0.000	0.000	0.001	0.004	0.003	0.000
Na	0.051	0.051	0.032	0.044	0.047	0.062	0.043	0.052	0.059
K	0.964	0.965	0.999	0.971	0.907	0.965	0.958	0.962	0.967
ΣA	1.014	1.016	1.031	1.015	0.954	1.028	1.005	1.016	1.026
F	0.005	0.005	0.005	0.005	0.005	0.005	0.005	0.005	0.005

Table IV.6: Major element analyses of muscovites. The single grain analyses were performed with an electron microprobe.

	BT08-63-M02-2	BT08-63-M02-3	BT08-63-M02-4	BT08-63-M02-5	BT08-63-M02-6	BT08-63-M02-7	BT08-63-M02-8	BT08-63-M02-10	BT08-63-M02-11
SiO ₂	45.29	45.75	45.04	45.46	45.34	45.13	45.14	45.14	45.39
Al ₂ O ₃	32.52	31.98	32.44	31.67	32.06	31.11	32.28	32.51	31.74
TiO ₂	1.19	0.84	1.42	1.52	1.57	1.63	1.44	0.92	1.61
FeO	4.10	4.37	3.92	4.00	3.75	4.59	3.85	4.05	3.73
MgO	0.88	1.26	0.79	0.97	0.85	1.35	0.88	0.88	0.93
MnO	0.00	0.03	0.01	0.05	0.01	0.03	0.02	0.02	0.05
K ₂ O	11.34	11.17	11.09	11.26	11.31	10.90	11.25	11.20	11.42
CaO	0.00	0.00	0.00	0.00	0.01	0.00	0.00	0.00	0.00
Na ₂ O	0.41	0.37	0.44	0.37	0.34	0.38	0.37	0.33	0.32
F	0.23	0.16	0.13	0.13	0.21	0.21	0.25	0.27	0.17
Total	95.95	95.93	95.27	95.44	95.45	95.33	95.48	95.32	95.36

Numbers of ions on the basis of 11 oxygens

Si	3.047	3.075	3.045	3.072	3.063	3.059	3.051	3.055	3.071
Al IV	0.953	0.925	0.955	0.928	0.937	0.941	0.949	0.945	0.929
ΣT	4.000	4.000	4.000	4.000	4.000	4.000	4.000	4.000	4.000
Al VI	1.627	1.609	1.630	1.595	1.616	1.544	1.622	1.648	1.602
Ti	0.060	0.042	0.072	0.077	0.080	0.083	0.073	0.047	0.082
Fe	0.208	0.221	0.200	0.204	0.191	0.234	0.196	0.206	0.190
Mg	0.088	0.126	0.079	0.098	0.085	0.137	0.088	0.089	0.094
Mn	0.000	0.002	0.000	0.003	0.001	0.001	0.001	0.001	0.003
ΣR	1.983	2.000	1.981	1.976	1.973	2.000	1.981	1.991	1.970
Ca	0.000	0.000	0.000	0.000	0.001	0.000	0.000	0.000	0.000
Na	0.054	0.048	0.058	0.048	0.044	0.049	0.049	0.044	0.042
K	0.973	0.958	0.956	0.971	0.975	0.942	0.970	0.967	0.986
ΣA	1.027	1.006	1.014	1.019	1.020	0.992	1.019	1.011	1.028
F	0.005	0.005	0.005	0.005	0.005	0.005	0.005	0.005	0.005

Table IV.6: Major element analyses of muscovites. The single grain analyses were performed with an electron microprobe.

	BT08-63-M02-12	BT08-26_M13_3	BT08-26_M13_4	BT08-26_M14_1	BT08-26_M14_2	BT08-26_M14_3	BT08-26_M14_4	BT08-26_M15_1	BT08-26_M15_2
SiO ₂	45.18	45.23	45.16	45.33	45.89	45.33	45.61	45.49	45.28
Al ₂ O ₃	32.44	32.15	32.20	32.72	32.95	32.63	32.97	33.44	32.63
TiO ₂	1.07	1.07	1.25	1.03	0.95	0.86	1.04	0.92	0.92
FeO	4.08	4.06	4.02	3.89	4.07	3.88	3.60	3.76	3.95
MgO	0.89	0.96	1.00	0.96	0.94	0.88	0.87	0.77	0.92
MnO	0.03	0.02	0.03	0.06	0.04	0.05	0.06	0.03	0.01
K ₂ O	11.39	11.19	11.19	11.21	11.12	10.94	11.02	10.68	11.16
CaO	0.00	0.00	0.00	0.00	0.00	0.00	0.01	0.01	0.00
Na ₂ O	0.42	0.41	0.38	0.36	0.42	0.47	0.29	0.35	0.40
F	0.13	0.18	0.43	0.35	0.24	0.31	0.15	0.24	0.33
Total	95.62	95.27	95.67	95.91	96.61	95.35	95.62	95.69	95.61

Numbers of ions on the basis of 11 oxygens

Si	3.049	3.061	3.052	3.050	3.059	3.062	3.062	3.049	3.055
Al IV	0.951	0.939	0.948	0.950	0.941	0.938	0.938	0.951	0.945
ΣT	4.000	4.000	4.000	4.000	4.000	4.000	4.000	4.000	4.000
Al VI	1.630	1.626	1.618	1.645	1.648	1.660	1.671	1.691	1.650
Ti	0.054	0.055	0.063	0.052	0.047	0.044	0.052	0.046	0.047
Fe	0.207	0.207	0.205	0.197	0.204	0.197	0.182	0.190	0.201
Mg	0.089	0.097	0.101	0.096	0.094	0.089	0.087	0.077	0.093
Mn	0.002	0.001	0.002	0.003	0.002	0.003	0.003	0.002	0.001
ΣR	1.982	1.986	1.989	1.994	1.995	1.993	1.996	2.006	1.991
Ca	0.000	0.000	0.000	0.000	0.000	0.000	0.001	0.001	0.000
Na	0.056	0.054	0.050	0.047	0.054	0.061	0.038	0.045	0.052
K	0.981	0.966	0.965	0.962	0.946	0.943	0.944	0.913	0.961
ΣA	1.036	1.020	1.015	1.009	1.000	1.004	0.983	0.959	1.013
F	0.005	0.005	0.005	0.005	0.005	0.005	0.005	0.005	0.005

Table IV.6: Major element analyses of muscovites. The single grain analyses were performed with an electron microprobe.

	BT08-26_M15_3	BT08-26_M15_4	BT08-26_M15_5	BT08-26_M15_6	BT08-26_M15_7	BT08-26_M15_8	BT08-26_M08_1	BT08-26_M08_2	BT08-26_M08_3
SiO ₂	45.22	44.90	45.28	45.50	44.98	44.86	46.03	46.81	45.55
Al ₂ O ₃	32.66	32.63	31.92	32.76	32.29	32.54	32.63	33.58	32.84
TiO ₂	1.09	1.13	0.94	1.10	0.95	1.16	0.86	0.48	0.72
FeO	4.12	4.28	4.13	4.06	4.09	4.01	3.70	3.69	3.80
MgO	0.96	0.94	0.97	0.95	1.03	0.94	0.94	0.93	0.94
MnO	0.03	0.04	0.07	0.04	0.04	0.04	0.04	0.04	0.05
K ₂ O	11.24	10.97	11.04	11.12	11.11	11.15	10.85	11.23	11.05
CaO	0.00	0.03	0.00	0.00	0.00	0.00	0.04	0.02	0.01
Na ₂ O	0.34	0.39	0.39	0.42	0.41	0.46	0.37	0.30	0.40
F	0.26	0.25	0.40	0.31	0.28	0.40	0.30	0.41	0.31
Total	95.92	95.56	95.14	96.28	95.19	95.56	95.76	97.49	95.67
<i>Numbers of ions on the basis of 11 oxygens</i>									
Si	3.043	3.032	3.074	3.049	3.050	3.035	3.087	3.087	3.065
Al IV	0.957	0.968	0.926	0.951	0.950	0.965	0.913	0.913	0.935
Σ T	4.000	4.000	4.000	4.000	4.000	4.000	4.000	4.000	4.000
Al VI	1.633	1.629	1.628	1.636	1.632	1.631	1.666	1.697	1.670
Ti	0.055	0.057	0.048	0.056	0.048	0.059	0.044	0.024	0.036
Fe	0.209	0.218	0.211	0.205	0.209	0.204	0.187	0.183	0.193
Mg	0.096	0.095	0.098	0.095	0.104	0.095	0.094	0.091	0.094
Mn	0.002	0.002	0.004	0.002	0.002	0.003	0.002	0.002	0.003
Σ R	1.995	2.001	1.989	1.994	1.996	1.992	1.993	1.998	1.996
Ca	0.000	0.002	0.000	0.000	0.000	0.000	0.003	0.001	0.001
Na	0.044	0.051	0.051	0.055	0.054	0.060	0.048	0.039	0.052
K	0.965	0.945	0.956	0.951	0.961	0.963	0.928	0.945	0.949
Σ A	1.009	0.998	1.007	1.005	1.016	1.023	0.980	0.985	1.002
F	0.005	0.005	0.005	0.005	0.005	0.005	0.005	0.005	0.005

Table IV.6: Major element analyses of muscovites. The single grain analyses were performed with an electron microprobe.

	BT08-26_M08_4	BT08-26_M08_7	BT08-26_M08_8	BT08-26_M07_1	BT08-26_M07_2	BT08-26_M07_3	BT08-26_M07_4	BT08-26_M06_2	BT08-26_M06_3
SiO ₂	45.33	45.53	45.33	45.18	45.40	45.29	45.50	45.55	45.45
Al ₂ O ₃	32.66	32.94	33.00	32.59	32.18	32.20	31.98	32.85	32.52
TiO ₂	0.57	0.48	0.48	1.05	0.98	0.97	1.05	1.09	0.93
FeO	3.92	3.81	3.74	3.82	3.85	3.83	3.78	4.03	3.97
MgO	0.97	0.96	0.98	0.98	0.98	0.96	1.09	0.89	0.91
MnO	0.06	0.05	0.06	0.02	0.02	0.05	0.06	0.06	0.08
K ₂ O	11.21	11.03	11.11	11.00	11.01	11.03	10.96	11.09	11.03
CaO	0.00	0.00	0.00	0.00	0.00	0.01	0.00	0.01	0.00
Na ₂ O	0.42	0.45	0.44	0.38	0.38	0.40	0.41	0.41	0.43
F	0.30	0.28	0.28	0.36	0.31	0.30	0.30	0.35	0.33
Total	95.45	95.53	95.41	95.38	95.11	95.05	95.14	96.33	95.65
<i>Numbers of ions on the basis of 11 oxygens</i>									
Si	3.063	3.067	3.059	3.053	3.075	3.070	3.080	3.050	3.064
Al IV	0.937	0.933	0.941	0.947	0.925	0.930	0.920	0.950	0.936
Σ T	4.000	4.000	4.000	4.000	4.000	4.000	4.000	4.000	4.000
Al VI	1.665	1.682	1.684	1.649	1.644	1.644	1.632	1.643	1.648
Ti	0.029	0.024	0.024	0.053	0.050	0.050	0.053	0.055	0.047
Fe	0.199	0.193	0.190	0.194	0.196	0.196	0.193	0.203	0.202
Mg	0.098	0.097	0.098	0.098	0.099	0.097	0.110	0.089	0.091
Mn	0.004	0.003	0.003	0.001	0.001	0.003	0.004	0.003	0.004
Σ R	1.994	1.999	2.000	1.997	1.990	1.989	1.992	1.993	1.992
Ca	0.000	0.000	0.000	0.000	0.000	0.001	0.000	0.001	0.000
Na	0.055	0.059	0.057	0.050	0.050	0.053	0.054	0.054	0.056
K	0.966	0.948	0.956	0.948	0.951	0.954	0.946	0.947	0.949
Σ A	1.021	1.007	1.014	0.998	1.001	1.007	1.001	1.002	1.005
F	0.005	0.005	0.005	0.005	0.005	0.005	0.005	0.005	0.005

Table IV.6: Major element analyses of muscovites. The single grain analyses were performed with an electron microprobe.

	BT08-26_M06_4	BT08-26_M06_5	BT08-26_M06_6	BT08-26_M06_7	BT08-26_M06_8	BT08-26_M06_9	BT08-26_M06_10	BT08-26_M06_11	BT08-26_M06_12
SiO ₂	45.49	45.62	45.71	45.87	45.35	45.43	45.51	45.51	45.36
Al ₂ O ₃	32.56	32.12	32.49	32.22	32.45	32.63	32.32	32.16	31.83
TiO ₂	0.94	1.00	1.05	1.00	0.82	0.90	0.96	0.94	0.88
FeO	3.97	4.02	3.91	3.96	4.01	3.86	3.95	4.20	4.13
MgO	0.95	0.92	0.93	0.92	0.91	0.93	0.97	1.02	1.06
MnO	0.05	0.04	0.05	0.01	0.05	0.07	0.05	0.06	0.04
K ₂ O	11.09	11.23	11.30	10.97	11.18	11.05	11.13	10.90	10.90
CaO	0.00	0.01	0.00	0.01	0.00	0.04	0.01	0.01	0.00
Na ₂ O	0.39	0.45	0.40	0.35	0.43	0.40	0.44	0.46	0.48
F	0.34	0.40	0.36	0.31	0.30	0.28	0.32	0.42	0.43
Total	95.77	95.81	96.20	95.62	95.49	95.57	95.66	95.67	95.10
<i>Numbers of ions on the basis of 11 oxygens</i>									
Si	3.062	3.076	3.067	3.087	3.064	3.062	3.069	3.070	3.079
Al IV	0.938	0.924	0.933	0.913	0.936	0.938	0.931	0.930	0.921
Σ T	4.000	4.000	4.000	4.000	4.000	4.000	4.000	4.000	4.000
Al VI	1.647	1.629	1.638	1.643	1.648	1.654	1.638	1.628	1.626
Ti	0.047	0.051	0.053	0.051	0.042	0.045	0.049	0.048	0.045
Fe	0.201	0.204	0.198	0.201	0.204	0.196	0.201	0.213	0.211
Mg	0.096	0.093	0.093	0.093	0.091	0.094	0.097	0.102	0.107
Mn	0.003	0.002	0.003	0.001	0.003	0.004	0.003	0.003	0.002
Σ R	1.993	1.979	1.984	1.988	1.988	1.993	1.987	1.995	1.991
Ca	0.000	0.000	0.000	0.001	0.000	0.003	0.001	0.001	0.000
Na	0.051	0.059	0.052	0.045	0.056	0.052	0.058	0.060	0.063
K	0.952	0.966	0.967	0.942	0.964	0.950	0.957	0.938	0.944
Σ A	1.004	1.026	1.019	0.988	1.020	1.004	1.016	0.998	1.007
F	0.005	0.005	0.005	0.005	0.005	0.005	0.005	0.005	0.005

Table IV.6: Major element analyses of muscovites. The single grain analyses were performed with an electron microprobe.

	BT08-26_M06_14	BT08-26_M05_1	BT08-26_M05_2	BT08-26_M05_3	BT08-26_M05_4	BT08-26_M05_5	BT08-26_M05_6	BT08-26_M05_7
SiO ₂	45.96	45.60	45.70	45.62	46.15	45.51	45.52	45.64
Al ₂ O ₃	32.26	33.36	32.85	32.54	32.41	32.86	32.55	32.44
TiO ₂	0.82	1.01	0.83	0.82	0.70	0.86	0.90	0.78
FeO	4.06	3.95	4.03	4.01	4.08	3.90	3.97	4.00
MgO	0.94	0.90	1.01	0.98	1.06	1.00	1.03	1.10
MnO	0.03	0.04	0.05	0.04	0.06	0.02	0.02	0.06
K ₂ O	11.12	11.19	10.98	11.14	11.08	10.99	11.20	11.16
CaO	0.00	0.00	0.00	0.00	0.00	0.00	0.00	0.01
Na ₂ O	0.43	0.41	0.48	0.39	0.47	0.44	0.48	0.46
F	0.41	0.22	0.37	0.34	0.24	0.43	0.28	0.22
Total	96.04	96.69	96.30	95.89	96.24	96.02	95.96	95.87
<i>Numbers of ions on the basis of 11 oxygens</i>								
Si	3.087	3.038	3.059	3.068	3.087	3.056	3.060	3.068
Al IV	0.913	0.962	0.941	0.932	0.913	0.944	0.940	0.932
Σ T	4.000	4.000	4.000	4.000	4.000	4.000	4.000	4.000
Al VI	1.642	1.658	1.651	1.648	1.643	1.658	1.639	1.639
Ti	0.041	0.050	0.042	0.041	0.035	0.043	0.046	0.040
Fe	0.205	0.198	0.203	0.203	0.205	0.197	0.201	0.202
Mg	0.094	0.090	0.101	0.098	0.105	0.100	0.103	0.110
Mn	0.002	0.002	0.003	0.002	0.003	0.001	0.001	0.003
Σ R	1.985	1.998	1.999	1.993	1.992	1.999	1.991	1.994
Ca	0.000	0.000	0.000	0.000	0.000	0.000	0.000	0.000
Na	0.056	0.053	0.063	0.051	0.061	0.057	0.062	0.060
K	0.953	0.951	0.938	0.956	0.946	0.942	0.960	0.957
Σ A	1.009	1.004	1.000	1.007	1.006	0.999	1.023	1.018
F	0.005	0.005	0.005	0.005	0.005	0.005	0.005	0.005

Table IV.6: Major element analyses of muscovites. The single grain analyses were performed with an electron microprobe.

	BT08-26_M05_8	BT08-26_M05_9	BT08-26_M04_2	BT08-26_M04_3	BT08-26_M04_4	BT08-26_M04_6	BT08-26_M03_1	BT08-26_M03_2	BT08-26_M03_3
SiO ₂	45.30	45.65	45.73	45.61	45.47	45.55	45.57	45.51	45.57
Al ₂ O ₃	32.57	32.81	32.95	32.79	32.95	32.76	32.91	32.77	32.65
TiO ₂	1.14	1.00	0.88	0.80	0.66	0.81	0.89	1.02	0.85
FeO	3.97	3.92	3.84	3.94	4.01	3.85	3.76	3.89	3.91
MgO	1.06	0.98	0.97	1.01	0.97	1.01	0.93	0.96	0.99
MnO	0.05	0.03	0.02	0.02	0.04	0.03	0.03	0.05	0.05
K ₂ O	11.08	11.12	11.07	11.20	11.18	11.20	11.24	11.06	11.27
CaO	0.00	0.00	0.00	0.00	0.00	0.00	0.00	0.00	0.00
Na ₂ O	0.51	0.47	0.39	0.45	0.41	0.42	0.37	0.39	0.37
F	0.47	0.26	0.34	0.35	0.26	0.39	0.36	0.24	0.38
Total	96.15	96.24	96.19	96.18	95.96	96.02	96.07	95.89	96.04

Numbers of ions on the basis of 11 oxygens

Si	3.045	3.056	3.061	3.059	3.054	3.060	3.058	3.056	3.063
Al IV	0.955	0.944	0.939	0.941	0.946	0.940	0.942	0.944	0.937
ΣT	4.000	4.000	4.000	4.000	4.000	4.000	4.000	4.000	4.000
Al VI	1.627	1.645	1.662	1.652	1.663	1.655	1.662	1.649	1.649
Ti	0.058	0.051	0.044	0.040	0.034	0.041	0.045	0.052	0.043
Fe	0.201	0.198	0.194	0.199	0.203	0.195	0.190	0.197	0.198
Mg	0.106	0.098	0.096	0.101	0.097	0.101	0.093	0.096	0.099
Mn	0.003	0.002	0.001	0.001	0.002	0.002	0.002	0.003	0.003
ΣR	1.995	1.993	1.997	1.994	1.998	1.994	1.992	1.997	1.992
Ca	0.000	0.000	0.000	0.000	0.000	0.000	0.000	0.000	0.000
Na	0.066	0.061	0.050	0.059	0.054	0.054	0.049	0.050	0.048
K	0.950	0.950	0.945	0.958	0.958	0.960	0.962	0.947	0.966
ΣA	1.017	1.010	0.995	1.017	1.012	1.014	1.011	0.998	1.014
F	0.005	0.005	0.005	0.005	0.005	0.005	0.005	0.005	0.005

Table IV.6: Major element analyses of muscovites. The single grain analyses were performed with an electron microprobe.

	BT08-26_M03_4	BT08-26_M03_5	BT08-26_M01_1	BT08-26_M01_2	BT08-26_M01_3	BT08-26_M01_4	BT08-26_M01_5	BT08-26_M01_6	BT08-26_M01_7
SiO ₂	45.70	45.53	46.74	45.59	45.67	45.51	45.53	45.60	45.74
Al ₂ O ₃	32.76	32.36	33.09	32.48	32.35	32.42	32.51	32.01	32.56
TiO ₂	0.97	0.89	0.73	0.99	0.78	0.83	0.83	0.79	0.77
FeO	4.02	3.87	3.55	3.98	3.97	3.84	3.99	4.11	3.87
MgO	1.00	1.00	0.93	0.94	0.95	0.92	0.96	0.99	0.98
MnO	0.03	0.05	0.01	0.06	0.03	0.03	0.02	0.04	0.05
K ₂ O	10.82	11.19	11.32	11.15	11.10	10.88	10.72	10.98	11.18
CaO	0.00	0.00	0.00	0.00	0.01	0.03	0.04	0.01	0.01
Na ₂ O	0.38	0.35	0.34	0.43	0.41	0.41	0.44	0.40	0.38
F	0.18	0.23	0.24	0.36	0.28	0.27	0.28	0.36	0.31
Total	95.87	95.46	96.96	95.98	95.56	95.14	95.32	95.29	95.85
<i>Numbers of ions on the basis of 11 oxygens</i>									
Si	3.062	3.072	3.095	3.065	3.079	3.076	3.071	3.085	3.075
Al IV	0.938	0.928	0.905	0.935	0.921	0.924	0.929	0.915	0.925
Σ T	4.000	4.000	4.000	4.000	4.000	4.000	4.000	4.000	4.000
Al VI	1.650	1.646	1.679	1.639	1.649	1.660	1.656	1.639	1.655
Ti	0.049	0.045	0.037	0.050	0.040	0.042	0.042	0.040	0.039
Fe	0.203	0.197	0.177	0.201	0.202	0.195	0.203	0.209	0.196
Mg	0.100	0.101	0.092	0.094	0.095	0.093	0.096	0.099	0.098
Mn	0.002	0.003	0.001	0.004	0.002	0.002	0.001	0.002	0.003
Σ R	2.004	1.991	1.985	1.989	1.988	1.992	1.998	1.990	1.991
Ca	0.000	0.000	0.000	0.000	0.001	0.002	0.003	0.001	0.001
Na	0.050	0.046	0.043	0.055	0.054	0.054	0.057	0.053	0.049
K	0.925	0.963	0.956	0.956	0.955	0.938	0.922	0.948	0.959
Σ A	0.975	1.009	1.000	1.012	1.010	0.994	0.982	1.001	1.009
F	0.005	0.005	0.005	0.005	0.005	0.005	0.005	0.005	0.005

Table IV.6: Major element analyses of muscovites. The single grain analyses were performed with an electron microprobe.

	BT08-31_M7-1	BT08-31_M7-2	BT08-31_M7-3	BT08-31_M8-1	BT08-31_M8-2	BT08-31_M8-3	BT08-31_M8-4	BT08-31_M10_1	BT08-31_M10_2
SiO ₂	45.24	45.50	44.90	45.11	45.33	45.50	45.87	45.87	45.48
Al ₂ O ₃	32.73	32.59	32.43	32.42	31.90	32.16	32.59	32.88	32.22
TiO ₂	1.60	1.03	1.48	1.46	2.03	1.85	0.91	0.77	1.22
FeO	3.91	4.47	4.16	4.32	3.98	4.06	4.27	3.74	3.97
MgO	0.81	1.05	0.89	0.92	0.99	0.93	0.91	0.95	0.92
MnO	0.01	0.01	0.01	0.04	0.01	0.04	0.05	0.01	0.02
K ₂ O	11.31	11.27	10.88	11.29	11.35	11.26	11.20	11.33	11.05
CaO	0.00	0.00	0.00	0.00	0.01	0.00	0.00	0.06	0.00
Na ₂ O	0.42	0.30	0.33	0.38	0.34	0.32	0.40	0.28	0.35
F	0.12	0.11	0.14	0.00	0.13	0.08	0.21	0.14	0.19
Total	96.14	96.33	95.22	95.95	96.08	96.20	96.40	96.02	95.42

Numbers of ions on the basis of 11 oxygens

Si	3.034	3.046	3.036	3.032	3.046	3.048	3.067	3.071	3.068
Al IV	0.966	0.954	0.964	0.968	0.954	0.952	0.933	0.929	0.932
ΣT	4.000	4.000	4.000	4.000	4.000	4.000	4.000	4.000	4.000
Al VI	1.621	1.618	1.620	1.601	1.572	1.589	1.635	1.667	1.631
Ti	0.081	0.052	0.075	0.074	0.103	0.093	0.046	0.039	0.062
Fe	0.197	0.225	0.212	0.219	0.201	0.205	0.215	0.189	0.202
Mg	0.080	0.105	0.089	0.092	0.099	0.093	0.091	0.095	0.092
Mn	0.000	0.000	0.001	0.002	0.000	0.002	0.003	0.000	0.001
ΣR	1.980	2.000	1.998	1.988	1.976	1.982	1.990	1.990	1.987
Ca	0.000	0.000	0.000	0.000	0.001	0.000	0.000	0.004	0.000
Na	0.054	0.039	0.043	0.050	0.045	0.041	0.051	0.036	0.046
K	0.968	0.963	0.938	0.968	0.973	0.962	0.955	0.968	0.951
ΣA	1.022	1.002	0.981	1.018	1.018	1.004	1.007	1.008	0.997
F	0.005	0.005	0.005	0.005	0.005	0.005	0.005	0.005	0.005

Table IV.6: Major element analyses of muscovites. The single grain analyses were performed with an electron microprobe.

	BT08-31_M10_3	BT08-31_M10_4	BT08-31_M10_6	BT08-31_M09_1	BT08-31_M09_2	BT08-31_M09_3	BT08-31_M09_4	BT08-31_M14_1	BT08-31_M14_2
SiO ₂	45.73	45.10	45.42	45.97	45.25	45.14	45.32	45.49	45.35
Al ₂ O ₃	32.17	32.68	32.27	33.15	33.12	32.89	32.49	32.38	32.33
TiO ₂	1.05	1.13	1.12	1.12	1.14	0.98	1.15	1.11	1.18
FeO	3.98	3.97	3.80	3.34	3.73	3.76	3.58	3.88	3.80
MgO	0.98	0.84	0.92	0.85	0.85	0.85	0.86	0.92	0.89
MnO	0.02	0.01	0.03	0.00	0.00	0.02	0.00	0.04	0.02
K ₂ O	11.28	11.29	11.19	11.19	11.32	10.97	11.17	11.19	11.06
CaO	0.01	0.00	0.01	0.00	0.00	0.03	0.01	0.00	0.01
Na ₂ O	0.30	0.33	0.30	0.30	0.42	0.33	0.44	0.42	0.37
F	0.21	0.19	0.18	0.17	0.16	0.05	0.32	0.14	0.23
Total	95.73	95.55	95.25	96.08	95.99	95.01	95.35	95.58	95.23
<i>Numbers of ions on the basis of 11 oxygens</i>									
Si	3.078	3.044	3.070	3.069	3.036	3.050	3.063	3.064	3.065
Al IV	0.922	0.956	0.930	0.931	0.964	0.950	0.937	0.936	0.935
Σ T	4.000	4.000	4.000	4.000	4.000	4.000	4.000	4.000	4.000
Al VI	1.631	1.644	1.641	1.679	1.656	1.669	1.652	1.636	1.642
Ti	0.053	0.058	0.057	0.056	0.058	0.050	0.058	0.056	0.060
Fe	0.202	0.202	0.193	0.168	0.188	0.191	0.182	0.197	0.193
Mg	0.098	0.084	0.093	0.084	0.085	0.086	0.087	0.093	0.089
Mn	0.001	0.000	0.002	0.000	0.000	0.001	0.000	0.002	0.001
Σ R	1.985	1.988	1.986	1.987	1.987	1.996	1.979	1.984	1.985
Ca	0.000	0.000	0.001	0.000	0.000	0.002	0.001	0.000	0.001
Na	0.039	0.043	0.040	0.039	0.055	0.044	0.058	0.054	0.049
K	0.969	0.972	0.965	0.953	0.969	0.945	0.963	0.962	0.954
Σ A	1.008	1.016	1.005	0.992	1.024	0.991	1.022	1.016	1.003
F	0.005	0.005	0.005	0.005	0.005	0.005	0.005	0.005	0.005

Table IV.6: Major element analyses of muscovites. The single grain analyses were performed with an electron microprobe.

	BT08-31_M14_3	BT08-31_M18_5	BT08-31_M04_2	BT08-31_M04_3	BT08-31_M04_5	BT08-31_M05_2	BT08-31_M05_3	BT08-31_M05_4	BT08-31_M03_3
SiO ₂	45.25	45.28	45.64	44.94	45.41	45.39	45.50	45.36	45.21
Al ₂ O ₃	32.23	32.25	32.44	32.45	32.58	32.87	32.24	32.35	32.15
TiO ₂	1.21	1.27	1.34	1.48	1.39	1.12	1.47	1.31	1.10
FeO	3.89	3.86	3.78	3.72	3.73	3.57	3.79	3.54	3.54
MgO	0.87	0.92	1.12	1.06	0.99	0.89	1.23	0.96	1.18
MnO	0.04	0.04	0.00	0.01	0.03	0.02	0.00	0.02	0.01
K ₂ O	11.21	11.03	10.88	11.21	11.36	11.16	11.03	11.15	11.16
CaO	0.00	0.00	0.04	0.01	0.03	0.03	0.07	0.03	0.06
Na ₂ O	0.45	0.43	0.24	0.34	0.30	0.32	0.40	0.29	0.30
F	0.20	0.06	0.20	0.10	0.11	0.17	0.16	0.16	0.34
Total	95.35	95.14	95.69	95.32	95.93	95.53	95.89	95.17	95.05
<i>Numbers of ions on the basis of 11 oxygens</i>									
Si	3.060	3.060	3.064	3.036	3.049	3.054	3.054	3.065	3.066
Al IV	0.940	0.940	0.936	0.964	0.951	0.946	0.946	0.935	0.934
Σ T	4.000	4.000	4.000	4.000	4.000	4.000	4.000	4.000	4.000
Al VI	1.629	1.630	1.631	1.621	1.627	1.662	1.605	1.642	1.636
Ti	0.062	0.065	0.068	0.075	0.070	0.057	0.074	0.067	0.056
Fe	0.198	0.196	0.191	0.189	0.189	0.181	0.192	0.180	0.181
Mg	0.088	0.093	0.112	0.107	0.099	0.090	0.123	0.097	0.119
Mn	0.002	0.002	0.000	0.000	0.002	0.001	0.000	0.001	0.001
Σ R	1.979	1.986	2.002	1.993	1.987	1.991	1.994	1.986	1.993
Ca	0.000	0.000	0.003	0.001	0.002	0.002	0.005	0.002	0.004
Na	0.059	0.057	0.032	0.044	0.039	0.041	0.052	0.038	0.039
K	0.967	0.951	0.932	0.966	0.973	0.958	0.945	0.961	0.966
Σ A	1.026	1.008	0.966	1.011	1.014	1.001	1.002	1.001	1.009
F	0.005	0.005	0.005	0.005	0.005	0.005	0.005	0.005	0.005

Table IV.6: Major element analyses of muscovites. The single grain analyses were performed with an electron microprobe.

	BT08-31_M03_4	BT08-31_M03_5	BT08-31_M02_1	BT08-31_M02_2	BT08-31_M02_3	BT08-31_M02_4	BT08-34-M02-5	BT08-80-M01-1	BT08-80-M01-3
SiO ₂	46.06	46.01	45.58	45.42	45.43	45.44	45.61	45.51	45.44
Al ₂ O ₃	32.52	32.77	32.40	32.48	32.91	32.51	34.05	33.34	34.36
TiO ₂	1.07	0.94	1.35	1.35	1.37	1.79	0.63	1.20	0.92
FeO	3.34	3.39	3.41	3.39	3.28	3.16	2.02	2.90	2.58
MgO	1.08	1.11	1.01	0.99	0.91	0.98	1.13	0.78	0.71
MnO	0.00	0.01	0.00	0.00	0.01	0.00	0.01	0.06	0.00
K ₂ O	11.35	11.48	11.46	11.41	11.28	11.34	11.22	11.32	11.01
CaO	0.05	0.00	0.00	0.00	0.01	0.02	0.04	0.02	0.03
Na ₂ O	0.25	0.30	0.32	0.35	0.37	0.34	0.42	0.34	0.36
F	0.18	0.24	0.33	0.28	0.20	0.21	0.07	0.06	0.13
Total	95.89	96.24	95.85	95.67	95.77	95.79	95.20	95.53	95.52
<i>Numbers of ions on the basis of 11 oxygens</i>									
Si	3.086	3.076	3.067	3.060	3.051	3.053	3.059	3.055	3.040
Al IV	0.914	0.924	0.933	0.940	0.949	0.947	0.941	0.945	0.960
Σ T	4.000	4.000	4.000	4.000	4.000	4.000	4.000	4.000	4.000
Al VI	1.655	1.659	1.637	1.640	1.657	1.628	1.752	1.693	1.750
Ti	0.054	0.047	0.068	0.068	0.069	0.090	0.032	0.061	0.046
Fe	0.169	0.171	0.173	0.172	0.166	0.160	0.102	0.147	0.130
Mg	0.108	0.110	0.101	0.099	0.091	0.098	0.113	0.078	0.070
Mn	0.000	0.000	0.000	0.000	0.001	0.000	0.000	0.003	0.000
Σ R	1.985	1.988	1.979	1.980	1.984	1.977	1.999	1.982	1.997
Ca	0.004	0.000	0.000	0.000	0.000	0.002	0.003	0.001	0.002
Na	0.032	0.039	0.041	0.046	0.048	0.044	0.055	0.044	0.047
K	0.970	0.979	0.984	0.981	0.967	0.972	0.960	0.969	0.940
Σ A	1.006	1.018	1.025	1.027	1.015	1.018	1.018	1.015	0.988
F	0.005	0.005	0.005	0.005	0.005	0.005	0.005	0.005	0.005

Table IV.6: Major element analyses of muscovites. The single grain analyses were performed with an electron microprobe.

	BT08-80-M04-3	BT08-80-M04-4	BT08-80-M02-2	BT08-80-M02-4	BT08-80-M02-5	BT08-80-M02-6	BT08-80-M06-1	BT08-80-M06-2	BT08-80-M06-3
SiO ₂	45.47	45.30	46.30	45.71	45.75	45.87	45.50	45.29	44.75
Al ₂ O ₃	33.87	34.20	33.42	33.96	33.83	33.93	33.24	34.10	34.37
TiO ₂	0.74	0.79	0.48	0.88	0.65	0.64	1.39	0.93	0.97
FeO	2.89	2.51	2.99	2.65	2.75	2.67	2.84	2.68	2.62
MgO	0.77	0.70	0.82	0.63	0.69	0.68	0.72	0.64	0.67
MnO	0.05	0.02	0.03	0.04	0.04	0.05	0.04	0.01	0.03
K ₂ O	11.37	11.28	11.03	11.25	11.61	11.54	10.96	11.19	11.44
CaO	0.03	0.03	0.03	0.01	0.00	0.00	0.01	0.02	0.00
Na ₂ O	0.32	0.40	0.35	0.45	0.27	0.33	0.29	0.37	0.35
F	0.09	0.05	0.01	0.15	0.13	0.10	0.06	0.10	0.20
Total	95.60	95.29	95.47	95.72	95.72	95.81	95.06	95.34	95.41

Numbers of ions on the basis of 11 oxygens

Si	3.049	3.042	3.096	3.058	3.065	3.067	3.061	3.041	3.013
Al IV	0.951	0.958	0.904	0.942	0.935	0.933	0.939	0.959	0.987
ΣT	4.000	4.000	4.000	4.000	4.000	4.000	4.000	4.000	4.000
Al VI	1.727	1.749	1.731	1.737	1.737	1.742	1.697	1.740	1.740
Ti	0.037	0.040	0.024	0.044	0.033	0.032	0.070	0.047	0.049
Fe	0.146	0.127	0.151	0.134	0.139	0.134	0.144	0.135	0.133
Mg	0.077	0.070	0.082	0.063	0.069	0.068	0.073	0.064	0.067
Mn	0.003	0.001	0.002	0.002	0.002	0.003	0.002	0.001	0.002
ΣR	1.989	1.987	1.990	1.980	1.980	1.980	1.986	1.988	1.992
Ca	0.003	0.002	0.002	0.001	0.000	0.000	0.001	0.001	0.000
Na	0.042	0.053	0.045	0.058	0.035	0.043	0.038	0.048	0.046
K	0.973	0.966	0.941	0.960	0.992	0.985	0.941	0.959	0.983
ΣA	1.017	1.021	0.988	1.019	1.027	1.028	0.979	1.007	1.028
F	0.005	0.005	0.005	0.005	0.005	0.005	0.005	0.005	0.005

Table IV.6: Major element analyses of muscovites. The single grain analyses were performed with an electron microprobe.

	BT08-80-M06-4	BT08-80-M06-5	BT08-80-M14-3	BT08-80-M14-4	BT08-80-M14-5	BT08-80-M14-6	BT08-80-M17-2	BT08-80-M17-3	BT08-80-M18-2
SiO ₂	45.85	45.17	45.54	45.58	45.55	45.63	45.18	47.35	45.43
Al ₂ O ₃	33.65	34.35	33.95	33.95	34.04	34.74	33.97	31.81	34.32
TiO ₂	0.80	0.62	1.23	1.02	0.81	0.48	1.04	1.45	0.81
FeO	2.74	2.69	2.36	2.46	2.59	2.38	2.71	2.92	2.50
MgO	0.84	0.66	0.61	0.63	0.63	0.57	0.67	0.76	0.64
MnO	0.02	0.03	0.00	0.02	0.05	0.02	0.02	0.02	0.01
K ₂ O	11.00	10.98	11.22	11.30	11.25	11.19	11.23	10.54	11.14
CaO	0.03	0.01	0.00	0.00	0.01	0.03	0.01	0.04	0.02
Na ₂ O	0.35	0.35	0.45	0.41	0.45	0.42	0.39	0.28	0.39
F	0.26	0.15	0.12	0.06	0.15	0.00	0.27	0.20	0.31
Total	95.54	95.01	95.48	95.44	95.53	95.47	95.49	95.36	95.56

Numbers of ions on the basis of 11 oxygens

Si	3.072	3.040	3.051	3.055	3.054	3.050	3.037	3.164	3.046
Al IV	0.928	0.960	0.949	0.945	0.946	0.950	0.963	0.836	0.954
ΣT	4.000	4.000	4.000	4.000	4.000	4.000	4.000	4.000	4.000
Al VI	1.729	1.765	1.733	1.738	1.744	1.787	1.728	1.669	1.758
Ti	0.040	0.032	0.062	0.051	0.041	0.024	0.053	0.073	0.041
Fe	0.138	0.136	0.119	0.124	0.131	0.120	0.137	0.147	0.126
Mg	0.084	0.067	0.061	0.063	0.063	0.057	0.067	0.075	0.063
Mn	0.001	0.002	0.000	0.001	0.003	0.001	0.001	0.001	0.000
ΣR	1.993	2.001	1.975	1.978	1.981	1.989	1.987	1.965	1.989
Ca	0.002	0.001	0.000	0.000	0.001	0.002	0.000	0.003	0.001
Na	0.046	0.046	0.058	0.054	0.059	0.054	0.051	0.036	0.051
K	0.940	0.943	0.959	0.966	0.962	0.954	0.963	0.898	0.953
ΣA	0.989	0.989	1.017	1.020	1.022	1.011	1.014	0.938	1.005
F	0.005	0.005	0.005	0.005	0.005	0.005	0.005	0.005	0.005

Table IV.6: Major element analyses of muscovites. The single grain analyses were performed with an electron microprobe.

	BT08-80-M18-3	BT08-80-M18-4	BT08-80-M18-5	BT08-80-M18-6	BT08-45-M01-1	BT08-45-M01-2	BT08-45-M02-2	BT08-45-M05-3	BT08-45-M04-1
SiO ₂	45.61	45.29	46.15	46.04	45.52	45.33	45.02	45.42	45.03
Al ₂ O ₃	33.38	34.09	33.80	34.21	33.52	32.82	32.93	32.50	33.27
TiO ₂	0.64	0.85	1.08	0.96	1.21	1.24	1.14	1.35	0.80
FeO	3.03	2.70	2.48	2.57	2.66	3.31	3.43	3.29	3.64
MgO	0.77	0.63	0.62	0.65	0.75	0.79	0.75	0.85	0.68
MnO	0.05	0.02	0.05	0.05	0.03	0.03	0.01	0.04	0.00
K ₂ O	11.07	11.15	11.16	10.75	11.36	11.27	11.21	11.06	11.33
CaO	0.01	0.01	0.00	0.00	0.00	0.00	0.00	0.01	0.00
Na ₂ O	0.35	0.48	0.43	0.36	0.40	0.46	0.52	0.42	0.36
F	0.13	0.15	0.08	0.15	0.23	0.16	0.15	0.26	0.23
Total	95.04	95.36	95.84	95.74	95.67	95.40	95.16	95.19	95.34

Numbers of ions on the basis of 11 oxygens

Si	3.073	3.042	3.076	3.066	3.054	3.056	3.044	3.068	3.042
Al IV	0.927	0.958	0.924	0.934	0.946	0.944	0.956	0.932	0.958
ΣT	4.000	4.000	4.000	4.000	4.000	4.000	4.000	4.000	4.000
Al VI	1.724	1.742	1.732	1.752	1.706	1.664	1.669	1.656	1.691
Ti	0.032	0.043	0.054	0.048	0.061	0.063	0.058	0.068	0.041
Fe	0.154	0.137	0.124	0.129	0.134	0.168	0.175	0.167	0.185
Mg	0.077	0.063	0.061	0.065	0.075	0.079	0.076	0.086	0.069
Mn	0.003	0.001	0.003	0.003	0.001	0.002	0.001	0.002	0.000
ΣR	1.991	1.985	1.975	1.997	1.977	1.976	1.978	1.979	1.986
Ca	0.001	0.001	0.000	0.000	0.000	0.000	0.000	0.000	0.000
Na	0.046	0.062	0.056	0.046	0.052	0.060	0.068	0.055	0.047
K	0.952	0.956	0.949	0.913	0.972	0.969	0.967	0.953	0.976
ΣA	0.998	1.019	1.005	0.959	1.024	1.029	1.035	1.009	1.023
F	0.005	0.005	0.005	0.005	0.005	0.005	0.005	0.005	0.005

Table IV.6: Major element analyses of muscovites. The single grain analyses were performed with an electron microprobe.

	BT08-45-M04-2	BT08-45-M03-1	BT08-45-M03-3	BT08-45-M03-4	BT08-45-M07-2	BT08-48-M00-2	BT08-48-M00-6	BT08-48-M02-1	BT08-48-M02-2
SiO ₂	45.12	45.28	45.04	45.47	45.11	45.15	45.59	45.70	45.92
Al ₂ O ₃	32.85	33.41	33.13	33.24	32.33	33.29	33.39	33.40	34.30
TiO ₂	1.20	0.82	1.00	1.02	1.88	1.25	1.20	0.75	0.47
FeO	3.54	3.39	3.47	3.40	3.62	3.11	2.94	2.91	2.78
MgO	0.74	0.73	0.75	0.81	0.87	0.95	0.93	1.02	0.98
MnO	0.01	0.03	0.01	0.02	0.02	0.02	0.03	0.03	0.00
K ₂ O	11.26	11.18	11.43	11.16	11.03	11.08	11.35	11.23	11.43
CaO	0.00	0.00	0.00	0.00	0.00	0.01	0.00	0.01	0.00
Na ₂ O	0.39	0.30	0.34	0.40	0.36	0.36	0.39	0.27	0.34
F	0.17	0.25	0.20	0.06	0.19	0.23	0.23	0.16	0.04
Total	95.28	95.40	95.37	95.58	95.41	95.44	96.04	95.49	96.26

Numbers of ions on the basis of 11 oxygens

Si	3.048	3.050	3.042	3.052	3.043	3.039	3.050	3.067	3.053
Al IV	0.952	0.950	0.958	0.948	0.957	0.961	0.950	0.933	0.947
ΣT	4.000	4.000	4.000	4.000	4.000	4.000	4.000	4.000	4.000
Al VI	1.664	1.704	1.680	1.683	1.615	1.680	1.684	1.709	1.741
Ti	0.061	0.042	0.051	0.051	0.095	0.063	0.060	0.038	0.024
Fe	0.180	0.172	0.176	0.172	0.184	0.158	0.148	0.147	0.139
Mg	0.075	0.073	0.075	0.081	0.087	0.095	0.093	0.102	0.097
Mn	0.001	0.002	0.000	0.001	0.001	0.001	0.001	0.002	0.000
ΣR	1.980	1.993	1.983	1.988	1.983	1.997	1.987	1.999	2.001
Ca	0.000	0.000	0.000	0.000	0.000	0.000	0.000	0.001	0.000
Na	0.051	0.039	0.045	0.053	0.047	0.046	0.050	0.035	0.044
K	0.970	0.961	0.985	0.956	0.949	0.951	0.969	0.961	0.969
ΣA	1.022	1.000	1.030	1.008	0.996	0.998	1.019	0.998	1.013
F	0.005	0.005	0.005	0.005	0.005	0.005	0.005	0.005	0.005

Table IV.6: Major element analyses of muscovites. The single grain analyses were performed with an electron microprobe.

	BT08-48-M03-2	BT08-48-M03-3	BT08-48-M03-4	BT08-48-M03-5	BT08-48-M03-6	BT08-48-M03-7	BT08-48-M04-2	BT08-48-M05-2	BT08-48-M05-3
SiO ₂	45.54	45.66	45.95	45.32	46.02	45.86	45.94	45.06	46.23
Al ₂ O ₃	33.70	33.28	33.56	33.34	33.07	33.30	32.67	31.91	33.01
TiO ₂	0.78	0.82	0.91	0.73	0.78	0.79	0.75	0.88	0.95
FeO	2.89	2.83	2.85	2.90	2.91	2.82	3.20	3.94	3.18
MgO	1.04	1.07	1.06	1.12	1.18	1.12	1.09	1.67	1.18
MnO	0.00	0.02	0.01	0.03	0.00	0.01	0.03	0.05	0.02
K ₂ O	11.17	11.14	11.16	11.38	11.12	11.14	11.03	11.29	11.33
CaO	0.00	0.02	0.00	0.00	0.00	0.00	0.04	0.00	0.00
Na ₂ O	0.44	0.46	0.40	0.44	0.49	0.41	0.22	0.29	0.33
F	0.16	0.23	0.14	0.12	0.25	0.02	0.04	0.24	0.15
Total	95.72	95.53	96.04	95.37	95.83	95.47	95.01	95.33	96.39

Numbers of ions on the basis of 11 oxygens

Si	3.050	3.066	3.064	3.051	3.080	3.072	3.093	3.053	3.078
Al IV	0.950	0.934	0.936	0.949	0.920	0.928	0.907	0.947	0.922
ΣT	4.000	4.000	4.000	4.000	4.000	4.000	4.000	4.000	4.000
Al VI	1.711	1.700	1.702	1.698	1.690	1.703	1.686	1.601	1.669
Ti	0.039	0.041	0.046	0.037	0.039	0.040	0.038	0.045	0.047
Fe	0.146	0.143	0.143	0.147	0.147	0.142	0.162	0.201	0.159
Mg	0.104	0.107	0.105	0.112	0.117	0.111	0.110	0.169	0.118
Mn	0.000	0.001	0.000	0.002	0.000	0.000	0.001	0.003	0.001
ΣR	1.999	1.993	1.997	1.995	1.993	1.997	1.998	2.018	1.995
Ca	0.000	0.002	0.000	0.000	0.000	0.000	0.003	0.000	0.000
Na	0.058	0.059	0.051	0.058	0.064	0.053	0.029	0.038	0.042
K	0.954	0.954	0.949	0.978	0.950	0.952	0.947	0.976	0.962
ΣA	1.012	1.015	1.001	1.035	1.013	1.005	0.979	1.013	1.005
F	0.005	0.005	0.005	0.005	0.005	0.005	0.005	0.005	0.005

Table IV.6: Major element analyses of muscovites. The single grain analyses were performed with an electron microprobe.

	BT08-48-M05-4	BT08-48-M13-1	BT08-48-M15-1	BT08-48-M15-2	BT08-48-M15-3	BT08-48-M15-4	BT08-48-M15-5	BT08-48-M17-1	BT08-48-M17-2
SiO ₂	45.74	45.90	46.11	46.08	45.85	45.70	46.03	45.94	45.86
Al ₂ O ₃	33.03	33.48	33.18	33.72	33.49	33.30	33.51	33.35	33.70
TiO ₂	0.89	0.73	0.53	0.41	0.46	0.71	0.62	1.11	0.69
FeO	3.22	3.07	3.29	3.10	3.01	2.83	3.02	2.90	2.91
MgO	1.11	0.97	1.11	1.12	1.04	1.02	1.00	0.99	0.98
MnO	0.03	0.02	0.05	0.02	0.00	0.00	0.02	0.01	0.01
K ₂ O	11.17	11.34	11.39	11.42	11.45	11.44	11.16	11.23	10.98
CaO	0.02	0.00	0.01	0.00	0.00	0.02	0.01	0.00	0.02
Na ₂ O	0.28	0.31	0.20	0.36	0.27	0.28	0.24	0.35	0.39
F	0.06	0.15	0.19	0.22	0.22	0.11	0.07	0.14	0.21
Total	95.55	95.97	96.07	96.46	95.80	95.42	95.69	96.03	95.75

Numbers of ions on the basis of 11 oxygens

Si	3.068	3.067	3.081	3.067	3.072	3.071	3.077	3.066	3.066
Al IV	0.932	0.933	0.919	0.933	0.928	0.929	0.923	0.934	0.934
ΣT	4.000	4.000	4.000	4.000	4.000	4.000	4.000	4.000	4.000
Al VI	1.680	1.705	1.695	1.713	1.718	1.709	1.717	1.689	1.722
Ti	0.045	0.037	0.027	0.021	0.023	0.036	0.031	0.056	0.035
Fe	0.163	0.154	0.166	0.155	0.152	0.143	0.152	0.146	0.146
Mg	0.111	0.096	0.111	0.111	0.104	0.103	0.099	0.099	0.098
Mn	0.002	0.001	0.003	0.001	0.000	0.000	0.001	0.000	0.000
ΣR	2.000	1.994	2.001	2.001	1.997	1.990	2.001	1.990	2.001
Ca	0.002	0.000	0.001	0.000	0.000	0.002	0.001	0.000	0.002
Na	0.036	0.040	0.026	0.047	0.035	0.036	0.031	0.046	0.050
K	0.956	0.967	0.971	0.970	0.979	0.981	0.952	0.956	0.936
ΣA	0.993	1.007	0.998	1.016	1.014	1.019	0.984	1.002	0.988
F	0.005	0.005	0.005	0.005	0.005	0.005	0.005	0.005	0.005

Table IV.6: Major element analyses of muscovites. The single grain analyses were performed with an electron microprobe.

	BT08-48-M17-3	BT08-48-M17-4	BT08-48-M17-5	BT08-48-M17-6	BT08-48-M17-7	BT08-48-M17-8	BT08-48-M17-9	BT08-48-M16-1	BT08-48-M16-2
SiO ₂	45.40	45.77	45.89	45.76	45.56	45.79	45.63	45.54	45.60
Al ₂ O ₃	33.51	33.90	33.67	33.44	33.62	33.61	33.14	33.70	33.70
TiO ₂	0.67	0.53	0.84	0.80	0.89	0.82	0.75	0.73	0.71
FeO	2.79	2.96	2.87	2.80	2.97	2.84	3.02	2.91	2.76
MgO	1.01	0.98	0.98	1.04	1.06	1.03	1.03	1.00	0.98
MnO	0.00	0.02	0.02	0.04	0.01	0.02	0.02	0.01	0.04
K ₂ O	11.21	11.15	11.28	11.31	11.23	11.32	11.29	11.34	11.30
CaO	0.00	0.01	0.00	0.00	0.00	0.00	0.00	0.00	0.00
Na ₂ O	0.40	0.41	0.41	0.38	0.40	0.41	0.33	0.37	0.41
F	0.20	0.32	0.22	0.15	0.29	0.11	0.10	0.21	0.09
Total	95.19	96.05	96.18	95.71	96.02	95.96	95.32	95.81	95.58

Numbers of ions on the basis of 11 oxygens

Si	3.058	3.058	3.061	3.065	3.048	3.059	3.070	3.051	3.057
Al IV	0.942	0.942	0.939	0.935	0.952	0.941	0.930	0.949	0.943
ΣT	4.000	4.000	4.000	4.000	4.000	4.000	4.000	4.000	4.000
Al VI	1.719	1.728	1.708	1.706	1.699	1.706	1.698	1.713	1.720
Ti	0.034	0.027	0.042	0.040	0.045	0.041	0.038	0.037	0.036
Fe	0.142	0.149	0.144	0.141	0.150	0.143	0.153	0.147	0.139
Mg	0.102	0.097	0.098	0.104	0.106	0.103	0.103	0.100	0.098
Mn	0.000	0.001	0.001	0.002	0.000	0.001	0.001	0.000	0.002
ΣR	1.996	2.001	1.993	1.993	2.000	1.994	1.993	1.997	1.994
Ca	0.000	0.001	0.000	0.000	0.000	0.000	0.000	0.000	0.000
Na	0.053	0.054	0.053	0.050	0.051	0.053	0.043	0.049	0.053
K	0.963	0.950	0.960	0.967	0.958	0.965	0.969	0.969	0.966
ΣA	1.016	1.005	1.013	1.016	1.010	1.018	1.012	1.018	1.019
F	0.005	0.005	0.005	0.005	0.005	0.005	0.005	0.005	0.005

Table IV.6: Major element analyses of muscovites. The single grain analyses were performed with an electron microprobe.

	BT08-48-M16-3	BT08-48-M16-4	BT08-48-M16-5	BT08-48-M18-1	BT08-48-M18-2	BT08-48-M18-3	BT08-48-M18-4	BT08-48-M18-5	BT08-48-M18-6
SiO ₂	45.53	46.11	45.72	45.83	45.51	45.75	45.59	45.32	45.28
Al ₂ O ₃	33.56	33.32	33.37	33.35	33.10	33.40	33.53	33.30	33.01
TiO ₂	0.76	0.69	0.97	1.43	1.23	1.35	1.55	1.49	1.29
FeO	2.98	2.98	2.80	2.85	3.07	2.89	2.93	2.81	2.89
MgO	1.02	1.07	0.94	0.98	1.02	0.95	0.96	0.89	0.96
MnO	0.03	0.00	0.01	0.00	0.01	0.00	0.01	0.00	0.00
K ₂ O	11.16	11.40	11.40	11.05	11.42	11.27	11.25	11.38	11.41
CaO	0.00	0.00	0.00	0.00	0.00	0.00	0.00	0.00	0.00
Na ₂ O	0.45	0.41	0.45	0.40	0.28	0.40	0.45	0.42	0.40
F	0.15	0.15	0.13	0.10	0.27	0.19	0.22	0.15	0.17
Total	95.64	96.13	95.79	95.99	95.91	96.20	96.49	95.76	95.41

Numbers of ions on the basis of 11 oxygens

Si	3.053	3.077	3.062	3.057	3.052	3.052	3.036	3.040	3.051
Al IV	0.947	0.923	0.938	0.943	0.948	0.948	0.964	0.960	0.949
ΣT	4.000	4.000	4.000	4.000	4.000	4.000	4.000	4.000	4.000
Al VI	1.706	1.698	1.697	1.679	1.670	1.679	1.668	1.674	1.672
Ti	0.038	0.035	0.049	0.072	0.062	0.068	0.078	0.075	0.065
Fe	0.150	0.150	0.141	0.143	0.155	0.145	0.147	0.142	0.147
Mg	0.101	0.107	0.094	0.097	0.102	0.094	0.095	0.089	0.096
Mn	0.002	0.000	0.000	0.000	0.000	0.000	0.000	0.000	0.000
ΣR	1.998	1.989	1.982	1.991	1.990	1.986	1.988	1.980	1.981
Ca	0.000	0.000	0.000	0.000	0.000	0.000	0.000	0.000	0.000
Na	0.059	0.053	0.058	0.051	0.037	0.052	0.058	0.054	0.053
K	0.955	0.970	0.974	0.940	0.977	0.959	0.956	0.974	0.981
ΣA	1.014	1.023	1.032	0.991	1.014	1.011	1.014	1.028	1.033
F	0.005	0.005	0.005	0.005	0.005	0.005	0.005	0.005	0.005

Table IV.6: Major element analyses of muscovites. The single grain analyses were performed with an electron microprobe.

	BT08-48-M18-7	BT08-48-M18-8	BT08-48-M08-1	BT08-48-M08-2	BT08-48-M08-3	BT08-48-M08-4	BT08-48-M08-5	BT08-48-M08-6	BT08-48-M08-7
SiO ₂	45.47	45.48	45.66	45.62	45.61	45.68	45.52	45.76	45.43
Al ₂ O ₃	33.19	33.31	33.50	33.48	33.62	33.39	33.37	33.61	33.47
TiO ₂	1.49	1.04	1.11	1.31	1.44	1.34	1.53	1.41	1.26
FeO	2.79	2.99	2.84	2.86	2.84	2.78	2.83	2.86	2.80
MgO	0.95	0.88	0.96	0.92	0.92	0.90	0.94	0.92	0.93
MnO	0.03	0.04	0.00	0.02	0.01	0.02	0.02	0.01	0.01
K ₂ O	11.33	11.57	11.20	11.22	11.26	11.25	11.23	11.21	11.23
CaO	0.00	0.01	0.00	0.00	0.00	0.00	0.00	0.00	0.01
Na ₂ O	0.39	0.24	0.39	0.41	0.39	0.40	0.44	0.38	0.43
F	0.22	0.04	0.15	0.27	0.13	0.12	0.11	0.33	0.06
Total	95.86	95.60	95.81	96.10	96.22	95.89	95.98	96.49	95.64

Numbers of ions on the basis of 11 oxygens

Si	3.048	3.054	3.055	3.049	3.040	3.054	3.042	3.046	3.045
Al IV	0.952	0.946	0.945	0.951	0.960	0.946	0.958	0.954	0.955
ΣT	4.000	4.000	4.000	4.000	4.000	4.000	4.000	4.000	4.000
Al VI	1.671	1.691	1.697	1.686	1.682	1.686	1.672	1.684	1.689
Ti	0.075	0.052	0.056	0.066	0.072	0.067	0.077	0.071	0.064
Fe	0.141	0.151	0.143	0.144	0.143	0.140	0.142	0.143	0.141
Mg	0.095	0.088	0.096	0.092	0.092	0.090	0.093	0.092	0.093
Mn	0.002	0.002	0.000	0.001	0.000	0.001	0.001	0.000	0.001
ΣR	1.983	1.985	1.991	1.988	1.989	1.984	1.985	1.990	1.987
Ca	0.000	0.000	0.000	0.000	0.000	0.000	0.000	0.000	0.001
Na	0.051	0.031	0.051	0.053	0.050	0.052	0.057	0.049	0.056
K	0.969	0.991	0.956	0.957	0.958	0.960	0.958	0.952	0.960
ΣA	1.020	1.023	1.007	1.009	1.008	1.012	1.014	1.001	1.017
F	0.005	0.005	0.005	0.005	0.005	0.005	0.005	0.005	0.005

Table IV.6: Major element analyses of muscovites. The single grain analyses were performed with an electron microprobe.

	BT08-48-M08-10	BT08-48-M09-1	BT08-48-M09-2	BT08-48-M09-3	BT08-48-M09-4	BT08-48-M09-5	BT08-48-M09-6	BT08-48-M09-7	BT08-48-M09-8
SiO ₂	45.21	45.87	46.08	45.81	45.86	45.89	45.53	45.96	45.99
Al ₂ O ₃	32.99	33.75	33.90	33.98	34.08	34.26	34.45	34.29	33.18
TiO ₂	1.31	1.05	1.08	0.94	0.95	0.68	0.65	0.64	0.84
FeO	3.03	2.65	2.72	2.77	2.70	2.90	2.84	2.88	2.90
MgO	0.91	0.90	0.91	0.93	0.88	0.87	0.90	0.96	0.94
MnO	0.00	0.00	0.01	0.02	0.00	0.02	0.03	0.03	0.03
K ₂ O	11.37	11.39	11.14	11.18	11.47	11.34	11.38	11.36	11.48
CaO	0.01	0.03	0.00	0.00	0.00	0.00	0.01	0.00	0.00
Na ₂ O	0.25	0.28	0.28	0.32	0.33	0.34	0.36	0.37	0.29
F	0.11	0.14	0.14	0.13	0.06	0.17	0.07	0.12	0.09
Total	95.18	96.06	96.26	96.08	96.32	96.48	96.22	96.61	95.74

Numbers of ions on the basis of 11 oxygens

Si	3.050	3.059	3.061	3.052	3.049	3.049	3.032	3.048	3.080
Al IV	0.950	0.941	0.939	0.948	0.951	0.951	0.968	0.952	0.920
ΣT	4.000	4.000	4.000	4.000	4.000	4.000	4.000	4.000	4.000
Al VI	1.674	1.713	1.716	1.720	1.721	1.732	1.736	1.729	1.699
Ti	0.066	0.053	0.054	0.047	0.047	0.034	0.032	0.032	0.042
Fe	0.154	0.133	0.136	0.139	0.135	0.145	0.142	0.144	0.146
Mg	0.091	0.089	0.090	0.092	0.087	0.086	0.089	0.095	0.094
Mn	0.000	0.000	0.000	0.001	0.000	0.001	0.002	0.002	0.002
ΣR	1.986	1.988	1.997	1.999	1.990	1.998	2.002	2.001	1.983
Ca	0.001	0.002	0.000	0.000	0.000	0.000	0.001	0.000	0.000
Na	0.032	0.036	0.036	0.041	0.042	0.044	0.047	0.048	0.038
K	0.979	0.969	0.944	0.950	0.973	0.961	0.967	0.961	0.981
ΣA	1.012	1.006	0.981	0.991	1.015	1.005	1.014	1.009	1.019
F	0.005	0.005	0.005	0.005	0.005	0.005	0.005	0.005	0.005

Table IV.6: Major element analyses of muscovites. The single grain analyses were performed with an electron microprobe.

	BT08-48-M09-10	BT08-48-M09-11	BT08-48-M09-13	BT08-48-M09-14	BT08-48-M09-15	BT08-48-M09-16	BT08-48-M09-17	BT08-48-M09-18	BT08-48-M09-19
SiO ₂	45.42	45.76	45.57	45.00	45.88	46.01	45.52	45.32	46.00
Al ₂ O ₃	33.36	33.42	33.90	33.82	34.04	33.61	33.76	33.68	33.72
TiO ₂	0.90	0.88	0.58	0.72	0.58	0.80	0.47	0.60	1.01
FeO	2.80	2.78	2.86	2.75	2.85	2.84	2.87	2.72	2.97
MgO	0.98	0.99	0.96	0.93	0.92	1.01	0.95	1.02	1.00
MnO	0.01	0.03	0.03	0.01	0.02	0.01	0.03	0.01	0.05
K ₂ O	11.41	10.82	11.40	11.16	11.47	10.50	11.34	11.09	11.20
CaO	0.05	0.05	0.00	0.02	0.00	0.06	0.01	0.02	0.00
Na ₂ O	0.24	0.25	0.28	0.38	0.30	0.24	0.33	0.36	0.30
F	0.08	0.05	0.12	0.25	0.18	0.02	0.23	0.21	0.18
Total	95.25	95.03	95.71	95.05	96.24	95.09	95.51	95.03	96.43
<i>Numbers of ions on the basis of 11 oxygens</i>									
Si	3.057	3.073	3.052	3.038	3.057	3.078	3.058	3.055	3.057
Al IV	0.943	0.927	0.948	0.962	0.943	0.922	0.942	0.945	0.943
Σ T	4.000	4.000	4.000	4.000	4.000	4.000	4.000	4.000	4.000
Al VI	1.705	1.718	1.729	1.730	1.731	1.730	1.732	1.732	1.699
Ti	0.046	0.045	0.029	0.036	0.029	0.040	0.024	0.030	0.051
Fe	0.142	0.141	0.144	0.140	0.143	0.143	0.145	0.138	0.149
Mg	0.098	0.099	0.095	0.094	0.091	0.101	0.095	0.102	0.099
Mn	0.000	0.002	0.002	0.001	0.001	0.000	0.001	0.000	0.003
Σ R	1.991	2.004	2.000	2.001	1.996	2.014	1.998	2.003	2.000
Ca	0.004	0.003	0.000	0.001	0.000	0.004	0.001	0.001	0.000
Na	0.031	0.033	0.037	0.050	0.039	0.031	0.042	0.048	0.039
K	0.980	0.927	0.974	0.961	0.975	0.896	0.972	0.954	0.950
Σ A	1.014	0.963	1.011	1.013	1.014	0.932	1.015	1.003	0.989
F	0.005	0.005	0.005	0.005	0.005	0.005	0.005	0.005	0.005

Table IV.6: Major element analyses of muscovites. The single grain analyses were performed with an electron microprobe.

	BT08-48-M09-20	BT08-48-M09-23	BT08-48-M09-24	BT08-48-M09-25	BT08-48-M09-26	BT08-15_M05_3	BT08-15_M05_4	BT08-15_M05_6	BT08-15_M05_8
SiO ₂	45.91	45.96	46.07	46.18	46.64	44.97	45.23	45.85	45.51
Al ₂ O ₃	33.83	33.95	33.94	33.71	33.04	33.74	33.03	33.66	33.66
TiO ₂	0.60	0.43	0.80	0.73	0.70	0.88	0.86	0.43	0.14
FeO	2.78	2.95	2.89	2.98	3.20	3.92	4.11	4.00	3.61
MgO	1.03	0.93	1.06	0.95	1.07	0.69	0.83	0.83	0.83
MnO	0.01	0.04	0.00	0.00	0.01	0.02	0.00	0.02	0.00
K ₂ O	11.15	11.37	11.13	11.14	11.06	11.10	11.40	11.35	11.41
CaO	0.01	0.00	0.00	0.04	0.01	0.03	0.00	0.00	0.02
Na ₂ O	0.35	0.26	0.40	0.32	0.22	0.28	0.33	0.24	0.29
F	0.23	0.17	0.07	0.13	0.20	0.12	0.12	0.26	0.03
Total	95.90	96.06	96.37	96.19	96.15	95.75	95.91	96.64	95.50
<i>Numbers of ions on the basis of 11 oxygens</i>									
Si	3.066	3.066	3.058	3.072	3.104	3.019	3.040	3.054	3.058
Al IV	0.934	0.934	0.942	0.928	0.896	0.981	0.960	0.946	0.942
Σ T	4.000	4.000	4.000	4.000	4.000	4.000	4.000	4.000	4.000
Al VI	1.729	1.736	1.713	1.716	1.696	1.690	1.657	1.697	1.725
Ti	0.030	0.022	0.040	0.037	0.035	0.045	0.044	0.022	0.007
Fe	0.140	0.148	0.144	0.149	0.160	0.198	0.208	0.201	0.183
Mg	0.103	0.092	0.105	0.095	0.106	0.069	0.083	0.082	0.083
Mn	0.001	0.002	0.000	0.000	0.001	0.001	0.000	0.001	0.000
Σ R	2.002	2.000	2.003	1.996	1.998	2.004	1.992	2.002	1.998
Ca	0.001	0.000	0.000	0.003	0.000	0.002	0.000	0.000	0.002
Na	0.046	0.034	0.051	0.041	0.029	0.036	0.043	0.031	0.037
K	0.950	0.968	0.942	0.945	0.939	0.951	0.977	0.964	0.978
Σ A	0.997	1.001	0.994	0.989	0.968	0.989	1.020	0.995	1.017
F	0.005	0.005	0.005	0.005	0.005	0.005	0.005	0.005	0.005

Table IV.6: Major element analyses of muscovites. The single grain analyses were performed with an electron microprobe.

	BT08-15_M01_1BT08-15_M01_2BT08-15_M01_3BT08-15_M02_1BT08-15_M02_2BT08-15_M02_4BT08-15_M02_5BT08-15_M02_6BT08-15_M03_2BT08-15_M03_3										
	45.28	45.70	45.34	45.07	45.35	44.94	45.20	44.96	45.01	45.35	
SiO ₂	45.28	45.70	45.34	45.07	45.35	44.94	45.20	44.96	45.01	45.35	
Al ₂ O ₃	33.19	33.90	33.41	33.95	33.10	32.96	33.29	33.49	33.23	33.12	
TiO ₂	1.19	0.38	0.98	1.05	1.67	1.24	0.97	0.92	1.07	0.78	
FeO	3.69	3.63	3.67	3.09	3.78	3.85	3.86	3.57	3.70	3.74	
MgO	0.77	0.75	0.81	0.66	0.76	0.75	0.76	0.75	0.80	0.84	
MnO	0.02	0.01	0.02	0.03	0.03	0.01	0.03	0.01	0.00	0.00	
K ₂ O	11.38	11.36	11.25	11.30	11.32	11.19	11.24	11.05	11.21	11.20	
CaO	0.00	0.00	0.00	0.00	0.00	0.00	0.00	0.02	0.02	0.04	
Na ₂ O	0.34	0.23	0.31	0.33	0.28	0.39	0.36	0.36	0.32	0.25	
F	0.26	0.05	0.00	0.10	0.11	0.00	0.03	0.03	0.11	0.19	
Total	96.12	96.00	95.79	95.58	96.39	95.32	95.74	95.16	95.46	95.51	
<i>Numbers of ions on the basis of 11 oxygens</i>											
Si	3.037	3.053	3.039	3.026	3.029	3.032	3.035	3.031	3.032	3.053	
AlIV	0.963	0.947	0.961	0.974	0.971	0.968	0.965	0.969	0.968	0.947	
Σ T	4.000	4.000	4.000	4.000	4.000	4.000	4.000	4.000	4.000	4.000	
AlVI	1.662	1.723	1.679	1.714	1.636	1.654	1.671	1.694	1.671	1.682	
Ti	0.060	0.019	0.050	0.053	0.084	0.063	0.049	0.047	0.054	0.039	
Fe	0.186	0.183	0.185	0.156	0.190	0.196	0.195	0.181	0.188	0.190	
Mg	0.077	0.075	0.081	0.066	0.075	0.075	0.076	0.075	0.080	0.084	
Mn	0.001	0.000	0.001	0.002	0.002	0.001	0.002	0.001	0.000	0.000	
Σ R	1.986	2.000	1.996	1.991	1.986	1.988	1.993	1.997	1.994	1.996	
Ca	0.000	0.000	0.000	0.000	0.000	0.000	0.000	0.001	0.001	0.003	
Na	0.044	0.030	0.040	0.043	0.036	0.050	0.047	0.048	0.042	0.033	
K	0.974	0.968	0.962	0.968	0.965	0.963	0.963	0.951	0.963	0.962	
Σ A	1.018	0.998	1.002	1.011	1.000	1.014	1.010	1.000	1.006	0.998	
F	0.005	0.005	0.005	0.005	0.005	0.005	0.005	0.005	0.005	0.005	

Table IV.7: Major element analyses of biotites. The single grain analyses were performed with an electron microprobe.

	BT09-80-B01-9	BT09-80-B01-10	BT09-80-B01-13	BT09-80-B01-15	BT09-80-B01-16	BT09-80-B02-1	BT09-80-B02-2	BT09-80-B02-3	BT09-80-B02-4
SiO ₂	35.18	34.89	34.46	35.29	35.11	35.29	35.28	35.16	35.17
Al ₂ O ₃	18.60	18.69	18.71	18.64	18.40	18.43	18.76	19.04	18.70
TiO ₂	3.28	3.27	2.92	2.89	3.16	3.14	3.13	3.18	1.71
FeO	20.62	20.92	20.45	20.58	20.67	21.11	21.22	20.21	21.17
MgO	7.89	7.85	7.91	7.78	8.11	7.76	7.72	7.56	7.80
MnO	0.38	0.34	0.35	0.33	0.34	0.37	0.34	0.34	0.35
K ₂ O	9.77	9.98	9.93	9.87	9.99	9.96	9.85	9.57	10.07
CaO	0.01	0.02	0.05	0.04	0.04	0.02	0.03	0.04	0.02
Na ₂ O	0.20	0.16	0.16	0.21	0.15	0.12	0.15	0.15	0.20
F	0.49	0.49	0.46	0.62	0.62	0.66	0.50	0.47	0.56
Total	96.41	96.61	95.40	96.25	96.59	96.87	96.97	95.73	95.75

Numbers of ions on the basis of 11 oxygens

Si	2.580	2.560	2.559	2.595	2.578	2.585	2.575	2.587	2.605
Al IV	1.420	1.440	1.441	1.405	1.422	1.415	1.425	1.413	1.395
Σ T	4.000	4.000	4.000	4.000	4.000	4.000	4.000	4.000	4.000
Al VI	0.187	0.176	0.196	0.211	0.170	0.177	0.190	0.239	0.239
Ti	0.181	0.180	0.163	0.160	0.174	0.173	0.172	0.176	0.095
Fe	1.138	1.156	1.143	1.140	1.143	1.165	1.166	1.120	1.181
Mg	0.862	0.858	0.875	0.853	0.887	0.847	0.840	0.829	0.861
Mn	0.023	0.021	0.022	0.021	0.021	0.023	0.021	0.021	0.022
Σ R	2.392	2.391	2.400	2.384	2.396	2.385	2.389	2.386	2.398
Ca	0.001	0.002	0.004	0.003	0.003	0.002	0.003	0.003	0.002
Na	0.028	0.022	0.024	0.030	0.021	0.017	0.021	0.021	0.029
K	0.914	0.934	0.941	0.926	0.936	0.931	0.917	0.898	0.952
Σ A	0.943								
F	0.005	0.005	0.005	0.005	0.005	0.005	0.005	0.005	0.005

Table IV.7: Major element analyses of biotites. The single grain analyses were performed with an electron microprobe.

	BT09-80-B02-5	BT09-80-B02-6	BT09-80-B02-7	BT09-80-B02-8	BT09-80-B02-9	BT09-80-B02-10	BT09-80-B03-1	BT09-80-B03-2	BT09-80-B03-3
SiO ₂	34.79	35.16	35.28	34.86	35.21	35.31	35.37	35.02	35.27
Al ₂ O ₃	18.54	18.46	18.57	18.94	18.78	18.47	18.41	18.39	18.54
TiO ₂	3.30	3.48	3.34	3.29	3.24	3.32	2.97	2.86	3.19
FeO	20.91	20.91	20.83	20.67	20.93	21.15	21.02	21.38	20.82
MgO	7.83	7.92	7.79	7.76	7.96	7.84	8.05	8.12	8.03
MnO	0.36	0.34	0.33	0.34	0.34	0.35	0.31	0.36	0.26
K ₂ O	10.04	9.84	10.15	10.27	10.09	10.21	10.34	9.81	10.21
CaO	0.01	0.00	0.00	0.00	0.00	0.00	0.00	0.00	0.01
Na ₂ O	0.18	0.15	0.12	0.13	0.19	0.15	0.08	0.09	0.14
F	0.62	0.59	0.62	0.66	0.68	0.54	0.79	0.88	1.02
Total	96.57	96.86	97.04	96.92	97.41	97.34	97.34	96.90	97.50

Numbers of ions on the basis of 11 oxygens

Si	2.559	2.572	2.579	2.555	2.566	2.575	2.586	2.572	2.577
Al IV	1.441	1.428	1.421	1.445	1.434	1.425	1.414	1.428	1.423
ΣT	4.000	4.000	4.000	4.000	4.000	4.000	4.000	4.000	4.000
Al VI	0.167	0.164	0.180	0.192	0.179	0.163	0.172	0.164	0.175
Ti	0.183	0.191	0.184	0.181	0.178	0.182	0.163	0.158	0.175
Fe	1.158	1.152	1.147	1.141	1.149	1.161	1.157	1.182	1.146
Mg	0.858	0.863	0.849	0.848	0.865	0.852	0.877	0.889	0.875
Mn	0.023	0.021	0.021	0.021	0.021	0.022	0.019	0.022	0.016
ΣR	2.389	2.392	2.379	2.383	2.391	2.380	2.389	2.415	2.386
Ca	0.000	0.000	0.000	0.000	0.000	0.000	0.000	0.000	0.001
Na	0.025	0.022	0.018	0.018	0.027	0.022	0.012	0.013	0.020
K	0.942	0.918	0.947	0.960	0.938	0.950	0.964	0.919	0.952
ΣA									
F	0.005	0.005	0.005	0.005	0.005	0.005	0.005	0.005	0.005

Table IV.7: Major element analyses of biotites. The single grain analyses were performed with an electron microprobe.

	BT09-80-B03-4	BT09-80-B03-5	BT09-80-B03-6	BT09-80-B03-7	BT09-80-B03-8	BT09-80-B09-1	BT09-80-B09-2	BT09-80-B09-3	BT09-80-B10-1
SiO ₂	35.25	35.35	35.39	35.26	35.51	34.83	34.88	34.85	34.99
Al ₂ O ₃	18.99	18.59	18.60	18.63	18.75	17.58	17.99	17.82	18.25
TiO ₂	3.24	2.94	3.09	2.84	2.84	3.38	3.18	3.07	3.17
FeO	20.49	20.65	20.80	21.30	21.20	21.10	20.78	20.78	20.31
MgO	8.14	8.35	7.97	8.06	8.16	8.53	8.41	8.13	7.99
MnO	0.29	0.30	0.35	0.30	0.33	0.34	0.31	0.35	0.33
K ₂ O	10.24	10.27	10.16	9.86	10.17	10.08	9.90	10.15	9.95
CaO	0.00	0.00	0.02	0.01	0.00	0.01	0.06	0.00	0.01
Na ₂ O	0.11	0.11	0.11	0.09	0.15	0.09	0.13	0.13	0.14
F	0.69	0.89	0.87	0.51	0.69	0.72	0.50	0.57	0.46
Total	97.43	97.45	97.36	96.85	97.79	96.65	96.14	95.84	95.59

Numbers of ions on the basis of 11 oxygens

Si	2.566	2.580	2.584	2.578	2.578	2.568	2.572	2.584	2.589
Al IV	1.434	1.420	1.416	1.422	1.422	1.432	1.428	1.416	1.411
ΣT	4.000	4.000	4.000	4.000	4.000	4.000	4.000	4.000	4.000
Al VI	0.195	0.180	0.186	0.183	0.183	0.096	0.136	0.142	0.181
Ti	0.177	0.161	0.170	0.156	0.155	0.187	0.176	0.171	0.176
Fe	1.123	1.135	1.144	1.173	1.159	1.171	1.154	1.160	1.132
Mg	0.883	0.908	0.867	0.878	0.883	0.937	0.924	0.898	0.881
Mn	0.018	0.019	0.022	0.018	0.020	0.021	0.020	0.022	0.020
ΣR	2.396	2.403	2.389	2.408	2.401	2.412	2.411	2.394	2.390
Ca	0.000	0.000	0.001	0.000	0.000	0.000	0.004	0.000	0.001
Na	0.015	0.016	0.016	0.012	0.021	0.013	0.018	0.018	0.020
K	0.951	0.956	0.947	0.920	0.942	0.948	0.931	0.960	0.939
ΣA									
F	0.005	0.005	0.005	0.005	0.005	0.005	0.005	0.005	0.005

Table IV.7: Major element analyses of biotites. The single grain analyses were performed with an electron microprobe.

	BT09-80-B10-2	BT09-80-B04-1	BT09-80-B04-2	BT09-80-B06-2	BT09-80-B07-1	BT09-80-B07-2	BT08-63-B08-1	BT08-63-B08-2	BT08-63-B08-3
SiO ₂	35.08	35.05	35.23	34.77	35.05	35.32	35.31	34.34	35.01
Al ₂ O ₃	18.20	17.87	18.12	18.76	18.76	18.51	17.74	17.72	17.59
TiO ₂	3.11	3.56	3.19	2.98	2.91	2.92	3.14	2.95	2.97
FeO	20.75	21.14	21.02	20.10	20.63	20.43	19.97	19.81	20.08
MgO	7.56	7.78	7.85	7.80	8.21	8.16	8.38	8.87	8.84
MnO	0.38	0.36	0.40	0.42	0.34	0.33	0.48	0.54	0.52
K ₂ O	10.08	10.01	10.25	9.91	10.18	10.12	10.15	10.02	9.85
CaO	0.01	0.01	0.00	0.09	0.00	0.00	0.02	0.05	0.01
Na ₂ O	0.10	0.13	0.10	0.17	0.14	0.18	0.08	0.08	0.15
F	0.48	0.38	0.51	0.46	0.54	0.57	0.71	0.96	0.81
Total	95.75	96.29	96.67	95.46	96.76	96.55	95.99	95.33	95.84

Numbers of ions on the basis of 11 oxygens

Si	2.596	2.581	2.588	2.576	2.568	2.591	2.611	2.569	2.596
Al IV	1.404	1.419	1.412	1.424	1.432	1.409	1.389	1.431	1.404
ΣT	4.000	4.000	4.000	4.000	4.000	4.000	4.000	4.000	4.000
Al VI	0.185	0.132	0.157	0.214	0.188	0.192	0.157	0.131	0.133
Ti	0.173	0.197	0.176	0.166	0.166	0.160	0.175	0.166	0.166
Fe	1.156	1.172	1.163	1.121	1.138	1.129	1.112	1.116	1.121
Mg	0.834	0.854	0.859	0.861	0.896	0.892	0.923	0.989	0.977
Mn	0.024	0.022	0.025	0.026	0.021	0.020	0.030	0.034	0.033
ΣR	2.372	2.378	2.380	2.389	2.410	2.393	2.397	2.436	2.430
Ca	0.001	0.001	0.000	0.007	0.007	0.000	0.002	0.004	0.001
Na	0.015	0.019	0.015	0.024	0.024	0.020	0.012	0.012	0.022
K	0.952	0.940	0.961	0.937	0.937	0.952	0.957	0.956	0.932
ΣA									
F	0.005	0.005	0.005	0.005	0.005	0.005	0.005	0.005	0.005

Table IV.7: Major element analyses of biotites. The single grain analyses were performed with an electron microprobe.

	BT08-63-B08-4	BT08-63-B09-1	BT08-63-B09-2	BT08-63-B09-3	BT08-63-B09-4	BT08-63-B01-1	BT08-63-B01-2	BT08-63-B01-3	BT08-63-B01-4
SiO ₂	35.03	35.54	35.61	35.64	35.64	36.06	35.96	35.86	35.54
Al ₂ O ₃	17.86	17.59	17.86	17.95	18.13	17.94	17.80	18.21	17.98
TiO ₂	2.82	3.08	2.84	2.97	2.96	2.87	2.99	3.02	2.58
FeO	20.01	20.08	20.46	19.99	20.19	19.16	19.33	19.19	19.36
MgO	8.65	8.72	8.57	8.74	8.61	9.35	9.33	9.64	9.38
MnO	0.53	0.51	0.51	0.49	0.52	0.54	0.53	0.52	0.46
K ₂ O	10.16	10.21	10.21	10.17	10.23	10.17	10.17	10.05	10.21
CaO	0.03	0.00	0.00	0.00	0.00	0.02	0.00	0.02	0.01
Na ₂ O	0.06	0.11	0.13	0.12	0.08	0.13	0.15	0.13	0.12
F	0.77	0.81	0.69	0.89	0.82	0.73	0.89	1.06	0.93
Total	95.92	96.66	96.88	96.96	97.18	96.96	97.15	97.70	96.57

Numbers of ions on the basis of 11 oxygens

Si	2.596	2.614	2.610	2.611	2.605	2.629	2.624	2.603	2.612
Al IV	1.404	1.386	1.390	1.389	1.395	1.371	1.376	1.397	1.388
Σ T	4.000	4.000	4.000	4.000	4.000	4.000	4.000	4.000	4.000
Al VI	0.156	0.138	0.154	0.161	0.167	0.172	0.155	0.161	0.170
Ti	0.157	0.170	0.157	0.164	0.163	0.157	0.164	0.165	0.143
Fe	1.117	1.112	1.129	1.103	1.111	1.052	1.062	1.049	1.071
Mg	0.955	0.956	0.936	0.954	0.938	1.016	1.015	1.043	1.027
Mn	0.033	0.032	0.032	0.031	0.032	0.033	0.033	0.032	0.029
Σ R	2.419	2.408	2.408	2.413	2.411	2.431	2.429	2.450	2.441
Ca	0.002	0.000	0.000	0.000	0.000	0.001	0.000	0.002	0.001
Na	0.009	0.016	0.018	0.017	0.012	0.018	0.022	0.019	0.017
K	0.961	0.958	0.955	0.951	0.954	0.946	0.947	0.931	0.957
Σ A									
F	0.005	0.005	0.005	0.005	0.005	0.005	0.005	0.005	0.005

Table IV.7: Major element analyses of biotites. The single grain analyses were performed with an electron microprobe.

	BT08-63-B01-5	BT08-63-B01-6	BT08-63-B01-7	BT08-63-B01-8	BT08-63-B01-9	BT08-63-B01-10	BT08-63-B01-11	BT08-63-B01-12	BT08-63-B01-13
SiO ₂	35.93	35.84	35.79	36.01	36.03	35.60	35.79	36.02	35.87
Al ₂ O ₃	17.98	18.04	17.47	17.11	17.37	17.40	17.62	17.55	17.74
TiO ₂	2.77	2.89	2.63	2.48	2.19	2.44	2.80	2.80	2.72
FeO	19.09	18.80	19.36	18.90	19.44	18.98	18.86	19.18	19.09
MgO	9.03	8.95	9.46	9.80	9.80	9.57	9.67	9.59	9.42
MnO	0.50	0.49	0.45	0.50	0.46	0.47	0.48	0.44	0.39
K ₂ O	10.22	10.14	10.20	10.33	10.09	10.28	10.17	10.06	10.21
CaO	0.00	0.00	0.01	0.00	0.01	0.01	0.01	0.00	0.01
Na ₂ O	0.09	0.13	0.14	0.05	0.08	0.11	0.14	0.08	0.11
F	0.88	0.86	0.86	0.98	0.77	0.83	1.06	0.85	0.81
Total	96.49	96.13	96.36	96.16	96.25	95.69	96.60	96.57	96.36

Numbers of ions on the basis of 11 oxygens

Si	2.637	2.636	2.634	2.658	2.650	2.638	2.629	2.639	2.634
Al IV	1.363	1.364	1.366	1.342	1.350	1.362	1.371	1.361	1.366
Σ T	4.000	4.000	4.000	4.000	4.000	4.000	4.000	4.000	4.000
Al VI	0.192	0.201	0.150	0.146	0.155	0.158	0.155	0.155	0.170
Ti	0.153	0.160	0.146	0.138	0.121	0.136	0.155	0.154	0.150
Fe	1.055	1.041	1.073	1.050	1.076	1.059	1.043	1.058	1.056
Mg	0.988	0.981	1.038	1.078	1.074	1.057	1.059	1.047	1.031
Mn	0.031	0.030	0.028	0.031	0.029	0.029	0.030	0.028	0.024
Σ R	2.418	2.413	2.434	2.443	2.456	2.439	2.442	2.442	2.431
Ca	0.000	0.000	0.001	0.000	0.001	0.001	0.001	0.000	0.001
Na	0.012	0.019	0.019	0.007	0.012	0.016	0.020	0.011	0.015
K	0.957	0.952	0.958	0.973	0.947	0.972	0.953	0.940	0.957
Σ A									
F	0.005	0.005	0.005	0.005	0.005	0.005	0.005	0.005	0.005

Table IV.7: Major element analyses of biotites. The single grain analyses were performed with an electron microprobe.

	BT08-63-B02-1	BT08-63-B02-2	BT08-63-B02-3	BT08-63-B02-4	BT08-63-B03-1	BT08-63-B03-2	BT08-26_B06_2	BT08-26_B06_3	BT08-26_B06_4
SiO ₂	35.95	35.82	35.95	35.79	35.80	35.90	35.75	36.04	35.66
Al ₂ O ₃	17.51	18.30	18.28	17.80	17.33	17.62	18.01	17.93	17.76
TiO ₂	3.43	2.85	3.00	2.98	2.51	2.61	3.24	2.39	2.56
FeO	19.78	18.70	18.90	19.41	20.83	20.60	19.05	18.45	18.49
MgO	8.74	9.31	9.10	9.20	8.62	8.48	8.22	9.13	8.87
MnO	0.45	0.45	0.49	0.49	0.51	0.50	0.64	0.62	0.70
K ₂ O	10.33	10.45	10.42	10.32	9.75	10.08	10.02	10.09	9.97
CaO	0.00	0.00	0.00	0.00	0.02	0.03	0.00	0.01	0.01
Na ₂ O	0.06	0.12	0.10	0.08	0.06	0.13	0.09	0.11	0.09
F	0.69	0.86	1.01	0.80	0.63	0.67	1.46	1.54	1.29
Total	96.94	96.86	97.25	96.87	96.06	96.62	96.48	96.31	95.41

Numbers of ions on the basis of 11 oxygens

Si	2.628	2.618	2.622	2.620	2.640	2.636	2.638	2.662	2.655
Al IV	1.372	1.382	1.378	1.380	1.360	1.364	1.362	1.338	1.345
Σ T	4.000	4.000	4.000	4.000	4.000	4.000	4.000	4.000	4.000
Al VI	0.138	0.196	0.193	0.156	0.147	0.161	0.206	0.223	0.213
Ti	0.189	0.157	0.165	0.164	0.139	0.144	0.180	0.133	0.143
Fe	1.089	1.029	1.038	1.070	1.157	1.139	1.059	1.026	1.036
Mg	0.952	1.014	0.989	1.004	0.947	0.928	0.904	1.005	0.984
Mn	0.028	0.028	0.030	0.030	0.032	0.031	0.040	0.039	0.044
Σ R	2.395	2.423	2.415	2.424	2.422	2.402	2.388	2.426	2.421
Ca	0.000	0.000	0.000	0.000	0.002	0.003	0.000	0.000	0.001
Na	0.009	0.017	0.014	0.011	0.009	0.018	0.013	0.015	0.013
K	0.964	0.975	0.969	0.964	0.917	0.944	0.943	0.951	0.947
Σ A									
F	0.005	0.005	0.005	0.005	0.005	0.005	0.005	0.005	0.005

Table IV.7: Major element analyses of biotites. The single grain analyses were performed with an electron microprobe.

	BT08-26_B06_6	BT08-26_B06_7	BT08-26_B06_8	BT08-26_B05_1	BT08-26_B05_3	BT08-26_B05_4	BT08-26_B05_5	BT08-26_B05_6	BT08-26_B05_7
SiO ₂	35.85	35.59	35.39	37.40	35.36	35.37	35.04	34.97	34.99
Al ₂ O ₃	17.97	18.37	18.02	18.49	17.30	17.23	17.20	16.75	17.02
TiO ₂	2.68	2.84	3.10	2.72	2.50	2.87	2.95	3.04	3.40
FeO	18.46	18.10	17.96	20.12	20.37	19.50	19.27	19.44	19.09
MgO	8.94	9.09	8.52	7.65	8.74	8.96	9.13	9.06	9.10
MnO	0.62	0.62	0.66	0.71	0.72	0.72	0.63	0.67	0.65
K ₂ O	9.86	10.00	10.04	10.09	10.01	10.08	10.02	10.14	9.96
CaO	0.02	0.00	0.00	0.01	0.06	0.01	0.01	0.01	0.01
Na ₂ O	0.09	0.14	0.10	0.08	0.16	0.10	0.11	0.12	0.09
F	1.30	1.50	1.45	0.85	1.34	1.39	1.50	1.44	1.48
Total	95.80	96.25	95.24	98.12	96.56	96.23	95.86	95.63	95.79

Numbers of ions on the basis of 11 oxygens

Si	2.653	2.628	2.641	2.691	2.622	2.627	2.615	2.621	2.612
Al IV	1.347	1.372	1.359	1.309	1.378	1.373	1.385	1.379	1.388
ΣT	4.000	4.000	4.000	4.000	4.000	4.000	4.000	4.000	4.000
Al VI	0.221	0.226	0.227	0.260	0.134	0.136	0.129	0.101	0.110
Ti	0.149	0.158	0.174	0.147	0.139	0.160	0.166	0.171	0.191
Fe	1.029	1.006	1.009	1.090	1.137	1.091	1.083	1.097	1.073
Mg	0.986	1.000	0.948	0.820	0.966	0.992	1.016	1.012	1.012
Mn	0.039	0.038	0.042	0.043	0.045	0.045	0.040	0.042	0.041
ΣR	2.424	2.429	2.400	2.361	2.422	2.425	2.433	2.423	2.427
Ca	0.002	0.000	0.000	0.001	0.005	0.001	0.001	0.001	0.001
Na	0.013	0.020	0.015	0.011	0.022	0.014	0.016	0.017	0.013
K	0.931	0.942	0.956	0.926	0.947	0.955	0.954	0.969	0.949
ΣA									
F	0.005	0.005	0.005	0.005	0.005	0.005	0.005	0.005	0.005

Table IV.7: Major element analyses of biotites. The single grain analyses were performed with an electron microprobe.

	BT08-26_B04_2	BT08-26_B04_3	BT08-26_B04_4	BT08-26_B04_5	BT08-26_B01_1	BT08-26_B01_2	BT08-26_B01_3	BT08-26_B01_4	BT08-26_B01_5
SiO ₂	36.17	35.42	35.26	34.62	36.21	35.29	35.59	35.20	35.22
Al ₂ O ₃	17.79	17.32	17.12	17.02	17.91	17.65	17.43	17.72	17.38
TiO ₂	3.07	2.93	3.03	2.80	2.36	2.81	2.63	2.89	3.10
FeO	20.12	19.83	20.06	20.27	19.55	19.69	20.17	20.02	19.95
MgO	8.13	8.55	8.48	8.95	8.72	8.76	8.98	8.77	8.90
MnO	0.66	0.68	0.60	0.65	0.50	0.54	0.60	0.65	0.66
K ₂ O	10.06	9.99	9.93	10.04	10.15	10.05	10.10	9.96	9.85
CaO	0.03	0.06	0.04	0.03	0.00	0.01	0.00	0.00	0.00
Na ₂ O	0.11	0.15	0.09	0.09	0.06	0.15	0.15	0.11	0.10
F	1.08	1.15	1.27	1.45	1.37	1.46	1.18	1.20	1.30
Total	97.22	96.07	95.88	95.93	96.83	96.40	96.83	96.52	96.47

Numbers of ions on the basis of 11 oxygens

Si	2.645	2.629	2.627	2.592	2.661	2.616	2.623	2.602	2.607
Al IV	1.355	1.371	1.373	1.408	1.339	1.384	1.377	1.398	1.393
ΣT	4.000	4.000	4.000	4.000	4.000	4.000	4.000	4.000	4.000
Al VI	0.179	0.145	0.131	0.095	0.212	0.159	0.137	0.146	0.123
Ti	0.169	0.164	0.170	0.158	0.130	0.157	0.146	0.161	0.173
Fe	1.108	1.108	1.125	1.143	1.082	1.099	1.119	1.114	1.112
Mg	0.886	0.946	0.942	0.999	0.955	0.968	0.986	0.966	0.982
Mn	0.041	0.043	0.038	0.041	0.031	0.034	0.038	0.041	0.042
ΣR	2.383	2.405	2.405	2.436	2.410	2.417	2.427	2.428	2.431
Ca	0.002	0.004	0.003	0.003	0.000	0.001	0.000	0.000	0.000
Na	0.016	0.022	0.013	0.014	0.009	0.022	0.021	0.015	0.014
K	0.939	0.946	0.944	0.959	0.951	0.951	0.950	0.939	0.930
ΣA									
F	0.005	0.005	0.005	0.005	0.005	0.005	0.005	0.005	0.005

Table IV.7: Major element analyses of biotites. The single grain analyses were performed with an electron microprobe.

	BT08-26_B01_6	BT08-31_B02_3	BT08-31_B03_1	BT08-31_B03_2	BT08-31_B03_3	BT08-31_B03_4	BT08-31_B01_1	BT08-31_B01_2	BT08-31_B01_3
SiO ₂	35.34	36.72	37.36	36.23	36.08	36.20	37.60	36.66	36.60
Al ₂ O ₃	17.89	17.41	17.67	17.31	17.21	17.23	16.82	17.03	17.34
TiO ₂	3.52	3.02	2.27	2.74	2.72	2.69	2.25	1.97	2.76
FeO	19.80	18.77	18.60	18.56	19.02	18.63	17.24	18.11	18.40
MgO	8.27	9.68	10.26	9.86	10.00	10.02	10.84	10.89	10.44
MnO	0.65	0.38	0.36	0.37	0.37	0.35	0.30	0.30	0.34
K ₂ O	10.18	10.37	10.26	10.17	10.08	10.28	9.94	10.44	10.39
CaO	0.01	0.01	0.04	0.03	0.02	0.03	0.09	0.02	0.00
Na ₂ O	0.12	0.08	0.06	0.07	0.12	0.08	0.41	0.08	0.11
F	1.03	1.01	1.08	1.11	0.98	1.03	0.93	1.08	1.00
Total	96.81	97.45	97.96	96.45	96.61	96.54	96.42	96.58	97.38

Numbers of ions on the basis of 11 oxygens

Si	2.600	2.667	2.692	2.661	2.646	2.657	2.738	2.686	2.659
Al IV	1.400	1.333	1.308	1.339	1.354	1.343	1.262	1.314	1.341
Σ T	4.000	4.000	4.000	4.000	4.000	4.000	4.000	4.000	4.000
Al VI	0.152	0.158	0.193	0.159	0.134	0.147	0.181	0.157	0.144
Ti	0.195	0.165	0.123	0.151	0.150	0.148	0.123	0.109	0.151
Fe	1.097	1.027	1.009	1.026	1.050	1.030	0.945	0.999	1.007
Mg	0.907	1.048	1.102	1.079	1.093	1.096	1.176	1.189	1.130
Mn	0.041	0.023	0.022	0.023	0.023	0.022	0.019	0.018	0.021
Σ R	2.391	2.420	2.449	2.439	2.450	2.443	2.445	2.472	2.453
Ca	0.001	0.000	0.003	0.002	0.002	0.002	0.007	0.002	0.000
Na	0.017	0.011	0.009	0.010	0.017	0.012	0.058	0.012	0.015
K	0.956	0.961	0.943	0.953	0.943	0.962	0.923	0.976	0.963
Σ A									
F	0.005	0.005	0.005	0.005	0.005	0.005	0.005	0.005	0.005

Table IV.7: Major element analyses of biotites. The single grain analyses were performed with an electron microprobe.

	BT08-31_B01_4	BT08-31_B01_5	BT08-31_B07_1	BT08-31_B07_2	BT08-31_B07_3	BT08-31_B08_1	BT08-31_B08_3	BT08-31_B08_6	BT08-31_B08_7
SiO ₂	36.61	36.90	35.16	35.56	35.39	35.90	35.19	35.45	35.50
Al ₂ O ₃	17.52	17.35	17.79	17.81	17.58	17.55	17.20	17.25	16.91
TiO ₂	2.56	2.79	2.39	2.40	2.39	3.02	3.54	3.79	3.49
FeO	18.35	18.39	19.79	19.54	19.94	18.88	19.86	19.32	19.59
MgO	10.51	10.31	8.59	8.78	8.81	9.21	9.03	8.80	9.24
MnO	0.31	0.35	0.49	0.46	0.42	0.34	0.41	0.47	0.39
K ₂ O	10.49	10.45	9.98	10.29	9.98	9.80	9.99	10.16	9.86
CaO	0.01	0.02	0.00	0.00	0.00	0.06	0.02	0.00	0.05
Na ₂ O	0.05	0.05	0.10	0.08	0.08	0.07	0.11	0.10	0.07
F	1.01	1.05	0.84	0.84	0.70	0.65	0.71	0.87	0.98
Total	97.42	97.67	95.13	95.76	95.29	95.49	96.06	96.20	96.08

Numbers of ions on the basis of 11 oxygens

Si	2.658	2.672	2.623	2.635	2.631	2.648	2.600	2.616	2.624
Al IV	1.342	1.328	1.377	1.365	1.369	1.352	1.400	1.384	1.376
ΣT	4.000	4.000	4.000	4.000	4.000	4.000	4.000	4.000	4.000
Al VI	0.158	0.154	0.188	0.191	0.172	0.174	0.098	0.117	0.097
Ti	0.140	0.152	0.134	0.134	0.134	0.168	0.197	0.210	0.194
Fe	1.003	1.003	1.112	1.090	1.116	1.049	1.105	1.074	1.090
Mg	1.137	1.113	0.955	0.970	0.976	1.012	0.994	0.968	1.018
Mn	0.019	0.022	0.031	0.029	0.026	0.021	0.026	0.029	0.025
ΣR	2.458	2.443	2.420	2.413	2.425	2.424	2.419	2.399	2.424
Ca	0.000	0.002	0.000	0.000	0.000	0.005	0.002	0.000	0.004
Na	0.007	0.007	0.015	0.011	0.011	0.011	0.016	0.014	0.010
K	0.972	0.966	0.950	0.973	0.947	0.922	0.942	0.957	0.930
ΣA									
F	0.005	0.005	0.005	0.005	0.005	0.005	0.005	0.005	0.005

Table IV.7: Major element analyses of biotites. The single grain analyses were performed with an electron microprobe.

	BT08-34-B03-1	BT08-34-B06-1	BT08-34-B06-2	BT08-34-B06-3	BT08-34-B08-3	BT08-34-B08-4	BT08-34-B13-1	BT08-34-B13-2	BT08-80-B03-1
SiO ₂	37.40	37.90	37.91	37.75	37.79	37.75	37.22	37.51	35.15
Al ₂ O ₃	18.02	18.91	19.08	19.10	18.77	19.22	18.59	18.97	17.44
TiO ₂	0.84	1.00	0.97	1.10	0.70	1.18	1.25	1.29	2.66
FeO	11.88	9.43	9.49	9.63	9.29	9.38	10.32	10.10	23.31
MgO	15.62	16.46	16.42	16.19	16.52	16.94	16.43	16.28	6.12
MnO	0.14	0.14	0.13	0.14	0.16	0.16	0.17	0.12	0.58
K ₂ O	10.02	10.51	10.49	10.61	10.45	9.44	10.38	10.10	10.16
CaO	0.05	0.01	0.00	0.02	0.02	0.01	0.01	0.04	0.00
Na ₂ O	0.10	0.13	0.16	0.10	0.13	0.09	0.11	0.15	0.03
F	0.94	1.01	0.95	1.19	1.29	0.91	0.86	0.91	0.49
Total	95.01	95.49	95.60	95.84	95.13	95.08	95.33	95.46	95.94

Numbers of ions on the basis of 11 oxygens

Si	2.719	2.726	2.722	2.714	2.736	2.707	2.689	2.698	2.619
Al IV	1.281	1.604	1.615	1.619	1.602	1.625	1.584	1.609	1.381
ΣT	4.000	4.330	4.337	4.333	4.338	4.332	4.273	4.307	4.000
Al VI	0.263	0.330	0.337	0.333	0.338	0.332	0.273	0.307	0.151
Ti	0.046	0.054	0.052	0.060	0.038	0.064	0.068	0.070	0.149
Fe	0.650	0.511	0.513	0.521	0.506	0.507	0.561	0.547	1.308
Mg	1.692	1.765	1.757	1.735	1.783	1.811	1.769	1.745	0.680
Mn	0.009	0.008	0.008	0.009	0.010	0.009	0.010	0.007	0.036
ΣR	2.660	2.668	2.668	2.658	2.676	2.722	2.681	2.676	2.324
Ca	0.004	0.001	0.000	0.002	0.001	0.001	0.000	0.003	0.000
Na	0.015	0.018	0.022	0.014	0.019	0.013	0.016	0.021	0.005
K	0.929	0.965	0.961	0.973	0.965	0.864	0.957	0.927	0.966
ΣA									
F	0.005	0.005	0.005	0.005	0.005	0.004	0.005	0.005	0.005

Table IV.7: Major element analyses of biotites. The single grain analyses were performed with an electron microprobe.

	BT08-80-B03-2	BT08-80-B02-1	BT08-80-B02-2	BT08-80-B02-3	BT08-80-B01-2	BT08-80-B01-3	BT08-80-B06-1	BT08-80-B06-3	BT08-80-B06-4
SiO ₂	35.03	34.37	34.59	34.03	35.16	35.15	34.91	34.86	34.78
Al ₂ O ₃	18.08	17.96	18.09	18.10	17.87	17.17	18.05	18.15	17.62
TiO ₂	2.61	2.61	2.89	2.97	1.55	2.31	2.90	2.78	2.69
FeO	23.84	23.85	23.69	24.01	23.53	23.97	23.88	23.85	24.43
MgO	6.19	6.14	6.02	6.03	6.67	6.08	5.84	6.18	6.04
MnO	0.63	0.61	0.56	0.56	0.59	0.63	0.65	0.64	0.54
K ₂ O	10.10	10.15	9.88	9.52	10.08	10.07	10.02	10.06	9.77
CaO	0.01	0.00	0.01	0.02	0.03	0.05	0.03	0.01	0.05
Na ₂ O	0.03	0.05	0.06	0.04	0.07	0.06	0.05	0.09	0.08
F	0.25	0.43	0.38	0.09	0.40	0.43	0.39	0.48	0.41
Total	96.77	96.17	96.16	95.38	95.95	95.91	96.72	97.11	96.40

Numbers of ions on the basis of 11 oxygens

Si	2.583	2.562	2.569	2.542	2.616	2.624	2.580	2.569	2.581
Al IV	1.417	1.438	1.431	1.458	1.384	1.376	1.420	1.431	1.419
ΣT	4.000	4.000	4.000	4.000	4.000	4.000	4.000	4.000	4.000
Al VI	0.155	0.140	0.153	0.135	0.184	0.135	0.153	0.146	0.123
Ti	0.145	0.146	0.161	0.167	0.087	0.130	0.161	0.154	0.150
Fe	1.324	1.339	1.325	1.350	1.318	1.347	1.329	1.324	1.365
Mg	0.680	0.682	0.666	0.671	0.740	0.676	0.643	0.679	0.668
Mn	0.040	0.038	0.035	0.035	0.037	0.040	0.041	0.040	0.034
ΣR	2.344	2.345	2.340	2.359	2.366	2.328	2.327	2.343	2.340
Ca	0.001	0.000	0.000	0.002	0.003	0.004	0.003	0.001	0.004
Na	0.004	0.008	0.009	0.006	0.010	0.008	0.007	0.013	0.012
K	0.950	0.965	0.936	0.907	0.957	0.959	0.945	0.946	0.925
ΣA									
F	0.005	0.005	0.005	0.005	0.005	0.005	0.005	0.005	0.005

Table IV.7: Major element analyses of biotites. The single grain analyses were performed with an electron microprobe.

	BT08-80-B06-5	BT08-80-B06-6	BT08-80-B06-7	BT08-80-B05-1	BT08-80-B05-2	BT08-80-B07-5	BT08-80-B12-1	BT08-80-B12-2	BT08-80-B12-3
SiO ₂	34.29	34.56	34.84	34.83	34.89	34.81	34.81	35.13	34.74
Al ₂ O ₃	18.13	17.98	17.84	18.22	17.82	17.80	17.55	17.89	17.92
TiO ₂	2.80	2.91	2.96	2.39	2.23	2.71	2.53	2.99	3.24
FeO	23.29	23.28	23.52	23.58	23.41	23.64	23.61	23.45	23.49
MgO	6.27	6.17	6.10	6.20	6.15	6.10	6.22	6.21	5.98
MnO	0.64	0.65	0.59	0.62	0.63	0.57	0.55	0.67	0.63
K ₂ O	9.91	9.89	9.98	9.95	10.02	9.83	10.09	9.92	10.15
CaO	0.06	0.04	0.05	0.01	0.00	0.05	0.02	0.00	0.00
Na ₂ O	0.10	0.13	0.09	0.03	0.08	0.09	0.05	0.07	0.08
F	0.49	0.44	0.36	0.37	0.43	0.33	0.29	0.52	0.49
Total	95.99	96.04	96.33	96.20	95.66	95.93	95.71	96.84	96.72

Numbers of ions on the basis of 11 oxygens

Si	2.556	2.571	2.583	2.584	2.606	2.598	2.591	2.571	2.571
Al IV	1.444	1.429	1.417	1.416	1.394	1.402	1.409	1.429	1.429
Σ T	4.000	4.000	4.000	4.000	4.000	4.000	4.000	4.000	4.000
Al VI	0.149	0.149	0.142	0.177	0.175	0.142	0.147	0.135	0.139
Ti	0.157	0.163	0.165	0.133	0.125	0.142	0.166	0.180	0.182
Fe	1.307	1.304	1.313	1.317	1.316	1.327	1.303	1.309	1.314
Mg	0.697	0.684	0.674	0.685	0.684	0.692	0.683	0.660	0.644
Mn	0.040	0.041	0.037	0.039	0.040	0.034	0.042	0.040	0.039
Σ R	2.351	2.341	2.331	2.352	2.341	2.337	2.340	2.324	2.318
Ca	0.005	0.003	0.004	0.001	0.000	0.001	0.000	0.000	0.000
Na	0.015	0.019	0.012	0.004	0.012	0.007	0.010	0.012	0.008
K	0.942	0.939	0.944	0.942	0.955	0.961	0.934	0.959	0.964
Σ A									
F	0.005	0.005	0.005	0.005	0.005	0.005	0.005	0.005	0.005

Table IV.7: Major element analyses of biotites. The single grain analyses were performed with an electron microprobe.

	BT08-80-B12-4	BT08-80-B12-5	BT08-80-B12-6	BT08-80-B13-1	BT08-80-B13-2	BT08-80-B13-3	BT08-80-B13-4	BT08-80-B13-5	BT08-80-B13-6
SiO ₂	34.51	34.65	35.17	35.35	34.44	34.96	34.25	34.82	34.55
Al ₂ O ₃	17.84	17.62	17.76	19.21	17.50	17.38	17.08	17.82	17.93
TiO ₂	3.25	3.45	3.37	2.34	3.25	3.68	3.27	3.13	2.79
FeO	23.41	23.79	23.43	22.99	23.66	23.80	24.71	23.48	23.62
MgO	5.80	5.80	6.03	5.61	6.02	5.88	5.78	5.89	6.08
MnO	0.62	0.63	0.57	0.57	0.65	0.54	0.67	0.61	0.63
K ₂ O	10.14	9.46	10.18	9.74	10.08	10.03	10.00	10.04	10.08
CaO	0.00	0.02	0.00	0.03	0.00	0.00	0.00	0.02	0.03
Na ₂ O	0.06	0.07	0.04	0.02	0.09	0.07	0.05	0.13	0.08
F	0.42	0.36	0.50	0.37	0.53	0.42	0.21	0.51	0.47
Total	96.05	95.85	97.06	96.23	96.22	96.76	96.02	96.45	96.26

Numbers of ions on the basis of 11 oxygens

Si	2.578	2.591	2.605	2.568	2.585	2.560	2.584	2.571	2.576
Al IV	1.422	1.409	1.395	1.432	1.415	1.440	1.416	1.429	1.424
ΣT	4.000	4.000	4.000	4.000	4.000	4.000	4.000	4.000	4.000
Al VI	0.123	0.133	0.273	0.107	0.099	0.065	0.142	0.143	0.147
Ti	0.193	0.187	0.130	0.182	0.205	0.184	0.175	0.156	0.156
Fe	1.333	1.300	1.276	1.329	1.325	1.391	1.312	1.323	1.334
Mg	0.643	0.662	0.616	0.669	0.648	0.644	0.651	0.674	0.663
Mn	0.039	0.036	0.035	0.041	0.034	0.042	0.038	0.040	0.033
ΣR	2.332	2.318	2.330	2.327	2.311	2.326	2.318	2.337	2.333
Ca	0.002	0.000	0.002	0.000	0.000	0.000	0.001	0.002	0.001
Na	0.010	0.006	0.003	0.013	0.010	0.007	0.018	0.012	0.007
K	0.898	0.957	0.916	0.959	0.946	0.954	0.950	0.957	0.951
ΣA									
F	0.005	0.005	0.005	0.005	0.005	0.005	0.005	0.005	0.005

Table IV.7: Major element analyses of biotites. The single grain analyses were performed with an electron microprobe.

	BT08-80-B13-7	BT08-45-B01-1	BT08-45-B01-2	BT08-45-B01-3	BT08-45-B02-1	BT08-45-B02-2	BT08-45-B02-3	BT08-45-B02-4	BT08-45-B06-1
SiO ₂	34.70	35.02	35.47	35.28	35.08	34.93	35.00	35.00	35.01
Al ₂ O ₃	17.96	18.07	18.34	18.16	17.70	17.70	17.26	18.12	17.35
TiO ₂	2.79	3.23	2.94	2.80	2.92	2.96	3.06	2.89	3.14
FeO	23.87	21.94	21.67	20.89	22.45	21.77	22.62	21.83	22.73
MgO	5.99	6.95	7.25	7.44	7.05	7.10	7.17	7.28	6.90
MnO	0.53	0.43	0.44	0.39	0.41	0.42	0.43	0.36	0.45
K ₂ O	10.04	10.03	10.13	10.07	9.86	9.82	9.93	10.01	9.98
CaO	0.02	0.00	0.00	0.01	0.03	0.09	0.05	0.05	0.02
Na ₂ O	0.05	0.15	0.12	0.17	0.13	0.17	0.07	0.13	0.08
F	0.21	0.60	0.80	0.79	0.81	0.69	0.70	0.75	0.81
Total	96.16	96.42	97.16	96.00	96.44	95.65	96.30	96.41	96.46

Numbers of ions on the basis of 11 oxygens

Si	2.576	2.587	2.600	2.613	2.598	2.601	2.598	2.587	2.598
Al IV	1.424	1.413	1.400	1.387	1.402	1.399	1.402	1.413	1.402
Σ T	4.000	4.000	4.000	4.000	4.000	4.000	4.000	4.000	4.000
Al VI	0.123	0.160	0.185	0.198	0.143	0.156	0.108	0.167	0.115
Ti	0.174	0.179	0.162	0.156	0.163	0.166	0.171	0.161	0.175
Fe	1.359	1.220	1.196	1.165	1.252	1.221	1.264	1.215	1.270
Mg	0.624	0.765	0.792	0.821	0.778	0.788	0.793	0.802	0.763
Mn	0.034	0.027	0.027	0.025	0.026	0.026	0.027	0.022	0.028
Σ R	2.313	2.352	2.363	2.365	2.361	2.357	2.363	2.367	2.351
Ca	0.001	0.000	0.000	0.001	0.002	0.007	0.004	0.004	0.001
Na	0.007	0.021	0.017	0.024	0.019	0.025	0.010	0.018	0.012
K	0.955	0.945	0.947	0.951	0.932	0.933	0.940	0.944	0.945
Σ A									
F	0.005	0.005	0.005	0.005	0.005	0.005	0.005	0.005	0.005

Table IV.7: Major element analyses of biotites. The single grain analyses were performed with an electron microprobe.

	BT08-45-B06-2	BT08-45-B06-3	BT08-45-B06-4	BT08-45-B04-1	BT08-45-B04-2	BT08-45-B04-3	BT08-45-B08-1	BT08-45-B08-2	BT08-45-B08-3
SiO ₂	34.64	34.87	34.76	35.34	35.03	35.12	35.17	35.73	35.40
Al ₂ O ₃	17.50	17.23	17.53	17.45	17.39	17.19	17.61	17.54	17.42
TiO ₂	2.93	3.01	2.77	3.22	3.68	3.81	2.73	2.79	2.54
FeO	23.19	23.22	22.78	22.39	22.08	21.98	22.02	22.39	23.10
MgO	6.90	6.91	6.97	6.58	6.58	6.54	7.07	7.03	7.49
MnO	0.42	0.44	0.42	0.46	0.43	0.43	0.41	0.37	0.43
K ₂ O	9.74	10.12	10.13	9.99	9.94	10.08	10.15	9.60	10.24
CaO	0.01	0.01	0.00	0.07	0.04	0.03	0.03	0.03	0.00
Na ₂ O	0.11	0.12	0.10	0.12	0.08	0.13	0.09	0.06	0.06
F	0.84	0.70	0.97	0.53	0.83	0.50	0.93	0.75	0.77
Total	96.28	96.63	96.43	96.15	96.07	95.80	96.21	96.30	97.46

Numbers of ions on the basis of 11 oxygens

Si	2.578	2.587	2.588	2.618	2.605	2.612	2.614	2.638	2.602
Al IV	1.422	1.413	1.412	1.382	1.395	1.388	1.386	1.362	1.398
ΣT	4.000	4.000	4.000	4.000	4.000	4.000	4.000	4.000	4.000
Al VI	0.113	0.094	0.126	0.143	0.129	0.119	0.158	0.164	0.111
Ti	0.164	0.168	0.155	0.179	0.206	0.213	0.153	0.155	0.140
Fe	1.299	1.297	1.277	1.249	1.236	1.231	1.233	1.245	1.278
Mg	0.765	0.764	0.773	0.727	0.729	0.725	0.783	0.773	0.820
Mn	0.027	0.027	0.027	0.029	0.027	0.027	0.026	0.023	0.027
ΣR	2.368	2.351	2.358	2.326	2.327	2.315	2.352	2.361	2.377
Ca	0.001	0.001	0.000	0.006	0.003	0.002	0.002	0.002	0.000
Na	0.016	0.018	0.015	0.018	0.011	0.018	0.013	0.009	0.009
K	0.925	0.958	0.962	0.944	0.943	0.956	0.963	0.904	0.960
ΣA									
F	0.005	0.005	0.005	0.005	0.005	0.005	0.005	0.005	0.005

Table IV.7: Major element analyses of biotites. The single grain analyses were performed with an electron microprobe.

	BT08-45-B08-4	BT08-45-B07-1	BT08-45-B07-2	BT08-45-B07-3	BT08-45-B07-4	BT08-45-B07-5	BT08-15_B01_1	BT08-15_B01_2	BT08-15_B01_4
SiO ₂	35.40	34.66	35.15	34.46	34.96	35.61	34.99	35.48	34.75
Al ₂ O ₃	17.91	17.77	17.74	17.33	17.79	17.70	17.37	18.04	17.76
TiO ₂	2.16	3.06	2.70	3.71	3.11	2.98	3.20	3.07	3.25
FeO	22.61	22.32	22.39	23.26	22.57	22.27	22.47	21.96	21.97
MgO	7.76	6.89	7.35	6.80	6.96	6.96	7.71	8.02	8.20
MnO	0.45	0.38	0.38	0.37	0.39	0.35	0.41	0.36	0.34
K ₂ O	9.94	9.89	10.14	10.02	9.87	10.31	9.92	10.15	10.14
CaO	0.00	0.01	0.01	0.03	0.03	0.00	0.07	0.02	0.00
Na ₂ O	0.06	0.16	0.09	0.05	0.14	0.07	0.09	0.10	0.11
F	0.84	0.76	0.88	0.79	0.73	0.66	0.29	0.59	0.45
Total	97.13	95.91	96.82	96.82	96.55	96.90	96.52	97.78	96.97

Numbers of ions on the basis of 11 oxygens

Si	2.602	2.582	2.597	2.555	2.585	2.620	2.579	2.582	2.553
Al IV	1.398	1.418	1.403	1.445	1.415	1.380	1.421	1.418	1.447
ΣT	4.000	4.000	4.000	4.000	4.000	4.000	4.000	4.000	4.000
Al VI	0.155	0.143	0.142	0.069	0.136	0.155	0.088	0.129	0.091
Ti	0.119	0.171	0.150	0.207	0.173	0.165	0.177	0.168	0.180
Fe	1.252	1.252	1.246	1.299	1.257	1.234	1.247	1.203	1.215
Mg	0.850	0.765	0.809	0.751	0.767	0.763	0.847	0.870	0.898
Mn	0.028	0.024	0.024	0.024	0.024	0.022	0.026	0.022	0.021
ΣR	2.404	2.355	2.371	2.350	2.358	2.339	2.385	2.393	2.405
Ca	0.000	0.001	0.001	0.002	0.002	0.000	0.006	0.001	0.000
Na	0.009	0.022	0.012	0.007	0.020	0.010	0.013	0.014	0.016
K	0.932	0.940	0.956	0.948	0.931	0.968	0.933	0.942	0.950
ΣA									
F	0.005	0.005	0.005	0.005	0.005	0.005	0.005	0.005	0.005

Table IV.7: Major element analyses of biotites. The single grain analyses were performed with an electron microprobe.

	BT08-15_B01_5	BT08-15_B01_7	BT08-15_B01_8	BT08-15_B01_9	BT08-15_B01_10	BT08-15_B03_1	BT08-15_B03_2	BT08-15_B02_2	BT08-15_B02_5
SiO ₂	35.20	33.70	35.07	35.28	35.11	35.64	35.10	35.08	34.95
Al ₂ O ₃	17.67	15.03	18.26	18.23	17.69	17.32	17.97	17.80	17.80
TiO ₂	2.67	4.73	3.36	3.04	2.89	2.93	2.75	2.40	3.78
FeO	21.90	21.13	21.88	21.84	21.96	22.40	22.88	22.98	22.59
MgO	8.31	6.70	7.68	7.75	8.17	7.80	7.63	7.83	7.60
MnO	0.31	0.23	0.35	0.33	0.33	0.31	0.35	0.37	0.38
K ₂ O	9.80	3.21	10.06	10.15	9.90	10.08	10.02	10.12	10.22
CaO	0.04	4.35	0.00	0.01	0.04	0.02	0.01	0.00	0.00
Na ₂ O	0.10	0.06	0.12	0.12	0.09	0.05	0.13	0.12	0.13
F	0.45	0.18	0.53	0.43	0.53	0.25	0.36	0.43	0.45
Total	96.44	89.32	97.31	97.18	96.71	96.81	97.18	97.13	97.91

Numbers of ions on the basis of 11 oxygens

Si	2.591	2.563	2.579	2.582	2.613	2.571	2.576	2.548	2.551
Al IV	1.409	1.437	1.421	1.418	1.387	1.429	1.424	1.452	1.449
ΣT	4.000	4.000	4.000	4.000	4.000	4.000	4.000	4.000	4.000
Al VI	0.124	0.137	0.149	0.116	0.110	0.123	0.117	0.077	0.103
Ti	0.148	0.185	0.167	0.160	0.162	0.151	0.133	0.207	0.202
Fe	1.214	1.204	1.202	1.216	1.237	1.262	1.271	1.240	1.229
Mg	0.911	0.837	0.844	0.895	0.852	0.833	0.857	0.826	0.810
Mn	0.019	0.022	0.020	0.021	0.019	0.021	0.023	0.024	0.024
ΣR	2.416	2.384	2.383	2.407	2.380	2.391	2.401	2.374	2.367
Ca	0.003	0.000	0.001	0.003	0.001	0.000	0.000	0.000	0.001
Na	0.014	0.016	0.017	0.012	0.008	0.018	0.017	0.018	0.015
K	0.920	0.938	0.946	0.929	0.943	0.936	0.948	0.950	0.956
ΣA									
F	0.005	0.005	0.005	0.005	0.005	0.005	0.005	0.005	0.005

Table IV.7: Major element analyses of biotites. The single grain analyses were performed with an electron microprobe.

	BT08-15_B02_6	BT08-15_B02_7	BT08-15_B01_1	BT08-15_B01_2	BT08-15_B01_3	BT08-15_B01_4
SiO ₂	35.00	34.99	34.82	35.11	35.67	34.83
Al ₂ O ₃	18.07	17.72	17.97	17.72	18.43	18.15
TiO ₂	3.41	3.28	3.66	4.13	4.35	3.36
FeO	22.81	22.67	22.28	21.95	20.83	21.28
MgO	7.26	7.32	7.42	7.49	6.97	7.86
MnO	0.37	0.43	0.38	0.34	0.34	0.39
K ₂ O	10.12	10.17	10.23	10.13	10.14	10.20
CaO	0.00	0.00	0.02	0.00	0.13	0.00
Na ₂ O	0.12	0.13	0.11	0.07	0.26	0.18
F	0.32	0.38	0.34	0.29	0.20	0.50
Total	97.49	97.08	97.23	97.23	97.33	96.76

Numbers of ions on the basis of 11 oxygens

Si	2.565	2.589	2.561	2.568	2.568	2.568
Al IV	1.435	1.411	1.439	1.432	1.432	1.432
ΣT	4.000	4.000	4.000	4.000	4.000	4.000
Al VI	0.091	0.165	0.134	0.129	0.116	0.154
Ti	0.227	0.237	0.186	0.188	0.197	0.177
Fe	1.207	1.138	1.178	1.183	1.184	1.182
Mg	0.815	0.754	0.861	0.861	0.843	0.834
Mn	0.021	0.021	0.025	0.024	0.024	0.025
ΣR	2.362	2.316	2.384	2.385	2.364	2.372
Ca	0.000	0.010	0.000	0.000	0.003	0.000
Na	0.009	0.037	0.025	0.032	0.049	0.034
K	0.944	0.939	0.957	0.936	0.949	0.959
ΣA						
F	0.005	0.005	0.005	0.005	0.005	0.005

Table IV.8: Major element analyses of chlorites. The single grain analyses were performed with an electron microprobe.

	BT09-80-C02-2	BT09-80-C02-3	BT09-80-C02-6	BT09-80-C02-7	BT09-80-C08-3	BT08-63-C07-1	BT08-63-C07-2	BT08-63-C07-3	BT08-63-C07-4
SiO ₂	25.58	25.34	26.91	28.04	25.73	25.23	25.25	25.43	25.23
Al ₂ O ₃	21.16	21.02	21.33	21.19	20.62	20.95	21.00	20.85	21.36
TiO ₂	0.15	0.21	0.39	0.72	0.28	0.07	0.07	0.04	0.06
FeO	29.36	29.21	27.79	26.41	28.81	27.38	27.32	27.49	27.22
MgO	11.59	11.66	11.17	10.61	11.47	13.50	13.02	13.21	13.00
MnO	0.46	0.43	0.42	0.37	0.44	0.96	0.89	0.99	0.95
K ₂ O	0.07	0.17	0.88	1.59	0.44	0.01	0.00	0.01	0.00
CaO	0.04	0.03	0.03	0.02	0.05	0.01	0.04	0.04	0.02
Na ₂ O	0.00	0.01	0.01	0.01	0.02	0.00	0.04	0.03	0.01
F	0.11	0.16	0.10	0.32	0.06	0.00	0.00	0.05	0.07
Total	88.52	88.23	89.02	89.28	87.92	88.12	87.64	88.14	87.92
<i>Numbers of ions on the basis of 14 oxygens</i>									
Si	2.563	2.551	2.597	2.572	2.525	2.532	2.546	2.553	2.536
Al IV	1.437	1.449	1.403	1.428	1.475	1.468	1.454	1.447	1.464
Σ T	4.000	4.000	4.000	4.000	4.000	4.000	4.000	4.000	4.000
Al VI	1.063	1.046	1.050	1.038	1.044	1.011	1.042	1.021	1.067
Ti	0.011	0.016	0.022	0.011	0.006	0.005	0.006	0.003	0.005
Fe	2.215	2.215	2.189	2.205	2.230	2.069	2.074	2.078	2.060
Mg	1.731	1.750	1.725	1.771	1.757	2.019	1.956	1.977	1.947
Mn	0.039	0.037	0.037	0.037	0.045	0.082	0.076	0.084	0.081
Σ R	5.059	5.063	5.024	5.061	5.083	5.187	5.155	5.163	5.160
Ca	0.004	0.003	0.006	0.003	0.002	0.001	0.005	0.004	0.002
Na	0.001	0.002	0.004	0.006	0.003	0.000	0.008	0.006	0.002
K	0.009	0.021	0.057	0.029	0.016	0.001	0.000	0.001	0.001
Σ A	0.013	0.026	0.067	0.038	0.020	0.003	0.013	0.012	0.005
F	0.000	0.000	0.000	0.000	0.000	0.000	0.000	0.000	0.000

Table IV.8: Major element analyses of chlorites. The single grain analyses were performed with an electron microprobe.

	BT08-63-C08-1	BT08-63-C08-3	BT08-63-C08-4	BT08-63-C08-5	BT08-63-C02-1	BT08-63-C02-2	BT08-63-C02-3	BT08-63-C02-4	BT08-63-C02-5
SiO ₂	25.95	25.51	25.54	25.22	25.47	25.22	25.93	25.32	25.12
Al ₂ O ₃	21.21	20.89	21.25	21.33	20.43	20.93	20.70	21.03	21.05
TiO ₂	0.22	0.14	0.08	0.06	0.37	0.10	0.14	0.11	0.11
FeO	27.28	27.03	27.64	26.73	26.62	26.88	26.83	27.38	27.26
MgO	12.62	12.99	12.52	12.43	13.74	13.29	13.32	13.34	13.26
MnO	0.78	0.82	0.85	0.86	0.90	0.90	0.85	0.91	0.91
K ₂ O	0.69	0.06	0.05	0.03	0.05	0.00	0.03	0.03	0.02
CaO	0.06	0.05	0.06	0.08	0.08	0.06	0.05	0.02	0.03
Na ₂ O	0.03	0.03	0.01	0.02	0.02	0.02	0.02	0.00	0.00
F	0.00	0.00	0.07	0.01	0.08	0.05	0.07	0.04	0.05
Total	88.83	87.52	88.05	86.76	87.77	87.45	87.93	88.19	87.81
<i>Numbers of ions on the basis of 14 oxygens</i>									
Si	2.585	2.572	2.564	2.562	2.564	2.547	2.600	2.539	2.530
Al IV	1.415	1.428	1.436	1.438	1.436	1.453	1.400	1.461	1.470
Σ T	4.000	4.000	4.000	4.000	4.000	4.000	4.000	4.000	4.000
Al VI	1.076	1.054	1.079	1.117	0.989	1.040	1.047	1.025	1.030
Ti	0.016	0.011	0.006	0.005	0.028	0.007	0.011	0.009	0.008
Fe	2.046	2.052	2.089	2.045	2.018	2.044	2.026	2.067	2.068
Mg	1.874	1.952	1.873	1.882	2.061	2.001	1.990	1.993	1.990
Mn	0.066	0.070	0.072	0.074	0.077	0.077	0.072	0.078	0.078
Σ R	5.077	5.138	5.119	5.121	5.173	5.168	5.145	5.172	5.174
Ca	0.006	0.005	0.006	0.008	0.009	0.007	0.005	0.002	0.003
Na	0.006	0.005	0.002	0.003	0.004	0.004	0.004	0.000	0.000
K	0.087	0.008	0.006	0.004	0.007	0.000	0.003	0.004	0.003
Σ A	0.099	0.019	0.013	0.016	0.020	0.011	0.012	0.006	0.006
F	0.000	0.000	0.000	0.000	0.000	0.000	0.000	0.000	0.000

Table IV.8: Major element analyses of chlorites. The single grain analyses were performed with an electron microprobe.

	BT08-63-C03-1	BT08-63-C03-2	BT08-63-C03-3	BT08-63-C03-4	BT08-63-C05-1	BT08-63-C05-2	BT08-63-C05-3	BT08-63-C01-3	BT08-63-C01-4
SiO ₂	26.14	25.75	26.08	25.48	26.74	25.85	25.84	25.41	25.22
Al ₂ O ₃	20.22	20.81	20.81	20.74	19.80	21.26	20.93	20.58	20.17
TiO ₂	0.11	0.00	0.05	0.03	0.03	0.08	0.06	0.03	1.02
FeO	27.06	26.90	26.77	26.77	26.50	26.89	27.42	26.50	26.57
MgO	12.94	13.31	13.42	13.42	12.25	12.93	12.59	12.74	12.54
MnO	0.89	0.85	0.84	0.87	0.78	0.82	0.81	0.76	0.73
K ₂ O	0.04	0.01	0.01	0.02	0.14	0.16	0.12	0.12	0.17
CaO	0.06	0.07	0.06	0.04	0.11	0.08	0.05	0.13	0.10
Na ₂ O	0.00	0.00	0.00	0.01	0.03	0.03	0.02	0.04	0.02
F	0.00	0.04	0.12	0.11	0.04	0.00	0.01	0.06	0.00
Total	87.46	87.75	88.16	87.48	86.41	88.10	87.84	86.37	86.54
<i>Numbers of ions on the basis of 14 oxygens</i>									
Si	2.635	2.587	2.607	2.572	2.720	2.586	2.596	2.595	2.574
Al IV	1.365	1.413	1.393	1.428	1.280	1.414	1.404	1.405	1.426
Σ T	4.000	4.000	4.000	4.000	4.000	4.000	4.000	4.000	4.000
Al VI	1.038	1.053	1.059	1.039	1.095	1.093	1.076	1.073	1.000
Ti	0.008	0.000	0.004	0.002	0.002	0.006	0.004	0.002	0.078
Fe	2.054	2.035	2.015	2.034	2.030	2.025	2.075	2.038	2.042
Mg	1.944	1.993	1.999	2.019	1.857	1.927	1.885	1.939	1.907
Mn	0.076	0.072	0.071	0.074	0.067	0.069	0.069	0.066	0.063
Σ R	5.119	5.154	5.148	5.169	5.052	5.121	5.108	5.118	5.090
Ca	0.006	0.007	0.006	0.004	0.012	0.008	0.005	0.014	0.011
Na	0.001	0.000	0.000	0.001	0.005	0.006	0.003	0.008	0.004
K	0.006	0.002	0.002	0.002	0.018	0.020	0.016	0.015	0.023
Σ A	0.013	0.009	0.008	0.008	0.035	0.034	0.024	0.038	0.037
F	0.000	0.000	0.000	0.000	0.000	0.000	0.000	0.000	0.000

Table IV.8: Major element analyses of chlorites. The single grain analyses were performed with an electron microprobe.

	BT08-26_C01_1	BT08-26_C01_2	BT08-26_C02_1	BT08-26_C02_3	BT08-26_C02_4	BT08-26_C05_1	BT08-26_C05_2	BT08-26_C05_3	BT08-26_C05_4
SiO ₂	25.37	24.71	25.68	25.26	26.20	25.59	25.72	25.26	25.45
Al ₂ O ₃	21.90	21.69	21.99	20.99	21.71	21.58	21.62	21.39	21.27
TiO ₂	0.13	0.15	0.04	0.16	0.00	0.10	0.03	0.00	0.15
FeO	26.81	27.24	27.02	26.57	26.20	26.52	26.46	26.41	26.58
MgO	11.91	12.10	11.77	12.10	10.76	12.32	12.37	12.87	12.22
MnO	1.06	1.14	1.11	1.13	1.04	0.78	0.72	0.79	0.83
K ₂ O	0.11	0.04	0.07	0.06	0.15	0.11	0.10	0.09	0.08
CaO	0.05	0.02	0.02	0.09	0.12	0.07	0.07	0.04	0.12
Na ₂ O	0.05	0.02	0.03	0.00	0.00	0.02	0.00	0.01	0.03
F	0.17	0.11	0.24	0.11	0.15	0.14	0.12	0.14	0.11
Total	87.55	87.21	87.98	86.46	86.33	87.24	87.19	86.99	86.83

Numbers of ions on the basis of 14 oxygens

Si	2.560	2.510	2.579	2.581	2.667	2.584	2.595	2.560	2.584
Al IV	1.440	1.490	1.421	1.419	1.333	1.416	1.405	1.440	1.416
ΣT	4.000	4.000	4.000	4.000	4.000	4.000	4.000	4.000	4.000
Al VI	1.165	1.108	1.182	1.110	1.273	1.153	1.166	1.116	1.130
Ti	0.010	0.011	0.003	0.012	0.000	0.008	0.002	0.000	0.011
Fe	2.037	2.084	2.043	2.044	2.008	2.017	2.010	2.016	2.032
Mg	1.791	1.832	1.761	1.843	1.632	1.854	1.860	1.944	1.849
Mn	0.090	0.098	0.095	0.098	0.090	0.067	0.061	0.068	0.071
ΣR	5.093	5.132	5.085	5.107	5.003	5.098	5.099	5.144	5.095
Ca	0.005	0.002	0.002	0.010	0.013	0.008	0.007	0.004	0.013
Na	0.009	0.003	0.007	0.000	0.000	0.004	0.000	0.001	0.006
K	0.015	0.005	0.009	0.008	0.019	0.015	0.012	0.011	0.010
ΣA	0.029	0.010	0.018	0.018	0.032	0.026	0.019	0.016	0.029
F	0.000	0.000	0.000	0.000	0.000	0.000	0.000	0.000	0.000

Table IV.8: Major element analyses of chlorites. The single grain analyses were performed with an electron microprobe.

	BT08-26_C08_1	BT08-26_C08_2	BT08-26_C08_3	BT08-26_C04_3	BT08-26_C04_4	BT08-26_C04_5	BT08-26_C04_7	BT08-31_C08_1	BT08-31_C09_2
SiO ₂	25.82	25.28	25.50	24.87	27.44	26.30	27.19	25.38	24.68
Al ₂ O ₃	21.15	21.26	21.10	20.94	21.36	21.19	20.98	20.96	20.25
TiO ₂	0.27	0.08	0.11	0.16	0.26	0.18	0.17	0.36	0.21
FeO	27.46	27.14	27.08	27.54	26.30	26.26	26.17	28.63	28.42
MgO	11.93	12.34	12.36	12.02	11.31	12.18	11.37	11.13	12.33
MnO	0.70	0.67	0.67	0.72	0.61	0.63	0.61	0.67	0.96
K ₂ O	0.11	0.06	0.08	0.08	0.39	0.33	0.28	0.13	0.02
CaO	0.10	0.11	0.07	0.07	0.16	0.11	0.15	0.05	0.06
Na ₂ O	0.04	0.03	0.01	0.06	0.01	0.03	0.06	0.07	0.00
F	0.27	0.10	0.10	0.27	0.17	0.18	0.22	0.00	0.00
Total	87.85	87.07	87.08	86.71	88.01	87.39	87.20	87.39	86.92
<i>Numbers of ions on the basis of 14 oxygens</i>									
Si	2.600	2.563	2.583	2.545	2.733	2.648	2.736	2.573	2.525
Al IV	1.400	1.437	1.417	1.455	1.267	1.352	1.264	1.427	1.475
Σ T	4.000	4.000	4.000	4.000	4.000	4.000	4.000	4.000	4.000
Al VI	1.110	1.104	1.103	1.071	1.241	1.163	1.224	1.079	0.967
Ti	0.020	0.006	0.009	0.012	0.019	0.013	0.013	0.027	0.016
Fe	2.082	2.072	2.066	2.122	1.973	1.991	1.983	2.186	2.189
Mg	1.790	1.865	1.866	1.833	1.679	1.828	1.705	1.682	1.880
Mn	0.060	0.058	0.058	0.062	0.052	0.054	0.052	0.058	0.083
Σ R	5.062	5.105	5.101	5.101	4.964	5.049	4.976	5.032	5.136
Ca	0.011	0.012	0.008	0.007	0.017	0.012	0.016	0.005	0.006
Na	0.008	0.006	0.002	0.011	0.002	0.006	0.012	0.015	0.000
K	0.014	0.007	0.010	0.011	0.050	0.043	0.036	0.017	0.002
Σ A	0.033	0.025	0.020	0.029	0.069	0.061	0.064	0.037	0.009
F	0.000	0.000	0.000	0.000	0.000	0.000	0.000	0.000	0.000

Table IV.8: Major element analyses of chlorites. The single grain analyses were performed with an electron microprobe.

	BT08-31_C10_2	BT08-31_C10_3	BT08-31_C14_1	BT08-31_C14_2	BT08-31_C14_3	BT08-31_C14_4	BT08-31_C14_5	BT08-31_C13_4	BT08-31_C13_5
SiO ₂	25.53	25.47	25.94	25.62	25.26	24.69	25.97	25.36	25.27
Al ₂ O ₃	20.25	20.33	21.11	20.77	20.80	20.39	21.05	20.44	20.12
TiO ₂	0.00	0.07	0.18	0.23	0.16	2.52	0.00	0.12	0.08
FeO	28.29	27.11	27.59	28.42	28.47	28.00	27.84	27.28	26.87
MgO	12.36	13.17	11.79	12.11	12.12	11.41	11.89	12.88	13.48
MnO	0.94	0.84	0.94	0.98	0.94	0.94	0.94	0.82	0.81
K ₂ O	0.03	0.10	0.03	0.05	0.04	0.03	0.09	0.23	0.05
CaO	0.03	0.04	0.07	0.02	0.01	0.01	0.04	0.04	0.04
Na ₂ O	0.08	0.01	0.04	0.02	0.01	0.00	0.04	0.07	0.01
F	0.00	0.14	0.00	0.16	0.09	0.00	0.06	0.00	0.01
Total	87.50	87.27	87.69	88.38	87.90	87.99	87.91	87.25	86.73
<i>Numbers of ions on the basis of 14 oxygens</i>									
Si	2.587	2.583	2.610	2.574	2.551	2.492	2.611	2.572	2.574
Al IV	1.413	1.417	1.390	1.426	1.449	1.508	1.389	1.428	1.426
Σ T	4.000	4.000	4.000	4.000	4.000	4.000	4.000	4.000	4.000
Al VI	1.006	1.013	1.114	1.033	1.028	0.919	1.106	1.017	0.990
Ti	0.000	0.005	0.014	0.017	0.012	0.191	0.000	0.009	0.006
Fe	2.159	2.070	2.090	2.150	2.165	2.128	2.107	2.084	2.061
Mg	1.867	1.990	1.768	1.813	1.824	1.717	1.781	1.947	2.046
Mn	0.081	0.072	0.080	0.084	0.081	0.080	0.080	0.071	0.070
Σ R	5.112	5.151	5.066	5.097	5.111	5.036	5.075	5.128	5.173
Ca	0.003	0.004	0.007	0.002	0.001	0.001	0.004	0.004	0.004
Na	0.015	0.001	0.009	0.004	0.002	0.000	0.007	0.015	0.001
K	0.004	0.013	0.004	0.006	0.005	0.004	0.011	0.029	0.007
Σ A	0.022	0.018	0.020	0.012	0.008	0.005	0.023	0.048	0.012
F	0.000	0.000	0.000	0.000	0.000	0.000	0.000	0.000	0.000

Table IV.8: Major element analyses of chlorites. The single grain analyses were performed with an electron microprobe.

	BT08-31_C12_1	BT08-31_C01_1	BT08-31_C01_2	BT08-31_C01_3	BT08-31_C01_4	BT08-31_C01_5	BT08-31_C01_6	BT08-31_C01_7	BT08-31_C03_9
SiO ₂	26.08	26.28	26.31	26.92	26.48	26.55	26.62	26.47	26.12
Al ₂ O ₃	21.11	20.85	20.61	20.88	19.93	20.20	19.77	19.80	20.91
TiO ₂	0.14	0.13	0.14	0.03	1.30	0.18	0.03	0.16	0.05
FeO	26.88	25.33	25.96	25.01	25.55	25.77	25.25	25.59	25.23
MgO	12.03	14.27	14.63	13.77	14.57	14.83	14.71	15.04	13.27
MnO	0.88	0.51	0.57	0.49	0.51	0.54	0.49	0.48	0.65
K ₂ O	0.08	0.18	0.10	0.08	0.06	0.07	0.11	0.08	0.13
CaO	0.08	0.04	0.03	0.06	0.03	0.04	0.10	0.11	0.05
Na ₂ O	0.07	0.04	0.01	0.02	0.05	0.02	0.04	0.02	0.04
F	0.00	0.14	0.12	0.07	0.00	0.01	0.18	0.00	0.05
Total	87.34	87.78	88.47	87.34	88.49	88.21	87.31	87.75	86.50
<i>Numbers of ions on the basis of 14 oxygens</i>									
Si	2.628	2.625	2.613	2.689	2.624	2.639	2.675	2.645	2.644
Al IV	1.372	1.375	1.387	1.311	1.376	1.361	1.325	1.355	1.356
Σ T	4.000	4.000	4.000	4.000	4.000	4.000	4.000	4.000	4.000
Al VI	1.136	1.081	1.025	1.149	0.952	1.006	1.017	0.977	1.140
Ti	0.011	0.010	0.010	0.002	0.097	0.014	0.003	0.012	0.004
Fe	2.040	1.905	1.941	1.881	1.906	1.929	1.911	1.925	1.923
Mg	1.807	2.125	2.165	2.050	2.152	2.197	2.203	2.240	2.002
Mn	0.075	0.043	0.048	0.042	0.043	0.045	0.042	0.041	0.056
Σ R	5.068	5.164	5.190	5.124	5.150	5.190	5.174	5.195	5.124
Ca	0.008	0.005	0.003	0.006	0.003	0.004	0.011	0.011	0.005
Na	0.013	0.008	0.002	0.004	0.010	0.004	0.008	0.005	0.009
K	0.010	0.023	0.012	0.010	0.008	0.009	0.014	0.010	0.017
Σ A	0.031	0.036	0.017	0.021	0.021	0.017	0.033	0.026	0.031
F	0.000	0.000	0.000	0.000	0.000	0.000	0.000	0.000	0.000

Table IV.8: Major element analyses of chlorites. The single grain analyses were performed with an electron microprobe.

	BT08-31_C05_1	BT08-31_C05_2	BT08-31_C05_3	BT08-31_C05_4	BT08-31_C05_5	BT08-31_C05_6	BT08-31_C05_7	BT08-80-C01-1	BT08-80-C02-1
SiO ₂	26.71	26.17	26.28	29.67	26.32	26.41	25.55	25.22	25.52
Al ₂ O ₃	21.05	21.97	21.34	20.28	21.19	21.53	21.27	20.41	19.97
TiO ₂	0.23	0.16	0.03	0.05	0.08	0.16	0.04	0.08	0.22
FeO	25.49	25.80	25.66	24.95	25.97	25.36	25.67	31.52	30.61
MgO	12.81	13.02	13.15	12.52	13.19	13.01	13.11	9.44	9.33
MnO	0.68	0.70	0.66	0.72	0.69	0.68	0.74	0.96	0.90
K ₂ O	0.06	0.02	0.11	0.02	0.16	0.06	0.01	0.07	0.21
CaO	0.08	0.04	0.06	0.03	0.06	0.04	0.05	0.06	0.08
Na ₂ O	0.08	0.01	0.00	0.04	0.03	0.02	0.05	0.00	0.06
F	0.02	0.00	0.05	0.00	0.00	0.04	0.08	0.00	0.00
Total	87.20	87.90	87.33	88.27	87.68	87.32	86.57	87.76	86.89
<i>Numbers of ions on the basis of 14 oxygens</i>									
Si	2.678	2.605	2.635	2.909	2.632	2.644	2.591	2.573	2.623
Al IV	1.322	1.395	1.365	1.091	1.368	1.356	1.409	1.427	1.377
Σ T	4.000	4.000	4.000	4.000	4.000	4.000	4.000	4.000	4.000
Al VI	1.166	1.183	1.158	1.253	1.131	1.184	1.134	1.027	1.043
Ti	0.017	0.012	0.002	0.004	0.006	0.012	0.003	0.006	0.017
Fe	1.924	1.934	1.938	1.842	1.956	1.912	1.960	2.421	2.369
Mg	1.914	1.932	1.965	1.829	1.966	1.941	1.982	1.435	1.429
Mn	0.057	0.059	0.056	0.060	0.058	0.058	0.063	0.083	0.078
Σ R	5.079	5.120	5.119	4.987	5.116	5.107	5.143	4.973	4.937
Ca	0.008	0.004	0.007	0.003	0.006	0.004	0.006	0.006	0.008
Na	0.015	0.002	0.000	0.007	0.006	0.004	0.010	0.000	0.011
K	0.008	0.003	0.014	0.002	0.020	0.008	0.002	0.009	0.027
Σ A	0.031	0.009	0.021	0.012	0.032	0.017	0.018	0.015	0.047
F	0.000	0.000	0.000	0.000	0.000	0.000	0.000	0.000	0.000

Table IV.8: Major element analyses of chlorites. The single grain analyses were performed with an electron microprobe.

	BT08-80-C07-2	BT08-80-C07-3	BT08-80-C08-2	BT08-80-C08-6	BT08-80-C09-1	BT08-80-C09-4	BT08-15_C03_1	BT08-15_C03_2	BT08-15_C03_3
SiO ₂	24.78	25.08	25.01	24.98	25.28	24.11	25.34	25.58	25.74
Al ₂ O ₃	20.66	20.28	20.72	20.66	20.44	21.11	19.57	20.28	20.15
TiO ₂	0.22	0.25	0.18	0.18	0.13	0.13	0.00	0.05	0.12
FeO	32.16	31.73	31.97	31.04	31.66	32.27	30.96	30.73	30.25
MgO	9.31	9.42	9.70	9.51	9.32	8.91	11.48	11.28	11.55
MnO	1.03	0.88	0.88	0.85	1.00	1.14	0.68	0.64	0.56
K ₂ O	0.06	0.44	0.10	0.17	0.14	0.01	0.01	0.02	0.04
CaO	0.06	0.07	0.03	0.03	0.06	0.05	0.09	0.07	0.09
Na ₂ O	0.00	0.03	0.02	0.03	0.03	0.04	0.01	0.05	0.00
F	0.00	0.04	0.03	0.00	0.03	0.00	0.00	0.00	0.00
Total	88.29	88.22	88.64	87.45	88.11	87.77	88.15	88.70	88.51

Numbers of ions on the basis of 14 oxygens

Si	2.521	2.555	2.531	2.555	2.572	2.472	2.569	2.571	2.587
Al IV	1.479	1.445	1.469	1.445	1.428	1.528	1.431	1.429	1.413
ΣT	4.000	4.000	4.000	4.000	4.000	4.000	4.000	4.000	4.000
Al VI	0.999	0.991	1.002	1.046	1.024	1.024	0.909	0.974	0.975
Ti	0.017	0.019	0.014	0.014	0.010	0.010	0.000	0.004	0.009
Fe	2.464	2.434	2.436	2.390	2.426	2.492	2.364	2.326	2.290
Mg	1.412	1.430	1.463	1.449	1.413	1.362	1.735	1.690	1.730
Mn	0.089	0.076	0.075	0.073	0.086	0.099	0.059	0.055	0.048
ΣR	4.980	4.951	4.990	4.973	4.959	4.986	5.066	5.047	5.052
Ca	0.007	0.007	0.004	0.004	0.007	0.006	0.010	0.008	0.009
Na	0.000	0.007	0.003	0.006	0.007	0.007	0.003	0.010	0.000
K	0.008	0.057	0.014	0.022	0.019	0.002	0.001	0.002	0.006
ΣA	0.015	0.071	0.021	0.032	0.032	0.015	0.014	0.020	0.015
F	0.000	0.000	0.000	0.000	0.000	0.000	0.000	0.000	0.000

Table IV.8: Major element analyses of chlorites. The single grain analyses were performed with an electron microprobe.

	BT08-15_C02_2	BT08-15_C02_3	BT08-15_C01_1	BT08-15_C01_2	BT08-15_C01_3	BT08-15_C01_4	BT08-15_C01_5	BT08-15_C01_6	BT10-33-C01-1
SiO ₂	24.69	25.89	24.56	24.80	25.26	24.70	25.05	24.67	26.29
Al ₂ O ₃	21.44	20.91	21.80	21.62	21.57	21.78	21.65	21.34	20.75
TiO ₂	0.11	0.02	0.15	0.11	0.05	0.02	0.06	0.07	0.04
FeO	29.51	29.14	30.00	29.82	29.54	29.68	29.48	29.21	24.00
MgO	11.74	11.21	10.89	10.96	11.22	11.40	11.30	11.07	14.07
MnO	0.53	0.54	0.74	0.72	0.71	0.77	0.74	0.70	0.56
K ₂ O	0.03	0.18	0.02	0.00	0.02	0.00	0.01	0.00	0.02
CaO	0.11	0.07	0.01	0.03	0.07	0.05	0.01	0.08	0.23
Na ₂ O	0.04	0.05	0.01	0.04	0.00	0.06	0.03	0.04	0.06
F	0.00	0.04	0.00	0.00	0.00	0.00	0.00	0.00	0.00
Total	88.21	88.05	88.17	88.10	88.44	88.47	88.33	87.18	86.02
<i>Numbers of ions on the basis of 14 oxygens</i>									
Si	2.488	2.606	2.480	2.503	2.535	2.484	2.518	2.514	2.663
Al IV	1.512	1.394	1.520	1.497	1.465	1.516	1.482	1.486	1.337
Σ T	4.000	4.000	4.000	4.000	4.000	4.000	4.000	4.000	4.000
Al VI	1.036	1.087	1.074	1.076	1.087	1.066	1.083	1.077	1.141
Ti	0.008	0.002	0.011	0.008	0.004	0.002	0.005	0.006	0.003
Fe	2.239	2.208	2.281	2.267	2.232	2.247	2.231	2.241	1.831
Mg	1.763	1.681	1.639	1.649	1.678	1.708	1.693	1.681	2.124
Mn	0.045	0.046	0.063	0.062	0.061	0.065	0.063	0.060	0.048
Σ R	5.092	5.024	5.068	5.061	5.061	5.088	5.075	5.066	5.147
Ca	0.012	0.007	0.001	0.003	0.008	0.006	0.001	0.008	0.025
Na	0.009	0.010	0.002	0.008	0.000	0.012	0.006	0.007	0.012
K	0.004	0.024	0.002	0.000	0.003	0.000	0.002	0.000	0.003
Σ A	0.025	0.041	0.005	0.012	0.010	0.018	0.008	0.016	0.039
F	0.000	0.000	0.000	0.000	0.000	0.000	0.000	0.000	0.000

Table IV.8: Major element analyses of chlorites. The single grain analyses were performed with an electron microprobe.

	BT10-33-C01-2	BT10-33-C01-3	BT10-33-C01-4	BT10-33-C01-5	BT10-33-C01-6	BT10-33-C02-1	BT10-33-C02-2	BT10-33-C02-4	BT10-33-C03-1	BT10-33-C03-3
SiO ₂	25.43	26.94	25.54	25.66	25.15	27.85	27.35	27.53	28.40	27.53
Al ₂ O ₃	20.79	21.87	21.31	21.12	20.86	19.79	19.62	19.53	19.82	19.82
TiO ₂	0.25	0.09	0.01	0.12	0.05	0.00	0.00	0.01	0.00	0.00
FeO	26.13	24.53	25.79	26.01	24.98	21.57	21.41	19.84	18.56	21.79
MgO	14.55	13.21	14.96	14.85	15.40	17.52	17.63	19.05	20.63	17.64
MnO	0.50	0.59	0.49	0.51	0.52	0.48	0.50	0.38	0.33	0.51
K ₂ O	0.02	0.03	0.02	0.02	0.00	0.00	0.02	0.02	0.00	0.02
CaO	0.11	0.19	0.09	0.06	0.07	0.18	0.12	0.12	0.06	0.19
Na ₂ O	0.02	0.08	0.03	0.02	0.03	0.06	0.01	0.06	0.00	0.01
F	0.00	0.00	0.00	0.00	0.10	0.08	0.07	0.06	0.29	0.09
Total	87.80	87.54	88.24	88.36	87.15	87.54	86.72	86.60	88.10	87.59

Numbers of ions on the basis of 14 oxygens

Si	2.547	2.677	2.540	2.550	2.534	2.749	2.727	2.735	2.763	2.721
AlIV	1.453	1.323	1.460	1.450	1.466	1.251	1.273	1.265	1.237	1.279
ΣT	4.000	4.000	4.000	4.000	4.000	4.000	4.000	4.000	4.000	4.000
AlVI	1.002	1.239	1.039	1.024	1.011	1.052	1.033	1.022	1.036	1.030
Ti	0.019	0.007	0.001	0.009	0.003	0.000	0.000	0.001	0.000	0.000
Fe	1.971	1.835	1.932	1.946	1.895	1.603	1.607	1.484	1.360	1.622
Mg	2.172	1.956	2.218	2.199	2.312	2.577	2.620	2.820	2.991	2.598
Mn	0.043	0.050	0.042	0.043	0.044	0.040	0.042	0.032	0.028	0.042
ΣR	5.206	5.087	5.230	5.222	5.266	5.273	5.302	5.359	5.414	5.292
Ca	0.012	0.021	0.009	0.006	0.007	0.019	0.013	0.013	0.006	0.020
Na	0.003	0.016	0.006	0.003	0.006	0.012	0.001	0.011	0.000	0.002
K	0.002	0.004	0.003	0.002	0.000	0.001	0.002	0.003	0.000	0.002
ΣA	0.018	0.040	0.018	0.012	0.014	0.031	0.016	0.026	0.007	0.023
F	0.000	0.000	0.000	0.000	0.000	0.000	0.000	0.000	0.000	0.000

Table IV.8: Major element analyses of chlorites. The single grain analyses were performed with an electron microprobe.

	BT10-33-C03-4	BT10-33-C03-5	BT10-33-C07-1	BT10-33-C07-2	BT10-33-C07-3	BT10-33-C06-1	BT10-33-C06-2	BT10-33-C06-3	BT10-33-C08-2	BT10-33-C09-2
SiO ₂	27.45	26.68	26.57	28.29	26.08	30.83	25.29	26.11	27.61	25.75
Al ₂ O ₃	19.74	21.71	20.25	19.57	20.08	20.43	20.08	20.63	20.10	21.85
TiO ₂	0.00	0.03	0.01	0.00	0.00	0.03	0.07	0.00	0.00	0.00
FeO	20.53	24.32	24.64	21.14	25.08	21.72	27.14	25.65	20.56	23.95
MgO	19.47	14.71	15.03	18.06	14.74	13.75	14.23	14.78	18.04	15.65
MnO	0.37	0.60	0.60	0.44	0.61	0.41	0.56	0.47	0.49	0.56
K ₂ O	0.00	0.00	0.02	0.03	0.02	0.03	0.00	0.00	0.01	0.02
CaO	0.09	0.24	0.18	0.18	0.15	0.29	0.13	0.13	0.21	0.16
Na ₂ O	0.00	0.04	0.03	0.05	0.02	1.32	0.05	0.02	0.00	0.00
F	0.18	0.01	0.00	0.13	0.00	0.01	0.00	0.00	0.19	0.08
Total	87.83	88.34	87.33	87.89	86.78	88.82	87.55	87.78	87.22	88.02

Numbers of ions on the basis of 14 oxygens

Si	2.698	2.631	2.658	2.777	2.633	2.980	2.552	2.606	2.731	2.554
AlIV	1.302	1.369	1.342	1.223	1.367	1.020	1.448	1.394	1.269	1.446
ΣT	4.000	4.000	4.000	4.000	4.000	4.000	4.000	4.000	4.000	4.000
AlVI	0.986	1.154	1.047	1.042	1.023	1.309	0.941	1.034	1.075	1.108
Ti	0.000	0.002	0.001	0.000	0.000	0.002	0.006	0.000	0.000	0.000
Fe	1.520	1.806	1.856	1.563	1.907	1.581	2.062	1.928	1.532	1.788
Mg	2.852	2.161	2.241	2.642	2.218	1.981	2.140	2.199	2.660	2.313
Mn	0.031	0.050	0.051	0.037	0.052	0.033	0.048	0.039	0.041	0.047
ΣR	5.389	5.173	5.195	5.284	5.199	4.907	5.197	5.200	5.307	5.257
Ca	0.009	0.026	0.019	0.018	0.016	0.030	0.014	0.014	0.022	0.017
Na	0.000	0.008	0.007	0.010	0.005	0.248	0.010	0.003	0.001	0.000
K	0.000	0.000	0.003	0.004	0.003	0.004	0.000	0.000	0.001	0.002
ΣA	0.009	0.033	0.028	0.032	0.024	0.282	0.024	0.017	0.025	0.019
F	0.000	0.000	0.000	0.000	0.000	0.000	0.000	0.000	0.000	0.000

Table IV.9: Chlorite geothermometry based on Vidal et al. (2005).

	SiO ₂ (wt %)	TiO ₂ (wt %)	Al ₂ O ₃ (wt %)	FeO (wt %)	Fe ₂ O ₃ (wt %)	MnO (wt %)	MgO (wt %)	CaO (wt %)	NaO (wt %)	K ₂ O (wt %)	X Fe ³⁺	Temperature (°C)
BT09-80-C08-5	25.02	0.40	21.28	29.52	0.00	0.53	11.70	0.01	0.02	0.02	1	486
BT08-15-C01_3	25.26	0.05	21.57	29.54	0.00	0.71	11.22	0.07	0.00	0.02	9	346
BT08-15-C01_5	25.05	0.06	21.65	29.48	0.00	0.74	11.30	0.01	0.03	0.01	3	421
BT08-15-C01_6	24.67	0.07	21.34	29.21	0.00	0.70	11.07	0.08	0.04	0.00	5	396
BT08-15-C03_2	25.58	0.05	20.28	30.73	0.00	0.64	11.28	0.07	0.05	0.02	20	300
BT08-31-C05_2	26.17	0.16	21.97	25.80	0.00	0.70	13.02	0.04	0.01	0.02	20	272
BT08-31-C10_2	25.53	0.00	20.25	28.29	0.00	0.94	12.36	0.03	0.08	0.03	22	300
BT08-31-C14_1	25.94	0.18	21.11	27.59	0.00	0.94	11.79	0.07	0.04	0.03	23	262
BT08-31-C14_4	24.69	2.52	20.39	28.00	0.00	0.94	11.41	0.01	0.00	0.03	28	249
BT08-63-C02-2	25.22	0.10	20.93	26.88	0.00	0.90	13.29	0.06	0.02	0.00	5	457
BT08-63-C02-3	25.93	0.14	20.70	26.83	0.00	0.85	13.32	0.05	0.02	0.03	23	292
BT08-63-C03-2	25.75	0.00	20.81	26.90	0.00	0.85	13.31	0.07	0.00	0.01	19	314
BT08-63-C03-3	26.08	0.05	20.81	26.77	0.00	0.84	13.42	0.06	0.00	0.01	23	290
BT08-63-C03-4	25.48	0.03	20.74	26.77	0.00	0.87	13.42	0.04	0.01	0.02	2	516
BT08-63-C07-2	25.25	0.07	21.00	27.32	0.00	0.89	13.02	0.04	0.04	0.00	5	451
BT08-63-C07-3	25.43	0.04	20.85	27.49	0.00	0.99	13.21	0.04	0.03	0.01	5	475
BT08-63-C08-5	25.22	0.06	21.33	26.73	0.00	0.86	12.43	0.08	0.02	0.03	13	326
BT10-33-C02-1	27.85	0.00	19.79	21.57	0.00	0.48	17.52	0.18	0.06	0.00	49	248
BT10-33-C02-2	27.35	0.00	19.62	21.41	0.00	0.50	17.63	0.12	0.01	0.02	46	262
BT10-33-C02-3	25.97	0.00	19.60	22.55	0.00	0.52	16.75	0.20	0.03	0.02	31	320
BT10-33-C03-2	27.00	0.00	19.58	21.53	0.00	0.51	16.17	0.19	0.05	0.01	46	238
BT10-33-C03-3	27.53	0.00	19.82	21.79	0.00	0.51	17.64	0.19	0.01	0.02	45	264
BT10-33-C03-4	27.45	0.00	19.74	20.53	0.00	0.37	19.47	0.09	0.00	0.00	45	295
BT10-33-C03-5	26.68	0.03	21.71	24.32	0.00	0.60	14.71	0.24	0.04	0.00	24	282
BT10-33-C06-3	26.11	0.00	20.63	25.65	0.00	0.47	14.78	0.13	0.02	0.00	23	313
BT10-33-C07-1	26.57	0.01	20.25	24.64	0.00	0.60	15.03	0.18	0.03	0.02	32	275
BT10-33-C07-3	26.08	0.00	20.08	25.08	0.00	0.61	14.74	0.15	0.02	0.02	28	293
BT10-33-C08-1	25.90	0.07	18.60	20.88	0.00	0.47	17.04	0.40	0.04	0.01	44	284
BT10-33-C08-2	27.61	0.00	20.10	20.56	0.00	0.49	18.04	0.21	0.00	0.01	47	256

APPENDIX
CHAPTER V

Table V.1: Oxygen isotope composition of Qz, Ms, Bt, Chl and Ep of samples from the BSZ.

Samples	Z (m)	Rocks	$\delta^{18}\text{O}_{\text{Qz}}$ (‰)	$\delta^{18}\text{O}_{\text{Ms}}$ (‰)	$\delta^{18}\text{O}_{\text{Bt}}$ (‰)	$\delta^{18}\text{O}_{\text{Chl}}$ (‰)	$\delta^{18}\text{O}_{\text{Ep}}$ (‰)	+/-
BT08-23	0	Breccia	2.4	-	-	-	-	-
BT10-01	-10	V2 Qz vein	-	8.4	-	-10.5	-10.8	0.2
BT10-02	-10	V2 Qz vein	-6.9	-	-	-	-12.6	0.1
BT10-09	-10	V1 Qz vein	10.5	-	-	-	-	-
BT10-12	-10	V2 Qz vein	-5.5	-	-	-10.4	-12.4	0.2
BT10-13	-10	V2 Qz vein	-6.8	-1.9	-	-9.6	-12.3	0.4
BT10-14	-10	V1 Qz vein	8.7	0.7	-	-	-	-
BT10-15	-10	V2 Qz vein	-6.6	6.8	-	-9.6	-7.6	0.1
BT10-19	-10	V2 Qz vein	-5.9	-1.7	-	-10.8	-12.4	0.0
BT10-30	-10	V1 Qz vein	9.5	-	-	-	-	-
BT10-31	-10	V2 Qz vein	-6.6	-	-	-	-14.1	0.2
BT08-21	-30	Mylonite	8.5	0.1	-	-	-	-
BT08-15	-40	Mylonite	10.6	8.1	1.3	-0.7	-	-
BT08-11	-50	Mylonite	9.0	7.6	-5.4	-8.8	-	-
BT08-45	-60	Mylonite	10.2	8.5	-	-	-	-
BT10-42	-60	V1 Qz vein	10.7	8.0	-	-	-	-
BT08-80	-120	Mylonite	10.5	8.1	2.4	2.4	-	-
BT08-37	-170	Mylonite	9.7	7.2	-	-	-	-
BT08-78	-178	Mylonite	10.9	8.0	-	-	-	-
BT08-30	-240	Mylonite	8.7	5.0	-	-	-	-
BT08-26	-265	Mylonite	10.9	8.4	4.2	4.7	-	-
BT08-75	-275	Mylonite	10.2	7.1	-	-	-	-
BT08-70	-315	Mylonite	10.3	7.0	-	-	-	-
BT08-71	-320	Mylonite	9.6	6.8	-	-	-	-
BT08-65	-370	Mylonite	9.6	6.2	0.4	-1.0	-	-
BT08-63	-380	Mylonite	10.0	6.0	-	-	-	-
BT10-51	-460	V1 Qz vein	9.9	-	-	-	-	-
BT10-52	-560	Protomylonite	9.6	7.2	4.7	4.5	-	-
BT10-49	-710	Granodiorite	9.8	7.7	4.5	4.1	-	-
BT08-02	-860	Granodiorite	9.3	7.4	-	-	-	-
BT09-80	-1060	Granodiorite	10.1	7.6	5.4	4.8	-	-

Table V.2: Hydrogen isotope composition of Ms, Bt, Chl, Ep and hydrogen, carbon and oxygen isotope composition of fluid inclusion in Qz.

Samples	Z (m)	Rocks	δD_{Ms} (‰)	+/-	δD_{Bt} (‰)	+/-	δD_{Chl} (‰)	+/-	δD_{Ep} (‰)	+/-	δD_{FI} (‰)	+/-	$\delta^{13}C$ (‰)	+/-	$\delta^{18}O_{CO2}$ (‰)	+/-
BT08-23	0	Breccia	-146	-	-	-	-	-	-	-	-	-	-	-	-	-
BT10-01	-10	V2 Qz vein	-133	-	-	-153	1	-127	13	-	-	-	-	-	-	-
BT10-02	-10	V2 Qz vein	-	-	-	-	-	-130	2	-98	3	-	-	-	-	-
BT10-09	-10	V1 Qz vein	-	-	-	-	-	-	-	-118	1	-11.7	0.1	14.1	0.2	0.2
BT10-12	-10	V2 Qz vein	-	-	-	-147	1	-120	1	-130	1	-	-	-	-	-
BT10-13	-10	V2 Qz vein	-143	0	-	-147	2	-139	2	-132	1	-	-	-	-	-
BT10-14	-10	V1 Qz vein	-	-	-	-	-	-	-	-123	1	-12.2	0.2	10.9	0.2	0.2
BT10-15	-10	V2 Qz vein	-142	5	-	-144	3	-127	1	-109	1	-	-	-	-	-
BT10-19	-10	V2 Qz vein	-139	1	-	-149	0	-139	5	-131	1	-	-	-	-	-
BT10-30	-10	V1 Qz vein	-	-	-	-	-	-136	3	-103	1	-	-	-	-	-
BT10-31	-10	V2 Qz vein	-	-	-	-	-	-	-	-108	3	-	-	-	-	-
BT08-21	-30	Mylonite	-	-	-	-	-	-	-	-73	3	-24.7	0.3	22.3	0.5	0.5
BT08-15	-40	Mylonite	-150	1	-153	1	-150	0	-	-93	3	-	-	-	-	-
BT08-11	-50	Mylonite	-150	1	-153	4	-152	0	-	-87	3	-	-	-	-	-
BT08-45	-60	Mylonite	-127	2	-136	3	-126	1	-	-53	3	-22.4	0.2	22.3	0.1	0.1
BT10-42	-60	V1 Qz vein	-132	1	-	-	-	-	-	-	-	-	-	-	-	-
BT08-80	-120	Mylonite	-127	12	-156	1	-139	9	-	-77	3	-	-	-	-	-
BT08-37	-170	Mylonite	-141	2	-143	0	-139	3	-	-	-	-	-	-	-	-
BT08-78	-178	Mylonite	-140	0	-	-	-	-	-	-	-	-	-	-	-	-
BT08-30	-240	Mylonite	-	-	-	-	-	-	-	-	-	-	-	-	-	-
BT08-26	-265	Mylonite	-142	1	-156	0	-141	2	-	-70	3	-20.6	0.2	22.0	0.2	0.2
BT08-75	-275	Mylonite	-144	0	-	-	-	-	-	-63	3	-22.9	0.3	20.7	0.1	0.1
BT08-70	-315	Mylonite	-144	3	-	-	-	-	-	-	-	-	-	-	-	-
BT08-71	-320	Mylonite	-144	3	-	-	-	-	-	-	-	-	-	-	-	-
BT08-65	-370	Mylonite	-139	0	-145	0	-149	0	-	-75	3	-	-	-	-	-
BT08-63	-380	Mylonite	-143	1	-155	8	-	-	-	-65	3	-	-	-	-	-
BT10-51	-460	V1 Qz vein	-	-	-	-	-	-	-	-	-	-	-	-	-	-
BT10-52	-560	Protomylonite	-65	3	-86	1	-75	0	-	-	-	-	-	-	-	-
BT10-49	-710	Granodiorite	-63	0	-93	1	-72	0	-	-	-	-	-	-	-	-
BT08-02	-860	Granodiorite	-61	0	-82	0	-71	1	-	-	-	-	-	-	-	-
BT09-80	-1060	Granodiorite	-69	3	-87	0	-79	0	-	-69	3	-22.5	0.3	20.7	0.2	0.2

Table V.3: Water content of Ms, Bt, Chl and fluid inclusion in quartz.

Samples	Z (m)	Rocks	Ms H₂O (wt%)	Bt H₂O (wt%)	Chl H₂O (wt%)	Epd H₂O (wt%)	Qz H₂O (mg / g)
BT08-23	0	Breccia	4.7	-	-	-	-
BT10-01	-10	V2 Qz vein	3.7	-	9.7	1.0	-
BT10-02	-10	V2 Qz vein	-	-	-	0.2	0.1
BT10-09	-10	V1 Qz vein	-	-	-	-	0.5
BT10-12	-10	V2 Qz vein	-	-	9.8	2.2	0.4
BT10-13	-10	V2 Qz vein	4.1	-	9.1	0.3	0.4
BT10-14	-10	V1 Qz vein	-	-	-	-	0.4
BT10-15	-10	V2 Qz vein	4.0	-	9.4	1.3	0.2
BT10-19	-10	V2 Qz vein	4.2	-	10.2	0.3	0.6
BT10-30	-10	V1 Qz vein	-	-	-	-	0.1
BT10-31	-10	V2 Qz vein	-	-	-	0.2	0.5
BT08-21	-30	Mylonite	-	-	-	-	0.3
BT08-15	-40	Mylonite	4.3	4.1	6.5	-	0.4
BT08-11	-50	Mylonite	4.1	5.4	7.9	-	0.3
BT08-45	-60	Mylonite	4.0	2.3	9.3	-	0.2
BT10-42	-60	V1 Qz vein	3.9	-	-	-	-
BT08-80	-120	Mylonite	4.7	3.1	8.3	-	0.2
BT08-37	-170	Mylonite	4.2	3.7	7.9	-	-
BT08-78	-178	Mylonite	4.0	-	-	-	-
BT08-30	-240	Mylonite	-	-	-	-	-
BT08-26	-265	Mylonite	4.0	3.9	5.6	-	0.2
BT08-75	-275	Mylonite	4.2	-	-	-	0.2
BT08-70	-315	Mylonite	4.0	-	-	-	-
BT08-71	-320	Mylonite	4.0	-	-	-	-
BT08-65	-370	Mylonite	3.9	4.5	6.9	-	0.3
BT08-63	-380	Mylonite	4.0	4.5	-	-	0.2
BT10-51	-460	V1 Qz vein	-	-	-	-	-
BT10-52	-560	Protomylonite	3.8	3.3	8.0	-	-
BT10-49	-710	Granodiorite	3.3	3.5	8.4	-	-
BT08-02	-860	Granodiorite	3.7	3.6	8.2	-	-
BT09-80	-1060	Granodiorite	4.3	3.6	8.8	-	0.2

Table V.4: Isotopic fractionation between minerals and fluid at a given temperature. Isotopic temperature were calculated with the Qz-Ms pairs, or Qz-Ep pairs when temperature are followed by " * ".

Sample	Z (m)	Rocks	T (°C)	δD _{wt} (‰)				δ ¹⁸ O _{wt} (‰)							
				Ms-wt	Bt-wt	Chl-wt	Ep-d-wt	Qz-wt	Ms-wt	GMWL (Ms)	Bt-wt	GMWL (Bt)	Chl-wt	GMWL (Chl)	Ep-d-wt
BT10-02	-10	V2 Qz vein	273*	-	-	-94	-94	-14.9	-	-	-	-	-13	-14.2	-13
BT10-12	-10	V2 Qz vein	205*	-	-	-	-	-16.8	-	-	-	-12.5	-	-16.1	-
BT10-13	-10	V2 Qz vein	287*	-83	-	-103	-103	-14.3	-3.6	-12	-	-9.9	-14	-13.6	-14
BT10-15	-10	V2 Qz vein	1167*	-	-	-101	-101	-7.1	7.8	-	-	-5.6	-14	-6.5	-14
BT10-19	-10	V2 Qz vein	226*	-91	-	-100	-100	-16.0	-5.1	-13	-	-12.4	-14	-15.3	-14
BT10-31	-10	V2 Qz vein	176*	-	-	-	-	-19.9	-	-	-	-	-	-19.1	-
BT08-15	-40	Mylonite	476	-129	-112	-119	-119	7.3	8.7	-17	3.7	1.2	-16	-	-
BT08-11	-50	Mylonite	725	-147	-129	-124	-124	7.6	8.9	-20	-3.0	-5.6	-17	-	-
BT08-45	-60	Mylonite	636	-119	-107	-98	-98	8.3	9.6	-16	-	-	-13	-	-
BT10-42	-60	V1 Qz vein	446	-108	-	-	-	6.9	8.4	-15	-	-	-	-	-
BT08-80	-120	Mylonite	485	-107	-116	-108	-108	7.3	8.7	-15	4.8	4.4	-15	-	-
BT08-37	-170	Mylonite	480	-121	-103	-109	-109	6.5	7.9	-16	-	-	-15	-	-
BT08-78	-178	Mylonite	423	-114	-	-	-	6.8	8.2	-15	-	-	-	-	-
BT08-30	-240	Mylonite	353	-	-	-	-	3.2	4.5	-	-	-	-	-	-
BT08-26	-265	Mylonite	472	-121	-115	-110	-110	7.5	9.0	-16	6.5	6.6	-15	-	-
BT08-75	-275	Mylonite	391	-113	-	-	-	5.6	7.0	-15	-	-	-	-	-
BT08-70	-315	Mylonite	376	-111	53	33	33	5.3	6.8	-15	-	5	3	-	-
BT08-71	-320	Mylonite	426	-118	-	-	-	5.6	7.0	-16	-	-	-	-	-
BT08-65	-370	Mylonite	369	-105	-90	-116	-116	4.4	5.8	-14	2.3	-0.1	-16	-	-
BT08-63	-380	Mylonite	320	-99	-92	-	-	3.6	4.9	-14	-	-	-	-	-
BT10-52	-560	Protomylonite	500	-47	-48	-45	-45	6.6	8.0	-7	7.1	6.6	-7	-	-
BT10-49	-710	Granodiorite	540	-49	-58	-43	-43	7.2	8.6	-7	7.0	6.4	-7	-	-
BT08-02	-860	Granodiorite	580	-49	-50	-42	-42	7.0	8.4	-7	-	-	-7	-	-
BT09-80	-1060	Granodiorite	469	-48	-46	-49	-49	6.7	8.1	-7	7.7	6.7	-7	-	-

APPENDIX
CHAPTER VI

Table VI.1: Major element analyses of muscovites. The single grain analyses were performed with an electron microprobe.

Analysis No.	1	2	4	6	7	4	5	6	7
	KE08-32-M02_1	KE08-32-M02_1	KE08-32-M02_1	KE08-32-M02_1	KE08-32-M02_1	KE08-32-M02_1	KE08-32-M02_2	KE08-32-M02_2	KE08-32-M02_2
SiO ₂	47.98	47.95	47.61	46.21	46.40	46.27	47.04	47.77	47.60
Al ₂ O ₃	34.86	35.07	35.45	34.88	35.29	34.20	35.34	35.82	35.77
TiO ₂	1.52	1.38	1.29	1.03	1.51	1.40	1.43	1.32	1.44
FeO	0.27	0.34	0.31	0.35	0.29	0.28	0.36	0.33	0.27
MgO	0.92	1.01	0.86	0.74	0.73	0.81	0.82	0.81	0.82
MnO	0.00	0.00	0.05	0.00	0.00	0.02	0.01	0.00	0.04
K ₂ O	9.35	9.43	9.41	10.44	9.59	10.07	9.29	9.32	9.23
CaO	0.04	0.01	0.03	0.01	0.06	0.05	0.02	0.02	0.00
Na ₂ O	0.25	0.34	0.53	0.30	0.33	0.26	0.23	0.28	0.28
F	0.00	0.00	0.00	0.00	0.00	0.00	0.00	0.00	0.00
Total	95.21	95.55	95.65	93.99	94.25	93.39	94.56	95.69	95.47
<i>Numbers of ions on the basis of 11 oxygens</i>									
Si	3.147	3.138	3.119	3.100	3.088	3.117	3.109	3.117	3.112
Al IV	0.853	0.862	0.881	0.900	0.912	0.883	0.891	0.883	0.888
Σ T	4.000	4.000	4.000	4.000	4.000	4.000	4.000	4.000	4.000
Al VI	1.842	1.842	1.855	1.857	1.856	1.832	1.862	1.872	1.869
Ti	0.075	0.068	0.063	0.052	0.076	0.071	0.071	0.065	0.071
Fe	0.015	0.019	0.017	0.020	0.016	0.016	0.020	0.018	0.015
Mg	0.090	0.098	0.084	0.074	0.073	0.081	0.081	0.079	0.080
Mn	0.000	0.000	0.003	0.000	0.000	0.001	0.001	0.000	0.002
Σ R	2.021	2.027	2.021	2.003	2.020	2.001	2.035	2.034	2.036
Ca	0.003	0.001	0.002	0.001	0.004	0.003	0.001	0.001	0.000
Na	0.032	0.042	0.067	0.040	0.043	0.034	0.030	0.035	0.035
K	0.782	0.787	0.786	0.893	0.814	0.866	0.783	0.776	0.770
Σ A	0.817	0.830	0.855	0.934	0.861	0.903	0.814	0.812	0.806
F	0.000	0.000	0.000	0.000	0.000	0.000	0.000	0.000	0.000

Table VI.1: Major element analyses of muscovites. The single grain analyses were performed with an electron microprobe.

Analysis No.	8	9	10	11	13	14	16	18	1
	KE08-32-M02_2	KE08-32-M02_2	KE08-32-M02_2	KE08-32-M02_2	KE08-32-M02_2	KE08-32-M02_2	KE08-32-M02_2	KE08-32-M02_2	KE08-32-M05_1
SiO ₂	47.29	47.10	47.85	47.23	47.08	46.85	47.34	48.77	47.47
Al ₂ O ₃	35.30	35.29	35.72	34.97	34.66	34.68	34.82	34.94	35.51
TiO ₂	1.26	1.20	1.39	1.43	1.49	1.44	1.47	1.46	1.58
FeO	0.32	0.27	0.27	0.28	0.25	0.30	0.24	0.28	0.33
MgO	0.82	0.81	0.81	0.88	0.89	0.91	0.94	0.99	0.75
MnO	0.00	0.07	0.00	0.03	0.03	0.00	0.04	0.01	0.03
K ₂ O	8.73	9.60	9.47	9.39	9.22	9.43	9.30	9.57	10.00
CaO	0.03	0.01	0.01	0.02	0.00	0.02	0.01	0.03	0.00
Na ₂ O	0.29	0.28	0.31	0.24	0.29	0.30	0.26	0.34	0.25
F	0.00	0.00	0.00	0.00	0.00	0.00	0.00	0.00	0.00
Total	94.07	94.64	95.88	94.49	93.93	93.96	94.47	96.45	95.94

Numbers of ions on the basis of 11 oxygens

Si	3.129	3.116	3.120	3.125	3.132	3.122	3.132	3.162	3.106
Al IV	0.871	0.884	0.880	0.875	0.868	0.878	0.868	0.838	0.894
ΣT	4.000	4.000	4.000	4.000	4.000	4.000	4.000	4.000	4.000
Al VI	1.882	1.867	1.864	1.852	1.848	1.845	1.847	1.831	1.844
Ti	0.063	0.060	0.068	0.071	0.074	0.072	0.073	0.071	0.078
Fe	0.017	0.015	0.015	0.016	0.014	0.017	0.013	0.015	0.018
Mg	0.080	0.080	0.079	0.087	0.088	0.090	0.093	0.095	0.073
Mn	0.000	0.004	0.000	0.002	0.001	0.000	0.002	0.001	0.002
ΣR	2.043	2.026	2.026	2.027	2.026	2.023	2.028	2.014	2.014
Ca	0.002	0.000	0.001	0.001	0.000	0.001	0.000	0.002	0.000
Na	0.037	0.036	0.040	0.031	0.038	0.039	0.033	0.042	0.031
K	0.737	0.810	0.788	0.792	0.782	0.802	0.785	0.791	0.835
ΣA	0.776	0.846	0.828	0.825	0.820	0.842	0.818	0.836	0.866
F	0.000	0.000	0.000	0.000	0.000	0.000	0.000	0.000	0.000

Table VI.1: Major element analyses of muscovites. The single grain analyses were performed with an electron microprobe.

Analysis No.	2	3	4	5	6	8	9	10	12
	KE08-32-M05_1	KE08-32-M05_1	KE08-32-M05_1	KE08-32-M05_1	KE08-32-M05_1	KE08-32-M05_1	KE08-32-M05_1	KE08-32-M05_1	KE08-32-M05_1
SiO ₂	47.59	47.34	45.54	47.23	49.02	47.22	47.55	46.67	46.71
Al ₂ O ₃	34.89	34.77	34.83	35.41	35.25	34.16	35.64	35.69	34.86
TiO ₂	1.53	1.49	1.37	1.41	1.41	1.48	1.54	1.58	1.32
FeO	0.30	0.33	0.32	0.31	0.29	0.31	0.29	0.30	0.24
MgO	1.03	0.94	0.74	0.82	1.00	0.99	0.72	0.68	0.71
MnO	0.03	0.00	0.02	0.02	0.07	0.01	0.00	0.02	0.01
K ₂ O	9.42	10.09	10.05	10.91	10.34	9.70	9.21	9.32	10.57
CaO	0.00	0.02	0.02	0.04	0.01	0.01	0.00	0.01	0.04
Na ₂ O	0.27	0.29	0.27	0.33	0.27	0.25	0.24	0.25	0.31
F	0.00	0.00	0.00	0.00	0.00	0.00	0.00	0.00	0.00
Total	95.05	95.29	93.18	96.52	97.68	94.14	95.23	94.57	94.87
<i>Numbers of ions on the basis of 11 oxygens</i>									
Si	3.130	3.122	3.077	3.093	3.151	3.144	3.116	3.087	3.107
Al IV	0.870	0.878	0.923	0.907	0.849	0.856	0.884	0.913	0.893
Σ T	4.000	4.000	4.000	4.000	4.000	4.000	4.000	4.000	4.000
Al VI	1.835	1.824	1.851	1.825	1.821	1.824	1.869	1.870	1.839
Ti	0.075	0.074	0.070	0.069	0.068	0.074	0.076	0.079	0.066
Fe	0.016	0.018	0.018	0.017	0.015	0.017	0.016	0.016	0.013
Mg	0.101	0.092	0.075	0.080	0.095	0.098	0.071	0.067	0.070
Mn	0.002	0.000	0.001	0.001	0.004	0.001	0.000	0.001	0.001
Σ R	2.029	2.009	2.014	1.993	2.004	2.014	2.031	2.033	1.990
Ca	0.000	0.001	0.001	0.002	0.001	0.001	0.000	0.001	0.002
Na	0.034	0.037	0.035	0.041	0.034	0.032	0.030	0.032	0.040
K	0.791	0.849	0.866	0.911	0.848	0.824	0.770	0.786	0.897
Σ A	0.825	0.887	0.903	0.955	0.882	0.857	0.800	0.819	0.940
F	0.000	0.000	0.000	0.000	0.000	0.000	0.000	0.000	0.000

Table VI.1: Major element analyses of muscovites. The single grain analyses were performed with an electron microprobe.

Analysis No.	6	7	10	11	12	13	14	15	16
SiO ₂	47.55	45.82	47.47	47.16	47.58	47.34	47.51	46.90	47.65
Al ₂ O ₃	35.79	34.20	35.61	35.47	35.52	35.38	34.80	34.92	34.86
TiO ₂	1.19	1.38	1.39	1.54	1.47	1.53	1.65	1.61	1.58
FeO	0.20	0.26	0.26	0.33	0.31	0.36	0.27	0.33	0.33
MgO	0.59	0.66	0.76	0.86	0.85	0.87	1.04	0.97	0.95
MnO	0.03	0.01	0.01	0.03	0.01	0.00	0.00	0.00	0.05
K ₂ O	10.50	10.62	9.03	8.92	9.09	8.92	8.86	9.37	9.08
CaO	0.00	0.00	0.01	0.01	0.02	0.00	0.01	0.00	0.00
Na ₂ O	0.32	0.24	0.24	0.26	0.23	0.23	0.22	0.25	0.25
F	0.00	0.00	0.00	0.00	0.00	0.00	0.00	0.00	0.00
Total	96.27	93.23	94.79	94.61	95.10	94.64	94.37	94.38	94.76

<i>Numbers of ions on the basis of 11 oxygens</i>									
Si	3.109	3.104	3.121	3.109	3.120	3.117	3.135	3.110	3.138
Al IV	0.891	0.896	0.879	0.891	0.880	0.883	0.865	0.890	0.862
ΣT	4.000	4.000	4.000	4.000	4.000	4.000	4.000	4.000	4.000
Al VI	1.867	1.834	1.880	1.864	1.865	1.863	1.842	1.839	1.842
Ti	0.058	0.070	0.068	0.076	0.073	0.076	0.082	0.080	0.078
Fe	0.011	0.015	0.014	0.018	0.017	0.020	0.015	0.019	0.018
Mg	0.057	0.067	0.074	0.084	0.083	0.085	0.102	0.095	0.093
Mn	0.002	0.000	0.001	0.001	0.001	0.000	0.000	0.000	0.003
ΣR	1.995	1.987	2.037	2.044	2.038	2.044	2.041	2.033	2.035
Ca	0.000	0.000	0.001	0.001	0.002	0.000	0.001	0.000	0.000
Na	0.041	0.031	0.030	0.034	0.030	0.029	0.028	0.032	0.032
K	0.876	0.917	0.757	0.750	0.760	0.749	0.746	0.792	0.762
ΣA	0.917	0.948	0.788	0.785	0.791	0.779	0.775	0.825	0.794
F	0.000	0.000	0.000	0.000	0.000	0.000	0.000	0.000	0.000

Table VI.1: Major element analyses of muscovites. The single grain analyses were performed with an electron microprobe.

Analysis No.	18	19	20	21	22	24	25	26	27
	KE08-32-M05_2	KE08-32-M05_2	KE08-32-M05_2	KE08-32-M05_2	KE08-32-M05_2	KE08-32-M05_2	KE08-32-M05_2	KE08-32-M05_2	KE08-32-M05_2
SiO ₂	47.89	47.19	46.59	46.92	45.91	46.61	46.94	46.97	46.13
Al ₂ O ₃	34.84	35.35	34.77	34.99	34.27	35.04	34.60	35.13	34.25
TiO ₂	1.52	1.35	1.30	1.44	1.45	1.42	1.42	1.40	1.36
FeO	0.29	0.29	0.31	0.30	0.27	0.25	0.26	0.29	0.22
MgO	0.92	0.90	0.88	0.85	0.69	0.79	0.85	0.82	0.71
MnO	0.00	0.00	0.05	0.01	0.01	0.02	0.00	0.00	0.02
K ₂ O	9.56	9.19	9.88	9.40	10.11	10.46	9.86	9.69	10.42
CaO	0.01	0.00	0.00	0.01	0.02	0.05	0.01	0.03	0.03
Na ₂ O	0.27	0.22	0.22	0.25	0.28	0.28	0.25	0.23	0.28
F	0.00	0.00	0.00	0.00	0.00	0.00	0.00	0.00	0.00
Total	95.32	94.50	94.00	94.20	93.05	94.96	94.21	94.55	93.45
<i>Numbers of ions on the basis of 11 oxygens</i>									
Si	3.142	3.117	3.111	3.116	3.106	3.094	3.125	3.112	3.112
Al IV	0.858	0.883	0.889	0.884	0.894	0.906	0.875	0.888	0.888
Σ T	4.000	4.000	4.000	4.000	4.000	4.000	4.000	4.000	4.000
Al VI	1.836	1.868	1.848	1.854	1.838	1.836	1.840	1.855	1.835
Ti	0.075	0.067	0.065	0.072	0.074	0.071	0.071	0.070	0.069
Fe	0.016	0.016	0.017	0.017	0.015	0.014	0.015	0.016	0.013
Mg	0.090	0.088	0.087	0.084	0.070	0.078	0.084	0.081	0.071
Mn	0.000	0.000	0.003	0.001	0.001	0.001	0.000	0.000	0.001
Σ R	2.018	2.039	2.020	2.028	1.998	2.000	2.010	2.021	1.989
Ca	0.000	0.000	0.000	0.001	0.002	0.003	0.001	0.002	0.002
Na	0.034	0.029	0.028	0.033	0.036	0.036	0.033	0.029	0.036
K	0.800	0.774	0.842	0.796	0.873	0.886	0.837	0.819	0.897
Σ A	0.835	0.803	0.870	0.830	0.910	0.925	0.871	0.850	0.935
F	0.000	0.000	0.000	0.000	0.000	0.000	0.000	0.000	0.000

Table VI.1: Major element analyses of muscovites. The single grain analyses were performed with an electron microprobe.

Analysis No.	KE08-32-M05_2		KE08-32-M05_2		KE08-32-M05_2		KE08-32-M05_2		KE08-32-M05_3		KE08-32-M05_3		KE08-32-M05_3	
	28	29	30	31	32	1	1	1	1	1	1	1	1	1
SiO ₂	46.44	46.86	47.14	47.06	46.83	46.46	47.52	47.44	47.06	47.44	47.06	47.06	47.06	47.06
Al ₂ O ₃	34.69	35.02	34.85	33.95	33.74	34.33	34.17	33.91	34.39	33.91	34.39	34.39	34.39	34.39
TiO ₂	1.28	1.41	1.50	1.52	1.45	1.43	1.50	1.47	1.53	1.47	1.53	1.53	1.53	1.53
FeO	0.28	0.28	0.23	0.33	0.36	0.27	0.33	0.28	0.26	0.28	0.26	0.26	0.26	0.26
MgO	0.78	0.77	0.86	0.99	1.02	0.87	1.08	1.16	0.94	1.16	0.94	0.94	0.94	0.94
MnO	0.00	0.00	0.05	0.03	0.00	0.00	0.00	0.00	0.00	0.00	0.00	0.00	0.00	0.00
K ₂ O	10.37	10.04	9.93	10.51	10.30	9.43	9.29	9.01	8.98	9.01	8.98	8.98	8.98	8.98
CaO	0.01	0.00	0.01	0.01	0.01	0.00	0.01	0.01	0.02	0.01	0.02	0.02	0.02	0.02
Na ₂ O	0.21	0.24	0.21	0.21	0.23	0.24	0.24	0.23	0.21	0.23	0.21	0.21	0.21	0.21
F	0.00	0.00	0.00	0.00	0.00	0.00	0.00	0.00	0.00	0.00	0.00	0.00	0.00	0.00
Total	94.08	94.63	94.77	94.62	93.95	93.05	94.15	93.53	93.39	93.53	93.39	93.39	93.39	93.39
<i>Numbers of ions on the basis of 11 oxygens</i>														
Si	3.108	3.110	3.120	3.135	3.139	3.125	3.154	3.163	3.141	3.163	3.141	3.141	3.141	3.141
Al IV	0.892	0.890	0.880	0.865	0.861	0.875	0.846	0.837	0.859	0.837	0.859	0.859	0.859	0.859
Σ T	4.000	4.000	4.000	4.000	4.000	4.000	4.000	4.000	4.000	4.000	4.000	4.000	4.000	4.000
Al VI	1.845	1.848	1.838	1.801	1.804	1.846	1.826	1.828	1.847	1.828	1.847	1.847	1.847	1.847
Ti	0.064	0.070	0.075	0.076	0.073	0.072	0.075	0.074	0.077	0.074	0.077	0.077	0.077	0.077
Fe	0.016	0.015	0.013	0.019	0.020	0.015	0.018	0.015	0.014	0.015	0.014	0.014	0.014	0.014
Mg	0.078	0.076	0.085	0.098	0.102	0.088	0.106	0.116	0.094	0.116	0.094	0.094	0.094	0.094
Mn	0.000	0.000	0.003	0.002	0.000	0.000	0.000	0.000	0.000	0.000	0.000	0.000	0.000	0.000
Σ R	2.002	2.011	2.013	1.995	1.999	2.022	2.026	2.032	2.032	2.032	2.032	2.032	2.032	2.032
Ca	0.001	0.000	0.001	0.000	0.001	0.000	0.001	0.000	0.001	0.000	0.001	0.001	0.001	0.001
Na	0.027	0.030	0.026	0.027	0.030	0.031	0.031	0.030	0.027	0.030	0.027	0.027	0.027	0.027
K	0.885	0.850	0.838	0.893	0.881	0.809	0.786	0.767	0.764	0.767	0.764	0.764	0.764	0.764
Σ A	0.913	0.880	0.865	0.920	0.912	0.840	0.818	0.797	0.793	0.797	0.793	0.793	0.793	0.793
F	0.000	0.000	0.000	0.000	0.000	0.000	0.000	0.000	0.000	0.000	0.000	0.000	0.000	0.000

Table VI.1: Major element analyses of muscovites. The single grain analyses were performed with an electron microprobe.

Analysis No.	1	1	1	1	2	3	4	5	6	7
	KE08-32-M05_4	KE08-32-M05_4	KE08-32-M05_4	KE08-32-M07_2	KE08-32-M07_2	KE08-32-M07_2	KE08-32-M07_2	KE08-32-M07_2	KE08-32-M07_2	KE08-32-M07_2
SiO ₂	48.67	49.28	48.48	47.50	47.07	47.31	47.64	47.77	47.13	47.13
Al ₂ O ₃	35.15	34.53	33.95	33.76	36.17	36.39	36.29	35.85	35.70	35.70
TiO ₂	1.47	1.43	1.32	0.66	1.35	1.32	1.59	1.77	1.64	1.64
FeO	0.25	0.31	0.28	0.22	0.27	0.27	0.29	0.29	0.31	0.31
MgO	0.99	1.22	1.17	0.85	0.71	0.73	0.76	0.84	0.84	0.84
MnO	0.09	0.06	0.07	0.03	0.00	0.03	0.00	0.05	0.01	0.01
K ₂ O	7.66	7.86	9.02	10.57	8.38	8.31	8.19	7.91	8.19	8.19
CaO	0.01	0.00	0.01	0.00	0.02	0.00	0.01	0.01	0.01	0.01
Na ₂ O	0.15	0.20	0.26	0.22	0.22	0.22	0.22	0.23	0.32	0.32
F	0.00	0.00	0.00	0.00	0.00	0.00	0.00	0.00	0.00	0.00
Total	94.45	94.92	94.63	93.83	94.20	94.57	95.01	94.76	94.20	94.20
<i>Numbers of ions on the basis of 11 oxygens</i>										
Si	3.177	3.206	3.193	3.184	3.101	3.102	3.107	3.120	3.106	3.106
Al IV	0.823	0.794	0.807	0.816	0.899	0.898	0.893	0.880	0.894	0.894
ΣT	4.000	4.000	4.000	4.000	4.000	4.000	4.000	4.000	4.000	4.000
Al VI	1.882	1.853	1.828	1.851	1.909	1.914	1.897	1.880	1.880	1.880
Ti	0.072	0.070	0.065	0.033	0.067	0.065	0.078	0.087	0.081	0.081
Fe	0.014	0.017	0.015	0.012	0.015	0.015	0.016	0.016	0.017	0.017
Mg	0.096	0.118	0.115	0.084	0.070	0.071	0.074	0.082	0.083	0.083
Mn	0.005	0.003	0.004	0.001	0.000	0.001	0.000	0.003	0.000	0.000
ΣR	2.069	2.062	2.027	1.983	2.061	2.066	2.065	2.068	2.061	2.061
Ca	0.001	0.000	0.001	0.000	0.001	0.000	0.001	0.000	0.001	0.001
Na	0.018	0.025	0.033	0.028	0.028	0.027	0.028	0.029	0.041	0.041
K	0.638	0.652	0.758	0.904	0.704	0.695	0.681	0.659	0.688	0.688
ΣA	0.657	0.677	0.792	0.932	0.733	0.722	0.710	0.689	0.730	0.730
F	0.000	0.000	0.000	0.000	0.000	0.000	0.000	0.000	0.000	0.000

Table VI.1: Major element analyses of muscovites. The single grain analyses were performed with an electron microprobe.

Analysis No.	8	9	10	11	12	13	2	3	4
	KE08-32-M07_2	KE08-32-M07_2	KE08-32-M07_2	KE08-32-M07_2	KE08-32-M07_2	KE08-32-M07_2	KE08-32-M07_3	KE08-32-M07_3	KE08-32-M07_3
SiO ₂	48.00	48.03	47.94	48.04	47.62	49.11	48.03	48.26	47.85
Al ₂ O ₃	35.80	35.79	35.32	35.56	35.36	36.57	36.88	36.40	36.28
TiO ₂	1.35	1.40	1.45	1.48	1.51	1.57	0.89	1.07	1.40
FeO	0.36	0.31	0.33	0.27	0.33	0.27	0.56	0.75	0.74
MgO	1.01	0.98	0.97	0.99	0.97	0.85	0.00	0.01	0.00
MnO	0.01	0.01	0.00	0.04	0.04	0.00	0.02	0.00	0.00
K ₂ O	8.21	7.92	8.38	7.77	7.90	8.50	10.56	9.82	9.01
CaO	0.01	0.00	0.00	0.01	0.00	0.03	0.28	0.34	0.19
Na ₂ O	0.30	0.25	0.23	0.24	0.25	0.22	0.21	0.23	0.21
F	0.00	0.00	0.00	0.00	0.00	0.00	0.00	0.00	0.00
Total	95.13	94.73	94.65	94.43	94.00	97.13	97.46	96.90	95.69
<i>Numbers of ions on the basis of 11 oxygens</i>									
Si	3.131	3.136	3.143	3.144	3.136	3.134	3.102	3.123	3.120
Al IV	0.869	0.864	0.857	0.856	0.864	0.866	0.898	0.877	0.880
Σ T	4.000	4.000	4.000	4.000	4.000	4.000	4.000	4.000	4.000
Al VI	1.882	1.891	1.872	1.886	1.879	1.884	1.910	1.899	1.908
Ti	0.066	0.069	0.071	0.073	0.075	0.075	0.043	0.052	0.068
Fe	0.019	0.017	0.018	0.015	0.018	0.014	0.030	0.040	0.040
Mg	0.098	0.095	0.095	0.096	0.096	0.081	0.000	0.001	0.000
Mn	0.000	0.001	0.000	0.002	0.002	0.000	0.001	0.000	0.000
Σ R	2.066	2.072	2.056	2.072	2.070	2.054	1.984	1.993	2.017
Ca	0.001	0.000	0.000	0.001	0.000	0.002	0.019	0.023	0.013
Na	0.038	0.032	0.029	0.031	0.031	0.027	0.026	0.029	0.027
K	0.683	0.660	0.701	0.648	0.664	0.692	0.870	0.810	0.750
Σ A	0.722	0.692	0.730	0.680	0.695	0.721	0.915	0.863	0.789
F	0.000	0.000	0.000	0.000	0.000	0.000	0.000	0.000	0.000

Table VI.1: Major element analyses of muscovites. The single grain analyses were performed with an electron microprobe.

Analysis No.	5	6	7	8	9	10	11	13	14
	KE08-32-M07_3	KE08-32-M07_3	KE08-32-M07_3	KE08-32-M07_3	KE08-32-M07_3	KE08-32-M07_3	KE08-32-M07_3	KE08-32-M07_3	KE08-32-M07_3
SiO ₂	46.37	46.18	46.64	46.92	47.27	46.89	47.53	46.96	46.59
Al ₂ O ₃	35.53	34.96	34.76	34.99	34.73	34.92	35.01	34.76	34.39
TiO ₂	1.66	1.72	1.73	1.49	1.49	1.51	1.60	1.52	1.51
FeO	0.72	0.76	0.86	0.97	0.98	0.94	0.91	0.91	0.94
MgO	0.03	0.02	0.00	0.03	0.00	0.02	0.00	0.00	0.02
MnO	0.03	0.01	0.00	0.00	0.01	0.03	0.03	0.00	0.01
K ₂ O	9.70	9.26	9.63	9.40	9.64	9.68	8.07	9.53	9.50
CaO	0.38	0.34	0.31	0.41	0.41	0.33	0.30	0.31	0.35
Na ₂ O	0.29	0.33	0.29	0.29	0.26	0.32	0.20	0.24	0.30
F	0.00	0.00	0.00	0.00	0.00	0.00	0.00	0.00	0.00
Total	94.75	93.63	94.26	94.52	94.82	94.69	93.68	94.24	93.65
<i>Numbers of ions on the basis of 11 oxygens</i>									
Si	3.081	3.097	3.113	3.119	3.136	3.117	3.153	3.129	3.129
Al IV	0.919	0.903	0.887	0.881	0.864	0.883	0.847	0.871	0.871
ΣT	4.000	4.000	4.000	4.000	4.000	4.000	4.000	4.000	4.000
Al VI	1.862	1.860	1.847	1.860	1.850	1.853	1.891	1.860	1.851
Ti	0.083	0.087	0.087	0.074	0.074	0.076	0.080	0.076	0.076
Fe	0.040	0.043	0.048	0.054	0.055	0.052	0.051	0.050	0.053
Mg	0.003	0.002	0.000	0.003	0.000	0.002	0.000	0.000	0.002
Mn	0.001	0.001	0.000	0.000	0.001	0.002	0.002	0.000	0.001
ΣR	1.989	1.992	1.982	1.991	1.980	1.985	2.023	1.986	1.982
Ca	0.027	0.025	0.022	0.029	0.029	0.024	0.021	0.022	0.025
Na	0.038	0.043	0.038	0.037	0.033	0.041	0.026	0.031	0.039
K	0.822	0.792	0.820	0.797	0.816	0.821	0.683	0.811	0.814
ΣA	0.887	0.860	0.880	0.863	0.878	0.885	0.730	0.864	0.878
F	0.000	0.000	0.000	0.000	0.000	0.000	0.000	0.000	0.000

Table VI.1: Major element analyses of muscovites. The single grain analyses were performed with an electron microprobe.

Analysis No.	15	17	18	19	20	21	22	23	24
	KE08-32-M07_3	KE08-32-M07_3	KE08-32-M07_3	KE08-32-M07_3	KE08-32-M07_3	KE08-32-M07_3	KE08-32-M07_3	KE08-32-M07_3	KE08-32-M07_3
SiO ₂	47.05	46.82	46.53	46.69	47.11	46.95	47.93	47.71	47.25
Al ₂ O ₃	34.78	35.32	34.97	35.15	34.72	34.70	35.45	35.30	34.97
TiO ₂	1.55	1.59	1.56	1.57	1.52	1.56	1.51	1.55	1.53
FeO	0.95	0.86	0.93	0.93	0.90	0.87	0.91	0.88	0.88
MgO	0.00	0.00	0.00	0.00	0.02	0.00	0.00	0.00	0.04
MnO	0.01	0.00	0.03	0.00	0.01	0.00	0.00	0.00	0.02
K ₂ O	9.38	9.37	9.42	9.07	9.00	9.38	9.44	9.26	9.28
CaO	0.30	0.30	0.29	0.31	0.25	0.30	0.36	0.28	0.26
Na ₂ O	0.23	0.25	0.23	0.33	0.27	0.27	0.34	0.26	0.28
F	0.00	0.00	0.00	0.00	0.00	0.00	0.00	0.00	0.00
Total	94.26	94.53	93.98	94.09	93.80	94.05	95.98	95.28	94.55
<i>Numbers of ions on the basis of 11 oxygens</i>									
Si	3.132	3.108	3.110	3.111	3.142	3.132	3.133	3.136	3.133
Al IV	0.868	0.892	0.890	0.889	0.858	0.868	0.867	0.864	0.867
Σ T	4.000	4.000	4.000	4.000	4.000	4.000	4.000	4.000	4.000
Al VI	1.860	1.870	1.865	1.871	1.871	1.861	1.864	1.870	1.865
Ti	0.077	0.079	0.078	0.079	0.076	0.078	0.074	0.077	0.076
Fe	0.053	0.048	0.052	0.052	0.050	0.049	0.050	0.049	0.049
Mg	0.000	0.000	0.000	0.000	0.002	0.000	0.000	0.000	0.004
Mn	0.001	0.000	0.001	0.000	0.001	0.000	0.000	0.000	0.001
Σ R	1.992	1.998	1.997	2.002	1.999	1.987	1.988	1.995	1.996
Ca	0.022	0.021	0.020	0.022	0.018	0.021	0.025	0.020	0.019
Na	0.030	0.032	0.030	0.042	0.034	0.035	0.043	0.034	0.036
K	0.796	0.793	0.803	0.771	0.766	0.798	0.787	0.776	0.785
Σ A	0.848	0.847	0.853	0.835	0.818	0.855	0.855	0.830	0.840
F	0.000	0.000	0.000	0.000	0.000	0.000	0.000	0.000	0.000

Table VI.1: Major element analyses of muscovites. The single grain analyses were performed with an electron microprobe.

Analysis No.	25	26	27	28	1	3	4	5	6
	KE08-32-M07_3	KE08-32-M07_3	KE08-32-M07_3	KE08-32-M07_3	KE08-45-M08_1	KE08-45-M08_2	KE08-45-M08_2	KE08-45-M08_2	KE08-45-M08_2
SiO ₂	46.72	47.16	46.90	46.88	49.03	49.15	44.97	47.55	46.27
Al ₂ O ₃	34.64	34.91	35.08	35.12	31.14	32.94	31.89	34.36	33.17
TiO ₂	1.50	1.54	1.53	1.55	0.52	0.72	0.76	0.72	0.81
FeO	0.91	0.83	0.85	0.80	4.02	4.30	4.11	4.27	4.43
MgO	0.02	0.08	0.00	0.02	1.06	1.11	0.79	0.78	0.76
MnO	0.03	0.02	0.02	0.03	0.00	0.00	0.00	0.03	0.00
K ₂ O	9.73	9.40	9.17	9.41	10.00	6.50	10.28	7.62	9.19
CaO	0.31	0.30	0.28	0.35	0.00	0.01	0.03	0.01	0.01
Na ₂ O	0.28	0.30	0.27	0.27	0.24	0.21	0.36	0.35	0.40
F	0.00	0.00	0.00	0.00	0.00	0.00	0.00	0.00	0.00
Total	94.18	94.57	94.12	94.45	96.02	94.93	93.21	95.70	95.04
<i>Numbers of ions on the basis of 11 oxygens</i>									
Si	3.123	3.129	3.122	3.115	3.260	3.233	3.111	3.134	3.113
Al IV	0.877	0.871	0.878	0.885	0.740	0.767	0.889	0.866	0.887
Σ T	4.000	4.000	4.000	4.000	4.000	4.000	4.000	4.000	4.000
Al VI	1.852	1.859	1.874	1.866	1.699	1.787	1.711	1.803	1.743
Ti	0.076	0.077	0.077	0.078	0.026	0.036	0.040	0.036	0.041
Fe	0.051	0.046	0.047	0.045	0.224	0.237	0.238	0.235	0.249
Mg	0.002	0.007	0.000	0.002	0.105	0.108	0.081	0.077	0.076
Mn	0.002	0.001	0.001	0.001	0.000	0.000	0.000	0.001	0.000
Σ R	1.982	1.991	1.999	1.991	2.054	2.168	2.070	2.152	2.110
Ca	0.022	0.021	0.020	0.025	0.000	0.001	0.002	0.001	0.000
Na	0.036	0.039	0.034	0.034	0.031	0.026	0.048	0.044	0.052
K	0.830	0.795	0.778	0.797	0.848	0.545	0.907	0.641	0.789
Σ A	0.888	0.855	0.832	0.857	0.880	0.572	0.957	0.686	0.841
F	0.000	0.000	0.000	0.000	0.000	0.000	0.000	0.000	0.000

Table VI.1: Major element analyses of muscovites. The single grain analyses were performed with an electron microprobe.

Analysis No.	8	9	10	11	12	13	14	15	16
SiO ₂	46.53	47.24	46.90	46.60	47.25	47.74	47.42	47.17	45.65
Al ₂ O ₃	33.67	33.95	33.79	32.24	33.48	33.05	32.84	33.23	32.24
TiO ₂	1.01	1.05	1.10	0.99	1.12	1.09	1.01	1.14	1.11
FeO	4.13	3.88	4.07	3.94	4.11	4.11	4.02	4.12	3.96
MgO	0.67	0.74	0.80	0.93	0.86	0.91	0.96	0.89	0.90
MnO	0.00	0.05	0.00	0.00	0.05	0.02	0.01	0.02	0.02
K ₂ O	9.17	8.89	9.11	9.88	8.94	10.35	8.91	9.30	9.18
CaO	0.03	0.01	0.00	0.03	0.01	0.00	0.05	0.01	0.01
Na ₂ O	0.39	0.46	0.48	0.46	0.47	0.51	0.48	0.48	0.40
F	0.00	0.00	0.00	0.00	0.00	0.00	0.00	0.00	0.00
Total	95.59	96.25	96.26	95.07	96.30	97.78	95.69	96.35	93.48

<i>Numbers of ions on the basis of 11 oxygens</i>									
Si	3.106	3.120	3.106	3.142	3.126	3.136	3.153	3.126	3.121
Al IV	0.894	0.880	0.894	0.858	0.874	0.864	0.847	0.874	0.879
ΣT	4.000	4.000	4.000	4.000	4.000	4.000	4.000	4.000	4.000
Al VI	1.754	1.762	1.744	1.704	1.736	1.695	1.728	1.721	1.719
Ti	0.051	0.052	0.055	0.050	0.056	0.054	0.051	0.057	0.057
Fe	0.230	0.214	0.225	0.222	0.227	0.226	0.223	0.228	0.227
Mg	0.067	0.073	0.079	0.093	0.085	0.089	0.095	0.088	0.091
Mn	0.000	0.003	0.000	0.000	0.003	0.001	0.001	0.001	0.001
ΣR	2.102	2.103	2.104	2.070	2.106	2.065	2.097	2.095	2.095
Ca	0.002	0.000	0.000	0.002	0.000	0.000	0.003	0.001	0.001
Na	0.051	0.058	0.062	0.060	0.060	0.065	0.061	0.061	0.053
K	0.781	0.749	0.770	0.850	0.755	0.867	0.756	0.786	0.801
ΣA	0.833	0.807	0.832	0.912	0.815	0.932	0.821	0.848	0.855
F	0.000	0.000	0.000	0.000	0.000	0.000	0.000	0.000	0.000

Table VI.1: Major element analyses of muscovites. The single grain analyses were performed with an electron microprobe.

Analysis No.	17	18	19	20	21	22	23	24	25
	KE08-45-M08_2	KE08-45-M08_2	KE08-45-M08_2	KE08-45-M08_2	KE08-45-M08_2	KE08-45-M08_2	KE08-45-M08_2	KE08-45-M08_2	KE08-45-M08_2
SiO ₂	47.27	47.31	48.72	47.34	46.93	46.80	47.35	47.67	47.20
Al ₂ O ₃	32.80	32.95	33.78	32.69	32.94	32.67	32.51	33.25	32.81
TiO ₂	1.07	1.09	1.13	1.11	1.07	1.17	1.14	1.14	1.08
FeO	4.05	3.93	4.16	4.11	4.08	4.01	3.77	3.90	3.99
MgO	0.97	0.98	0.97	0.94	0.93	0.92	0.91	0.91	0.91
MnO	0.00	0.03	0.02	0.00	0.01	0.01	0.00	0.02	0.01
K ₂ O	9.49	8.99	6.94	9.16	9.24	9.12	10.27	8.47	8.71
CaO	0.00	0.02	0.00	0.00	0.00	0.00	0.01	0.03	0.02
Na ₂ O	0.44	0.52	0.36	0.47	0.46	0.47	0.43	0.42	0.47
F	0.00	0.00	0.00	0.00	0.00	0.00	0.00	0.00	0.00
Total	96.09	95.81	96.08	95.84	95.66	95.17	96.38	95.81	95.20
<i>Numbers of ions on the basis of 11 oxygens</i>									
Si	3.143	3.144	3.179	3.151	3.131	3.137	3.149	3.153	3.151
Al IV	0.857	0.856	0.821	0.849	0.869	0.863	0.851	0.847	0.849
Σ T	4.000	4.000	4.000	4.000	4.000	4.000	4.000	4.000	4.000
Al VI	1.713	1.724	1.777	1.715	1.722	1.718	1.698	1.745	1.733
Ti	0.054	0.054	0.055	0.055	0.054	0.059	0.057	0.057	0.054
Fe	0.225	0.219	0.227	0.229	0.228	0.225	0.210	0.215	0.223
Mg	0.096	0.097	0.095	0.094	0.093	0.092	0.090	0.089	0.090
Mn	0.000	0.001	0.001	0.000	0.000	0.000	0.000	0.001	0.000
Σ R	2.087	2.096	2.155	2.093	2.097	2.094	2.055	2.108	2.101
Ca	0.000	0.001	0.000	0.000	0.000	0.000	0.001	0.002	0.002
Na	0.057	0.067	0.045	0.060	0.060	0.061	0.055	0.053	0.060
K	0.805	0.762	0.578	0.778	0.787	0.779	0.871	0.715	0.742
Σ A	0.862	0.830	0.623	0.838	0.846	0.840	0.927	0.771	0.804
F	0.000	0.000	0.000	0.000	0.000	0.000	0.000	0.000	0.000

Table VI.1: Major element analyses of muscovites. The single grain analyses were performed with an electron microprobe.

Analysis No.	26	28	29	30	31	32	33	34	35
	KE08-45-M08_2	KE08-45-M08_2	KE08-45-M08_2	KE08-45-M08_2	KE08-45-M08_2	KE08-45-M08_2	KE08-45-M08_2	KE08-45-M08_2	KE08-45-M08_2
SiO ₂	47.71	47.42	46.48	46.65	46.85	47.67	46.48	47.06	46.71
Al ₂ O ₃	32.45	32.44	31.86	32.14	33.25	34.06	32.86	33.66	33.54
TiO ₂	1.14	1.06	1.06	0.97	0.98	0.99	0.87	0.86	1.11
FeO	3.94	3.93	3.70	3.92	4.16	3.74	3.77	3.52	4.03
MgO	0.98	0.96	0.88	0.89	0.77	0.73	0.79	0.81	0.72
MnO	0.03	0.00	0.01	0.01	0.00	0.00	0.01	0.00	0.05
K ₂ O	9.94	10.00	10.52	10.47	10.00	10.14	10.10	9.93	10.15
CaO	0.12	0.04	0.00	0.01	0.00	0.01	0.02	0.00	0.02
Na ₂ O	0.53	0.49	0.44	0.42	0.46	0.36	0.39	0.35	0.44
F	0.00	0.00	0.00	0.00	0.00	0.00	0.00	0.00	0.00
Total	96.84	96.36	94.97	95.50	96.47	97.72	95.30	96.20	96.78

Numbers of ions on the basis of 11 oxygens

Si	3.157	3.153	3.148	3.143	3.116	3.120	3.126	3.123	3.099
Al IV	0.843	0.847	0.852	0.857	0.884	0.880	0.874	0.877	0.901
ΣT	4.000	4.000	4.000	4.000	4.000	4.000	4.000	4.000	4.000
Al VI	1.687	1.696	1.690	1.694	1.722	1.747	1.731	1.756	1.722
Ti	0.057	0.053	0.054	0.049	0.049	0.049	0.044	0.043	0.055
Fe	0.218	0.218	0.209	0.221	0.231	0.205	0.212	0.195	0.223
Mg	0.097	0.095	0.089	0.089	0.076	0.071	0.079	0.080	0.072
Mn	0.002	0.000	0.001	0.001	0.000	0.000	0.001	0.000	0.003
ΣR	2.060	2.063	2.043	2.054	2.078	2.071	2.067	2.075	2.075
Ca	0.008	0.003	0.000	0.001	0.000	0.001	0.001	0.000	0.001
Na	0.068	0.064	0.058	0.055	0.059	0.045	0.050	0.045	0.057
K	0.839	0.848	0.909	0.900	0.848	0.847	0.867	0.840	0.859
ΣA	0.915	0.915	0.967	0.955	0.907	0.893	0.919	0.885	0.917
F	0.000	0.000	0.000	0.000	0.000	0.000	0.000	0.000	0.000

Table VI.1: Major element analyses of muscovites. The single grain analyses were performed with an electron microprobe.

Analysis No.	36	37	38	39	2	3	4	5	6
	KE08-45-M08_2	KE08-45-M08_2	KE08-45-M08_2	KE08-45-M08_2	KE08-45-M08_3	KE08-45-M08_3	KE08-45-M08_3	KE08-45-M08_3	KE08-45-M08_3
SiO ₂	46.65	46.65	46.87	47.75	46.99	48.82	45.55	47.08	48.40
Al ₂ O ₃	33.34	33.66	33.68	32.42	33.87	34.84	32.07	33.45	32.31
TiO ₂	1.07	1.07	0.91	0.73	1.05	1.08	0.89	1.01	1.05
FeO	4.13	3.71	3.68	3.82	4.05	3.87	3.57	4.38	4.12
MgO	0.71	0.71	0.68	0.72	0.74	0.77	0.73	0.73	1.02
MnO	0.01	0.03	0.04	0.05	0.04	0.03	0.02	0.01	0.00
K ₂ O	9.82	9.82	9.23	11.17	9.82	10.09	10.65	10.60	10.85
CaO	0.00	0.01	0.00	0.00	0.01	0.01	0.00	0.00	0.01
Na ₂ O	0.43	0.39	0.39	0.34	0.44	0.44	0.34	0.42	0.31
F	0.00	0.00	0.00	0.00	0.00	0.00	0.00	0.00	0.00
Total	96.16	96.05	95.48	97.01	97.02	99.95	93.82	97.70	98.08
<i>Numbers of ions on the basis of 11 oxygens</i>									
Si	3.109	3.105	3.124	3.170	3.102	3.120	3.125	3.106	3.175
Al IV	0.891	0.895	0.876	0.830	0.898	0.880	0.875	0.894	0.825
Σ T	4.000	4.000	4.000	4.000	4.000	4.000	4.000	4.000	4.000
Al VI	1.728	1.746	1.769	1.707	1.736	1.744	1.718	1.707	1.673
Ti	0.054	0.054	0.046	0.036	0.052	0.052	0.046	0.050	0.052
Fe	0.230	0.206	0.205	0.212	0.224	0.207	0.205	0.242	0.226
Mg	0.070	0.071	0.068	0.071	0.073	0.073	0.074	0.072	0.100
Mn	0.000	0.001	0.002	0.003	0.002	0.001	0.001	0.000	0.000
Σ R	2.082	2.078	2.090	2.030	2.087	2.077	2.044	2.071	2.050
Ca	0.000	0.001	0.000	0.000	0.001	0.000	0.000	0.000	0.001
Na	0.055	0.051	0.051	0.044	0.057	0.054	0.045	0.054	0.040
K	0.835	0.834	0.785	0.946	0.827	0.823	0.932	0.892	0.908
Σ A	0.890	0.886	0.835	0.990	0.884	0.877	0.977	0.946	0.948
F	0.000	0.000	0.000	0.000	0.000	0.000	0.000	0.000	0.000

Table VI.1: Major element analyses of muscovites. The single grain analyses were performed with an electron microprobe.

Analysis No.	10	11	12	7	11	16	10	1	2
	KE08-45-M10_1	KE08-45-M10_1	KE08-45-M10_1	KE08-45-M10_3	KE08-45-M10_4	KE08-45-M10_4	KE08-45-M11_1	KE08-45-M11_3	KE08-45-M11_3
SiO ₂	49.63	48.49	47.36	47.35	47.35	52.29	47.64	49.01	49.79
Al ₂ O ₃	33.45	32.28	32.58	33.86	33.64	32.59	33.19	32.41	31.31
TiO ₂	0.95	1.05	1.16	0.25	1.03	0.23	1.05	1.15	1.04
FeO	0.92	0.88	0.93	0.10	0.11	0.15	0.12	4.06	4.09
MgO	0.75	0.83	0.74	0.69	0.69	1.15	0.78	1.20	1.50
MnO	0.00	0.03	0.00	0.00	0.01	0.00	0.00	0.00	0.00
K ₂ O	10.31	10.06	10.19	10.56	9.79	9.47	9.81	9.05	9.12
CaO	0.02	0.03	0.04	0.01	0.00	0.01	0.00	0.00	0.00
Na ₂ O	0.43	0.29	0.45	0.32	0.46	0.14	0.43	0.46	0.45
F	0.00	0.00	0.00	0.00	0.00	0.00	0.00	0.00	0.00
Total	96.48	93.95	93.45	93.14	93.08	96.03	93.03	97.35	97.31

Numbers of ions on the basis of 11 oxygens

Si	3.235	3.246	3.198	3.194	3.185	3.372	3.205	3.201	3.252
Al IV	0.765	0.754	0.802	0.806	0.815	0.628	0.795	0.799	0.748
ΣT	4.000	4.000	4.000	4.000	4.000	4.000	4.000	4.000	4.000
Al VI	1.805	1.792	1.790	1.885	1.852	1.849	1.838	1.695	1.663
Ti	0.047	0.053	0.059	0.013	0.052	0.011	0.053	0.056	0.051
Fe	0.050	0.049	0.052	0.006	0.006	0.008	0.007	0.222	0.223
Mg	0.073	0.082	0.074	0.069	0.069	0.111	0.079	0.116	0.146
Mn	0.000	0.002	0.000	0.000	0.000	0.000	0.000	0.000	0.000
ΣR	1.976	1.978	1.976	1.972	1.979	1.980	1.976	2.090	2.083
Ca	0.001	0.002	0.003	0.001	0.000	0.000	0.000	0.000	0.000
Na	0.055	0.038	0.059	0.042	0.060	0.017	0.056	0.058	0.057
K	0.857	0.859	0.877	0.908	0.840	0.779	0.842	0.753	0.760
ΣA	0.913	0.899	0.940	0.951	0.900	0.796	0.898	0.812	0.818
F	0.000	0.000	0.000	0.000	0.000	0.000	0.000	0.000	0.000

Table VI.1: Major element analyses of muscovites. The single grain analyses were performed with an electron microprobe.

Analysis No.	3	4	5	6	8	9	1	2	3
	KE08-45-M11_3	KE08-45-M11_3	KE08-45-M11_3	KE08-45-M11_3	KE08-45-M11_3	KE08-45-M11_3	KE08-52-M2_1	KE08-52-M2_1	KE08-52-M2_1
SiO ₂	48.43	47.99	48.12	47.49	49.27	51.38	48.13	47.99	47.97
Al ₂ O ₃	31.46	32.64	33.48	33.61	31.05	30.27	34.97	35.05	34.77
TiO ₂	1.07	1.16	1.16	1.08	0.18	0.09	0.56	0.63	0.78
FeO	4.16	4.01	4.25	4.28	3.34	2.58	3.16	3.37	3.41
MgO	1.46	1.10	0.88	0.84	1.64	1.21	0.95	0.80	0.84
MnO	0.05	0.00	0.00	0.04	0.05	0.00	0.01	0.03	0.00
K ₂ O	8.57	9.30	8.97	9.74	10.12	10.26	8.07	8.68	8.85
CaO	0.00	0.00	0.00	0.00	0.00	0.02	0.02	0.00	0.00
Na ₂ O	0.42	0.42	0.48	0.52	0.23	0.27	0.39	0.49	0.55
F	0.00	0.00	0.00	0.00	0.00	0.00	0.00	0.00	0.00
Total	95.63	96.63	97.34	97.60	95.89	96.07	96.26	97.03	97.18
<i>Numbers of ions on the basis of 11 oxygens</i>									
Si	3.216	3.166	3.147	3.117	3.271	3.381	3.142	3.125	3.125
Al IV	0.784	0.834	0.853	0.883	0.729	0.619	0.858	0.875	0.875
ΣT	4.000	4.000	4.000	4.000	4.000	4.000	4.000	4.000	4.000
Al VI	1.678	1.703	1.727	1.717	1.701	1.728	1.832	1.815	1.794
Ti	0.053	0.058	0.057	0.053	0.009	0.004	0.028	0.031	0.038
Fe	0.231	0.221	0.232	0.235	0.185	0.142	0.172	0.183	0.186
Mg	0.145	0.108	0.085	0.082	0.162	0.118	0.092	0.077	0.082
Mn	0.003	0.000	0.000	0.002	0.003	0.000	0.000	0.002	0.000
ΣR	2.110	2.090	2.101	2.089	2.061	1.993	2.124	2.108	2.100
Ca	0.000	0.000	0.000	0.000	0.000	0.001	0.001	0.000	0.000
Na	0.054	0.054	0.061	0.066	0.029	0.034	0.049	0.061	0.069
K	0.725	0.783	0.748	0.815	0.857	0.861	0.672	0.721	0.735
ΣA	0.779	0.837	0.810	0.881	0.886	0.896	0.722	0.782	0.805
F	0.000	0.000	0.000	0.000	0.000	0.000	0.000	0.000	0.000

Table VI.1: Major element analyses of muscovites. The single grain analyses were performed with an electron microprobe.

Analysis No.	4	5	6	7	8	9	10	2	3
	KE08-52-M2_1	KE08-52-M2_1	KE08-52-M2_1	KE08-52-M2_1	KE08-52-M2_1	KE08-52-M2_1	KE08-52-M2_1	KE08-52-M2_2	KE08-52-M2_2
SiO ₂	47.08	47.30	48.26	47.94	47.15	47.27	47.81	47.95	47.78
Al ₂ O ₃	34.16	34.51	34.58	34.56	34.02	34.06	33.23	33.50	33.07
TiO ₂	0.86	0.97	0.88	1.06	1.54	1.55	1.52	1.52	1.49
FeO	3.49	3.53	3.60	3.56	3.64	3.72	3.67	3.34	3.57
MgO	0.87	0.89	0.92	0.91	0.86	0.91	1.15	1.10	1.13
MnO	0.00	0.03	0.00	0.02	0.05	0.02	0.06	0.00	0.02
K ₂ O	9.40	8.65	9.00	8.77	8.35	8.38	8.50	8.39	8.82
CaO	0.04	0.01	0.01	0.00	0.02	0.03	0.00	0.01	0.00
Na ₂ O	0.52	0.58	0.58	0.55	0.55	0.54	0.54	0.55	0.50
F	0.00	0.00	0.00	0.00	0.00	0.00	0.00	0.00	0.00
Total	96.43	96.48	97.82	97.40	96.19	96.50	96.50	96.37	96.39
<i>Numbers of ions on the basis of 11 oxygens</i>									
Si	3.108	3.107	3.129	3.119	3.105	3.105	3.141	3.145	3.146
Al IV	0.892	0.893	0.871	0.881	0.895	0.895	0.859	0.855	0.854
Σ T	4.000	4.000	4.000	4.000	4.000	4.000	4.000	4.000	4.000
Al VI	1.766	1.779	1.771	1.770	1.746	1.742	1.714	1.734	1.712
Ti	0.043	0.048	0.043	0.052	0.076	0.077	0.075	0.075	0.074
Fe	0.193	0.194	0.195	0.194	0.200	0.204	0.202	0.183	0.197
Mg	0.086	0.087	0.089	0.088	0.085	0.089	0.113	0.108	0.111
Mn	0.000	0.002	0.000	0.001	0.003	0.001	0.003	0.000	0.001
Σ R	2.088	2.109	2.098	2.105	2.110	2.113	2.107	2.099	2.095
Ca	0.003	0.000	0.001	0.000	0.002	0.002	0.000	0.001	0.000
Na	0.067	0.074	0.073	0.070	0.070	0.068	0.069	0.070	0.064
K	0.792	0.725	0.744	0.728	0.702	0.702	0.713	0.701	0.741
Σ A	0.862	0.799	0.818	0.797	0.774	0.772	0.782	0.772	0.805
F	0.000	0.000	0.000	0.000	0.000	0.000	0.000	0.000	0.000

Table VI.1: Major element analyses of muscovites. The single grain analyses were performed with an electron microprobe.

Analysis No.	4	5	6	7	2	3	4	5	6
SiO ₂	47.72	47.58	47.78	47.49	47.41	47.39	46.99	47.89	45.50
Al ₂ O ₃	33.75	32.96	33.28	34.07	34.00	33.60	33.42	33.93	32.76
TiO ₂	1.42	1.44	1.40	1.17	1.60	1.51	1.59	1.46	1.50
FeO	3.14	3.26	3.36	3.16	3.42	3.65	3.69	3.62	3.70
MgO	0.96	1.03	1.03	0.76	0.85	0.90	0.91	0.90	0.84
MnO	0.00	0.01	0.00	0.00	0.01	0.07	0.00	0.00	0.00
K ₂ O	8.77	9.47	8.74	9.37	9.09	8.96	8.98	9.66	9.71
CaO	0.01	0.02	0.01	0.00	0.02	0.01	0.01	0.04	0.04
Na ₂ O	0.50	0.55	0.52	0.45	0.46	0.54	0.48	0.55	0.53
F	0.00	0.00	0.00	0.00	0.00	0.00	0.00	0.00	0.00
Total	96.27	96.32	96.13	96.46	96.87	96.64	96.08	98.09	94.62
<i>Numbers of ions on the basis of 11 oxygens</i>									
Si	3.136	3.144	3.149	3.125	3.109	3.118	3.112	3.116	3.085
Al IV	0.864	0.856	0.851	0.875	0.891	0.882	0.888	0.884	0.915
ΣT	4.000	4.000	4.000	4.000	4.000	4.000	4.000	4.000	4.000
Al VI	1.750	1.711	1.733	1.767	1.737	1.724	1.721	1.718	1.702
Ti	0.070	0.072	0.069	0.058	0.079	0.075	0.079	0.071	0.076
Fe	0.173	0.180	0.185	0.174	0.187	0.201	0.204	0.197	0.210
Mg	0.094	0.102	0.101	0.074	0.083	0.089	0.090	0.087	0.085
Mn	0.000	0.001	0.000	0.000	0.001	0.004	0.000	0.000	0.000
ΣR	2.087	2.065	2.089	2.074	2.087	2.093	2.094	2.074	2.073
Ca	0.001	0.001	0.001	0.000	0.002	0.001	0.001	0.003	0.003
Na	0.063	0.070	0.066	0.057	0.058	0.069	0.061	0.069	0.069
K	0.735	0.798	0.734	0.787	0.761	0.752	0.759	0.801	0.840
ΣA	0.799	0.870	0.802	0.844	0.820	0.821	0.821	0.874	0.912
F	0.000	0.000	0.000	0.000	0.000	0.000	0.000	0.000	0.000

Table VI.1: Major element analyses of muscovites. The single grain analyses were performed with an electron microprobe.

Analysis No.	7	8	9	1	2	4	5	6	7
	KE08-52-M3_1	KE08-52-M3_1	KE08-52-M3_1	KE08-52-M6_1	KE08-52-M6_1	KE08-52-M6_1	KE08-52-M6_1	KE08-52-M6_1	KE08-52-M6_1
SiO ₂	48.31	45.53	47.28	45.38	47.07	47.22	46.70	47.32	48.10
Al ₂ O ₃	34.29	32.40	33.92	31.92	33.74	33.66	33.40	33.69	34.19
TiO ₂	1.57	1.52	1.70	1.10	1.12	1.25	1.29	1.32	1.29
FeO	3.52	3.65	3.21	3.73	3.58	3.48	3.38	3.37	3.30
MgO	0.85	0.78	0.80	0.94	0.89	0.79	0.81	0.80	0.77
MnO	0.00	0.00	0.00	0.02	0.00	0.00	0.01	0.01	0.05
K ₂ O	9.37	9.97	9.68	10.01	10.20	10.27	10.40	10.23	10.27
CaO	0.01	0.01	0.00	0.05	0.01	0.01	0.00	0.00	0.03
Na ₂ O	0.55	0.50	0.36	0.38	0.45	0.43	0.48	0.46	0.45
F	0.00	0.00	0.00	0.00	0.00	0.00	0.00	0.00	0.00
Total	98.47	94.39	96.96	93.54	97.08	97.12	96.48	97.20	98.47
<i>Numbers of ions on the basis of 11 oxygens</i>									
Si	3.120	3.097	3.105	3.116	3.105	3.112	3.104	3.114	3.121
Al IV	0.880	0.903	0.895	0.884	0.895	0.888	0.896	0.886	0.879
Σ T	4.000	4.000	4.000	4.000	4.000	4.000	4.000	4.000	4.000
Al VI	1.730	1.695	1.731	1.700	1.728	1.727	1.719	1.727	1.735
Ti	0.076	0.078	0.084	0.057	0.056	0.062	0.064	0.065	0.063
Fe	0.190	0.208	0.176	0.214	0.197	0.192	0.188	0.186	0.179
Mg	0.082	0.079	0.078	0.096	0.088	0.078	0.080	0.078	0.075
Mn	0.000	0.000	0.000	0.001	0.000	0.000	0.000	0.001	0.003
Σ R	2.078	2.060	2.069	2.068	2.069	2.059	2.052	2.056	2.054
Ca	0.001	0.001	0.000	0.004	0.001	0.000	0.000	0.000	0.002
Na	0.068	0.066	0.046	0.051	0.058	0.054	0.062	0.058	0.056
K	0.772	0.865	0.811	0.877	0.858	0.863	0.882	0.858	0.850
Σ A	0.841	0.931	0.857	0.931	0.916	0.918	0.944	0.917	0.908
F	0.000	0.000	0.000	0.000	0.000	0.000	0.000	0.000	0.000

Table VI.1: Major element analyses of muscovites. The single grain analyses were performed with an electron microprobe.

Analysis No.	8	9	10	11	12	13	14	16	17
	KE08-52-M6_1	KE08-52-M6_1	KE08-52-M6_1	KE08-52-M6_1	KE08-52-M6_1	KE08-52-M6_1	KE08-52-M6_1	KE08-52-M6_1	KE08-52-M6_1
SiO ₂	47.46	48.13	46.56	47.98	47.30	47.44	47.07	47.40	45.59
Al ₂ O ₃	34.07	34.25	33.40	33.96	33.53	33.35	33.45	32.81	31.36
TiO ₂	1.33	1.46	1.46	1.34	1.43	1.47	1.55	1.48	1.54
FeO	3.17	3.47	3.66	3.58	3.63	3.69	3.78	3.72	3.82
MgO	0.73	0.84	0.91	0.91	0.88	0.90	0.90	1.06	1.04
MnO	0.06	0.00	0.00	0.00	0.00	0.02	0.01	0.00	0.03
K ₂ O	9.36	9.56	9.30	9.91	9.89	10.18	9.28	9.45	9.86
CaO	0.04	0.01	0.01	0.01	0.00	0.00	0.00	0.02	0.02
Na ₂ O	0.40	0.50	0.52	0.54	0.54	0.54	0.53	0.52	0.48
F	0.00	0.00	0.00	0.00	0.00	0.00	0.00	0.00	0.00
Total	96.62	98.22	95.81	98.24	97.22	97.62	96.59	96.46	93.75
<i>Numbers of ions on the basis of 11 oxygens</i>									
Si	3.120	3.119	3.100	3.119	3.112	3.115	3.109	3.136	3.125
Al IV	0.880	0.881	0.900	0.881	0.888	0.885	0.891	0.864	0.875
Σ T	4.000	4.000	4.000	4.000	4.000	4.000	4.000	4.000	4.000
Al VI	1.759	1.735	1.721	1.721	1.712	1.696	1.712	1.694	1.658
Ti	0.066	0.071	0.073	0.066	0.071	0.073	0.077	0.074	0.079
Fe	0.174	0.188	0.204	0.194	0.200	0.202	0.209	0.206	0.219
Mg	0.071	0.081	0.090	0.088	0.086	0.088	0.089	0.104	0.106
Mn	0.003	0.000	0.000	0.000	0.000	0.001	0.001	0.000	0.002
Σ R	2.074	2.075	2.087	2.069	2.068	2.061	2.087	2.078	2.064
Ca	0.002	0.000	0.001	0.001	0.000	0.000	0.000	0.001	0.002
Na	0.051	0.063	0.067	0.068	0.069	0.069	0.068	0.067	0.064
K	0.785	0.791	0.790	0.821	0.829	0.853	0.782	0.798	0.862
Σ A	0.839	0.854	0.858	0.890	0.899	0.922	0.850	0.866	0.928
F	0.000	0.000	0.000	0.000	0.000	0.000	0.000	0.000	0.000

Table VI.1: Major element analyses of muscovites. The single grain analyses were performed with an electron microprobe.

Analysis No.	18	19	1	2	3	4	5	6	7	8
	KE08-52-M6_1	KE08-52-M6_1	KE08-52-M6_2	KE08-52-M6_2	KE08-52-M6_2	KE08-52-M6_2	KE08-52-M6_2	KE08-52-M6_2	KE08-52-M6_2	KE08-52-M6_2
SiO ₂	47.73	46.74	45.66	46.99	46.84	51.94	46.10	47.14	47.62	46.83
Al ₂ O ₃	33.08	32.71	32.69	33.23	32.60	34.66	32.15	32.89	33.32	33.15
TiO ₂	1.55	1.46	1.42	1.54	1.51	1.54	1.48	1.52	1.48	1.56
FeO	3.59	3.47	3.44	3.55	3.65	3.94	3.60	3.67	3.69	3.52
MgO	1.06	1.04	0.70	0.79	1.07	1.13	1.05	0.97	1.06	0.98
MnO	0.01	0.00	0.00	0.02	0.04	0.00	0.01	0.00	0.00	0.04
K ₂ O	9.79	9.73	10.63	10.47	9.36	3.68	9.66	9.37	9.26	9.09
CaO	0.02	0.03	0.03	0.01	0.00	0.02	0.00	0.00	0.01	0.00
Na ₂ O	0.55	0.50	0.40	0.53	0.50	0.21	0.52	0.50	0.53	0.49
F	0.00	0.00	0.00	0.00	0.00	0.00	0.00	0.00	0.00	0.00
Total	97.36	95.69	94.98	97.14	95.58	97.14	94.56	96.07	96.97	95.67
<i>Numbers of ions on the basis of 11 oxygens</i>										
Si	3.132	3.122	3.093	3.106	3.128	3.264	3.121	3.130	3.128	3.116
Al IV	0.868	0.878	0.907	0.894	0.872	0.736	0.879	0.870	0.872	0.884
Σ T	4.000	4.000	4.000	4.000	4.000	4.000	4.000	4.000	4.000	4.000
Al VI	1.690	1.697	1.704	1.695	1.693	1.831	1.685	1.703	1.708	1.715
Ti	0.076	0.074	0.072	0.076	0.076	0.073	0.075	0.076	0.073	0.078
Fe	0.197	0.194	0.195	0.196	0.204	0.207	0.204	0.204	0.203	0.196
Mg	0.103	0.103	0.071	0.078	0.107	0.106	0.105	0.096	0.104	0.097
Mn	0.001	0.000	0.000	0.001	0.002	0.000	0.000	0.000	0.000	0.002
Σ R	2.067	2.068	2.041	2.047	2.082	2.217	2.070	2.079	2.087	2.089
Ca	0.001	0.002	0.002	0.000	0.000	0.002	0.000	0.000	0.000	0.000
Na	0.070	0.065	0.053	0.068	0.065	0.025	0.068	0.065	0.067	0.063
K	0.820	0.829	0.919	0.883	0.798	0.295	0.834	0.794	0.775	0.772
Σ A	0.891	0.897	0.974	0.952	0.863	0.322	0.902	0.858	0.843	0.835
F	0.000	0.000	0.000	0.000	0.000	0.000	0.000	0.000	0.000	0.000

Table VI-2: Ar/Ar analyses of muscovites from the Kettle DSZ.

ID	Temp (°C)	⁴⁰ Ar/ ³⁹ Ar	³⁷ Ar/ ³⁹ Ar	³⁶ Ar/ ³⁹ Ar (x 10 ⁻³)	³⁹ Ar _k (x 10 ⁻¹⁵ mol)	K/Ca	⁴⁰ Ar* (%)	³⁹ Ar (%)	Age (Ma)	±1σ (Ma)
KE08-032 , Muscovite, 5.01 mg, J=0.0015864±0.07%, D=1.005±0.001, NM-233L, Lab#=59598-01										
Xi A	600	23.63	0.0187	26.71	1.95	27.22	66.6	1.0	44.46	0.46
X B	650	19.40	0.0020	3.802	2.13	251.7	94.2	2.0	51.55	0.36
X C	700	18.98	0.0009	2.184	3.69	584.2	96.6	3.8	51.70	0.22
X D	750	18.46	-0.0005	1.394	6.46	-	97.8	7.0	50.90	0.15
X E	800	18.48	0.0005	1.298	9.5	995.1	97.9	11.7	51.03	0.12
F	850	18.57	-0.0001	2.187	17.0	-	96.5	20.0	50.56	0.10
G	880	18.22	0.0000	0.7709	24.3	-	98.7	32.0	50.752	0.085
H	940	18.09	0.0002	0.5795	35.8	2462	99.1	49.6	50.552	0.085
I	1000	18.17	0.0002	0.7649	24.1	2319	98.8	61.4	50.61	0.10
J	1050	18.14	-0.0001	0.9699	14.8	-	98.4	68.7	50.369	0.095
K	1100	18.19	0.0000	1.204	13.4	-	98.0	75.3	50.294	0.097
L	1170	18.23	0.0001	0.7646	35.4	7289	98.8	92.7	50.779	0.081
M	1220	18.28	-0.0005	1.248	10.9	-	98.0	98.1	50.52	0.11
N	1650	34.88	-0.0004	57.30	3.91	-	51.5	100.0	50.64	0.46
Integrated age ± 1σ			n=14		203.4		K2O=9.83%		50.599	0.073
Plateau ± 1σ			steps F-N	n=9	MSWD=3.03	179.6		88.3	50.57	0.07
KE08-039 , Muscovite, 4.03 mg, J=0.0015877±0.07%, D=1.005±0.001, NM-233L, Lab#=59594-01										
Xi A	550	37.05	0.0350	92.25	1.25	14.57	26.4	0.7	27.8	1.1
X B	600	25.77	0.0162	24.01	0.939	31.46	72.5	1.3	52.70	0.95
X C	650	22.84	0.0035	14.45	1.61	145.2	81.3	2.2	52.40	0.61
X D	700	21.40	0.0016	9.470	2.59	313.2	86.9	3.7	52.47	0.42
X E	730	20.37	0.0004	5.866	2.73	1319	91.5	5.3	52.57	0.35
X F	770	21.03	0.0026	9.197	4.32	195.0	87.1	7.8	51.69	0.28
G	800	22.66	0.0000	15.92	8.45	-	79.2	12.7	50.69	0.21
H	820	20.35	-0.0001	8.406	10.2	-	87.8	18.6	50.44	0.16
I	840	19.22	0.0001	4.350	12.9	4338	93.3	26.1	50.62	0.13
J	870	18.56	-0.0002	2.365	17.6	-	96.2	36.3	50.416	0.099
K	900	18.37	0.0004	1.891	14.9	1408	97.0	44.9	50.29	0.12
L	930	18.58	0.0003	2.362	12.3	1484	96.2	52.1	50.48	0.13
M	960	18.84	0.0016	3.388	9.34	313.7	94.7	57.5	50.37	0.16
N	1020	19.35	0.0009	4.956	11.8	552.5	92.4	64.3	50.48	0.15
O	1060	19.49	0.0003	5.394	9.8	1881	91.8	70.0	50.52	0.14
X P	1110	19.06	0.0000	3.522	26.8	-	94.5	85.5	50.86	0.10
X Q	1170	18.39	0.0000	1.045	24.9	-	98.3	100.0	51.02	0.10
Integrated age ± 1σ			n=17		172.5		K2O=10.36%		50.57	0.08
Plateau ± 1σ			steps G-O	n=9	MSWD=0.70	107.3		62.2	50.46	0.06

Table VI-2: Ar/Ar analyses of muscovites from the Kettle DSZ.

ID	Temp (°C)	⁴⁰ Ar/ ³⁹ Ar	³⁷ Ar/ ³⁹ Ar	³⁶ Ar/ ³⁹ Ar (x 10 ⁻³)	³⁹ Ar _k (x 10 ⁻¹⁵ mol)	K/Ca	⁴⁰ Ar* (%)	³⁹ Ar (%)	Age (Ma)	±1σ (Ma)
KE08-044 , Muscovite, 7.06 mg, J=0.0015928±0.10%, D=1.005±0.001, NM-233L, Lab#=59595-01										
Xi A	600	22.65	0.0112	31.19	6.01	45.64	59.3	2.2	38.18	0.29
X B	700	21.33	0.0017	5.930	10.5	294.3	91.8	6.1	55.38	0.15
X C	750	19.56	0.0014	2.910	10.4	361.5	95.6	10.0	52.93	0.12
X D	800	19.40	0.0008	3.552	13.1	641.0	94.6	14.8	51.94	0.12
E	830	19.00	0.0008	3.412	14.1	662.1	94.7	20.0	50.96	0.12
F	860	18.64	0.0004	2.346	18.5	1310	96.3	26.9	50.830	0.095
G	900	18.55	0.0001	1.807	22.2	3916	97.1	35.1	51.025	0.097
H	960	18.55	0.0001	1.994	31.3	5752	96.8	46.6	50.866	0.078
I	1020	18.45	0.0003	1.868	43.3	1888	97.0	62.6	50.687	0.083
J	1060	18.41	0.0005	1.549	42.7	1100	97.5	78.4	50.830	0.074
K	1120	18.19	0.0002	0.9533	51.0	2439	98.5	97.3	50.710	0.073
L	1220	18.95	0.0032	3.229	5.13	158.7	95.0	99.2	50.97	0.20
M	1650	50.83	0.0260	109.5	2.20	19.66	36.4	100.0	52.32	0.86
Integrated age ± 1σ		n=13		270.6		K2O=9.24%		50.86	0.08	
Plateau ± 1σ steps E-M		n=9		MSWD=1.82		230.6		85.2	50.83	0.06
KE08-045 , Muscovite, 4.66 mg, J=0.0015948±0.11%, D=1.005±0.001, NM-233L, Lab#=59596-01										
Xi A	550	31.46	0.0212	54.37	1.53	24.07	48.9	0.8	43.72	0.78
X B	600	21.46	0.0141	10.76	1.43	36.16	85.2	1.6	51.81	0.57
X C	650	20.41	0.0052	5.575	2.51	97.34	91.9	2.9	53.18	0.37
X D	700	19.52	0.0025	4.501	4.42	204.9	93.2	5.2	51.56	0.25
X E	750	19.09	0.0025	3.556	7.07	201.9	94.5	8.9	51.14	0.17
X F	730	18.04	0.0018	0.0491	2.20	289.4	99.9	10.1	51.10	0.35
G	770	19.04	0.0019	4.038	4.59	274.6	93.7	12.5	50.60	0.21
H	800	19.59	0.0006	6.263	8.07	897.6	90.5	16.8	50.30	0.16
I	820	19.05	0.0006	3.990	16.2	842.6	93.8	25.3	50.66	0.12
J	850	18.42	0.0005	1.893	18.8	1037	97.0	35.2	50.641	0.095
K	880	18.25	0.0004	1.366	20.3	1185	97.8	45.9	50.603	0.093
L	900	18.24	0.0009	1.627	15.4	596.4	97.4	54.0	50.35	0.11
M	930	18.41	0.0003	2.093	14.0	1759	96.6	61.3	50.45	0.11
N	960	18.59	0.0006	2.342	12.3	819.9	96.3	67.8	50.75	0.12
O	990	18.69	0.0004	3.239	10.6	1177	94.9	73.4	50.28	0.14
P	1020	19.03	0.0005	3.815	9.25	956.9	94.1	78.3	50.75	0.15
X Q	1060	18.88	0.0005	3.150	15.4	1003	95.1	86.4	50.89	0.11
X R	1110	18.28	0.0003	0.9571	22.3	1548	98.5	98.2	51.035	0.094
X S	1170	18.50	0.0020	1.621	3.50	254.6	97.4	100.0	51.08	0.25
Integrated age ± 1σ		n=19		189.9		K2O=9.81%		50.68	0.09	
Plateau ± 1σ steps G-P		n=10		MSWD=1.90		129.5		68.2	50.55	0.08

Table VI-2: Ar/Ar analyses of muscovites from the Kettle DSZ.

ID	Temp (°C)	⁴⁰ Ar/ ³⁹ Ar	³⁷ Ar/ ³⁹ Ar	³⁶ Ar/ ³⁹ Ar (x 10 ⁻³)	³⁹ Ar _k (x 10 ⁻¹⁵ mol)	K/Ca	⁴⁰ Ar* (%)	³⁹ Ar (%)	Age (Ma)	±1σ (Ma)
KE08-047 , Muscovite, 6.8 mg, J=0.0015844±0.08%, D=1.005±0.001, NM-233L, Lab#=59593-01										
Xi A	550	32.24	0.0185	60.53	2.05	27.55	44.5	0.8	40.55	0.63
X B	600	22.84	0.0064	14.34	1.87	79.51	81.4	1.5	52.39	0.45
C	650	21.04	0.0037	9.733	3.24	138.6	86.3	2.8	51.15	0.30
D	700	19.98	0.0021	5.944	5.71	246.2	91.2	5.0	51.33	0.19
E	730	19.24	0.0002	3.839	6.34	2431	94.1	7.4	51.00	0.17
F	760	19.23	0.0005	3.853	7.63	1055	94.1	10.3	50.96	0.17
G	790	20.38	0.0008	8.284	10.2	628.6	88.0	14.3	50.51	0.15
H	820	19.91	0.0007	6.625	18.9	751.0	90.2	21.6	50.56	0.12
I	850	18.85	0.0003	2.917	30.7	1717	95.4	33.4	50.661	0.095
J	870	18.47	0.0000	1.559	24.6	-	97.5	42.9	50.741	0.092
K	900	18.53	0.0000	1.658	24.2	-	97.4	52.3	50.805	0.095
L	930	18.76	0.0003	2.218	20.5	1608	96.5	60.2	51.00	0.11
M	990	18.85	0.0001	2.971	32.8	3807	95.3	72.8	50.626	0.087
N	1060	19.41	0.0005	4.707	29.5	1120	92.8	84.2	50.75	0.10
O	1170	18.45	0.0005	1.592	40.9	1068	97.4	100.0	50.641	0.082
Integrated age ± 1σ			n=15		259.2		K2O=9.24%		50.67	0.08
Plateau ± 1σ			steps E-O	n=11	MSWD=1.82	246.3		95.0	50.72	0.06
KE08-049 , Muscovite, 1.21 mg, J=0.0015914±0.08%, D=1.005±0.001, NM-233L, Lab#=59597-01										
Xi A	600	33.19	0.1401	58.79	0.490	3.641	47.7	1.3	44.9	1.6
B	700	20.66	0.0148	10.60	1.15	34.57	84.8	4.3	49.62	0.69
C	750	18.92	0.0014	2.658	1.36	366.9	95.8	7.8	51.31	0.52
D	800	19.92	0.0028	8.096	1.78	180.7	88.0	12.5	49.60	0.44
E	830	19.76	-0.0005	6.786	2.90	-	89.8	20.1	50.23	0.31
F	900	18.50	0.0004	2.976	10.8	1224	95.2	48.1	49.87	0.12
G	960	18.55	-0.0003	2.645	5.60	-	95.8	62.7	50.26	0.18
H	1020	18.92	0.0007	4.042	3.66	724.7	93.7	72.3	50.16	0.23
I	1060	18.99	-0.0028	4.060	3.53	-	93.7	81.5	50.35	0.26
Xi J	1120	18.49	0.0002	1.843	7.11	2294	97.1	100.0	50.76	0.15
Integrated age ± 1σ			n=10		38.4		K2O=7.65%		50.16	0.10
Plateau ± 1σ			steps B-I	n=8	MSWD=1.82	30.8		80.2	50.08	0.12

Table VI-2: Ar/Ar analyses of muscovites from the Kettle DSZ.

Sample	L#	Mineral	Plateau Age					Integrated Age	
			% ³⁹ Ar	n	MSWD	Age (Ma)	± 1s	Age (Ma)	± 1s
KE08-032	59598	Muscovite	88.3	9	3.0	50.57	0.07	50.60	0.07
KE08-039	59594	Muscovite	62.2	9	0.70	50.46	0.06	50.57	0.08
KE08-044	59595	Muscovite	85.2	9	1.8	50.83	0.06	50.86	0.08
KE08-045	59596	Muscovite	68.2	10	1.9	50.55	0.08	50.68	0.09
KE08-047	59593	Muscovite	95.0	11	1.8	50.72	0.06	50.67	0.08
KE08-049	59597	Muscovite	80.2	8	1.8	50.08	0.12	50.16	0.10

Notes:

Isotopic ratios corrected for blank, radioactive decay, and mass discrimination, not corrected for interfering reactions.

Errors quoted for individual analyses include analytical error only, without interfering reaction or J uncertainties.

Integrated age calculated by summing isotopic measurements of all steps.

Integrated age error calculated by quadratically combining errors of isotopic measurements of all steps.

Plateau age is inverse-variance-weighted mean of selected steps.

Plateau age error is inverse-variance-weighted mean error (Taylor, 1982) times root MSWD where MSWD>1.

Plateau error is weighted error of Taylor (1982).

Decay constants and isotopic abundances after Steiger and Jäger (1977).

X preceding sample ID denotes analyses excluded from plateau age calculations.

i preceding sample ID denotes analyses excluded from isochron age calculations.

Weight percent K₂O calculated from ³⁹Ar signal, sample weight, and instrument sensitivity.

Ages calculated relative to FC-2 Fish Canyon Tuff sanidine interlaboratory standard at 28.02 Ma

Decay Constant (LambdaK (total)) = 5.543e-10/a

- in K/Ca indicates nondetected ³⁷Ar above blank.

D is 1 AMU mass discrimination in favor of light isotopes.

Correction factors:

$$(^{39}\text{Ar}/^{37}\text{Ar})_{\text{Ca}} = 0.0007 \pm 5\text{e-}05$$

$$(^{36}\text{Ar}/^{37}\text{Ar})_{\text{Ca}} = 0.00028 \pm 2\text{e-}05$$

$$(^{40}\text{Ar}/^{39}\text{Ar})_{\text{K}} = 0.010 \pm 0.002$$

Table VI.3: Table of hydrogen and oxygen isotope compositions of mylonite from the KSZ.

Distance to the detachment (m)	Rocks	UTM 11N	WGS84	$\delta^{18}\text{O Qz}$ (+/-) (‰)	$\delta^{18}\text{O Ms}$ (+/-) (‰)	$\delta\text{D Ms}$ (+/-) (‰)	$\delta\text{D Fl Qz}$ (+/-) (‰)	$T_{\text{Qz-Ms}}$ (+/-) (°C)	+/-				
KE08-032	Quartzite	400611	5361720	5.56	0.55	7.17	0.13	-130	1.3	-	-	-	
KE08-033	Quartzite	400588	5361643	10.72	0.09	8.89	0.06	-132	-	-109	1	664	10
KE08-035	Quartzite	400566	5361630	12.91	0.07	-	-	-	-	-39	3	-	-
012-03	Quartzite	400564	5361620	8.13	0.05	4.65	0.05	-128	2	-	-	361	20
KE08-037	Quartzite	400556	5361631	3.95	0.72	6.43	0.39	-135	1.0	-	-	-	-
KE08-039	Lens in Micaschiste	400556	5361631	11.47	1.27	8.19	0.88	-133	0.3	-40	3	383	28
KE08-043	Lens in Micaschiste	400517	5361608	12.51	0.01	5.62	0.08	-129	-	-48	3	168	2
KE08-044	Quartzite	400517	5361608	11.10	0.22	7.29	0.08	-132	1.2	-	-	333	8
KE08-045	Quartzite	400489	5361572	12.75	0.16	8.96	0.44	-134	0.9	-88	1	335	16
011-03	Quartzite	400521	5361623	12.22	0.05	9.37	0.05	-120	2	-	-	428	26
KE08-046	Quartzite	400511	5361605	11.23	0.28	7.61	0.24	-130	0.3	-	-	351	32
KE08-047	Quartzite	400505	5361604	12.90	0.21	9.72	0.21	-131	1.4	-	-	393	31
010-03	Quartzite	400506	5361627	12.48	0.05	8.92	0.09	-129	2	-	-	354	27
KE08-048	Quartzite	400497	5361598	11.94	0.08	8.29	0.23	-132	5.5	-	-	342	15
009-03	Quartzite	400487	5361607	5.03	0.25	4.89	0.10	-129	2	-	-	-	-
KE08-049	Quartzite	400478	5361610	12.23	0.17	8.72	0.52	-134	4.3	-75	3	368	29
007-03	Quartzite	400477	5361601	12.39	0.05	9.46	0.05	-129	2	-	-	418	25
004-03	Quartzite	400514	5361602	8.61	0.36	6.48	0.21	-129	2	-	-	536	240
KE08-052	Quartzite	400466	5361593	12.54	0.03	8.83	0.20	-133	0.7	-73	3	342	10
000-03	Quartzite	400418	5361426	12.46	0.07	8.96	0.17	-130	2	-	-	360	48

Table VI.4: List of samples from the KSZ.

Sample	Description	Localities	UTM (11N)	WGS84	Elevation
			(m)	(m)	(m)
KE08-001	Myl	Road 20 (dir. Kettle Falls)	0415359	5382495	532
KE08-002	Pegmatite	Road 20 (dir. Kettle Falls)	0415359	5382495	532
KE08-003	Amphibolite	Road 20 (dir. Kettle Falls)	0415359	5382495	532
KE08-004	Folded Qz vein	Road 20 (dir. Kettle Falls)	0415359	5382495	532
KE08-005	Pegmatite	Road 20 (dir. Kettle Falls)	0417194	5387119	500
KE08-006	Am+Qz+My	Road 20 (dir. Kettle Falls)	0417194	5387119	500
KE08-007	Chlorite	Road 20 (dir. Kettle Falls)	0417194	5387119	500
KE08-008	Quartzite	Quartzite quarry (rd 395)	0417052	5388311	565
KE08-009	Quartzite	Quartzite quarry (rd 395)	0417055	5388266	557
KE08-010	Quartzite	Quartzite quarry (rd 395)	0417068	5388255	547
KE08-011	Quartzite	Quartzite quarry (rd 395)	0417058	5388242	541
KE08-012	Quartzite	Quartzite quarry (rd 395)	0417072	5388191	529
KE08-013	Quartzite	Quartzite quarry (rd 395)	0417064	5388178	523
KE08-014	Pure Ms layer	Quartzite quarry (rd 395)	0417080	5388176	515
KE08-015	Qzt+Ms layer	Quartzite quarry (rd 395)	0417096	5388177	511
KE08-016	Pure Ms layer	Quartzite quarry (rd 395)	0417096	5388177	511
KE08-017	Quartzite	Quartzite quarry (rd 395)	0417488	5387422	427
KE08-018	Myl	Matsen Creek Rd	0412833	5400738	856
KE08-019	Felsic layer	Matsen Creek Rd	0412802	5400725	860
KE08-020	Quartzite	Matsen Creek Rd	0412890	5400913	845
KE08-021	Myl	Matsen Creek Rd	0412921	5400917	841
KE08-022	Quartzite	Matsen Creek Rd	0413048	5399464	789
KE08-023	Quartzite	Matsen Creek Rd	0413372	5399409	763
KE08-024	Pegmatite	Matsen Creek Rd	0413372	5399409	763
KE08-025	Qzt	Matsen Creek Rd	0413606	5399113	732
KE08-026	Qzt	Matsen Creek Rd	0414522	5398956	657
KE08-027	Meta-sediment	Matsen Creek Rd	0415816	5398150	523
KE08-028	Quartzite	Matsen Creek Rd	0415795	5398050	514
KE08-029	Meta-sediment	Matsen Creek Rd	0416994	5398402	418
KE08-030	Qz vein+Meta-sediment	Matsen Creek Rd	0417959	5400203	405
KE08-031	Micaschiste	Hall Creek quarry	0400630	5361714	836
KE08-032	Quartzite	Hall Creek quarry	0400611	5361720	824
KE08-033	Quartzite	Hall Creek quarry	0400588	5361643	817
KE08-034	Quartzite	Hall Creek quarry	0400566	5361630	811
KE08-035	Quartzite	Hall Creek quarry	0400566	5361630	811
KE08-036	Quartzite	Hall Creek quarry	0400564	5361628	808
KE08-037	Micaschiste	Hall Creek quarry	0400556	5361631	807 ?
KE08-038	Pegmatite	Hall Creek quarry	0400556	5361631	807 ?
KE08-039	Qzt+Ms	Hall Creek quarry	0400556	5361631	807 ?
KE08-040	Quartzite	Hall Creek quarry	0400556	5361631	807 ?
KE08-041	Micaschiste	Hall Creek quarry			

Table VI.4: List of samples from the KSZ.

Sample	Description	Localities	UTM (11N)	WGS84	Elevation
			(m)	(m)	(m)
KE08-042	Quartzite	Hall Creek quarry	0400559	5361624	806 ?
KE08-043	Quartzite	Hall Creek quarry	0400517	5361608	790
KE08-044	Quartzite	Hall Creek quarry	0400517	5361608	790
KE08-045	Quartzite	Hall Creek quarry	0400489	5361572	771
KE08-046	Quartzite	Hall Creek quarry	0400511	5361605	761
KE08-047	Quartzite	Hall Creek quarry	0400505	5361604	755
KE08-048	Quartzite	Hall Creek quarry	0400497	5361598	747
KE08-049	Quartzite	Hall Creek quarry	0400478	5361610	735
KE08-050	Qzt+Ms	Hall Creek quarry	0400478	5361610	735
KE08-051	Micaschiste	Hall Creek quarry	0400464	5361605	733
KE08-052	Quartzite	Hall Creek quarry	0400466	5361593	726
KE09-001	Quartzite	Overlook Dead's man Crk	0409274	5399262	1429
KE09-002	Quartzite	Overlook Dead's man Crk	0409239	5308979	1436
KE09-003	Quartzite	Overlook Dead's man Crk	040739	5397380	1524
KE09-004	Orthogneiss mylonite	Overlook Dead's man Crk	0407011	5397463	1545
KE09-005	Orthogneiss mylonite	Overlook Dead's man Crk	0406938	5397468	1551
KE09-006	Quartzite	Overlook Dead's man Crk	0407023	5397381	1531
KE09-007	Granodiorite	Overlook Dead's man Crk	0413088	5394747	684
KE09-008	Pegmatite	Overlook Dead's man Crk	0413088	5394747	684
KE09-009	Pegmatite	Overlook Dead's man Crk	0417832	5388169	426
KE09-010	Amphibolite	Overlook Dead's man Crk	0417832	5388169	426
KE09-011	Pegmatite	Overlook Dead's man Crk	0417832	5388169	426
KE09-012	Sandstone	Cattle outcrop (5 miles Kamloops	0422889	5395833	533
KE09-013	Calcite vein	Cattle outcrop (5 miles Kamloops	0422889	5395833	533
KE09-014	Micaschiste	Bridge Kamloops Island	0417766	5391988	402
KE09-015	Quartzite	Bridge Kamloops Island	0417766	5391988	402
KE09-016	Mylo mafic	Bridge Kamloops Island	0417694	5391981	401
KE09-017	Qz veins	Bridge Kamloops Island	0417694	5391981	401
KE09-018	Calcite vein	Ricky canyon	0418069	5372919	896
KE09-019	Quartzite	Ricky canyon	0418618	5368800	895
KE09-020	Qz veins	Hw 25 toward Kettle	0414154	5371898	453
KE09-021	Calcite vein	Hw 25 toward Kettle	0414154	5371898	453
KE09-022	Quartzite	Hw 25 toward Kettle	0417790	5379864	413
KE09-023	Orthogneiss mylonite	section Kettle Falls bridge	0416655	5387350	609
KE09-024	Orthogneiss mylonite	section Kettle Falls bridge	0416363	5387339	724
KE09-025	Pegmatite	section Kettle Falls bridge	0416363	5387339	724
KE09-026	Pegmatite	section Kettle Falls bridge	0416363	5387339	724
KE09-027	Pegmatite	section Kettle Falls bridge	0416323	5387289	755
KE09-028	Pegmatite	section Kettle Falls bridge	0416469	5387389	675
KE09-029	Leucocrate vein	section Kettle Falls bridge	0416544	5387435	650

Table VI.4: List of samples from the KSZ.

Sample	Description	Localities	UTM (11N)	WGS84	Elevation
			(m)	(m)	(m)
KE09-030	Orthogneiss mylonite	section Kettle Falls bridge	0416798	5387237	532
KE09-031	Orthogneiss mylonite	section Kettle Falls bridge	0417118	5386971	458
KE09-032	Orthogneiss mylonite	section Kettle Falls bridge	0417033	5386912	450
KE09-033	Pegmatite	section Kettle Falls bridge	0417237	5386852	441
KE09-034	Amphibolite	section Kettle Falls bridge	0417237	5386852	441
KE09-035	Schiste	Road above Hall Crk	0399861	5363942	1145
KE09-036	Qz veins	Road above Hall Crk	0399861	5363942	1145
KE09-037	Quartzite	Road above Hall Crk	0399341	5363553	1142
KE09-038	Micaschiste	Road above Hall Crk	0399341	5363553	1142
KE09-039	Quartzite	Road above Hall Crk	0399565	5363051	954
KE09-040	Pegmatite	Road above Hall Crk	0395672	5365930	770
KE09-041	Pegmatite	Road above Hall Crk	0395959	5367708	951
KE09-042	Quartzite	Road above Hall Crk	0395959	5367708	951
KE09-043	Amphibolite	Road above Hall Crk	0395959	5367708	951
KE09-044	Pegmatite	Road above Hall Crk	0396118	5368040	1095
KE09-045	Orthogneiss mylonite	Road above Hall Crk	0396118	5368040	1095
KE09-046	Micaschiste	Road above Hall Crk	0396118	5368040	1095
KE09-047	Quartzite	Road above Hall Crk	0396358	5368375	1172
KE09-048	Pegmatite	Road above Hall Crk	0396358	5368375	1172
KE09-049	Quartzite	Road above Hall Crk	0397601	5368654	1354
KE09-050	Pegmatite	Road above Hall Crk	0397601	5368654	1354
KE09-051	Micaschiste	Road above Hall Crk	0397573	5368448	1380
KE09-052	Quartzite	Road above Hall Crk	0397573	5368448	1380
KE09-053	Pegmatite	Road above Hall Crk	0397875	5368007	1439
KE09-054	Orthogneiss mylonite	Road above Hall Crk	0398136	5367548	1490
KE09-055	Chlorite layer	Road above Hall Crk	0398091	5367903	1451
KE09-056	Quartzite	Little White Mtn	0397736	5367255	1552
KE09-057	Quartzite	Little White Mtn	0397536	5367269	1500
KE09-058	Quartzite	Little White Mtn	0397359	5367222	1443
KE09-059	Quartzite	Hall Crk / Little White Mtn	0399160	5363208	1128
KE09-060	Quartzite	Hall Crk / Little White Mtn	0399190	5363168	1108
KE09-061	Quartzite	Hall Crk / Little White Mtn	0399248	5363116	1078
KE09-062	Quartzite	Hall Crk / Little White Mtn	0399290	5363108	1058
KE09-063	Quartzite	Hall Crk / Little White Mtn	0399355	5363136	1034
KE09-064	Quartzite	Hall Crk / Little White Mtn	0399454	5363143	1002
KE09-065	Quartzite	Hall Crk / Little White Mtn	0399506	5363102	980
KE09-066	Quartzite	Hall Crk / Little White Mtn	0399527	5363051	954
KE09-067	Quartzite	Hall Crk / Little White Mtn	0399557	5362998	933
KE09-068	Quartzite	Hall Crk / Little White Mtn	0399578	5362971	906
KE09-069	Quartzite	Hall Crk / Little White Mtn	0399596	5362899	881
KE09-070	Quartzite	Hall Crk / Little White Mtn	0399585	5362850	840
KE09-071	Micaschiste	Hall Crk / Little White Mtn	0399619	5362788	813

Table VI.4: List of samples from the KSZ.

Sample	Description	Localities	UTM (11N)	WGS84	Elevation
			(m)	(m)	(m)
KE09-072	Quartzite	Hall Crk / Little White Mtn	0399677	5362625	767
KE09-073	Qtz+Micaschiste	Hall Crk / Little White Mtn	0398994	5362409	721
KE09-074	Mylo Qtz	Hall Crk / Little White Mtn	0398994	5362409	721
KE09-075	Leucogranite	Hall Crk / Little White Mtn	0398994	5362409	721
KE09-076	Mudstone		0403488	5360554	618
KE09-077	Sandstone		0403488	5360554	618
KE09-078	Breccia		0401725	5361952	1055
KE09-079	Breccia		0401197	5362470	1021
KE10-001	Qz vein cross-cutting S1	Hall Creek	0400466	5361593	
KE10-002	Quartzite	Hall Creek	0400519	5361603	774
KE10-003	Qz vein cross-cutting S1	Hall Creek	0400511	5361596	686
KE10-004	Qz vein in pegmatite	Hall Creek	0400511	5361596	686
KE10-005	Qz vein in Qtz	Hall Creek	0400556	5361552	795
KE10-006A	Quartzite proto-myl.	Hall Creek	0400556	5361552	795
KE10-006B	Folded Micaschiste	Hall Creek	0400556	5361552	795
KE10-007	Quartzite proto-myl.	Hall Creek	0400616	5361678	834
KE10-008	Quartzite proto-myl.	Hall Creek	0400636	5361696	842
KE10-009	Qz vein transposed	Hall Creek	0400647	5361724	846
KE10-010	Quartzite	Hall Creek	0400438	5361439	660
KE10-011	Phyllonite	Hall Creek (base of the section)	0399242	5362312	740
KE10-012	Silicified Pegmatite	Hall Creek (base of the section)	0399162	5362360	732
KE10-013	"Fresh" aplite	Hall Creek (base of the section)	0399162	5362360	732
KE10-014	Fresh pegmatite	Hall Creek (base of the section)	0399033	5362414	719
KE10-015	Crushed peg. Or aplite (???)	Hall Creek (base of the section)	0399033	5362414	719
KE10-016	Qz vein parrallel	Hall Creek (base of the section)	0399033	5362414	719
KE10-017	Cataclasite	Hall Creek (base of the section)	0399598	5362808	811
KE10-018	Qz vein +/- cataclased	Hall Creek (base of the section)	0399598	5362808	811
KE10-019	Qz vein cross-cutting S1	Hall Creek (Hanging wall ?)	0401556	5362013	1042
KE10-020	Silicified "blue rock"	Hall Creek (Hanging wall ?)	0401556	5362013	1042
KE10-021	Silicified rock+ mineralistation	Hall Creek (Hanging wall ?)	0401556	5362013	1042
KE10-022	Breccia	Hall Creek (Hanging wall ?)	0401556	5362013	1042
KE10-023	Structural plan silicified	Hall Creek (Hanging wall ?)	0401633	5362031	1061
KE10-023	Amphibolite	Hwy 395 and KF bridge	0415359	5382495	532
KE10-024	Pegmatite	Hwy 395 and KF bridge	0415359	5382495	532
KE10-025	Orthogneiss	Hwy 395 and KF bridge	0415359	5382495	532
KE10-026	amphibolite with Chl+Py	Hwy 395 and KF bridge	0415359	5382495	532
KE10-027	Cataclasite (Hz pipe)	Matsen crk rd	0415795	5398050	514

Table VI.4: List of samples from the KSZ.

Sample	Description	Localities	UTM (11N)	WGS84	Elevation
			(m)	(m)	(m)
KE10-028A	Cataclasite (Vt pipe)	Matsen crk rd	0415795	5398050	514
KE10-028B	Cataclasite (Vt pipe)	Matsen crk rd	0415795	5398050	514
KE10-029	Silicified unit+hydrothermalism	Matsen crk rd	0415795	5398050	514
KE10-030	Silicified unit+hydrothermalism	Matsen crk rd	0415795	5398050	514
KE10-031	Silicified migmatite -> Qzt	Matsen crk rd	0412583	5401953	849
KE10-032	Silicified Marble (?)	Matsen crk rd	0412625	5404583	790

